



TECHNICAL REPORT 01-03

Contaminant Transport in Fracture Networks with Heterogeneous Rock Matrices: The PICNIC Code

February 2001

W. Barten
P.C. Robinson

TECHNICAL REPORT 01-03

Contaminant Transport in Fracture Networks with Heterogeneous Rock Matrices: The PICNIC Code

February 2001

W. Barten ¹⁾
P.C. Robinson ²⁾

¹⁾ PSI, Würenlingen and Villigen

²⁾ QuantiSci Limited, Henley-on-Thames, UK
present adress: Quintessa Limited, Henley-on-Thames, UK

This report was prepared on behalf of Nagra. The viewpoints presented and conclusions reached are those of the author(s) and do not necessarily represent those of Nagra.

PREFACE

The Laboratory for Waste Management at the Paul Scherrer Institut is performing work to develop and test models as well as to acquire specific data relevant to performance assessments of planned Swiss nuclear waste repositories. These investigations are undertaken in close co-operation with, and with the financial support of, the National Co-operative for the Disposal of Radioactive Waste (Nagra). The present report is issued simultaneously as a PSI-Bericht and a Nagra Technical Report.

ISSN 1015-2636

"Copyright © 2001 by Nagra, Wettingen (Switzerland) / All rights reserved.

All parts of this work are protected by copyright. Any utilisation outwith the remit of the copyright law is unlawful and liable to prosecution. This applies in particular to translations, storage and processing in electronic systems and programs, microfilms, reproductions, etc."

Abstract

In the context of safety assessment of radioactive waste repositories, complex radionuclide transport models covering key safety-relevant processes play a major role. In recent Swiss safety assessments, such as Kristallin-I, an important drawback was the limitation in geosphere modelling capability to account for geosphere heterogeneities. In marked contrast to this limitation in modelling capabilities, great effort has been put into investigating the heterogeneity of the geosphere as it impacts on hydrology. Structural geological methods have been used to look at the geometry of the flowpaths on a small scale and the diffusion and sorption properties of different rock materials have been investigated. This huge amount of information could however be only partially applied in geosphere transport modelling.

To make use of these investigations the “PICNIC project” was established as a joint cooperation of PSI/Nagra and QuantiSci to provide a new geosphere transport model for Swiss safety assessment of radioactive waste repositories. The new transport code, PICNIC, can treat all processes considered in the older geosphere model RANCHMD generally used in the Kristallin-I study and, in addition, explicitly accounts for the heterogeneity of the geosphere on different spatial scales.

The effects and transport phenomena that can be accounted for by PICNIC are a combination of (advective) macro-dispersion due to transport in a network of conduits (legs), micro-dispersion in single legs, one-dimensional or two-dimensional matrix diffusion into a wide range of homogeneous and heterogeneous rock matrix geometries, linear sorption of nuclides in the flowpath and the rock matrix and radioactive decay and ingrowth in the case of nuclide chains. Analytical and numerical Laplace transformation methods are integrated in a newly developed hierarchical linear response concept to efficiently account for the transport mechanisms considered which typically act on extremely different timescales. To account for one-dimensional matrix diffusion into homogeneous planar or cylindrical rock layers, analytical relations in the Laplace domain are used. To deal with one-dimensional or two-dimensional matrix diffusion into heterogeneous rock matrices, a finite-element method is embedded. The capability of the code for handling two-dimensional matrix diffusion is - to our knowledge - unique in fracture network modelling.

To ensure the reliability of the code, which merges methods from graph theory, Laplace transformation, finite-element methods, analytical and algebraic transformations and a convolution to calculate complex radionuclide transport processes over a large and diverse application range, implementation of the code and careful verification have been alternated for iterative improvement and especially the elimination of bugs. The internal mathematical structure of PICNIC forms the basis of the verification strategy.

The code is verified in a series of seven steps with increasing complexity of the rock matrix. Calculations for single nuclides and nuclide decay chains are carefully tested and analysed for radionuclide transport in single legs, in pathways and in networks. Different sources and boundary conditions are considered. Quantitative estimates of the accuracy of the code are derived from comparisons with analytical solutions, cross-comparisons with other codes and different types of self-consistency tests, including extended testing of different refinements of the embedded finite-element method for different rock matrix geometries. The geosphere barrier efficiency is a good single indicator of the code accuracy. Application ranges with reduced accuracy of the code are also considered.

For one-dimensional matrix diffusion into homogeneous and heterogeneous rock matrices, cross-

comparisons with other codes are performed. For two-dimensional matrix diffusion, however, no code for cross-comparison is available. Consequently, the verification for these geometries relies chiefly on the verification for one-dimensional matrix diffusion, on qualitative estimates and on different self-consistency tests. The steady-state release for a single nuclide is additionally verified quantitatively.

PICNIC has been verified as far as possible at present to allow application with confidence in performance assessment and in modelling of transport experiments. It is shown that structural geological information on small-scale heterogeneity can be entered easily into PICNIC. It is explained, e.g. that considering two-dimensional matrix diffusion into the layer of altered wallrock adjacent to open channels in the cataclastic zone can strongly increase the performance of the geosphere for migrating radionuclides, depending however on the properties of the nuclides and the rock. Considering the effects of matrix diffusion into a second rock layer can also be highly beneficial.

Zusammenfassung

Im Zusammenhang mit der Beurteilung der Langzeitsicherheit von Endlagern für radioaktive Abfälle spielen komplexe Modelle, die die wichtigsten Effekte des Radionuklidtransports einschliessen, eine bedeutende Rolle. In den jüngsten schweizerischen Sicherheitsanalysen wie zum Beispiel Kristallin-I war die eingeschränkte Möglichkeit, die Heterogenität der Geosphäre zu berücksichtigen, ein wichtiger Nachteil. Im scharfen Gegensatz zu diesen Einschränkungen bei den Möglichkeiten der Transportmodellierung, wurde die Heterogenität der Geosphäre mit grossem Aufwand untersucht. So wurde der Einfluss der Heterogenität der Geosphäre auf die Hydrologie erforscht. Mit strukturgeologischen Methoden wurde die Geometrie der Fliesspfade analysiert, und Diffusions- und Sorptionseigenschaften der unterschiedlichen Gesteinstypen wurden erforscht. Von dieser umfangreichen Wissensbasis konnte jedoch nur ein kleiner Teil für die Transportmodellierung verwendet werden.

Um die Ergebnisse solcher aufwendigen Untersuchungen zukünftig nutzen zu können, wurde das "PICNIC Projekt" als eine Zusammenarbeit von PSI/Nagra und QuantiSci begründet, um ein neues Geosphären-Transportmodell für schweizerische Sicherheitsanalysen für Endlager radioaktiver Abfälle zu schaffen. Der neue Transport-Code PICNIC kann alle Prozesse behandeln, die im älteren Geosphären-Transportmodell RANCHMD betrachtet wurden, das als Hauptwerkzeug für den Geosphären-Transport in der Kristallin-I Studie eingesetzt wurde. Darüber hinaus berücksichtigt PICNIC ausdrücklich die Heterogenität der Geosphäre auf verschiedenen räumlichen Skalen.

PICNIC umfasst die folgenden Transportphänomene und Effekte: (advective) Makro-Dispersion auf Grund des Transports der Nuklide in einem Netzwerk von wasserführenden Spalten (Teilstrecken); Mikro-Dispersion in den einzelnen Teilstrecken; Matrixdiffusion in verschiedenen homogenen und heterogenen Gesteinsmatrix-Geometrien; lineare Sorption im Bereich des fliessenden Wassers und in der Gesteinsmatrix sowie radioaktiver Zerfall und Aufbau von Nuklidketten. Um die verschiedenen Transportmechanismen effizient zu berücksichtigen, die typischerweise auf extrem unterschiedlichen Zeitskalen wirken, sind analytische und numerische Methoden der Laplacetransformation in einem dafür entwickelten hierarchischen Linearen Responsmodell integriert. Die eindimensionale Matrixdiffusion in homogene Gesteinsschichten mit ebener oder zylindrischer Geometrie wird im Laplaceraum analytisch behandelt. Für eindimensionale oder zweidimensionale Diffusion in eine heterogene Gesteinsmatrix wird eine Finite-Elemente Methode benutzt. Die Fähigkeit von PICNIC, zweidimensionale Matrixdiffusion zu berücksichtigen, ist - unseres Wissens nach - zur Zeit einzigartig für ein Klufnetzwerkmodell.

PICNIC verbindet Methoden aus der Graphentheorie, der Laplacetransformation, Finite-Elemente Methoden, analytische und algebraische Transformationen und die Berechnung von Faltungsintegralen, um komplexen Radionuklidtransport in einem weiten und vielfältigen Anwendungsbereich zu berechnen. Um die Verlässlichkeit des Codes zu gewährleisten, wurde der Code abwechselnd entwickelt und verifiziert. Dadurch wurde der Code iterativ verbessert, insbesondere wurden vorhandene Fehler sukzessive beseitigt. Das Vorgehen bei der Verifikation basiert auf der inneren mathematischen Struktur von PICNIC.

Der Code wird in sieben Hauptschritten mit wachsender Komplexität der Gesteinsmatrix verifiziert. Der Transport von Einzelnukliden und auch von Nuklidketten wird analysiert, sowohl für Teilstrecken, für ganze Transportwege als auch für Netzwerke. Der Effekt von verschiedenen Nuklidquellen und Randbedingungen wird untersucht. Die Genauigkeit des Codes wird abgeschätzt mit Hilfe von analytischen Lösungen, soweit möglich über Quervergleiche mit anderen Rechen-

Codes sowie mittels verschiedenen Selbstkonsistenztests und ausgedehnten Tests mit verschiedenen Diskretisierungen der Finiten-Elemente Gitter für die unterschiedlichen Gesteinsmatrixgeometrien. Dabei hat sich die sogenannte Geosphären-Barriereneffizienz als ein gutes Mass für die Rechengenauigkeit des Codes herausgestellt. Anwendungsbereiche des Codes mit reduzierter Rechengenauigkeit werden aufgezeigt.

Für den Fall von eindimensionaler Matrixdiffusion in homogene und auch in heterogene Gesteinsmatrizen werden Quervergleiche mit anderen Codes gemacht. Für zweidimensionale Matrixdiffusion ist jedoch kein Code für Quervergleiche vorhanden. Deshalb baut die Verifikation für diese Art von Gesteinsmatrix auf der Verifikation für eindimensionale Matrixdiffusion auf, sowie auf qualitativen Abschätzungen und auf verschiedenen Selbstkonsistenztests. Zusätzlich wird der Spezialfall des stationären Nuklidtransports quantitativ verifiziert.

PICNIC wurde so weit als zur Zeit möglich verifiziert und kann vertrauensvoll für die Geosphären-Transportmodellierung im Zusammenhang mit Sicherheitsanalysen und für die Modellierung von Transportexperimenten verwendet werden. Darüber hinaus wird gezeigt, dass Informationen aus der Strukturgeologie, zum Beispiel über die kleinräumige Heterogenität von kataklastischen Scherzonen einfach bei PICNIC-Rechnungen berücksichtigt werden können. So wird beispielsweise aufgezeigt, dass die Berücksichtigung von zweidimensionaler Diffusion in eine alterierte Zone bei offenen Kanälen die Wirksamkeit der Geosphäre als Transportbarriere für mobile Radionuklide stark verbessern kann; dies ist aber abhängig von den Eigenschaften der betreffenden Nuklide und des Gesteins. Die Auswirkungen von Matrixdiffusion in eine zweite Gesteinszone können ebenfalls hochwillkommen sein.

Résumé

Dans le contexte de l'évaluation de sûreté, les modèles complexes de transport de radionucléides jouent un rôle déterminant. Dans les exercices d'évaluation de sûreté menés récemment en Suisse, comme par exemple Kristallin-I, une limitation importante résidait dans la capacité réduite à prendre en compte les hétérogénéités au sein de la géosphère. Contrastant de façon marquante avec les limitations existant au niveau de la capacité de modélisation, un effort important a été consacré à l'étude des hétérogénéités de la géosphère. Ainsi, on a mené des investigations quant à l'impact de l'hétérogénéité de la géosphère sur les régimes d'écoulement. Des méthodes géologiques structurales ont été mises au point pour observer la géométrie des chemins privilégiés d'écoulement à petite échelle et les propriétés diffusives et sorptives des différentes roches ont été étudiées. Néanmoins, seule une part réduite des informations obtenues ont pu être intégrées dans la modélisation du transport dans la géosphère.

Le projet PICNIC a été construit sur la base d'une coopération PSI/Cédra et QuantiSci, avec pour objectif de doter l'évaluation de sûreté des stockages de déchets radioactifs en Suisse d'un nouveau modèle de transport dans la géosphère intégrant les résultats des investigations. Le nouveau code de transport PICNIC est à même de traiter tous les phénomènes pris en compte par le modèle précédent RANCHMD, utilisé dans l'étude Kristallin-I. Il traite de plus explicitement l'hétérogénéité de la géosphère pour différentes échelles spatiales.

Les phénomènes de transport suivants sont pris en compte par PICNIC: macro dispersion résultant du transport convectif de nucléides dans un réseau de chemins d'écoulement privilégiés (tubes); micro dispersion dans les tubes unitaires; diffusion matricielle 1D ou 2D dans une large gamme de géométrie de blocs matriciels correspondant à des milieux homogènes ou hétérogènes; adsorption linéaire de nucléides le long des chemins privilégiés d'écoulement; décroissance radioactive et filiation. Des méthodes de transformées de Laplace tant analytiques que numériques sont intégrées dans un concept linéaire hiérarchique afin de rendre compte de façon efficace des mécanismes de transport considérés et qui impliquent typiquement des échelles temporelles très différentes. La diffusion matricielle 1D dans des couches géologiques de géométries planes ou cylindriques est traitée par transformée de Laplace analytique. Pour rendre compte de diffusion matricielle dans des blocs matriciels 1D ou 2D hétérogènes, une méthode aux éléments finis est implémentée. La possibilité offerte par le code PICNIC de prendre en compte une diffusion matricielle 2D est à notre connaissance unique dans le domaine de la modélisation en réseau de fractures.

PICNIC rassemble des méthodes issues de la théorie des graphes, la transformée de Laplace, les éléments finis, des transformations analytiques et algébriques, des convolutions, afin de modéliser le transport complexe de radionucléides pour un champ d'application large. Afin de vérifier les performances du code, on a fait alterner les phases de développement et de validation. Par cette démarche, le code a été amélioré de façon itérative et en particulier les erreurs ont pu être progressivement écartées. La démarche suivie dans les phases de vérification s'appuie sur la structure mathématique interne de PICNIC.

Le code est validé en sept étapes avec des niveaux de complexité croissants. Le transport de nucléides ainsi que de chaînes de nucléides est analysé tant pour les tubes que pour les chemins de transport et les réseaux. Les effets de différents types de sources et de conditions aux limites sont étudiés. La précision du code est estimée en faisant appel à des solutions analytiques, par des comparaisons croisées avec d'autres codes de calcul et par des tests de consistance interne incluant un raffinement de la discrétisation adoptée pour la méthode des éléments finis dans le cas des blocs

matriciels hétérogènes. Il est apparu que la capacité de rétention de la géosphère est un bon critère pour la précision du code. On signale les domaines d'application du code correspondant à une précision inférieure du code.

Pour les cas incluant une diffusion matricielle 1D dans des milieux homogènes et hétérogènes, des comparaisons croisées avec d'autres codes sont menées. Pour une diffusion matricielle 2D, il n'y a par contre pas de code disponible. C'est pourquoi les vérifications pour ce type de blocs matriciels reposent sur des analyses menées pour des blocs 1D ainsi que des estimations qualitatives et des tests de consistance interne. En complément, le cas permanent du transport de radionucléides est validé de façon quantitative.

PICNIC a été validé autant qu'il est possible de le faire à ce jour et peut en conséquence être utilisé avec confiance pour la modélisation du transport dans la géosphère dans le cadre d'analyses de sûreté et pour la modélisation d'expériences de transport de radioéléments. Il est montré que PICNIC peut prendre facilement en compte une information d'hétérogénéité structurelle géologique à petite échelle (par exemple au niveau des failles cataclastiques). On a ainsi pu montrer que la prise en compte de diffusion matricielle 2D dans les zones altérées accroît de façon significative les capacités de rétention de la géosphère; ce résultat générique est bien sûr à moduler en fonction des propriétés du milieu poreux ainsi que du radionucléide concerné. Il peut être profitable de considérer la diffusion dans un bloc matriciel hétérogène incluant une zone de diffusion supplémentaire.

Riassunto

Nell' ambito delle analisi di sicurezza per il confinamento di scorie radioattive, modelli complessi descriventi il trasporto di radionuclidi e tenenti conto di processi rilevanti per la sicurezza hanno un ruolo importante. Nelle più recenti analisi di sicurezza, quali "Kristallin I", un serio limite di tali modelli era l' impossibilità di tener conto dell' eterogeneità della geosfera. In stridente contrasto con tali limiti nei modelli sta il grande lavoro di ricerca sull' impatto delle eterogeneità geosferiche sull' idrologia. Metodi di geologia strutturale sono stati usati al fine di determinare, su piccola scala, la geometria delle traiettorie idrologiche, come pure le proprietà diffusive e di assorbimento delle varie rocce investigate. Questo grande volume di informazioni non ha potuto tuttavia venir utilizzato che in misura parziale nei modelli di trasporto attraverso la geosfera.

Il progetto "PICNIC" è stato iniziato in cooperazione tra PSI/Cisra e QuantiSci al fine di ottenere un nuovo modello di trasporto nella geosfera atto all' analisi di sicurezza per depositi di scorie radioattive e in grado di utilizzare i dati provenienti dalle ricerche summenzionate. Il nuovo programma di trasporto PICNIC può trattare tutti i processi considerati in RANCHMD, il modello usato precedentemente per la geosfera nell' analisi di sicurezza Kristallin-I, ed inoltre può tener conto in modo esplicito dell' eterogeneità della geosfera su varie scale di dimensioni spaziali.

Gli effetti e i fenomeni di trasporto che vengono considerati in PICNIC sono, in combinazione: la macro-dispersione (avvettiva), dovuta al trasporto in una rete di traiettorie (segmenti), della diffusione in matrice uni- o bidimensionale in una grande varietà di geometrie della matrice rocciosa, l' assorbimento lineare di nuclidi lungo la traiettoria e nella matrice rocciosa, il decadimento radioattivo e, nel caso di catene di nuclidi, la produzione di nuclidi. Metodi per trasformazioni di Laplace di tipo analitico e numerico sono stati integrati in un nuovo concetto gerarchico di risposta lineare, al fine di poter considerare in modo efficiente dei meccanismi di trasporto agenti su scale temporali differenti. Per tener conto della diffusione unidimensionale nella matrice in formazioni rocciose a geometria planare o cilindrica sono state applicate relazioni analitiche nello spazio di Laplace. Per risolvere problemi di diffusione uni- o bidimensionale in matrici eterogenee, è stato incluso un metodo di elementi finiti. La capacità del programma di calcolare la diffusione in matrice in due dimensioni è, a nostra conoscenza, unica nel campo della modellizzazione di sistemi di fratture.

Per garantire l' affidabilità del programma, che unisce metodi provenienti dalla teoria dei grafici, trasformazioni di Laplace, metodi di elementi finiti, trasformazioni analitiche ed algebriche, e una convoluzione per calcolare il trasporto complesso dei radionuclidi in un grande e svariato campo di applicazioni, esso è stato implementato e verificato attraverso una procedura iterativa di miglioramento ed eliminazione degli errori di programmazione. La struttura matematica interna di PICNIC funge da base per una strategia di verifica del programma di calcolo.

Il programma è stato verificato in una serie di sette passi comprendenti matrici rocciose progressivamente più complesse. Calcoli per nuclidi singoli e catene di nuclidi sono verificati ed analizzati con cura in relazione al trasporto in singoli segmenti, in traiettorie idrologiche e in sistemi di traiettorie, considerando diversi luoghi di iniezione e condizioni limite. Stime quantitative sulla precisione del programma sono state derivate per mezzo di un confronto con soluzioni analitiche, e si sono fatti confronti per quanto possibile con altri programmi come pure test di compatibilità intrinseca, comprendenti prove su vari affinamenti del metodo ad elementi finiti per varie geometrie della matrice rocciosa. In tale contesto l' efficienza della barriera geosferica si è rivelata un buon indicatore della precisione del programma. Domini di applicazione ove la precisione è ridotta sono

stati identificati.

Nel caso della diffusione unidimensionale in matrici sia omogenee che eterogenee sono stati effettuati dei confronti con altri programmi. Poichè non esistono altri programmi descriventi la diffusione bidimensionale nella matrice idonei per un confronto, la verifica si basa in questo caso sulla diffusione unidimensionale, su stime qualitative ed altri tests di compatibilità intrinseca. Inoltre il rilascio di nuclidi singoli è stato verificato quantitativamente in condizioni stazionarie.

PICNIC è stato verificato nei limiti attualmente possibili e può quindi venir applicato in modo affidabile nelle analisi di sicurezza e nella modellizzazione di esperimenti sul trasporto. Si dimostra che con PICNIC si possono utilizzare agevolmente dati di geologia strutturale quantificanti le eterogeneità su piccola scala. E' stato chiarito, per esempio, che l'efficienza della geosfera nel limitare il rilascio di radionuclidi migliora notevolmente se si considera la diffusione bidimensionale nello strato di roccia alterata adiacente a condotti aperti, all' interno di zone cataclastiche. Questo effetto tuttavia dipende dalle proprietà dei nuclidi e della roccia. Simili effetti benefici si ottengono anche quando si considera la diffusione nella matrice di un secondo strato di roccia.

TABLE OF CONTENTS

1. INTRODUCTION.....	1
2. THE SYSTEM.....	8
2.1. WATER AND NUCLIDE BALANCE ON THE SCALE OF THE NETWORK.....	8
2.1.1. <i>Definitions</i>	8
2.1.2. <i>Water Balance</i>	10
2.1.3. <i>Nuclide Balance</i>	10
2.1.4. <i>Pathways and Tree</i>	12
2.1.5. <i>Laplace Transformed Source Terms</i>	14
2.1.6. <i>Source Terms in the Time Domain</i>	15
2.1.7. <i>Geosphere Barrier Efficiency</i>	16
2.2. WATER AND NUCLIDE BALANCE ON THE SCALE OF A LEG.....	18
2.2.1. <i>Water Balance</i>	18
2.2.2. <i>Nuclide Balance</i>	19
2.2.3. <i>Interface with the Rock Matrix</i>	21
2.2.4. <i>Initial Conditions</i>	23
2.2.5. <i>Boundary Conditions</i>	24
2.3. TRANSPORT OF A SINGLE NUCLIDE IN A LEG.....	25
2.3.1. <i>Balance Equations</i>	25
2.3.2. <i>Limit of Infinite Peclet Number</i>	26
2.3.3. <i>General Solution for a Finite Peclet Number</i>	27
2.3.4. <i>At-Infinity Boundary Condition</i>	28
2.3.5. <i>Zero-Concentration Boundary Condition</i>	28
2.3.6. <i>Zero-Gradient Boundary Condition</i>	29
2.4. TRANSPORT IN THE ROCK MATRIX.....	30
2.4.1. <i>Balance Equations</i>	30
2.4.2. <i>Boundary Conditions</i>	33
2.4.3. <i>Determination of the Rock Matrix Response</i>	34
2.5. EXAMPLES OF ROCK MATRIX GEOMETRIES.....	36
2.5.1. <i>One-Dimensional Planar Rock Matrix</i>	36
2.5.2. <i>Single Nuclide in a One-Dimensional Planar Rock Matrix</i>	39
2.5.3. <i>Unlimited and Strongly Limited Rock Matrix Diffusion and the Limit of an Infinite Peclet Number for a Single Nuclide</i>	44
2.5.4. <i>Single Nuclide in a One-Dimensional Two-Layer Planar Rock Matrix</i>	46
2.5.5. <i>One-Dimensional Cylindrical Rock Matrix</i>	50
2.6. LINEAR SORPTION.....	53
2.6.1. <i>Retardation Constant in the Rock Matrix</i>	53
2.6.2. <i>Retardation Constant in the Area of Flowing Water</i>	53
2.7. LAPLACE TRANSFORM INVERSION.....	56
2.7.1. <i>Talbot's Algorithm</i>	56
2.7.2. <i>Cut-off Times</i>	57
2.7.3. <i>Peak Values</i>	58
2.8. STRUCTURE OF THE INPUT FILE.....	59
3. STRUCTURE AND VERIFICATION STRATEGY OF PICNIC.....	62
3.1. PICNIC FLOW SCHEME.....	62
3.1.1. <i>Analytical Rock Matrix Response and Time-Dependent Source</i>	62
3.1.2. <i>Analytical Source in the Laplace Domain</i>	66
3.1.3. <i>Nuclide Decay Chains</i>	66
3.1.4. <i>Condensed Flow Scheme</i>	67
3.2. POSSIBLE ERRORS.....	68
3.3. APPLICATION RANGE OF PICNIC TO BE VERIFIED.....	70
3.4. VERIFICATION STRATEGY.....	72
3.4.1. <i>Homogeneous One-Dimensional Planar Rock Matrix</i>	74
3.4.2. <i>Homogeneous Cylindrical Rock Matrix</i>	77
3.4.3. <i>Using the Embedded Finite-Element Method to Approximate Matrix Diffusion into a Homogeneous One-</i>	

<i>Dimensional Planar Rock Matrix</i>	78
3.4.4. <i>Two-Layer One-Dimensional Planar Rock Matrix</i>	81
3.4.5. <i>One-Dimensional Matrix Diffusion into Heterogeneous Geometries</i>	82
3.4.6. <i>Homogeneous Two-Dimensional Planar Rock Matrix</i>	84
3.4.7. <i>Two-Dimensional Matrix Diffusion into Heterogeneous Geometries</i>	86
4. HOMOGENEOUS ONE-DIMENSIONAL PLANAR ROCK MATRIX	88
4.1. SINGLE NUCLIDES IN A SINGLE LEG: GRIMSEL DIPOLE EXPERIMENT	88
4.1.1. <i>Comparison with RANCHMD</i>	88
4.1.2. <i>Comparison with GIMRT</i>	92
4.1.3. <i>Comparison with PAWorks/LTG</i>	95
4.1.4. <i>Peclet Number Dependence and Boundary Conditions</i>	98
4.1.5. <i>Parameter Self-Consistency</i>	103
4.1.6. <i>Self-Consistency Tests of the Network Feature</i>	105
4.1.7. <i>Technical Test: Dependence on Number of Partial Sums in Talbot Series</i>	106
4.1.8. <i>Technical Test: Dependence on Output Times</i>	106
4.2. SINGLE NUCLIDES AND NUCLIDE DECAY CHAINS, SINGLE LEGS AND PATHWAYS: VARIATIONS OF THE GRIMSEL DIPOLE EXPERIMENT	108
4.2.1. <i>Single Nuclide and Nuclide Decay Chain in a Single Leg</i>	108
4.2.2. <i>Single Nuclide and Nuclide Decay Chain in a Pathway</i>	118
4.3. TRANSPORT OF SINGLE NUCLIDES AND A NUCLIDE DECAY CHAIN IN NETWORKS	123
4.3.1. <i>No Rock Matrix</i>	126
4.3.2. <i>Same Rock Matrix in Each Leg</i>	128
4.3.3. <i>Different Rock Matrix in Different Legs: Single Nuclide and Nuclide Decay Chain</i>	130
4.4. CASES RELATED TO PERFORMANCE ASSESSMENT	136
4.4.1. <i>Single Nuclides in a Single Planar Channel</i>	136
4.4.2. <i>Decay Chain in a Single Planar Channel</i>	141
4.4.3. <i>Single Nuclides in a Small Network of Planar Channels</i>	144
4.4.4. <i>INTRACOIN Chain Decay Test Case</i>	152
4.5. SUMMARY.....	154
5. HOMOGENEOUS CYLINDRICAL ROCK MATRIX	157
5.1. VARIATIONS OF THE GRIMSEL DIPOLE EXPERIMENT	157
5.2. CASES RELATED TO PERFORMANCE ASSESSMENT	160
5.2.1. <i>Single Vein</i>	160
5.2.2. <i>Vein Network</i>	164
5.3. SUMMARY.....	168
6. USING THE EMBEDDED FINITE-ELEMENT METHOD TO APPROXIMATE MATRIX DIFFUSION INTO A HOMOGENEOUS ONE-DIMENSIONAL PLANAR ROCK MATRIX	170
6.1. ONE-DIMENSIONAL MATRIX DIFFUSION	171
6.2. WEAKLY TWO-DIMENSIONAL MATRIX DIFFUSION	177
6.3. TEST OF FINITE-ELEMENT MESH REFINEMENT	182
6.4. TEST OF MULTIPLE ROCK MATRIX LAYERS	190
6.5. EXTREMELY SMALL AREAS OF ROCK MATRIX	196
6.6. TRANSPORT IN A NETWORK	203
6.7. SUMMARY.....	210
7. TWO-LAYER ONE-DIMENSIONAL PLANAR ROCK MATRIX	212
7.1. CASES RELATED TO PERFORMANCE ASSESSMENT	213
7.1.1. <i>Geometry of a Cataclastic Zone</i>	213
7.1.2. <i>Release Curves and Geosphere Barrier Efficiency</i>	215
7.1.3. <i>Discretisation Tests with Subdivided Rock Matrix Layers</i>	223
7.1.4. <i>Self-Consistency Test of Network Feature</i>	234
7.1.5. <i>Varying the Porosity of the Second Rock Layer</i>	237
7.2. VARIATIONS OF THE GRIMSEL DIPOLE EXPERIMENT	239
7.2.1. <i>Single Nuclide</i>	239
7.2.2. <i>Nuclide Decay Chain</i>	244
7.3. SUMMARY.....	248

8. ONE-DIMENSIONAL MATRIX DIFFUSION INTO HETEROGENEOUS GEOMETRIES	250
8.1. TWO INDEPENDENT HOMOGENEOUS REGIONS FOR MATRIX DIFFUSION	250
8.2. TWO INDEPENDENT TWO-LAYER REGIONS FOR MATRIX DIFFUSION	259
8.3. TRANSPORT IN A PATHWAY	266
8.3.1. <i>Two Independent Homogeneous Matrix Areas and 3 Legs</i>	266
8.3.2. <i>Two Independent Homogeneous Matrix Areas and 5 Legs</i>	271
8.3.3. <i>Two Independent Two-Layer Matrix Areas and 5 Legs</i>	276
8.4. TRANSPORT IN A NETWORK	281
8.5. SUMMARY	287
9. HOMOGENEOUS TWO-DIMENSIONAL PLANAR ROCK MATRIX	289
9.1. CASES RELATED TO PERFORMANCE ASSESSMENT	291
9.1.1. <i>Release Curves and Geosphere Barrier Efficiency</i>	291
9.1.2. <i>Effect of Mesh Refinement for a Pulse-Like Source</i>	305
9.1.3. <i>Spot-Check for an Even More Refined Mesh</i>	313
9.1.4. <i>Vertically Subdivided Rock Matrix</i>	315
9.2. VARIATIONS OF THE GRIMSEL DIPOLE EXPERIMENT	318
9.2.1. <i>Single Nuclide</i>	318
9.2.2. <i>Nuclide Decay Chain</i>	320
9.2.3. <i>The "Numerical Effect" of Rotating the Rock Matrix</i>	324
9.2.4. <i>The "Numerical Effect" of a Daughter on its Parent</i>	329
9.3. TRANSPORT IN A NETWORK	331
9.4. SUMMARY	336
10. TWO-DIMENSIONAL MATRIX DIFFUSION INTO HETEROGENEOUS GEOMETRIES	339
10.1. TWO-LAYER ROCK MATRIX	339
10.1.1. <i>Single Nuclide</i>	341
10.1.2. <i>Nuclide Decay Chain</i>	343
10.2. ROCK MATRIX WITHIN THE FRACTURE	347
10.2.1. <i>The "Numerical Effect" of Rotating the Rock Matrix</i>	348
10.2.2. <i>The "Numerical Effect" of a Daughter on its Parent</i>	350
10.3. SUMMARY	352
11. CONCLUSIONS AND OUTLOOK	354
11.1. FUNDAMENTALS AND CAPABILITIES OF THE CODE	354
11.2. ANALYTICALLY IMPLEMENTED ONE-DIMENSIONAL MATRIX DIFFUSION	355
11.3. EMBEDDED FINITE-ELEMENT METHOD FOR ONE-DIMENSIONAL MATRIX DIFFUSION INTO A HETEROGENEOUS ROCK MATRIX	355
11.4. EMBEDDED FINITE-ELEMENT METHOD FOR TWO-DIMENSIONAL MATRIX DIFFUSION	356
11.5. REMAINING OPEN QUESTIONS AND RESTRICTIONS	357
11.6. PERFORMANCE ASSESSMENT MODELLING ASPECTS	359
11.7. EXPERIMENT MODELLING ASPECTS	359
11.8. OUTLOOK	359
12. ACKNOWLEDGEMENTS	361
13. NOTATION	362
14. REFERENCES	366

1. Introduction

In the context of safety assessment of radioactive waste repositories, complex radionuclide transport models covering key safety-relevant processes play a major role. This report presents the major aspects of the new Swiss geosphere code PICNIC and discusses in particular the topic of code verification.

In the Swiss safety assessment Kristallin-I [Nagra, 1994] for high-level radioactive waste disposal, a model chain for the near-field, the far-field (or geosphere) and the biosphere was used. However, an important drawback in Kristallin-I was the limitation in geosphere modelling capability to account for large-scale and small-scale geosphere heterogeneities. The geosphere model RANCHMD [Hadermann and Rösel, 1985] used in the Kristallin-I study uses a single flowpath with constant parameters along the flowpath. The small-scale heterogeneity of the water-conducting feature (wcf) is considered in such a way that the area of flowing water is in contact with a homogeneous porous rock matrix available for one-dimensional matrix diffusion. Matrix diffusion is an important retardation mechanism [Foster, 1975; Grisak and Pickens, 1980; Neretnieks, 1980; Tang, Frind and Sudicky, 1981; Nagra, 1994; Hadermann and Heer, 1996; Jakob, 1997; Rasilainen, 1997]. It considers the exchange of nuclides between the water flowing in rock fractures and the stagnant porewater of the surrounding wallrock and the diffusion of the nuclides into the pore space. *Limited matrix diffusion* as considered by RANCHMD assumes that the available rock matrix is finite.

In marked contrast to this limitation in modelling capabilities, the heterogeneity of the geosphere has been investigated with great effort. Considering the hydrology of the geosphere, it has been shown that water flows through a network of fractures or wcf [Nagra, 1994; Thury et al., 1994]. This means that the heterogeneity of the geosphere on a larger scale should also be considered. On the other hand, using structural geological methods, the geometry of the flowpaths is considered on a smaller scale and simplified for performance assessment modelling [Thury et al., 1994; particularly section 10.3]. This shows that water flows in channels through different types of wcf (cataclastic zones, jointed zones, etc.), where the rock matrix adjacent to the channels available for matrix diffusion is heterogeneous and the assumption of one-dimensional matrix diffusion into a homogeneous zone is an oversimplification. For performance assessment purposes the sorption properties [OECD NEA, 1992] of different rock materials involved are also investigated [Stenhouse, 1995]. These investigations of the hydrology, structural geology and sorption properties indicate that the geosphere is heterogeneous on different scales. The heterogeneity of the geosphere could be taken into account for performance assessment modelling. More credit could thus be taken for knowledge of the heterogeneity and over-conservatism in the transport modelling could be reduced. (This holds in particular when the release curves for the homogeneous model and the more detailed model are of strongly different shapes.)

Another example of a Swiss repository project where it could be beneficial to take into account geosphere heterogeneity in transport modelling is the planned repository for low- and intermediate level radioactive waste at the Wellenberg site in the Canton of Nidwalden. At Wellenberg also the water flows through a system of fractures or wcf [Nagra, 1997]. Based on results of structural geological investigations, the flowpaths are heterogeneous on a small scale. Cataclastic zones, discrete shear zones and connected calcareous marl/limestone layers were identified and simplified for performance assessment modelling [Nagra, 1997; especially section 5.7]. For various conditions,

which are relevant from a performance assessment point of view, the sorption properties of the involved rock materials are carefully investigated for different rock porewater chemistries [Bradbury and Baeyens, 1997a; 1997b].

To deal with heterogeneities in the geosphere and to describe transport in heterogeneous fractured rock, a series of fracture network transport models have been developed in the past; see Bear, Tsang and deMarsily [1993] and section 6 in National Research Council [1996] for an overview. One group of models deals with numerical finite-element calculations in the Laplace or time domain, e.g. Sudicky and McLaren [1992], Küpper, Schwartz and Steffler [1995], and Novakowski and Bogan [1999]. These models also consider diffusion into the stagnant porewater of the rock matrix as an important transport process [Nagra, 1994] using a one-dimensional approximation and assuming the available rock matrix to be unlimited. *Unlimited matrix diffusion* is mathematically easier to deal with and is, for some purposes, a good approximation for nuclide diffusion into stagnant rock porewater. But this approach does not take into account the finite extent of the available rock matrix and can give non-conservative results, particularly for long times. The Laplace transformation method (e.g. Hadermann [1980a]; Tang, Frind and Sudicky [1981; Barker [1982]; Sudicky and Frind [1984]; Barker [1985]; Hodgkinson and Maul [1988]; Robinson and Maul [1991]) is widely used and is efficient for solving linear partial differential equations with time-independent parameters.

Another group of models (“channel network models”) describes contaminant transport in a network by considering individual pathways between inflow and outflow positions. These models can, on the one hand, describe transport in large and complex networks, but normally the transport processes considered in the individual fractures of the network are strongly restricted. Typical examples are the network models of Robinson [1984], Cacas et al. [1990], Grindrod et al. [1991], Dverstorp, Andersson and Nordqvist [1992], Herbert and Lanyon [1992], Berkowitz [1994] and Clemo and Smith [1997], which include advection (with some retardation factors) and micro-dispersion in the individual fractures. All these network models account for *macro-dispersion* and *micro-dispersion*. *Macro-dispersion* means that different flowpaths through the network have different advection times, since different fractures or channels in the network have different water flow velocities and different lengths. This concept also includes the effect of retarded advection by *linear sorption* of the nuclides, i.e. nuclides in the water and nuclides sorbed on the rock are in instantaneous and linear chemical equilibrium. *Micro-dispersion* means that, in a channel or fracture, different flowpaths exist with different advection times. All these channel network models calculate nuclide transport through the network by superimposing the transport through different pathways. Consequently, they are restricted to linear processes in the sense of partial differential equations.

More complex transport behaviour in the individual fractures can be handled, but at the cost of long computation times or particularly strong restrictions on the size and complexity of the network. This is done in the channel network model VAPFRAC of Nordqvist et al. [1992, 1996], which considers a two-dimensional transmissivity field in each fracture. To allow for variability of the flowpaths within the fracture planes, this model uses *residence time spectra* of the fractures instead of one single residence time and combines the residence time spectra of the fractures to obtain the residence time spectrum of the network. Such a residence time spectrum can also be regarded as the *linear response function* of the fracture or the network in the time domain [Barten, 1996a]. The linear response theory is well known and is considered in the time domain, Laplace domain or Fourier domain depending on the system considered. Green’s functions and the fluctuation-dissipation theorem [Kubo, 1966] are among the best known examples from physics.

Overall, these models and codes were not able to fulfil the requirement to make efficient use of the knowledge of the heterogeneity of the geosphere in transport modelling. Therefore the PICNIC (PSI/QuantiSci Interactive Code for Networks of Interconnected Channels) project presented in this report was established as a cooperation of Paul Scherrer Institute (PSI)/Nagra and QuantiSci to provide a new geosphere transport model for Swiss safety assessment of radioactive waste repositories. In addition to the long timescales and transport distances considered in performance assessments, PICNIC can also deal with the small scales typical for transport experiments in the laboratory or in the field. For a description of the early concepts, which laid the fundamentals for the present form of the code, see Robinson [1993]; Barten [1994]; Smith and Robinson [1995]; Barten [1995]. PICNIC is a type of channel network model. It can deal with all processes accounted for in the geosphere model RANCHMD used in the Kristallin-I study. In addition, PICNIC explicitly accounts for the heterogeneity of the geosphere on a large scale, considering transport in a network and on a small scale, considering the heterogeneity of the rock matrix available for matrix diffusion. Due to the complex geometry and the different and particularly long timescales for transport, care had to be taken to select the relevant processes and to use efficient mathematical and numerical methods. Therefore the fast and efficient combination of a hierarchical linear response concept with Laplace transformation methods is used. PICNIC has considerable flexibility to deal with multiple source locations and nuclide sources of arbitrary time-dependent form.

PICNIC has been developed in two phases. The first phase [Barten and Robinson, 1996] concentrated on the geosphere heterogeneity on a large scale, dealing with transport in a fracture network, with one-dimensional matrix diffusion into a limited homogeneous planar or cylindrical rock domain being considered, as in the Kristallin-I study. A network in PICNIC is defined by a number of nodes, called junctions, and the directional connections, called legs, between these nodes (Figure 1.1, top). This PICNIC phase has recently been applied in preliminary studies in the context of Swiss performance assessments [Schneider et al., 1996; 1998].

In the current phase now the flexibility of PICNIC to account for the small-scale heterogeneity of the geosphere is considerably increased and PICNIC accounts in more detail for the geometry of the wallrock accessible for matrix diffusion. PICNIC now takes into account one-dimensional and two-dimensional matrix diffusion into a heterogeneous rock matrix [Robinson, 1997a]. In Figure 1.1, bottom, the case of a two-layer rock matrix is shown as an example for two-dimensional matrix diffusion into a heterogeneous rock matrix. First examples of the effect of one-dimensional matrix diffusion into a two-layer rock matrix geometry for cases related to Kristallin-I have recently been presented [Barten, Robinson and Schneider, 1998]. Most recently, first examples of the effect of two-dimensional matrix diffusion into a single-layer rock matrix geometry for cases related to Kristallin-I have been presented [Barten, Robinson and Tirbonod, 2000]. This capability of PICNIC to handle more complicated geometries for matrix diffusion allows use of the detailed structural knowledge mentioned above that is available from rock characterisation work.

The main strengths of the very efficient and fast code are the flexibility to account for the large-scale heterogeneity of the flowpaths (network effects) and the small-scale heterogeneity (variability and geometry of the rock available for matrix diffusion). It is also very useful for safety assessment that PICNIC can account for decay of nuclide chains. This is one of the key features of PICNIC. Additionally, PICNIC can deal with branching and recombining nuclide chains. This is not considered explicitly in this report, but could be of some use in special applications. The main weaknesses of PICNIC are that it cannot account for nonlinear effects, such as nonlinear sorption, and it cannot account for time-dependent parameters, such as water flow rate or porosity.

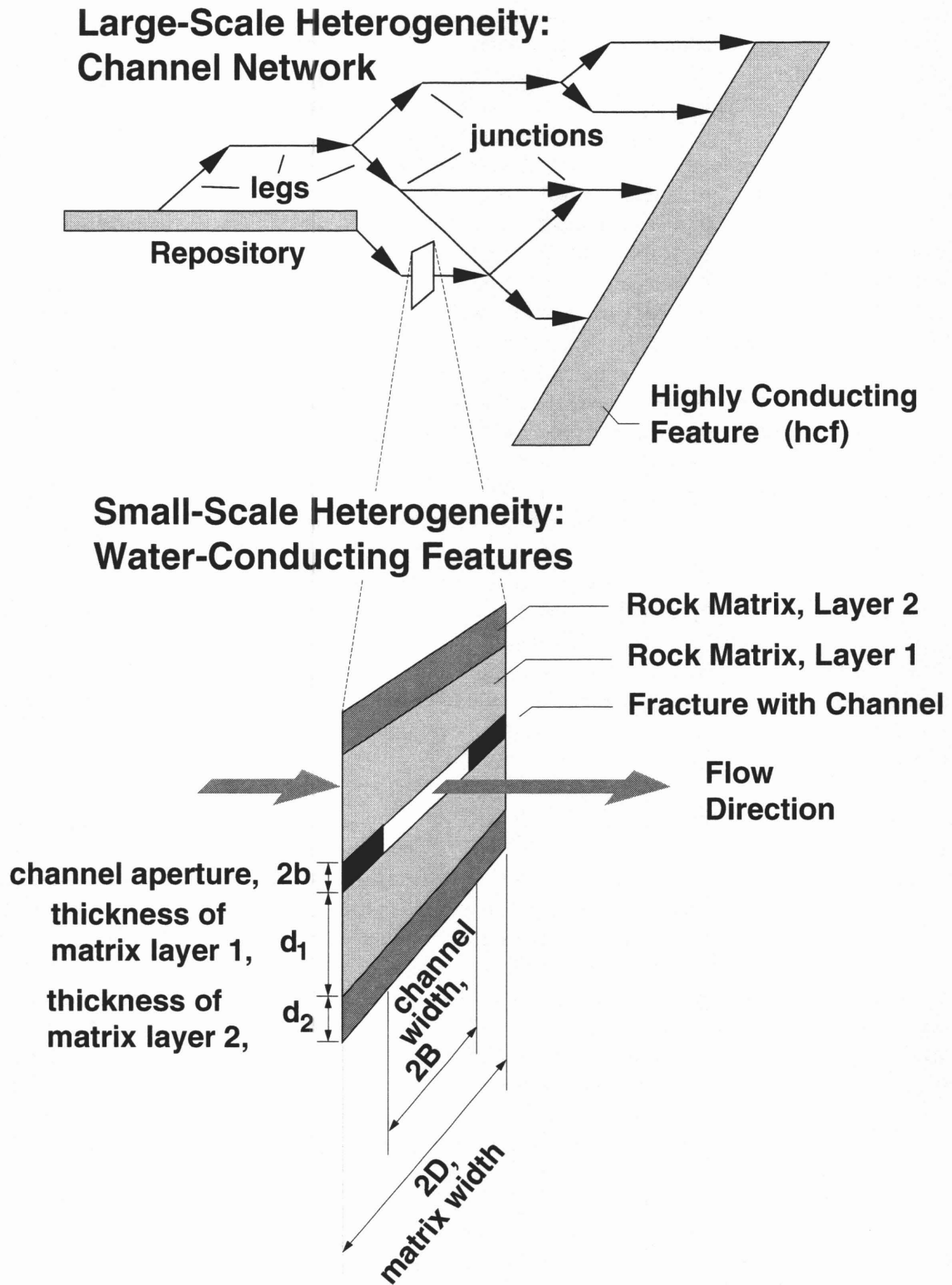


Figure 1.1. Network representing large-scale heterogeneity (top) and an example cross-section of a flowpath consisting of a channel within a fracture with adjacent two-layer rock matrix representing the small-scale heterogeneity considered by PICNIC (bottom). For $D = B$, matrix diffusion is one-dimensional.

This report concentrates on the capability of PICNIC to calculate nuclide flow rates¹ at junctions or out of legs into junctions. The calculation of nuclide flow rates is critical to performance assessment applications. Additionally, PICNIC can calculate mass² in the area of flowing water, nuclide exchange³ between the area of flowing water and the porous rock matrix and mass in the rock matrix for specified legs. These additional features, not considered explicitly in this report, can support the understanding of transport behaviour in a network, but are hard to verify quantitatively considering the limited availability of data from other codes, especially for more complicated rock matrix geometries.

Two recent further developments of other codes were very beneficial for the verification of PICNIC described in this report, especially because they use a different method for inverse Laplace transformation. The PAWorks/LTG code [Dershowitz et al., 1998] has been further developed to account for limited one-dimensional matrix diffusion into more than one homogeneous area of rock matrix in combination with transport in a fracture network. A finite-element method in the Laplace domain was used. Also, the RIP code [Miller and Kossik, 1998] has been further developed to consider one-dimensional matrix diffusion into more than one two-layer area of rock matrix in combination with transport in a network. Therefore, in a channel network type model, similar to PICNIC, a hierarchical linear response concept in the Laplace domain has been applied. RIP and PAWorks/LTG use numerical Laplace transformation methods, which are different from the method applied in PICNIC, to consider transport in networks in combination with different geometries for one-dimensional matrix diffusion.

This report is structured as follows. Following this introductory section, giving the motivation for the development of PICNIC, the system, its describing **balance equations**, the **solution concept** and, as far as necessary for this report, **some detailed solutions** are presented in section 2.

The **verification strategy** for PICNIC is described in section 3, based on an analysis of the mathematical and numerical methods in PICNIC. To ensure the reliability of PICNIC, the **verification of the key features is of primary importance**. It therefore forms the main part of this report. The verification strategy consists of **seven steps with increasing complexity** of the rock matrix and/or of the numerical methods applied, which are described in sections 4 to 10. As tests, mainly cases related to the Kristallin-I study and the Grimsel dipole transport experiments [Heer and Hadermann, 1994] are selected.

In section 4, test cases with **one-dimensional matrix diffusion into a homogeneous planar rock matrix** are considered. The tests are extended in section 5 to **one-dimensional matrix diffusion into a homogeneous cylindrical rock matrix**. These were the two rock matrix geometries considered in the Kristallin-I study using RANCHMD. Consequently, cross-comparisons with

¹ We use the term “nuclide flow” which has the unit $1[\text{mol}/\text{a}]$, to distinguish it from “nuclide flux”, which denotes here the “nuclide flow per unit area” in units of $1[\text{mol}/(\text{a}*\text{m}*\text{m})]$. Note that in many performance assessment applications, where it is not necessary to distinguish sharply between these two quantities, the term “flux” is often used also for “nuclide flow”. We use the term “breakthrough curve” when the time-dependent form of “nuclide flow” is of particular interest. Also coming from performance assessment, the terms “nuclide release” or “release curve” are preferred when “nuclide flow” is considered at inner junctions of a network, while the term “breakthrough curve” is often reserved for “nuclide flow” at the end of the model chain for the repository near-field, the geosphere and the biosphere (or less rigidly for “nuclide flow” out of a network).

² “Mass” here means the amount of nuclides in units of $1[\text{mol}]$.

³ “Nuclide exchange” here means the nuclide flow in units of $1[\text{mol}/\text{a}]$ at the flowing water/rock matrix interface integrated over the entire leg.

RANCHMD are performed for single legs, for both **single nuclides** and **nuclide decay chains**. For verification of the **network capability** in PICNIC, a sequence of RANCHMD calculations for each individual leg in the network are combined to obtain the nuclide release of the network. The agreement with this so-called “assembled RANCHMD” result is excellent. Self-consistency checks are conducted to test analytical relations. Additional cross-comparisons with the code PAWorks/LTG contribute to the basis for the next verification steps for more complicated rock matrix geometries. These two steps verify the capabilities of PICNIC to deal with transport in a **pathway** and a **network** of legs, to deal with different **leg outlet boundary conditions** and to handle **single or multiple sources of different time-dependent form**.

The further verification steps consider mainly the transport of **single nuclides** and **nuclide decay chains** in single **legs**, while the capability of PICNIC to deal with pathways and networks is occasionally spot-checked to increase confidence in the verification. While the rock matrix response in the Laplace domain is **implemented analytically** for the rock matrix geometries of sections 4 and 5, in sections 6 to 10, for **increased flexibility in terms of rock matrix diffusion**, a **finite-element method** for calculating the rock matrix response is **embedded** in PICNIC, forming a hybrid type code. Because of the embedded finite-element method used, “**discretisation tests**” considering different refinements in the finite-element mesh for calculation of the rock matrix response are generally used to indicate the accuracy of the code.

Different geometries for **one-dimensional matrix diffusion** are considered in sections 6 to 8. In section 6 the embedded finite-element method in PICNIC is verified in terms of dealing with a **homogeneous planar layer of rock matrix** by comparison with the PICNIC option with the analytically implemented rock matrix response (considered in section 4). The agreement with the latter indicates the **accuracy of the finite-element method** for this type of geometry. The relative difference functions (i.e. functions giving the relative difference between two results) act as “**calibration curves**” for the more complicated rock matrix geometries.

In section 7, for **one-dimensional matrix diffusion into a two-layer rock matrix**, the steady-state flow rate of a single nuclide is compared to the analytical result. For the full time-dependent behaviour, a cross-comparison with the RIP code is performed⁴, both for single nuclides and for nuclide decay chains.

Section 8 completes the analysis of one-dimensional matrix diffusion with some example geometries. For **one-dimensional matrix diffusion into two independent homogeneous areas of rock matrix**, a cross-comparison with the PAWorks/LTG code is performed. A similar cross-comparison with the RIP code is performed for **two independent two-layer areas of rock matrix** in a leg.

For two-dimensional matrix diffusion considered in sections 9 and 10, no analytical solution for the rock matrix response is available, nor any code for cross-comparison of the time-dependent behaviour. Thus, the verification for **two-dimensional matrix diffusion** relies mainly on the verification of the embedded finite-element method for one-dimensional matrix diffusion, on qualitative estimates and on “**discretisation tests**”, both for single nuclides and nuclide decay chains. In section 9, for **two-dimensional matrix diffusion into a homogeneous rock matrix**

⁴ Note that the rock matrix geometries considered in sections 7 to 10 go beyond the geometries considered for geosphere transport in Kristallin-I and are not within the capability of RANCHMD.

layer, the PICNIC result for the steady-state release of a single nuclide is additionally compared to a result derived from a calculation using the finite-element code ADINA [ADINA, 1992].

Section 10 completes the verification of PICNIC, particularly for two-dimensional matrix diffusion, with discretisation tests and consistency tests for a few example geometries. A single nuclide and a nuclide decay chain are considered in a leg **with two-dimensional matrix diffusion into a two-layer rock matrix**. Finally, a case with an area of **rock matrix in a fracture** is spot-checked for inaccuracies in the code observed in previous sections.

Conclusions and an **outlook** are given in section 11. For this verification, the PICNIC version of October 1998 was chosen as the common basis. Since then, small inconveniences and a few bugs have been eliminated from the code, which, however, are estimated to change the numerical results of this report only slightly; see also section 11.

2. The System

In this section we describe the system considered together with the balance equations describing the system. The mathematical and numerical methods used in PICNIC to solve the balance equations are presented to support the verification of the code. PICNIC uses a hierarchical concept to deal with transport in heterogeneously fractured rock. This section is organised according to the geometric structures of the rock that are described. Each hierarchical level derives the information it utilises from the level beneath it.

On the highest hierarchical level, **transport in a network** is considered in section 2.1. The network consists of a system of junctions connected by discrete legs. The interaction of the different legs is only via the junctions.

Transport in the legs is discussed in section 2.2.

To illustrate the structure of the code, in section 2.3 the **solution method for a single nuclide in a single leg** is described in more detail. The cross-section of a leg consists of areas of flowing water and areas of porous rock matrix filled with stagnant porewater. The transverse dispersion in the area of flowing water is approximated as instantaneous mixing such that transport in the leg parallel to the water flow is one-dimensional.

Diffusive transport in the porewater of the porous rock matrix is described in section 2.4. Because diffusion in the porous rock matrix parallel to the direction of flowing water is neglected, it is sufficient to consider the two-dimensional diffusion in the rock matrix and the nuclide exchange with the area of flowing water in the cross-section of the leg. For illustration, the case of a single nuclide in a one-dimensional homogeneous planar rock matrix is discussed.

In section 2.5 **different rock matrix geometries** are considered and discussed in detail.

In section 2.6 we show how PICNIC accounts for **linear sorption** in the porous rock zone and in the area of flowing water.

In section 2.7 Talbot's method used in PICNIC for numerical inverse Laplace transformation is described.

Finally in section 2.8, we outline the structure of the **input file** which describes how the network and its parameters are entered into PICNIC.

2.1. Water and Nuclide Balance on the Scale of the Network

This section describes **transport on the scale of the network**. It begins with the nomenclature used to describe the geometry of a network and then considers the flow of water, which is assumed to be time-independent. This has a fundamental influence on the transport of nuclides described later. The balance equations are solved by the pathway method, or more technically speaking, by the tree method in the Laplace domain. For accuracy reasons, the implementation of this method differs when the nuclide source is defined in the Laplace domain and when an arbitrary time-dependent source is entered to PICNIC. For later use in the verification, we finally define the so-called geosphere barrier efficiency.

2.1.1. Definitions

The network is described using definitions adopted from graph theory, e.g. Abell and Braselton [1994a].

- A directed network is defined by a set of **junctions** (nodes) in the network and a set of **legs** in the

network.

- A **leg** lg is a direct connection between two junctions. The direction is defined by the **tail** $tl(lg)$ and the **head** $hd(lg)$ of the leg lg ; see Figure 2.1a. The definitions of the head and tail of a leg come from graph theory and should not be confused with the “hydraulic head”. Note that the head of a leg has a lower “hydraulic head” than the tail of a leg; water therefore flows from tail to head.
- A leg ar is denoted as an **arriving leg** of a junction ju , when ju is the head of the leg ar ; see Figure 2.1b. A leg dp is denoted as a **departing leg** of a junction ju , when ju is the tail of dp . The set of legs $Ar(ju)$ is the **set of arriving legs** of the junction ju . The set of legs $Dp(ju)$ is the **set of departing legs** of the junction ju .
- A junction an is an **ancestor** of a junction ju where there is a leg that is an arriving leg of the junction ju and a departing leg of the junction an . A junction da is a **daughter** of a junction ju where there is a leg that is a departing leg of the junction ju and an arriving leg of the junction da . The set of junctions $An(ju)$ is the **set of ancestors** of the junction ju . The set of junctions $Da(ju)$ is the **set of daughters** of the junction ju .

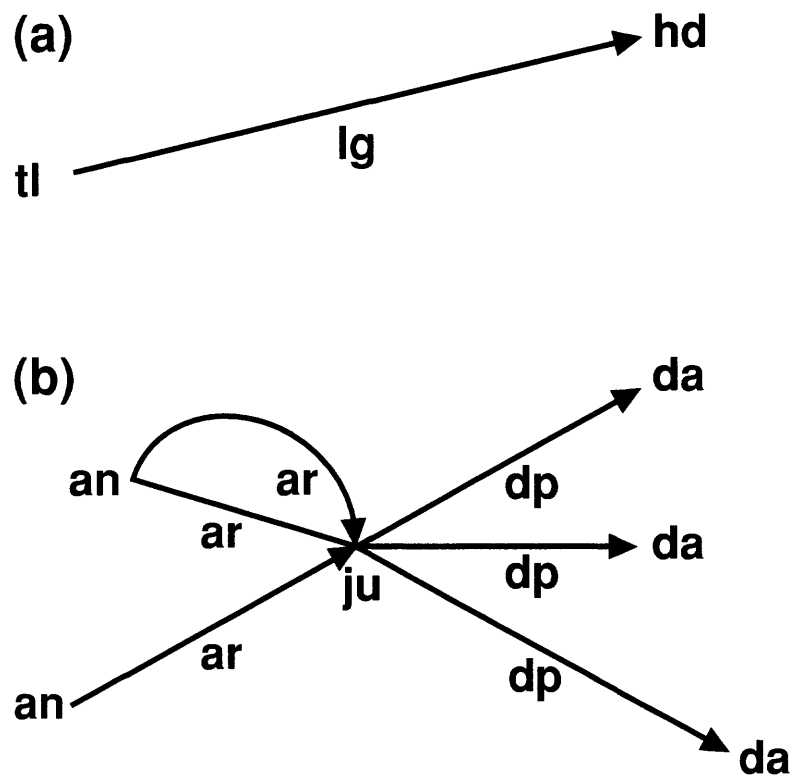


Figure 2.1. (a) A leg lg is shown with the junctions tl and hd , which are the **tail** and the **head** of the leg, respectively. (b) Part of a network is shown with a junction ju that has three **arriving legs**, indicated as ar , and three **departing legs**, indicated as dp . There are two junctions indicated as an that are **ancestors** of ju . (Notice that there are two arriving legs of ju which have the same tail in common.) There are three junctions indicated as da that are **daughters** of the junction ju . The arrows indicate the flow direction in the legs. The arrowhead in one of the legs is omitted to keep the drawing tidy.

2.1.2. Water Balance

We consider situations where the water flow rates Q_{lg} are predefined in each leg lg in the network. The directions of water flow in the legs are most important, because they organise the “network” and also define the direction of transport in the network, as discussed below. In PICNIC, time-independent water flow rates are considered. For some comments on time-dependent water flow rates in the network see Barten [1997]. The mass of water is conserved in each leg of the network. The junctions can act as sources or sinks of water. Thus the amount of flowing water, Qt_{ju} , at a junction ju is, on the one hand, the amount of water entering the junction,

$$Qt_{ju} = Qs_{ju} + \sum_{ar \in Ar(ju)} Q_{ar} , \quad (2.1)$$

which is described by any possible source of water at the junction, Qs_{ju} , and the inflowing water from the arriving legs, $\sum_{ar \in Ar(ju)} Q_{ar}$. At junctions without a source of water, we define $Qs_{ju} = 0$ to

be consistent with the above notation. On the other hand, because of the conservation of mass of water, Qt_{ju} is equal to the amount of water leaving the junction and entering the departing legs,

$$Qt_{ju} = \sum_{dp \in Dp(ju)} Q_{dp} . \quad (2.2)$$

A possible sink of water at ju is treated, for the sake of brevity, as a leg to a junction that has lower hydraulic head than the junctions of interest.

2.1.3. Nuclide Balance

The typical situation considered is that there are some junctions that are source locations where nuclides are released into the network. The source locations of water and nuclides can be different. We need to calculate the time-dependent nuclide flow rate $J_{out}(t)$ at a specific junction out in a network, and therefore assume that the time-dependent nuclide flow rate $J_{ju}(t)$ at an arbitrary junction ju in a network is described, on the one hand, by the nuclides entering the junction,

$$J_{ju}(t) = S_{ju}(t) + \sum_{ar \in Ar(ju)} Out_{ar}(t) , \quad (2.3)$$

where $S_{ju}(t)$ is the nuclide source. $Out_{ar}(t)$ denotes the nuclide outflow of the arriving legs $ar \in Ar(ju)$ at the junction ju . At junctions without a source, we define $S_{ju}(t) = 0$ to be consistent with the above notation. The nuclide flow rate can be described, on the other hand, by the nuclides leaving the junction

$$J_{ju}(t) = \sum_{dp \in Dp(ju)} In_{dp}(t) , \quad (2.4)$$

where $In_{dp}(t)$ denotes the nuclide flow rate into the departing legs $dp \in Dp(ju)$ at the junction ju . Expressed in a general manner, we consider situations where the nuclide outflow rate of a leg lg can be expressed by applying an operator N_{lg} to the nuclide inflow rate,

$$Out_{lg}(t) = N_{lg}(In_{lg}(t)). \quad (2.5)$$

For the linear transport processes considered here, there is a response function, $\mathfrak{R}_{lg}(t)$, of the leg, such that the nuclide outflow rate can be calculated as the convolution, (*), of the nuclide inflow rate with the response function of the leg,

$$Out_{lg}(t) = \mathfrak{R}_{lg}(t) * In_{lg}(t) = \int_0^t dt' \mathfrak{R}_{lg}(t-t') \cdot In_{lg}(t'). \quad (2.6)$$

The nuclide inflow rate of a leg

$$In_{lg}(t) = w_{lg} J_{tl(lg)}(t), \quad (2.7)$$

is determined by the nuclide flow rate at the tail of the leg, $J_{tl(lg)}(t)$, and the probability w_{lg} of a nuclide at the tail of the leg entering the leg. In PICNIC w_{lg} is time-independent and no probabilistic calculations are performed. w_{lg} is the fraction of the amount of nuclides reaching the tail that enters the leg. The above formulation in equation (2.7) inherently ensures conservation of mass at the junctions as a boundary condition. The predefined probability depends on the water flow rates Q_{dp} of the departing legs at $tl(lg)$ and, in general, we assume perfect mixing at the junctions,

$$w_{lg} = \frac{Q_{lg}}{Q_{tl(lg)}}. \quad (2.8)$$

The junction in denotes a member in the set of inflow positions In .⁵ Because of the superposition principle for the linear transport processes considered, the nuclide flow rate at a junction ju can be calculated as the superposition of the nuclide flows arising from the different sources,

$$J_{ju}(t) = \sum_{in \in In} J_{ju,in}(t), \quad (2.9)$$

where the nuclide flows arising from the different sources can be considered independently. $J_{ju,in}(t)$ denotes the nuclide flow rate at the junction ju due to the source at the junction in .

⁵ For simplicity we indicate the sources here by their location. However, more than one nuclide source at the same junction is also possible.

2.1.4. Pathways and Tree

Again because of the linear processes considered for a single source, the nuclide flow rate is the superposition of the nuclide flow rates through the different possible pathways between the junctions *in* and *ju*,

$$J_{ju,in}(t) = \sum_{w \in W} J_{ju,in;w}(t), \quad (2.10)$$

where W denotes the set of different pathways between the junctions *in* and *ju*. The set of pathways is represented in PICNIC as a tree. A tree is a special kind of directed network where each junction (besides the first junction) has exactly one arriving leg. A pathway is a special kind of tree where each junction (besides the last junction) has exactly one departing leg. Thus a pathway consists of one or more legs in series. See for explanation the small network in Figure 2.2a. There are 9 different pathways between the junctions *in* and *out* which are depicted in Figure 2.2b as a tree.

Using equations (2.6) and (2.7), the nuclide flow rate at the junctions can be calculated straightforwardly as

$$J_{ju,in;w}(t) = w_{ar(ju);w} \mathfrak{R}_{ar(ju);w}(t) * J_{tl(ar),in;w}(t), \quad (2.11)$$

starting with

$$J_{in,in;w}(t) = S_{in}(t) \quad (2.12)$$

and ending with the requested outflow position, *out*, in the network. Here $ar(ju)$ denotes the single arriving leg of the junction *ju* in the pathway w (or the tree) and $tl(ar)$ is the single ancestor of the junction *ju*. Only the leg response functions, $\mathfrak{R}_{lg}(t)$, are needed for all legs in the pathways between the inflow positions and the outflow position. The above equations (2.8)-(2.12) then give a complete algorithm for calculation of the nuclide flow rates at arbitrary junctions in the network and particularly at a requested outflow position *out*. However this is rather time-consuming because, for each leg in each tree, a convolution has to be performed. Even more important, calculating the time-dependent leg response functions, $\mathfrak{R}_{lg}(t)$, would need a larger effort. Therefore PICNIC works mainly in the Laplace domain.

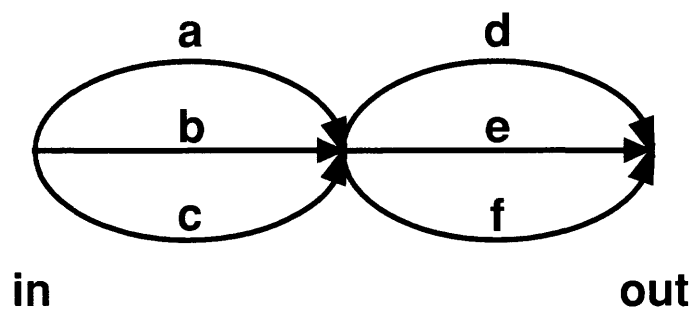
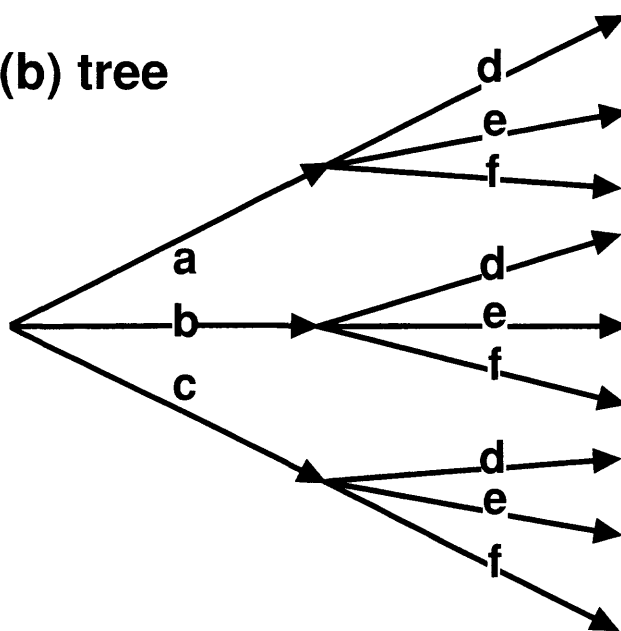
(a) network**(b) tree**

Figure 2.2. (a) A small 6-leg network transformed to (b) a tree. The arrows indicate the flow directions in the legs.

2.1.5. Laplace Transformed Source Terms

The Laplace transformed function $\bar{f}(s)$ of an (arbitrary) time-dependent function $f(t)$ is defined as

$$\bar{f}(s) = \int_0^{\infty} dt e^{-st} f(t). \quad (2.13)$$

One variant of PICNIC considers source terms in the Laplace domain, $\bar{S}_{in}(s)$. Then the relations in the Laplace domain

$$\bar{J}_{ju,in}(s) = \sum_{w \in W} \bar{J}_{ju,in;w}(s), \quad (2.14)$$

$$\bar{J}_{ju,in;w}(s) = w_{ar(ju);w} \bar{\mathfrak{R}}_{ar(ju);w}(s) \cdot \bar{J}_{il(ar);in;w}(s), \quad (2.15)$$

$$\bar{J}_{in,in;w}(s) = \bar{S}_{in}(s) \quad (2.16)$$

replace the equations (2.10)-(2.12). Finally, Talbot's method (Talbot [1979]) for numerical inverse Laplace transformation is used in PICNIC to calculate $J_{ju,in}(t)$.

2.1.6. Source Terms in the Time Domain

In most applications, time-dependent functions are entered to PICNIC in tabular form as source terms $S_{in}(t)$. The Laplace transformation of this type of source term to obtain $\bar{S}_{in}(s)$ in combination with the numerical inverse Laplace transformation applied later is, in many cases, not very accurate and could lead to large inaccuracies of the entire algorithm. To maintain the advantages of the Laplace transformation method, we modify our algorithm and use the linear response concept described here.

Because of the linearity of the transport mechanisms considered, there is a linear response function or residence time spectrum, $T_{ju,in}(t)$, of the tree between the junctions in and ju ,

$$J_{ju,in}(t) = T_{ju,in}(t) * S_{in}(t). \quad (2.17)$$

$T_{ju,in}(t)$ depends only on the properties of the network between in and ju and is independent of the source itself. Note that this notation distinguishes clearly between the response function of a leg, $\mathfrak{R}_{lg}(t)$, which is determined by the properties of the leg only, and the response function of the nuclide flow rate at a junction, $T_{ju,in}(t)$, which also depends on the inflow position. The tree response function is calculated in the Laplace domain according to

$$\bar{T}_{ju,in}(s) = \sum_{w \in W} \bar{T}_{ju,in;w}(s), \quad (2.18)$$

$$\bar{T}_{ju,in;w}(s) = w_{ar(ju);w} \bar{\mathfrak{R}}_{ar(ju);w}(s) \cdot \bar{T}_{l(ar);in;w}(s), \quad (2.19)$$

starting with the identity function, I , at the source location,

$$\bar{T}_{in,in;w}(s) = I. \quad (2.20)$$

This set of equations considering response functions replaces the equations (2.14) to (2.16) which considered the nuclide flow rate. (Equation (2.20) follows from $\bar{J}_{in,in;w}(s) = \bar{T}_{in,in;w}(s) \cdot \bar{S}_{in}(s) = \bar{S}_{in}(s)$.) Finally, Talbot's method (Talbot [1979]) for numerical inverse Laplace transformation is used in PICNIC to calculate $T_{ju,in}(t)$ and the convolution with the source $S_{in}(t)$ is performed according to equation (2.17). The methods of linear response are very similar for a single nuclide and nuclides of a decay chain. For a single nuclide, it is sufficient to use a single response function, while e.g. $\mathfrak{R}_{ar}(t)$ and $T_{ju,in}(t)$ are tensors or "matrices" of response functions in the case of a decay chain. Note that, for a decay chain, the term $T_{ju,in}(t) * S_{in}(t)$ means, in addition to the convolution in time, a matrix-vector product and $\mathfrak{R}_{ar}(t) * T_{l(ar);in}(t)$ means a matrix-matrix product in addition to the convolution in time.

2.1.7. Geosphere Barrier Efficiency

As an aside we introduce the geosphere barrier efficiency in this subsection. We start with the nuclide flow rate at a junction in its Laplace transformed form arising from a nuclide source. This is

$$\bar{J}_{ju,in}(s) = \bar{T}_{ju,in}(s) \cdot \bar{S}_{in}(s), \quad (2.21)$$

because a convolution in the time domain transforms into a simple product in the Laplace domain, cf. equation (2.17). For a nuclide decay chain $1 \rightarrow \dots \rightarrow i \rightarrow i+1 \rightarrow \dots \rightarrow I$ the quantities above are vectors or tensors of functions and we obtain explicitly

$$\bar{J}_{ju,in}^{(i)}(s) = \sum_{j=1}^I \bar{T}_{ju,in}^{(i,j)}(s) \cdot \bar{S}_{in}^{(j)}(s), \quad (2.22)$$

where $\bar{J}_{ju,in}^{(i)}(s)$ denotes the flow rate of the nuclide (i). Thus $\bar{T}_{ju,in}^{(i,j)}(s)$ describes the influence of a source of nuclides of type (j) at a junction in on the flow rate of nuclides of type (i) at the junction ju . With the defining equation (2.13) of the Laplace transform, in the limit of $s \rightarrow 0$,

$$\bar{f}(s=0) = \int_0^{\infty} dt f(t), \quad (2.23)$$

the time integral of the nuclide flow rate at a junction

$$\bar{J}_{ju,in}^{(i)}(s=0) = \int_0^{\infty} dt J_{ju,in}^{(i)}(t) \quad (2.24)$$

and the time integral of a nuclide source

$$\bar{S}_{in}^{(j)}(s=0) = \int_0^{\infty} dt S_{in}^{(j)}(t) \quad (2.25)$$

are given by the ($s=0$) components of their Laplace transforms. Thus $\bar{T}_{ju,in}^{(i,j)}(s=0)$ describes the influence of the time integral of a source of nuclides of type (j) at a junction in on the time integral flow rate of nuclides of type (i) at the junction ju by

$$\int_0^{\infty} dt J_{ju,in}^{(i)}(t) = \sum_{j=1}^I \bar{T}_{ju,in}^{(i,j)}(s=0) \cdot \int_0^{\infty} dt S_{in}^{(j)}(t). \quad (2.26)$$

When a single nuclide, but not a nuclide decay chain, is considered, then

$$\bar{T}_{ju,in}(s=0) = \frac{\bar{J}_{ju,in}(s)}{S_{in}(s)} = \frac{\int_0^{\infty} dt J_{ju,in}(t)}{\int_0^{\infty} dt S_{in}(t)}, \quad (2.27)$$

where, for simplicity, we omit the upper index for the nuclide. We then call $\bar{T}_{ju,in}(s=0)$ (for historical reasons) “1 minus the geosphere barrier efficiency” of the network between the junctions in and ju . Note that the “geosphere barrier efficiency” is zero for a non-decaying nuclide with $\bar{T}_{ju,in}(s=0) = 1$ and is highest for a strongly decaying nuclide with $\bar{T}_{ju,in}(s=0) \rightarrow 0$. For a constant source, $S_{in}(t) = S_{in} = \text{constant}$ for $t > 0$,

$$\frac{J_{ju,in}(t)}{S_{in}} \xrightarrow{t \rightarrow \infty} \bar{T}_{ju,in}(s=0), \quad (2.28)$$

also describes the long-time behaviour of the nuclide flow rate.

For transport in a single leg lg , with

$$\bar{T}_{hd(lg),nl(lg)}(s) = w_{lg} \bar{\mathfrak{R}}_{lg}(s), \quad (\text{with } w_{lg} = 1) \quad (2.29)$$

the “geosphere barrier efficiency” is $1 - \bar{\mathfrak{R}}_{lg}(s=0)$. To our knowledge, this concept was given its name and was first analysed for specific boundary conditions by Smith [1991], both for a planar and a cylindrical rock matrix geometry.

2.2. Water and Nuclide Balance on the Scale of a Leg

Till now we have considered transport on the scale of the network. We have shown that, for this, we only need the nuclide flow rates at the junctions which can be derived from the nuclide sources, the flow of water which enters into the probabilities, w_{lg} , at the junctions and the leg response functions which are addressed now. Therefore, in this subsection the flow of water and the balance equations for the nuclides in the area of the flowing water in a leg are discussed. The flowing water/rock matrix interface is analysed and the initial conditions and boundary conditions are presented.

2.2.1. Water Balance

Water may flow in a leg in the z -direction from the inflow position at $z = 0$ to the outflow position at $z = L$. Note that z is the direction along the leg parallel to the flow of water and x and y are coordinates normal to z , i.e. into the rock matrix (see below). The index for the leg is omitted in this subsection. Because we consider stationary flow of water and because the mass of water is conserved in the leg, the water flow rate Qe_z is independent of time and z -position. The leg may have a cross-sectional area A_f in the x - y plane. Thus the specific discharge of the leg is

$$q = \frac{Q}{A_f}. \quad (2.30)$$

Water flow is confined to the part of the leg with area A_i , while there is no flow of water in the rest of the leg. The area A_i may have infill with porosity ε_i . With this geometry, the flow porosity in the leg is defined as

$$\varepsilon_f = \frac{A_i}{A_f} \varepsilon_i \quad (2.31)$$

and the velocity of the flowing water is

$$v = \frac{Q}{A_i \varepsilon_i} = \frac{q}{\varepsilon_f} \quad (2.32)$$

which is regarded as independent of position in the area A_i .

2.2.2. Nuclide Balance

Nor does the nuclide concentration $C_f^{(i)}(z; t)$ in flowing water depend on the x or y position, i.e. fast transverse dispersion is considered. The upper index “(i)” denotes the nuclide in the decay chain $1 \rightarrow \dots \rightarrow i \rightarrow i+1 \rightarrow \dots \rightarrow I \rightarrow$. We consider a small slice of the leg of length Δz in the z -direction with volume $V_f = A_f \Delta z$ and with volume, $V_i = A_i \Delta z$, of the “area” with flowing water. The rest of the volume V_f may be porous rock filled with stagnant porewater or solid rock. The nuclide inventory in the flowing water in V_i is $V_i \varepsilon_i C_f^{(i)} = V_f \varepsilon_f C_f^{(i)}$. If we assume linear equilibrium sorption of the nuclides on the infill and the surfaces of the volume V_i , we can define (e.g. Hadermann and Rösler [1985]) a retardation factor $R_f^{(i)}$ for each nuclide (i) that gives the ratio of the amount of nuclide in the volume V_i to the amount of nuclide in the flowing water. Thus the amount of nuclide in V_i is

$$N_f^{(i)} = V_f \varepsilon_f R_f^{(i)} C_f^{(i)} = V_i \varepsilon_i R_f^{(i)} C_f^{(i)}. \quad (2.33)$$

The amount of nuclides in V_i can change with time only by radioactive decay and ingrowth and transport through the bounding surfaces of V_i . Thus the balance equation for $N_f^{(i)}$ can be approximated as

$$\begin{aligned} \partial_t N_f^{(i)}(z; t) = & - \left[J^{(i)}(z + \Delta z/2; t) - J^{(i)}(z - \Delta z/2; t) \right] - A_m \left\langle \mathbf{j}_p^{(i)} \cdot \mathbf{e}_n \right\rangle_{A_m}(z; t), \\ & - \lambda^{(i)} N_f^{(i)}(z; t) + \lambda^{(i-1)} N_f^{(i-1)}(z; t) \end{aligned} \quad (2.34)$$

where $- \left[J^{(i)}(z + \Delta z/2; t) - J^{(i)}(z - \Delta z/2; t) \right]$ describes nuclide transport through the front- and back-side of V_i . The transport through the side-walls of V_i orthogonal to the water flow is expressed as the spatially averaged nuclide flux through the side walls, $- \left\langle \mathbf{j}_p^{(i)} \cdot \mathbf{e}_n \right\rangle_{A_m}(z; t)$, multiplied by the area of the side-walls, A_m . There $\mathbf{j}_p^{(i)}(x, y, z; t)$ is the nuclide flux at the side-walls of V_i and $\mathbf{e}_n(x, y)$ is the normal vector of the side-walls. The symbol $\langle \dots \rangle$ denotes the spatial average over the side-walls. Radioactive decay is described by the decay constants $\lambda^{(i)}$. Branched decay can also be dealt with in PICNIC, but is not discussed here explicitly. In the limit case of small Δz we get approximately

$$\begin{aligned} \partial_t N_f^{(i)}(z; t) = & - \Delta z \partial_z J^{(i)}(z; t) - A_m \left\langle \mathbf{j}_p^{(i)} \cdot \mathbf{e}_n \right\rangle_{A_m}(z; t), \\ & - \lambda^{(i)} N_f^{(i)}(z; t) + \lambda^{(i-1)} N_f^{(i-1)}(z; t) \end{aligned} \quad (2.35)$$

where $\lambda^{(0)} = 0$, consistent with the above notation. Assuming advection-dominated transport in the

flowing water, together with micro-dispersion, the nuclide flow rate is⁶

$$J^{(i)}(z;t) = J_f^{(i)}(z;t) = Q \left[C_f^{(i)}(z;t) - a_L \partial_z C_f^{(i)}(z;t) \right], \quad (2.36)$$

where $QC_f^{(i)}(z;t)$ is the advective contribution and $-Q a_L \partial_z C_f^{(i)}(z;t)$ is the dispersive contribution in Fickian form. The dispersion length a_L is assumed to be nuclide-independent. It can be expressed by the channel Peclet number Pe or the nuclide-independent dispersion constant D_f of the channel,

$$a_L = \frac{L}{Pe} = \frac{D_f \varepsilon_f}{q_f}. \quad (2.37)$$

Altogether, the balance equation for nuclide concentration in the flowing water is

$$\begin{aligned} \partial_t C_f^{(i)}(z;t) = & \frac{D_f}{R_f^{(i)}} \partial_z^2 C_f^{(i)}(z;t) - \frac{q}{R_f^{(i)} \varepsilon_f} \partial_z C_f^{(i)}(z;t) - \frac{\delta_f}{R_f^{(i)} \varepsilon_i} \left\langle \mathbf{j}_p^{(i)} \cdot \mathbf{e}_n \right\rangle_{A_m} (z;t) \\ & - \lambda^{(i)} C_f^{(i)}(z;t) + \lambda^{(i-1)} \frac{R_f^{(i-1)}}{R_f^{(i)}} C_f^{(i-1)}(z;t) \end{aligned}, \quad (2.38)$$

$$\text{where} \quad \delta_f = \frac{A_m}{V_i} \quad (2.39)$$

is the geometric surface to volume ratio of the area of flowing water.

⁶ The lower index "f" in the nuclide flow in the area of flowing water is mostly dropped for brevity.

2.2.3. Interface with the Rock Matrix

Up to now, we have not discussed the behaviour in the rock matrix. The only “information” from the rock matrix that enters into the nuclide balance equation (2.38) for the area of flowing water is the nuclide flow rate from the area of flowing water to the rock matrix, $A_m \langle \mathbf{j}_p^{(i)} \cdot \mathbf{e}_n \rangle_{A_m}(z;t)$. On the other hand, as will be described below, the nuclide concentration in the flowing water acts as a boundary condition for the nuclide concentration in the rock matrix. Assuming a perfectly connected pore space in the area of flowing water and the rock matrix, PICNIC uses the continuity condition

$$C_p^{(i)}(x,y,z;t) = C_f^{(i)}(z;t) \quad (2.40)$$

for (x,y) at the flowing water/rock matrix interface. As will be described in section 2.4, within the rock matrix there is only transport in the x - y plane and transport in the z -direction parallel to the flowing water is neglected. Thus, because of the linearity of the balance equations, there is a rock matrix response tensor $(\eta^{(i,j)})^{i=1\dots I, j=1\dots I}(t)$, such that the nuclide flow rate between the flowing water and the rock matrix is

$$-A_m \langle \mathbf{j}_p^{(i)} \cdot \mathbf{e}_n \rangle_{A_m}(z;t) = \sum_{j=1}^I \eta^{(i,j)}(t) * C_f^{(j)}(z;t). \quad (2.41)$$

Because a parent nuclide influences its daughter, but not vice versa, $\eta^{(i,j)}(t) = 0$ holds for $i > j$. Thus the balance equations in the flowing water read

$$\begin{aligned} \partial_t C_f^{(i)}(z;t) = & \frac{D_f}{R_f^{(i)}} \partial_z^2 C_f^{(i)}(z;t) - \frac{q}{R_f^{(i)} \varepsilon_f} \partial_z C_f^{(i)}(z;t) + \frac{1}{R_f^{(i)} V_i \varepsilon_i} \sum_{j=1}^i \eta^{(i,j)}(t) * C_f^{(j)}(z;t) \\ & - \lambda^{(i)} C_f^{(i)}(z;t) + \lambda^{(i-1)} \frac{R_f^{(i-1)}}{R_f^{(i)}} C_f^{(i-1)}(z;t) \end{aligned}, \quad (2.42)$$

where the rock matrix response tensor $\eta(t)$ is the only quantity where the properties of the rock matrix enter.

We Laplace transform now this linear integro-partial differential equation (2.42). Therefore we use that the Laplace transformed of a time differentiation of a function, $\partial_t f(t)$, is just $s\bar{f}(s)$ when $f(t=0) = 0$. In addition we use that the convolution of time-dependent functions is transformed into a simple product in the Laplace domain. All other terms are transformed straightforwardly. Thus the Laplace transformed balance equations in the area of flowing water are a coupled system of ordinary differential equations,

$$s\bar{C}_f^{(i)}(z;s) = \frac{D_f}{R_f^{(i)}} \partial_z^2 \bar{C}_f^{(i)}(z;s) - \frac{q}{R_f^{(i)} \varepsilon_f} \partial_z \bar{C}_f^{(i)}(z;s) + \frac{1}{R_f^{(i)} V_i \varepsilon_i} \sum_{j=1}^i \bar{\eta}^{(i,j)}(s) \cdot \bar{C}_f^{(j)}(z;s) - \lambda^{(i)} \bar{C}_f^{(i)}(z;s) + \lambda^{(i-1)} \frac{R_f^{(i-1)}}{R_f^{(i)}} \bar{C}_f^{(i-1)}(z;s) \quad , \quad (2.43)$$

cf. equation (2.42). The above equation can be written as

$$0 = \frac{D_f}{R_f^{(i)}} \partial_z^2 \bar{C}_f^{(i)}(z;s) - \frac{q}{R_f^{(i)} \varepsilon_f} \partial_z \bar{C}_f^{(i)}(z;s) - \left[s + \lambda^{(i)} - \frac{\bar{\eta}^{(i,i)}(s)}{R_f^{(i)} V_i \varepsilon_i} \right] \bar{C}_f^{(i)}(z;s) + \frac{1}{R_f^{(i)} V_i \varepsilon_i} \sum_{j=1}^{i-1} \bar{\eta}^{(i,j)}(s) \cdot \bar{C}_f^{(j)}(z;s) + \lambda^{(i-1)} \frac{R_f^{(i-1)}}{R_f^{(i)}} \bar{C}_f^{(i-1)}(z;s) \quad . \quad (2.44)$$

This system of second order differential equations for the nuclide concentrations $\left(C_f^{(i)}(z;t) \right)^{i=1\dots I}$ can be rewritten as a system of first order differential equations for the nuclide flow rate $\left(J^{(i)}(z;t) \right)^{i=1\dots I}$ and the advective nuclide flow rate $\left(QC_f^{(i)}(z;t) \right)^{i=1\dots I}$,

$$\partial_z \bar{J}^{(i)}(z;s) = - \frac{R_f^{(i)}}{q/\varepsilon_f} \left[s + \lambda^{(i)} - \frac{\bar{\eta}^{(i,i)}(s)}{R_f^{(i)} V_i \varepsilon_i} \right] QC_f^{(i)}(z;s) + \frac{1}{V_i \varepsilon_i q/\varepsilon_f} \sum_{j=1}^{i-1} \bar{\eta}^{(i,j)}(s) \cdot QC_f^{(j)}(z;s) + \lambda^{(i-1)} \frac{R_f^{(i-1)}}{q/\varepsilon_f} QC_f^{(i-1)}(z;s) \quad , \quad (2.45)$$

which is completed by the definition of the nuclide flow rate

$$\partial_z QC_f^{(i)}(z;s) = - \frac{Pe}{L} \left[\bar{J}^{(i)}(z;s) - QC_f^{(i)}(z;s) \right], \quad (2.46)$$

such that we have $2I$ balance equations for $2I$ independent quantities. The system of balance equations (2.45-46) can be formally written as

$$\partial_z \begin{pmatrix} \bar{J}^{(1)}(z;s) \\ QC_f^{(1)}(z;s) \\ \vdots \\ \bar{J}^{(I)}(z;s) \\ QC_f^{(I)}(z;s) \end{pmatrix} = \mathbf{A}(s) \begin{pmatrix} \bar{J}^{(1)}(z;s) \\ QC_f^{(1)}(z;s) \\ \vdots \\ \bar{J}^{(I)}(z;s) \\ QC_f^{(I)}(z;s) \end{pmatrix} . \quad (2.47)$$

This system of first order differential equations can be treated as an eigenvalue problem. The solution is in general⁷

$$\begin{pmatrix} \bar{J}^{(1)}(z; s) \\ Q\bar{C}_f^{(1)}(z; s) \\ \vdots \\ \bar{J}^{(l)}(z; s) \\ Q\bar{C}_f^{(l)}(z; s) \end{pmatrix} = \sum_{v=1}^{2l} \mathbf{a}'_v(s) \exp(zK_v(s)) \quad (2.48)$$

with the $2l$ eigenvalues $K_1(s) \dots K_{2l}(s)$ of the matrix $\mathbf{A}(s)$. The $2l$ vectors $\mathbf{a}'_1(s) \dots \mathbf{a}'_{2l}(s)$ depend on the boundary conditions described below and must be determined to calculate the response function tensor of the leg. This will be illustrated in section 2.3 for the case of a single nuclide.

2.2.4. Initial Conditions

Because only the nuclide concentrations due to the nuclide sources are considered in our method, the concentrations in the area of flowing water and the rock matrix are zero at $t = 0$,

$$C_f^{(i)}(z; t = 0) = 0 \quad \text{for all } z, \quad (2.49a)$$

$$C_p^{(i)}(x, y, z; t = 0) = 0 \quad \text{for all } x, y, z, \quad (2.49b)$$

when the nuclide sources start after $t = 0$.

⁷ This general form is not valid when different nuclides of a decay chain have the same parameters and especially the same half-life. Therefore we exclude the non-generic, artificial case that different nuclides of the decay chain have exactly the same half-life.

2.2.5. Boundary Conditions

The $2I \times 2I$ -matrix $\mathbf{A}(s)$ is z -independent, so that we obtain an eigenvalue equation, for which we need $2I$ independent boundary conditions. The first I boundary conditions are given by fixing the nuclide flow rate at the inflow position,

$$J^{(i)}(z=0;t) = In^{(i)}(t) \quad (2.50)$$

in the time domain or equivalently $\overline{J}^{(i)}(z=0;s) = \overline{In}^{(i)}(s)$ in the Laplace domain. For the next I boundary conditions, PICNIC has three different options:

$$\partial_z C_f^{(i)}(z=L;t) = 0, \quad (\text{ZG}) \quad (2.51a)$$

$$C_f^{(i)}(z=L;t) = 0, \quad (\text{ZC}) \quad (2.51b)$$

$$C_f^{(i)}(z \rightarrow \infty;t) = 0, \quad (\text{AI}) \quad (2.51c)$$

for all nuclides $i = 1 \dots I$ or the equivalent boundary conditions in the Laplace domain. Zero-gradient (ZG) means that the nuclide flow rate at the channel outlet is purely advective, whereas for zero-concentration (ZC) the nuclide outflow is purely dispersive. Zero-concentration is sometimes considered to describe dilution at the channel outlet. At-infinity (AI) is an artificial boundary condition that has benefits for analytical considerations. These options for the boundary conditions specify that the behaviour in a leg depends only on the properties of the leg and the rate of nuclide flow into it, but not for example on the rate of nuclide flow at the head of the leg. This is basic to the applicability of the pathway/tree method presented in section 2.1.

With the boundary conditions (2.50) and (2.51a, b or c), the eigenvalue problem equation (2.47) can be solved and the vectors $\mathbf{a}'_1(s) \dots \mathbf{a}'_{2I}(s)$ can be determined to obtain the full solution of equation (2.48). Using this solution via

$$\overline{Out}^{(i)}(s) = \sum_{j=1}^I \overline{\mathfrak{R}}^{(i,j)}(z=L;s) \cdot \overline{In}^{(j)}(s) = \overline{J}^{(i)}(z=L;s), \quad (2.52)$$

(cf. equation (2.6)), the response function tensor $\overline{\mathfrak{R}}^{(i,j)}(z=L;s)$ of the leg can be determined. For illustration purpose of illustration this is done in the next subsection for a single nuclide. For a decay chain, the structure of the solution is similar.

2.3. Transport of a Single Nuclide in a Leg

In this subsection we concentrate on transport of a single nuclide in a single leg to illustrate the solution procedure. First the system of balance equations is given in the Laplace domain. The solution is first derived for the case of vanishing micro-dispersion, and the general solution for the case with micro-dispersion is then derived. In this case, the pre-factors ahead of the eigenvectors in this solution depend on the outlet boundary condition of the leg. For the three possible outlet boundary conditions used in PICNIC, the pre-factors are calculated and the leg response function in the Laplace domain is given.

2.3.1. Balance Equations

For a single nuclide, the system of equations (2.45) to (2.46) reduces to

$$\partial_z \begin{pmatrix} \bar{J}(z; s) \\ Q\bar{C}_f(z; s) \end{pmatrix} = \mathbf{A}(s) \begin{pmatrix} \bar{J}(z; s) \\ Q\bar{C}_f(z; s) \end{pmatrix} = \begin{pmatrix} 0 & \Lambda(s) \\ -Pe/L & Pe/L \end{pmatrix} \begin{pmatrix} \bar{J}(z; s) \\ Q\bar{C}_f(z; s) \end{pmatrix}, \quad (2.53)$$

where for brevity the upper index for the nuclide is dropped. Here the eigenvalue is

$$\Lambda(s) = -\frac{\alpha}{L} \left[s + \lambda - \frac{\bar{\eta}(s)}{R_f V_i \varepsilon_i} \right], \quad (2.54)$$

$$\text{and} \quad \alpha = \frac{R_f L}{q/\varepsilon_f} \quad (2.55)$$

is the advection time. As already noted, the only contribution from matrix diffusion is in $\bar{\eta}(s)$. In section 2.5 we will discuss examples for the rock matrix response function $\bar{\eta}(s)$. Here we proceed to calculate the solution. First we consider, for purposes of illustration, the limit of an infinite Peclet number.

2.3.2. Limit of Infinite Peclet Number

When we neglect micro-dispersion in the limit case of $Pe \rightarrow \infty$, the advective nuclide flow rate $QC_f(z; s)$ equals the entire nuclide flow rate $\bar{J}(z; s)$. The first row of the matrix equation above can then be reformulated to

$$\partial_z \bar{J}(z; s) = \Lambda(s) \cdot \bar{J}(z; s), \quad (2.56)$$

while the equation in the second row diverges. With the nuclide flow rate at the inlet as the boundary condition, the z -dependent nuclide flow rate is

$$\bar{J}(z; s) = \bar{\mathfrak{R}}(z; s) \cdot \bar{J}(z=0; s) = e^{z\Lambda(s)} \cdot \bar{J}(z=0; s). \quad (2.57)$$

Particularly at the outlet of the leg at $z = L$ we obtain

$$\bar{\mathfrak{R}}_{Pe \rightarrow \infty}(z=L; s) = e^{L\Lambda(s)} = \exp\left(-\alpha \left[s + \lambda - \frac{\bar{\eta}(s)}{R_f V_i \varepsilon_i} \right]\right), \quad (2.58)$$

which is the response function of the leg needed in the formalism on the scale of the network discussed in section 2.1. Because of conservation of mass, for non-negative, real-valued s , $\bar{\mathfrak{R}}(z; s)$ is positive and real-valued and moreover less than or equal to 1. Thus, $\Lambda(s)$ is real-valued for non-negative real-valued s and moreover less than zero or exactly zero.

2.3.3. General Solution for a Finite Peclet Number

For a finite Peclet number, the eigenvalues of the system of two balance equations (2.53) are

$$K_{1,2}(s) = \frac{Pe}{2L} \left[1 \pm \frac{2\chi(s)}{Pe} \right], \quad (2.59)$$

$$\text{with } \chi(s) = \frac{Pe}{2} \sqrt{1 + \frac{-4L\Lambda(s)}{Pe}}. \quad (2.60)$$

From section 2.3.1, where we considered $\Lambda(s)$, we know that $\chi(s)$ is real-valued for real-valued s , and in particular $\chi(s) \geq Pe/2$ for real-valued s . The general solution of the balance equations is

$$\begin{aligned} \begin{pmatrix} \bar{J}(z; s) \\ Q\bar{C}_f(z; s) \end{pmatrix} &= \left[\mathbf{a}'(s) \exp(zK_1(s)) + \mathbf{b}'(s) \exp(-zK_2(s)) \right] \\ &= \left[\mathbf{a}'(s) \exp\left(\frac{z}{L} \chi(s)\right) + \mathbf{b}'(s) \exp\left(-\frac{z}{L} \chi(s)\right) \right] \exp\left(\frac{z}{L} \frac{Pe}{2}\right), \end{aligned} \quad (2.61a)$$

or equivalently

$$\begin{pmatrix} \bar{J}(z; s) \\ Q\bar{C}_f(z; s) \end{pmatrix} = \begin{bmatrix} a_1(s) \\ a_2(s) \end{bmatrix} \cosh\left(\frac{z-L}{L} \chi(s)\right) + \begin{bmatrix} b_1(s) \\ b_2(s) \end{bmatrix} \sinh\left(\frac{z-L}{L} \chi(s)\right) \exp\left(\frac{z-L}{L} \frac{Pe}{2}\right), \quad (2.61b)$$

see also Robinson, Sharp and Kreisel [1998]. Equation (2.61b) is preferred over equation (2.61a), because of the useful formal relations $\partial_x \sinh(x) = \cosh(x)$, $\partial_x \cosh(x) = \sinh(x)$, $\sinh(-x) = -\sinh(x)$, $\cosh(-x) = \cosh(x)$, $\sinh(x=0) = 0$, $\cosh(x=0) = 1$. The vectors $\mathbf{a}' = \begin{pmatrix} a'_1 \\ a'_2 \end{pmatrix}, \mathbf{b}'$ or equivalently \mathbf{a}, \mathbf{b} must be determined, depending on the boundary conditions, to

calculate $\bar{\mathfrak{R}}(z=L; s)$. In general, for determination of the four parameters, two relations are provided by the eigenvalues of the system and the remaining two conditions are given by the boundary conditions; however we will calculate the parameters here straightforwardly.

2.3.4. At-Infinity Boundary Condition

As mentioned above, we need a second boundary condition in addition to the nuclide inflow rate at $z=0$, and PICNIC has three options. Here we consider the at-infinity boundary condition

$$Q\bar{C}_f(z \rightarrow \infty; s) = 0, \quad (\text{AI}) \quad (2.62)$$

From sections 2.3.1 and 2.3.2, where we considered $\Lambda(s)$, we know that $\chi(s)$ is real-valued for real-valued s , and $\chi(s) \geq \frac{Pe}{2}$. Thus $\mathbf{a}' = 0$, and

$$\bar{\mathfrak{R}}_{AI}(z = L; s) = e^{Pe/2} [\cosh\chi(s) + \sinh\chi(s)]^{-1} = e^{Pe/2 - \chi(s)}. \quad (2.63)$$

2.3.5. Zero-Concentration Boundary Condition

The zero-concentration boundary condition,

$$Q\bar{C}_f(z = L; s) = 0, \quad (\text{ZC}) \quad (2.64)$$

means $a_2 = 0$ in equation (2.60b) and thus

$$Q\bar{C}_f(z; s) = b_2(s) \sinh\left(\frac{z-L}{L} \chi(s)\right) \exp\left(\frac{z-L}{L} \frac{Pe}{2}\right). \quad (2.65)$$

With the definition of $\bar{J}(z; s)$ in equation (2.36) this gives

$$\bar{J}(z; s) = \frac{1}{2} b_2(s) \left[-\frac{2\chi(s)}{Pe} \cosh\left(\frac{z-L}{L} \chi(s)\right) + \frac{1}{2} \sinh\left(\frac{z-L}{L} \chi(s)\right) \right] \exp\left(\frac{z-L}{L} \frac{Pe}{2}\right). \quad (2.66)$$

and particularly

$$\bar{J}(z = 0; s) = \frac{1}{2} b_2(s) \left[-\frac{2\chi(s)}{Pe} \cosh(\chi(s)) - \frac{1}{2} \sinh(\chi(s)) \right] \exp\left(-\frac{Pe}{2}\right) \quad (2.67)$$

and
$$\bar{J}(z = L; s) = \frac{1}{2} b_2(s) \left[-\frac{2\chi(s)}{Pe} \right]. \quad (2.68)$$

This gives in turn

$$\bar{\mathfrak{R}}_{ZC}(z = L; s) = e^{Pe/2} \left\{ \cosh\chi(s) + \frac{Pe}{2\chi(s)} \sinh\chi(s) \right\}^{-1}. \quad (2.69)$$

2.3.6. Zero-Gradient Boundary Condition

For the zero-gradient boundary condition,

$$\partial_z \bar{Q} \bar{C}_f(z=L; s) = 0, \quad (\text{ZG}) \quad (2.70)$$

using equation (2.61b) we start with the ansatz

$$\bar{Q} \bar{C}_f(z; s) = \left[a_2(s) \cosh\left(\frac{z-L}{L} \chi(s)\right) + b_2(s) \sinh\left(\frac{z-L}{L} \chi(s)\right) \right] \exp\left(\frac{z-L}{L} \frac{Pe}{2}\right), \quad (2.71)$$

for the advective nuclide flow rate, which in turn gives

$$-\frac{L}{Pe} \partial_z \bar{Q} \bar{C}_f(z; s) = -\frac{1}{2} \left\{ \begin{aligned} & \left[a_2(s) + \frac{2\chi(s)}{Pe} b_2(s) \right] \cosh\left(\frac{z-L}{L} \chi(s)\right) \\ & + \left[b_2(s) + \frac{2\chi(s)}{Pe} a_2(s) \right] \sinh\left(\frac{z-L}{L} \chi(s)\right) \end{aligned} \right\} \exp\left(\frac{z-L}{L} \frac{Pe}{2}\right) \quad (2.72)$$

for the dispersive nuclide flow rate. For evaluation at $z=0$ we obtain

$$b_2(s) = -\frac{Pe}{2\chi(s)} a_2(s), \quad (2.73)$$

using the ZG boundary condition. Then the definition of $\bar{J}(z; s)$ in equation (2.36) gives

$$\bar{J}(z; s) = a_2(s) \left\{ \cosh\left(\frac{z-L}{L} \chi(s)\right) - \frac{1}{2} \left[\frac{Pe}{2\chi(s)} + \frac{2\chi(s)}{Pe} \right] \sinh\left(\frac{z-L}{L} \chi(s)\right) \right\} \exp\left(\frac{z-L}{L} \frac{Pe}{2}\right). \quad (2.74)$$

With evaluation at $z=0$ and $z=L$,

$$\bar{J}(z=0; s) = a_2(s) \left\{ \cosh(\chi(s)) + \frac{1}{2} \left[\frac{Pe}{2\chi(s)} + \frac{2\chi(s)}{Pe} \right] \sinh(\chi(s)) \right\} \exp\left(-\frac{Pe}{2}\right) \quad (2.75)$$

$$\text{and} \quad \bar{J}(z=L; s) = a_2(s), \quad (2.76)$$

we obtain in turn

$$\bar{\mathfrak{R}}_{ZG}(z=L; s) = e^{Pe/2} \left\{ \cosh\chi(s) + \frac{1}{2} \left[\frac{Pe}{2\chi(s)} + \frac{2\chi(s)}{Pe} \right] \sinh\chi(s) \right\}^{-1}. \quad (2.77)$$

2.4. Transport in the Rock Matrix

Till now we have considered transport on the scale of the network and, on the scale of flowing water in the leg, we have calculated the response function. For the balance equation for the nuclide concentration in the flowing water we still require to know the **rock matrix response tensor**

$\left(\frac{-}{\eta^{(i,j)}}\right)^{i=1\dots I, j=1\dots I}$ (s) which is determined by the nuclide flow rate $-A_m \langle \mathbf{j}_p^{(i)} \cdot \mathbf{e}_n \rangle_{A_m}(z;t)$ from

the region of flowing water into the porous rock matrix. All other quantities are already known.

Therefore in this subsection we analyse the **nuclide balance in the porous rock matrix**.

Boundary and continuity conditions are given and finally it is **discussed how the rock matrix response is determined**.

2.4.1. Balance Equations

For the nuclide balance we consider a small volume $V_p = \Delta x \Delta y \Delta z$, situated at x, y, z , with side-lengths Δx , Δy , Δz respectively. The accessible porosity in the volume filled with stagnant porewater is $\varepsilon_p(x, y)$, and $C_p^{(i)}(x, y, z; t)$ denotes the nuclide concentration of the nuclide (i) in the stagnant porewater. The nuclide inventory in the porewater of this volume is $V_p \varepsilon_p C_p^{(i)}$. If we assume linear equilibrium sorption of the nuclides on the rock matrix, we can again define [e.g. Hadermann and Rösel, 1985] a retardation factor $R_p^{(i)}(x, y)$ that gives the ratio of the amount of nuclides in the entire volume V_p to the amount of nuclides in the rock porewater. Thus the amount of nuclides in V_p is

$$N_p^{(i)}(x, y, z; t) = V_p \varepsilon_p(x, y) R_p^{(i)}(x, y) C_p^{(i)}(x, y, z; t). \quad (2.78)$$

The amount of nuclides in V_p can change with time only by radioactive decay and ingrowth and transport through the bounding surfaces of V_p . Thus the balance equation for $N_p^{(i)}$ can be approximated as

$$\begin{aligned} \partial_t N_p^{(i)}(z; t) = & -\Delta y \Delta z \left[\mathbf{j}_p^{(i)}(x + \Delta x/2, y, z; t) - \mathbf{j}_p^{(i)}(x - \Delta x/2, y, z; t) \right] \cdot \mathbf{e}_x \\ & - \Delta x \Delta z \left[\mathbf{j}_p^{(i)}(x, y + \Delta y/2, z; t) - \mathbf{j}_p^{(i)}(x, y - \Delta y/2, z; t) \right] \cdot \mathbf{e}_y \\ & - \Delta x \Delta y \left[\mathbf{j}_p^{(i)}(x, y, z + \Delta z/2; t) - \mathbf{j}_p^{(i)}(x, y, z - \Delta z/2; t) \right] \cdot \mathbf{e}_z \\ & - \lambda^{(i)} N_p^{(i)}(x, y, z; t) + \lambda^{(i-1)} N_p^{(i-1)}(x, y, z; t) \end{aligned} \quad (2.79)$$

which can be further approximated for small Δx , Δy , Δz as

$$\partial_t N_p^{(i)}(x, y, z; t) = -V_p \nabla \cdot \mathbf{j}_p^{(i)}(x, y, z; t) - \lambda^{(i)} N_p^{(i)}(x, y, z; t) + \lambda^{(i-1)} N_p^{(i-1)}(x, y, z; t) \quad (2.80)$$

Assuming Fickian diffusion, the nuclide flux in the rock matrix is

$$\mathbf{j}_p^{(i)}(x, y, z; t) = -\varepsilon_p(x, y)D_p^{(i)}(x, y)\nabla C_p^{(i)}(x, y, z; t). \quad (2.81)$$

when we restrict to scalar diffusion constants $D_p^{(i)}(x, y)$. We restrict to cases where the overall transport behaviour in the leg parallel to the water flow is dominated by the transport in the flowing water and neglect diffusive flux in the rock matrix parallel to the flow of water. Then the nuclide flux in the rock matrix can be approximated as

$$\mathbf{j}_p^{(i)}(x, y, z; t) = -\varepsilon_p(x, y)D_p^{(i)}(x, y)\nabla_{\perp}C_p^{(i)}(x, y, z; t) \quad (2.82)$$

with $\nabla_{\perp} = \mathbf{e}_x\partial_x + \mathbf{e}_y\partial_y$. Thus the balance equation for the nuclide concentration in the porewater is

$$\begin{aligned} \partial_t C_p^{(i)}(x, y, z; t) = & -\frac{1}{\varepsilon_p(x, y)R_p^{(i)}(x, y)}\nabla_{\perp} \cdot \mathbf{j}_p^{(i)}(x, y, z; t) \\ & -\lambda^{(i)}C_p^{(i)}(x, y, z; t) + \lambda^{(i-1)}\frac{R_p^{(i-1)}(x, y)}{R_p^{(i)}(x, y)}C_p^{(i-1)}(x, y, z; t) \end{aligned} \quad (2.83)$$

or explicitly

$$\begin{aligned} \partial_t C_p^{(i)}(x, y, z; t) = & \frac{1}{\varepsilon_p(x, y)R_p^{(i)}(x, y)}\nabla_{\perp} \cdot \left[\varepsilon_p(x, y)D_p^{(i)}(x, y)\nabla_{\perp}C_p^{(i)}(x, y, z; t) \right] \\ & -\lambda^{(i)}C_p^{(i)}(x, y, z; t) + \lambda^{(i-1)}\frac{R_p^{(i-1)}(x, y)}{R_p^{(i)}(x, y)}C_p^{(i-1)}(x, y, z; t) \end{aligned} \quad (2.84)$$

Till now we have discussed the case that the parameters in the rock matrix such as $D_p^{(i)}(x, y)$ or $\varepsilon_p(x, y)$ may vary in general within the rock matrix. In PICNIC we consider cases where the cross-sectional area of the flowpath is subdivided into a set of part areas or “cells”. Some of these cells are occupied by flowing water and the rock matrix occupies the rest. The cells may be indicated for example by a location (X, Y) within the area or by the rock type in this part area. The parameters $D_p^{(i)}(x, y) = D_p^{(i)}(X, Y)$, $R_p^{(i)}(x, y) = R_p^{(i)}(X, Y)$, $\varepsilon_p(x, y) = \varepsilon_p(X, Y)$ indicate the properties of the rock matrix type in the respective area. The properties may vary from cell to cell, but are constant within each cell. Thus the balance equation in such a cell with rock matrix reduces to

$$\begin{aligned} \partial_t C_p^{(i)}(x, y, z; t) = & \frac{D_p^{(i)}(X, Y)}{R_p^{(i)}(X, Y)}\nabla_{\perp}^2 C_p^{(i)}(x, y, z; t) \\ & -\lambda^{(i)}C_p^{(i)}(x, y, z; t) + \lambda^{(i-1)}\frac{R_p^{(i-1)}(X, Y)}{R_p^{(i)}(X, Y)}C_p^{(i-1)}(x, y, z; t) \end{aligned} \quad (2.85)$$

with $\nabla_{\perp}^2 = \partial_x^2 + \partial_y^2$ and

$$\mathbf{j}_p^{(i)}(x, y, z; t) = -\varepsilon_p(X, Y) D_p^{(i)}(X, Y) \nabla_{\perp} C_p^{(i)}(x, y, z; t). \quad (2.86)$$

See Figure 2.3 for a general example of such a cross-sectional area which, in PICNIC, is subdivided like a checkerboard. (PICNIC can also deal with so-called veins which have a cylindrical geometry, see section 5.)

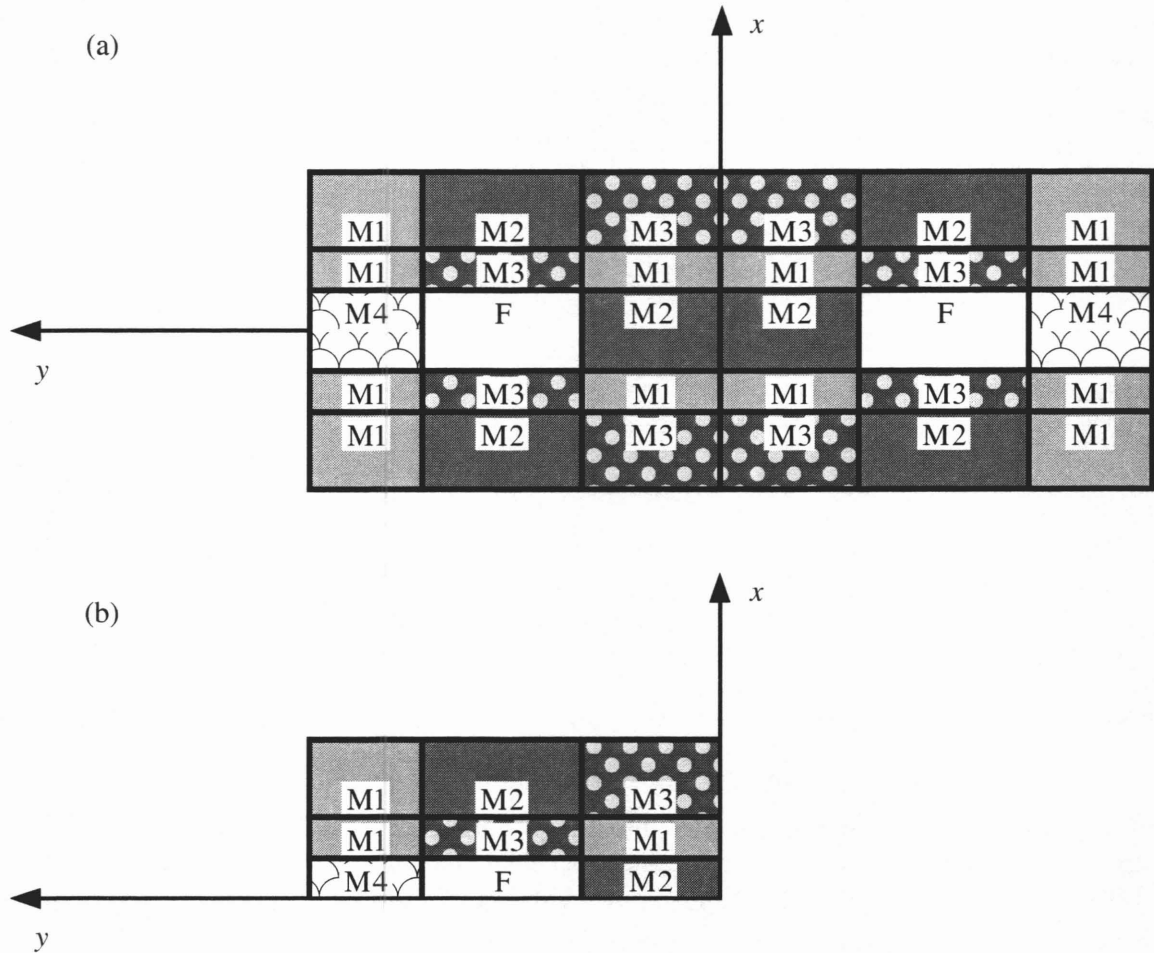


Figure 2.3. (a) Sketch of the cross-section of a leg which is subdivided like a checkerboard of 6 columns and 5 rows into areas of flowing water (F) and areas of rock matrix (M1, M2, M3 or M4). PICNIC requires that the cross-section is mirror-symmetric with respect both to the x -axis and the y -axis, which are indicated by the thinner lines. In (b) the quarter of the cross-sectional area is depicted which needs to be analysed using these symmetries.

The balance equations are transformed into the Laplace domain, giving

$$0 = \frac{D_p^{(i)}(X,Y)}{R_p^{(i)}(X,Y)} \nabla_{\perp}^2 \bar{C}_p^{(i)}(x,y,z;s) - [s + \lambda^{(i)}] \bar{C}_p^{(i)}(x,y,z;s) + \lambda^{(i-1)} \frac{R_p^{(i-1)}(X,Y)}{R_p^{(i)}(X,Y)} \bar{C}_p^{(i-1)}(x,y,z;s) \quad (2.87)$$

$$\text{and} \quad \vec{j}_p^{(i)}(x,y,z;s) = -\varepsilon_p(X,Y) D_p^{(i)}(X,Y) \nabla_{\perp} \bar{C}_p^{(i)}(x,y,z;s). \quad (2.88)$$

Using these symmetries, the combined diffusion/decay/ingrowth problem of equation (2.87) needs to be solved only in a quarter of the cross-sectional area, see Figure 2.3b.⁸ In the example of Figure 2.3b, this is the rate of nuclide flow to the left into the rock matrix type M4, upwards into the rock matrix type M3 and to the right into the rock matrix type M2.

2.4.2. Boundary Conditions

We now explain the boundary conditions for the example of the rock matrix type M4 in Figure 2.3b, which contains all four different possible situations.

(i) The y -axis acting as symmetry line is at the lower boundary of the area M4. Because of this symmetry there is no nuclide flux through this boundary, $\vec{j}_p^{(i)} \cdot \mathbf{e}_n = 0$.

(ii) There is also no flux through the left, outer boundary of M4, $\vec{j}_p^{(i)} \cdot \mathbf{e}_n = 0$, because outer boundaries are assumed to be impermeable.

(iii) The upper boundary of the area M4 is in contact with another type of rock matrix. This type of inner boundary needs 2I boundary or continuity conditions, i.e. two boundary conditions for each nuclide of the decay chain. The first I conditions are given by the continuity of the normal component of the nuclide flux, $\vec{j}_p^{(i)} \cdot \mathbf{e}_n$, at this interface. This ensures conservation of mass in the rock matrix. As the remaining I conditions in PICNIC, the continuity of nuclide concentration $\bar{C}_p^{(i)}(x,y,z;s)$ is assumed at the interface. This means that the pore space in the rock matrix described by $\varepsilon_p(X,Y)$ is well connected, also at the interface of different types of rock matrix.

(iv) Finally at the right side, the area M4 is in contact with the area of flowing water. As mentioned already in section 2.2.3 the continuity of the nuclide concentration

$$\bar{C}_p^{(i)}(x,y,z;s) = \bar{C}_f^{(i)}(z;s) \quad (2.89)$$

⁸ In PICNIC at present it is required to enter leg cross-sections which are symmetrical with respect to the x - and y -axis. Thus for some rock matrix geometries it is necessary to use these symmetry axes to construct a respective leg cross-section to be entered into PICNIC.

for (x,y) at the flowing water/rock matrix interface is used in PICNIC also assuming a well connected pore space at this interface.

2.4.3. Determination of the Rock Matrix Response

We now discuss how the rock matrix response is determined. In our hierarchical linear response concept, the behaviour in the area of flowing water is on a higher level than the behaviour in the rock matrix. From the linearity and the z -independence of the balance equations we know that there is a rock matrix response tensor of functions, $\left(\bar{\eta}^{(i,j)}\right)_{i=1\dots I, j=1\dots I}(s)$, such that

$$-A_m \left\langle \bar{\mathbf{j}}_p^{(i)} \cdot \mathbf{e}_n \right\rangle_{A_m}(z;s) = \sum_{j=1}^I \bar{\eta}^{(i,j)}(s) \cdot \bar{C}_f^{(j)}(z;s), \quad (2.90)$$

cf. equation (2.41). The ‘‘coefficients’’ $\bar{\eta}^{(i,j)}(s)$ are the only quantities which enter into the balance equation in the flowing water and which we need to determine. In general we know, when we perform a test calculation using

$$\bar{C}_f^{(j)}(z;s) = \delta_{j,k} \left[\text{a mol/m}^3 \right] \quad (2.91)$$

in the boundary condition (2.89), with the Kronecker-delta $\delta_{j,k} = 1$ for $j=k$ and $\delta_{j,k} = 0$ for $j \neq k$, then we can determine one column of the coefficient matrix immediately using

$$-A_m \left\langle \bar{\mathbf{j}}_p^{(i)} \cdot \mathbf{e}_n \right\rangle_{A_m}(s) = \sum_{j=1}^I \bar{\eta}^{(i,j)}(s) \cdot \delta_{j,k} \left[\text{a mol/m}^3 \right] = \bar{\eta}^{(i,k)}(s) \left[\text{a mol/m}^3 \right]. \quad (2.92)$$

After going through the different $k = 1\dots I$ test calculations (for each s considered), the entire coefficient matrix $\left(\bar{\eta}^{(i,k)}\right)_{i=1\dots I, k=1\dots I}(s)$ is determined.

In order to determine the rock matrix response $\bar{\eta}^{(i,k)}(s)$, the two-dimensional structure (see Figure 2.3b) is discretised using bilinear finite elements. The system of ‘‘diffusion equations’’ (2.87) for complex ‘‘decay’’ rates $\left[s + \lambda^{(i)} \right]$ with boundary conditions described above is then solved for each Laplace integration point. These equations form a linear algebraic system for a complex concentration value at each node. In PICNIC, this system is solved using a direct solver that has been written for the purpose.

The discretisation uses a rectilinear grid, with the number of elements and their sizes determined from the level of refinement set by the user.

Two factors are important in determining the accuracy of the finite-element approximation. These are the total number of elements and the size of the elements near to interfaces. The importance of the former is obvious, while the latter needs a little more explanation. The need for care at interfaces

arises because there can be steep gradients in cases where the properties change across the interface. It is necessary for the elements to be small enough to accommodate these gradients. The potential inaccuracy that can be caused by not modelling the gradients accurately is exacerbated in cases where the sorption properties differ markedly; even a small error in the aqueous concentration can lead to a large error in the mass distribution. Once the size of the elements next to the interfaces is determined, the other sizes are set as a geometric sequence.

PICNIC determines an appropriate element size by considering the extreme case where the concentration field is constant in one block and then dips sharply to zero in a neighbouring block. The relative mass in this neighbour is proportional to the size of the first element, and this can thus be used to determine a suitable element size.

The user specifies a REFINE level, which is used to scale both the number of elements and their size (via controlling the potential relative mass error). The following Table 2.1 gives the implemented scheme. The number of elements is for each block in each direction. In the overall discretisation, the largest number of elements and smallest element sizes are used for each row and column of the geometry. The number of elements increases if a block has flow neighbours, since the boundary gradients here are directly used in determining the response function. A maximum of 20 elements is imposed. For more details see Robinson [1997a].

REFINE	Elements if no flow block neighbours	Elements if one flow block neighbour	Elements if two flow block neighbours	Factor for relative mass error
1	2	4	6	0.015
2	4	8	12	0.011
3	6	12	18	0.0081
4	8	16	20	0.0060
5	10	20	20	0.0045
6	12	20	20	0.0033
7	14	20	20	0.0024

Table 2.1. Implemented scheme of embedded finite-element method. For more details see text.

We briefly discuss the tensor $\bar{\eta}^{(i,k)}(s)$. For the mother nuclide, $i = 1$, with $\lambda^{(0)} = 0$ the balance equation (2.87) means

$$0 = \frac{D_p^{(1)}(X,Y)}{R_p^{(1)}(X,Y)} \nabla_{\perp}^2 \bar{C}_p^{(1)}(x,y,z;s) - [s + \lambda^{(1)}] \bar{C}_p^{(1)}(x,y,z;s) . \quad (2.93)$$

For $k > 1$ in equation (2.90) it follows that $\bar{C}_p^{(1)}(x,y,z;s) = 0$ and thus $\bar{\eta}^{(1,k)}(s) = 0$. By similar argument we can infer that

$$\bar{\eta}^{(i,k)}(s) = 0 \quad \text{for } i < k , \quad (2.94)$$

and that ingrowth has no influence on the diagonal elements $\bar{\eta}^{(k,k)}(s)$.

2.5. Examples of Rock Matrix Geometries

In the previous subsection we described how the rock matrix response is calculated in principle. In this subsection we consider **some example rock matrix geometries** in more detail.

First we consider the balance equations and the solution for **one-dimensional matrix diffusion of a nuclide decay chain into a homogeneous planar rock matrix layer**.

Then the **solution for a single nuclide** is derived in detail. This solution determines the **timescales** relevant for transport as **lumped parameters**.

For later use in the verification, the limit of an **infinite Peclet number** is then considered in particular for a **very small or a very large rock matrix layer thickness**. Within these limits it is possible to calculate the time-dependent solution analytically.

Then a **single nuclide in a one-dimensional two-layer rock matrix geometry** is considered.

Finally the balance equations are given for a **cylindrical vein geometry** with a surrounding, finite, homogeneous rock matrix layer.

2.5.1. One-Dimensional Planar Rock Matrix

We start with the example of a **homogeneous planar rock matrix** below and above an area of flowing water, as depicted in Figure 2.4. First the system of balance equations is given in the Laplace domain together with the boundary conditions. Then the solution in the Laplace domain is derived.

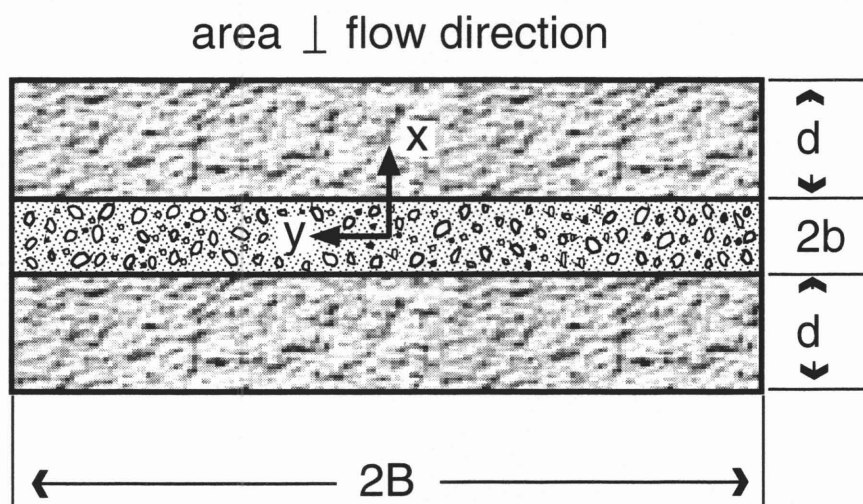


Figure 2.4. Sketch of a cross-section through a parallel plate channel with an adjacent rock layer accessible for matrix diffusion. The sketch is not to scale. Thickness of the water-conducting feature is $2b$. Thickness of the rock matrix below and above the water-conducting feature, that is available for matrix diffusion, is d .

A leg of length L in the z -direction is considered with a rectangular cross-section. The area of flowing water centered at $x = 0$, $y = 0$ is filled with infill of porosity ε_i . The aperture of the area of flowing water in the x -direction is $2b$ and the width in y -direction is $2B$. Thus, for simplicity⁹,

⁹ When more than one fracture with the same properties is considered in the same leg, then the cross-sectional area of the flowing water increases accordingly.

$A_i = 2b2B$ is the cross-section of the area of flowing water and we again define a volume of the "area" with flowing water as $V_i = A_i \Delta z$ for a slice of length Δz . The whole cross-section of the leg considered, A_f , may be larger. The flow porosity is ε_f and water flows with constant velocity $(q / \varepsilon_f) \mathbf{e}_z$ through the channel. Below and above the area of flowing water, a homogeneous layer of rock with porosity ε_p is situated. The width of the porous rock matrix is $2B$, as for the area of flowing water. The thickness of the rock matrix layers available for matrix diffusion is d . Because of the cross-sectional geometry of the leg, the behaviour in the rock matrix is y -independent and matrix diffusion is one-dimensional in the x -direction only. Thus $C_p^{(i)}(x, z; t)$ describes the nuclide concentration in the porewater and, for the rock matrix, there exists only a single set of parameters $D_p^{(i)}$, $R_p^{(i)}$ and ε_p . In this case, transport of nuclides in the rock matrix is described by the balance equations

$$\partial_t C_p^{(i)}(x, z; t) = \frac{D_p^{(i)}}{R_p^{(i)}} \partial_x^2 C_p^{(i)}(x, z; t) - \lambda^{(i)} C_p^{(i)}(x, z; t) + \lambda^{(i-1)} \frac{R_p^{(i-1)}}{R_p^{(i)}} C_p^{(i-1)}(x, z; t) \quad (2.95)$$

for the concentrations of the nuclides $i = 1 \dots I$ in the rock matrix.

At the interface between the channel and the rock matrix at $|x| = b$, the continuity condition

$$C_p^{(i)}(|x| = b, z; t) = C_f^{(i)}(z; t) \quad (2.96)$$

is assumed for all z and t . For the limited matrix diffusion considered here, there is zero nuclide flux beyond the given distance d from the edge of the water-conducting feature,

$$j_p^{(i)}(|x| = b + d, z; t) = 0 \quad (2.97)$$

for all t , where the nuclide flux in the rock matrix is $\mathbf{j}_p^{(i)}(x, z; t) = \mathbf{e}_x j_p^{(i)}(x, z; t)$ with

$$j_p^{(i)}(x, z; t) = -\varepsilon_p D_p^{(i)} \partial_x C_p^{(i)}(x, z; t). \quad (2.98)$$

The Laplace transformed balance equations and nuclide flux in the rock matrix are

$$0 = \frac{D_p^{(i)}}{R_p^{(i)}} \partial_x^2 \bar{C}_p^{(i)}(x, z; s) - [s + \lambda^{(i)}] \bar{C}_p^{(i)}(x, z; s) + \lambda^{(i-1)} \frac{R_p^{(i-1)}}{R_p^{(i)}} \bar{C}_p^{(i-1)}(x, z; s) \quad (2.99)$$

and
$$\bar{j}_p^{(i)}(x, z; s) = -\varepsilon_p D_p^{(i)} \partial_x \bar{C}_p^{(i)}(x, z; s). \quad (2.100)$$

When we again define a slice of the leg of length Δz , the nuclide flow rate in the rock matrix in this slice is

$$\bar{\mathbf{J}}_p^{(i)}(x,z;s) = A_p \bar{\mathbf{J}}_p^{(i)}(x,z;s) = \mathbf{e}_x A_p \bar{J}_p^{(i)}(x,z;s), \quad (2.101)$$

with the area $A_p = 2B \Delta z$. The system of second order differential equations (2.99) for the nuclide concentrations $\left(\bar{C}_p^{(i)}\right)^{i=1\dots I}(x,z;s)$ can be rewritten as a system of first order differential equations for the nuclide flow rate $\left(\bar{J}_p^{(i)}\right)^{i=1\dots I}(x,z;s)$ and the nuclide concentration:

$$\partial_x \bar{J}_p^{(i)}(x,z;s) = -A_p \varepsilon_p R_p^{(i)} \left[s + \lambda^{(i)} \right] \bar{C}_p^{(i)}(x,z;s) + A_p \varepsilon_p R_p^{(i-1)} \lambda^{(i-1)} \bar{C}_p^{(i-1)}(x,z;s) \quad (2.102)$$

which is completed by the definition of the nuclide flow rate

$$\partial_x \bar{C}_p^{(i)}(x,z;s) = -\frac{1}{A_p \varepsilon_p D_p^{(i)}} \bar{J}_p^{(i)}(x,z;s), \quad (2.103)$$

such that we have $2I$ balance equations for $2I$ independent quantities. Similar to the behaviour in a leg considered in section 2.2.3, the system of balance equations (2.102) to (2.103) is an eigenvalue equation system,

$$\partial_z \begin{pmatrix} \bar{C}_p^{(1)}(x,z;s) \\ \bar{J}_p^{(1)}(x,z;s) \\ \vdots \\ \bar{C}_p^{(I)}(x,z;s) \\ \bar{J}_p^{(I)}(x,z;s) \end{pmatrix} = \mathbf{A}(s) \begin{pmatrix} \bar{C}_p^{(1)}(x,z;s) \\ \bar{J}_p^{(1)}(x,z;s) \\ \vdots \\ \bar{C}_p^{(I)}(x,z;s) \\ \bar{J}_p^{(I)}(x,z;s) \end{pmatrix}. \quad (2.104)$$

Because of the linearity of this equation system and because of the constant parameters in $\mathbf{A}(s)$, the solution of this system of balance equations is in general

$$\begin{pmatrix} \bar{C}_p^{(1)}(x,z;s) \\ \bar{J}_p^{(1)}(x,z;s) \\ \vdots \\ \bar{C}_p^{(I)}(x,z;s) \\ \bar{J}_p^{(I)}(x,z;s) \end{pmatrix} = \bar{\mathbf{M}}(x;s) \begin{pmatrix} \bar{C}_p^{(1)}(b,z;s) \\ \bar{J}_p^{(1)}(b,z;s) \\ \vdots \\ \bar{C}_p^{(I)}(b,z;s) \\ \bar{J}_p^{(I)}(b,z;s) \end{pmatrix} \quad (2.105)$$

with the $(2I \times 2I)$ -dimensional response tensor $\bar{\mathbf{M}}(x;s)$. To obtain $\bar{\mathbf{M}}(x;s)$ the eigenvalue equation (2.104) has to be solved. Also the boundary conditions (2.96) to (2.97) have to be used to

calculate the rock matrix response function tensor $\left(\bar{\eta}^{(i,j)}\right)^{i=1\dots I, j=1\dots I}(s)$ via equation (2.90). For this geometry

$$-A_m \left\langle \bar{\mathbf{j}}_p^{(i)} \cdot \mathbf{e}_n \right\rangle_{A_m}(z; s) = -\left[\bar{J}_p^{(i)}(x=b, z; s) - \bar{J}_p^{(i)}(x=-b, z; s) \right] = -2\bar{J}_p^{(i)}(x=b, z; s), \quad (2.106)$$

for symmetry reasons.

2.5.2. Single Nuclide in a One-Dimensional Planar Rock Matrix

Now we derive and discuss the **solution for a single nuclide** in a one-dimensional rock matrix geometry, because we will use it later for the verification of PICNIC. For a single nuclide, the system of equations (2.102) to (2.103) reduces to

$$\partial_z \begin{pmatrix} \bar{C}_p(x, z; s) \\ \bar{J}_p(x, z; s) \end{pmatrix} = \mathbf{A}(s) \begin{pmatrix} \bar{C}_p(x, z; s) \\ \bar{J}_p(x, z; s) \end{pmatrix} = \begin{pmatrix} 0 & -\frac{1}{A_p \varepsilon_p D_p} \\ -A_p R_p \varepsilon_p [s + \lambda] & 0 \end{pmatrix} \begin{pmatrix} \bar{C}_p(x, z; s) \\ \bar{J}_p(x, z; s) \end{pmatrix}, \quad (2.107)$$

where, for brevity, the upper index for the nuclide is dropped. The solution of this system of equations is in general

$$\begin{pmatrix} \bar{C}_p(x, z; s) \\ \bar{J}_p(x, z; s) \end{pmatrix} = \begin{pmatrix} \bar{\mathbf{M}}^{(1,1)}(x; s) & \bar{\mathbf{M}}^{(1,2)}(x; s) \\ \bar{\mathbf{M}}^{(2,1)}(x; s) & \bar{\mathbf{M}}^{(2,2)}(x; s) \end{pmatrix} \begin{pmatrix} \bar{C}_p(b, z; s) \\ \bar{J}_p(b, z; s) \end{pmatrix}. \quad (2.108)$$

Taking into account the continuity equation (2.96) at the flowing water/rock matrix interface and the zero-flow boundary condition (2.97), evaluating at the end of the rock matrix at $x = b + d$ gives

$$\begin{pmatrix} \bar{C}_p(x=b+d, z; s) \\ 0 \end{pmatrix} = \begin{pmatrix} \bar{\mathbf{M}}^{(1,1)}(x=b+d; s) & \bar{\mathbf{M}}^{(1,2)}(x=b+d; s) \\ \bar{\mathbf{M}}^{(2,1)}(x=b+d; s) & \bar{\mathbf{M}}^{(2,2)}(x=b+d; s) \end{pmatrix} \begin{pmatrix} \bar{C}_f(z; s) \\ \bar{J}_p(b, z; s) \end{pmatrix}. \quad (2.109)$$

Evaluating the second row gives

$$\bar{J}_p(x=b, z; s) = -\frac{1}{2} \bar{\eta}(s) \bar{C}_f(z; s). \quad (2.110)$$

$$\text{with} \quad \frac{1}{2} \bar{\eta}(s) = \frac{\bar{\mathbf{M}}^{(2,1)}(x=b+d; s)}{\bar{\mathbf{M}}^{(2,2)}(x=b+d; s)}, \quad (2.111)$$

which we wished to calculate.¹⁰ Note that inserting $\bar{\eta}(s)$ into equation (2.108) yields nuclide flow rate and concentration in the rock matrix via

$$\begin{pmatrix} \bar{C}_p(x, z; s) \\ \bar{J}_p(x, z; s) \end{pmatrix} = \begin{pmatrix} \bar{M}^{(1,1)}(x; s) & \bar{M}^{(1,2)}(x; s) \\ \bar{M}^{(2,1)}(x; s) & \bar{M}^{(2,2)}(x; s) \end{pmatrix} \begin{pmatrix} 1 \\ \frac{1}{2} \bar{\eta}(s) \end{pmatrix} \bar{C}_f(z; s). \quad (2.112)$$

Now it remains to calculate the (2×2) -dimensional response tensor $\bar{M}(x; s)$ by solving the eigenvalue equation (2.108). The eigenvalues of (2.108) as functions of s are

$$\Gamma_{1,2}(s) = \pm \Gamma(s) = \pm \sqrt{\frac{[s + \lambda] R_p}{D_p}}. \quad (2.113)$$

We denote the corresponding eigenvectors as $\mathbf{v}_1(s)$ and $\mathbf{v}_2(s)$ and

$$\begin{pmatrix} \bar{C}_p(x, z; s) \\ \bar{J}_p(x, z; s) \end{pmatrix} = A(s) \mathbf{v}_1(s) \exp(\Gamma(s)[x - b]) + B(s) \mathbf{v}_2(s) \exp(-\Gamma(s)[x - b]), \quad (2.114)$$

with the coefficients $A(s)$ and $B(s)$. In the basis system $(\bar{C}_p(s), \bar{J}_p(s))$, the eigenvectors are represented by

$$\mathbf{v}_1(s) = \begin{pmatrix} \frac{1}{A_p \varepsilon_p D_p} \\ -\Gamma(s) \end{pmatrix}, \quad \mathbf{v}_2(s) = \begin{pmatrix} \frac{1}{A_p \varepsilon_p D_p} \\ \Gamma(s) \end{pmatrix}. \quad (2.115)$$

Thus the transformation matrix from the eigenvector basis system to the $(\bar{C}_p(s), \bar{J}_p(s))$ basis system is

$$\bar{\mathbf{D}}^{-1}(s) = \begin{pmatrix} \frac{1}{A_p \varepsilon_p D_p} & \frac{1}{A_p \varepsilon_p D_p} \\ -\Gamma(s) & \Gamma(s) \end{pmatrix}, \quad (2.116)$$

and the transformation matrix from the $(\bar{C}_p(s), \bar{J}_p(s))$ basis system to the eigenvector basis system is

¹⁰ Note that the quantity $\frac{1}{2} \bar{\eta}(s)$ was denoted as $\eta(s + \lambda)$ in Barten [1996a].

$$\bar{\mathbf{D}}(s) = \begin{pmatrix} \frac{A_p \varepsilon_p D_p}{2} & -\frac{1}{2\Gamma(s)} \\ \frac{A_p \varepsilon_p D_p}{2} & \frac{1}{2\Gamma(s)} \end{pmatrix}. \quad (2.117)$$

The propagation ($x = b$) \rightarrow ($x = b + x_1$) in the eigenvector system is given by the diagonal matrix

$$\bar{\mathbf{P}}(x; s) = \begin{pmatrix} \exp([x - b]\Gamma(s)) & 0 \\ 0 & \exp(-[x - b]\Gamma(s)) \end{pmatrix} \quad (2.118)$$

for positive x . Negative x are related by symmetry. Thus the response tensor is determined through

$$\bar{\mathbf{M}}(x; s) = \bar{\mathbf{D}}^{-1}(s) \bar{\mathbf{P}}(x; s) \bar{\mathbf{D}}(s) \quad (2.119)$$

$$\begin{aligned} \bar{\mathbf{M}}(x; s) &= \begin{pmatrix} \cosh([x - b]\Gamma(s)) & -\frac{\sinh([x - b]\Gamma(s))}{A_p \varepsilon_p D_p \Gamma(s)} \\ -A_p \varepsilon_p D_p \Gamma(s) \sinh([x - b]\Gamma(s)) & \cosh([x - b]\Gamma(s)) \end{pmatrix} \\ \text{as} & \\ &= \cosh([x - b]\Gamma(s)) \begin{pmatrix} 1 & -\frac{\tanh([x - b]\Gamma(s))}{A_p \varepsilon_p D_p \Gamma(s)} \\ -A_p \varepsilon_p D_p \Gamma(s) \tanh([x - b]\Gamma(s)) & 1 \end{pmatrix}. \end{aligned} \quad (2.120)$$

for positive x . Using (2.111) and evaluating $\bar{\mathbf{M}}(x; s)$ at $x = b + d$ we arrive at

$$\frac{1}{2} \bar{\eta}(s) = -A_p \varepsilon_p D_p \Gamma(s) \tanh(d\Gamma(s)) = -A_p \varepsilon_p \sqrt{D_p R_p} \sqrt{s + \lambda} \tanh\left(\sqrt{\frac{d^2 R_p}{D_p}} \sqrt{s + \lambda}\right). \quad (2.121)$$

See Robinson and Maul [1991] for a similar response coefficient function. We now discuss some special cases. If there is no nuclide diffusion into the rock matrix, $J_p = 0$, then

$$\frac{1}{2} \bar{\eta}(s) = 0. \quad (2.122)$$

For a thin rock matrix with fast diffusion processes, i.e. heuristically for “small” $\sqrt{\frac{d^2 R_p}{D_p}} \sqrt{s + \lambda}$, with $\tanh(X) \approx X$, then we get

$$\frac{1}{2} \bar{\eta}(s) \approx -A_p \varepsilon_p R_p d [s + \lambda]. \quad (2.123)$$

For unlimited matrix diffusion, i.e. heuristically for “large” $\sqrt{\frac{d^2 R_p}{D_p} \sqrt{s + \lambda}}$, with $\tanh(X \rightarrow \infty) \approx 1$, then

$$\frac{1}{2} \bar{\eta}(s) = -A_p \varepsilon_p \sqrt{D_p R_p} \sqrt{s + \lambda}. \quad (2.124)$$

The rock matrix response function $\bar{\eta}(s)$ enters into the area of flowing water eigenvalue $\Lambda(s)$, cf. equation (2.54),

$$\begin{aligned} L\Lambda(s) &= -[s + \lambda] \alpha - \frac{L \varepsilon_p \sqrt{D_p R_p}}{q/\varepsilon_f} \frac{2A_p}{V_i \varepsilon_i} \sqrt{s + \lambda} \tanh \left(\sqrt{\frac{d^2 R_p}{D_p} \sqrt{s + \lambda}} \right), \\ &= -[s + \lambda] \alpha - \gamma \sqrt{s + \lambda} \tanh(\beta \sqrt{s + \lambda}) \end{aligned} \quad (2.125)$$

with the geometrical **surface to volume ratio** $\delta_f = \frac{2A_p}{V_i} = \frac{1}{b}$. (2.126)

$L\Lambda(s)$ is determined by four **timescales**:

the **advection time** $\alpha = \frac{R_f L}{q/\varepsilon_f}$, (2.127)

the **matrix diffusion time** $\beta^2 = \frac{d^2 R_p}{D_p}$, (2.128)

the **matrix delay time** $\gamma^2 = \left[\frac{L \varepsilon_p \sqrt{D_p R_p}}{q/\varepsilon_f} \frac{\delta_f}{\varepsilon_i} \right]^2$, (2.129)

and the **nuclide half-life** $T_{1/2} = \frac{\ln 2}{\lambda}$. (2.130)

The finite Peclet number introduces a further independent timescale for transport in a single leg. The notation and names of α, β, γ are from Barten [1996a]; Barten and Robinson [1996]. Only the definition of γ is slightly extended, because we now distinguish between ε_f and ε_i .

As an aside, note that other definitions for the timescales and another notation are also possible, cf. for example literature on the Grimsel dipole experiment (where $\varepsilon_i = 1$ was used). Note that the timescales from the Grimsel literature can be related to the time scales β^2 and γ^2 as

$$\frac{2}{3}t_{MD} = \frac{2}{3}\tau_0 = \frac{1}{6}\gamma^2 \quad (2.131)$$

$$\text{and} \quad t_{MP} = \frac{1}{5}t_p(2d) = \frac{1}{5}\beta^2. \quad (2.132)$$

In the Grimsel literature the quantity τ_0 is denoted as a delay parameter [page 41 in Heer and Hadermann, 1994] or as a time shift [page 93 in Hadermann and Heer, 1996]. The quantity $t_p(x)$ is denoted as penetration time [equation (31e) on page 53 in Heer and Hadermann, 1994]. Heer and Smith [1998] denote the quantity t_{MD} as matrix diffusion time and t_{MP} as matrix propagation time.

Let us now return to the **special cases**. If there is **no nuclide diffusion** into the rock matrix, then

$$L\Lambda(s) = -[s + \lambda]\alpha. \quad (2.133)$$

For a **thin rock matrix** with fast diffusion processes, then

$$L\Lambda(s) \approx -[s + \lambda][\alpha + \beta\gamma] = -[s + \lambda]\alpha \left[1 + \frac{\beta\gamma}{\alpha}\right], \quad (2.134)$$

and matrix diffusion acts like linear sorption in the area of flowing water. The increased retardation is determined by

$$\text{the nuclide capacity ratio} \quad \frac{\beta\gamma}{\alpha} = \frac{\varepsilon_p R_p}{\varepsilon_i R_f} d\delta_f, \quad (2.135)$$

of the rock matrix and the area of flowing water, where $d\delta_f = \frac{d}{b}$ is the geometrical volume ratio.

For **unlimited matrix diffusion**,

$$L\Lambda(s) = -[s + \lambda]\alpha - \gamma\sqrt{s + \lambda}. \quad (2.136)$$

2.5.3. Unlimited and Strongly Limited Rock Matrix Diffusion and the Limit of an Infinite Peclet Number for a Single Nuclide

We have seen that we can calculate solutions for the rock matrix response and thus also the response functions of single legs and entire networks fully analytically in the Laplace domain. However, in general for the inverse Laplace transformation a numerical method like Talbot's method [Talbot, 1979] has to be used, see section 2.7. This is done in PICNIC. Analytical solutions, which are discussed in this subsection, however, (already in limit cases, like for long times) have many benefits: they are very instructive, help to understand the transport behaviour and support the verification. In the limit of an infinite Peclet number¹¹, in some cases the analytical solution can be derived also in the time domain.

In this subsection we consider the response function of a **single nuclide in a single leg with an unlimited rock matrix**.

At the end of this subsection we will also give the solution for a **strongly limited rock matrix**.

When we **neglect micro-dispersion** in the limit of $Pe \rightarrow \infty$, the Laplace transformed response function of a single leg is

$$\overline{\mathfrak{R}}_{Pe \rightarrow \infty}(s) = e^{L\Lambda(s)} = \exp(-[s + \lambda]\alpha - \gamma\sqrt{s + \lambda}), \quad (2.137)$$

using equations (2.58) and (2.124). The time-dependent response function is

$$\mathfrak{R}_{Pe \rightarrow \infty}(t) = L^{-1}\{\overline{\mathfrak{R}}_{Pe \rightarrow \infty}(s)\} = L^{-1}\{\exp(-[s + \lambda]\alpha - \gamma\sqrt{s + \lambda})\}, \quad (2.138)$$

where L^{-1} formally indicates the numerical inverse Laplace transformation. Using the formal relation

$$L^{-1}\{\overline{f}(as + b)\}(t) = \frac{1}{a} \exp\left(-\frac{bt}{a}\right) \cdot f\left(\frac{t}{a}\right), \quad (2.139)$$

given e.g. in equation (1.1.1.4) in Prudnikov, Brychkov and Marichev [1992], we obtain

$$\mathfrak{R}_{Pe \rightarrow \infty}(t) = e^{-\lambda t} L^{-1}\{\overline{\mathfrak{R}}_{Pe \rightarrow \infty, \lambda \rightarrow 0}(s)\}(t) = e^{-\lambda t} L^{-1}\{e^{-s\alpha} \exp(-\gamma\sqrt{s})\}(t). \quad (2.140)$$

We would like to mention here that the first half of this relation holds in general for single nuclides, because the quantities s and λ are found only in the combined form $[s + \lambda]$ in the balance equations in the area of flowing water and the rock matrix. Using further

$$L^{-1}\{e^{-bs} \overline{f}(as)\}(t) = \frac{1}{a} \theta(t - a) \cdot f\left(\frac{t - b}{a}\right), \quad (2.141)$$

¹¹ Note that the limit of an infinite Peclet number is not implemented in PICNIC. And, as we will see later, it actually cannot be approached by PICNIC, because of numerical instabilities.

given e.g. in equation (1.1.2.1) in Prudnikov, Brychkov and Marichev [1992], we obtain

$$\begin{aligned}\mathfrak{R}_{Pe \rightarrow \infty}(t) &= e^{-\lambda t} \theta(t - \alpha) \cdot L^{-1} \left\{ \overline{\mathfrak{R}}_{Pe \rightarrow \infty, \lambda \rightarrow 0, \alpha \rightarrow 0}(s) \right\} (t - \alpha) \\ &= e^{-\lambda t} \theta(t - \alpha) \cdot L^{-1} \left\{ \exp(-\gamma \sqrt{s}) \right\} (t - \alpha)\end{aligned}\quad (2.142)$$

We would like to mention here that also the first half of this relation holds in general for single nuclides, because of the form of $\Lambda(s)$ in equations (2.54) and (2.58). Using further

$$L^{-1} \left\{ \exp(a \sqrt{s}) \right\} (t) = \frac{a}{2\sqrt{\pi}} t^{-3/2} \cdot \exp\left(-\frac{a^2}{4t}\right), \quad (2.143)$$

given e.g. in equation (2.2.1.9) in Prudnikov, Brychkov and Marichev [1992], we obtain finally

$$\mathfrak{R}_{Pe \rightarrow \infty}(t) = e^{-\lambda t} \theta(t - \alpha) \cdot \frac{\gamma}{2\sqrt{\pi}} [t - \alpha]^{-3/2} \cdot \exp\left(-\frac{\gamma^2}{4[t - \alpha]}\right). \quad (2.144)$$

This form of the response function, which also gives directly the nuclide flow rate for a δ -function source and variants of it are well known in the literature, e.g. Hadermann [1981]; Sudicky and Frind [1984]; Lever and Bradbury [1985]; appendix 3 in Jakob and Hadermann [1994] and references cited therein).

Considering this nuclide flow rate for a δ -function source in the case of a non-decaying nuclide, $\lambda = 0$, the advection time α gives the breakthrough time of the system when only advection is considered. Because of the factor $\theta(t - \alpha)$ no release is observed for $t < \alpha$. The maximum of the nuclide flow rate is at

$$t_{\max} = \alpha + \frac{\gamma^2}{6} \quad \text{with a maximum value} \quad \sqrt{\frac{3}{2\pi e^3}} \frac{6}{\gamma^2} = \sqrt{\frac{3}{2\pi e^3}} \frac{1}{t_{\max} - \alpha}. \quad (2.145)$$

For **long times**, $4[t - \alpha] \gg \gamma^2$, the **non-decaying nuclide** shows the typical $t^{-3/2}$ fingerprint [Heer and Hadermann, 1994; Hadermann and Heer, 1996] of **unlimited matrix diffusion**,

$$\mathfrak{R}_{Pe \rightarrow \infty}(t) \sim [t - \alpha]^{-3/2}. \quad (2.146)$$

We finally consider the case of **strongly limited matrix diffusion**, where the Laplace transformed response function of a single leg is

$$\overline{\mathfrak{R}}_{Pe \rightarrow \infty}(s) = e^{L\Lambda(s)} = \exp\left(-[s + \lambda][\alpha + \beta\gamma]\right), \quad (2.147)$$

using equations (2.58) and (2.134). The time-dependent response function is then

$$\Re_{Pe \rightarrow \infty}(t) = e^{-\lambda t} \cdot \delta(t - [\alpha + \beta\gamma]), \quad (2.148)$$

with $\delta(t)$ being the Dirac delta function. L^{-1} indicates the numerical inverse Laplace transformation.

The cases with a finite rock matrix lie between these two cases. The matrix diffusion time β^2 is the typical timescale for diffusion in the rock matrix. For $t \ll \beta^2$, the system behaves as if matrix diffusion were unlimited. On the other hand, for $t \gg \beta^2$ the concentration in the rock matrix can be considered as being in “instantaneous” equilibrium with the concentration in the flowpath. Then the rock matrix acts like surface sorption in the flowpath.

2.5.4. Single Nuclide in a One-Dimensional Two-Layer Planar Rock Matrix

We now derive and discuss the solution for a **single nuclide** in a one-dimensional **two-layer planar rock matrix geometry**, because we will use it later for the verification of PICNIC. This situation is similar to the single-layer case, cf. Figure 2.4. Above and below the flowpath there is again a finite rock matrix filled with stagnant porewater. This rock matrix now consists, however, of two adjacent layers of rock matrix in series, layer 1 with extent d_1 and layer 2 with extent d_2 as depicted in Figure 2.5.

The transport in the porous rock layers is purely diffusive with

$$\begin{aligned} \partial_t C_p(x,z;t) &= \frac{D_{p,1}}{R_{p,1}} \partial_x^2 C_p(x,z;t) - \lambda C_p(x,z;t) \\ \partial_t C_p(x,z;t) &= \frac{D_{p,2}}{R_{p,2}} \partial_x^2 C_p(x,z;t) - \lambda C_p(x,z;t) \end{aligned} \quad (2.149)$$

in rock layers 1 and 2, respectively. $D_{p,1}$ is the diffusion constant, $R_{p,1}$ is the retardation constant due to linear sorption, $\varepsilon_{p,1}$ is the porosity in rock layer 1. Similar definitions hold for rock layer 2. For symmetry reasons, there is again no diffusion in the y -direction. Consequently, the nuclide flux in the rock matrix is

$$j_p(x,z;t) = -\varepsilon_{p,1} D_{p,1} \partial_x C_p(x,z;t) \quad \text{in layer 1} \quad (2.150a)$$

$$j_p(x,z;t) = -\varepsilon_{p,2} D_{p,2} \partial_x C_p(x,z;t) \quad \text{in layer 2.} \quad (2.150b)$$

Thus, for the one-dimensional rock matrix geometry considered here we obtain the well known relation

$$\langle \mathbf{j}_p \cdot \mathbf{e}_n \rangle(z;t) = j_p(x = b,z;t) = -\varepsilon_{p,1} D_{p,1} \partial_x C_p(x = b,z;t), \quad (2.151)$$

for the rock matrix diffusion term.

At the interface between the two porous rock layers the concentration in the porewater and the nuclide flux normal to the interface are continuous,

$$C_p(|x| = b + d_{1,-}, z; t) = C_p(|x| = b + d_{1,+}, z; t), \quad (2.152a)$$

$$j_p(|x| = b + d_{1,-}, z; t) = j_p(|x| = b + d_{1,+}, z; t). \quad (2.152b)$$

For the limited matrix diffusion considered, there is a zero nuclide flux beyond a given distance $d_1 + d_2$ from the edge of the water-conducting feature,

$$j_p(|x| = b + d_1 + d_2, z; t) = 0. \quad (2.153)$$

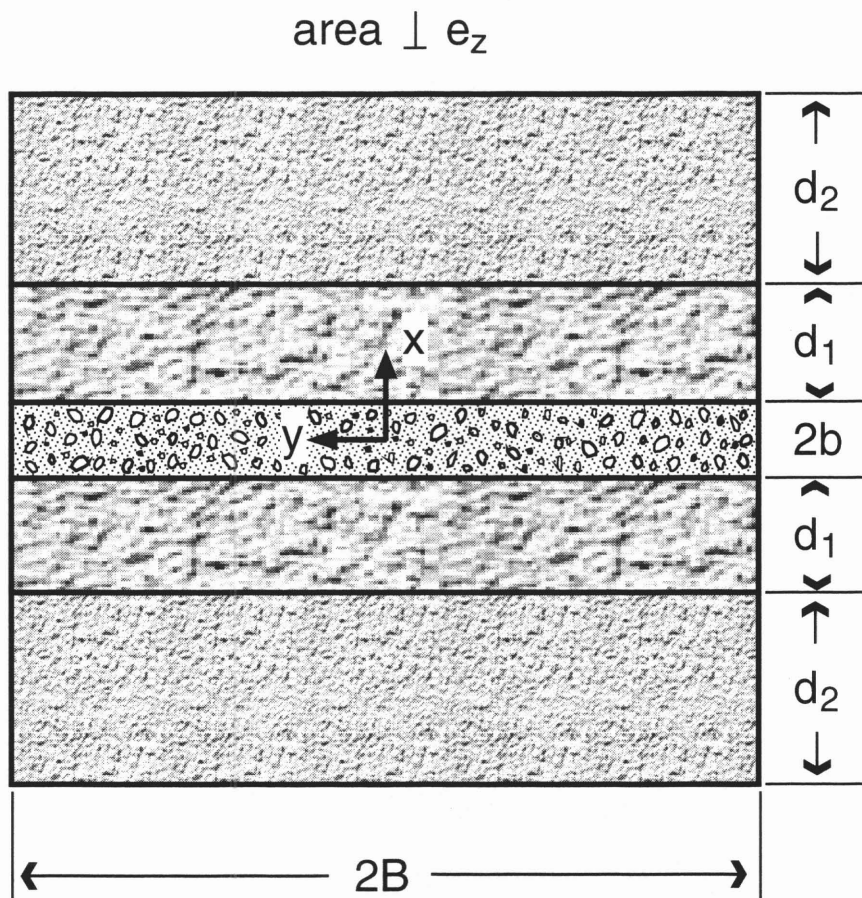


Figure 2.5. Sketch of a cross-section through a parallel plate channel with two rock layers in series.

For this system of balance equations we can again define two 2×2 rock matrix response tensors $\overline{M}_1(x; s)$ and $\overline{M}_2(x; s)$, as for the single-layer case, such that

$$\begin{pmatrix} \bar{C}_p(x, z; s) \\ \bar{J}_p(x, z; s) \end{pmatrix} = \bar{M}_1(x; s) \begin{pmatrix} \bar{C}_p(b, z; s) \\ \bar{J}_p(b, z; s) \end{pmatrix} \quad \text{for } b \leq x \leq b + d_1 \quad (2.154)$$

$$\text{and } \begin{pmatrix} \bar{C}_p(x, z; s) \\ \bar{J}_p(x, z; s) \end{pmatrix} = \bar{M}_2(x; s) \begin{pmatrix} \bar{C}_p(b + d_1, z; s) \\ \bar{J}_p(b + d_1, z; s) \end{pmatrix} \quad \text{for } b + d_1 \leq x \leq b + d_1 + d_2. \quad (2.155)$$

(For negative x we can use the symmetry of the system.) The tensors $\bar{M}_1(x; s)$ and $\bar{M}_2(x; s)$ have the same form as for the single-layer case in equation (2.120). Using the continuity conditions (2.152a,b) at the interface, $|x| = b + d_1$, between the two rock layers, we can directly define a rock matrix response tensor, $\bar{M}(x; s)$, for the whole rock matrix, such that

$$\begin{pmatrix} \bar{C}_p(x, z; s) \\ \bar{J}_p(x, z; s) \end{pmatrix} = \bar{M}(x; s) \begin{pmatrix} \bar{C}_p(b, z; s) \\ \bar{J}_p(b, z; s) \end{pmatrix} \quad \text{for } b \leq x \leq b + d_1 + d_2 \quad (2.156)$$

$$\text{with } \bar{M}(x; s) = \bar{M}_1(x; s) \quad \text{for } b \leq x \leq b + d_1 \quad \text{and } (2.157)$$

$$\bar{M}(x = b + d_1 + x_2; s) = \bar{M}_2(b + d_1 + x_2; s) \bar{M}_1(b + d_1; s) \quad \text{for } b + d_1 \leq x \leq b + d_1 + d_2. \quad (2.158)$$

At the end of the accessible rock matrix we obtain for

$$\begin{aligned} \bar{M}(x; s) = & \cosh(d_1 \Gamma_1(s)) \cdot \cosh(d_2 \Gamma_2(s)) \cdot \\ & \left(\begin{array}{l} 1 + \frac{\left\{ A_p \varepsilon_p D_p \Gamma(s) \right\}_1}{\left\{ A_p \varepsilon_p D_p \Gamma(s) \right\}_2} \tanh(d_1 \Gamma_1(s)) \tanh(d_2 \Gamma_2(s)) \\ - \left\{ A_p \varepsilon_p D_p \Gamma(s) \tanh(d \Gamma(s)) \right\}_1 - \left\{ A_p \varepsilon_p D_p \Gamma(s) \tanh(d \Gamma(s)) \right\}_2 \\ - \left[\frac{\tanh(d \Gamma(s))}{A_p \varepsilon_p D_p \Gamma(s)} \right]_1 - \left[\frac{\tanh(d \Gamma(s))}{A_p \varepsilon_p D_p \Gamma(s)} \right]_2 \\ 1 + \frac{\left\{ A_p \varepsilon_p D_p \Gamma(s) \right\}_2}{\left\{ A_p \varepsilon_p D_p \Gamma(s) \right\}_1} \tanh(d_1 \Gamma_1(s)) \tanh(d_2 \Gamma_2(s)) \end{array} \right) \end{aligned} \quad (2.159)$$

With an argument similar to that for the single-layer case, taking into account the continuity equation (2.152a,b) at the flowing water/rock matrix interface and the zero-flow boundary condition (2.153), evaluating at the end of the rock matrix at $x = b + d_1 + d_2$ gives

$$\begin{aligned} \left(\begin{array}{c} \bar{C}_p(x = b + d_1 + d_2, z; s) \\ 0 \end{array} \right) = \\ = \begin{pmatrix} \bar{M}^{(1,1)}(x = b + d_1 + d_2; s) & \bar{M}^{(1,2)}(x = b + d_1 + d_2; s) \\ \bar{M}^{(2,1)}(x = b + d_1 + d_2; s) & \bar{M}^{(2,2)}(x = b + d_1 + d_2; s) \end{pmatrix} \begin{pmatrix} \bar{C}_f(z; s) \\ \bar{J}_p(b, z; s) \end{pmatrix}. \end{aligned} \quad (2.160)$$

Evaluating the second row gives

$$\bar{J}_p(x = b, z; s) = -\frac{1}{2} \bar{\eta}(s) \bar{C}_f(z; s). \quad (2.161)$$

$$\text{with} \quad \frac{1}{2} \bar{\eta}(s) = \frac{\bar{M}^{(2,1)}(x = b + d_1 + d_2; s)}{\bar{M}^{(2,2)}(x = b + d_1 + d_2; s)}, \quad (2.162)$$

which we wished to calculate. Using equation (2.159) gives

$$\begin{aligned} \frac{1}{2} \bar{\eta}(s) &= \frac{1}{2} \bar{\eta}_{d_2=0}(s) \cdot f_2(s) = -\left\{ A_p \varepsilon_p D_p \Gamma(s) \tanh(d\Gamma(s)) \right\}_1 \cdot f_2(s) \\ &= -\left\{ A_p \varepsilon_p D_p \Gamma(s) \tanh(d\Gamma(s)) \right\}_1 \frac{1 + \frac{\left\{ A_p \varepsilon_p D_p \Gamma(s) \right\}_2 \tanh(d_2 \Gamma_2(s))}{\left\{ A_p \varepsilon_p D_p \Gamma(s) \right\}_1 \tanh(d_1 \Gamma_1(s))}}{1 + \frac{\left\{ A_p \varepsilon_p D_p \Gamma(s) \right\}_2 \tanh(d_1 \Gamma_1(s)) \cdot \tanh(d_2 \Gamma_2(s))}{\left\{ A_p \varepsilon_p D_p \Gamma(s) \right\}_1}}. \end{aligned} \quad (2.163)$$

Thus the rock matrix response $\frac{1}{2} \bar{\eta}(s)$ of the two-layer case can be regarded as the rock matrix response of the single-layer case, $\frac{1}{2} \bar{\eta}_{d_2=0}(s)$, modified with the (slightly reformulated) analytically determinable correction function

$$f_2(s) = \frac{1 + \frac{\gamma_2 \tanh(\beta_2 \sqrt{s + \lambda})}{\gamma_1 \tanh(\beta_1 \sqrt{s + \lambda})}}{1 + \frac{\gamma_2 \tanh(\beta_2 \sqrt{s + \lambda}) \tanh(\beta_1 \sqrt{s + \lambda})}{\gamma_1}}, \quad (2.164)$$

cf. Barten, Robinson and Schneider [1998] where this has been published. The values β_1 , β_2 , γ_1 , γ_2 are defined according to β and γ for the single-layer case in equations (2.128) and (2.129). This system with two layers of rock matrix has also been analysed in the Laplace domain by Barten [1996a] using a slightly different notation, but in the limit of infinite Peclet number only, thus neglecting micro-dispersion. Robinson, Sharp and Kreisel [1998] considered advection and micro-dispersion in a single leg with two layers of rock matrix, but using a Heaviside step function for the

concentration as inlet boundary condition and at-infinity (see equation 2.51c) as outlet boundary condition.

To account for more general cases, i.e. two-dimensional rock matrix diffusion, $\bar{\eta}(s)$ is calculated numerically in one variant of PICNIC using a finite-element method for the evaluation of the Laplace transformed balance equations. Our analytical result for $\bar{\eta}(s)$ for the two-layer geometry is not implemented in PICNIC, but will be used in section 7 for the verification of the code. Note that a similar method to that presented in this subsection was implemented very recently in the RIP code [Miller and Kossik, 1998].

2.5.5. One-Dimensional Cylindrical Rock Matrix

The rock matrix geometries considered up till now can all be seen as special cases of the checkerboard-like geometry of Figure 2.3. PICNIC, however, has also the additional option of dealing with **cylindrical geometry** with a single homogeneous rock matrix layer as depicted in Figure 2.6.

In this section we give the time-dependent mass balance equations for nuclide transport in a single channel and the surrounding rock matrix, together with the boundary conditions. We consider a cylindrical channel of length L in the z -direction. Such a channel is called a **vein** and πR^2 is the cross-sectional area of the channel with R being the radius of the channel. The channel is filled with a porous medium, the *infill* of the channel, with infill porosity ε_i . The flow porosity is again ε_f and water flows with constant velocity $(q / \varepsilon_f) \mathbf{e}_z$ through the veins. For a single vein we can consider transport in a channel with cross-sectional area $A_f = \pi R^2$ and obtain $\varepsilon_f = \varepsilon_i$. However, if we consider a single vein in a larger area $A_f \neq \pi R^2$ then ε_f and ε_i are different for this water-

conducting feature, $\varepsilon_f = \varepsilon_i \frac{\pi R^2}{A_f}$. If we consider a block of host rock as a water-conducting feature containing a bundle of n veins with the same properties, as shown in Figure 2.6, then¹²

$$\varepsilon_f = \varepsilon_i \frac{n \pi R^2}{A_f}.$$

The channel is surrounded by a rock matrix with porosity ε_p accessible to rock matrix diffusion and pores filled with *stagnant water*. The thickness in the radial direction of the rock matrix around the water-conducting feature of a vein that is available for matrix diffusion is d . The geometry considered is radially symmetrical, such that the nuclide concentration in the porewater can be described as $C_p^{(i)}(r, z; t)$, where r describes the radial dependency which is the same around each vein. Transport of nuclides is described by the balance equations (2.38) in the area of flowing water and

¹² As described below, the porosities and cross-sectional area are defined independently in PICNIC, such that n is not necessarily a natural number (positive integer) here.

$$\begin{aligned} \partial_t C_p^{(i)}(r,z;t) = & \frac{D_p^{(i)}}{R_p^{(i)}} \left(\partial_r^2 C_p^{(i)}(r,z;t) - \frac{1}{r} \partial_r C_p^{(i)}(r,z;t) \right) \\ & - \lambda^{(i)} C_p^{(i)}(r,z;t) + \lambda^{(i-1)} \frac{R_p^{(i-1)}}{R_p^{(i)}} C_p^{(i-1)}(r,z;t) \end{aligned} \quad (2.165)$$

for the concentration of the nuclides $i = 1 \dots I$ in the rock matrix substituting equations (2.85). Here we have used the operator identity for radial symmetrical geometries, $\partial_r^2 - \frac{1}{r} \partial_r = \partial_\perp^2 = \partial_x^2 + \partial_y^2$.

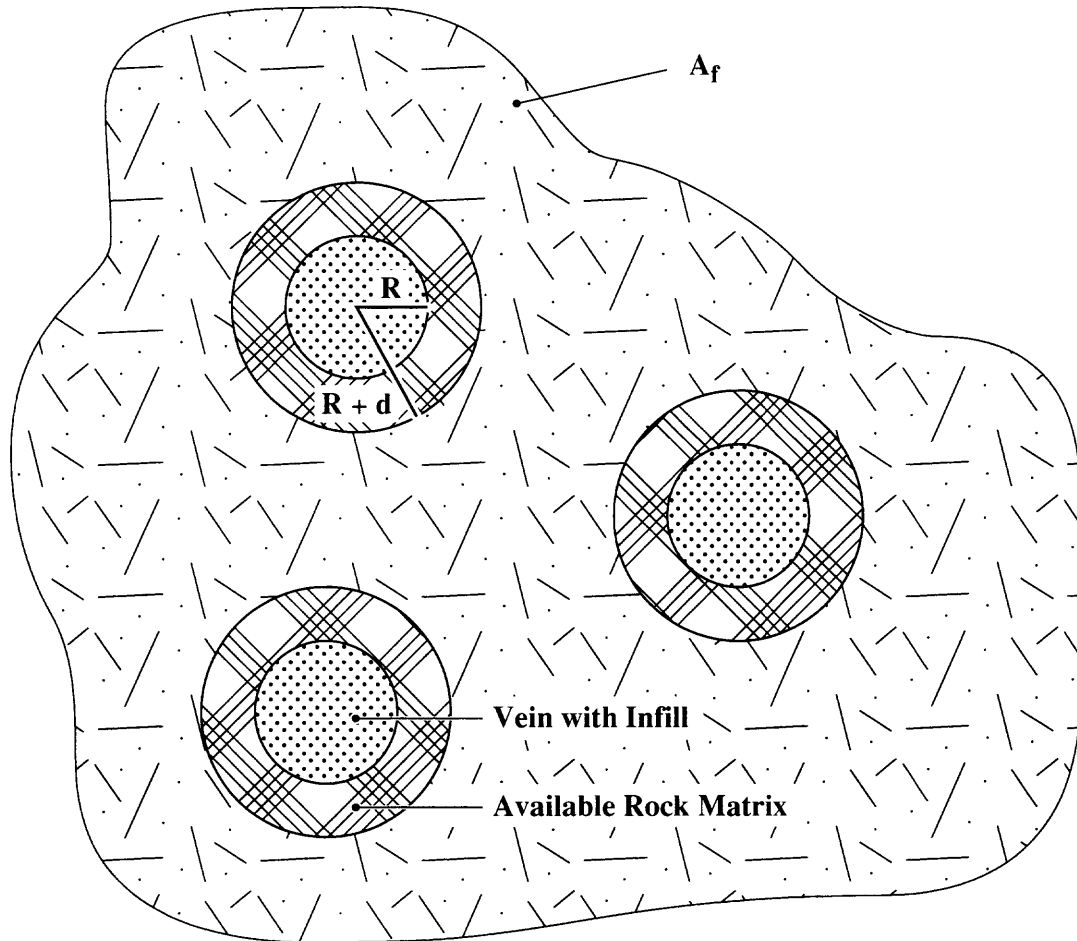


Figure 2.6. Cross-section of a water-conducting feature with area A_f containing a number of n veins with the same properties. Each vein has radius R and is surrounded by an accessible rock matrix of thickness d .

At the interface between the channel and the rock matrix, at $r = R$, the continuity condition

$$C_p^{(i)}(r = R, z; t) = C_f^{(i)}(z; t) \quad (2.166)$$

is assumed for all z and t . For the limited matrix diffusion considered here, there is zero nuclide flux

beyond the given distance d from the edge of the water-conducting feature,

$$j_p^{(i)}(r = R + d, z; t) = 0 \quad (2.167)$$

for all t , where the nuclide flux in the rock matrix, $\mathbf{j}_p^{(i)}(r, z; t) = \mathbf{e}_r j_p^{(i)}(r, z; t)$, is purely radial with

$$j_p^{(i)}(r, z; t) = -\varepsilon_p D_p^{(i)} \partial_r C_p^{(i)}(r, z; t), \quad (2.168)$$

and \mathbf{e}_r is the normal radial vector. The Laplace transformed balance equations and nuclide flux in the rock matrix are

$$0 = \frac{D_p^{(i)}}{R_p^{(i)}} \left[\partial_r^2 - \frac{1}{r} \partial_r \right] \bar{C}_p^{(i)}(r, z; s) - \left[s + \lambda^{(i)} \right] \bar{C}_p^{(i)}(r, z; s) + \lambda^{(i-1)} \frac{R_p^{(i-1)}}{R_p^{(i)}} \bar{C}_p^{(i-1)}(r, z; s) \quad (2.169)$$

$$\text{and} \quad \bar{j}_p^{(i)}(r, z; s) = -\varepsilon_p D_p^{(i)} \partial_r \bar{C}_p^{(i)}(r, z; s). \quad (2.170)$$

When we again define a slice of the leg of length Δz , then the nuclide flow rate in the rock matrix in this slice is

$$\bar{\mathbf{J}}_p^{(i)}(r, z; s) = A_p(r) \bar{\mathbf{j}}_p^{(i)}(r, z; s) = \mathbf{e}_r A_p(r) \bar{j}_p^{(i)}(r, z; s), \quad (2.171)$$

$$\text{with the area} \quad A_p(r) = n 2\pi r \Delta z. \quad (2.172)$$

The factor n in $A_p(r)$ accounts for multiple veins in the leg. Thus the nuclide flow rate at the interface between the flowing water and the rock matrix is

$$-\frac{A_m}{V_i} \left\langle \bar{\mathbf{j}}_p^{(i)} \cdot \mathbf{e}_n \right\rangle_{A_m}(z; s) = -\delta_f \left\langle \bar{\mathbf{j}}_p^{(i)} \cdot \mathbf{e}_n \right\rangle_{A_m}(z; s) = -\frac{2}{R} \bar{j}_p^{(i)}(r = R, z; s), \quad (2.173)$$

with $A_m = A_p(r = R)$ and

$$\delta_f = \frac{2}{R}, \quad (2.174)$$

for the cylindrical geometry considered. This is analysed in PICNIC using analytical relations to obtain $\bar{\eta}^{(i,j)}(s)$ according to equation (2.41). For details see Robinson [1997a].

2.6. Linear Sorption

Till now we have considered transport on the scale of the network, in the area of flowing water of the legs and finally in the rock matrix. Thereby, we have discussed the entire range of heterogeneities considered in PICNIC. Thus, now the transport behaviour is determined, when the parameters are entered in PICNIC.

In this subsection we discuss two of these parameters. These are the **retardation constants in the rock matrix**, $R_p^{(i)}$, and the **retardation constants in the areas of flowing water**, $R_f^{(i)}$. These retardation constants describe the effect of linear equilibrium sorption of the nuclides on different rock surfaces.

2.6.1. Retardation Constant in the Rock Matrix

The retardation constant in an area of the rock matrix of a leg, $R_p^{(i)} = R_p^{(i)}(x, y; z)$, is defined in PICNIC as

$$R_p^{(i)} = R_{0,p}^{(i)} + \frac{1 - \varepsilon_p}{\varepsilon_p} \rho_p K_{d,p}^{(i)}. \quad (2.175)$$

$R_{0,p}^{(i)}$ is the base matrix retention, ε_p is the porosity and ρ_p is the mass density of the rock matrix. $K_{d,p}^{(i)}$ is the volume-based linear sorption equilibrium distribution coefficient for nuclide (i). This definition has the technical advantage that the retardation constant can be set directly by defining $R_{p,0}^{(i)}$ and setting $K_{d,p}^{(i)}$ to zero. Alternatively, setting the base matrix retention $R_{p,0}^{(i)} = 1$ gives the standard definition used e.g. in performance assessments [Nagra, 1994].

In the form of the second term it is assumed that the entire mass of the rock matrix is accessible for sorption. This might not always be valid, e.g. for extremely small porosities ε_p . In these cases the retardation constants might be defined differently by $R_{0,p}^{(i)}$. The same holds below for the retardation constant in the flowing water. Overall it should be kept in mind that these considerations are only rough approximations for the sorption behaviour in a real porous rock zone.

2.6.2. Retardation Constant in the Area of Flowing Water

We discuss the retardation in the area of the flowing water first for the situation where the area of flowing water is in contact with one type of rock matrix only. Then the retardation constant is defined as

$$\begin{aligned} R_f^{(i)} &= R_{0,f}^{(i)} + \frac{1 - \varepsilon_i}{\varepsilon_i} \rho_i K_{d,f}^{(i)} + \left[1 - \varepsilon_p\right] \frac{A_m}{V_i \varepsilon_i} K_{a,f}^{(i)} \\ &= R_{0,f}^{(i)} + \frac{1 - \varepsilon_i}{\varepsilon_i} \rho_i K_{d,f}^{(i)} + \left[1 - \varepsilon_p\right] \frac{\delta_f}{\varepsilon_i} K_{a,f}^{(i)}, \end{aligned} \quad (2.176)$$

where the first two terms are defined similarly as in the rock matrix. $R_{0,f}^{(i)}$ is the base retardation, ε_i is the infill porosity and ρ_i is the mass density of the infill material. $K_{d,f}^{(i)}$ is the volume-based linear sorption equilibrium coefficient for nuclide (i).

In the third term, sorption on the surfaces in the area of the flowing water is taken into account. $K_{a,f}^{(i)}$ is the linear surface-based sorption equilibrium distribution coefficient for nuclide (i) in the water-conducting feature. The factor $[1 - \varepsilon_p]$ takes into consideration that there is a porous rock matrix with porosity ε_p around the area of flowing water and the surface available for sorption is reduced by the factor $(1 - \varepsilon_p)$. There $\delta_f = \frac{A_m}{V_i}$ is the geometrical surface to volume ratio, e.g. for a planar fracture geometry $\delta_f = 1/b$. The surface sorption term accounts for the infill porosity ε_i in the denominator, which means that the sorbing surface does not change with changing ε_i , while the water volume is proportional to ε_i . This assumption is, for example, valid when the infill material touches the surface like hard spheres on a hard plane.

Another, actually not implemented assumption is, that the sorbing surface of the area of flowing water is reduced by the fracture infill. For instance, Barten, Niemeyer and Heer [1997] suggested that the infill material covers the surface of the volume V_i to the same amount as it covers the volume itself.¹³ This would mean omitting the denominator ε_i in the surface sorption term, and

$$R_f^{(i)} = R_{0,f}^{(i)} + \frac{1 - \varepsilon_i}{\varepsilon_i} \rho_i K_{d,f}^{(i)} + [1 - \varepsilon_p] \delta_f K_{a,f}^{(i)}, \quad (2.177)$$

and, specifically for a planar fracture geometry,

$$R_f^{(i)} = R_{0,f}^{(i)} + \frac{1 - \varepsilon_i}{\varepsilon_i} \rho_i K_{d,f}^{(i)} + [1 - \varepsilon_p] \frac{1}{b} K_{a,f}^{(i)}. \quad (2.178)$$

The two concepts are visualised in Figure 2.7.

In the case where more than one type of porous rock matrix is in contact with the area of flowing water, the contributions from the different surfaces to the retardation factor should be summed. This, however, is not considered in PICNIC till now. This means that in the embedded finite-element option used in PICNIC the surface sorption part in the retardation constant $R_f^{(i)}$ is actually not implemented. Note that in most performance assessment cases to date, no infill material and no retardation in the area of flowing water have been considered.

¹³ For $\varepsilon_f = \varepsilon_i$ this is also consistent with equation (2.3) in Barten [1995].

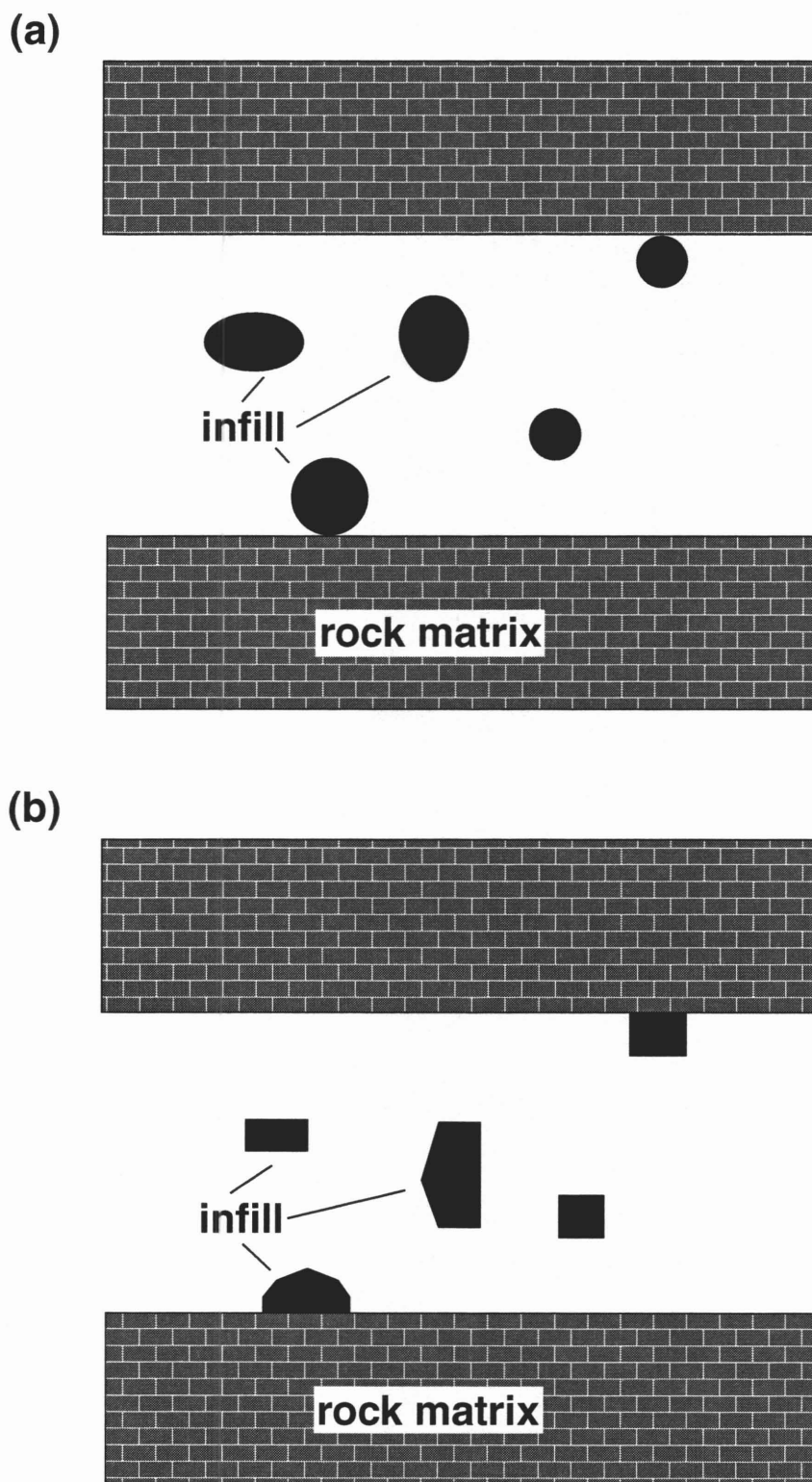


Figure 2.7. Concept of surface sorption in the area of flowing water explained for the special case without matrix diffusion. (a) conceptualises infill touching the surface of a channel like hard spheres which do not reduce the sorbing area. (b) conceptualises the sorbing surface being reduced by the infill.

2.7. Laplace Transform Inversion

In this subsection Talbot's algorithm is described which is used in PICNIC for numerical inverse Laplace transformation [Robinson, 1997b].

2.7.1. Talbot's Algorithm

The approach to Laplace transform inversion that we use is not specific to the particular forms of PICNIC. We therefore describe it in general terms for a generic function $f(t)$.

The requirement is to evaluate $f(t)$, at a particular set of times, given an ability to calculate the transform $\bar{f}(s)$. There are many algorithms for numerically inverting Laplace transforms [Davis and Martin, 1979], but experience has shown that the Talbot algorithm [Talbot, 1979] performs very well in this type of problem. The Talbot algorithm involves numerical integration along a contour in the complex plane. This contour is a deformed version of the Bromwich contour, which is usually used in Laplace transform inversion. The algorithm includes four parameters, λ, σ, ν and n , which can be adjusted to give the desired accuracy. In practice it is found that most inversions can be performed to sufficient accuracy by a standard set of choices and this approach is used in PICNIC. The inversion formula given by Talbot can be written as

$$f(t) \approx \frac{1}{n} \sum'_{k=0}^{n-1} \text{Re} \left[w_k e^{s_k t} \bar{f}(s_k) \right], \quad (2.179)$$

where Σ' implies that the $k=0$ term is given a weight of one half, and

$$\begin{aligned} s_k &= \lambda(\alpha_k + i\nu\theta_k) + \sigma \\ \theta_k &= \frac{k\pi}{n} \\ \alpha_k &= \theta_k \cot \theta_k \\ w_k &= \lambda(\nu + i\beta_k) \\ \beta_k &= \theta_k + \frac{\alpha_k(\alpha_k - 1)}{\theta_k}. \end{aligned} \quad (2.180)$$

The standard choice of parameters suggested by Talbot are $\sigma = 0$, $\nu = 1$, $\lambda = 6/(t - t_0)$, with n chosen to give sufficient accuracy, but typically $n = 32$. Here t_0 is the effective time-origin, and is discussed later. For the types of problem relevant to PICNIC, $\nu = 1.5$ is found to be better and is used as the default in PICNIC. In this form the Talbot algorithm requires a new contour for every different time, t . In practice it is possible to reuse the contour for neighbouring values. This works best if a contour set from a later time is reused for an earlier time - this is equivalent to using a smaller value of λ than the standard one for the earlier time. With this approach a single contour can be used to evaluate results at times spanning a factor of 3 to 5 in times.

To extend this capability further, we add an additional point on the contour in the position where the final point would be for n twice as large as that being used. The inversion formula is adjusted to account for this, by weighting the $k = n - 1$ point. This is done by noting that the inversion formula is in fact a simple trapezoidal integration formula along the contour described by s_k . This extra

point can extend the time range over which the contour is valid by up to a factor of 2. In PICNIC, its main effect is to maintain the accuracy over the full time range.

Talbot's algorithm is at its least accurate for very early times if $f(t)$ is small or zero there. We can prevent this being a problem by: calculating a cut-off time, before which $f(t)$ is assumed to be zero; and, setting an accuracy criterion based on the overall size of $f(t)$. Each of these is discussed later in this section.

The Talbot algorithm converges very rapidly with the number of contour points in most circumstances. Thus an appropriate measure of accuracy is the difference between the result obtained with n points and that obtained with $n/2$ points. The latter is trivial to calculate because it just uses every second point in the full set. A relative accuracy measure is appropriate in most cases, but to deal with cases where the result is near zero, and so is affected by round-off errors, an absolute error criterion, as discussed above, is required. The absolute and relative errors parameters η and ε can be set and a result accepted if

$$|f_n - f_{n/2}| < \varepsilon [|f_n| + |f_{n/2}|], \quad (2.181)$$

or if

$$|f_n| < \eta f_{\max}, \quad (2.182)$$

where f_n is the result with n points and f_{\max} is the (estimated) maximum value of $f(t)$. Typically $\varepsilon = 10^{-4}$ and $\eta = 10^{-6}$. If neither of these conditions is met when a contour is being reused, then the standard contour is used instead. If neither is met when the standard contour is in use, then the number of points is doubled.

There is a limit to the maximum number of points (128) and if a satisfactory result cannot be obtained with this number then a warning must be issued. Even in this case the results might still be acceptable but the user will have to make this judgement.

2.7.2. Cut-off Times

To find an early cut-off time before which $f(t)$ can be thought of as zero, and an earlier time still at which the time-origin for $f(t)$ can be considered to be, we can use some inequalities relating the Laplace transform to the integral of $f(t)$.

These are only valid for positive definite $f(t)$ and so are not be used for the flux from fracture to matrix, which changes sign. The appropriate cut-off and origin times for this are those of the incoming flux.

Let

$$F(t) = \int_0^t f(\tau) d\tau. \quad (2.183)$$

Then, if $f(t)$ is positive for all t and s is a real, positive number,

$$\begin{aligned}
F(t) &\leq \int_0^t e^{st} e^{-s\tau} f(\tau) d\tau \\
&\leq e^{st} \int_0^{\infty} e^{-s\tau} f(\tau) d\tau \quad . \\
&= e^{st} \bar{f}(s)
\end{aligned} \tag{2.184}$$

Also $F(\infty) = \bar{f}(0)$, thus

$$\frac{F(t)}{F(\infty)} \leq \frac{e^{st} \bar{f}(s)}{\bar{f}(0)} \quad \forall s \geq 0 \quad . \tag{2.185}$$

By searching through a set of values of s (chosen to cover the range of timescales of interest), a bound can be put on the value of $F(t)$ that is on the proportion as the area under $f(t)$. We can then define the cut-off time to be that for which $F(t)/F(\infty) \leq \epsilon_c = 10^{-8}$ say. The effective time origin, t_0 , could be defined as the time for which $F(t)/F(\infty) \leq \epsilon_0 = 10^{-10}$ say. In practice, the latter was not found to be useful and a time origin of zero is used throughout.

2.7.3. Peak Values

In order to work out an estimated peak value for use in the accuracy criterion we can again use the Laplace transform values along the positive real axis. If $F(t)$ is positive everywhere then taking the first few moments and fitting a Gaussian shape works fairly well. The moments can be evaluated by calculating the derivatives of the Laplace transform at $s = 0$, since

$$\begin{aligned}
\bar{f}(0) &= \int_0^{\infty} f(t) dt \\
\bar{f}'(0) &= - \int_0^{\infty} t f(t) dt \quad . \\
\bar{f}''(0) &= \int_0^{\infty} t^2 f(t) dt.
\end{aligned} \tag{2.186}$$

Therefore

$$\begin{aligned}
\langle t \rangle &= - \frac{\bar{f}'(0)}{\bar{f}(0)} \\
\langle t^2 \rangle &= \frac{\bar{f}''(0)}{\bar{f}(0)} \quad ,
\end{aligned} \tag{2.187}$$

and the peak value can be approximated as

$$f_{\max} \approx \frac{\bar{f}(0)}{\sqrt{\pi} \sqrt{\langle t^2 \rangle - \langle t \rangle^2}} \quad . \tag{2.188}$$

An additional inequality that can be used to give a lower bound on the peak value is

$$\bar{f}(s) \leq \int_0^{\infty} f_{\max} e^{-st} dt \quad , \quad (2.189)$$

which is valid for any $f(t)$ and gives the inequality

$$f_{\max} \geq s\bar{f}(s) \quad \forall s \geq 0 \quad , \quad (2.190)$$

In practice, the derivatives are not evaluated at $s=0$ but for small values of s , since the calculated derivatives near the origin are often subject to large rounding errors. While the inversion is being performed the peak value can be updated if larger values than the estimates are found. If significantly larger values are found (more than a factor of ten larger) then a warning would be issued to the user.

2.8. Structure of the Input File

In the previous subsections we have explained the fundamentals of PICNIC. In this subsection we briefly outline how the geometry of the network and the parameters of the individual legs and rock matrix areas are entered as an **input file** to PICNIC. This input file can be written either directly or via a Graphical User Interface (GUI). For a description of the details of the GUI see Robinson [1997a]. For the details of the syntax of the input file see Robinson and Cooper [1997]; Robinson [1997b]. Here we give an overview of the aspects relevant to this report. The overview should assist in orientation and is not intended to be complete. The input file is subdivided into the sections specified below, each of which starts with a keyword. For identification purposes, in this subsection the keywords are written in capitals.

(DECAYS) The nuclides considered, and their names, are entered in a section beginning with the keyword DECAYS. For each parent nuclide that decays to a daughter nuclide, the name of the parent and the daughter are typed, together with the half-life. If no daughter nuclide needs to be considered, the name of the daughter is omitted. For simplicity, entering "0.0" as half-life is interpreted by PICNIC as meaning that the nuclide is stable. PICNIC analyses the DECAYS section, constructs the nuclide decay chains and identifies the single nuclides. The transport of each single nuclide and each nuclide decay chain is then considered separately.

(CONTROLS) In the CONTROLS section, use of the keyword CALCULATE-FLOWS indicates whether the DARCY velocities in the LEG section are entered or if it is necessary to calculate the DARCY velocities using the HYDRAULIC-CONDUCTIVITY of the LEG section together with boundary conditions in the JUNCTION section. NTALB gives the number of elements in the Talbot series for the inverse Laplace transformation. REFINE gives the level of mesh refinement in the case where the rock matrix response is calculated numerically by a finite-element method.

(LEG) The geometry of a leg and its name are entered in a section beginning with the keyword LEG. The name of the junction which is the tail of the leg (the upstream end) is entered by the keyword FROM. For the head of the leg (the downstream end), the name is entered following the keyword TO. q_f is entered by DARCY-VELOCITY. Optionally, instead of entering q_f , the HYDRAULIC-CONDUCTIVITY of the leg can be entered. In this case, the Darcy velocity is

calculated by PICNIC, and the tail and the head of the leg may be exchanged by PICNIC. The LENGTH L , CSA A_f (the cross-sectional area), and PECLET Pe are entered. BC-TYPE specifies one of the three possible options for the outlet boundary condition, AT-INFINITY, ZERO-CONCENTRATION or ZERO-GRADIENT. The name of the ROCK-TYPE is entered. The properties of the rock type are defined either as 1D-ROCK-TYPE or so-called 2D-ROCK-TYPE, see below.

(1D-ROCK-TYPE) is the keyword when the rock matrix response, $\bar{\eta}(s)$, is analytically known and implemented in PICNIC. Currently, there are two different options. Either the MATRIX-GEOMETRY is PLANAR or CYLINDRICAL. The keyword PLANAR means that matrix diffusion is one-dimensional into a homogeneous block of rock matrix; see section 4. The keyword CYLINDRICAL indicates one-dimensional matrix diffusion into a homogeneous cylindrical rock matrix geometry; see section 5. The FLOW-POROSITY ε_f is entered. The implemented definition

of the SPECIFIC-SURFACE-AREA $\frac{\delta_f}{\varepsilon_i} = \frac{A_m}{V_i \varepsilon_i}$ also contains the infill porosity. The

PENETRATION-DEPTH d gives the thickness of the rock matrix below and above the area of flowing water. The FLOW-BLOCK-NAME and the MATRIX-BLOCK-NAME are entered, where the properties must be defined in the FLOW-BLOCK and the MATRIX-BLOCK section discussed below. For the CYLINDRICAL matrix geometry the RADIUS R of the area of flowing water is entered. There are a number of other analytical solutions, but they are not actually implemented in PICNIC.

(2D-ROCK-TYPE) As depicted in Figure 2.3a, a cross-sectional area of a leg can also be entered in checkerboard form to PICNIC, where each cell is either a FLOW-BLOCK or a MATRIX-BLOCK, see below. The number of rows and of columns of the “checkerboard” are entered using the keyword SIZE. The FLOW-POROSITY ε_f is either entered directly or defaults to the physical porosity specified in the geometry. The heights of the individual rows and the widths of the columns of the “checkerboard” are entered using the ROW-HEIGHTS and the COL-WIDTHS keywords. The names of the FLOW-BLOCK or the MATRIX-BLOCK assigned to the individual cells of the “checkerboard” are entered using the BLOCKS keyword.

(FLOW-BLOCK) This section gives the material properties of a named area of flowing water. These are the BASE-RETARDATION $R_{0,f}^{(i)}$, the INFILL-KD $K_{d,f}^{(i)}$ and the FRACTURE-KA $K_{a,f}^{(i)}$ for each nuclide considered, and the INFILL-POROSITY ε_i and the INFILL-DENSITY ρ_i .

(MATRIX-BLOCK) This section gives the material properties of a named area of rock matrix. These are the BASE-MATRIX-RETENTION $R_{0,p}^{(i)}$, the MATRIX-KD $K_{d,p}^{(i)}$, and the MATRIX-DIFFUSION $D_p^{(i)}$ for each nuclide considered, and the MATRIX-POROSITY ε_p and the MATRIX-DENSITY ρ_p .

(JUNCTION) gives, optionally, the INFLOW rate or OUTFLOW rate of water, $Q_{s_{ju}}$, at specific junctions ju in the network. For the CALCULATE-FLOWS option in the CONTROLS section, these quantities or alternatively the hydraulic HEAD are required at some junctions.

(SOURCE-TERM) A source $S_{in}^{(i)}(t)$ or $\bar{S}_{in}^{(i)}(s)$ is named and entered in this section. With the keyword AT, the position *in* of the source is entered. For a time-dependent source $S_{in}^{(i)}(t)$, the keyword FILE together with the file name and the type of the file is entered, which can presently be TABLE or HARTLEY. TABLE means that the time and flow rates of the nuclides considered are entered in a table format in the file considered. The keyword HARTLEY means that the same information is now in a Hartley-file format, which is the output format of some repository near-field codes. Predefined sources can be entered using the keyword ANALYTIC and the type of source which can be SIMPLE-LEACHING, TOP-HAT-RELEASE, BAND-RELEASE or DELTA-FUNCTION. SIMPLE-LEACHING and DELTA-FUNCTION are implemented as analytical sources in the Laplace domain, while TOP-HAT-RELEASE and BAND-RELEASE are implemented in the time domain. SIMPLE-LEACHING is described by the keywords INVENTORY and LEACH-RATE. DELTA-FUNCTION is described by INVENTORY. TOP-HAT-RELEASE is described by the keywords INVENTORY and RELEASE-TIME. BAND-RELEASE, which is the nuclide decay chain version of TOP-HAT-RELEASE, is also described by the keywords INVENTORY and RELEASE-TIME. In all cases the source can be re-scaled using the keyword SCALE-FACTOR.

(OUT-LOCATIONS) In this section it is specified what kind of output will be generated at what position. Using the keyword JUNCTION, together with the name of a junction *out*, and the keyword FLUX, it is specified that the nuclide flow rate $J_{out}^{(i)}(t)$ will be generated. Using the keyword LEG, together with the name of the leg *lg*, and the keyword FLUX, it is specified that the nuclide flow rate at the outflow position of the leg into the junction, which is the tail of the leg, is specified. The other output options for a leg MASS-IN-FRACTURE, FLUX-TO-MATRIX or MASS-IN-MATRIX are not considered in this report.

(OUT-FILES) In this section the name of the output file is given and the nuclides which are considered in the output file are specified.

(OUT-TIMES) This section gives the NUMBER-OF-TIMES for the output. The keyword LINEAR specifies that the output times are equidistant on a linear timescale or, alternatively, the keyword GEOMETRIC specifies equidistant output times on a logarithmic timescale. The START-TIME and the FINAL-TIME of the output times are entered. Some additional output times can be specified using the keyword EXTRA-TIMES.

3. Structure and Verification Strategy of PICNIC

In the preceding section the system considered was described, together with the derivation of the (mathematical) fundamentals.

In this section we now describe **how these fundamentals are efficiently combined in the PICNIC code** as a tool for describing nuclide transport in heterogeneous fractured rock.

Possible sources of errors in the flow of control within PICNIC (the “PICNIC flow scheme”) are discussed.

The **application range** of PICNIC is then reconsidered with respect to its verification.

The analysis of the architecture and the application range of PICNIC is then used as the basis for a **verification strategy appropriate to the program**.

3.1. PICNIC Flow Scheme

The flow of control within PICNIC (the “PICNIC flow scheme”) for the calculation of nuclide flow rate at a junction is depicted in Table 3.1.¹⁴ Note that the code structure follows this algorithm. The case of transport of a single nuclide is discussed explicitly, although the treatment of a nuclide decay chain has the same concept. The calculation in PICNIC is different depending chiefly on whether the nuclide source is known in the Laplace domain or in the time domain, and depending on the geometry of the rock matrix.

In this subsection the **PICNIC flow scheme** is discussed first for sources entered to PICNIC in the time domain.

In PICNIC special sources are also **implemented analytically in the Laplace domain**.

The PICNIC flow scheme is then compared for **single nuclides and nuclide decay chains**.

Finally the **PICNIC flow scheme** is presented in a further **simplified** way for extraction of the logical structure.

3.1.1. Analytical Rock Matrix Response and Time-Dependent Source

We first consider the situation where a time-dependent nuclide source is entered to PICNIC (column 5 in Table 3.1). PICNIC works along a series of levels which we consider now, with special emphasis on verification.

(0) The input file with all parameters is first read and analysed in PICNIC. In this way, the nuclides and decay chains are identified. The rock types, types of flow blocks and matrix blocks are also read. The geometry of the network, the location of the sources and the output positions are read. The network is analysed and the set of pathways between the source location, *in*, and the output position, *out*, are thus determined for each source and presented as a tree.

In the next code levels, the nuclide flow rate is constructed in a hierarchical manner like a “Russian doll”, starting from the innermost “doll”.

¹⁴ The flow scheme for the other output options (compare the OUT-LOCATIONS section of the input file in section 2.8) is conceptually the same.

(1) On the “lowest” hierarchical level in this flow scheme, for each rock type the rock matrix response in the Laplace domain $\bar{\eta}(s)$ is calculated. Analytical solutions of the rock matrix response exist for a number of cases of one-dimensional matrix diffusion. Presently, the cases of limited one-dimensional diffusion into a homogeneous planar or cylindrical rock matrix geometry are implemented in PICNIC, cf. e.g. equation (2.121). As an alternative, PICNIC has the option to enter the geometry of the cross-section of a leg in a kind of checkerboard geometry, cf. Figure 2.3 and discussion in section 2.4. PICNIC then uses a finite-element method to calculate the rock matrix response $\bar{\eta}(s)$.¹⁵

(2) In the next four levels, the leg response in the Laplace domain is calculated by analytical and algebraic relations. In this code level the effect of advection is accounted for, which means that the eigenvalue $L\Lambda(s)$ is calculated from $\bar{\eta}(s)$ using equation (2.54) in section 2.3.1.

(3) In the next level, micro-dispersion is accounted for with finite Pe , which means that the eigenvalue $\chi(s)$, and therefrom $K_v(s)$, are calculated from $L\Lambda(s)$ using equations (2.59) and (2.60) in section 2.3.3.

(4) The leg response function¹⁶ is then calculated from $\chi(s)$ using equations (2.63), (2.69) or (2.77), depending on the outlet boundary condition considered, i.e. $\bar{\mathfrak{R}}_{ZG}(s)$ for the zero-gradient boundary condition.

(5) As mentioned above, we consider here the case that the source is known in the time domain only, but not in the Laplace domain. The method with the tree response function is then used in the next four levels, see section 2.1.6. In this code level formally the response function in the Laplace domain of a pathway between a source location *in* and the junction *in* is initialised to the identity function, see equation (2.20).

(6) In the next level, for each pathway between the source location considered and the output location, the pathway response function $\bar{T}_{out,in;w}(s)$ is calculated using equation (2.19). This level needs level (5) and uses the results from level (4) several times.

¹⁵ This option is especially useful for cases of two-dimensional matrix diffusion where the rock matrix response in the Laplace domain $\bar{\eta}(s)$ cannot in general be determined analytically.

¹⁶ Remember that, for a single nuclide, a response function in the time domain is proportional to the nuclide release for a δ -function source. A leg response function describes the nuclide release of a single leg for a δ -function source. In this code level the Laplace transformed response functions are considered. The pathway response function describes the nuclide release at the end of a pathway. The tree response function describes the nuclide release of the sum of all pathways between a source location and a junction.

PICNIC Flow Scheme

				arbitrary "time-dependent" nuclide source	nuclide source implemented as function in the Laplace domain
"code" level	transport geometry	features, processes	quantities	selected mathematical procedure	
0	network	problem definition	q_f, ϵ_p, \dots legs, junctions	reading of parameters and eventually calculation of water flow rates from conductivities to obtain q_f , generation of trees	
Laplace Domain:				↓	
1	rock matrix	matrix diffusion	rock matrix response, $\bar{\eta}(s)$	embedded with analytical relations for homogeneous one-dimensional rock matrix geometries or embedded with a finite-element method for heterogeneous rock matrices	
				↓	
2	leg	advection ($Pe \rightarrow \infty$)	eigenvalue, $L\Lambda(s)$	analytical transformations	
				↓	
3	leg	micro-dispersion (finite Pe)	eigenvalues, $\chi(s), K_v(s)$	analytical transformations	
				↓	
4	leg	outlet boundary condition	leg response, $\bar{\mathfrak{R}}_{ZG}(s), \bar{\mathfrak{R}}_{AI}(s),$ or $\bar{\mathfrak{R}}_{ZC}(s)$	3 variants (ZG, ZC, AI), analytical transformations	
				↓	
5	source	location (and form) of source	pathway / tree initialisation, $\bar{T}_{in,in,w}(s)$ or $\bar{J}_{in,in,w}(s)$	response, analytical transformations	flow rate, analytical transformations
				↓	↓

6	pathway	network geometry, location of source and output	pathway response or flow, $\bar{T}_{out,in;w}(s)$ or $\bar{J}_{out,in;w}(s)$	↓ response, analytical transformations	↓ flow rate, analytical transformations
7	tree	network geometry, location of source and output	tree response or flow, $\bar{T}_{out,in}(s)$ or $\bar{J}_{out,in}(s)$	↓ response, analytical transformations	↓ flow rate, analytical transformations
8	tree	inverse Laplace transformation	tree response or flow, $T_{out,in}(t)$ or $J_{out,in}(t)$	↓ response, using numerical Talbot scheme	↓ flow rate, using numerical Talbot scheme
Time Domain:				↓	↓
9	source	form of source	tree flow, $J_{out,in}(t) = T_{out,in}(t) * S_{in}(t)$	flow rate, calculated by convolution of the tree response with the time-dependent source	
10	network	multiple sources	network flow, $J(t)$	↓ superposition of nuclide flow rates from different sources	

Table 3.1. This table summarises the flow of control within PICNIC (the PICNIC flow scheme) consisting of the main cords given in columns 5 and 6 of the table. Each cord consists of a problem definition part (code level 0) followed by a “Russian doll” structure (code levels 1 to 10) given in the rows of the table. Code levels (1) to (7) work in the Laplace domain and levels (9) and (10) work in the time domain. Level (8) is the numerical inverse Laplace transformation. Column 5 of the table considers the case that a time-dependent source is entered at user-supplied times. Column 6 considers that the nuclide source is implemented in PICNIC as a function in the Laplace domain. The rock matrix response in code level 1 is implemented analytically for a homogeneous planar or cylindrical rock matrix geometry, while a finite-element method is embedded to account also for one-dimensional or two-dimensional matrix diffusion into heterogeneous rock matrices. Column 1 of the table gives the “code level” where PICNIC works. Column 2 denotes the geometry that is considered, while column 3 gives the features and processes PICNIC deals with, together with the respective (mathematical) quantities in column 4. For more details see text.

(7) The pathway response functions are then combined to give the tree response function $\bar{T}_{out,in}(s)$ using equation (2.18).

(8) From level (1) to level (7) we have worked in the Laplace domain. In this level, the tree response function is numerically inverse Laplace transformed using Talbot's method (Talbot [1979]) to obtain $T_{out,in}(t)$.

(9) As mentioned above, here we consider a nuclide source which is entered to PICNIC explicitly in its time-dependent form. This nuclide source is convoluted with the tree response function to obtain the nuclide release $J_{out,in}(t)$, see equation (2.17).

(10) In the case of multiple sources, the releases originating from the different sources are finally superimposed using equation (2.10). Now we are back on the uppermost level of the network or the outermost "doll" of the "Russian doll".

3.1.2. Analytical Source in the Laplace Domain

In the case where the form of the nuclide source is known in the Laplace domain, the procedure is slightly different; see column 6 of the PICNIC flow scheme in Table 3.1. Different to the case with the source in the time domain, in the code levels (5) to (7) the nuclide release in the Laplace domain, $\bar{J}_{out,in}(s)$, is calculated instead of $\bar{T}_{out,in}(s)$, cf. equations (2.14-16). Also the time-dependent nuclide release $J_{out,in}(t)$ is calculated in level (8) by numerical inverse Laplace transformation. Thus it is not necessary to perform the convolution in code level (9). Note that δ -function sources¹⁷ and simple-leaching sources are actually implemented in PICNIC as analytical functions in the Laplace domain. Top-hat sources and band-release sources are implemented as time-dependent functions. Thus, internally in PICNIC, these sources are handled like arbitrary time-dependent sources, although the Laplace transforms of these sources are known analytically. This is, because, during the development of PICNIC, this calculation variant proved to be much more stable.

3.1.3. Nuclide Decay Chains

For nuclide decay chains of length I , PICNIC has the same flow scheme as given in Table 3.1 for single nuclides. The only difference is that we deal now with sets of eigenvalues instead of single eigenvalues and with vectors or tensors (matrices) of functions instead of single functions. This means, for code level (1), that the rock matrix response $\bar{\eta}(s)$ is an $(I \times I)$ -matrix of functions. Instead of the single exponent $LA(s)$, in code level (2) there is a set of I different exponents. Instead of the single exponent part $\chi(s)$ and the two eigenvalues $K_\nu(s)$ in code level (3), there is a set of $2I$ different exponents $K_\nu(s)$.

While for single nuclides, $\bar{\mathfrak{R}}_{ZG}(s)$, $T_{out,in}(t)$, $J(t)$,... in code levels (4-10) are single s - or t -valued functions, for nuclide decay chains the response tensors $\bar{\mathfrak{R}}_{ZG}(s)$, $T_{out,in}(t)$,... are lower triangle

¹⁷ For a δ -function source (discarding the physical units), the nuclide release $J_{out,in}(t)$ is identical to the tree response function $T_{out,in}(t)$ and is thus the base case for all cords in the flow scheme.

$(I \times I)$ -matrices and the nuclide flow rates $J(t), \dots$ are vectors of length I , where each component is a s - or t -valued function. More explicitly, now $\overline{\mathfrak{R}}_{ZG}(s)$ in code level (4) is an $(I \times I)$ -matrix of leg response functions. A pathway is initialised in code level (5) by defining a vector or a matrix of functions instead of a single function. Matrix-matrix or matrix-vector products of functions are performed in code level (6), instead of products of single functions. Vectors or matrices of functions are summed in code level (7). The numerical inverse Laplace transformation in code level (8) is performed for each component of the vector or matrix of functions. For each component of the nuclide flow rate, I functions are summed in code level (9), where each is calculated as a convolution of two functions. For multiple sources, vectors of functions are summed in code level (10) instead of single functions.

While conceptually the step from a single nuclide to a nuclide decay chain contains “only some algebra”, for the verification it is necessary to verify the behaviour of decay chains and one cannot rely on the verification procedure for a single nuclide.

3.1.4. Condensed Flow Scheme

Condensing the structure of the flow scheme of PICNIC further, it consists of a problem definition part (0), followed by a “Russian doll” structure (1-10), see Table 3.2.

The image of a “Russian doll” is chosen because one level interacts only with the next level and the succession of the levels is necessarily in this order. (The tree initialisation level (5) can also be executed before the levels (1) to (4).) Another interpretation of the flow scheme could be the picture of a hierarchical linear “pathway” of processes or (more precisely) a “directed network” of processes. Note, for the pathway level (6), several legs must be considered in level (4).

This flow scheme relies on the linearity of the processes and on the fact that all processes only act locally. Matrix diffusion (in code level 1) acts locally at one position in the leg and locally at one s -value in the Laplace domain. The effects of advection (2) and micro-dispersion (3) in the legs can be separated into the eigenvalues of the partial differential equations. The leg outlet boundary condition (4) influences only the pre-factors of the eigenvectors, but not the eigenvectors themselves. The pathways/tree initialisation (5) is independent of all other levels. The pathway calculation (6) only makes use of the pathway initialisation (5) and of the leg response functions calculated in level (4). The tree calculation (7) uses only the pathway result of level (6). The inverse Laplace transformation (8) is applied only to the results of the tree calculation (7). If necessary, the source is convoluted in (9) with the time-dependent tree response function (8). For multiple sources (10) the single sources results (9) are superimposed.

Condensed PICNIC Flow Scheme — “Russian Doll Structure”

level 0	problem definition
	↓
1	matrix diffusion: embedded with analytical relations or with finite-element method
	↓
2	Advection in leg
	↓
3	micro-dispersion in leg
	↓
4	leg outlet boundary conditions
	↓
5	initialisation of the pathways/tree; form of source in “Laplace domain”
	↓
6	pathway (sequence of legs between a source at <i>in</i> and the junction <i>out</i>)
	↓
7	tree (representing all pathways from a source to the junction <i>out</i>)
	↓
8	numerical inverse Laplace transformation (Talbot’s method)
	↓
9	convolution with “time-dependent” source
	↓
10	multiple sources

Table 3.2. Condensed PICNIC flow scheme consisting of the problem definition part in code level (0), followed by the “Russian doll structure” in code levels (1) to (10).

3.2. Possible Errors

Based on the structure of the code and the mathematical and numerical procedures used, we now discuss the **possible sources of errors**¹⁸ and the parts of the code, which can conceal errors.

(refer to code level 0; see section 3.1.1) The correct reading of the input file needs some effort from a software point of view. However, from a verification point of view, bugs in this level should show up after a few tests. The same holds for the generation of the trees from the geometry of the

¹⁸ A source of errors, which in principle cannot be neglected, is the bias in the verification due to the skills and opinions of the persons involved in the tests (i.e. the human factor) and the “phase of the moon”. These errors are hard to control. To reduce their probability, a principle in the verification of each code should be to incorporate some redundancy and random factors into the selection of the test cases. Because of the involved increased expense, as typical in most practical cases this will be done for PICNIC only to a limited extent. An example of “redundancy” is the overlap of the selected test cases considered for the different rock matrix geometries. An example of the involvement of “random factors” is the selection of part of the test cases which were strongly influenced by the availability of results from other codes.

network, and the source and output locations, which uses graph theory. The calculation of the Darcy velocities from hydraulic conductivities and hydraulic heads should also need only a few tests, because errors should directly show up there.

(refer to code level 1) The calculation of the analytically available rock matrix response $\bar{\eta}(s)$ will also need only a few tests. However, the generation of numerical inaccuracies is inevitable using the finite-element method for the calculation of the rock matrix response. The finite-element calculation of the rock matrix response for nuclide decay chains, from a numerical point of view, is even more complicated, because now a coupled system of balance equations has to be computed with yet more processes interacting on different timescales. The effects of all these inaccuracies need to be analysed in detail!

(refer to code levels 2-4,6,7) By contrast, the errors in the remaining analytical transformations in the Laplace domain should show up already for simple test cases.

(refer to point 3) However, the calculation of $\chi(s)$ (or better $K_v(s)$) can increase existing errors for

high Peclet numbers. (Consider, e.g. $K_2(s) = \frac{Pe}{2L} \left[1 - \sqrt{1 + \frac{-4L\Lambda(s)}{Pe}} \right]$ for a single nuclide which is

about $K_2(s) \approx \Lambda(s)$ for large Peclet numbers. Inaccuracies in $\Lambda(s)$ can however be strongly increased in $K_2(s)$ because of loss of trailing digits from $\Lambda(s)$ which is due to *cancellation*.)

(refer to code level 4) The calculation of the leg response functions, e.g. $\bar{\mathfrak{K}}_{ZG}(s)$, can be an even stronger error amplifier, particularly because of the exponential functions involved. This is particularly of concern for cases where the rock matrix response is calculated in code level (1) using the finite-element method and some inaccuracies are inevitably generated already in code level (1).

(refer to code level 8) Talbot's method for the inverse Laplace transformation is a key point for the reliability of the code. It involves numerical integration in the complex plane approximated as the sum of a finite series. Particularly for high Peclet numbers, when the nuclide flow rate sharply increases or sometimes sharply decreases, these series are not always well behaved. Thus, the numerical inverse Laplace transformation can act both as a source and as an amplifier of numerical errors.

(refer to code level 9) A limited accuracy is also inherent in the numerical convolution with the source. A user of the code should also keep in mind that PICNIC interprets a time-dependent source as a function which is piece-wise linear between the user-supplied times. This can be regarded as another source of error. However, the convolution is very late in the PICNIC flow scheme, so that its inaccuracies are not amplified and its consequences in terms of errors can be demonstrated in a few tests.

(refer to code level 10) Also, the superposition of the nuclide flow rate for multiple sources should need a few tests only.

The "end product" of PICNIC, i.e. time-dependent release curves, should be analysed and verified. Simply verifying early code components (such as the finite-element method in code level 1) in particular is not sufficient because different code components work differently well for different parameter regions and especially because of the "error amplifiers" (3,4,8) in the code. On the other

hand, it must be borne in mind that considering “only” the end product can also conceal errors which potentially exist in an intermediate level of the flow scheme.

Also multiple sources (10) lead to a superposition of release curves, where errors can be balanced. A broad source (5,9) leads to smoothed release curves with smoothed or damped errors. Considering networks (7) or pathways (6) also leads to a convolution of leg response functions and possible smoothed or balanced errors. Thus it is expected that considering a single, short pulse-like or δ -function source should result in most clear information on the errors.

3.3. Application Range of PICNIC to be Verified

In this subsection the **diverse application range** of PICNIC (Table 3.3) is discussed with respect to its verification.

PICNIC Application Range

	Features	“code levels” involved
A	single nuclides or nuclide decay chains;	all
B	a single leg, a pathway (legs in series), or a network of legs;	6, 7 for pathways and networks
C	3 different leg outlet boundary conditions (ZG, ZC or AI)	4
D	different forms of the source function; one or more sources;	5, 9, 10
E	one-dimensional or two-dimensional matrix diffusion and different rock matrix geometries;	1
F	together with the variation of all parameters.	all

Table 3.3. Summary of the application range of PICNIC, i.e. the combination of points A-F described in the second column. The base case includes advective and dispersive transport in a single leg in the area of flowing water, together with linear sorption in the area of flowing water and in the rock matrix. The respective “code levels” involved in the PICNIC flow scheme of Table 3.1 are given in the third column. For more details see text.

(A in Table 3.3) The capability to deal with single nuclides is included as a special case in the capability of PICNIC to deal with nuclide decay chains. Thus, in principle, it is sufficient to consider nuclide decay chains. However, to increase the complexity of the test cases gradually, in most cases we will consider first a single nuclide and then a nuclide decay chain. See also the discussion in section 3.1.3 where it is argued that it is not sufficient to deal with single nuclides only, because the difference between a single nuclide and a nuclide decay chain enters into all “code levels” of PICNIC.

(B) The capability to deal with a network includes the capability to deal with a pathway, which again contains the capability to deal with a single leg.¹⁹ Thus it would be sufficient to verify the capability of PICNIC to deal in general with networks. The difference between dealing with a single leg and dealing with a pathway or network is contained in PICNIC only in the code levels (6) and (7), which are used only in a very simple way for a “network” consisting of a single leg. These

¹⁹ This is because a leg is a special case of a pathway and a pathway is a special case of a network.

levels only contain analytical transformations which, however, can conceal or smooth possible inaccuracies of other code levels, as mentioned above. Thus our most test cases will deal with single legs. The capability for pathways and networks will be verified only by a few tests, mainly depending on the availability of results from other codes for comparison.

(C) The only difference in PICNIC for the zero-gradient (ZG), zero-concentration (ZC) or at-infinity (AI) leg outlet boundary conditions is in code level (4), which contains only analytical transformations. Thus we will ensure that each boundary condition is considered in some tests, but in most cases we will use the option which is most convenient. This depends particularly on the available results from other codes for comparison.

(D) The capability to deal with multiple sources includes the capability to deal with a single source. Thus it would be sufficient to verify the capability in PICNIC to deal with multiple sources. However, the difference between dealing with a single source and dealing with multiple sources is contained in PICNIC only in the code level (10), which means a superposition of release curves. Thus nearly all of our test cases will deal with a single source, in particular because the superposition can conceal or smooth possible inaccuracies in other code levels. The capability for multiple sources will be spot-checked. The two different options in PICNIC to enter the form of a source have to be tested. On the one hand, the Laplace transformed forms of some sources are implemented in PICNIC as analytical formulae. This is considered in code level (5) in column 6 in Table 3.1 and will be tested at least once for each possibility implemented. On the other hand, arbitrary time-dependent sources can be entered to PICNIC in files. This is implemented in PICNIC as the initialisation of the pathway/tree response function tensor as the identity function tensor in code level (5) and the convolution in the (late) code level (9) in column 5 in Table 3.1. The accuracy of the convolution will be tested for different sources. The convolution can also conceal or smooth inaccuracies in earlier code levels. Thus, as already mentioned, in most test cases we will consider short, pulse-like or δ -function sources.

(E) In PICNIC a wide variety of different rock matrix geometries for matrix diffusion can be considered. For a homogeneous planar or cylindrical rock matrix geometry, the rock matrix response is calculated analytically in code level (1). As an alternative to these analytical formulae, the rock matrix geometry can also be entered to PICNIC by giving the cross-section of a leg in a checkerboard manner as described in section 2.4.3. PICNIC then uses a finite-element method for calculation of the rock matrix response. In this case, one-dimensional or two-dimensional matrix diffusion into homogeneous or heterogeneous rock matrices can be considered. It is necessary to show that both options, the analytically implemented rock matrix response and the embedded finite-element method work correctly. The capability of PICNIC to deal with different types of matrix diffusion will be used to organise the verification strategy given below.

(F) For practical reasons, it is not possible to consider thoroughly the variation of all possible parameters in a verification study (and additional tests can always be conceived). We therefore concentrate on the main operation ranges of PICNIC. These are the modelling of field experiments on one hand and the application in performance assessment on the other, where matrix diffusion is a relevant effect. As key examples, (theoretical) variations of the Grimsel dipole experiment and cases related to the Kristallin-I performance assessment are considered. These cases are selected because the parameters used in these studies are well founded. A practical and historical reason for this selection was also the availability of release curves for comparison, especially with the RANCHMD code. Another reason is that the form of the time-dependent nuclide release strongly depends on the timescales, particularly the relative timescales of the different processes such as advection, matrix

diffusion and radioactive decay. It is an advantage that the Grimsel and Kristallin-I cases span different ranges of these timescales and show different transport behaviour.

3.4. Verification Strategy

In this subsection we explain the strategy for verifying the PICNIC code, based on considerations of the PICNIC architecture and possible sources of error and considering the range of application of PICNIC in the preceding subsections. The capability to deal with matrix diffusion into a variety of different rock matrix geometries (point E in Table 3.3) organises the verification scheme (Table 3.4), which consists of seven steps (I to VII) of increasing complexity. These seven steps (performed in sections 4 to 10) are described in sections 3.4.1 to 3.4.7.

For one-dimensional matrix diffusion into a homogeneous planar or cylindrical rock matrix geometry, the rock matrix response is calculated analytically in PICNIC. The respective tests are described in steps I and II below.

As an alternative to these analytical formulae the rock matrix geometry can also be entered to PICNIC by giving the cross-section of a leg in a checkerboard manner as described in section 2.4.3. The rock matrix response is then calculated by PICNIC using a finite-element method.

The verification strategy is described in the verification steps III to VII below. The complexity of the rock matrix is gradually increased from step III, which considers the same single-layer planar rock matrix geometry as step I, over different heterogeneous rock matrix geometries for one-dimensional matrix diffusion considered in steps IV and V and ends with two-dimensional matrix diffusion in steps VI and VII.

The strategy has been further developed and changed during the verification process. The test cases considered are historically strongly influenced by the availability of results from the literature or from other codes for direct comparison with PICNIC. Each verification step is further subdivided into points (a) to (f) (Table 3.4), depending on whether a single nuclide or a nuclide decay chain are considered (point A in Table 3.3) and depending on whether transport is in a single leg, a pathway or a network (point B in Table 3.3).

PICNIC Verification Scheme

step	section	rock matrix geometry	A	b	c	d	e	f
			single leg		pathway		network	
			single nuclide	decay chain	single nuclide	decay chain	single nuclide	decay chain
I	4	planar geometry	C,S,K	C,K	C,K	C,K	C,K	C,K
II	5	vein geometry	C	C				C
III	6	one-dimensional, single layer	P-I,S,R	P-I,R			P-I,R	P-I,R
IV	7	one-dimensional, two-layer	C,S,R	C,R			K	
V	8	one-dimensional, heterogeneous	C,R	C,R	C,R	C,R	C,R	C,R
VI	9	two-dimensional, single layer	S,R,K	R,K			R	R
VII	10	two-dimensional, heterogeneous	R,K	R,K				

Table 3.4. Summary of PICNIC verification. The symbols in the cells denote tests of different kind where PICNIC calculations have been performed. **Empty cells are implicitly tested.** Legend:

C: comparison with other computer code;

K: consistency tests;

P-I: comparison of “embedded finite-element” results in PICNIC with “analytically” implemented results in PICNIC;

R: “discretisation test” with different mesh refinements in the finite-element results in PICNIC;

S: stationary behaviour tested.

3.4.1. Homogeneous One-Dimensional Planar Rock Matrix

In verification step I (documented in section 4), the effect of one-dimensional matrix diffusion into a homogeneous planar rock matrix geometry (Figure 2.4) is considered; see Table 3.5. The test cases presented in Barten [1996b, 1996c]; Barten and Robinson [1996]; Niemeier and Barten [1997] are reviewed and extended. For this geometry, the analytical solution for the rock matrix response $\bar{\eta}(s)$ is available and implemented in PICNIC; almost the full range of possible combinations of the points A to D in Table 3.3 are considered. Comparisons with the codes RANCHMD, GIMRT [Steeffel and Yabusaki, 1996] and, very recently, PAWorks/LTG [Dershowitz et al., 1998] are performed together with a series of self-consistency tests considering analytical relations.

step	rock matrix geometry	a	b	c	d	e	f
		single leg		pathway		network	
		single nuclide	decay chain	single nuclide	decay chain	single nuclide	decay chain
I	planar geometry	C,S,K	C,K	C,K	C,K	C,K	C,K

Table 3.5. Summary verification scheme for a planar rock matrix geometry excerpted from Table 3.4. C: comparison with other computer code; K: consistency tests; S: stationary behaviour tested. The structure of the verification scheme, especially for this planar rock matrix geometry, is only very roughly represented by this table. For more details see the verification matrix in Table 4.16.

(Transport experiment cases) More explicitly, we start with test cases related to the Grimsel dipole experiment where results from the RANCHMD code [Hadermann and Rösel, 1985] were available [Heer and Hadermann, 1994; Hadermann and Heer, 1996] for direct comparison. The transport of the single “nuclides” strontium and uranium in a single leg (a in Table 3.5) is considered, which show strongly different timescales for transport. The zero-gradient outlet boundary condition is used. The effect of variation of the Peclet number is illustrated for the different boundary conditions. Some technical tests of the stability of the numerical inverse Laplace transformation in code level (8) and the convolution with a time-dependent source in code level (9) of the PICNIC flow scheme are performed.

It is shown that PICNIC can encounter numerical instabilities for high Peclet numbers ($Pe > 100$).

For strontium, self-consistency tests are performed in such a way that the parameters are varied but the timescales for transport stay exactly the same. It is checked that the nuclide flow rate is the same in these calculations. This demonstrates our analytical understanding of the system and verifies that PICNIC deals correctly with the parameter values entered.

In another self-consistency test for a single nuclide in a leg with the at-infinity outlet boundary condition, a network (e) with multiple sources is constructed to behave as the single leg. A similar self-consistency test, comparing transport in a network with transport in a single leg, is performed for a nuclide decay chain (f) consisting of a parent nuclide with a non-decaying daughter.

Considering different types of short pulse-like sources, it is shown that how this source is generated has almost no influence: using a file to enter a square or triangular form of the source function, or

using an analytically implemented δ -pulse or a simple-leaching source, or using the top-hat release option in PICNIC.

The capability to deal with the band-release source [Bateman, 1908-1910] is verified for a nuclide decay chain in a single leg (b) using analytical relations and results from the literature. This should be sufficient, because this type of source (as the top-hat source) is implemented in PICNIC analytically in the time domain and then convoluted with the time-dependent response function. The option for a simple-leaching source which is implemented analytically in the Laplace domain is verified for a single nuclide in a single leg (a) using an analytical relation in a self-consistency test.

The capability for the analytically implemented simple-leaching source is also verified for a nuclide decay chain.

Fortunately, very recently it was also possible to perform inter-comparisons with the PAWorks/LTG code. This inter-comparison is already very useful in step I, but becomes most valuable in verification step V, where rock matrix geometries are considered which go beyond the capabilities of the RANCHMD code. The inter-comparison is done for the zero-gradient leg outlet boundary condition, because PAWorks/LTG is presently restricted to this boundary condition. Therefore hypothetical variations of the Grimsel uranine case are considered for a single nuclide or a nuclide decay chain in a single leg or a pathway (a,b,c,d). PAWorks/LTG uses a different definition of the probabilities w_{lg} of the nuclides to enter a leg at a junction. Not only arriving legs, but also departing legs can be entered by the nuclides (which is by definition not possible in PICNIC, see section 2.1.3). The differences in the release curves between PICNIC and PAWorks/LTG appear to be much smaller for the pathways than for the networks considered below.

For a network, this difference influences the transport behaviour more strongly in such a way that no exact agreement is expected or indeed encountered in the code inter-comparison with PAWorks/LTG. The transport behaviour of a single nuclide in three different networks (e) is considered (where the parameters are not Grimsel-related). In one of these networks also a nuclide decay chain (f) is considered. However, PICNIC and PAWorks/LTG do not consider exactly the same physical system. Different boundary conditions at the inner junctions in the network are considered. Thus the sub-points (e) and (f) (Table 3.5) cannot be regarded as fully verified by the cross-comparison with PAWorks/LTG alone.

(Performance assessment cases) To enter into another parameter region, and in particular to show that PICNIC can be used with confidence for performance assessment applications, test cases related to the Kristallin-I performance assessment are considered. Direct comparisons with the Swiss geosphere transport code RANCHMD are performed for single legs. Arbitrary time-dependent near-field releases are entered to PICNIC in tabular form in a file.²⁰ This also verifies the capability of PICNIC to deal with these types of sources. The transport of different single nuclides is considered for a single leg (a), and for multiple sources in a small network (e). This also verifies the capability of PICNIC to deal with single nuclides in pathways (c). A nuclide decay chain is considered in a single leg (b). For historical reasons, the verification of the transport of a (performance assessment-relevant) nuclide decay chain in a network (f) is performed in verification step II. Considering the leg outlet boundary conditions, the zero-concentration boundary condition is used for the single leg. In the network the zero-gradient and the zero-concentration leg outlet

²⁰ Both the simple tabular form and the 'Hartley' file format are tested.

boundary conditions are used, thereby verifying the capability of PICNIC for these boundary conditions. For a single nuclide in a single leg (a), the steady-state release is compared to the analytical result for all outlet boundary conditions, at-infinity, zero-gradient, and zero-concentration.

Note that, for the verification of the network capability in PICNIC, a sequence of RANCHMD calculations for each individual leg in the network is combined to obtain the nuclide release of the network. The agreement with this so-called “assembled RANCHMD” result is excellent.

(Implications for the following verification steps) Together with the understanding of the PICNIC flow scheme, it is shown that PICNIC can deal with one or more sources and different forms of source functions (point D in the PICNIC application range, Table 3.3). This means that, for the rock matrix geometries considered below, only appropriate single sources need to be considered and not a range of sources. In most cases we will consider short pulse-like sources. However, constant sources are also very useful, especially because analytical results and numerical calculations from other codes are often available for steady-state release, but not the time-dependent behaviour.

Our tests covering the three different leg outlet boundary conditions indicate that this code level in PICNIC works correctly (point C in Table 3.3). This means that, for the further verification steps, it should not matter what leg outlet boundary condition is considered.

After verification step I (and once we have considered, in step II below, the transport of a nuclide decay chain in a network), we will conclude that the parts in the PICNIC flow scheme dealing with pathways or networks of legs also work correctly (point B in Table 3.3).

This first verification step for a planar rock matrix geometry supports the verification in all the following steps. This means that, for the further verification, we can restrict to the transport of a single nuclide and a nuclide decay chain in a single leg (a,b). It is only necessary to perform spot-checks for the transport in a pathway or a network (c to f) in combination with different types of rock matrix in the legs.

3.4.2. Homogeneous Cylindrical Rock Matrix

In verification step II (documented in section 5), the effect of one-dimensional matrix diffusion into a homogeneous cylindrical rock matrix geometry (Figure 2.6) is considered, see Table 3.6. The test cases presented in Barten, Niemeyer and Heer [1997] are reviewed. For this geometry, the analytical solution for the rock matrix response $\bar{\eta}(s)$ is also coded in PICNIC. The calculation of the rock matrix response $\bar{\eta}(s)$ is the only difference to the procedure in PICNIC for the planar rock matrix geometry considered in step I. Thus, as mentioned in section 3.4.1, it is not necessary to consider the full range of combinations of the points (A) to (D) of the PICNIC application range. The same holds for the verification steps III to VII described below.

step	rock matrix geometry	a	b	c	d	e	f
		single leg		pathway		network	
		single nuclide	decay chain	single nuclide	decay chain	single nuclide	decay chain
II	vein geometry	C	C				C

Table 3.6. Summary verification scheme for a cylindrical rock matrix geometry. C: comparison with other computer code.

For a single nuclide in a single leg (a in Table 3.6), two hypothetical variations of the Grimsel dipole parameters for uranium are considered and compared to RANCHMD results.

To show that PICNIC can be used with confidence for performance assessment applications for vein geometry, again test cases related to the Kristallin-I performance assessment are used as sources from performance assessment. Direct comparisons with RANCHMD are performed for the transport of a nuclide decay chain in a single leg (b).

“Assembled PICNIC” calculations (similar to the “assembled RANCHMD” calculations mentioned above) are performed for a test case with multiple sources of a nuclide decay chain in a small network (f). This also verifies implicitly the capability of PICNIC to deal with transport of a nuclide decay chain in a pathway (d) and of a single nuclide in a pathway or a network (c,e).

3.4.3. Using the Embedded Finite-Element Method to Approximate Matrix Diffusion into a Homogeneous One-Dimensional Planar Rock Matrix

In verification steps III to VII, cases are considered where the rock matrix response $\bar{\eta}(s)$ is calculated using the finite-element method. To find a first estimate for the numerical error in PICNIC due to the finite-element method, in verification step III (documented in section 6) test cases are considered (Table 3.7), which are the same or very close to the one-dimensional planar rock geometry cases described in step I. In “discretisation tests”, different refinements to the finite-element method are compared to each other and to the results for the analytically derived rock matrix response of verification step I. Regarding the source terms, we concentrate on short pulses and on constant sources.

step	rock matrix geometry	a	b	c	d	e	f
		single leg		pathway		network	
		single nuclide	decay chain	single nuclide	decay chain	single nuclide	decay chain
III	one-dimensional, single layer	P-I,S,R	P-I,R			P-I,R	P-I,R

Table 3.7. Summary verification scheme for a one-dimensional planar rock matrix geometry approximated using the finite-element option in PICNIC. “P-I” indicates that the finite-element result in PICNIC is compared to the analytically implemented result in PICNIC. R: “discretisation test” considering different mesh refinements in the finite-element results in PICNIC; S: stationary behaviour tested.

(Transport experiment cases) More explicitly, the transport of uranium (a in Table 3.7) and a nuclide decay chain in a single leg (b) is considered for a δ -function source. The effect of mesh refinement in the finite-element method is analysed and the results are compared to PICNIC calculations of step I with the analytical rock matrix response. Then, for almost the same test cases, it is checked that small side-columns of rock matrix (Figure 3.1a) and the associated weakly two-dimensional matrix diffusion can also be handled in PICNIC.

(Performance assessment cases) Performance assessment parameters are then considered for a constant source of single nuclides in a single leg (a). The effect of mesh refinement in the finite-element method is analysed in detail for a weakly decaying nuclide (with weak influence of radioactive decay on the transport behaviour) and a strongly decaying nuclide (with strong influence of radioactive decay on the transport behaviour). The long-time limit nuclide flow rate for the constant source gives, in particular, information on the accuracy of the geosphere barrier efficiency (see section 2.1.7), which is used in the more complicated rock matrix geometries in the steps below.

The effect of subdividing the rock matrix layer horizontally (Figure 3.1b) is then analysed. This subdivision enforces an increased number of finite-element meshes in the rock matrix and additionally a local refinement of the finite-element mesh for calculation of the rock matrix response, see section 2.4.3.

It is shown that extremely small sub-columns of rock should be avoided²¹, because they might lead to increased numerical error of the results. This is considered for the geometries of Figures 3.1a-d.

Finally, the effects of different mesh refinements on transport of a **single nuclide** (e) and a **nuclide decay chain** in a **network** (f) are analysed. Therefore we consider a network where we have performed, in step I, a cross-comparison with the PAWorks/LTG code.

(Implications) These self-consistency tests within PICNIC in particular show that the finite-element method for numerical calculation of the rock matrix response works for this homogeneous one-dimensional rock matrix geometry. The tests, moreover, give indications of (mainly small) differences between the different PICNIC results for the same physical system. These investigations should also help in steps IV to VII, by providing “calibration curves” for errors generated by the finite-element method. Note that the forms of these relative difference functions between different PICNIC results are very useful, particularly because they can also be generated (and compared to the “calibration curves” of this verification step) for cases with two-dimensional matrix diffusion in steps VI and VII, where no reference code for the time-dependent behaviour is available.

²¹ In the example considered, “extremely small” means smaller than 10^{-12} [m].

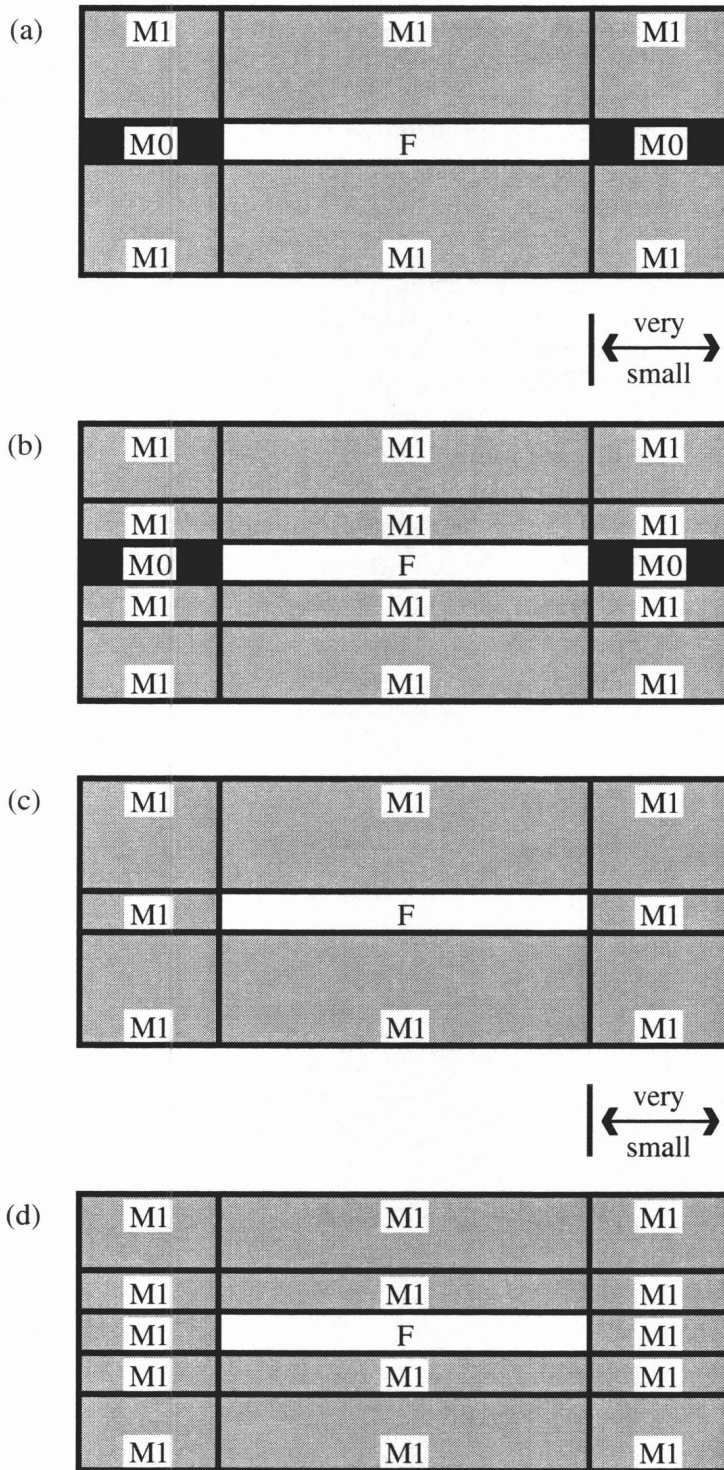


Figure 3.1. Different cross-sections of legs entered in a checkerboard manner to PICNIC. “F” indicates an area of flowing water, “M1” indicates a porous rock matrix and “M0” is a rock matrix area which is impermeable. Matrix diffusion in these geometries is nearly one-dimensional, because the side-columns are assumed to be very small (the sketch is not to scale). In (a,c), one row of rock matrix is considered below and above the area of flowing water. In (b,d) physically the same system is considered as in (a,c) but the rock layer is subdivided horizontally.

3.4.4. Two-Layer One-Dimensional Planar Rock Matrix

In verification step IV (documented in section 7), the effect of one-dimensional matrix diffusion into a two-layer rock matrix (Figure 2.5) is considered, see Table 3.8. The test cases presented in Barten, Robinson and Schneider [1998] are reviewed and considerably extended. For this geometry, the analytical solution for the rock matrix response $\bar{\eta}(s)$ is available. It is, however, not coded in PICNIC. Cross-comparisons with the code RIP [Miller and Kossik, 1998] are performed for single nuclides and nuclide decay chains. PICNIC results for steady-state release of single nuclides are compared to an analytical result.

step	rock matrix geometry	A	b	c	d	e	f
		single leg		pathway		network	
		single nuclide	decay chain	single nuclide	decay chain	single nuclide	decay chain
IV	one-dimensional, two-layer	C,S,R	C,R			K	

Table 3.8. Summary verification scheme for one-dimensional matrix diffusion into a two-layer rock matrix geometry. C: comparison with other computer code; K: consistency tests; R: "discretisation test" considering different mesh refinements in the finite-element results in PICNIC; S: stationary behaviour tested.

(Performance assessment cases) More explicitly, performance assessment parameters are considered for single nuclides in a single leg (a in Table 3.8). The effect of mesh refinement and of subdivision of rock matrix layers is analysed. For the long-time nuclide flow rate in the case of a constant source, the PICNIC result is compared to the analytical result. For a δ -function source, the forms of the relative difference functions between different PICNIC results are analysed. Thereby the effect of mesh refinement in the finite-element method is considered in detail for different extents of the second rock matrix layer and three different nuclides. For a self-consistency test, a network is constructed that behaves like a single leg (e). As a further test for different parameters, the effect of variation of the porosity of the second rock layer is considered for the long-time limit of a constant source.

(Transport experiment cases) To enter into another parameter range, Grimsel uranium parameters are considered for a single nuclide (a) and a nuclide decay chain in a single leg (b). Again the effects of mesh refinement and rock layer subdivision on the PICNIC results are considered. Here, too, an inter-comparison with the code RIP was possible. Because RIP is presently restricted to the at-infinity boundary condition, this leg outlet boundary condition is used.

3.4.5. One-Dimensional Matrix Diffusion into Heterogeneous Geometries

In verification step V (documented in section 8) the effect of one-dimensional matrix diffusion into different heterogeneous rock matrix geometries (Figure 3.2) is considered, see Table 3.9. For these geometries, the analytical solution for the rock matrix response $\bar{\eta}(s)$ is available, but is not implemented in PICNIC. Cross-comparisons with the codes PAWorks/LTG and RIP are performed. The effects of mesh refinement and rock layer subdivision on the PICNIC results are considered.

step	rock matrix geometry	a	b	c	d	e	f
		single leg		pathway		network	
		single nuclide	decay chain	single nuclide	decay chain	single nuclide	decay chain
V	one-dimensional, heterogeneous	C,R	C,R	C,R	C,R	C,R	C,R

Table 3.9. Summary verification scheme for one-dimensional matrix diffusion into a two-layer rock matrix geometry. C: comparison with other computer code; R: “discretisation test” considering different mesh refinements in the finite-element results in PICNIC.

We start with the transport of a single nuclide (a in Table 3.9) and of a nuclide decay chain in a single leg (b), with matrix diffusion into two independent homogeneous rock matrix areas (Figure 3.2a). For PICNIC, this situation looks like two-dimensional matrix diffusion, but to ensure nearly one-dimensional matrix diffusion the available rock matrix areas are separated by nearly impermeable rock. Grimsel uranium parameters are used. A comparison with PAWorks/LTG is performed. This leg is also considered within a 3-leg pathway and within a 5-leg pathway (c,d) to spot-check the capability of PICNIC for pathways.

Two independent two-layer regions for matrix diffusion (Figure 3.2b) are then considered for a single nuclide (a) and for a nuclide decay chain in a single leg (b). This leg is also considered within a 5-leg pathway (c,d). A code inter-comparison with RIP is performed for the single nuclide and the nuclide decay chain in the single leg and the pathway (a,b,c,d).

Finally, a network considered earlier in step I is varied to contain some legs with two independent two-layer rock matrices for one-dimensional matrix diffusion (Figure 3.2c). A code inter-comparison with RIP is performed for the single nuclide and the nuclide decay chain in the network (e,f).

In verification steps III to V, we have considered different (heterogeneous) rock matrix geometries for one-dimensional matrix diffusion. PICNIC can deal with all these situations with increasing complexity. We have also exhausted code inter-comparisons as far as possible to conclude that the capability of PICNIC to deal with one-dimensional matrix diffusion is verified. The checks for the mesh refinement in the finite-element method give estimates of the code accuracy.

These test cases of step V are treated in PICNIC as two-dimensional matrix diffusion, in such a way that PICNIC constructs a spatially two-dimensional finite-element mesh for calculation of the rock matrix response. Thus, the tests of step V also contribute as limiting cases to the verification performed in steps VI and VII for really two-dimensional matrix diffusion.

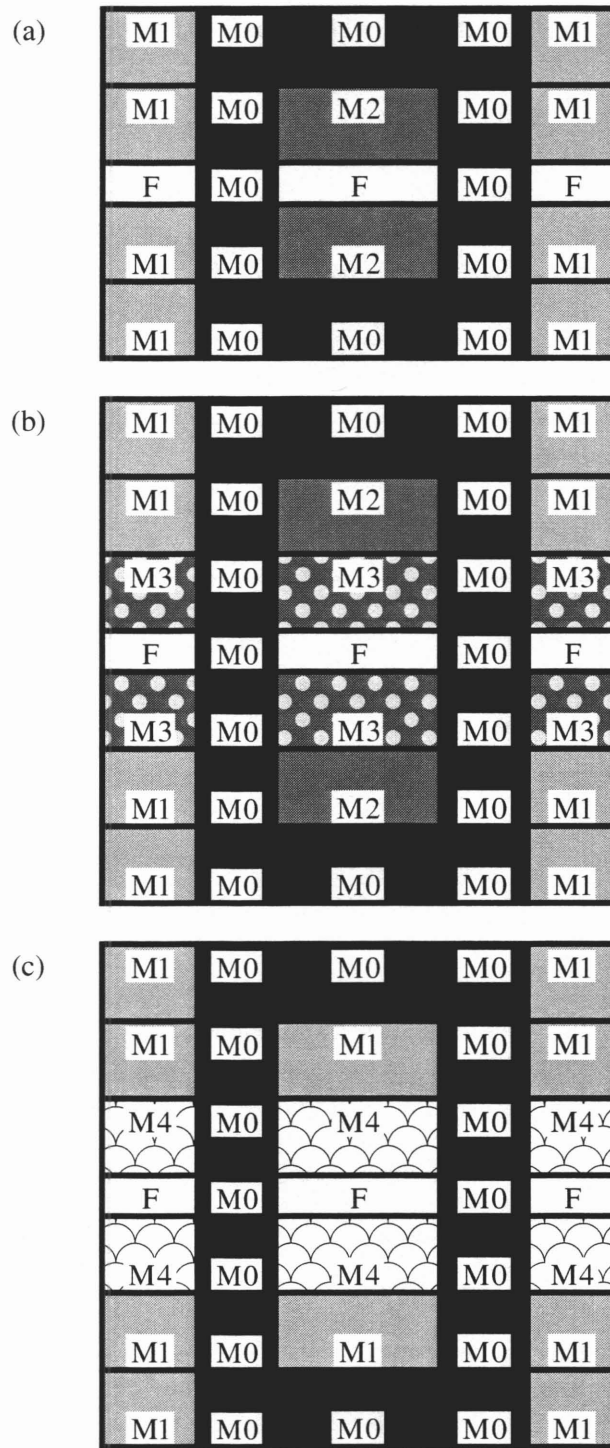


Figure 3.2. Different cross-sections of legs entered in a checkerboard manner to PICNIC. The sketches are not to scale. “F” indicates an area of flowing water, “M1,M2,M3,M4” indicate different types of porous rock matrix. Because of the impermeable rock matrix areas of type “M0”, one-dimensional matrix diffusion into two independent areas of rock matrix is approximated. In (a) two homogeneous areas of rock are considered, while matrix diffusion is into two-layer rock matrix areas in (b) and (c).

3.4.6. Homogeneous Two-Dimensional Planar Rock Matrix

In verification step VI (documented in section 9), the effect of two-dimensional matrix diffusion into a homogeneous area of rock matrix (Figure 3.3) is considered, see Table 3.10. These test cases presented in Barten, Robinson and Tirbonod [2000] are reviewed and considerably extended. For this geometry, no analytical solution of the rock matrix response $\bar{\eta}(s)$ is available. No code for comparison was found that can deal in general with two-dimensional matrix diffusion and the particular geometry considered in the test cases. This strongly reduces the possibilities for code verification. As a way round this drawback, the verification rests primarily on verification of the embedded finite-element method for one-dimensional matrix diffusion, on qualitative estimates and on “discretisation tests” for single nuclides and nuclide decay chains. It was also possible to compare PICNIC results for steady-state release of a single nuclide to a result derived from a calculation using the ADINA-T code [ADINA, 1992].

step	rock matrix geometry	a	b	c	d	e	f
		single leg		pathway		network	
		single nuclide	decay chain	single nuclide	decay chain	single nuclide	decay chain
VI	two-dimensional, single layer	S,R,K	R,K			R	R

Table 3.10. Summary verification scheme for two-dimensional matrix diffusion into a homogeneous rock matrix layer. R: “discretisation test” considering different mesh refinements in the finite-element results in PICNIC; S: stationary behaviour tested.

(Performance assessment cases) More explicitly, performance assessment parameters are considered for single nuclides in a single leg (a in Table 3.10). For the steady-state release of a single decaying nuclide, the PICNIC result is compared to a result derived from a calculation using the ADINA-T code [ADINA, 1992]. For a δ -function source, the form of relative difference functions between different PICNIC results are analysed. Thereby, for three different nuclides the effect of mesh refinement in the finite-element method is analysed in detail for different ratios of the width of the rock matrix to the width of the area of flowing water. The differences for different PICNIC results for this matrix geometry are also compared to those in steps III to V to check consistency.

(Transport experiment cases) To enter into another parameter range, Grimsel uranine parameters are considered for a single nuclide (a) and for a nuclide decay chain in a single leg (b). Again the effects of mesh refinement and rock layer subdivision on the PICNIC results are considered.

In further tests it is found that PICNIC results are different when the x - and y -axes in the cross-section of the legs (compare Figure 2.3) are exchanged and the orthogonal problem is considered. This numerical effect is physically not correct, because symmetry relations are violated. (In the most recent version of PICNIC, this bug is eliminated.)

In a self-consistency test for nuclide decay chains (b), it is also found that the behaviour of a parent nuclide depends numerically on the parameters of the daughter. This numerical result is physically not correct, see comments in section 11.5.

In an additional spot-check, “discretisation tests” are performed for a single nuclide (e) and for a nuclide decay chain in a network (f).

Besides the two inconsistencies mentioned above, with these tests the capability of PICNIC is verified as far as possible/useful for this rock matrix geometry. The “discretisation tests” considering mesh refinement and rock matrix subdivision in the finite-element method give estimates of the accuracy of code.

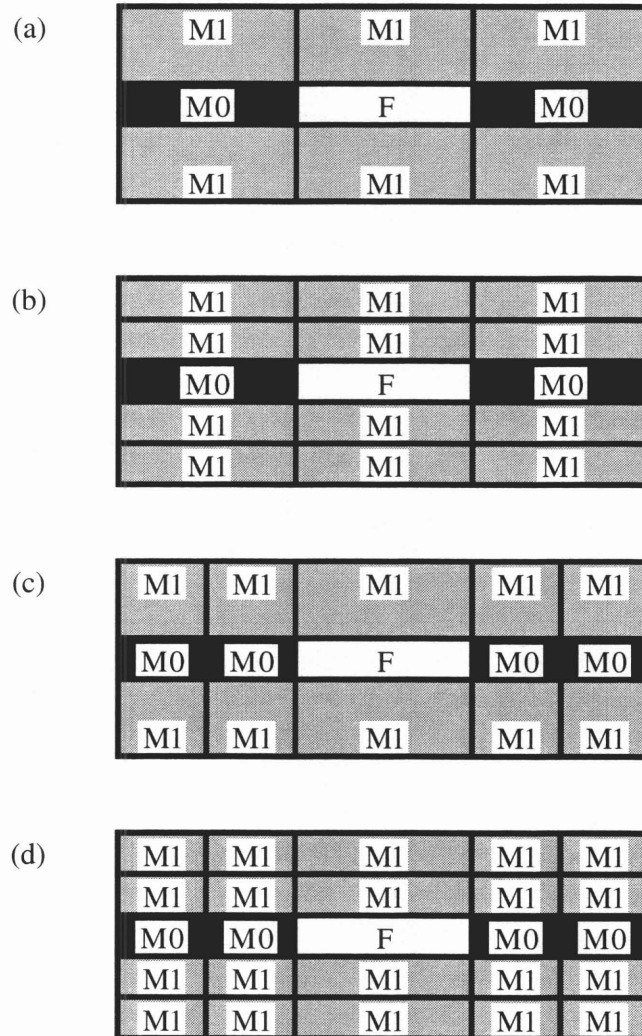


Figure 3.3. The same cross-section of a leg is entered in 4 different ways in a checkerboard manner to PICNIC. Two-dimensional matrix diffusion into a homogeneous rock layer is considered. “F” indicates an area of flowing water, “M1” indicates a porous rock matrix and “M0” is a rock matrix area which is impermeable. In (a) 3 columns and 3 rows are used as a minimal representation. In (b) the rock layer below and above the area of flowing water is subdivided horizontally. In (c) the side-columns are subdivided vertically. In (d) the rock layer is subdivided horizontally and the side-columns are subdivided vertically.

3.4.7. Two-Dimensional Matrix Diffusion into Heterogeneous Geometries

In the final verification step VII (documented in section 10), two further rock matrix geometries are considered, see Table 3.11. Again the effects of mesh refinement and rock layer subdivision on the PICNIC results are analysed in “discretisation tests”. This gives indications of the accuracy of the results.

step	rock matrix geometry	a	b	c	d	e	f
		single leg		pathway		network	
		single nuclide	decay chain	single nuclide	decay chain	single nuclide	decay chain
VII	two-dimensional, heterogeneous	R,K	R,K				

Table 3.11. Summary verification scheme for two-dimensional matrix diffusion into heterogeneous rock matrix geometries. K: consistency tests; R: “discretisation test” considering different mesh refinements in the finite-element results in PICNIC.

More explicitly, two-dimensional matrix diffusion into a two-layer rock matrix (Figure 3.4a,b) is considered for a single nuclide (a in Table 3.11) and for a nuclide decay chain in a single leg (b).

Finally the two small inconsistencies mentioned in step VI are spot-checked using Grimsel uranine parameters for another rock matrix geometry for two-dimensional matrix diffusion (Figure 3.4c,d).

The verification again relies on the earlier verification steps and on “discretisation tests” for these geometries providing estimates of the accuracy of the code. A more extended verification plan would be of restricted use only, as long as no analytical results or results from other codes are available.

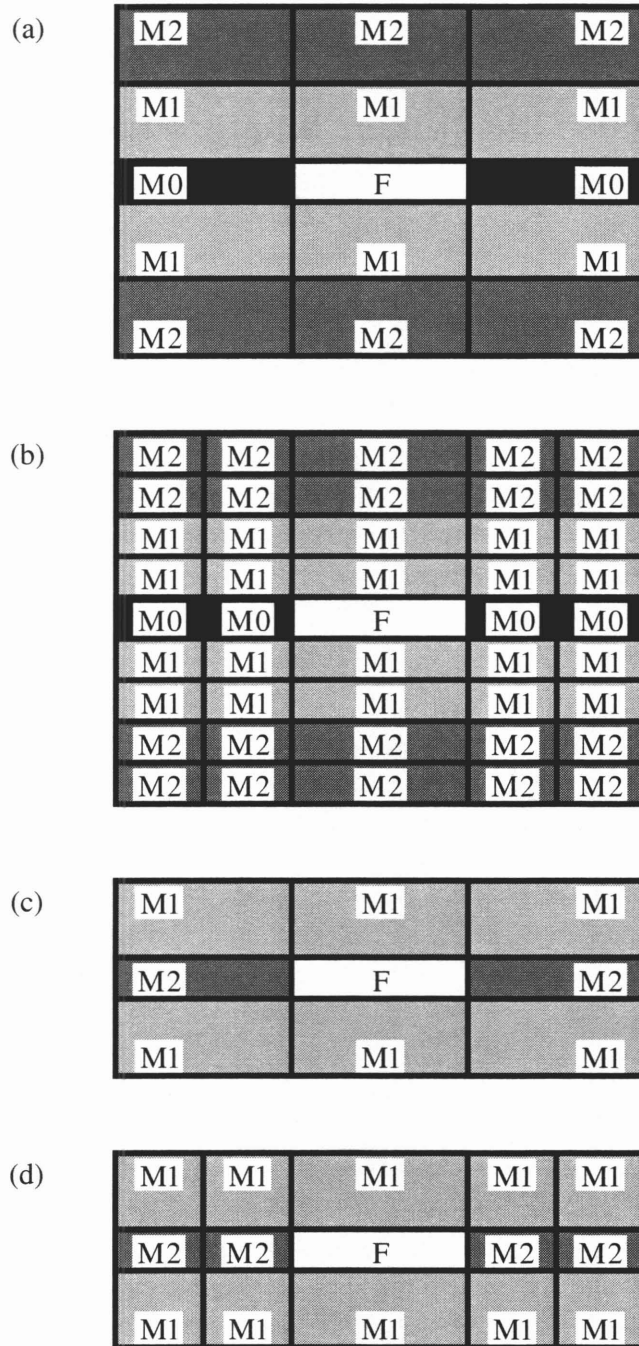


Figure 3.4. Different cross-sections of legs entered in a checkerboard manner to PICNIC. The sketches are not to scale. "F" indicates an area of flowing water, "M0,M1,M2" indicate different types of porous rock matrix. (a,b) give a geometry for two-dimensional matrix diffusion into a two-layer rock matrix of types "M1" and "M2". (c,d) give a rock matrix geometry with a single-layer rock matrix of type "M1" below and above a fracture. Within the fracture there is an area of flowing water. The rest of the fracture is impermeable for matrix type "M0" in (a,b), while it is accessible to matrix diffusion for matrix type "M2" in (c,d). The geometries are entered in (a,c) in the standard way, while in (b) the rock matrix is horizontally and vertically subdivided, and in (d) the side-columns are vertically subdivided.

4. Homogeneous One-Dimensional Planar Rock Matrix

In this section we consider the effect of matrix diffusion into a homogeneous planar rock matrix geometry. This is step I of the verification of PICNIC; see the verification strategy in section 3.4.1. For this geometry, the analytical solution for the rock matrix response $\bar{\eta}(s)$ is available and implemented in PICNIC; cf. the PICNIC flow scheme in Table 3.1. In this section, the test cases presented in Barten [1996b]; Barten [1996c]; Barten and Robinson [1996]; Niemeyer and Barten [1997] are reviewed (in sections 4.1 and 4.4) and considerably extended. The parameter definition and the balance equations for the planar rock matrix geometry are given in sections 2.2.2 and 2.5.1. Because this verification step is the base for all further verification steps in the next sections, a large series of combinations of the capabilities of PICNIC in Table 3.3 has to be performed. This means that different boundary conditions and different sources are considered in combination with the verification sub-steps (a-f); cf. Table 3.4.

We start in section 4.1 with the transport of **single nuclides in a single leg**. These cases are related to the Grimsel dipole experiment. Code inter-comparisons with RANCHMD, GIMRT and PAWorks/LTG are performed. A series of self-consistency tests and technical tests are conducted.

In section 4.2, the transport of **single nuclides and nuclide decay chains in a single leg and in a pathway** are considered in a code inter-comparison with PAWorks/LTG.

In section 4.3, in a more qualitative way, the transport of a single nuclide and of a nuclide decay chain in networks is considered again in a code inter-comparison with PAWorks/LTG.

In section 4.4, **test cases related to the Kristallin-I performance assessment** are considered in a code inter-comparison with RANCHMD. The transport of **single nuclides in a single leg and in a small network** is analysed. For the network, a comparison with the so-called “assembled RANCHMD” method is performed. A **nuclide decay chain is considered in a single leg**. This subsection ends with an INTRACOIN **chain decay** test case for transport **in a single leg**.

Section 4.5 gives a summary.

4.1. Single Nuclides in a Single Leg: Grimsel Dipole Experiment

We start our verification of the fracture geometry case for matrix diffusion by testing the accuracy of PICNIC for a **single non-decaying nuclide in a single leg**. With this aim, PICNIC results are compared mainly with results from RANCHMD [Hadermann and Rösel, 1985], which is the Swiss geosphere transport model currently used in safety assessments [Nagra, 1994]. A short code inter-comparison with GIMRT [Steeffel and Yabusaki, 1996] and PAWorks/LTG [Dershowitz et al., 1998] is done. Parameters from the Grimsel dipole transport experiment are used. Then, instability of the code for high Peclet numbers is considered. A series of self-consistency tests and technical tests of PICNIC are performed.

4.1.1. Comparison with RANCHMD

We start our verification of the code by testing the accuracy of PICNIC for a single non-decaying nuclide in a single channel with parallel plate geometry for matrix diffusion. Therefore, we consider RANCHMD calculations related to the 5 m dipole transport experiments at the Grimsel Test Site with strontium and uranine. These are among the best known applications of the Swiss geosphere transport model RANCHMD. Heer and Hadermann [1994] and Hadermann and Heer

[1996] describe the experiments, as well as detailed quantitative modelling with RANCHMD. For modelling these experiments it was generally sufficient to conduct a single RANCHMD calculation, which corresponds to transport through a single leg in PICNIC.²² The length of the leg considered is²³ $L = 5[\text{m}]$. There is no infill considered in the area of flowing water, thus the infill porosity $\varepsilon_i = 1$. The aperture of the area of flowing water is $2b$ which is entered to PICNIC via the surface to volume ratio $\delta_f = 1/b = 21505.4[1/\text{m}]$. The flow porosity is $\varepsilon_f = 1$ and, for simplicity, the cross-sectional area of the leg is chosen as $A_f = 1[\text{m}^2]$. Thus the Darcy velocity, $q_f = 16830.7[\text{m/a}]$, gives the velocity of the flowing water. There is no sorption considered in the area of flowing water, thus the retardation constant is $R_f = 1$. The Peclet number is $Pe = 20$, which defines the dispersion length a_L and the dispersion constant D_f of the leg, see equation (2.37). The thickness of the rock matrix below and above the area of flowing water is $d = 6.2 \cdot 10^{-3}[\text{m}]$, and the matrix porosity is $\varepsilon_p = 0.0062$. The matrix diffusion constant in the rock matrix is $D_p = 788.94 \cdot 10^{-6}[\text{m}^2/\text{a}]$. The retardation constant in the rock matrix is $R_p = 1$ for strontium and $R_p = 905.36$ for uranine, which is the only difference between the two nuclides²⁴ considered. To test the capability of the code for very short times for nuclide injection, the calculations assume a top-hat injection of $J_f / Q_f = 31.250[\text{mol} / \text{m}^3]$ over $1[\text{minute}] = 1.901285 \cdot 10^{-6}[\text{a}]$, while in the experiments the injection time was $1[\text{hour}]$.²⁵ Zero-gradient (see equation 2.51a) is used as the leg outlet boundary condition. In addition to this outlet boundary condition, the release of non-decaying nuclides is determined by four independent parameters: the advection time α , the matrix diffusion time β^2 , the matrix delay time γ^2 and the leg Peclet number Pe . For a discussion of such combined parameters, see section 2.5.2 and e.g. Heer and Smith [1998] and references cited therein. The parameters considered for strontium are

$$\alpha = 2.97076 \cdot 10^{-4}[\text{a}], \quad \beta^2 = 44.1124[\text{a}], \quad \gamma^2 = 0.112053[\text{a}], \quad (4.1)$$

and $Pe = 20$. All these timescales are much larger than the timescale for release of the nuclide source which is smaller than $2 \cdot 10^{-6}[\text{a}]$. Thus the source can be considered as pulse-like. As expected from the considerations for infinite Peclet number (section 2.5.3), (nearly) no release is observed for $t < \alpha$ and the time to maximum release is in the order of $\alpha + \frac{1}{6}\gamma^2 \approx \frac{1}{6}\gamma^2 \approx 0.2[\text{a}]$, compare solid line in Figure 4.1 and column 2 in Table 4.1. Because of the very large matrix diffusion time, β^2 , in the graphical representation of the breakthrough curve in Figure 4.1, no indication of the limitation of the rock matrix is observed. Because the rock matrix diffusion time β^2 is much larger than the time interval of $1[\text{a}]$ considered, the system appears to behave as if rock matrix diffusion were unlimited, and for larger times a $t^{-3/2}$ tailing is observed.

²² It is beneficial to compare PICNIC to RANCHMD results for these test cases, because the comparison is in a parameter range where the reference code RANCHMD has been successfully applied to experiments. Thus this comparison with the RANCHMD calculations also shows that PICNIC can be applied to such experiments.

²³ In the original modelling of the experiments $L = 4.9[\text{m}]$ was used.

²⁴ For simplicity, we consider the dye uranine also to be a nuclide.

²⁵ For single nuclides we omit the upper index ($i = 1$).

For uranine there is no sorption in the rock matrix, thereby $R_p = 1.0$, thus reducing β and γ and keeping α and Pe constant:

$$\alpha = 297076 \cdot 10^{-4} [\text{a}], \quad \beta^2 = 4.87236 \cdot 10^{-2} [\text{a}], \quad \gamma^2 = 1.23766 \cdot 10^{-4} [\text{a}]. \quad (4.2)$$

The uranine release curve is given as dashed line in Figure 4.1 and in column 5 in Table 4.1. As expected from the considerations for infinite Peclet number (section 2.5.3), the time to maximum release is in the order of $\alpha + \frac{1}{6}\gamma^2 \approx \alpha \approx 3 \cdot 10^{-4} [\text{a}]$. Because $\alpha \gg \frac{1}{6}\gamma^2$, the nuclide flow rate sharply increases at the rising edge of the release curve. For $10^{-3} [\text{a}] < t < 10^{-2} [\text{a}]$, matrix diffusion behaves as nearly unlimited. The influence of the limitation of the rock matrix is observed for times in the order of the matrix diffusion time β^2 , see the hump on top of the $t^{-3/2}$ tailing for $t > 10^{-2} [\text{a}]$.

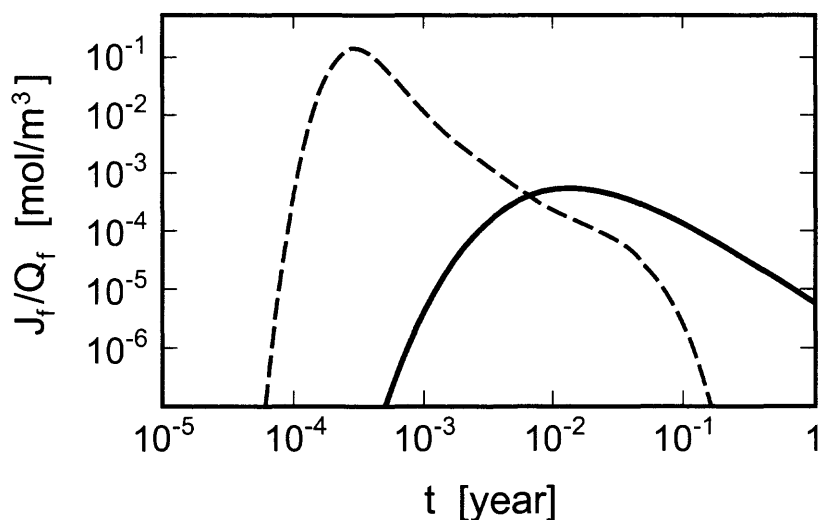


Figure 4.1. Breakthrough curves for strontium (solid line) and uranine (dashed line) in a double-logarithmic scale. Figure adopted from Hadermann and Heer [1996].

These first quantitative tests show excellent agreement between PICNIC and results from the verified code RANCHMD, see Table 4.1. For this verification exercise the RANCHMD calculations were performed with greater accuracy than the calculations performed in Hadermann and Heer [1996], which were not intended for verification purposes.

time [a]	strontium		uranine	
	J_f / Q_f [mol / m ³]	difference [%], $100 \frac{P-R}{R}$	J_f / Q_f [mol / m ³]	difference [%], $100 \frac{P-R}{R}$
$5 \cdot 10^{-5}$			$< O(10^{-10})$	
10^{-4}			$3.347 \cdot 10^{-4}$	-1.44
$2 \cdot 10^{-4}$	$< O(10^{-11})$		$6.637 \cdot 10^{-2}$	-0.19
$5 \cdot 10^{-4}$	$7.511 \cdot 10^{-8}$	-4.24	$6.041 \cdot 10^{-2}$	0.08
10^{-3}	$3.877 \cdot 10^{-6}$	-1.49	$1.031 \cdot 10^{-2}$	0.01
$2 \cdot 10^{-3}$	$4.837 \cdot 10^{-5}$	-0.65	$2.669 \cdot 10^{-3}$	-0.02
$5 \cdot 10^{-3}$	$2.945 \cdot 10^{-4}$	-0.28	$5.793 \cdot 10^{-4}$	0.04
10^{-2}	$4.934 \cdot 10^{-4}$	-0.17	$2.137 \cdot 10^{-4}$	-0.01
$2 \cdot 10^{-2}$	$4.833 \cdot 10^{-4}$	-0.10	$1.091 \cdot 10^{-4}$	0.02
$5 \cdot 10^{-2}$	$2.641 \cdot 10^{-4}$	0.01	$2.580 \cdot 10^{-5}$	-0.07
10^{-1}	$1.264 \cdot 10^{-4}$	0.01	$2.341 \cdot 10^{-6}$	-0.33
$2 \cdot 10^{-1}$	$5.268 \cdot 10^{-5}$	0.07	$1.903 \cdot 10^{-8}$	-0.92
$5 \cdot 10^{-1}$	$1.477 \cdot 10^{-5}$	0.01	$O(10^{-14})$	
1	$5.411 \cdot 10^{-6}$	0.02		
maximum of J_f / Q_f [mol / m ³]	$5.182 \cdot 10^{-4}$	-0.03	$1.303 \cdot 10^{-1}$	0.06
t_{\max} [a]	$1.337 \cdot 10^{-2}$	< 0.01	$3.008 \cdot 10^{-4}$	< 0.01

Table 4.1. Comparison of PICNIC and RANCHMD calculations. In the first column, time is given and in the second and fourth columns the PICNIC results for J_f / Q_f for strontium and uranine, respectively. In the third and fifth columns the relative deviation of the PICNIC results (P) from the RANCHMD results (R) is presented. The two bottom rows give the maximum value, and the time of the maximum, t_{\max} , of the breakthrough curve.

4.1.2. Comparison with GIMRT

The code RANCHMD is restricted to one-dimensional matrix diffusion into homogeneous planar or cylindrical rock matrix geometries and cannot be used for verification of PICNIC for more complicated rock matrix geometries considered in sections 7-10. Other potential candidates for an inter-comparison with PICNIC must also be considered. One of these is the code pair GIMRT/OS3D of Steefel and Yabusaki [1996] which utilises a finite-difference time-stepping method. From its definition, for a constant nuclide source GIMRT/OS3D can model transport in a heterogeneous porous medium; thus it can also model transport in a fracture with surrounding heterogeneous rock matrix. It should be negligible that diffusion in the rock matrix is always considered locally isotropically in GIMRT and thus diffusion parallel to the advection direction in the flowing water cannot be suppressed — this is different to PICNIC. Thereby GIMRT can consider transport problems which are spatially two-dimensional, while OS3D is also applicable for spatially three-dimensional problems. Thus GIMRT can be applied to transport problems with one-dimensional matrix diffusion, while OS3D in principle also has the capability for two-dimensional matrix diffusion.

To test the accuracy of GIMRT, and especially whether GIMRT/OS3D could be used later for the verification of two-dimensional matrix diffusion, we consider here the transport of uranine in the Grimsel 5 m dipole experiment with its one-dimensional matrix diffusion. (Here we know already from the comparisons with RANCHMD, that PICNIC gives reliable results.) The release curve considering a constant source $S(t) = 1 \text{ [mol/a]}$ is given in Figure 4.2a on a linear scale for the nuclide flow rate and in Figure 4.2b on a logarithmic scale, while the time is given on a logarithmic scale. For late times with high nuclide flow rates and small concentration gradients in the leg, the GIMRT results show a very good agreement with the PICNIC result. However the increase of the release curve for early times up to the half of the steady-state nuclide flow rate (with strong concentration gradients in the leg) is much earlier for the GIMRT results compared to the PICNIC result.

A harder test case than this steady-state approach is the behaviour for short, pulse-like injection of nuclides into the leg with $S(t) = \delta(t) \text{ [mol/a]}$. Using GIMRT, this cannot be calculated directly. However this release curve (Figures 4.2c,d) can be generated by differentiation in time of the release curve for a constant source (Figures 4.2a,b). For this case, considerable differences to the PICNIC result are encountered. The difference in the time to maximum release is in the order of 5%, and nearly 10% for the maximum.²⁶ Compare also Figure 4.3 where time is presented on a linear scale. These differences are, in particular, much greater than the differences between PICNIC and RANCHMD results. However it should be noted that the present application of GIMRT/OS3D, in particular the behaviour for short times, can be considered to be outside the typically geochemical application range of the code.

Overall, this inter-comparison indicates that, for verification of two-dimensional matrix diffusion and using the present spatial resolution, GIMRT/OS3D could possibly have some value for qualitative considerations and considering trends, but the value for the quantitative verification of PICNIC is expected to be rather restricted. Given these results, perhaps besides the steady-state behaviour, it is presently not planned to perform further inter-comparisons with GIMRT/OS3D (at

²⁶ For an increased spatial resolution for better results it would also be necessary to reduce the finite-difference step in time, which would considerably increase the computation time. The computation times for two-dimensional matrix diffusion which would need to be performed using OS3D are expected to be even longer.

least with the spatial resolution applied).

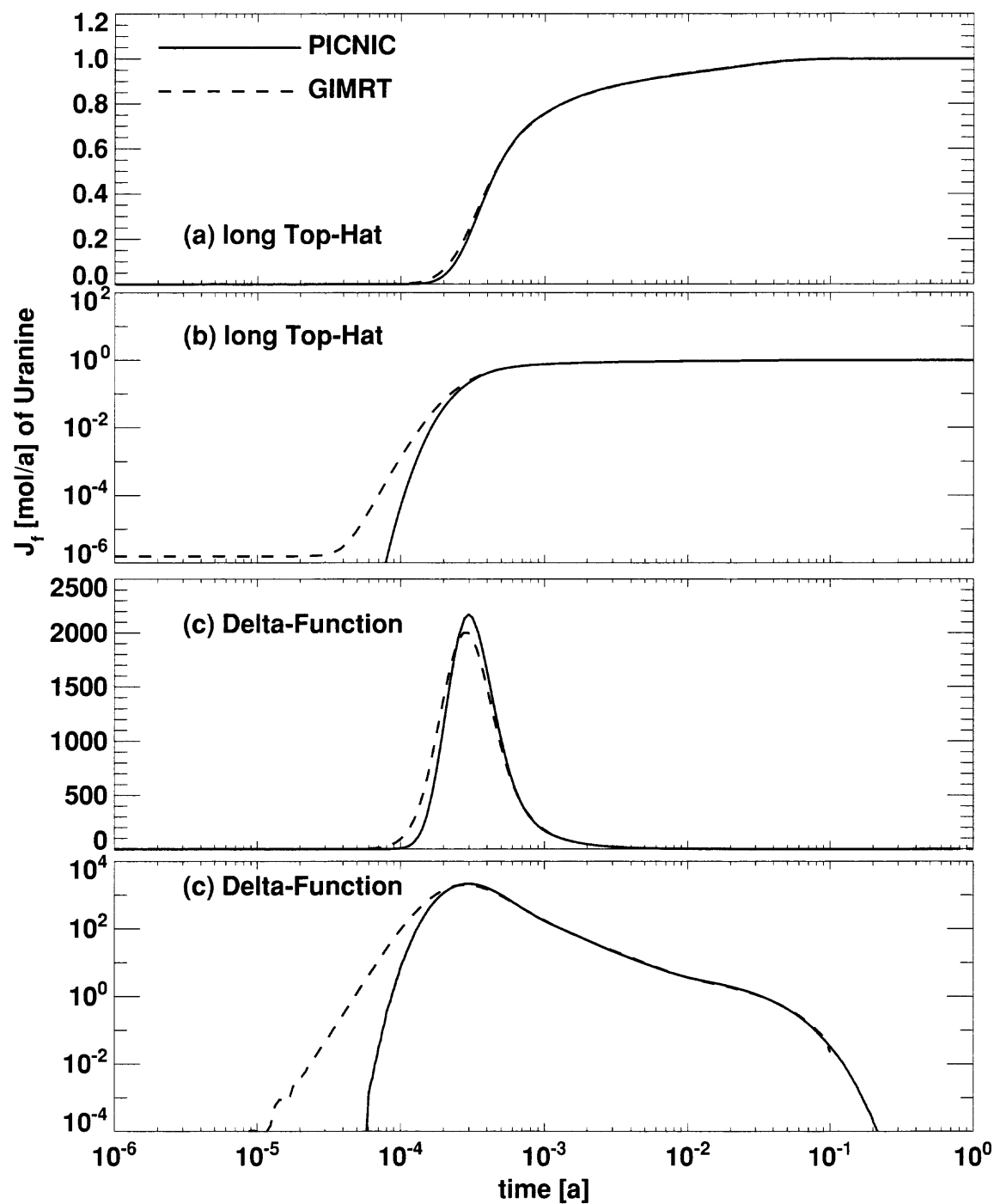


Figure 4.2. Comparison of the release curves of GIMRT (dashed lines) with results from PICNIC (solid lines) for uranium parameters. In (a,b) a constant source and in (c,d) a δ -function source are considered. The GIMRT calculations were performed up to the time $t=0.1$ [a].

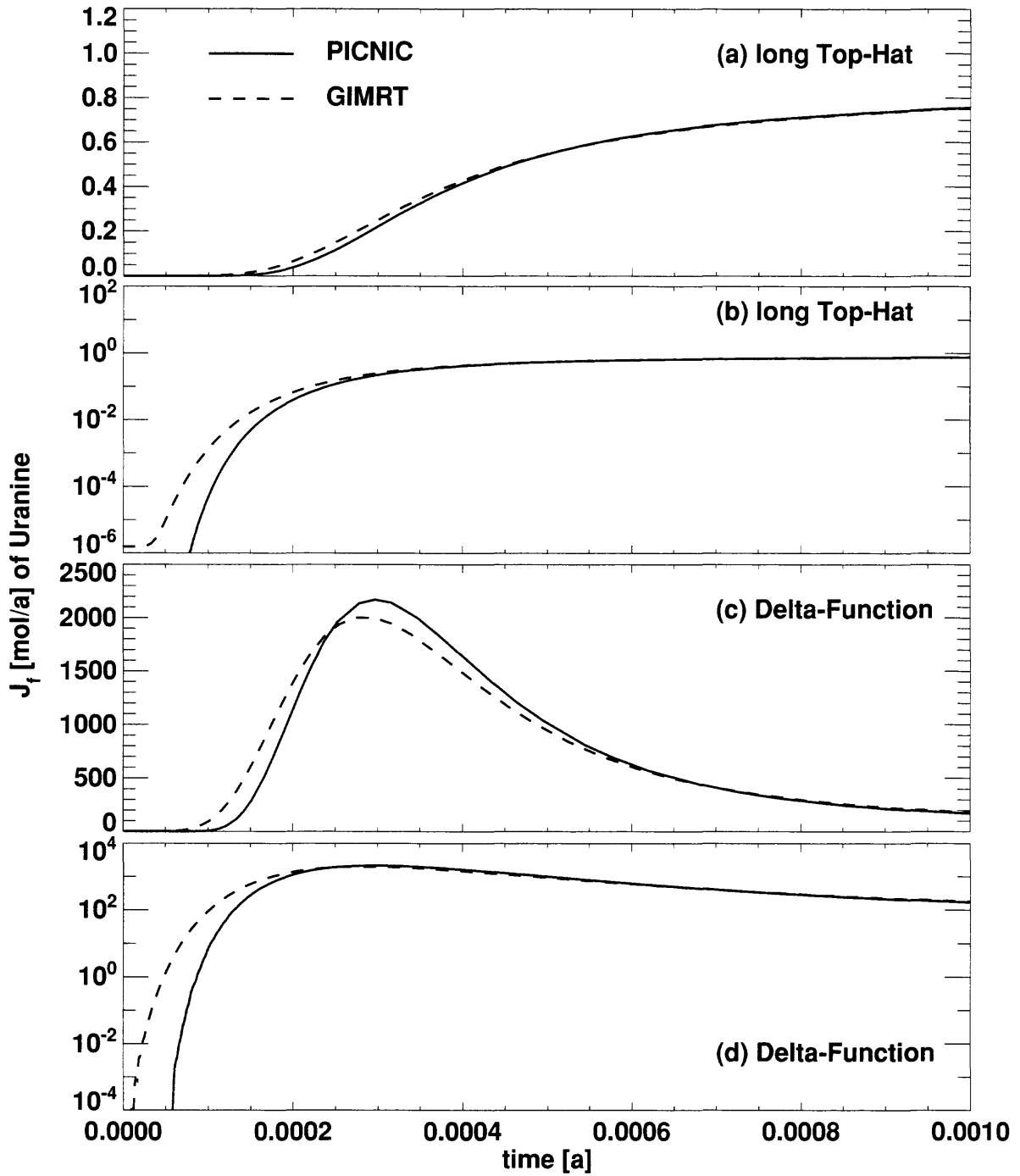


Figure 4.3. Comparison of the release curves of GIMRT (dashed lines) with results from PICNIC (solid lines) for uranine parameters as in Figure 4.2. The time is given here on a linear scale for better resolution of the maximum in (c,d).

4.1.3. Comparison with PAWorks/LTG

The code PAWorks/LTG [Dershowitz et al., 1998] can consider one-dimensional matrix diffusion into two or more independent homogeneous planar rock matrix areas (see section 8), which goes beyond the capabilities of RANCHMD. In this code a new variant of the finite-element method in the Laplace domain [Sudicky, 1989, 1990] is used. For the numerical inverse Laplace transformation, the variant of deHoog, Knight and Stokes [1982] of Crump's [1976] method is applied, which is different to Talbot's method applied in PICNIC. Like PICNIC, PAWorks/LTG can deal with the transport of radionuclide decay chains in one-dimensional channels in combination with matrix diffusion into the neighbouring rock matrix. PAWorks/LTG is presently restricted to the zero-gradient boundary condition. In the recent verification report [Shuttle and Eiben, 1998] of PAWorks/LTG, the strontium and the uranine cases of Figure 4.1 were considered. The agreement of the PICNIC and the PAWorks/LTG result is excellent, see Figure 4.4 for the strontium case and Figure 4.5 for the uranine case. In the region from middle of the rising edge to the tailing of the breakthrough curve the relative difference to the PICNIC result is within 1% for both nuclides. Only for very early times is the increase of the LTG result somewhat later. This excellent agreement contributes to the verification of both codes.

After this promising start the inter-comparison with PAWorks/LTG will be extended to nuclide decay chains and pathways in section 4.2 and to networks in section 4.3.

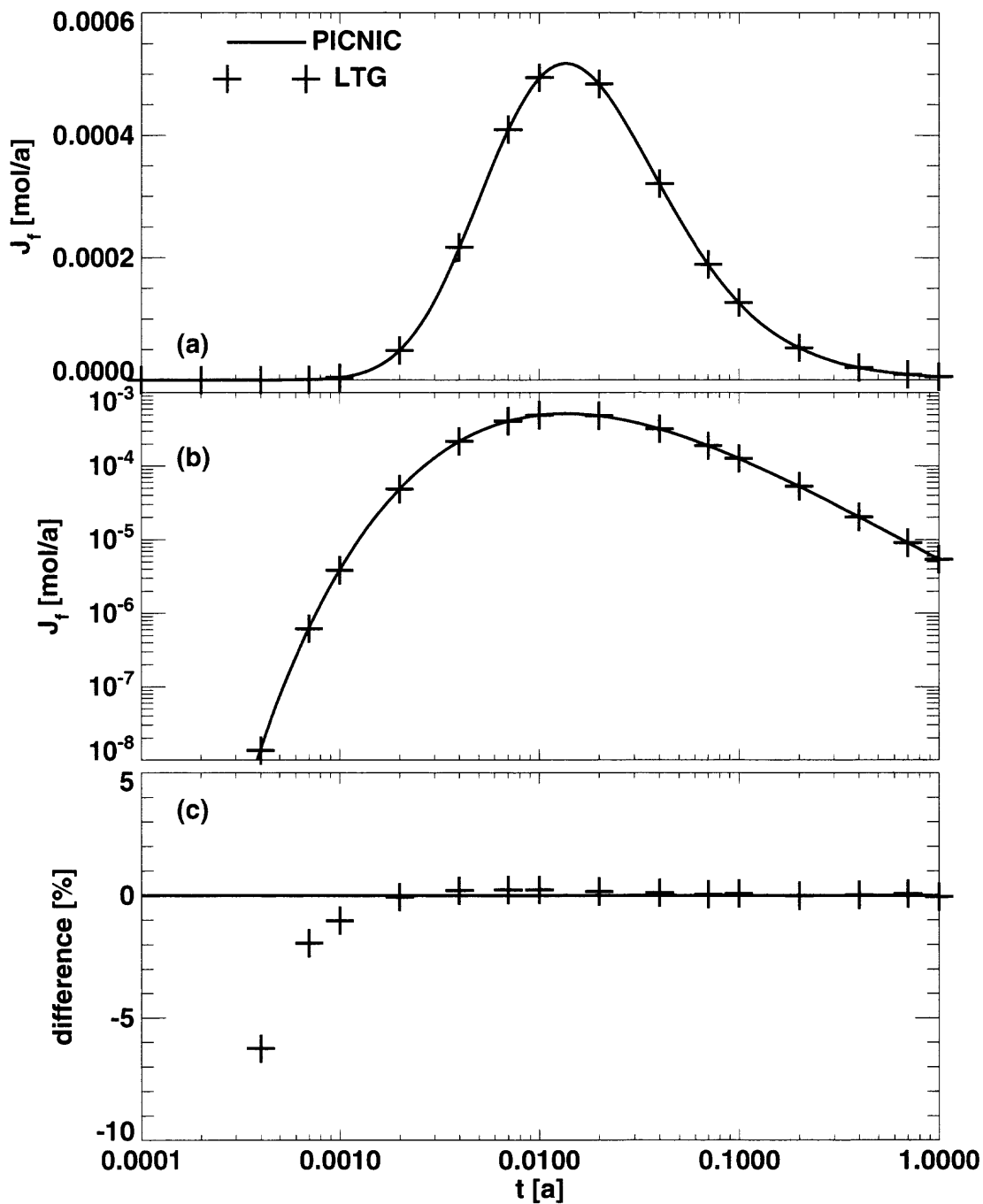


Figure 4.4. The result of a PAWorks/LTG calculation (the crosses indicate the data points available) is compared to the respective PICNIC result (solid lines) for the release of strontium. The PAWorks/LTG results are from Shuttle and Eiben [1998]. The top-hat source over 1 minute and units of the nuclide flow rate are the same as for the solid line in Figure 4.1. The release curves are given in (a) on a linear scale and in (b) on a logarithmic scale. The relative difference of the PAWorks/LTG result to the PICNIC result is given in (c).

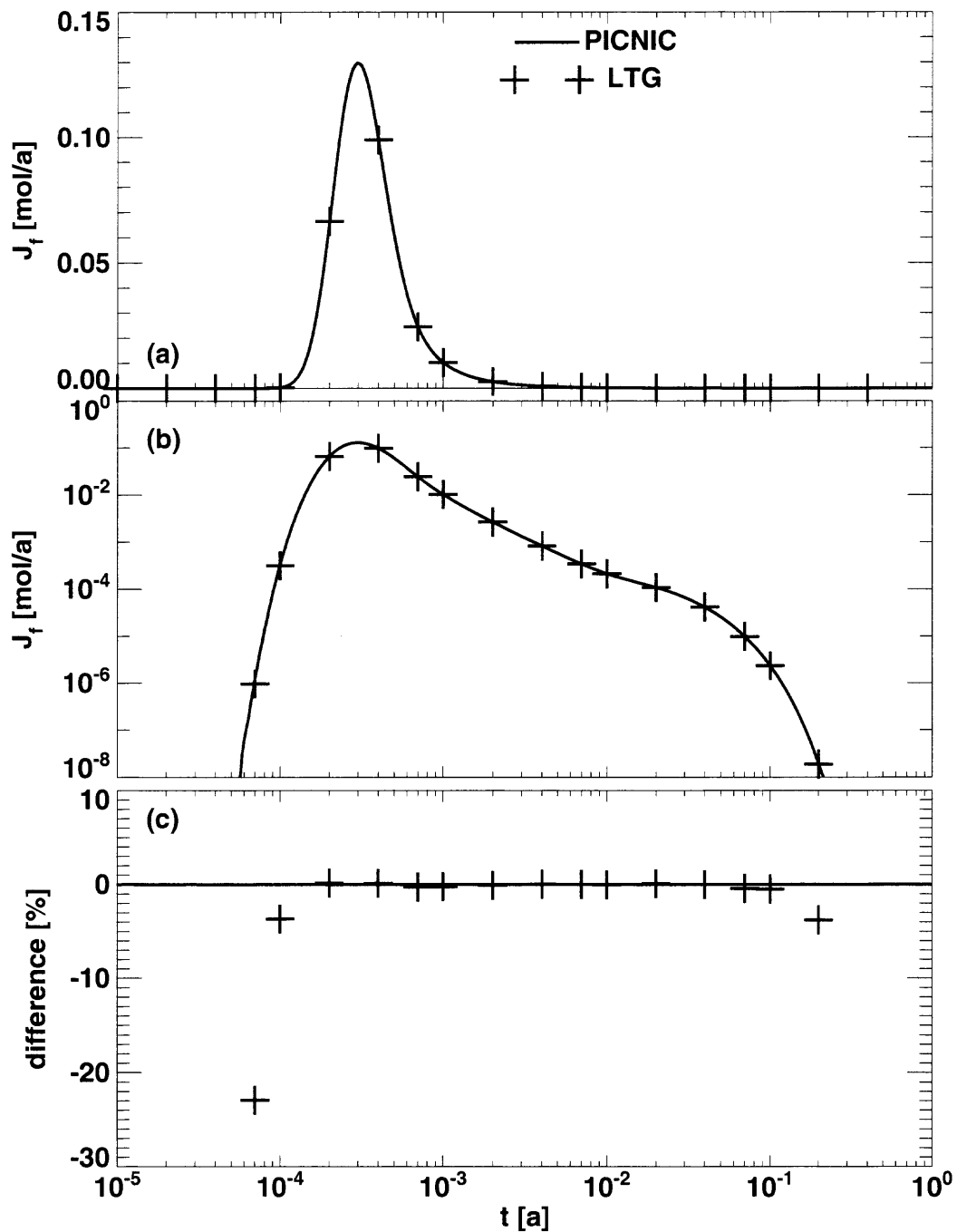


Figure 4.5. The result of a PAWorks/LTG calculation (the crosses indicate the data points available) is compared to the respective PICNIC result (solid lines) for the release of uranium. The PAWorks/LTG results are from Shuttle and Eiben [1998]. The top-hat source over 1 minute and units of the nuclide flow rate are the same as for the dashed line in Figure 4.1. The release curves are given in (a) on a linear scale and in (b) on a logarithmic scale. The relative difference of the PAWorks/LTG result to the PICNIC result is given in (c).

4.1.4. Peclet Number Dependence and Boundary Conditions

We continue testing PICNIC for single nuclides in single channels. To test here in a qualitative manner for the outflow boundary condition, a δ -function input $S(t) = J_f(z = 0; t) = \delta(t)[a]$ of uranine is applied.²⁷ While up till now zero-gradient was used as the outflow boundary condition, we compare here the effect of the three available boundary conditions given in equations (2.51a,b,c). Till now the experimental Peclet number, $Pe=20$, was used. For this Peclet number, the breakthrough curves for the outflow boundary conditions zero-gradient (ZG, solid line), zero-concentration (ZC, long-dashed line) and at-infinity (AI, short-dashed line) are nearly identical when presented on a double-logarithmic scale (Figure 4.6b). Figure 4.7 gives the curves of Figure 4.6 on a linear scale for better resolution of the maxima.

For a much larger Peclet number, $Pe=200$, the outflow boundary condition is yet less relevant and the curves for the different boundary conditions cannot be distinguished (Figures 4.6a and 4.7a). In the limit of neglected micro-dispersion, $Pe \rightarrow \infty$ (dash-dotted line in Figure 4.7a), only one boundary condition in the flowing water, the inflow boundary condition, is necessary (section 2.3.2). Note, that for this high Peclet number, at the sharp rising edge of the nuclide pulse PICNIC produces very strong numerical oscillations caused by the calculation of the eigenvalues and the execution of the Talbot scheme for numerical inverse Laplace transformation. See also the shaded area in Table 4.3, where the breakthrough curves for the different boundary conditions and Peclet numbers are listed.

To demonstrate, on a double-logarithmic scale, the influence of the different outflow boundary conditions, we consider in Figure 4.6c the small Peclet number $Pe=2$. For zero-concentration the breakthrough is earliest, followed by at-infinity and zero-gradient, but, all in all, the breakthrough curves show similar behaviour. Note that the assumption of Fickian dispersion has to be questioned for such a small Peclet number. The examined range of Peclet numbers, $2 \leq Pe \leq 200$, covers the scope of relevant Peclet numbers generally considered in safety assessments and in modelling of experiments.

²⁷ Note that for strontium at $Pe = 20$, the peak region and the tail of the breakthrough curve are almost insensitive to the leg outflow boundary condition. Thus the breakthrough curve is almost completely determined by the behaviour in the rock matrix.

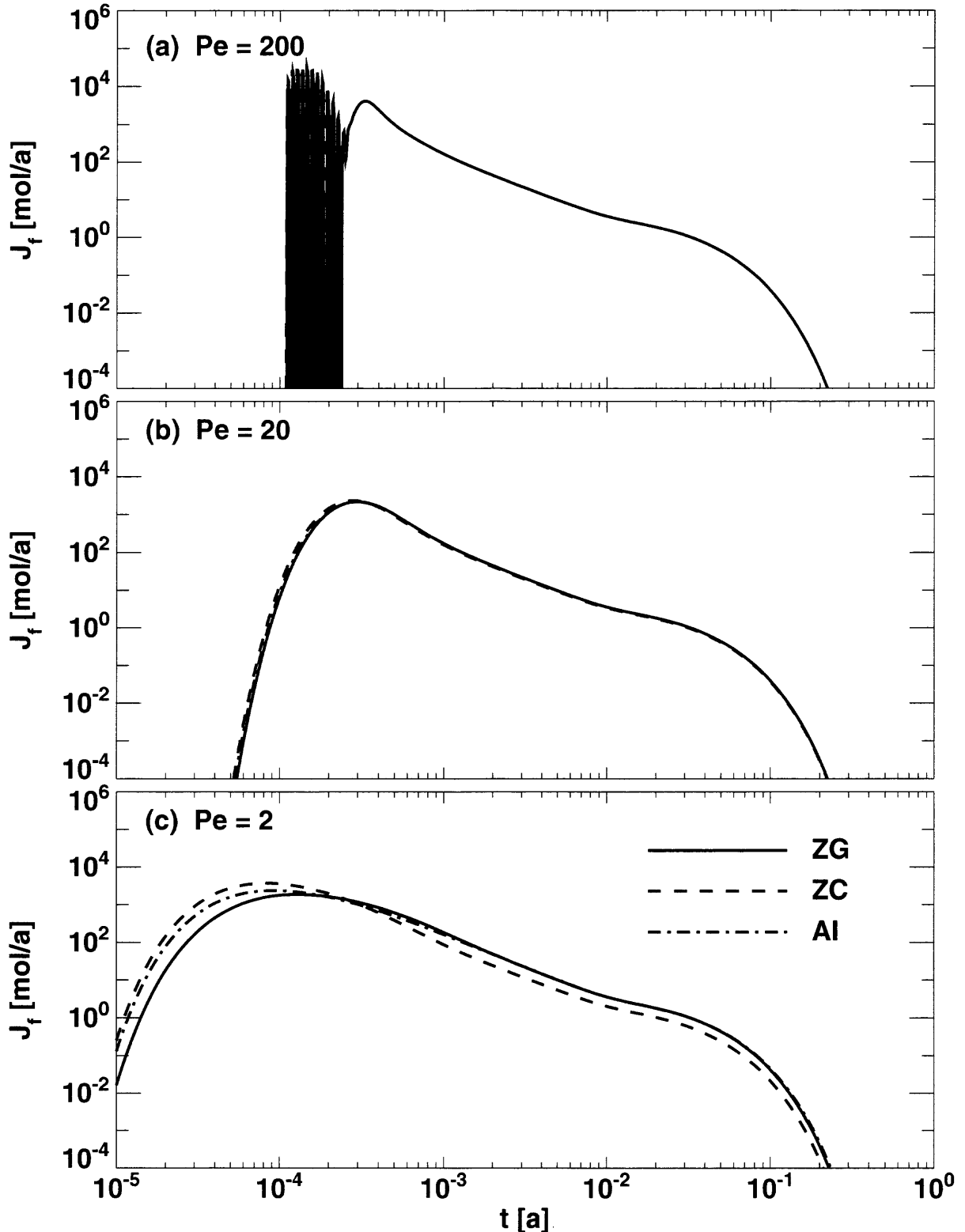


Figure 4.6. Effect of different values for the Peclet number Pe on tracer breakthrough using different boundary conditions, as indicated in the legends. (Note: zero-gradient means a zero-gradient at the leg outlet boundary condition, ZC a zero-concentration at the leg outlet boundary condition, and AI means a zero-concentration at-infinity boundary condition.) For all 9 calculations a δ -function source was assumed. The early tracer breakthrough for small Peclet numbers is due to increased dispersion only. Note the large numerical oscillations at the rising edge of the release curve for $Pe = 200$.

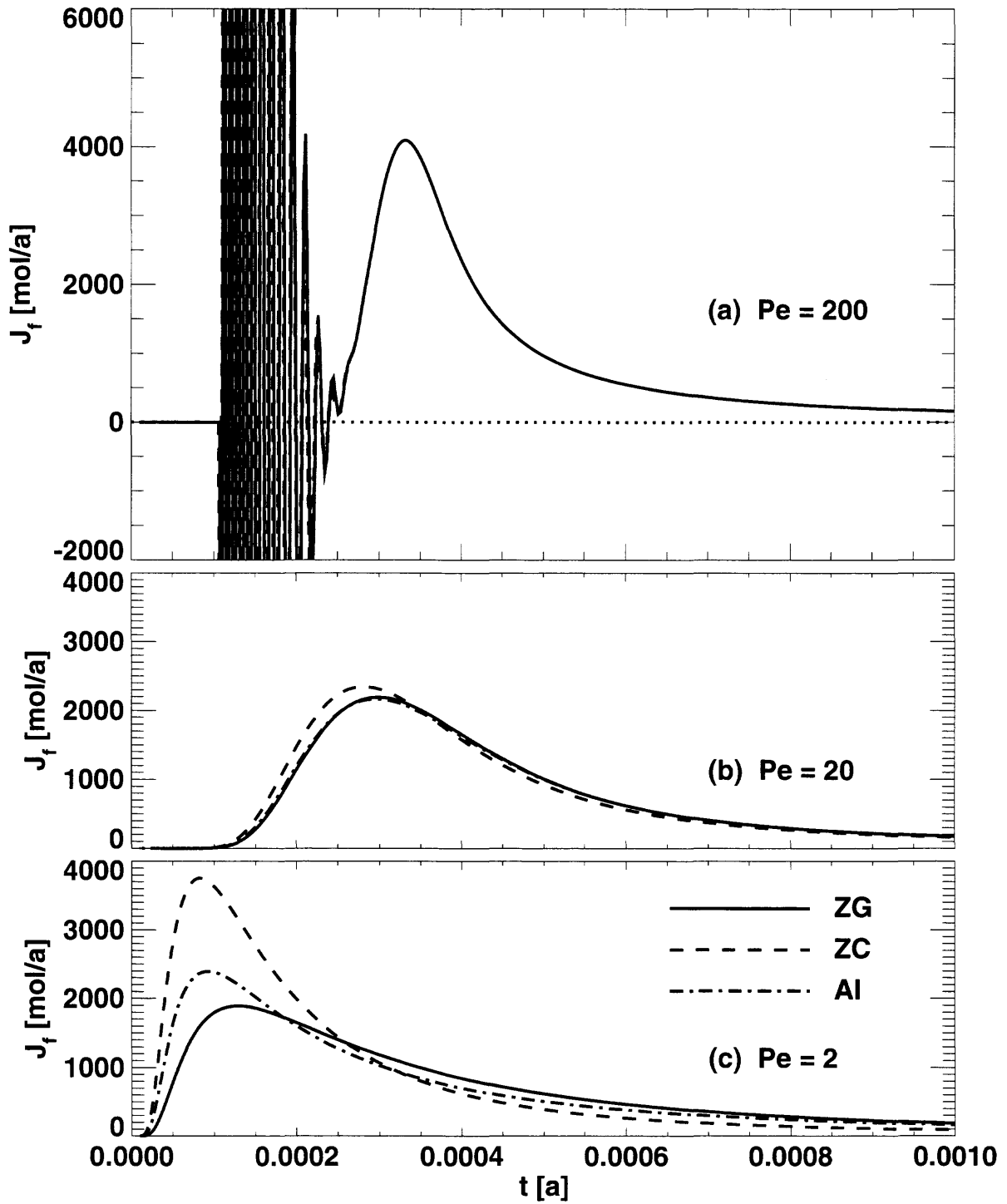


Figure 4.7. The same as for Figure 4.6, but on linear scale for better resolution of the maxima. Time and value of the maxima are given in Table 4.2.

Comparing the Peclet numbers, the behaviour for early times shows most influence. The breakthrough is earliest for the smallest Pe . This could become relevant, if radioactive decay were taken into consideration. The maxima differ within only a factor of 2 for the different boundary conditions and for this large range of Peclet numbers (Table 4.2). See also Figure 4.7 where the breakthrough curves are given on a linear scale for better resolution of the peak region. For the tail of the breakthrough curves the overall behaviour is very similar (Figure 4.6). Thus it is determined by the behaviour in the rock matrix.

We now briefly consider the influence of the numerical oscillations²⁸ found for $Pe=200$, see shaded area in Table 4.3. These oscillations could mask the transport behaviour when a network consisting of at least two pathways is considered, where the maximum of the breakthrough curve of one pathway lies in the area of the numerical oscillations of the second pathway. It should be borne in mind that applying such an unrealistic high Peclet number is a kind of testing to the extreme. For the zero-gradient boundary conditions we have considered the numerical oscillations for a range of Peclet numbers, see Table 4.4. The numerical oscillations do indeed generate (non-physical) negative values for parts of the breakthrough curves. Taking the value for the minimum of these oscillations (which go to negative values) as a measure yields 3.0 for the ratio of numerical oscillations and the maximum of the breakthrough curve for $Pe=200$, which is not acceptable for a calculation of breakthrough curves over the entire time range. This ratio clearly decreases to $3.15 \cdot 10^{-3}$ for $Pe=175$, which might be acceptable at least for safety assessments. Note that no numerical oscillations going to negative values for the nuclide flow rate could be seen for $Pe=100$.

Pe	(a) $t_{max} [10^{-4} \text{ a}]$			(b) $J_f(z=L; t_{max}) [10^3 \text{ mol/a}]$		
	ZG	ZC	AI	ZG	ZC	AI
200	3.318	3.318	3.318	4.099	4.099	4.099
20	2.985	2.812	2.959	2.191	2.344	2.165
2	1.291	0.830	0.928	1.892	3.755	2.393

Table 4.2. (a) Time and (b) maximum of the breakthrough curves for various Peclet numbers and leg outflow boundary conditions. For the breakthrough curves see Figures 4.6 and 4.7.

²⁸ The numerical oscillations are caused by Talbot's method for numerical inverse Laplace transformation which has problems resolving the extremely sharp increase of the rising edge of the breakthrough curves.

Peclet number	200	200	200
boundary condition	ZG	ZC	AI
Talbot points	129	129	129
time	J_f [mol/a]		
1.7E-04	0.0000E+00	0.0000E+00	0.0000E+00
1.8E-04	4.6156E+03	1.3753E+04	3.2657E+03
1.9E-04	-1.0725E+04	-8.3139E+03	-7.8860E+03
2.0E-04	-4.9904E+02	-1.9842E+03	-1.9945E+02
2.1E-04	4.2393E+03	2.6842E+03	2.8561E+03
2.2E-04	-2.2612E+03	-1.4954E+03	-1.6808E+03
2.3E-04	6.3082E+02	2.9668E+02	5.5149E+02
2.4E-04	1.4172E+02	2.1862E+02	7.2436E+01
2.5E-04	1.8224E+02	1.3586E+02	2.3959E+02
2.6E-04	6.6565E+02	7.2267E+02	6.4684E+02
2.7E-04	1.0664E+03	1.0611E+03	1.0729E+03
2.8E-04	1.7273E+03	1.7228E+03	1.7224E+03
2.9E-04	2.4158E+03	2.4065E+03	2.4179E+03
3.0E-04	3.0802E+03	3.0830E+03	3.0807E+03
5.0E-04	9.6917E+02	9.6917E+02	9.6917E+02
1.0E-03	1.6231E+02	1.6231E+02	1.6231E+02
2.0E-03	4.3965E+01	4.3965E+01	4.3965E+01
3.0E-03	2.2112E+01	2.2112E+01	2.2112E+01
5.0E-03	9.6827E+00	9.6827E+00	9.6827E+00
1.0E-02	3.5940E+00	3.5940E+00	3.5940E+00
2.0E-02	1.8398E+00	1.8398E+00	1.8398E+00
3.0E-02	1.1322E+00	1.1322E+00	1.1322E+00
5.0E-02	4.3221E-01	4.3221E-01	4.3221E-01
1.0E-01	3.8797E-02	3.8797E-02	3.8797E-02
2.0E-01	3.0876E-04	3.0876E-04	3.0876E-04
3.0E-01	2.4231E-06	2.4231E-06	2.4231E-06
5.0E-01	1.4428E-10	1.4428E-10	1.4428E-10
1.0E+00	0.0000E+00	0.0000E+00	0.0000E+00
maximum	4.0988E+03	4.0987E+03	4.0987E+03
t_{\max}	3.3180E-04	3.3180E-04	3.3180E-04

Table 4.3. Breakthrough curves are given for $Pe=200$. The shaded area of the table shows very strong numerical oscillations in the rising edge of the breakthrough curves. For the considered $Pe = 200$ the number of Talbot points is increased to 129 (see also section 4.1.7), but this reduces the numerical oscillations only slightly.

Pe	100	125	150	175	200
start time of numerical oscillations		1.47E-04	1.55E-04	1.63E-04	1.71E-04
end time of numerical oscillations		~1.6E-04	~1.8E-04	~2.1E-04	~2.5E-04
amplitude of numerical oscillations		4.318481E-02	6.102405E-01	1.243846E+01	1.229279E+04
maximum of breakthrough curve	3.403020E+03	3.619367E+03	3.795371E+03	3.954907E+03	4.095780E+03
time of maximum	3.30E-04	3.30E-04	3.30E-04	3.30E-04	3.30E-04
numerical oscillations to maximum ratio		1.19E-05	1.61E-04	3.15E-03	3.00

Table 4.4. Numerical oscillations for different Peclet numbers. The zero-gradient boundary condition is applied. The number of partial sums in the Laplace domain is increased to 129 (compare section 2.7 and 2.8). As a rough measure for the amplitude of the numerical oscillations in row 4, the absolute value of the minimum of these oscillations, which go also to negative values, is given. The ratio of the amplitude of the numerical oscillations (given in row 4) to the maximum of the breakthrough curve is given in row 6.

4.1.5. Parameter Self-Consistency

In this subsection we use self-consistency tests to check whether the parameters are correctly entered to the code. We have already shown that the behaviour of the system depends on combined parameters. For a non-decaying single nuclide these combined parameters are $\alpha, \beta, \gamma, Pe$. If the primary parameters (like $R_f, R_p, \varepsilon_f, \dots$) change, but the combined parameters $\alpha, \beta, \gamma, Pe$ are kept constant, then the result, i.e. the breakthrough curve, is the same. We consider the strontium case with $Pe = 20$ and the zero-gradient boundary condition with a δ -function source term. For these test cases, the δ -function source term is approximated in the calculation by a simple-leaching source term²⁹ with a very high release rate of 10^7 [a]. This is case (a) in Table 4.5. When we multiply $q_f, \varepsilon_f, \varepsilon_i, \varepsilon_p$ by a common factor A , e.g. $A = 10$, then the parameter combinations $\alpha, \beta, \gamma, Pe$ do not change. For this case, called (b), and the other cases listed in Table 4.5, the agreement of the breakthrough curves with each other has been verified with six to seven digits accuracy. In case (d) we have verified that PICNIC also can handle retardation by linear sorption in the flowpath. This has been done by multiplying R_f with a factor A^{-2} , ε_p with a factor A^{-1} , and ε_f and L with a factor A .

²⁹ Note that the release curves agree within six to seven digits accuracy with the result, when the δ -function source is entered as "analytical source" to PICNIC. The agreement is in the same order of magnitude when the pulse-like source has a triangular form.

For a δ -function input and non-zero λ , the breakthrough curve is simply multiplied by a factor $e^{-\lambda t}$ - this is also verified.

For a time-shifted source term, the breakthrough curve is also simply time-shifted - this is also verified for a top-hat source term that is entered by a tabular file.

We check now check the sensitivity of the PICNIC code to the area A_f . We consider the same channel as discussed above, but with the at-infinity boundary condition. The sensitivity to A_f cannot be checked for a single leg, so, we subdivide the channel, which is 5 m long here, into two channels of lengths 2 m and 3 m with the same properties, but with the area of the first leg multiplied by a factor A^{-1} . Note that we have to change the Peclet number of the legs, since the system length changes. For continuity of the water flow rate $Q_f = A_f q_f$ at the junction of the two channels we have to multiply q_f by the factor A in the first leg. To keep the typical timescales constant we can now apply (b) of Table 4.5 and also multiply $\varepsilon_f, \varepsilon_i, \varepsilon_p$ with the factor A . It is verified that this 2-leg pathway does produce the same breakthrough curve as the single leg, with six to seven digits accuracy.

	q_f	D_f	ε_f	ε_i	L	R_f	d	R_p	D_p	ε_p	δ_f
(a)											
(b)	A		A	A						A	
(c)	A	A				A					A
(d)			A	A	A	A^{-2}				A^{-1}	
(f)							A		A^2		A^{-1}
(g)								A	A		A^{-1}

Table 4.5. Matrix for self-consistency tests. The first column denotes the test case and the first row gives the parameters. In the bulk of the table the factors of the parameters compared to the case (a) are given. An empty field indicates a factor of 1. All cases produce the same results, because they yield the same values for the combined transport parameters $\alpha, \beta, \gamma, Pe$.

4.1.6. Self-Consistency Tests of the Network Feature

In this subsection we list first tests of the network feature of PICNIC done by constructing **networks that behave like a single leg**. This is possible when the outflow boundary condition at-infinity is applied. In this case the response function in Laplace space of a single nuclide in a single channel has the form $\overline{\mathfrak{R}}(z; s) = e^{-K_2(s)z}$ with an eigenvalue function $K_2(s)$ that does not depend on the length of the channel, see sections 2.3.2-2.3.4. For the outflow boundary condition at-infinity, as in the limit $Pe \rightarrow \infty$, only one eigenvalue function $LK_2(s) \xrightarrow{Pe \rightarrow \infty} L\Lambda(s)$ determines the transport behaviour, while two eigenvalue functions are needed for the boundary conditions zero-gradient and zero-concentration, see sections 2.3.5 and 2.3.6. Thus, for at-infinity a single channel can be subdivided into several parts, all having the boundary condition at-infinity without affecting the transport behaviour. Also, giving nuclides the possibility to choose one of several legs, all of them having the same transport properties, does not change the breakthrough curves.

The network shown in figure 4.8 has the same transport behaviour as uranine in the single leg of length 5 m discussed in section 4.1.1. The legs a, d, e have length 2 m, the legs b, f, g have length 3 m, and the legs c, h have zero length (indicated as dashed lines); hence every flowpath has the same total length. PICNIC is also able to deal with more than one source location, e.g. a source S_1 at junction 1 and a second source S_5 at junction 5. This means that the source S_1 is connected to junction 4 by the network of legs a, b, c building up one pathway, while the source S_5 is connected to junction 4 by the network of legs d, b, c, e, f, g, h building up three pathways, (d, b, c) , (e, f, c) and (e, g, h) . The network facility is verified for the network of Figure 4.8 by evaluating the breakthrough curves at junctions 3 and 4 and at leg b . For all checks, an agreement with six to seven digits accuracy was found in comparison with PICNIC calculations for a single leg.

These self-consistency tests have been extended successfully in a next step to a **nuclide chain** consisting of a parent and a non-decaying daughter, where parent and daughter have the same transport properties.

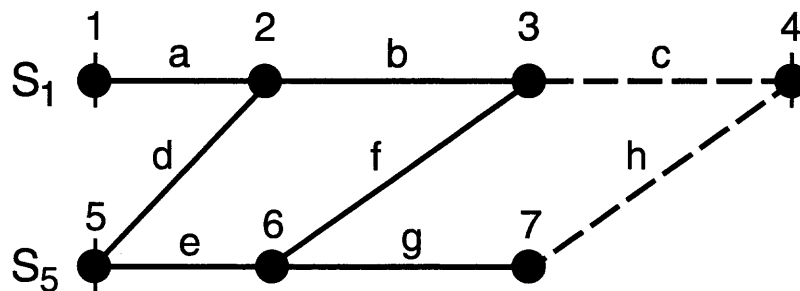


Figure 4.8. Small network with two source locations at junctions 1 and 5, which shows the transport behaviour of a single leg. Flow is from left to right. The legs c and h have zero length (indicated as dashed lines) to combine the nuclide outflow rates at the junctions 3 and 7 at the junction 4. The legs a, d, e have the same length, (2 m), and the legs b, f, g have a different length, (3 m).

4.1.7. Technical Test: Dependence on Number of Partial Sums in Talbot Series

The numerical inverse Laplace transformation is made [Robinson 1997a] using **Talbot's method** [Talbot 1979] as an integration in the complex number plane on a default contour. The integration is approximated by a series, using 33 partial sums in default. For the strontium and the uranine cases documented in section 4.1.1 we found agreement within six to seven digits accuracy for calculations with 17, 33, 65, 100 and 129 partial sums. This indicates that the standard value of 33 partial sums is chosen appropriately for these cases. For even lower values the results were not satisfactory for the edges of the breakthrough curves, although the maximum was calculated with three to four digits accuracy, even with this poor resolution.

4.1.8. Technical Test: Dependence on Output Times

The manner in which PICNIC calculates the breakthrough curves depends on the output times that are required. To demonstrate and quantify this dependence, the results for strontium in section 4.1.1 for different output time options are considered in Table 4.6, (cf. section 2.8 for the keywords in the input file. These output times can be (a) equidistant on a linear timescale or (b) equidistant on a logarithmic timescale. In principle, the results should be least accurate, when the ratio of the largest output time and the smallest (non-zero) output time is large. Such large ratios are most often produced using the logarithmic timescale. For the case considered, the results for the different requested output times agree very well and differences are in the order of 1% or lower. Only for the last requested output time in a PICNIC calculation are there large big differences to other PICNIC calculations, when the ratio of the biggest output time and the smallest (non-zero) output time is large, see shaded elements in Table 4.6. **Till now, this is an unresolved bug.**³⁰ These problems are found when a source term is entered as a table so that a **convolution** with the time-dependent response function has to be performed. For an analytic δ -function source term we did not encounter these problems.

³⁰ Note that the bug for the last output time depends on the FORTRAN compiler in use. The actual calculations were performed using a FORTRAN 90 compiler on workstation using DIGITAL UNIX, while the bug was not observed for a FORTRAN 77 compiler or a FORTRAN 90 compiler on a PC. The influence of the requested output times on the PICNIC result can be reduced when an internal parameter in PICNIC, MXRT, is increased.

(a)

start-time	1.0E-3	0.0E-4	0.0E-4	0.0E-4	0.0E-4
final-time	1.0E-0	2.0E-0	1.0E-2	1.0E-1	1.0E-1
number-of-times	1000	2001	1001	101	1001
lin/log	linear	linear	linear	linear	linear
time					
1.000000E-04			0.000000E+00		0.000000E+00
1.000000E-03	3.877440E-06	3.863006E-06	3.879774E-06	3.881503E-06	3.883637E-06
1.000000E-02	4.934448E-04	4.936836E-04	4.932764E-04	4.936231E-04	4.936634E-04
1.000000E-01	1.264145E-04	1.263345E-04		1.263621E-04	1.242528E-04
1.000000E+00	4.506955E-06	5.411109E-06			

(b)

start-time	1.0E-6	1.0E-6	1.0E-3	1.0E-6	1.0E-4
final-time	1.0E+6	1.0E+0	1.0E+0	1.0E+1	1.0E+0
number-of-times	13	13	25	15	25
lin/log	logarithmic	logarithmic	logarithmic	logarithmic	logarithmic
time					
1.000000E-04	0.000000E+00	0.000000E+00		0.000000E+00	0.000000E+00
1.000000E-03	3.939527E-06	3.882258E-06	3.862396E-06	3.894417E-06	3.862397E-06
1.000000E-02	4.918980E-04	4.934930E-04	4.937214E-04	4.930936E-04	4.937214E-04
1.000000E-01	1.262318E-04	1.264583E-04	1.263252E-04	1.264232E-04	1.263252E-04
1.000000E+00	5.408750E-06	3.701080E-06	5.410073E-06	5.413810E-06	4.677834E-06
1.000000E+01	2.050253E-07			4.004882E-19	
1.000001E+02	1.607171E-09				
1.000001E+03	0.000000E+00				

Table 4.6. The relevance of the output time options in PICNIC is presented (a) for equidistant output times on a linear timescale, (b) for equidistant output times on a logarithmic timescale and for different start time, final time and number of times. Below this parameter part in both part tables in the first column the time is given. The following columns give the breakthrough curves for the different cases. The shaded table elements indicate large errors for the last output time.

4.2. Single Nuclides and Nuclide Decay Chains, Single Legs and Pathways: Variations of the Grimsel Dipole Experiment

Up till now we have mainly considered a single nuclide in a single leg and only a few self-consistency tests for a nuclide decay chain and a small network have been performed. In this section we consider **a single nuclide and a nuclide decay chain in a single leg and a two-leg pathway** as hypothetical variations of the Grimsel uranine case. These test cases have been performed as a cross-comparison between PAWorks/LTG and PICNIC. Selections of the PAWorks/LTG simulations presented in this section and section 8 have been used in the verification of PAWorks/LTG, see also Shuttle and Ahlstrom [1999].

4.2.1. Single Nuclide and Nuclide Decay Chain in a Single Leg

We start with the uranine case considered in sections 4.1.1 and 4.1.3, but now use a δ -function source. The agreement of the PICNIC (solid lines in Figure 4.9) and the PAWorks/LTG result (crosses) is again excellent. As expected from the earlier test case presented in Figure 4.5 (where we considered a top-hat source), in the peak and the tail region the relative difference of the PAWorks/LTG result to the PICNIC result is within 1%. Only for very early times is the increase of the LTG result somewhat later with respect to the PICNIC result.

To test the accuracy for a **nuclide decay chain** we now consider the nuclide chain $\text{ANUC} \rightarrow \text{BNUC} \rightarrow \text{CNUC}$. The half-life of ANUC is defined as 10^{-3} [a], the half-life of BNUC is 10^{-4} [a] while CNUC is assumed to be stable. Thus BNUC is in radioactive equilibrium with ANUC to test also this situation. ANUC, BNUC and CNUC are assumed to have the same properties as the non-decaying uranine, apart from the retardation factor in the rock matrix. ANUC has the same retardation factor in the rock matrix as uranine, $R_p = 1.0$, while the retardation factor of BNUC is $R_p = 2.0$ and the retardation factor of CNUC is $R_p = 10.0$. A δ -function source of the parent ANUC is considered. The release of ANUC (Figure 4.10), BNUC (Figure 4.11) and CNUC (4.12) is again modelled with PICNIC (solid lines) and LTG (crosses) and the results compared. For all nuclides of the decay chain the agreement is excellent, within 1% in the relevant region, with a somewhat later increase of the LTG result for very early times.

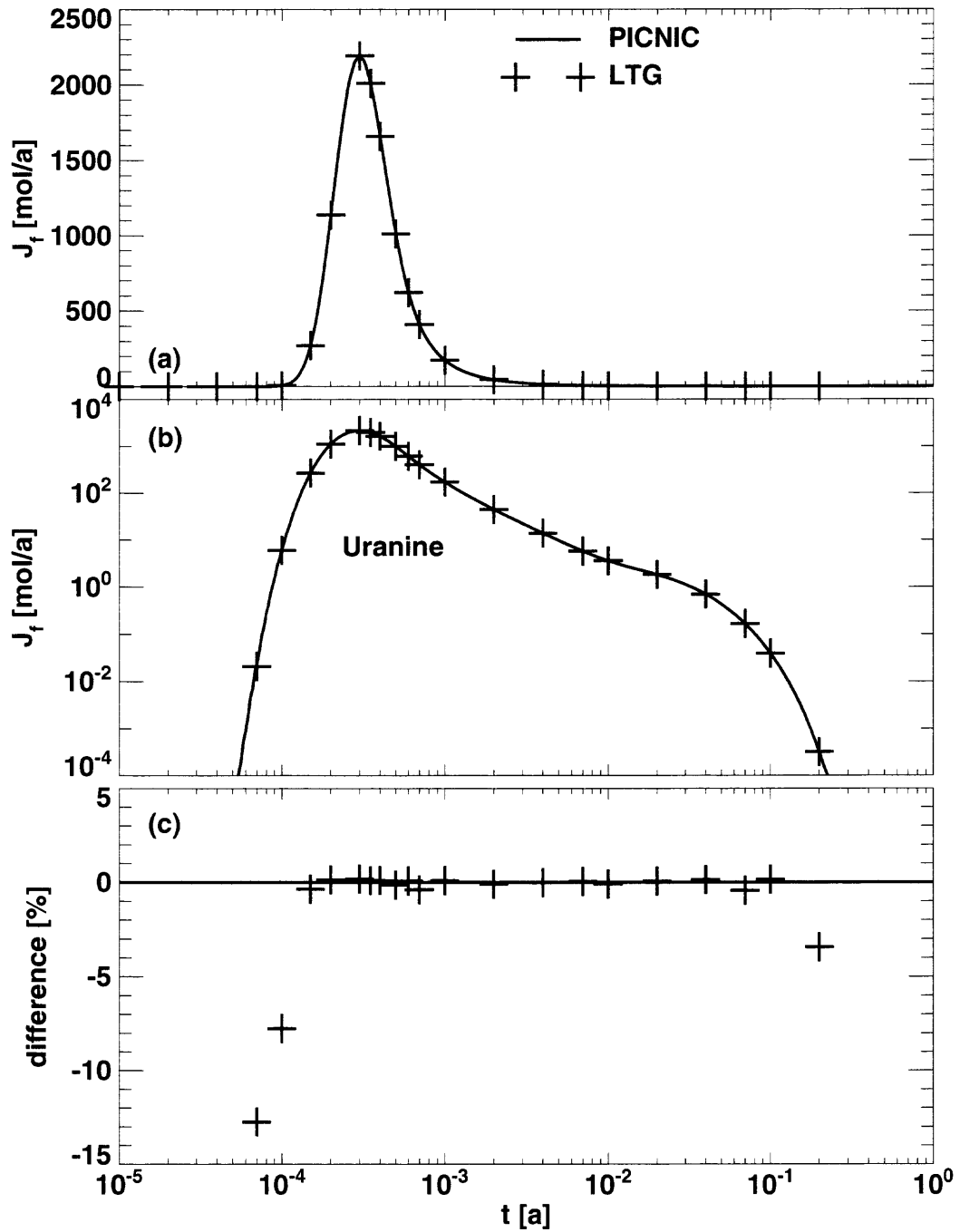


Figure 4.9. The result of a PAWorks/LTG calculation (crosses) is compared to the PICNIC result (solid lines) for the release of uranine. A δ -function source is considered. This is the only difference to the situation in Figure 4.3 where a top-hat source over 1 minute was considered. The release curves are given in (a) on a linear scale and in (b) on a logarithmic scale. The relative difference of the PAWorks/LTG result to the PICNIC result is given in (c).

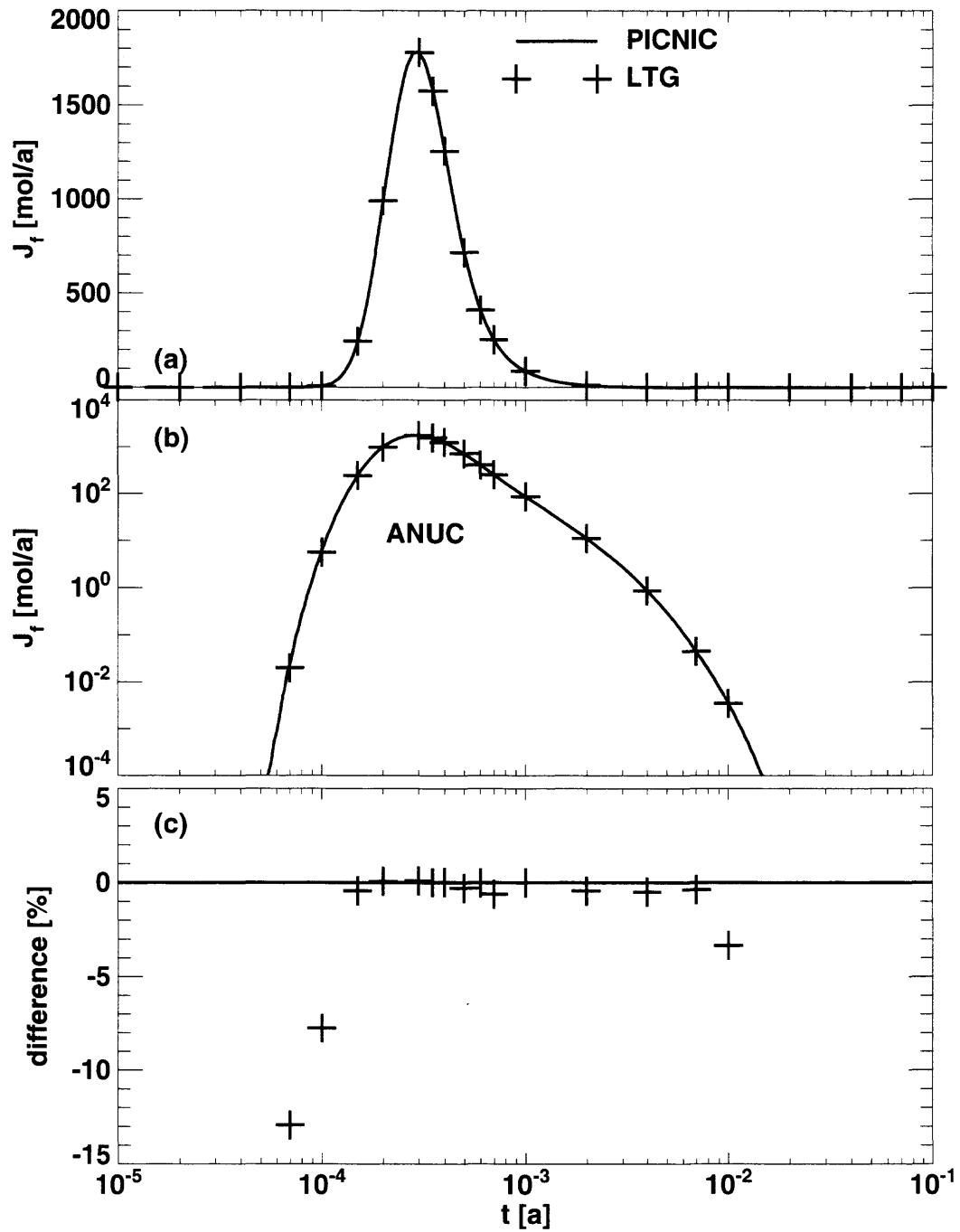


Figure 4.10. Hypothetical variation of the Grimsel uranium dipole experiment for a nuclide decay chain. Presented is the nuclide ANUC of the decay chain $\text{ANUC} \rightarrow \text{BNUC} \rightarrow \text{CNUC}$. A δ -function source of the parent ANUC is considered. The nomenclature is as in Figure 4.9.

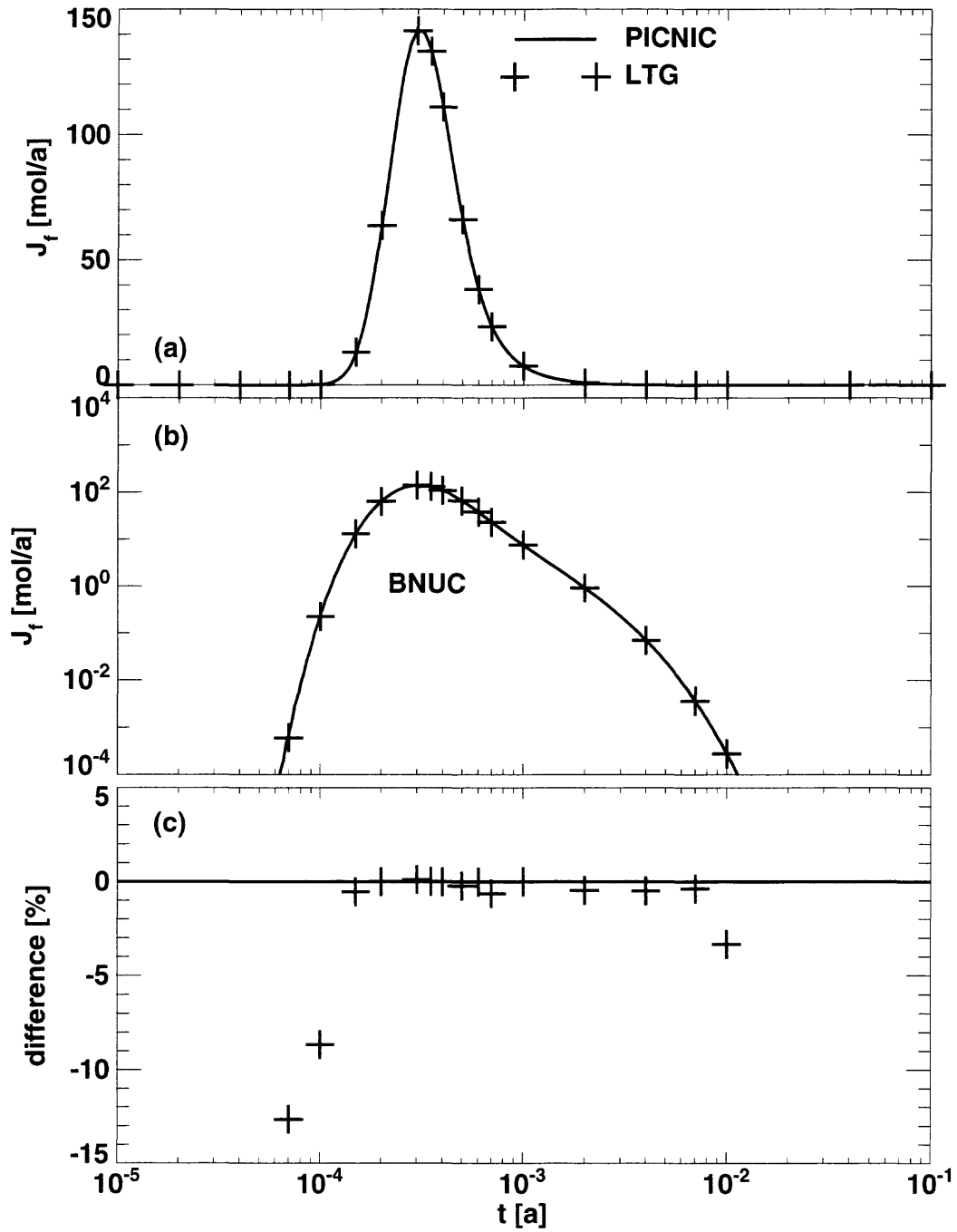


Figure 4.11. Hypothetical variation of the Grimsel uranium dipole experiment for a nuclide decay chain. Presented is the nuclide BNUC of the decay chain $\text{ANUC} \rightarrow \text{BNUC} \rightarrow \text{CNUC}$. A δ -function source of the parent ANUC is considered. The nomenclature is as in Figure 4.9.

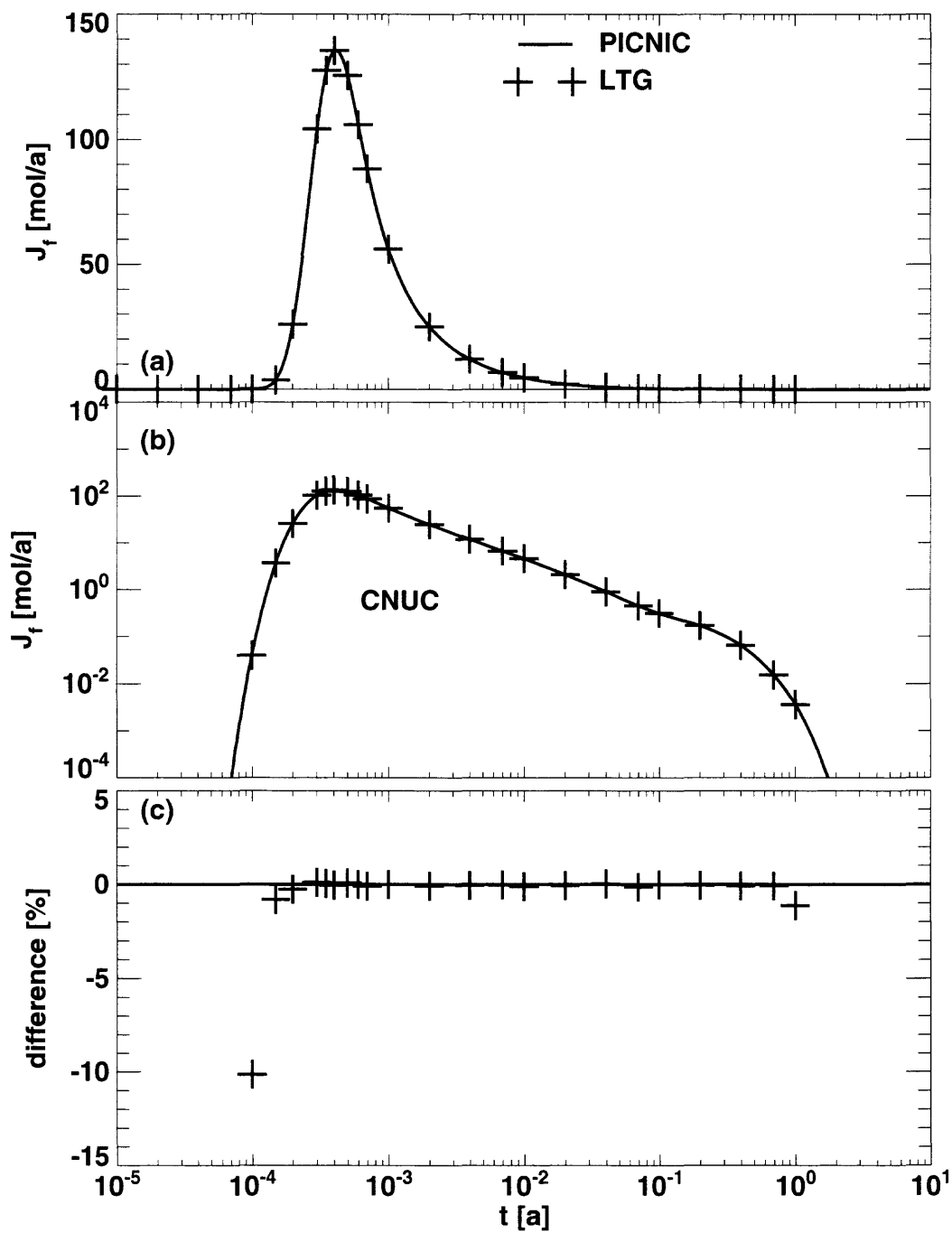


Figure 4.12. Hypothetical variation of the Grimsel uranium dipole experiment for a nuclide decay chain. Presented is the nuclide CNUC of the decay chain $ANUC \rightarrow BNUC \rightarrow CNUC$. A δ -function source of the parent ANUC is considered. The nomenclature is as in Figure 4.9.

As the next step we consider a parameter variation of the uranine case in such a way that the rock matrix thickness is reduced by a factor of 12.4 to $d = 0.5 \cdot 10^{-3} [\text{m}]$, while the retardation in the rock matrix is increased by a factor of 10 to $R_p = 10$. Thus the matrix delay time γ^2 increases by a factor of 10, the matrix diffusion time β^2 reduces by about a factor of 15, while α and Pe do not change:

$$\alpha = 297076 \cdot 10^{-4} [\text{a}], \quad \beta^2 = 3.16881 \cdot 10^{-3} [\text{a}], \quad \gamma^2 = 1.23766 \cdot 10^{-3} [\text{a}]. \quad (4.3)$$

Now matrix diffusion time and matrix delay time are nearly in the same order of magnitude. This case is considered, especially because the order of magnitude of the time to maximum release, $\alpha + \frac{1}{6}\gamma^2 \approx 5 \cdot 10^{-4} [\text{a}]$, is determined both³¹ by α and $\frac{1}{6}\gamma^2$. Also for this situation, the agreement of the PICNIC (solid lines in Figure 4.13) and the PAWorks/LTG result (crosses) is excellent. In the relevant region the relative difference to the PICNIC result is within 1%. Only for very early times is the increase of the LTG result somewhat later; for very late times the decrease is somewhat earlier with respect to the PICNIC result.

We also consider for this rock matrix the **nuclide decay chain** ANUC \rightarrow BNUC \rightarrow CNUC, where the half-life of ANUC is $10^{-3} [\text{a}]$, the half-life of BNUC is $10^{-4} [\text{a}]$ while CNUC is assumed to be stable. For the rock matrix considered, the retardation factors are assumed to be $R_p = 10.0$ for ANUC as for the single nuclide, while the retardation factor of BNUC is $R_p = 20.0$ and the retardation factor of CNUC is $R_p = 100.0$. Thus all retardation factors are a factor of 10 larger than in the original rock matrix considered. Again a δ -function source of the parent ANUC is considered. The release of ANUC (Figure 4.14), BNUC (Figure 4.15) and CNUC (4.16) is again modelled with PICNIC (solid lines) and LTG (crosses) and the results compared. For all nuclides of the decay chain the agreement is excellent, within 1% in the relevant region, with a somewhat later increase of the LTG result for very early times.

³¹ Remember that the time to maximum release was determined mainly by α for the original uranine case, while it was determined by $\frac{1}{6}\gamma^2$ for the strontium case.

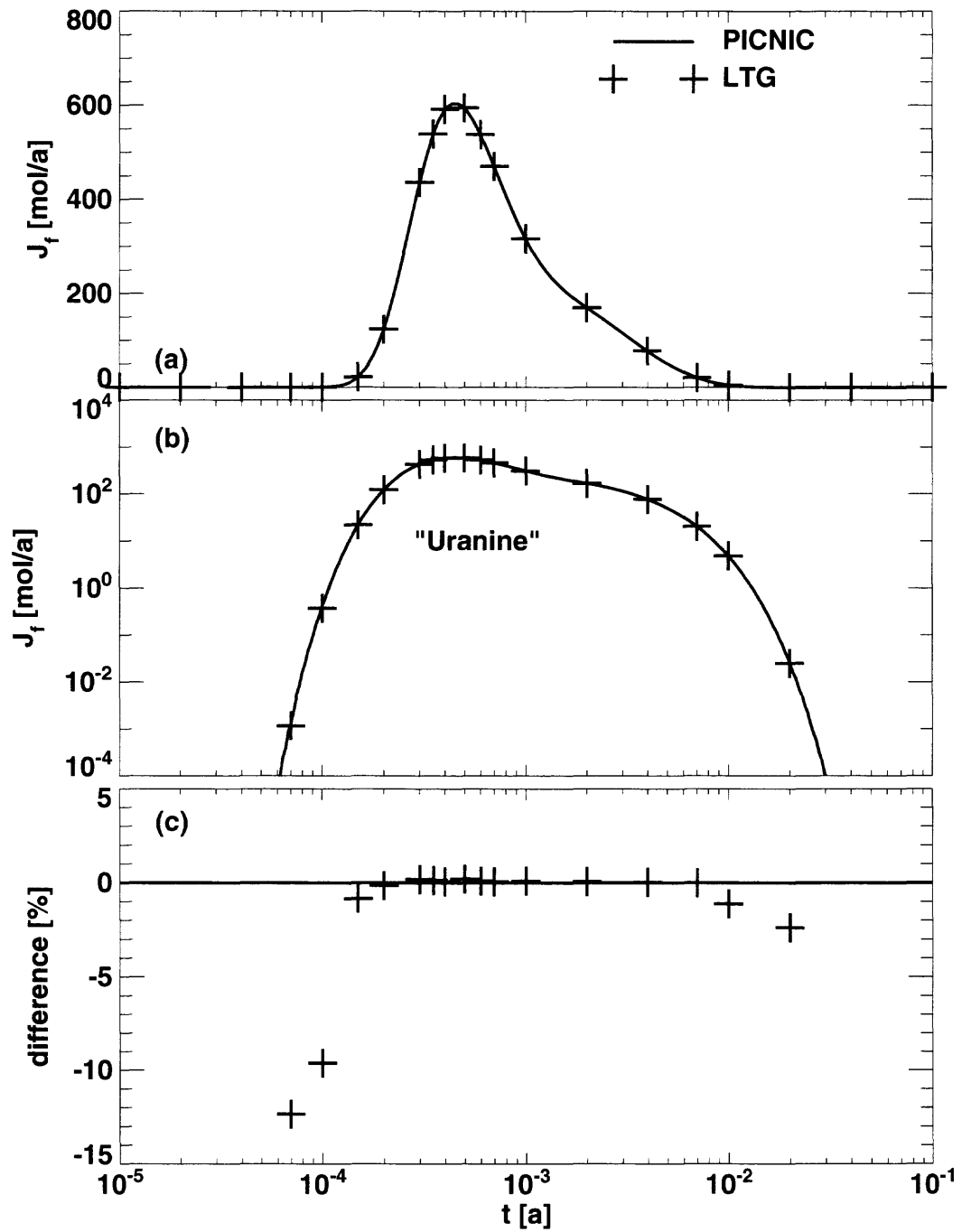


Figure 4.13. Hypothetical variation of the Grimsel uranine dipole experiment for a different rock matrix. A δ -function source is considered.

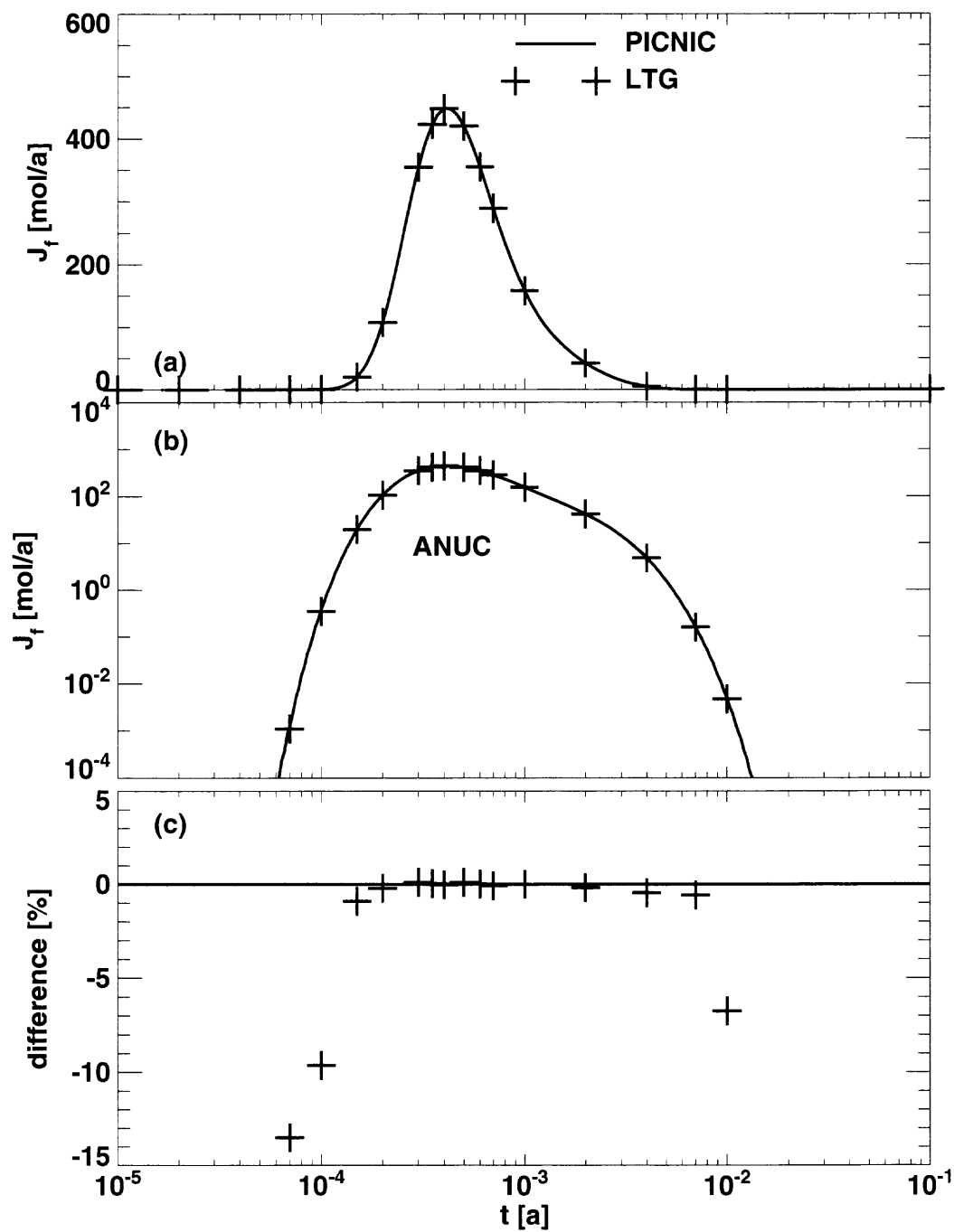


Figure 4.14. Hypothetical variation of the Grimsel uranine dipole experiment for a nuclide decay chain and a different rock matrix. Presented is the nuclide ANUC of the decay chain $\text{ANUC} \rightarrow \text{BNUC} \rightarrow \text{CNUC}$. A δ -function source of ANUC is considered.

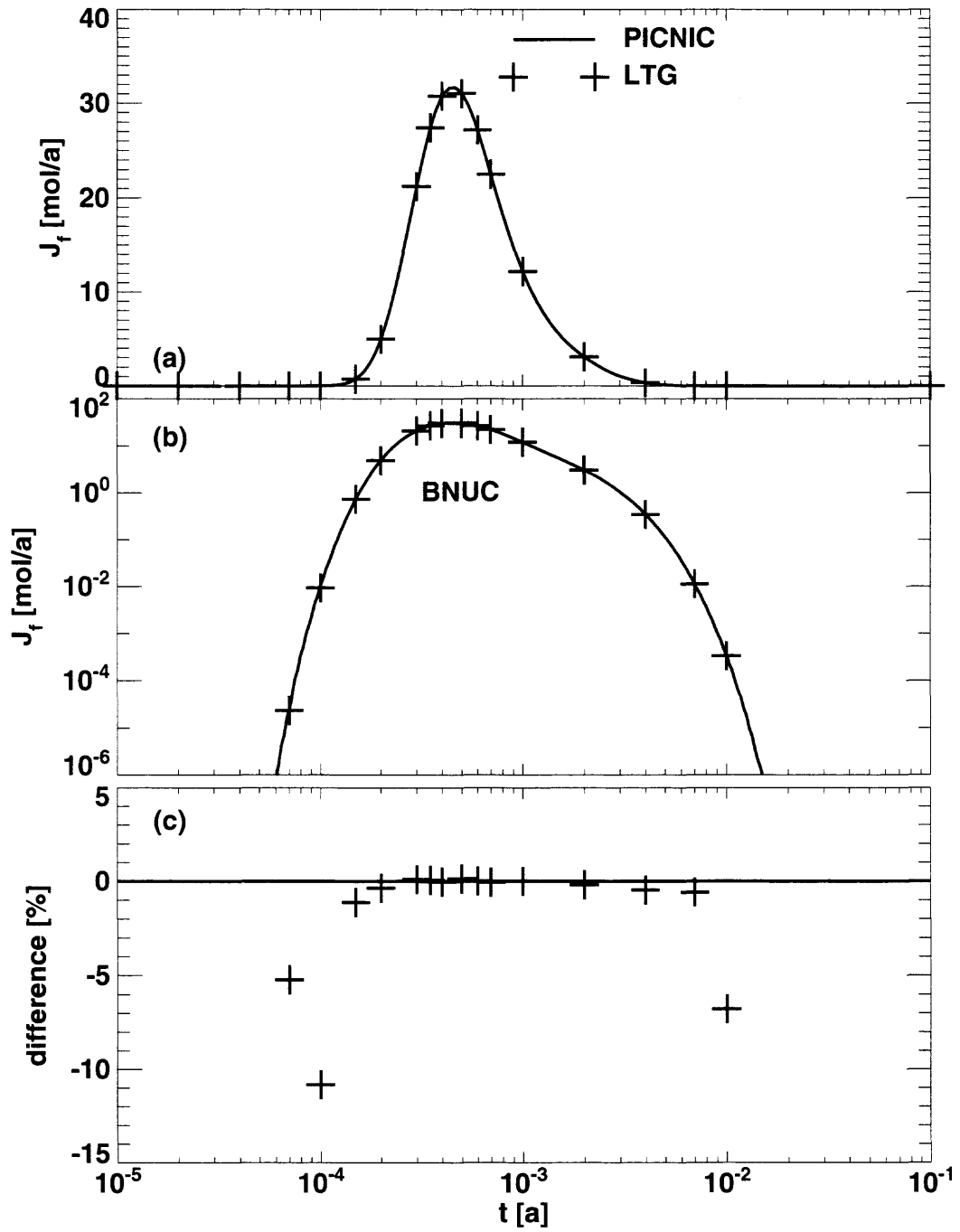


Figure 4.15. Hypothetical variation of the Grimsel uranine dipole experiment for a nuclide decay chain and a different rock matrix. Presented is the nuclide BNUC of the decay chain $ANUC \rightarrow BNUC \rightarrow CNUC$. A δ -function source of the parent ANUC is considered.

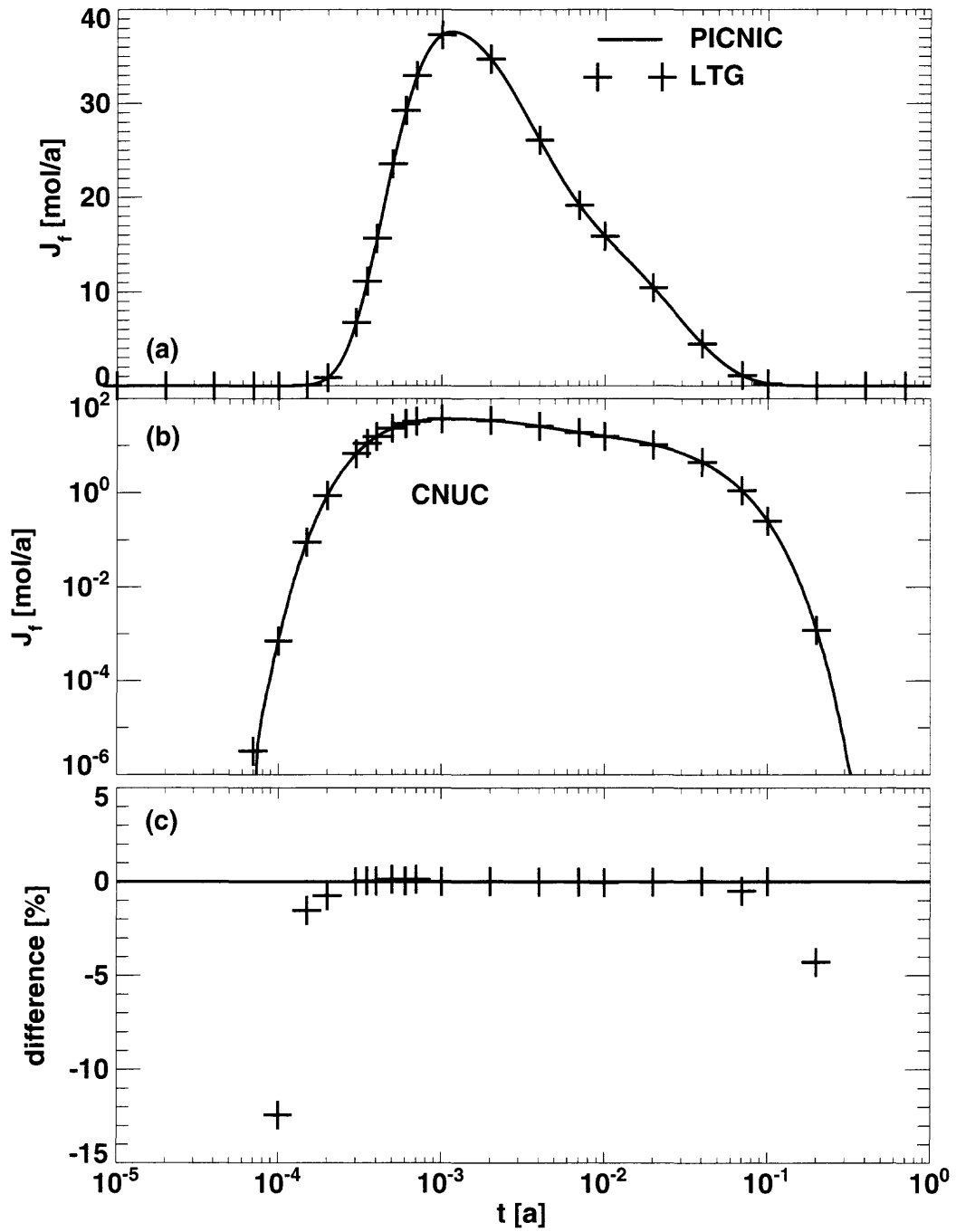


Figure 4.16. Hypothetical variation of the Grimsel uranine dipole experiment for a nuclide decay chain and a different rock matrix. Presented is the nuclide CNUC of the decay chain $\text{ANUC} \rightarrow \text{BNUC} \rightarrow \text{CNUC}$. A δ -function source of the parent ANUC is considered.

4.2.2. Single Nuclide and Nuclide Decay Chain in a Pathway

To test the network feature in PICNIC, we now consider transport in a **pathway** consisting of two legs, see Figure 4.17. Again a variation of the uranine transport in the Grimsel dipole experiment is considered. The first leg is assumed to have a length $L = 2$ [m] and the rock matrix (which we denote as of type M1) and dispersion length are as in the original uranine case. Thus the length of the leg is the only difference to the original single leg case. The second leg is assumed to be of length $L = 3$ [m]. The rock matrix of the second leg (which we denote as type M2) is changed in such a way that the rock matrix thickness is reduced by a factor of 12.4 to $d = 0.5 \cdot 10^{-3}$ [m], while the retardation in the rock matrix is increased by a factor of 10 to $R_p = 10$. Thus, the rock matrix is as in the single leg case considered in Figure 4.13. A δ -function source is assumed at the inlet of the first leg.

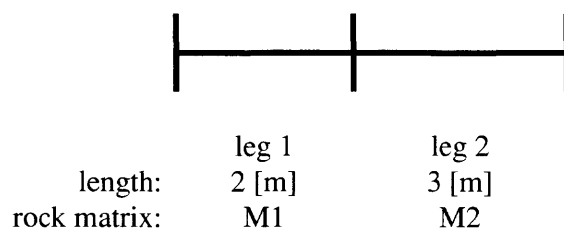


Figure 4.17. Pathway consisting of two legs. For details see text.

Also for this situation the agreement of the PICNIC (solid lines in Figure 4.18) and the PAWorks/LTG result (crosses) is very good. In the relevant region, the relative difference to the PICNIC result is now within 2%, and for early times the increase of the LTG result is somewhat earlier than for the PICNIC result. This somewhat increased and different deviation from the PICNIC result is presumably caused by the different boundary condition at the interface of the two legs. Compare also the code cross-comparison for the 3-leg pathway in section 8.3.1.

The code cross-comparison for the **nuclide decay chain** ANUC (Figure 4.19) \rightarrow BNUC (Figure 4.20) \rightarrow CNUC (Figure 4.21) also shows very good agreement and has a similar signature as for the single nuclide. We have considered again a δ -function source of the parent ANUC. In the rock matrix of the first leg the retardation factor of ANUC is $R_p = 1.0$, as for the single nuclide, while the retardation factor of BNUC is $R_p = 2.0$ and the retardation factor of CNUC is $R_p = 10.0$. The retardation factors in the rock matrix of the second leg are ten times larger.

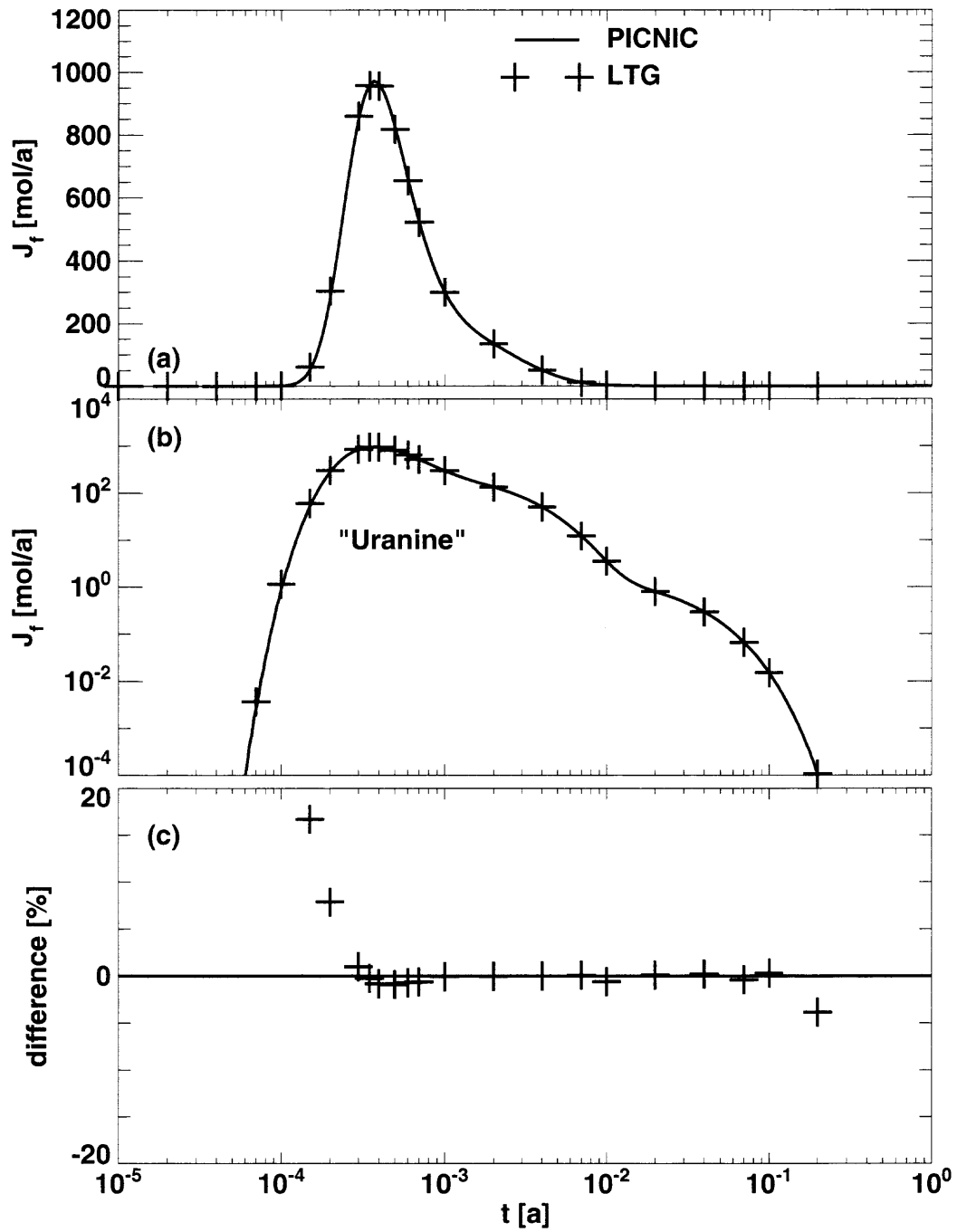


Figure 4.18. Hypothetical variation of the Grimsel uranine dipole experiment for a 2-leg pathway. A δ -function source is considered.

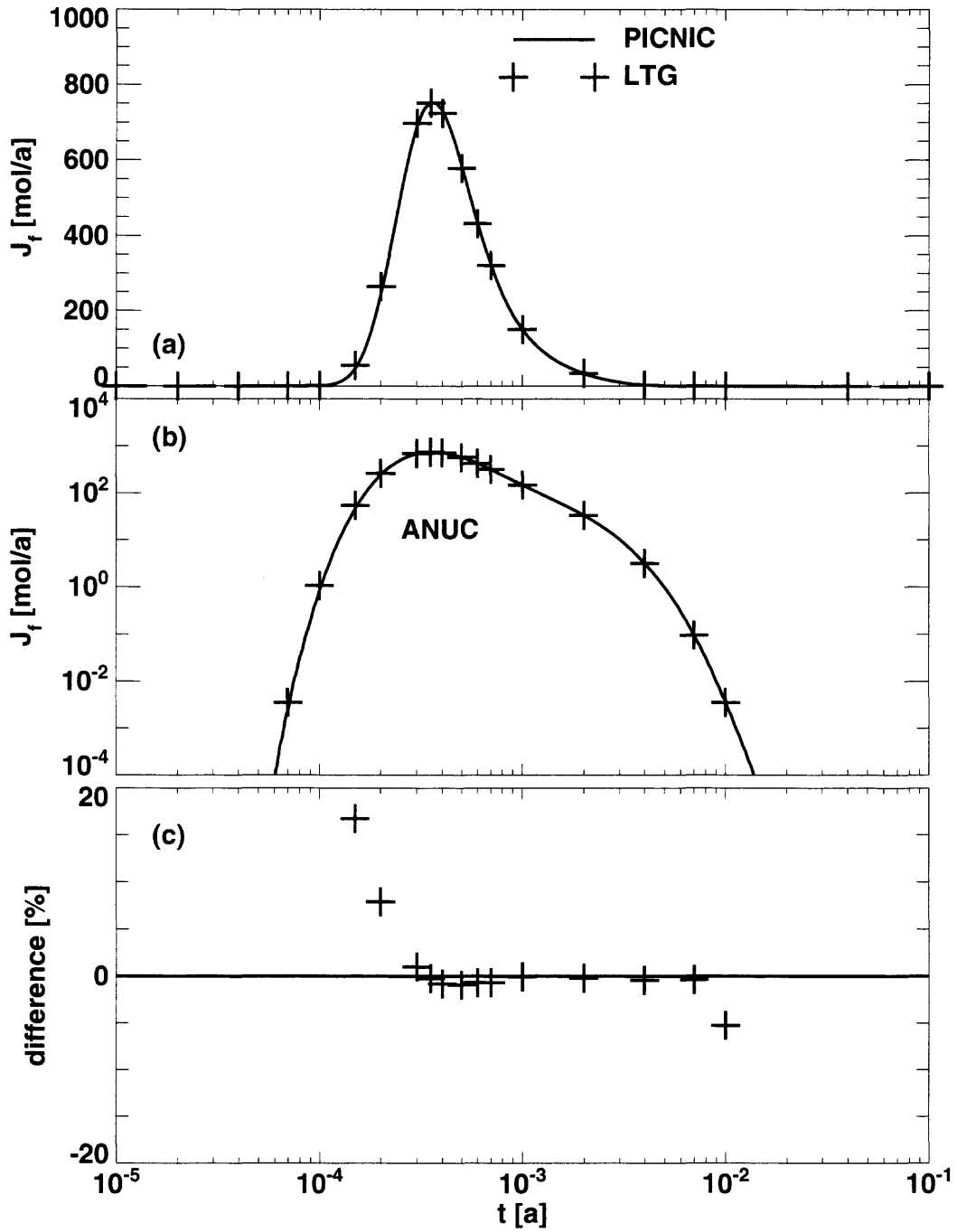


Figure 4.19. Hypothetical variation of the Grimsel uranine dipole experiment for a nuclide decay chain and a 2-leg pathway. Presented is the nuclide ANUC of the decay chain $ANUC \rightarrow BNUC \rightarrow CNUC$. A δ -function source of the parent ANUC is considered.

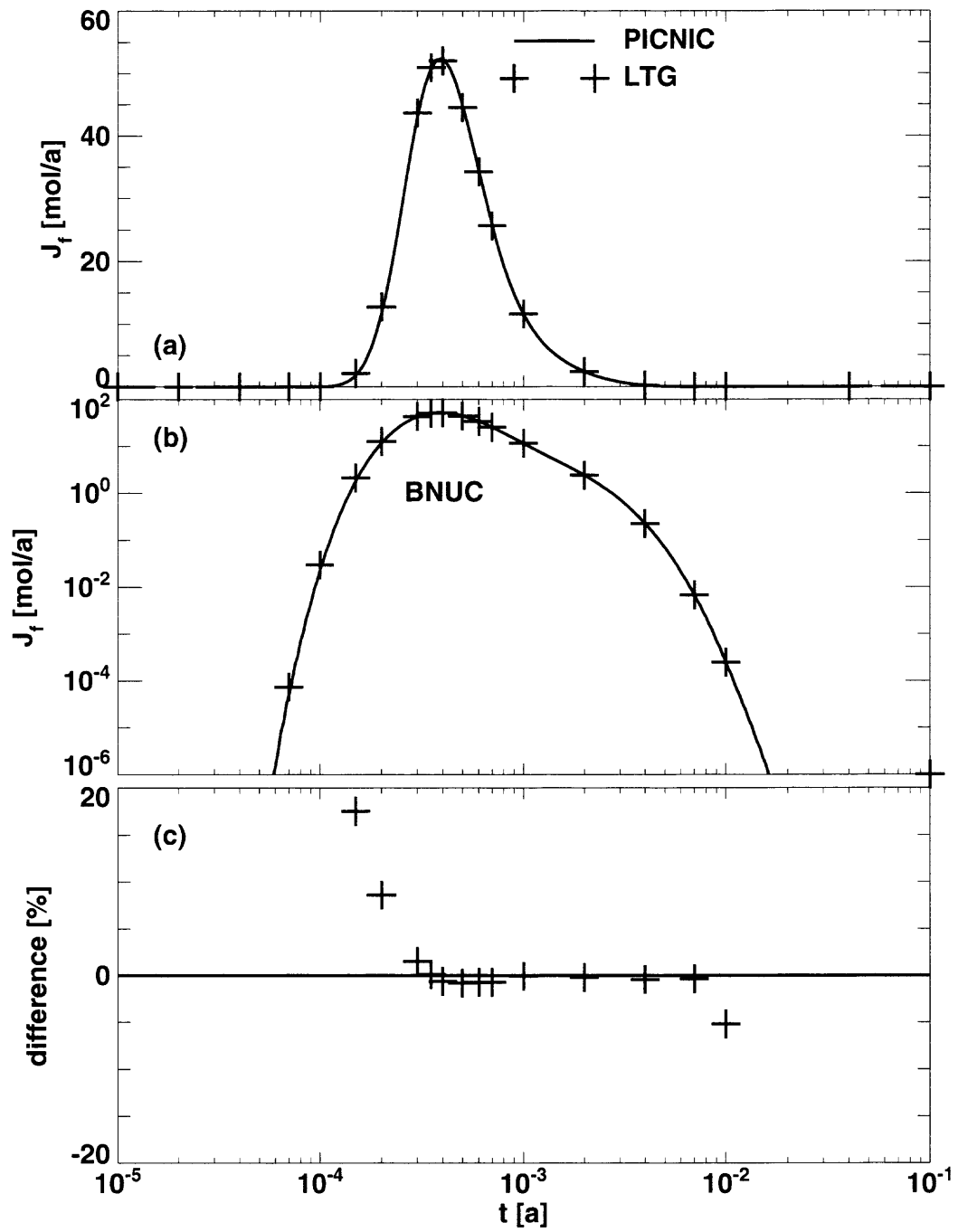


Figure 4.20. Hypothetical variation of the Grimsel uranium dipole experiment for a nuclide decay chain and a 2-leg pathway. Presented is the nuclide BNUC of the decay chain $\text{ANUC} \rightarrow \text{BNUC} \rightarrow \text{CNUC}$. A δ -function source of the parent ANUC is considered.

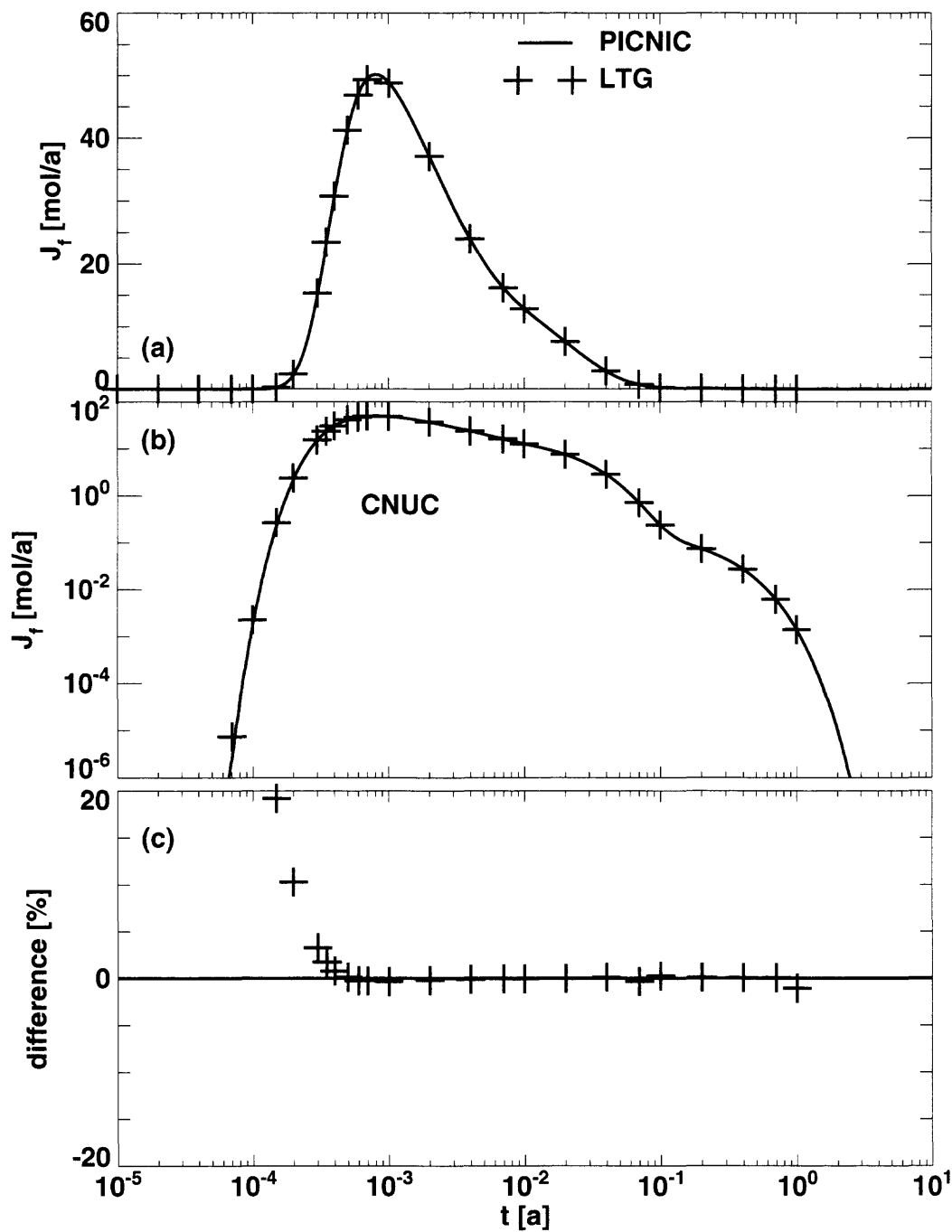


Figure 4.21. Hypothetical variation of the Grimsel uranine dipole experiment for a nuclide decay chain and a 2-leg pathway. Presented is the nuclide CNUC of the decay chain $ANUC \rightarrow BNUC \rightarrow CNUC$. A δ -function source of the parent ANUC is considered.

4.3. Transport of Single Nuclides and a Nuclide Decay Chain in Networks

In this subsection we consider transport in **networks**. The test cases are again a cross-comparison between PAWorks/LTG and PICNIC. The geometry of the network, as depicted in Figure 4.22, has the form of a grid. It is quite similar to the network sketched in Figure 4.1 in Shuttle and Eiben [1998]. For all networks considered, the area of flowing water in the legs, and thereby the velocity field, is the same. The nuclide source is always situated at the junction $in = 17$ and the nuclide flow rate is evaluated at the junction $out = 18$. The cross-sectional area and the hydraulic conductivities of the legs are given in Table 4.7. Artificial values of the parameters are used. There is no sorption in the area of flowing water, $R_f = 1$. The length of each leg is $L = 20[m]$, the Peclet number is $Pe = 20$, and the flow porosity and the infill porosity of each leg are $\varepsilon_f = \varepsilon_i = 1$. Together with the hydraulic head difference of $1[m]$ between the junctions in and out , this defines the flow of water in the legs, see the Darcy velocities in Table 4.7. It is checked with the respective PAWorks/LTG result that **PICNIC calculates the Darcy velocities correctly from the hydraulic conductivities**.

The considered networks differ only in terms of the rock matrix of the legs.

First we consider a **single nuclide in the network without rock matrix**.

As the next test case it is considered that the **rock matrix in the different legs has the same properties**.

Finally we consider a **network with different types of rock matrix**, first for a **single nuclide** and then for a **nuclide decay chain**.

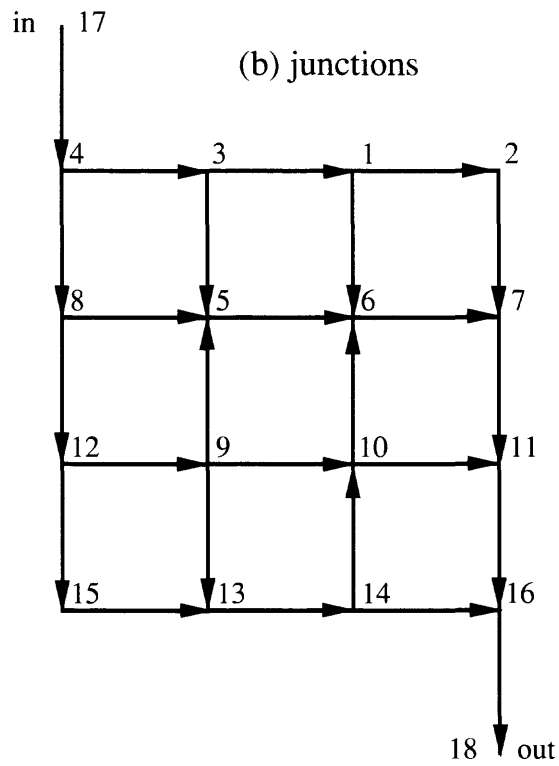
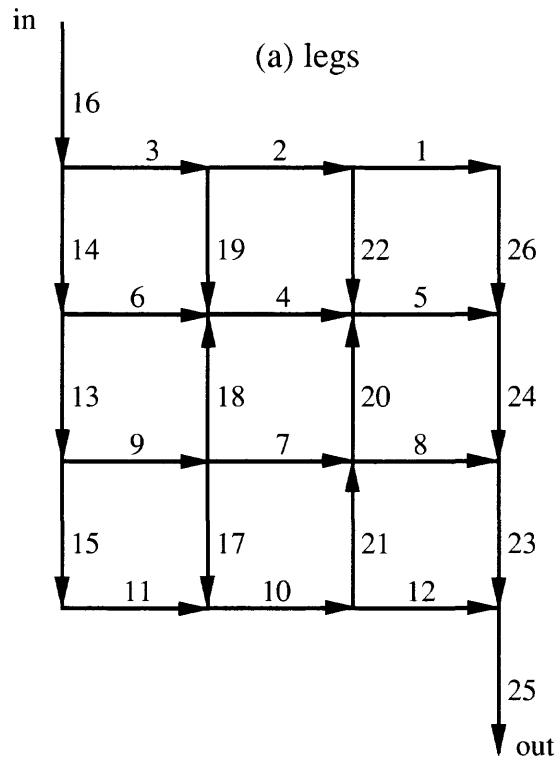


Figure 4.22. In (a) the legs and in (b) the junctions of a 26-leg network are indicated. The flow of water in the horizontal legs is always from left to right. The flow of water in the vertical junctions is always from top to bottom, except for the legs 18, 20 and 21 where water flows (slowly) from bottom to top.

leg	cross-sectional area A_f [m ²]	hydraulic conductivity [m/a]	Darcy velocity q_f [m/a]	surface to volume ratio $\delta_f = \frac{1}{b}$ [1/m]
1	0.009645625	4989.344	84.92689	3162.055336
2	0.01278282	4989.346	68.832	3162.056573
3	0.017457	4989.344	74.93047	3162.055336
4	0.017888	7056.708	97.06961	2236.135957
5	0.02365688	7056.708	120.649	2236.135957
6	0.01211912	7056.708	98.8398	2236.135957
7	0.0253	9978.688	136.3278	1581.027668
8	0.01714075	9978.688	175.2803	1581.027668
9	0.03057505	9978.688	127.5381	1581.027668
10	0.03817726	14111.84	191.4073	1117.942985
11	0.04046718	14111.84	172.1722	1117.942985
12	0.02508178	14111.84	266.9243	1117.942985
13	0.14176	63115.20	76.6565	250
14	0.1808	63115.20	66.7317	250
15	0.18144	63115.20	38.39944	250
16	0.29856	63115.20	44.78969	250
17	0.19288	63115.20	1.760973	250
18	0.16	63115.20	0.6880622	250
19	0.1484	63115.20	2.884482	250
20	0.16	63115.20	6.605059	250
21	0.13784	63115.20	4.443344	250
22	0.17328	63115.20	0.3503324	250
23	0.08272001	63115.20	80.72749	250
24	0.16	63115.20	22.95846	250
25	0.1224	63115.20	109.2543	250
26	0.16032	63115.20	5.109822	250

Table 4.7. Parameters of the legs which are common to the networks depicted in Figure 4.22. Note that PAWorks/LTG defines the cross-sectional area A_f of the area of flowing water by the aperture $2b$ and the perimeter $A_f/2b$. Also the transmissivity is defined there instead of the hydraulic conductivity of the legs.

4.3.1. No Rock Matrix

First we consider the nuclide transport in the **network without rock matrix** in the legs. For this network we consider a pulse-like source $S_{in}(t) = 10\delta(t)$ [mol/a]. The nuclide flow rate at the junction *out* has the double-peaked structure (with the maxima at $t \approx 2[a]$ and $t \approx 6[a]$) and the two shoulders/tailings (following at $t \approx 10[a]$ and $t \approx 100[a]$), given in Figure 4.23. Qualitatively the PICNIC results assuming the zero-gradient boundary condition in each leg (solid lines) and the PAWorks/LTG results (short-dashed lines) are very similar. However there are quantitative differences, see the relative difference functions of the LTG result from the PICNIC result in Figure 4.23c. The first maximum of the LTG result is slightly smaller and somewhat later. Also the decrease of the LTG result to late times is earlier. The most striking difference between the LTG and the PICNIC result is in the minimum between the two maxima. This minimum is strongly pronounced for PICNIC, indicating a linear superposition of the release from different pathways, while it appears to be smeared out in the LTG result (compare Figure 4.23b). Using at-infinity in PICNIC as the boundary condition in all legs (dash-dotted lines in Figure 4.23) does not mitigate this difference between the LTG and the PICNIC result. Note that these calculations are in contradistinction, but not contradiction to each other, because LTG does not fix the boundary condition at inner junctions in the network. This especially influences the distribution of nuclides at junctions to the legs. For instance in PICNIC nuclides only enter departing legs, while in the LTG method it might be possible that nuclides at a junction also enter an arriving leg.

Note that for this case without matrix diffusion, the PICNIC code produces, in the release curve for early times, $t \approx 1[a]$, some non-physical oscillations also to negative values. These oscillations, however, are three orders of magnitude below the maximum value of the breakthrough curve.

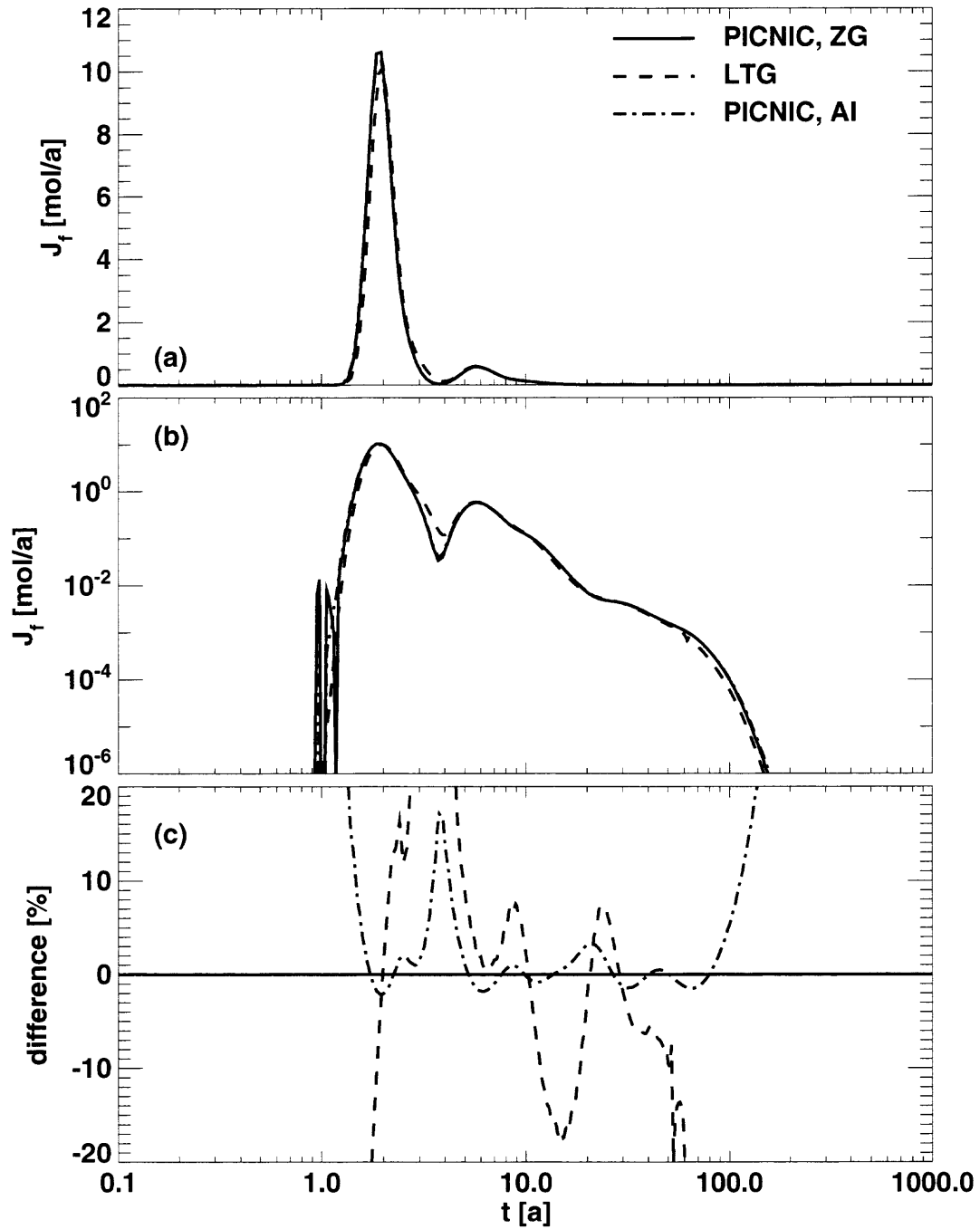


Figure 4.23. The result of a PAWorks/LTG calculation (short-dashed lines) for a 26-leg network without matrix diffusion is compared to the PICNIC result with the zero-gradient boundary condition in each leg (solid lines). The release curves are given in (a) on a linear scale and in (b) on a logarithmic scale. The relative difference of the PAWorks/LTG result to the PICNIC result is given in (c). For reference the PICNIC result for the at-infinity boundary condition in each leg (dash-dotted lines) is also given.

4.3.2. Same Rock Matrix in Each Leg

Next we consider the **same type of rock matrix in each leg of the network**, but δ_f changes from leg to leg (Table 4.7). The parameters of the rock matrix are $d = 0.05[\text{m}]$, $\varepsilon_p = 0.1$, $D_p = 0.031536[\text{m}^2/\text{a}]$ and $R_p = 26.0$. A top-hat source is considered: $S_{in}(t) = 10[\text{mol/a}]$ for $0 < t < 10[\text{a}]$, and $S_{in}(t) = 0$ for $t < 0[\text{a}]$ and for $t > 10[\text{a}]$.

The release for this network shows a strong maximum and then a kind of shoulder (at $t \approx 100[\text{a}]$), see Figure 4.24. Again the PICNIC results for the zero-gradient boundary condition in each leg (solid lines) and the PAWorks/LTG results (short-dashed lines) are qualitatively very similar, and there are again quantitative differences. As in the former case, the increase of the LTG result for early times is later with respect to the PICNIC result. The maximum is also later and smaller, indicating a stronger “macro-dispersion” in the network due to the different boundary conditions for the LTG method at inner junctions. Again these differences cannot be mitigated using the at-infinity boundary condition in PICNIC (dash-dotted lines).

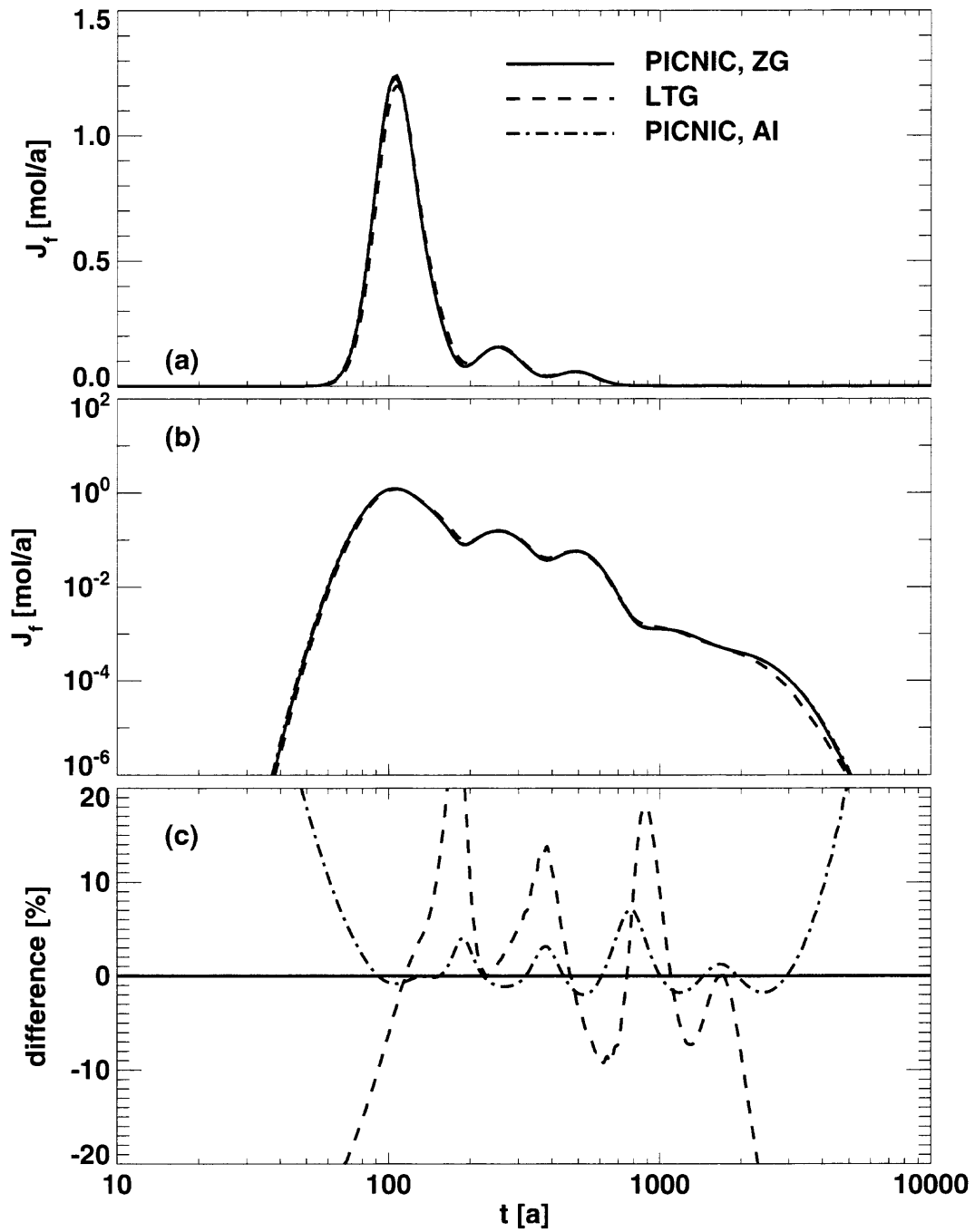


Figure 4.24. Same as Figure 4.23. Now the same rock matrix in each leg is considered. The result of a PAWorks/LTG calculation (short-dashed lines) and the PICNIC result with the at-infinity boundary condition in each leg (dash-dotted lines) are compared to the PICNIC result with the zero-gradient boundary condition in each leg (solid lines).

4.3.3. Different Rock Matrix in Different Legs: Single Nuclide and Nuclide Decay Chain

As the next test case we consider the **network with different types of rock matrix in different legs**. All other properties remain the same as in the former example. The rock matrix parameters of the network are given in Table 4.8. We consider again a top-hat source, $S_{in}(t) = 10$ [mol/a] for $0 < t < 10$ [a] and $S_{in}(t) = 0$ for $t < 0$ [a] and $t > 10$ [a].

legs	matrix porosity ε_p	matrix thickness d [m]	retardation R_p of ANUC and single nuclide	retardation R_p of BNUC	retardation R_p of CNUC
1,2,3	0.1	0.05	26	17.5	23.5
4,5,6	0.1	0.05	26	17.5	23.5
7,8,9	0.1	0.05	26	17.5	23.5
10,11,12	0.001	1	2501	1651	2251
13,14,15,16	0.001	1	2501	1651	2251
17,18,19	0.1	0.05	26	17.5	23.5
20,21,22	0.1	0.05	26	17.5	23.5
23,24,25,26	0.001	1	2501	1651	2251

Table 4.8. Parameter values of the rock matrix for the single nuclide and the nuclide decay chain calculation. The first column gives the legs. The second column gives the rock matrix porosity ε_p and the third column gives the rock matrix thickness d . Columns 4 to 6 give the retardation factors R_p in the rock matrix of the nuclides ANUC, BNUC and CNUC. ANUC has the same retardation properties as the single nuclide considered. The legs 1 to 9 have the same rock matrix properties as in the former case. The diffusion constant in the rock matrix is $D_p = 0.031536$ [m²/a] for all legs and all nuclides.

The release for this network shows a very pronounced first maximum at $t \approx 16$ [a], followed by smaller maxima at $t \approx 100$ [a] and $t \approx 180$ [a], a shoulder at $t \approx 400$ [a] and a very long tailing up to about $t \approx 10^5$ [a], see Figure 4.25. Qualitatively the PICNIC result for the zero-gradient boundary condition in each leg (solid lines) and the PAWorks/LTG result (short-dashed lines) are very similar and again there are quantitative differences. The increase of the LTG result for early times is again later. The maximum is also later and smaller, indicating again a stronger macro-dispersion in the network due to the different boundary conditions for the LTG method at inner junctions. In the tailing the differences between the LTG and the PICNIC result decrease with some oscillations, see Figure 4.25c. Again these differences cannot be mitigated using the at-infinity boundary condition in PICNIC (dash-dotted lines).

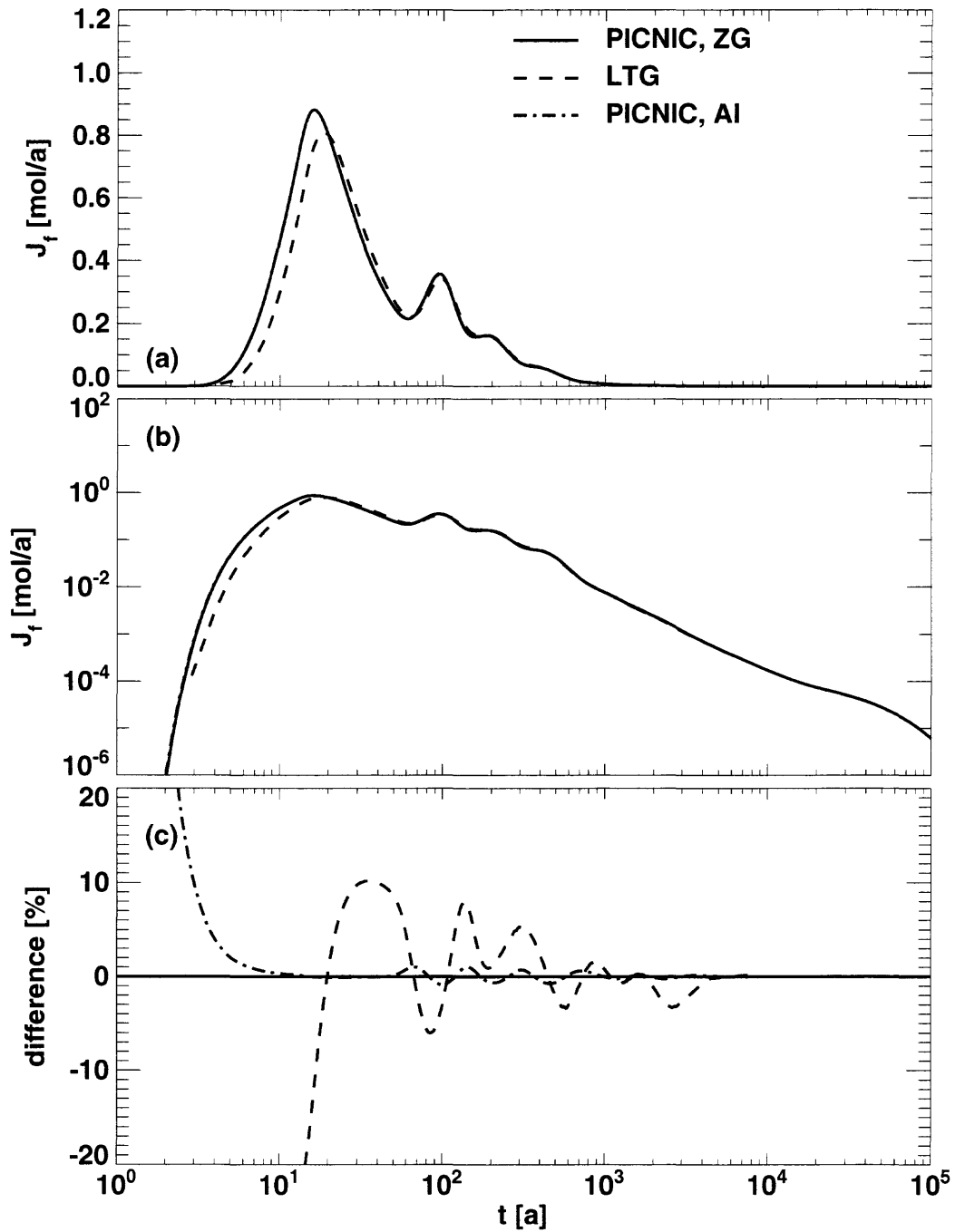


Figure 4.25. Same as Figure 4.23 but considered are different rock matrices in the legs. The result of a PAWorks/LTG calculation (short-dashed lines) and the PICNIC result with the at-infinity boundary condition in each leg (dash-dotted lines) are compared to the PICNIC result with the zero-gradient boundary condition in each leg (solid lines). The LTG result has been calculated up to $t \approx 10^4$ [a].

To test the accuracy in this **network** for a **nuclide decay chain**, we now consider the chain³² $\text{ANUC} \rightarrow \text{BNUC} \rightarrow \text{CNUC} \rightarrow$, where the half-life of ANUC is 17.32868 [a], the half-life of BNUC is 13.86294 [a] and the half-life of the nearly stable CNUC is 6931.472 [a]. ANUC is assumed to have the same transport properties as the non-decaying nuclide above. BNUC and CNUC are assumed to have the same properties as ANUC, except for retardation in the rock matrix, see Table 4.8. The release of ANUC (Figure 4.26), BNUC (Figure 4.27) and CNUC (4.28) is again calculated using PAWorks/LTG (short-dashed lines) and PICNIC with the zero-gradient boundary condition in each leg (solid lines) and with the at-infinity boundary condition in each leg (dash-dotted lines) and compared. Again the PICNIC results for the zero-gradient boundary condition in each leg (solid lines) and the PAWorks/LTG results (short-dashed lines) are qualitatively very similar and there are quantitative differences. Again, these differences cannot be mitigated using the at-infinity boundary condition in PICNIC (dash-dotted lines).

Overall we can conclude that there are different boundary conditions in inner junctions of the LTG method and the pathways/tree method applied in PICNIC. This leads to quantitatively different results, while the results are qualitatively very similar.³³ These differences appear to be considerably greater for networks (this subsection) than for pathways (sections 4.2 and 8.3). This might be because, for pathways, the response functions of the legs are (slightly) different³⁴ in the LTG code compared with the PICNIC method. For networks, the definition of the probabilities w_{lg} of the nuclides to enter a leg at a junction additionally comes into play. These probabilities are different for PAWorks/LTG and PICNIC. For PAWorks/LTG, not only arriving legs but also departing legs can be entered by the nuclides. This is by definition not possible in PICNIC, because w_{lg} is determined solely by the water flow rates (compare section 2.1.3). Because of the differences in the definition of w_{lg} , the tests described in this subsection verified the capability for transport in a network in a qualitative way, but the network capability cannot be regarded as being fully quantitatively verified by the cross-comparison with PAWorks/LTG alone.³⁵

³² Note that this decay chain does not have the same properties as the decay chain sometimes considered in single legs or pathways, e.g. in section 4.2.

³³ Our calculations, especially for the network without matrix diffusion, have shown that matrix diffusion is **not** the reason behind the differences between PAWorks/LTG and PICNIC. Also considering nuclide decay chains does **not** lead to increased differences.

³⁴ Except for in the last leg, where the zero-gradient outlet boundary condition is also explicitly specified in PAWorks/LTG.

³⁵ Note that the definition of legs and junctions and also the boundary conditions at junctions are only approximations of real physical behaviour. Thus, in situations where particular differences become very important - such as boundary conditions at inner junctions - results should be considered with care.

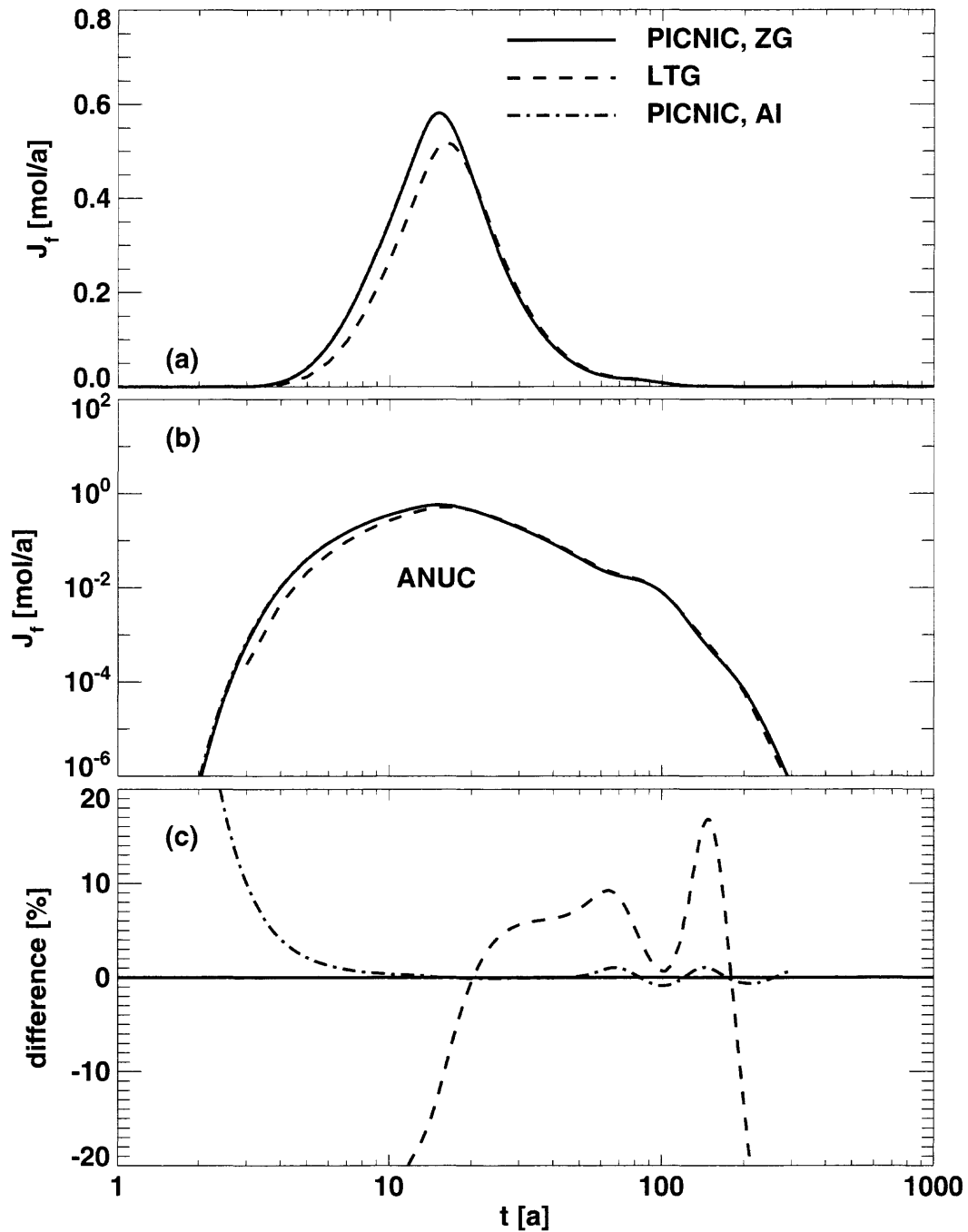


Figure 4.26. Same as Figure 4.25. The only difference is that the nuclide ANUC of the decay chain ANUC \rightarrow BNUC \rightarrow CNUC \rightarrow is considered. A top-hat source is considered. The result of a PAWorks/LTG calculation (short-dashed lines) and the PICNIC result with the at-infinity boundary condition in each leg (dash-dotted lines) are compared to the PICNIC result with the zero-gradient boundary condition in each leg (solid lines).

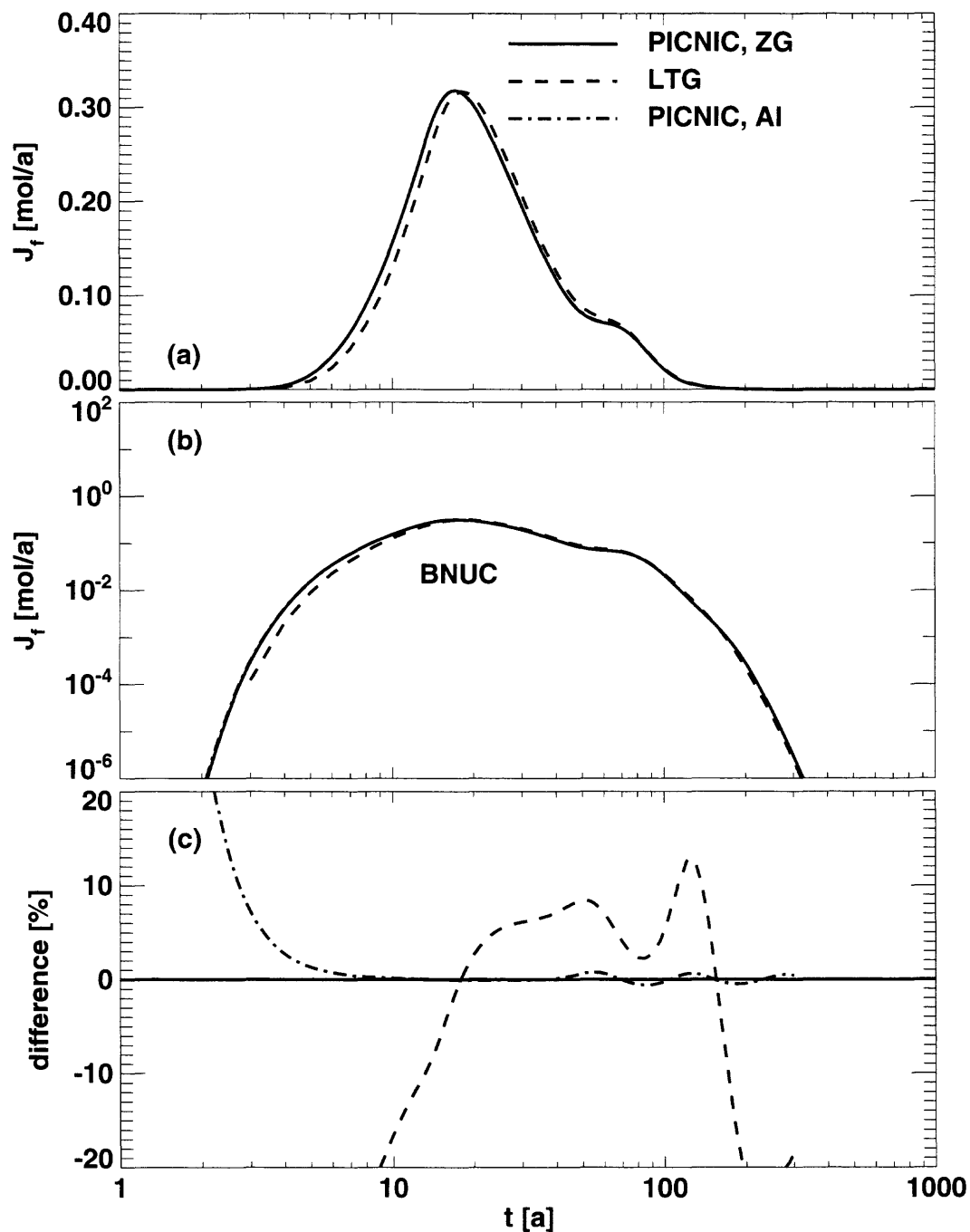


Figure 4.27. Same as Figure 4.25. The only difference is that the nuclide BNUC of the decay chain ANUC \rightarrow BNUC \rightarrow CNUC \rightarrow is considered. A top-hat source of the parent ANUC is considered. The result of a PAWorks/LTG calculation (short-dashed lines) and the PICNIC result with the at-infinity boundary condition in each leg (dash-dotted lines) are compared to the PICNIC result with the zero-gradient boundary condition in each leg (solid lines).

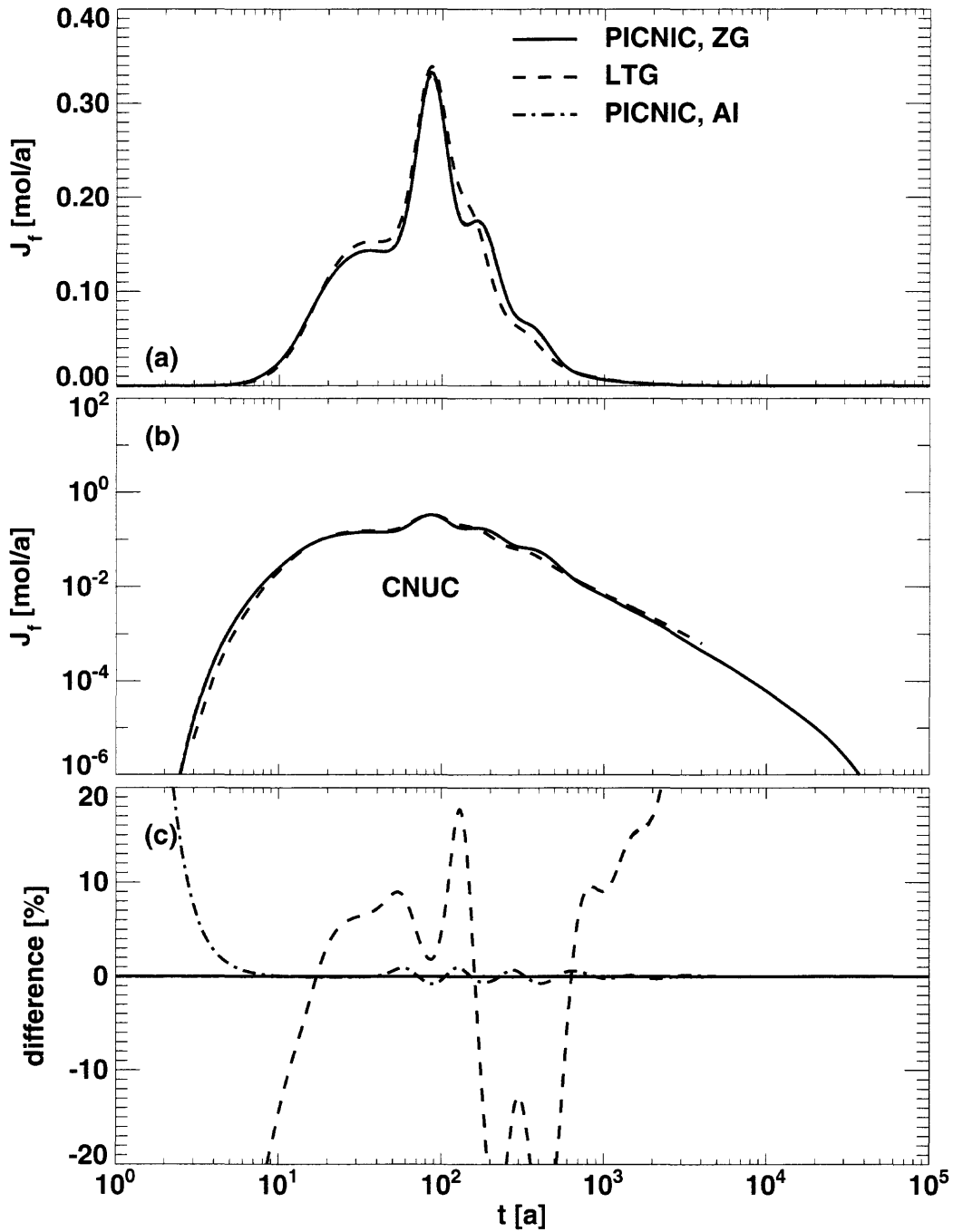


Figure 4.28. Same as Figure 4.25. The only difference is that the nuclide CNUC of the decay chain $\text{ANUC} \rightarrow \text{BNUC} \rightarrow \text{CNUC} \rightarrow$ is considered. A top-hat source of the parent ANUC is considered. The result of a PAWorks/LTG calculation (short-dashed lines) and the PICNIC result with the at-infinity boundary condition in each leg (dash-dotted lines) are compared to the PICNIC result with the zero-gradient boundary condition in each leg (solid lines). The LTG result has been calculated up to $t \approx 4 \cdot 10^3$ [a].

4.4. Cases Related to Performance Assessment

In this subsection we continue with **tests related to performance assessment**. In the main part of this subsection, cases related to the Kristallin-I study [Nagra, 1994] are considered and a cross-comparison with the RANCHMD code is performed. This is mainly a review of the verification cases presented by Niemeyer and Barten [1997]. Typical releases from the repository near-field are used as sources to the geosphere.

First the Kristallin-I reference case for **single nuclides** is considered and modelled as a PICNIC leg. Next a **nuclide decay chain in a single leg** is analysed.

Then the transport of **single nuclides in a small network** of legs with **multiple sources** is considered and compared to the so-called “assembled RANCHMD” calculations.

Finally a variation of an INTRACOIN chain decay test case without matrix diffusion is modelled as a PICNIC leg. Thereby the capability of PICNIC to deal with a **band-release source** and a **simple-leaching source** are verified.

4.4.1. Single Nuclides in a Single Planar Channel

In this section we consider the **Kristallin-I reference case for single nuclides**. The planar rock matrix geometry is as described in Nagra [1994], Figure 5.3.5 and Tables 5.3.1 to 5.3.3, and is designated as Geometry 6. The release from the near-field³⁶, which was calculated using the near-field model STRENG [Grindrod et al., 1990] and is shown in Figure 4.29a, is read by PICNIC from a file (“**Hartley**”-file format). This also verifies the capability of PICNIC to deal with this very special file format. Geosphere release curves, as calculated by PICNIC, are presented in Figure 4.29b, together with results given by RANCHMD (dashed lines) for comparison. For the RANCHMD calculations, the discretisation scheme was that for the Kristallin-I safety assessment.

From Figure 4.29b it can be seen that the release rates calculated by PICNIC and RANCHMD are in very good agreement, both qualitatively and quantitatively. Table 4.9 lists the maximum release rate and the time to maximum release for each of the seven radionuclides, again showing very good agreement between the two calculations. The calculated times to maximum release show excellent agreement, with the worst case being for ⁷⁹Se where PICNIC indicates a maximum 0.15% earlier than RANCHMD. The maximum rates predicted by PICNIC are generally around 1% to 2% higher than those given by the RANCHMD calculations.

³⁶ The time axis in all figures and tables in Kristallin I-related cases in this report refers to „Time after canister failure“.

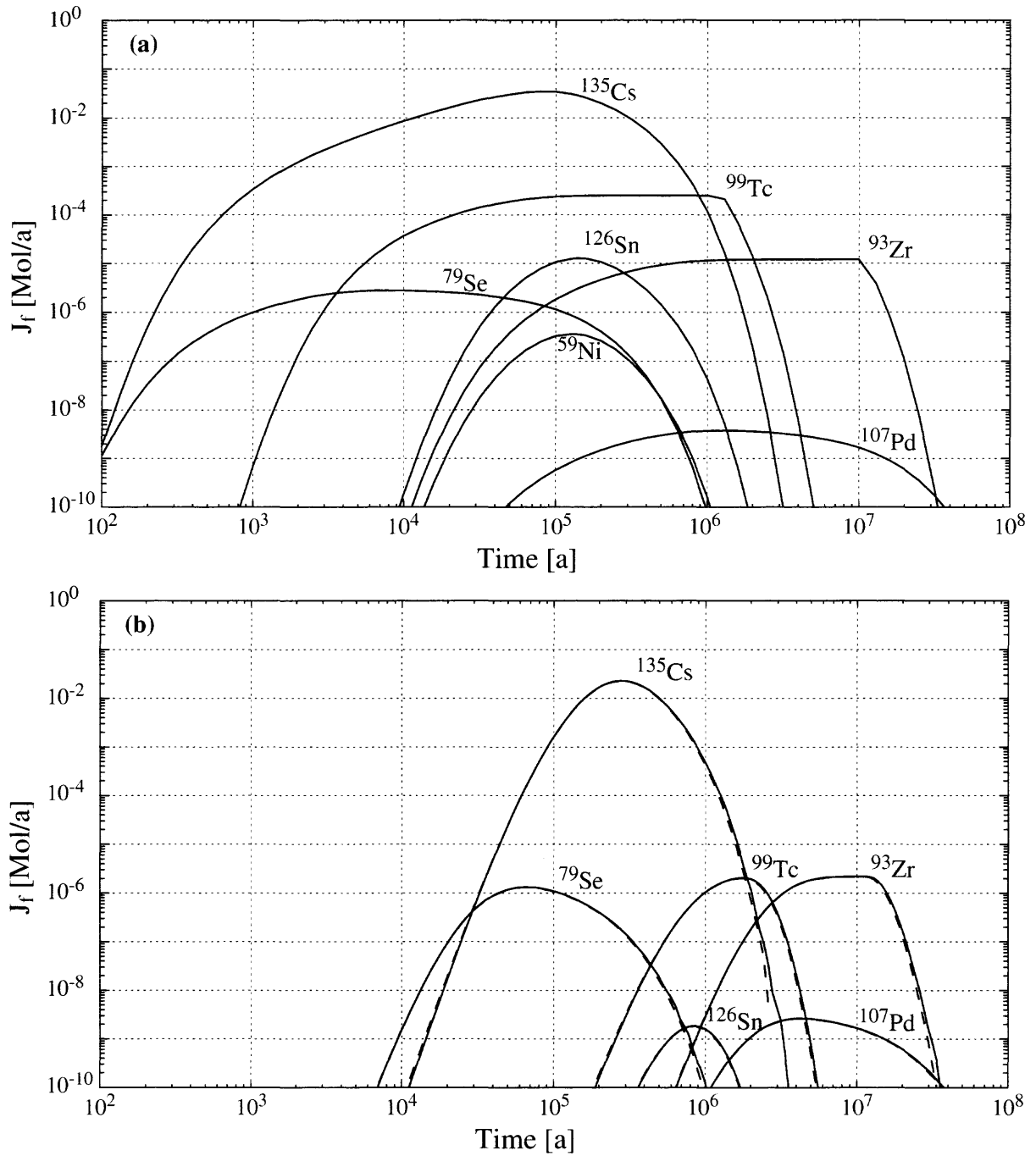


Figure 4.29. Nuclide release rates (a) from the near-field (i.e. source for geosphere) and (b) from the geosphere, for the single nuclides of the Kristallin-I reference case with the planar Geometry 6, (see Tables 5.3.1 to 5.3.3 in Nagra [1994]), presented on a double-logarithmic scale. In (b) PICNIC calculations (solid lines) and RANCHMD calculations (dashed lines) are shown for comparison.

nuclide	$T_{1/2}$	Maximum of J_f [mol / a]			time [a] of maximum		
		PICNIC	RANCHMD	diff.(P,R) [%]	PICNIC	RANCHMD	diff.(P,R) [%]
¹³⁵ Cs	2.3E+06	2.279E-02	2.250E-02	1.29	2.783E+05	2.784E+05	
¹²⁶ Sn	1.0E+05	1.835E-09	1.803E-09	1.77	8.254E+05	8.255E+05	
¹⁰⁷ Pd	6.5E+06	2.649E-09	2.621E-09	1.07	4.354E+06	4.354E+06	
⁹⁹ Tc	2.13E+05	2.054E-06	2.018E-06	1.78	1.778E+06	1.778E+06	
⁹³ Zr	1.53E+06	2.176E-06	2.148E-06	1.30	1.066E+07	1.066E+07	
⁷⁹ Se	6.5E+04	1.325E-06	1.309E-06	1.22	6.813E+04	6.823E+04	-0.15
⁵⁹ Ni	7.6E+04	1.261E-11	1.244E-11	1.37	7.263E+05	7.264E+05	

Table 4.9. Comparison of maximum release rate and time to maximum release for seven single radionuclides as calculated by PICNIC (P) and RANCHMD (R) for the Kristallin-I reference case with Geometry 6. The first and second columns specify the nuclides and their corresponding half-life. The maximum release rate and the time of that maximum as calculated by PICNIC are given in columns 3 and 6 respectively. The corresponding results from RANCHMD are given in columns 4 and 7 respectively. Columns 5 and 8 present the relative differences between the results of the two calculations, i.e. $100*(P-R)/R$. Comparing the time to maximum release with the nuclide half-life gives a first indication how strongly radioactive decay influences the breakthrough curves.

Table 4.10 presents a detailed comparison of the release curves predicted by the two codes for ¹³⁵Cs, the nuclide which shows the highest maximum release rate, and ⁹⁹Tc, for which the difference between the maximum rate predicted by PICNIC and RANCHMD is the largest. It appears that the release curves predicted by PICNIC are slightly behind those given by RANCHMD. This can also be seen in Figure 4.29b.³⁷ See also Figure 4.30a where the absolute values of the relative differences of PICNIC calculations from RANCHMD calculations for ¹³⁵Cs (solid line) and ⁹⁹Tc (dashed line) are visualised graphically on a double-logarithmic scale. The spikes to very small values indicate where the difference changes sign; compare columns 4 and 7 of Table 4.10.

³⁷ On the rising edge of the release curves the two codes agree to within 30% for release rates less than six orders of magnitude below the maximum. For the trailing edge the agreement is within 70% up to four decades below the maximum. Given that the comparison of these edges (especially when they represent sharp fronts) is an extreme test, the two codes exhibit an acceptable level of agreement over the range of interest. Following the maximum, the release rate predicted by RANCHMD approaches zero somewhat faster than that calculated by PICNIC. However, it is well known that RANCHMD results can only be considered reliable down to approximately five orders of magnitude below the maximum according to the specified accuracy for the time integration (A. Jakob, private communication).

time [a]	¹³⁵ Cs			⁹⁹ Tc		
	PICNIC	RANCHMD	diff.(P,R) [%]	PICNIC	RANCHMD	diff.(P,R) [%]
1.000e+04	3.436499E-11	5.150E-11	-33.27			
2.021e+04	1.865308E-08	2.209E-08	-15.56	0.000000E+00	1.434E-20	
2.966e+04	4.543692E-07	4.978E-07	-8.72	0.000000E+00	2.617E-18	
4.948e+04	2.250884E-05	2.309E-05	-2.52	1.557535E-16	9.553E-16	-83.70
1.000e+05	1.602232E-03	1.587E-03	0.96	4.961286E-13	7.222E-13	-31.30
2.021e+05	1.705289E-02	1.685E-02	1.20	1.629669E-10	1.915E-10	-14.90
2.966e+05	2.265289E-02	2.234E-02	1.40	2.637213E-09	2.882E-09	-8.49
4.948e+05	1.036036E-02	1.005E-02	3.08	6.281497E-08	6.448E-08	-2.58
1.000e+06	4.808598E-04	4.240E-04	13.41	1.031917E-06	1.023E-06	0.87
2.021e+06	1.116503E-06	6.550E-07	70.46	1.937023E-06	1.876E-06	3.25
2.966e+06	4.577960E-09	1.000E-30		4.254351E-07	3.703E-07	14.89
4.948e+06	1.149834E-13			9.121636E-10	5.612E-10	62.54
1.000e+07				6.732752E-18	1.000E-30	
2.021e+07				1.697234E-27		

Table 4.10. Comparison between PICNIC (P) and RANCHMD (R) calculations of time-dependence of output for ¹³⁵Cs and ⁹⁹Tc for the Kristallin-I reference case. In the first column, time is given and in the second and fifth columns the PICNIC results for ¹³⁵Cs and ⁹⁹Tc, respectively. In the third and sixth columns the RANCHMD results are presented. The fourth and seventh columns give the relative differences of PICNIC and RANCHMD results, i.e. 100*(P-R)/R.

A higher degree of discretisation in the RANCHMD calculations reduces the differences with respect to PICNIC. For ¹³⁵Cs the difference in the maximum release rate could be reduced by a factor of three to around 0.5%, while the differences on the rising edge could be cut by up to twenty times, to less than 0.7% within 5 decades of the maximum. On the trailing edge the differences were practically unaffected. Finally, interpolation between the data points in the source file is performed linearly in PICNIC, while RANCHMD uses an exponential interpolation. This could contribute to the remaining differences in the results.

Finally we have checked that the analytical result (sections 2.1.7, 2.3.4, 2.3.5 and 2.3.6) for a steady-state release is calculated by PICNIC with six to seven digits accuracy for the single nuclides considered in Figure 4.29. This check has been done for the boundary conditions zero-gradient, zero-concentration and at-infinity and using a very long top-hat release over 10⁸[a].

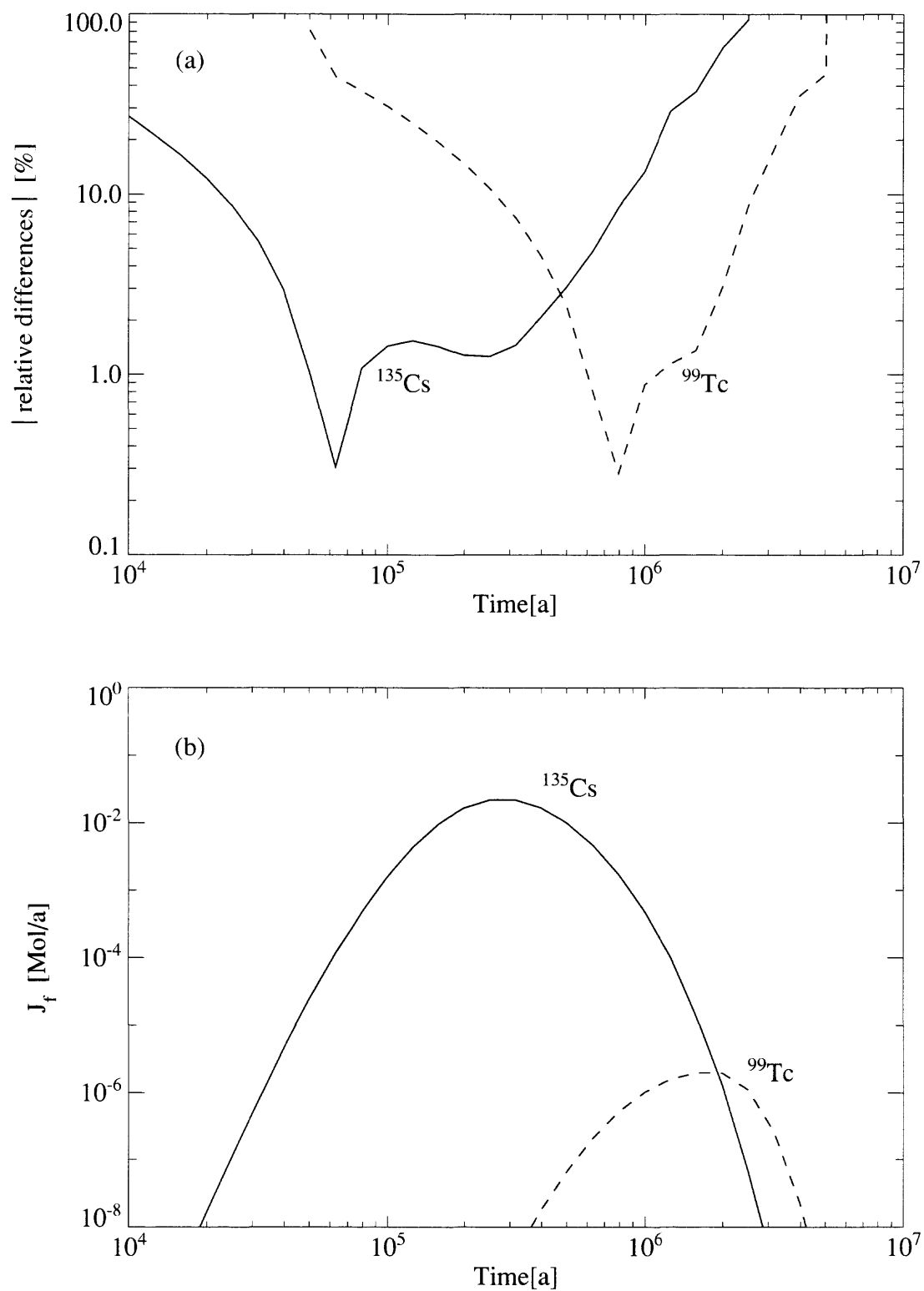


Figure 4.30. (a) Absolute values of the relative differences of PICNIC calculations from RANCHMD calculations for ^{135}Cs (solid line) and ^{99}Tc (dashed line). The spikes to very small values indicate where the difference changes sign, compare columns 4 and 7 of Table 4.10. The release rates are given in (b) for better orientation, see also Figure 4.29b.

4.4.2. Decay Chain in a Single Planar Channel

In this subsection we consider the reference case in Kristallin-I for the $4N+2$ **decay chain** $^{246}\text{Cm} \rightarrow ^{242}\text{Pu} \rightarrow ^{238}\text{U} \rightarrow ^{234}\text{U} \rightarrow ^{230}\text{Th} \rightarrow ^{226}\text{Ra} \rightarrow \dots \rightarrow ^{206}\text{Pb}$. As in the previous case the geometry is Geometry 6, as described in Nagra [1994] Figure 5.3.5 and Tables 5.3.1 to 5.3.3. The release from the near-field, as shown in Figure 4.31a, is read from a file in “Hartley”-file format. This verifies the capability of PICNIC to deal also with nuclide decay chains with this file format. Geosphere release curves, as calculated by PICNIC, are presented in Figure 4.31b, once again with results given by RANCHMD (dashed lines) for comparison. As for the single nuclides discussed in the preceding section, a qualitatively and quantitatively good agreement is found for all nuclides.

The excellent agreement between the two codes for the time of maximum release for all chain members except ^{242}Pu can be clearly seen in Table 4.11. The difference of 6.6% in the time-points of the maximum nuclide release may be due to the time discretisation of RANCHMD which is of the same order. This nuclide also shows the largest difference in the maximum release rate predicted by the two programs, 3.26% smaller, as compared with approximately 1% larger for the other members of the decay chain. However, the time of the maximum release rate for ^{242}Pu is greater than ten times the half-life of this nuclide, a fact which is reflected in the very small value of the maximum.

When the release starts at times significantly greater than the half-life, the value of the maximum is known to be very sensitive to the form of the release curve. Bearing these various points in mind, the degree of agreement between the two calculations is very good.

The first member of the decay chain, ^{246}Cm , has a relatively short half-life and hence there is no release. Indeed the near-field release rate for this nuclide is so small that it does not even appear at the down-stream boundary. The next chain member, ^{242}Pu , also decays to an almost insignificant level during geosphere transport. The relatively short half-life values, in comparison with the time to maximum release, for the decay products of ^{238}U mean that these nuclides are released in secular equilibrium with their long-lived precursor. This indicates that such a steady-state radioactive decay is correctly treated by PICNIC.

Table 4.12 presents a detailed comparison of the release rates for ^{238}U and ^{234}U , those nuclides with the highest maximum values. The rising edge of the release curve for ^{238}U shows good agreement, within 15%, even at eight orders of magnitude below the maximum, while for ^{234}U the same level of agreement is seen from seven decades below the maximum. For the trailing edge the agreement is within 2% for the period up to 10^8 [a], the end of the calculation time. This cut-off time is a factor five greater than the time to maximum release and sufficient for safety assessment purposes.

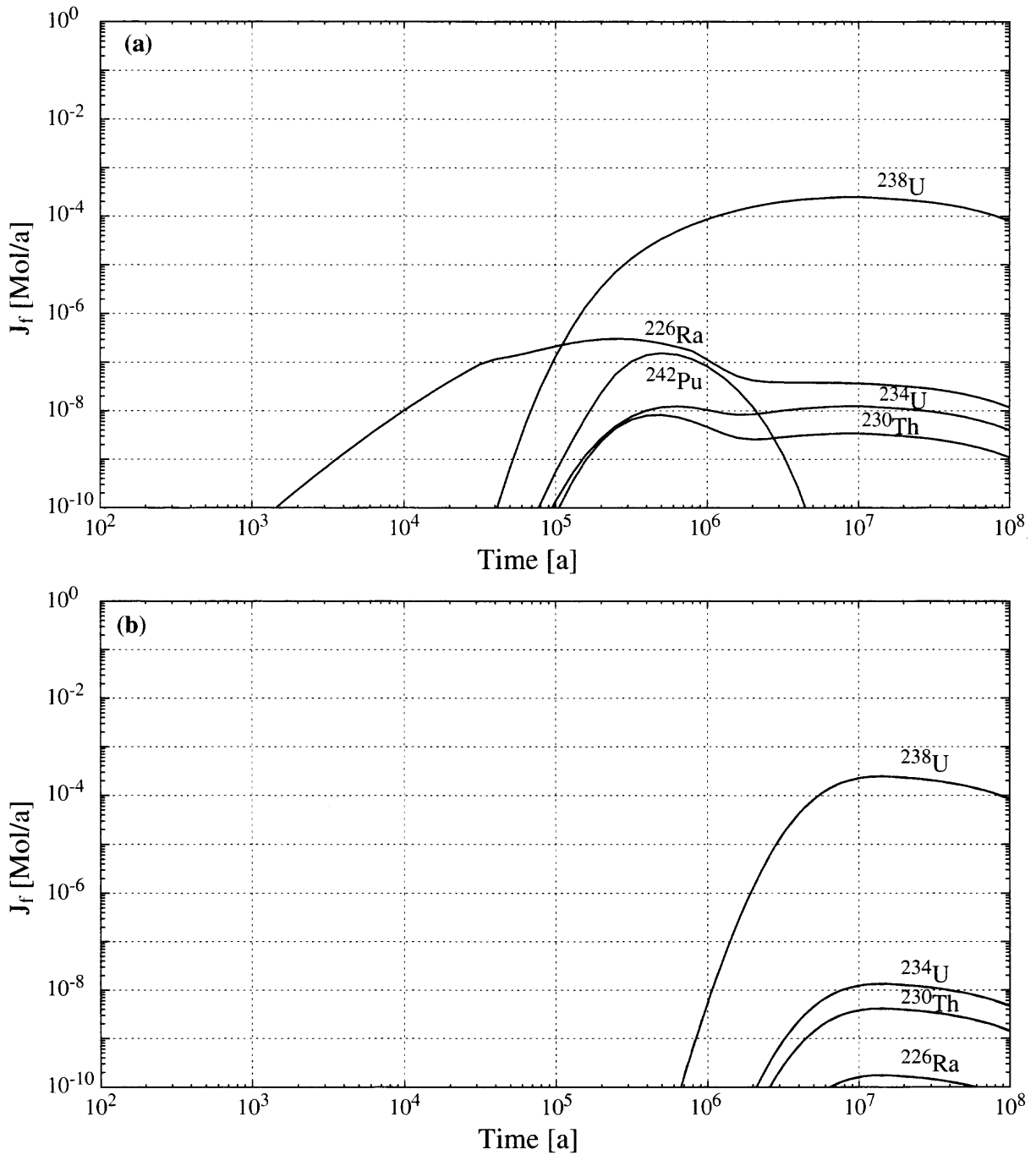


Figure 4.31. Nuclide release rates, (a) from the near-field source and (b) from the geosphere of the 4N+2 nuclide chain, presented on a double-logarithmic scale. Considered is the Kristallin-I reference case with the planar Geometry 6. In (b) PICNIC calculations (solid lines) and RANCHMD calculations (dashed lines) are shown for comparison. Because of the excellent agreement between PICNIC and RANCHMD calculations, the dashed lines are invisible in the area presented.

nuclide	$T_{1/2}$ [a]	maximum of J_f [mol / a]			time [a] of maximum		
		PICNIC	RANCHMD	diff.(P,R) [%]	PICNIC	RANCHMD	diff.(P,R) [%]
^{246}Cm	4.753E+03						
^{242}Pu	3.73E+05	5.700E-14	5.892E-14	-3.26	4.084E+06	3.831E+06	6.60
^{238}U	4.468e+09	2.443E-04	2.419E-04	0.99	1.377E+07	1.377E+07	
^{234}U	2.455E+05	1.342E-08	1.329E-08	0.98	1.377E+07	1.377E+07	
^{230}Th	7.538E+04	4.122E-09	4.082E-09	0.98	1.377E+07	1.377E+07	
^{226}Ra	1.6E+03	1.750E-10	1.733E-10	0.98	1.377E+07	1.377E+07	

Table 4.11. Comparison of maximum release rate and time of maximum release for the 4N+2 radionuclide decay chain as calculated by PICNIC and RANCHMD for the Kristallin-I reference case with Geometry 6. The first and second columns specify the decay chain members and their corresponding half-life. The maximum release rate and the time of that maximum as calculated by PICNIC are given in columns 3 and 6 respectively. The corresponding results from RANCHMD are given in columns 4 and 7 respectively. Columns 5 and 8 present the relative differences between the results of the two calculations. A breakthrough of ^{246}Cm is not seen, because it has a half-life that is small compared to its transport time. The very low maximum release of ^{242}Pu (roughly seven orders of magnitude smaller than the source) is due to its short half-life.

time	^{238}U			^{234}U		
	PICNIC	RANCHMD	diff.(P,R) [%]	PICNIC	RANCHMD	diff.(P,R) [%]
1.000e+05	0.0000E+00	4.178E-22	-100	4.5387E-27	4.383E-25	≈ -100
2.021e+05	1.0736E-18	5.959E-17	≈ -100	3.0125E-20	4.692E-20	-35.79
2.966e+05	7.5132E-15	1.100E-14	-31.70	5.0444E-18	6.701E-18	-24.72
4.948e+05	3.9788E-12	4.543E-12	-12.42	1.4434E-15	1.670E-15	-13.57
1.000e+06	5.1358E-09	5.266E-09	-2.47	6.5214E-13	6.743E-13	-3.29
2.021e+06	1.3388E-06	1.319E-06	1.50	7.8713E-11	7.758E-11	1.46
2.966e+06	1.1857E-05	1.165E-05	1.78	6.5424E-10	6.430E-10	1.75
4.948e+06	7.9458E-05	7.846E-05	1.27	4.3652E-09	4.311E-09	1.26
1.000e+07	2.2347E-04	2.214E-04	0.93	1.2278E-08	1.217E-08	0.89
2.021e+07	2.3150E-04	2.290E-04	1.09	1.2720E-08	1.259E-08	1.03
2.966e+07	2.0557E-04	2.032E-04	1.17	1.1295E-08	1.117E-08	1.12
4.948e+07	1.6013E-04	1.579E-04	1.41	8.7985E-09	8.674E-09	1.44
1.000e+08	8.4767E-05	8.313E-05	1.97	4.6575E-09	4.567E-09	1.98

Table 4.12. Comparison between PICNIC and RANCHMD calculations of time-dependent output for ^{238}U and ^{234}U for the Kristallin-I reference case. In the first column, time is given and in the second and fifth columns the PICNIC results for ^{238}U and ^{234}U , respectively. In the third and sixth columns the RANCHMD results are presented. The fourth and seventh columns give the relative differences of PICNIC and RANCHMD results.

4.4.3. Single Nuclides in a Small Network of Planar Channels

In this section we consider a modification of the Kristallin-I reference case for **single nuclides** discussed in section 4.4.1. The nuclides are assumed to be transported in a small **network** consisting of six legs, as shown in Figure 4.32, to test the network capabilities of PICNIC. This network has been considered earlier, see Schneider et al. [1996]. The network represents the following conceptual model: The repository area is intersected by three different types of water-conducting feature (wcf). After 100 m transport distance, these join to one larger structure regarded as a “mixing tank”. From here transport continues through three types of wcf to the highly conducting feature (*hcf*) which is assumed to have a shortcut to the biosphere. The overall transport length is 200m and the hydraulic head difference is 4m, the same as in the reference case of Kristallin-I. The properties of the rock matrix are also the same. However the three types of wcf differ in their hydraulic conductivity, resulting in a different Darcy velocity for each type. Type 1, represented by leg 1 and leg 4, is assumed to have a Darcy velocity, q_1 and q_4 respectively, which is equal to the Darcy velocity q_r in the reference case. The Darcy velocities of type 2 (leg 2 and leg 5) and type 3 (leg 3 and leg 6) are ten and one hundred times larger, respectively, $q_2 = q_5 = 10q_r$ and $q_3 = q_6 = 100q_r$. Water-conducting features of type 1 govern flow in 50% of the cross-sectional area of the host rock. Type 2 features govern 47% and the remaining 3% of the section is governed by type 3.

The nuclide flow rate at the mixing tank is given as the sum of the nuclide releases of leg 1, leg 2 and leg 3. From the mixing tank, the nuclides are distributed to leg 4, leg 5 and leg 6 in proportion to the water flow rate in each leg. The water flow rate is given as product of Darcy velocity and cross-sectional area, i.e. $Q_4 = 0.5Q_r$, $Q_5 = 4.7Q_r$ and $Q_6 = 3.0Q_r$, with Q_r being the water flow rate in the reference case. Thus, $0.5/8.2$ of the nuclides follow leg 4 between the mixing tank at junction 4 and the *hcf* at junction 5, $4.7/8.2$ follow leg 5, and $3.0/8.2$ follow the fast leg 6, even though this represents only 3% of the cross-sectional area. This can be regarded as a simple example of channeling. The release to the *hcf* at the end of the network is the sum of the releases of leg 4, leg 5 and leg 6.

The nuclide release from the repository is calculated using the near-field model STRENG [Grindrod et al., 1990] and is read by PICNIC from source files. The nuclide release from the repository near-field into the geosphere depends on the water flow rate at the interface of near-field and geosphere; thus the three different sources (S_1 at junction 1, S_2 at junction 2, and S_3 at junction 3) given in Figure 4.33 had to be calculated. The total inventory of the repository is allocated to the three sources according to their relative cross-sectional area. For a more detailed discussion see Nagra [1994]. It is assumed that the dispersion length of every leg in the network is the same as in the reference case considered in section 4.3.1, i.e. $a_L = 20\text{m}$. Hence the Peclet number is $Pe = 5$. The boundary condition for outflow at the mixing tank is chosen as zero-gradient (equation 2.51a) for the purpose of better comparison between PICNIC and RANCHMD calculations. Schneider et al. [1996] used the at-infinity boundary condition (equation 2.51c), which cannot be applied exactly in RANCHMD calculations. At the end of the network the presence of a *hcf* is assumed. Thus, the outflow boundary condition is zero-concentration (equation 2.51b), as in the reference case.

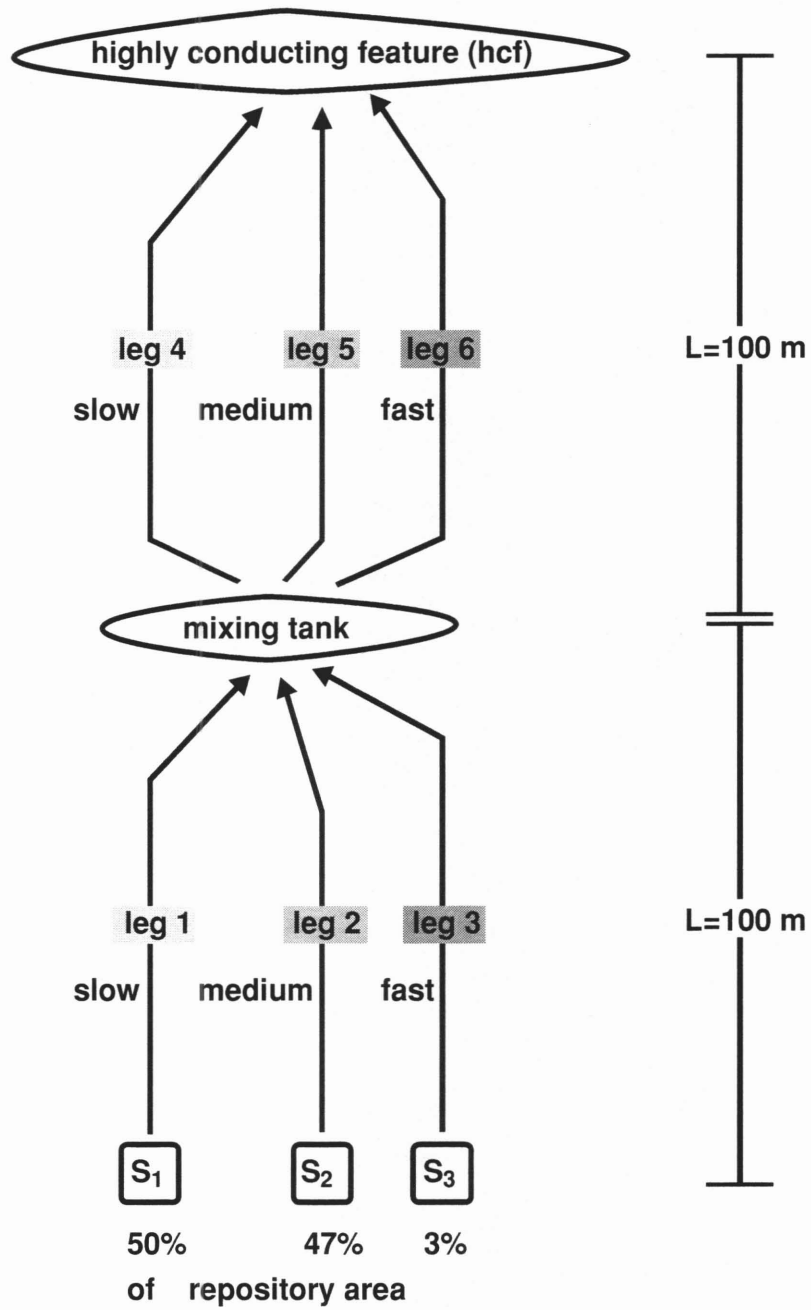


Figure 4.32. Small six-leg network, as described in detail in the text.

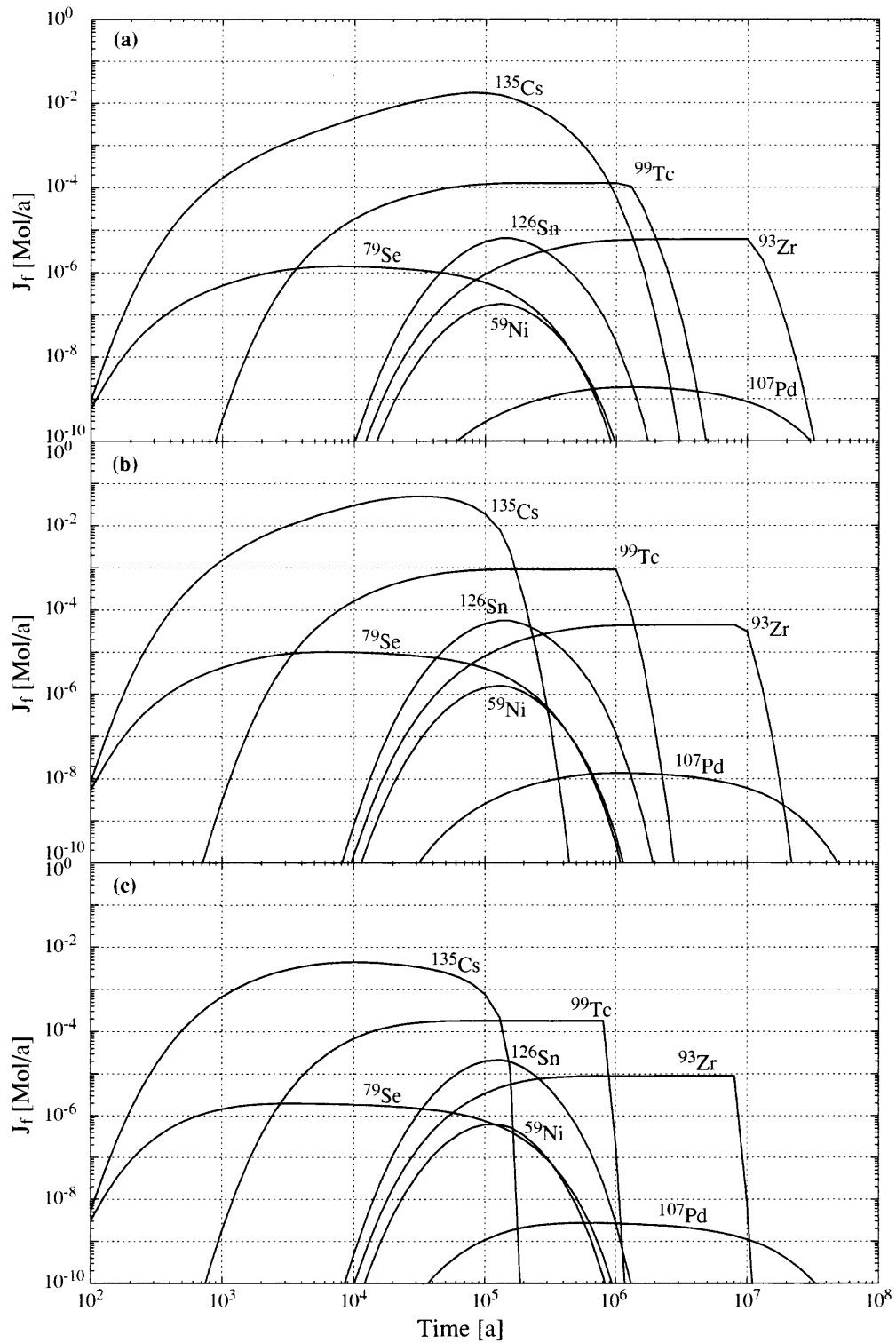


Figure 4.33. Near-field release sources of the network of Figure 4.32 for different radionuclides. (a) Source S_1 of leg 1 at junction 1, (b) source S_2 of leg 2 at junction 2, and (c) source S_3 of leg 3 at junction 3. The total inventory of the repository is allocated to the three sources according to their relative cross-sectional area: 50% is allocated to S_1 , 47% to S_2 , and the remaining 3% to S_3 .

Transport in this network can also be evaluated by performing a separate RANCHMD calculation for each leg. The superimposed result is called “assembled RANCHMD”. The PICNIC results (solid lines in Figure 4.34) and the “assembled RANCHMD” results (dashed lines in Figure 4.34) are in very good agreement. Table 4.13 presents the maximum release rate of each nuclide, and the corresponding time of maximum, (a) at the inflow to the mixing tank, and (b) at the release to the *hcf* for both the PICNIC and the “assembled RANCHMD” calculations. At the mixing tank the maximum release rate values show very good agreement, as do most of the calculated times of maximum release rate. For the two nuclides ^{135}Cs and ^{126}Sn , PICNIC predicts a time of maximum some 6% greater than that given by RANCHMD. However, this difference is not much more than the time increment of the printout and the actual difference could therefore be somewhat smaller. The largest difference in the maximum release rate calculated by the two methods is 0.6% for ^{126}Sn . The details of the release curve for ^{135}Cs presented in Table 4.14a (left hand side) show very good agreement on the rising edge, with a maximum difference in the order of 15% even five orders of magnitude below the maximum. On the trailing edge the differences are much larger when the release rate has fallen two decades below the maximum, at some 20 times the time of the release maximum. This could be due to the very fast decrease of the source at leg 2 (see Figure 4.33b) and leg 3 (see Figure 4.33c) after about $10^5[\text{a}]$. The behaviour of ^{99}Tc (left hand side of Table 4.14b) is similar to that of ^{135}Cs .

At the outflow into the *hcf*, the predicted times of maximum release rate for both calculation methods are generally in good agreement, see Table 4.13b. For ^{93}Zr , however, PICNIC calculates a maximum some 12% earlier than that of the assembled RANCHMD calculations. This difference can be attributed to the form of the release curve for this nuclide, which appears to attain a stationary condition after some $2 \cdot 10^6[\text{a}]$, thus making the identification of the time of maximum somewhat arbitrary. The values for maximum release rate differ by only small amounts in the range 0.3% (for ^{79}Se and ^{93}Zr) to 1.3% (for ^{59}Ni). The time-dependence of ^{135}Cs (right hand side of Table 4.14a) shows similar behaviour as at the mixing tank (left hand side of Table 4.14a). The same holds for ^{99}Tc (right hand side of Table 4.14b).

(a) mixing tank	maximum of J_f [mol / a]			time [a] of maximum		
nuclide	PICNIC	assembled RANCHMD	diff.(P,R) [%]	PICNIC	assembled RANCHMD	diff.(P,R) [%]
¹³⁵ Cs	5.084E-02	5.082E-02	< 0.05	4.642E+04	4.364E+04	6.37
¹²⁶ Sn	3.660E-05	3.637E-05	0.63	1.778E+05	1.669E+05	6.53
¹⁰⁷ Pd	1.696E-08	1.695E-08		1.468E+06	1.468E+06	
⁹⁹ Tc	8.228E-04	8.230E-04	< 0.05	7.743E+05	7.744E+05	
⁹³ Zr	5.068E-05	5.068E-05		7.263E+06	7.263E+06	
⁷⁹ Se	1.162E-05	1.162E-05		1.136E+04	1.146E+04	-0.87
⁵⁹ Ni	9.641E-07	9.633E-07	0.08	1.565E+05	1.566E+05	

(b) <i>hcf</i>	maximum of J_f [mol / a]			time [a] of maximum		
nuclide	PICNIC	assembled RANCHMD	diff.(P,R) [%]	PICNIC	assembled RANCHMD	diff.(P,R) [%]
¹³⁵ Cs	4.711E-02	4.690E-02	0.45	5.275E+04	5.285E+04	-0.19
¹²⁶ Sn	2.214E-05	2.190E-05	1.10	2.154E+05	2.155E+05	
¹⁰⁷ Pd	1.650E-08	1.644E-08	0.36	1.668E+06	1.668E+06	
⁹⁹ Tc	6.492E-04	6.473E-04	0.29	7.743E+05	7.744E+05	
⁹³ Zr	4.642E-05	4.629E-05	0.28	6.813E+06	7.743E+06	-12.0
⁷⁹ Se	1.084E-05	1.081E-05	0.28	1.468E+04	1.478E+04	-0.68
⁵⁹ Ni	5.398E-07	5.331E-07	1.26	1.896E+05	1.897E+05	

Table 4.13. Comparison of maxima and time of maxima of PICNIC and assembled RANCHMD output for the network of Figure 4.32 for single nuclides (a) at the mixing tank and (b) at the highly conducting feature (*hcf*). The first and second columns specify the nuclides and their corresponding half-life. The maximum release rate and the time of that maximum as calculated by PICNIC are given in columns 3 and 6 respectively. The corresponding assembled RANCHMD results are given in columns 4 and 7 respectively. Columns 5 and 8 present the relative differences between the results of the two calculations. Columns 5 of Tables 4.9 and 4.13 can also be found as a chart in Figure 4.35.

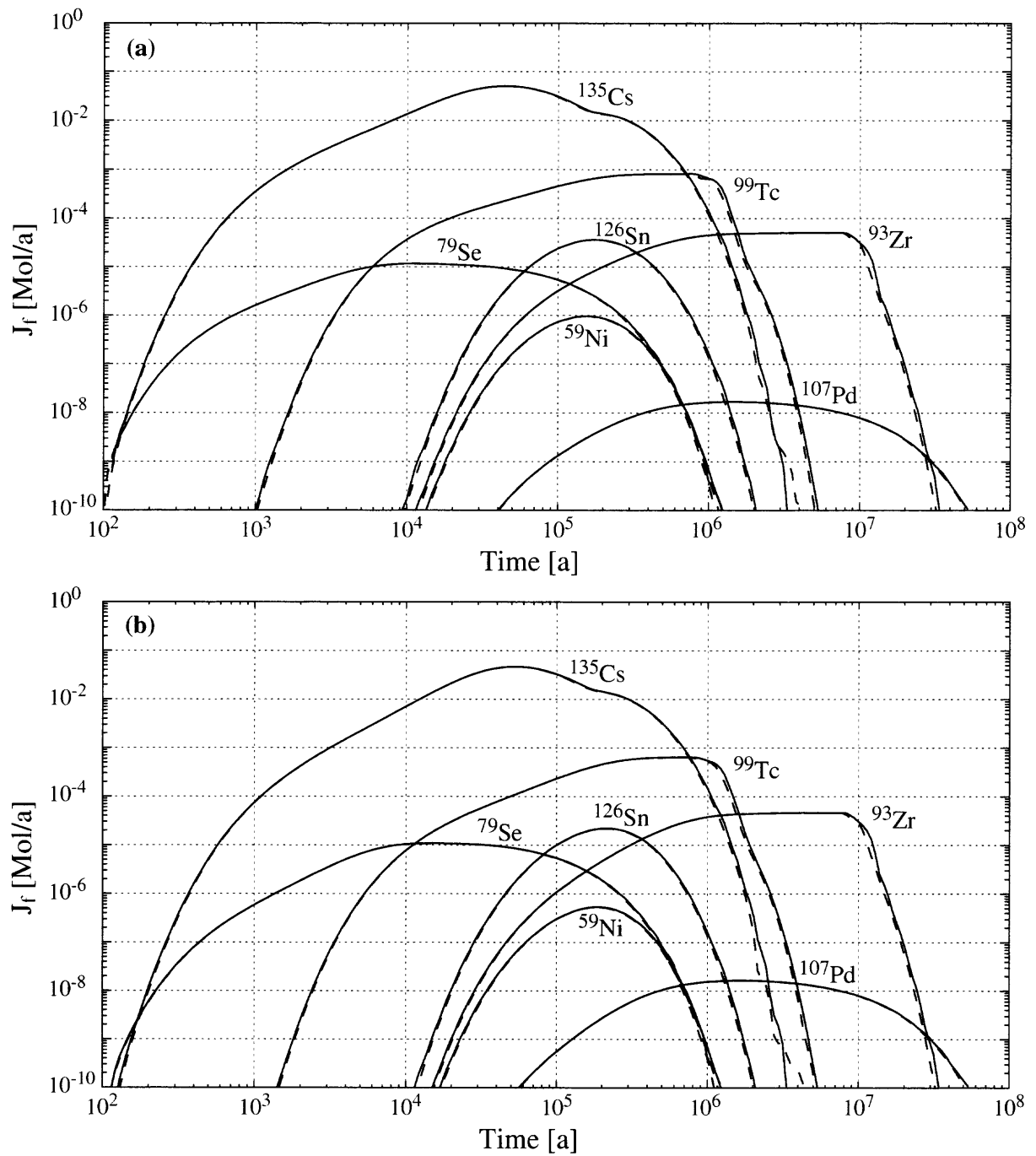


Figure 4.34. Release curves (a) at the mixing tank and (b) at the outlet to the highly conducting feature (*hcf*), presented on a double-logarithmic scale. The transport of single nuclides in the network of Figure 4.32 is considered. PICNIC calculations (solid lines) and assembled RANCHMD calculations (dashed lines) are shown for comparison.

Relative differences of maximal release rates between PICNIC and RANCHMD calculations

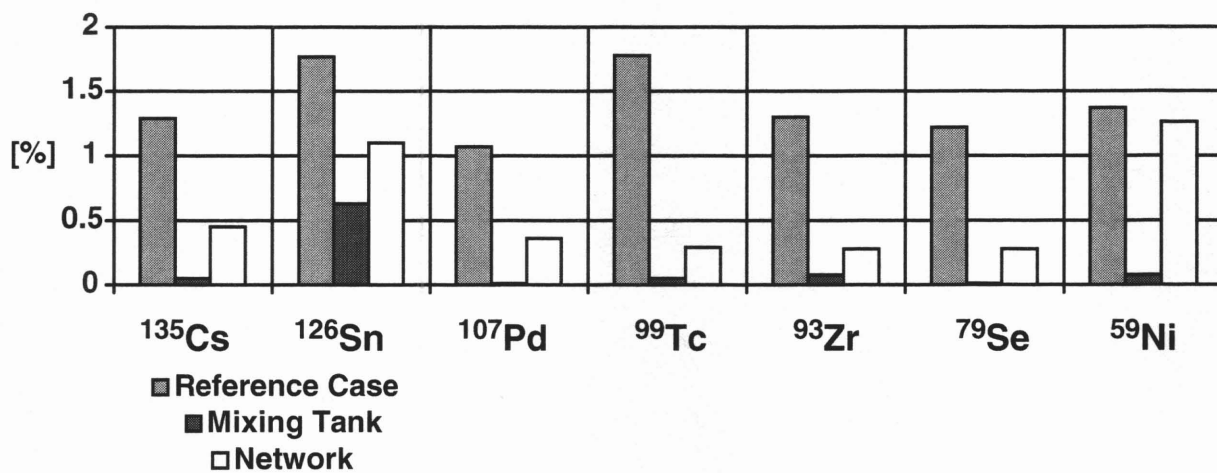


Figure 4.35. Relative differences in maximum release rates between PICNIC and RANCHMD calculations for the Kristallin-I reference case from column 5 in Table 4.9 and for the mixing tank and the network from column 5 in Table 4.13 for different nuclides.

(a) ¹³⁵ Cs	mixing tank			hcf		
	time [a]	PICNIC	assembled RANCHMD	diff.(P,R) [%]	PICNIC	assembled RANCHMD
1.000e+02	0.0000E+00			0.0000E+00		
2.021e+02	2.0335E-07	1.811E-7	12.29	1.2637E-08	1.047E-8	20.70
2.966e+02	2.8399E-06	2.537E-6	11.94	2.5207E-07	2.238E-7	12.63
4.948e+02	3.5784E-05	3.454E-5	3.60	4.9459E-06	4.701E-6	5.21
1.000e+03	3.5729E-04	3.541E-4	0.90	7.5330E-05	7.411E-5	1.65
2.021e+03	1.5048E-03	1.502E-3	0.19	4.3235E-04	4.296E-4	0.65
2.966e+03	2.6983E-03	2.699E-3	-0.03	8.9959E-04	8.963E-4	0.37
4.948e+03	5.3975E-03	5.403E-3	-0.10	2.1717E-03	2.166E-3	0.26
1.000e+04	1.3706E-02	1.390E-2	-1.40	7.1240E-03	7.107E-3	0.24
2.021e+04	3.2571E-02	3.262E-2	-0.15	2.2088E-02	2.204E-2	0.22
2.966e+04	4.4686E-02	4.473E-2	-0.10	3.5204E-02	3.513E-2	0.20
4.948e+04	5.0539E-02	5.048E-2	0.12	4.6929E-02	4.675E-2	0.39
1.000e+05	3.1062E-02	3.051E-02	1.81	3.2905E-02	3.227E-02	1.97
2.021e+05	1.3728E-02	1.349E-02	1.77	1.4511E-02	1.414E-02	2.62
2.966e+05	9.7880E-03	9.676E-03	1.16	1.0261E-02	1.011E-02	1.49
4.948e+05	3.1299E-03	3.016E-03	3.78	3.3539E-03	3.227E-03	3.93
1.000e+06	1.3969E-04	1.173E-04	19.09	1.4976E-04	1.259E-04	18.95
2.021e+06	3.2205E-07	1.470E-07	> 100	3.4969E-07	1.592E-07	> 100
2.966e+06	1.8258E-09	1.991E-09	-8.30	1.8764E-09	8.304E-10	> 100
4.948e+06	3.8615E-14	8.080E-12	≈ -100	4.0962E-14	2.369E-12	≈ -100
1.000e+07	1.6147E-14	3.082E-18	> 100	1.6647E-14	2.427E-18	> 100

(b) ⁹⁹ Tc	mixing tank			hcf		
	time	PICNIC	assembled RANCHMD	diff.(P,R) [%]	PICNIC	assembled RANCHMD
2.966e+02	1.2584E-17	5.737E-18	> 100	2.2670E-20	3.734E-20	-39.28
4.948e+02	1.2584E-17	1.091E-14	≈ -100	1.0878E-16	6.535E-17	66.46
1.000e+03	9.7347E-11	7.297E-11	33.41	1.9913E-12	1.429E-12	9.35
2.021e+03	4.9778E-08	4.412E-8	12.82	2.7188E-09	2.327E-9	16.85
2.966e+03	5.6541E-07	5.160E-7	9.57	4.6572E-08	4.262E-8	9.27
4.948e+03	5.4719E-06	5.330E-6	2.66	7.2777E-07	7.011E-7	3.804
1.000e+04	3.7014E-05	3.686E-5	0.42	7.7405E-06	7.663E-6	1.01
2.021e+04	1.0718E-04	1.072E-4		3.0874E-05	3.075E-5	0.40
2.966e+04	1.5910E-04	1.593E-4	-0.12	5.3168E-05	5.303E-5	0.26
4.948e+04	2.5191E-04	2.521E-4	-0.08	1.0085E-04	1.006E-4	0.25
1.000e+05	4.5813E-04	4.590E-04	-0.20	2.3399E-04	2.337E-04	0.12
2.021e+05	7.0832E-04	7.091E-04	-0.11	4.6410E-04	4.631E-04	0.22
2.966e+05	7.8685E-04	7.873E-04	-0.06	5.7488E-04	5.734E-04	0.26
4.948e+05	8.1780E-04	8.180E-04	-0.02	6.3851E-04	6.367E-04	0.28
1.000e+06	6.6009E-04	6.513E-04	1.34	5.5295E-04	5.245E-04	5.42
2.021e+06	5.7926E-06	4.753E-06	21.88	6.4459E-06	5.088E-06	26.69
2.966e+06	3.3515E-07	2.642E-07	26.85	3.3874E-07	2.656E-07	27.54
4.948e+06	3.6042E-10	1.606E-10	> 100	3.7184E-10	2.384E-10	55.97
1.000e+07	3.4106E-15	3.000E-30		2.6734E-15	4.823E-16	> 100
2.021e+07	1.1035E-27	3.000E-30		9.7506E-28	3.126E-30	

Table 4.14. Comparison between PICNIC and assembled RANCHMD calculations of time-dependence for (a) ¹³⁵Cs and (b) ⁹⁹Tc for the network of Figure 4.32. In the first column, time is given and in the second and fifth columns the PICNIC results at the mixing tank and the highly conducting feature are compiled. In the third and sixth columns the assembled RANCHMD results are presented. The fourth and seventh columns give the relative differences of PICNIC and assembled RANCHMD results. See also Figure 4.34.

4.4.4. INTRACOIN Chain Decay Test Case

In this section we deal with transport of a **nuclide decay chain in a single leg. Band-release** over 10^5 [a] of the chain ($^{245}\text{Cm} \rightarrow ^{237}\text{Np} \rightarrow ^{233}\text{U} \rightarrow$) into a channel of length $L=500$ [m] is considered. The inventory of the source at $t=0$, given in arbitrary particle units [*const.mol*], and the half-lives $T_{1/2}^{(i)} = \ln(2)/\lambda^{(i)}$ of the nuclides $i=1..3$ are presented in Table 4.15 together with the parameters of the flowpath. The nuclide sources $S_{in}^{(i)}(t) = \left(J_f^{(i)}\right)^{i=1..3} (z=0;t)$ are given in Figure 4.36a on a double-logarithmic scale. The inventory of the (on the timescale considered) slowly decaying daughter ^{237}Np is much larger than the inventory of the fast decaying parent ^{245}Cm and the grand-daughter ^{233}U . Thus, the source function of the daughter is nearly constant in time, while the source function of the parent considerably decreases and the source function of the grand-daughter shows ingrowth. It is checked that the band-release calculated by PICNIC agrees with the analytical solution calculated using the code Maple V [Abell and Braselton, 1994b]. The solution for the band-release source was first presented by Bateman [1908-1910], see also the calculation method by Hadermann [1980b].

(i)	1	2	3
nuclide	^{245}Cm	^{237}Np	^{233}U
$T_{1/2}^{(i)}$ [a]	$8.5 \cdot 10^3$	$2.14 \cdot 10^6$	$1.592 \cdot 10^5$
$\alpha^{(i)}$ [a]	$3 \cdot 10^4$	10^5	$3 \cdot 10^4$
$R_f^{(i)}$	60	200	60
inventory $N^{(i)}(t)$ at $t=0$	$8.5840 \cdot 10^3$	$3.0874 \cdot 10^6$	$9.1871 \cdot 10^2$
$J_f^{(i)}(z=0;t=10^5[\text{a}])$	$2.4970 \cdot 10^{-5}$	$2.9973 \cdot 10^1$	$8.0475 \cdot 10^{-1}$
$J_f^{(i)}(z=L;t_{\max}^{(i)})$	$4.694 \cdot 10^{-3}$	$2.404 \cdot 10^1$	1.322
$t_{\max}^{(i)}$ [a]	$2.547 \cdot 10^4$	$1.402 \cdot 10^5$	$1.120 \cdot 10^5$

Table 4.15. Parameters and results of transport of INTRACOIN test case of a nuclide decay chain. Release time for band-release is 10^5 [a]. Length of the channel is $L=500$ m and $Pe=10$. See also Figure 4.36.

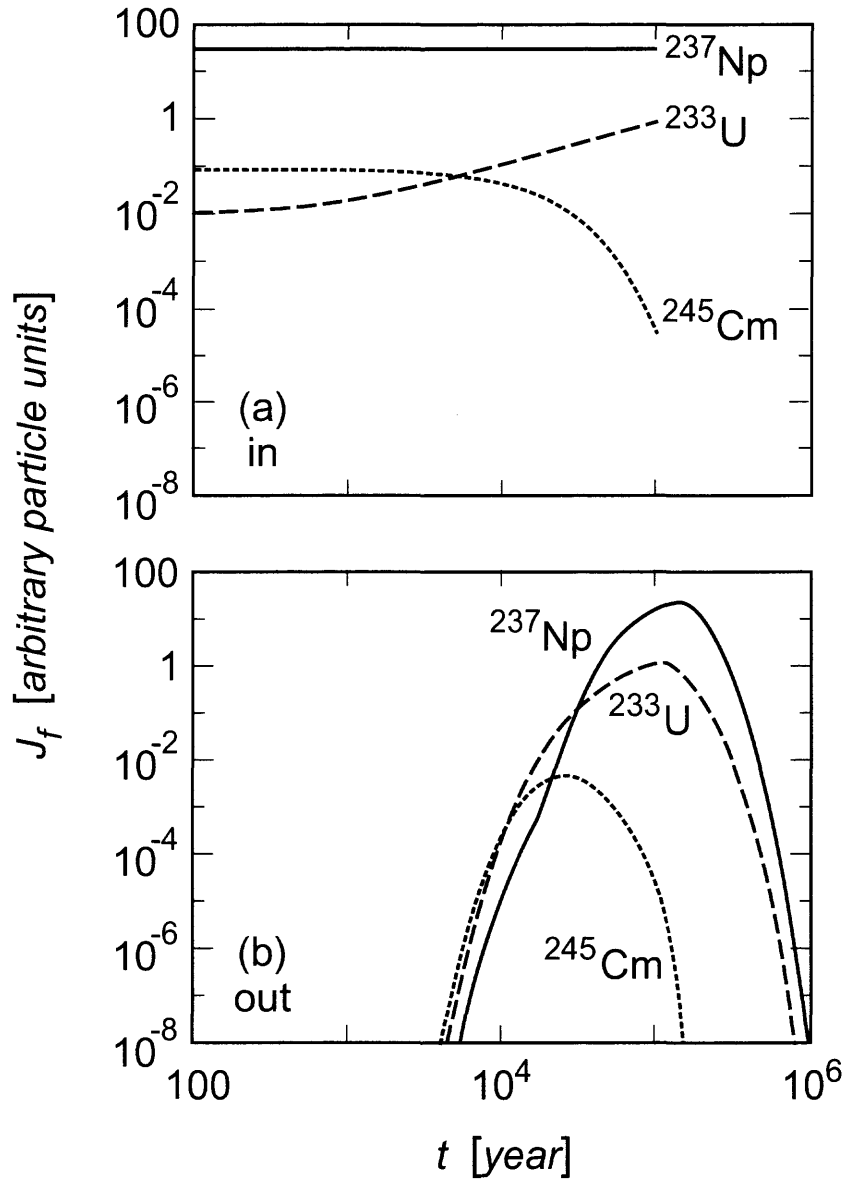


Figure 4.36. (a) Nuclide source and (b) breakthrough curves of the decay chain, $^{245}\text{Cm} \rightarrow ^{237}\text{Np} \rightarrow ^{233}\text{U} \rightarrow$, are presented on a double-logarithmic scale. For the parameters and the maxima of the breakthrough curves see Table 4.15.

No matrix diffusion is considered in the channel, so that the characteristic times for $\gamma^{(i)} = 0$ and $\beta^{(i)}$ are irrelevant. The behaviour in the channel is described by the advection times $\alpha^{(i)}$, the Peclet number Pe and the half-lives $T_{1/2}^{(i)}$ of the nuclides $i = 1..3$. The outflow boundary condition at-infinity (see equation 2.51c) is used. The breakthrough curves $\left(J_f^{(i)}\right)^{i=1..3}(z=L;t)$ are presented in Figure 4.36b. The transport behaviour of the daughter and the grand-daughter are almost independent of that of the parent, for similar reasons as discussed for the inflow position. Because the advection time of the daughter is larger than that of the parent and the grand-daughter, the

daughter ^{237}Np shows the latest breakthrough. The maximum of $J_f^{(i=2)}(z=L;t)$ of the daughter is decreased compared to $J_f^{(i=2)}(z=0;t=10^5[\text{a}])$, because of its decay and micro-dispersion, see Table 4.15. On the other hand, because of the decay of the daughter, the maximum of the grand-daughter breakthrough curve shows further ingrowth, when compared with the inflow at the end of the release-time, at $t=10^5[\text{a}]$.

This case considered is very similar to an INTRACOIN Level 1 benchmark that was also calculated with the codes RANCH and RANCHN (see Hadermann and Rösel [1983], especially Figure 1.4, Table 7.3 and Table 9.4)³⁸. The only differences from our case are the inflow boundary conditions. The band-release, given in Figure 4.36a, was assigned in this early INTRACOIN case only to the advective part $Q_f C_f^{(i)}(z=0;t)$ of the nuclide inflow

$$J_f^{(i)}(z=0;t) = Q_f \left[C_f^{(i)}(z=0;t) - \frac{L}{Pe} \partial_z C_f^{(i)}(z=0;t) \right].$$

For $Pe=10$ the advective contribution is the dominant part in the nuclide flow rate. Despite this difference in the inflow boundary conditions, the RANCHN, RANCH and the PICNIC results agree within the resolution of the printout given in Table 9.4 of Hadermann and Rösel [1983], or 0.1% relative difference, for the maxima of the breakthrough curves and the time $t_{\max}^{(i)}$ of the maxima. For $t_{\max}^{(i=1)}$, PICNIC agrees with RANCH, and both disagree with the RANCHN printout by 2.5%.

In a further test case we consider a variation of this INTRACOIN test case assuming a **simple-leaching** source. This source is described by the system of differential equations

$\partial_t N^{(i)}(t) = -[k^{(i)} + \lambda^{(i)}]N^{(i)}(t) + \lambda^{(i-1)}N^{(i-1)}(t)$ for the inventory of the source $N^{(i)}(t)$. The initial inventory $N^{(i)}(t=0)$ and the leach rates $k^{(i)}$ for all nuclides of the decay chain ($i=1\dots I$) are specified by the user of PICNIC and determine the source $S^{(i)}(t) = k^{(i)}N^{(i)}(t)$. This source is implemented in PICNIC as an analytical solution in the Laplace domain. For the selected leach rates $k^{(1)} = 10^{-4}[1/\text{a}]$, $k^{(2)} = 3 \cdot 10^{-5}[1/\text{a}]$, $k^{(3)} = 10^{-5}[1/\text{a}]$ and the parameters of Table 4.15, we have verified that the simple-leaching source $S^{(i)}(t)$ calculated by PICNIC agrees with the analytical solution calculated using the code Maple V [Abell and Braselton, 1994b].

4.5. Summary

As step I in the verification scheme, in this section, we have verified the capability of PICNIC to deal with a homogeneous planar rock matrix; see the detailed verification matrix in Table 4.16. Transport of a single nuclide in a single leg was evaluated and compared to RANCHMD calculations for a limited and an effectively unlimited rock matrix. The cross-comparison was extended to the code PAWorks/LTG and, for a quick check, to the GIMRT code. This was done using the parameters of the Grimsel dipole experiment with the tracer uranine. PAWorks/LTG, PICNIC and RANCHMD calculations showed a very good agreement with each other. GIMRT

³⁸ Note that Hadermann and Rösel [1983] use arbitrary activity units for the inventory and thus their breakthrough curves give $\lambda^{(i)} J_f^{(i)}(z=L;t)$ in units of $[const' \cdot \text{becquerel}/\text{a}]$ or $[const \cdot \text{mol}/\text{a}^2]$.

showed a very good agreement for late times, while there were differences for early times and in the maximum region. A numerical instability of PICNIC for high Peclet numbers was considered.³⁹ Parameter self-consistency checks supported the understanding of the transport processes involved and verified that PICNIC correctly reads the input parameters. A self-consistency test started the verification of the network feature in PICNIC. In technical tests the numerically implemented inverse Laplace transformation and the convolution with a time-dependent source were analysed for their numerical stability.

For a single nuclide and a nuclide decay chain in a single leg and in a 2-leg pathway, a cross-comparison with PAWorks/LTG was performed and showed a very good agreement. (Note that this cross-comparison will be extended in section 8 to more complicated rock matrices.) In this section the cross-comparison was extended to single nuclides and a nuclide decay chain in a 26-leg network. Thereby the capability of PICNIC to calculate the water flow rates from hydraulic conductivities of the legs and hydraulic heads at some junctions was verified. However, the comparison for the nuclide transport in the networks was regarded more as a qualitative test, because the leg outlet boundary conditions of PICNIC and PAWorks/LTG were slightly different at inner junctions of the network.

Test cases related to the Kristallin-I safety assessment were considered in a cross-comparison with RANCHMD. These were in a completely different parameter range to the cases above. Single nuclides and a nuclide decay chain in a single leg were considered with typical nuclide sources used in performance assessments. As a parameter variation, the transport of single nuclides in a small 6-leg pathway with multiple sources was considered. Results from a simulation of this case using PICNIC were compared to so-called “assembled RANCHMD” calculations which used the code RANCHMD in each leg and a different network technique. The excellent agreement between PICNIC and “assembled RANCHMD” results verified the network capability of PICNIC for single nuclides. Thereby the capability of PICNIC to calculate the flow of water from hydraulic conductivities of the legs and hydraulic heads at some junctions was verified quantitatively also in transport calculations. The network capability for nuclide decay chains is left to the verification step in the next section for a vein geometry. The capability to deal with the analytically implemented band-release source and the simple-leaching source was verified using an INTRACOIN test case.

These investigations have verified the capability of PICNIC to deal with planar fracture geometry. Using the considerations in section 3, this verification step I also serves as a basis for the verification of the other rock matrix geometries in the next steps.

³⁹ In the 1999 version of PICNIC, a small bug was eliminated which reduces some inaccuracies for high Peclet numbers. However, the instability for high Peclet numbers (which are outside the application range considered for PICNIC) appears to be inherent to Talbot’s method, which is actually implemented in PICNIC for inverse Laplace transformation.

single leg		(a) single nuclide			(b) nuclide decay chain		
planar rock matrix geometry		ZG	ZC	AI	ZG	ZC	AI
source in Laplace domain	δ -pulse	C ⁴⁰ ,K	K	K	C ⁴¹ ,K		
	simple-leaching	A			A ⁴²		
source in time domain	short pulse						
	long top-hat	S ⁴³	S	S	S ⁴⁴	S	S
	band-release			L ⁴⁵ ,A,K			
	general	C ⁴⁶	C ⁴⁷		C ⁴⁸	C ⁴⁹	

pathway		(c) single nuclide			(d) nuclide decay chain		
planar rock matrix geometry		ZG	ZC	AI	ZG	ZC	AI
source in Laplace domain	δ -pulse	C ⁵⁰			C ⁵¹		K
	simple-leaching						
source in time domain	short pulse			K			
	long top-hat						
	band-release						
	general			K			K

network		(e) single nuclide			(f) nuclide decay chain		
planar rock matrix geometry		ZG	ZC	AI	ZG	ZC	AI
source in Laplace domain	δ -pulse						K
	simple-leaching						
source in time domain	short pulse	K		K	K		K
	long top-hat	K		K	K		
	band-release						
	general	C ⁵²	C ⁵³	K	C ⁵⁴		K

Table 4.16. Performed test calculations for a planar fracture geometry using, in PICNIC, the analytically implemented solution for the rock matrix response. Note: All test cases represented by empty fields in the scheme were implicitly verified by any of the specified examples. Such a procedure is strongly based on the internal structure of PICNIC as outlined in more detail in section 3. Legend: A: analytical solution available; C: comparison with other computer code; K: consistency tests; L: check with information from the literature; S: steady-state solution checked.

⁴⁰ Comparison with PAWorks/LTG.

⁴¹ Comparison with PAWorks/LTG.

⁴² The nuclide flow rate at the source location is considered. Comparison with Maple V.

⁴³ Comparison with analytical result. The same for ZC and AI.

⁴⁴ Comparison with analytical result. Only a parent nuclide decaying into a non-decaying daughter nuclide which has the same properties as the parent nuclide are considered. The same for ZC and AI.

⁴⁵ Only advection and dispersion are considered and no matrix diffusion. The same for AI.

⁴⁶ Comparison with PAWorks/LTG and RANCHMD.

⁴⁷ Comparison with RANCHMD.

⁴⁸ Comparison with PAWorks/LTG and RANCHMD.

⁴⁹ Comparison with PAWorks/LTG and RANCHMD.

⁵⁰ Comparison with PAWorks/LTG.

⁵¹ Comparison with PAWorks/LTG.

⁵² Comparison with assembled RANCHMD and "qualitative" comparison with PAWorks/LTG.

⁵³ Comparison with assembled RANCHMD.

⁵⁴ "Qualitative" comparison with PAWorks/LTG.

5. Homogeneous Cylindrical Rock Matrix

In this section we consider the effect of matrix diffusion into a homogeneous cylindrical rock matrix geometry. This is step II of the verification of PICNIC; see section 3.4.2. The test cases presented in Barten, Niemeyer and Heer [1997] are reviewed. The only difference in the PICNIC flow scheme (Table 3.1) for the vein geometry with respect to the planar fracture geometry considered in section 4 is the calculation of $\bar{\eta}(s)$. Because the analytical solution for the rock matrix response $\bar{\eta}(s)$ is implemented in PICNIC also for this matrix geometry, it is mainly necessary to consider the transport of a **single nuclide and of a nuclide decay chain in a single leg**. As mentioned in section 4 it remains to consider the transport of a **nuclide decay chain in a network**. The parameter definition and the balance equations for the vein geometry are given in section 2.5.5.

We start in section 5.1 with (a) a **single nuclide in a single leg** considering a hypothetical variation of the Grimsel dipole parameters for uranine. The PICNIC results are compared to results from RANCHMD.

In section 5.2, test cases related to the Kristallin-I performance assessment are considered for a **nuclide decay chain in a single vein and in a small network of veins**. For the single leg, the PICNIC results are compared to results from RANCHMD. For the network, a comparison with the so-called “assembled PICNIC” method is performed.

Section 5.3 gives a summary.

5.1. Variations of the Grimsel Dipole Experiment

In this subsection we start our verification of the vein case for matrix diffusion by testing the accuracy of PICNIC for a **single non-decaying nuclide in a single vein**. With this aim, PICNIC results are compared with results from RANCHMD.

For the planar fracture geometry with matrix diffusion, the first quantitative comparison (section 4.1) of PICNIC and RANCHMD calculations was based on data from the Grimsel migration experiment with the tracers uranine and strontium [Heer and Hadermann, 1994; Hadermann and Heer, 1996]. This had the advantage that the reference code RANCHMD was applied in a parameter range where the code has been used to model experiments. For the first test of the vein geometry, now the same data as in the dipole experiment in the Grimsel rock laboratory with the non-sorbing tracer uranine are used. However, a geologically reasonable vein radius of $R = 0.001[\text{m}]$ has to be applied, see p. 240 of Nagra [1994]. This leads to a considerably smaller surface to volume ratio of the water-conducting feature than in the fracture geometry of Grimsel. In order to achieve a well structured breakthrough curve (peak, tail, tail end perturbation) for this vein radius and, in addition, a substantial geometric effect of the vein geometry, the Darcy velocity was reduced to $q_f = 78.25[\text{m/a}]$ and the penetration depth was selected as $d = 0.017466[\text{m}]$. The Darcy velocity is equal to the actual water velocity, because no infill within the water-conducting feature is considered. Zero-gradient (see equation 2.51a) is used as the outflow boundary condition, as for the fracture geometry case. The calculations assume a top-hat injection over $200[\text{minutes}] = 3.80258 \cdot 10^{-4}[\text{a}]$ to test the capability of the code for a short-duration nuclide injection. For the RANCHMD calculations, an inventory of the source of $1[\text{mol}]$ and flow through

a cross-sectional area of $1\text{[m}^2\text{]}$ were assumed. RANCHMD provides $J_f(t)/Q_f$ in units of $[\text{mol}/\text{m}^3]$ as output. See Heer and Hadermann [1997] for a more detailed discussion of nuclide flow and rock matrix diffusion in a vein and the comparison to the fracture case. PICNIC provides $J(t)$ in units of $[\text{mol}/\text{a}]$ as output.

The inventory of the source is entered in the PICNIC input file for a direct comparison of J_f/Q_f with the RANCHMD result. The left hand side of Table 5.1 and Figure 5.1 show the calculated breakthrough curves and relative differences of PICNIC and RANCHMD results. The maximum of the breakthrough curve is about 2% earlier and 0.23% smaller for the PICNIC calculation compared to the RANCHMD calculation. In the rising and trailing edges of the breakthrough curve the values of the PICNIC calculations are several percent smaller than the values of the RANCHMD calculations.

To test the asymptotic behaviour of the tail for effectively unlimited matrix diffusion (case pv02), we increase the penetration depth to $d = 1.699\text{[m]}$. The maximum of the breakthrough curve is again about 2% earlier and 0.39% smaller for the PICNIC calculation compared to the RANCHMD calculation. See the right hand side of Table 5.1 and Figure 5.1 for the breakthrough curves and relative differences of PICNIC and RANCHMD results. In the rising edge of the breakthrough curve, the values of the PICNIC calculations are several percent smaller than the values of the RANCHMD calculations. In the trailing edge of the breakthrough curve the RANCHMD calculation shows up to 1% smaller values than, the RANCHMD calculations, as long as the system behaves as if matrix diffusion were unlimited. PICNIC responds to the finite matrix thickness slightly earlier than RANCHMD.

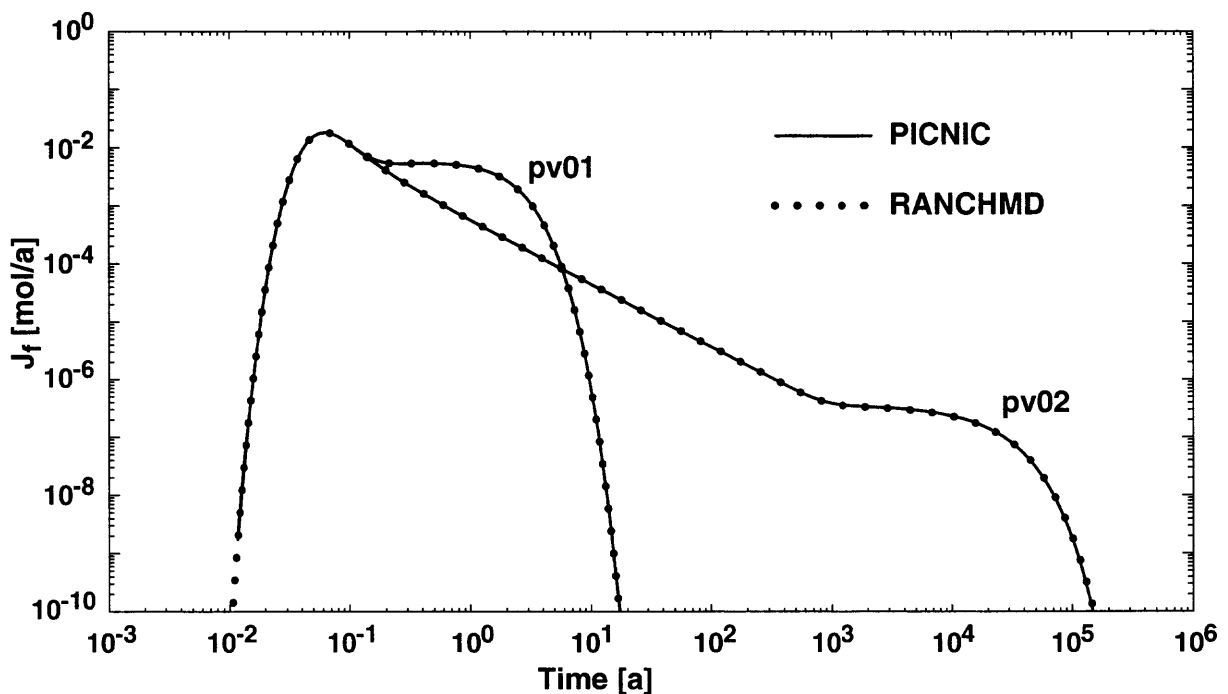


Figure 5.1. Breakthrough curve for uranium in a vein with limited rock matrix (pv01) and effectively unlimited rock matrix (pv02) in a double-logarithmic scale. PICNIC calculations (solid lines) are compared to RANCHMD calculations (dots).

These first quantitative tests for the vein case show excellent agreement between PICNIC and the verified code RANCHMD, (Table 5.1). This positive result has also been observed for the fracture case with matrix diffusion, see section 4.1.1. There, the differences between PICNIC calculations and (higher resolution) RANCHMD calculations were slightly smaller than in the present case.

time [a]	pv01		pv02	
	J_f / Q_f [mol / m ³]	difference [%], $100 \frac{P-R}{R}$	J_f / Q_f [mol / m ³]	difference [%], $100 \frac{P-R}{R}$
1.0e-2	0.0		0.0	
2.0e-2	3.6156E-05	-3.17	3.6157E-05	-3.19
3.0e-2	1.9926E-03	-0.96	1.9927E-03	-1.06
5.0e-2	1.5491E-02	-0.32	1.5491E-02	-0.44
1.0e-1	1.1491E-02	0.01	1.1460E-02	-0.26
2.0e-1	5.5144E-03	0.26	4.0284E-03	-0.36
3.0e-1	5.3083E-03	0.25	2.3548E-03	-0.43
5.0e-1	5.3091E-03	0.25	1.2606E-03	-0.51
1.0	4.6960E-03	0.17	5.6629E-04	-0.55
2.0	2.7064E-03	-0.10	2.6124E-04	-0.63
3.0	1.2538E-03	-0.41	1.6720E-04	-0.65
5.0	1.9159E-04	-1.04	9.5616E-05	-0.71
1.0e+1	7.0162E-07	-2.74	4.4944E-05	-0.79
2.0e+1	0(1.E-11)		2.1173E-05	-0.88
3.0e+1			1.3642E-05	-0.86
5.0e+1			7.8444E-06	-0.92
1.0e+2			3.7036E-06	-1.00
2.0e+2			1.7498E-06	-0.97
3.0e+2			1.1293E-06	-0.50
5.0e+2			6.5598E-07	0.84
1.0e+3			3.8424E-07	1.84
2.0e+3			3.3534E-07	2.18
3.0e+3			3.2033E-07	2.11
5.0e+3			2.9279E-07	1.95
1.0e+4			2.3254E-07	1.46
2.0e+4			1.4367E-07	0.47
3.0e+4			8.6828E-08	-0.60
5.0e+4			3.0183E-08	-2.85
1.0e+5			1.7840E-09	-8.89
2.0e+5			<O(1.E-11)	
maximum of J_f / Q_f [mol / m ³]	1.8098E-02	-0.23	1.8099E-02	-0.39
t_{\max} [a]	6.33E-02	≈ 2 (for typeout)	6.33E-02	≈ 2 (for typeout)

Table 5.1. Comparison of PICNIC and RANCHMD calculations. In the first column, time is given and in the second and fourth columns the PICNIC results for J_f / Q_f of case pv01 and pv02, respectively. In the third and sixth columns the relative differences of the PICNIC results (P) from the RANCHMD results (R) are presented, i.e. $100*(P-R)/R$. The two bottom rows give the maximum value and the time of the maximum, t_{\max} , of the breakthrough curves.

5.2. Cases Related to Performance Assessment

In this subsection we continue with tests related to the Kristallin-I performance assessment for a **nuclide decay chain**. We consider first a **single vein** and then a **small network of veins with multiple sources**.

5.2.1. Single Vein

We consider the Kristallin-I reference case for the 4N+2 decay chain $^{246}\text{Cm} \rightarrow ^{242}\text{Pu} \rightarrow ^{238}\text{U} \rightarrow ^{234}\text{U} \rightarrow ^{230}\text{Th} \rightarrow ^{226}\text{Ra} \rightarrow \dots \rightarrow ^{206}\text{Pb}$. The geometry is a vein geometry as described in Nagra [1994], Figure 5.3.5 and Tables 5.3.1 to 5.3.3, and designated there as Geometry 4. To achieve more pronounced release curves (by a factor of one hundred), we reduced the transport length (to $L=2$ m) and the hydraulic head difference. The release from the near-field was calculated by the near-field model STRENG [Grindrod et al., 1990]. It is the same as for the fracture case with matrix diffusion shown in Figure 4.29a. The release curves are presented in Figure 5.2 as solid lines and the respective RANCHMD calculations (dots) are shown for comparison. For the RANCHMD calculations the level of discretisation was that normally used in the Kristallin-I safety assessments,⁵⁵ the same as in the fracture case. As for the decay chain in the fracture geometry a qualitatively and quantitatively good agreement is found for all nuclides.

The excellent agreement between the two codes for the time of maximum release for all chain members except ^{246}Cm and ^{242}Pu can be clearly seen in Table 5.2. The difference of about 6.5% noted for these two nuclides is approximately the same magnitude as the selected resolution of the printout. We chose the output resolution normally used in the Kristallin-I safety assessments, here 36 output times per decade. At the same time, these nuclides show the largest difference in the maximum release rate predicted by the two programs, about 3.5% as compared with less than 1% for the other members of the decay chain. However, the maxima of these nuclides are so small that they do not even appear in Figure 5.2. The relatively short half-life values (column 2 in Table 5.2), in comparison to the time to maximum release (columns 6 and 7), for the decay products of ^{238}U mean that these nuclides are released in secular equilibrium with their long-lived precursor. This indicates that such steady-state radioactive decay is correctly treated by PICNIC, also for veins.

Figure 5.3 and Table 5.3 present a detailed comparison of the release curves for ^{238}U and ^{234}U , those nuclides with the highest maximum release rates. The rising edge of the release curve for ^{238}U shows good agreement, within 20%, even at eight orders of magnitude below the maximum, while for ^{234}U the same level of agreement is seen from seven decades below the maximum. For the trailing edge, the agreement is within 2% for the period up to 10^8 [a], the end of the calculation time. This cut-off time is a factor of five greater than the time to maximum release and sufficient for safety assessment purposes.

⁵⁵ These are 40 grid points (exponentially spaced) in the rock matrix and 47 grid points in the water-conducting feature.

nuclide	$T_{1/2}$ [a]	maximum of J_f [mol / a]			time t_{\max} [a] of maximum,		
		PICNIC	RANCHMD	diff.(P,R) [%]	PICNIC	RANCHMD	diff.(P,R) [%]
^{246}Cm	4.753E+03	1.274E-22	1.234E-22	3.24	7.743E+04	7.273E+04	6.46
^{242}Pu	3.73E+05	3.631E-11	3.511E-11	3.42	1.066E+06	1.000E+06	6.6
^{238}U	4.468e+09	2.382E-04	2.361E-04	0.89	1.668E+07	1.668E+07	
^{234}U	2.455E+05	1.303E-08	1.297E-08	0.46	1.668E+07	1.668E+07	
^{230}Th	7.538E+04	3.995E-09	3.981E-09	0.35	1.668E+07	1.668E+07	
^{226}Ra	1.6E+03	1.696E-10	1.693E-10	0.18	1.668E+07	1.668E+07	

Table 5.2. Comparison of maximum release rate and time of maximum release for the 4N+2 radionuclide decay chain as calculated by PICNIC (P) and RANCHMD (R) for the Kristallin-I reference case with Geometry 4. The first and second columns specify the decay chain members and their corresponding half-life. The maximum release rate and the time of that maximum as calculated by PICNIC are given in columns 3 and 6, respectively. The corresponding results from RANCHMD are given in columns 4 and 7, respectively. Columns 5 and 8 present the relative differences between the results of the two calculations, i.e. $100 \cdot (P-R)/R$.

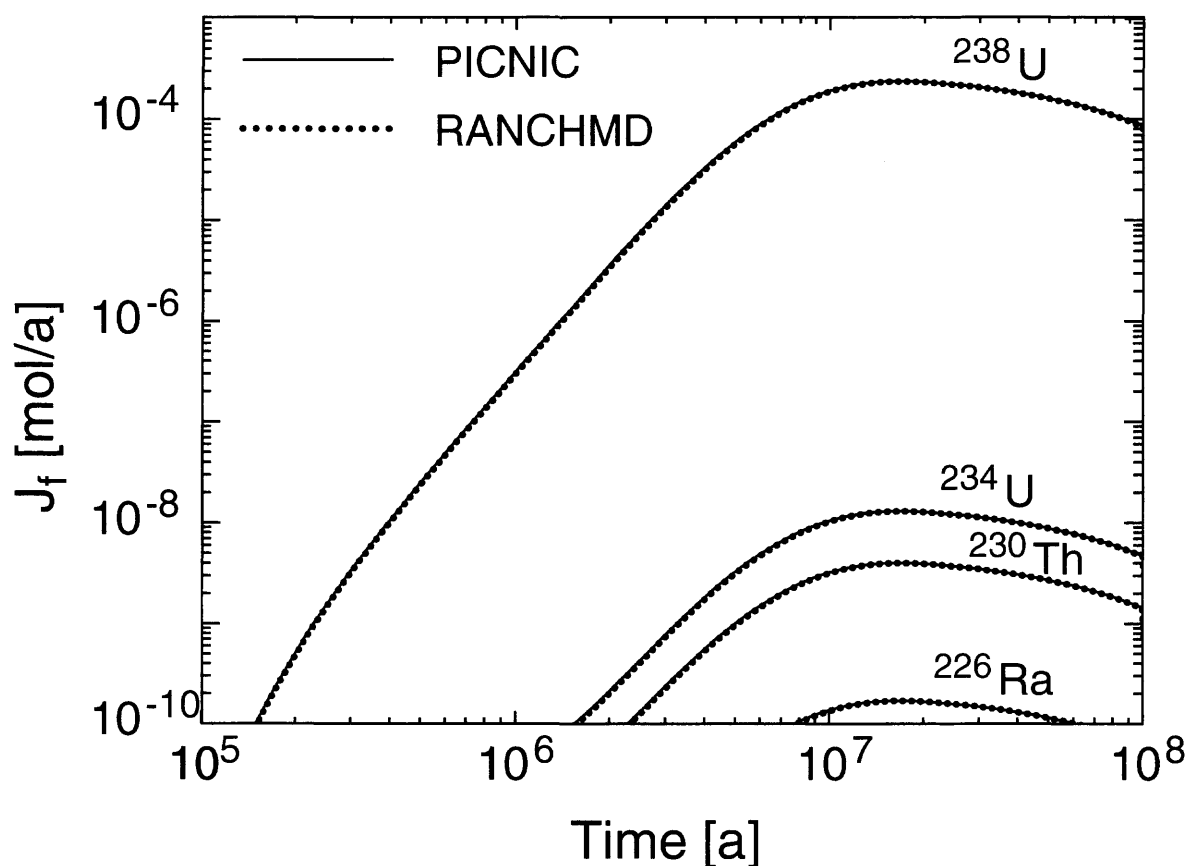


Figure 5.2. Nuclide release rates from the geosphere presented on a double-logarithmic scale. The Kristallin-I reference case with the vein Geometry 4 is considered for the 4N+2 nuclide chain, see Tables 5.3.1 to 5.3.3 in Nagra [1994]. PICNIC calculations (solid lines) and RANCHMD calculations (dots) are shown for comparison.

time	²³⁸ U			²³⁴ U		
	PICNIC	RANCHMD	diff.(P,R) [%]	PICNIC	RANCHMD	diff.(P,R) [%]
1.000E+04	5.163E-25	2.508E-23	≈ -100	6.844E-28	2.969E-24	≈ -100
2.000E+04	4.139E-20	2.336E-20	77.14	5.323E-23	1.108E-22	-51.97
3.000E+04	1.620E-17	8.712E-18	85.95	2.016E-20	1.197E-20	68.45
5.000E+04	8.273E-15	5.852E-15	41.38	9.723E-18	6.947E-18	39.97
1.000E+05	6.048E-12	5.133E-12	17.81	6.148E-15	5.284E-15	16.36
2.000E+05	4.948E-10	4.646E-10	6.49	3.807E-13	3.617E-13	5.27
3.000E+05	3.245E-09	3.079E-09	5.37	1.895E-12	1.824E-12	3.89
5.000E+05	2.424E-08	2.312E-08	4.84	8.508E-12	8.189E-12	3.89
1.000E+06	3.059E-07	2.900E-07	5.48	3.814E-11	3.624E-11	5.24
2.000E+06	3.596E-06	3.393E-06	5.98	2.106E-10	1.987E-10	5.99
3.000E+06	1.384E-05	1.309E-05	5.76	7.607E-10	7.193E-10	5.77
5.000E+06	5.859E-05	5.597E-05	4.68	3.215E-09	3.072E-09	4.64
1.000E+07	1.905E-04	1.866E-04	2.09	1.046E-08	1.025E-08	2.05
2.000E+07	2.340E-04	2.323E-04	0.70	1.280E-08	1.276E-08	0.32
3.000E+07	2.081E-04	2.066E-04	0.73	1.139E-08	1.135E-08	0.36
5.000E+07	1.617E-04	1.602E-04	0.92	8.849E-09	8.801E-09	0.55
1.000E+08	8.623E-05	8.484E-05	1.64	4.719E-09	4.660E-09	1.27

Table 5.3. Comparison between PICNIC (P) and RANCHMD (R) calculations of time-dependence of output for ²³⁸U and ²³⁴U for the Kristallin-I reference case with vein geometry, but with reduced length $L=2$ m. The first and second columns specify the nuclides and their corresponding half-life. The maximum release rate and the time of that maximum as calculated by PICNIC are given in columns 3 and 6, respectively. The corresponding results from RANCHMD are given in columns 4 and 7, respectively. Columns 5 and 8 present the relative differences between the results of the two calculations, i.e. $100*(P-R)/R$. For comparison of the data at the selected times, a cubic spline interpolation on a double-logarithmic scale was used.

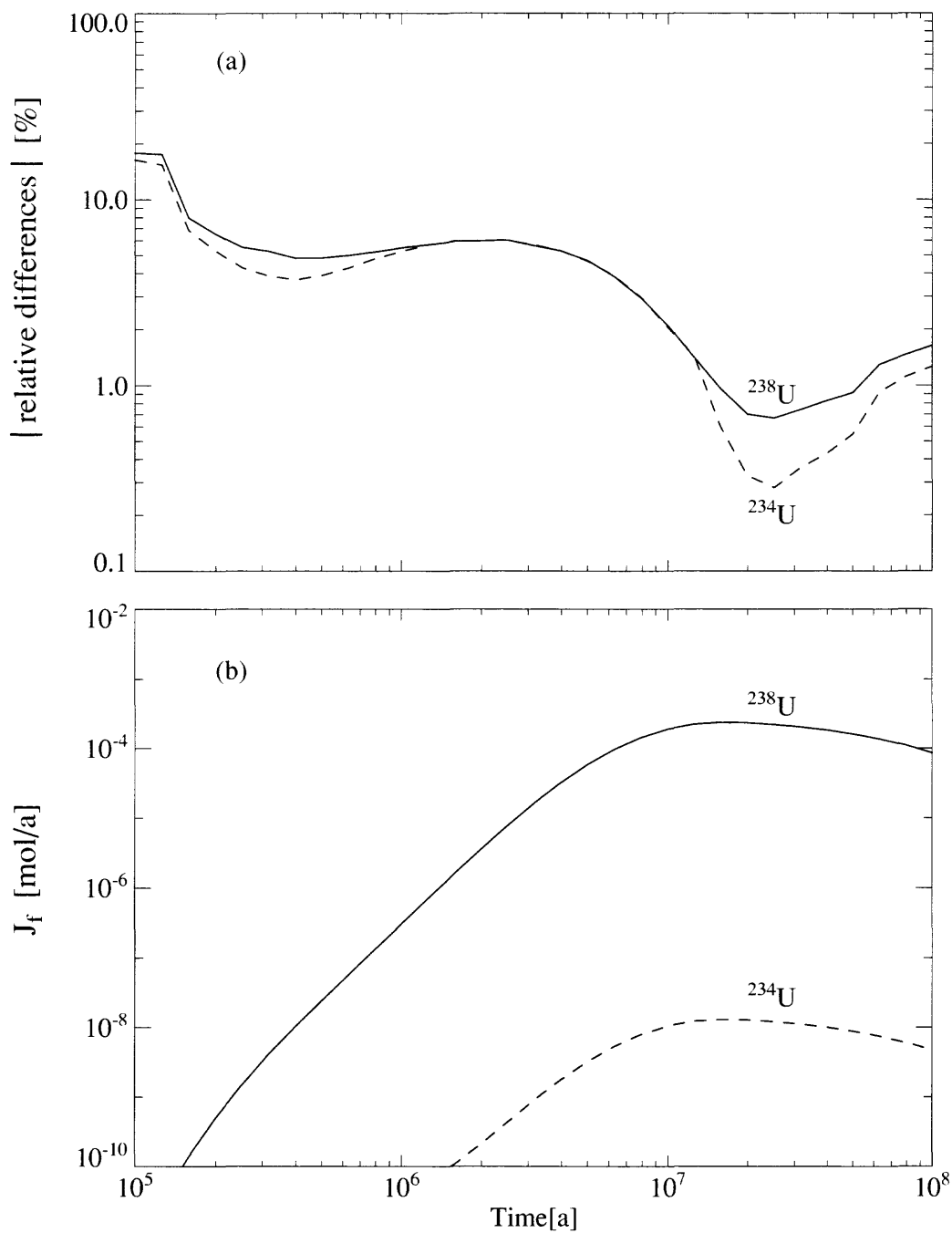


Figure 5.3. (a) The absolute values of the relative differences of PICNIC calculations from RANCHMD calculations for ^{238}U (solid line) and ^{234}U (dashed line) are given on a double-logarithmic scale, compare columns 4 and 7 of Table 5.3. The release rates are given also in part (b) for better orientation.

5.2.2. Vein Network

In this subsection we describe the testing of PICNIC for the case of transport of a **nuclide decay chain in a network of veins** (with surrounding homogeneous rock matrix). With that aim we consider a further modification of the Kristallin-I reference case for the 4N+2 decay chain $^{246}\text{Cm} \rightarrow ^{242}\text{Pu} \rightarrow ^{238}\text{U} \rightarrow ^{234}\text{U} \rightarrow ^{230}\text{Th} \rightarrow ^{226}\text{Ra} \rightarrow \dots \rightarrow ^{206}\text{Pb}$ [Table 3.7.1 in Nagra, 1994]. The nuclides are assumed to be transported in the small vein network consisting of six legs, which we have considered already in the fracture case, see Figure 4.32. For more pronounced breakthrough curves in our test case all transport lengths and the hydraulic head difference are reduced by a factor of ten⁵⁶ compared to the reference case of Kristallin-I. This means that the total transport length is 20m, the mixing tank is after 10m and the dispersion length in each leg is 2 m. Leg 1 and leg 4 are assumed to have a Darcy velocity $q_1 = q_4 = q_r$, as in the reference case. The Darcy velocities of leg 2 and leg 5 are ten times larger and the Darcy velocities of leg 3 and leg 6 are one hundred times larger.

The nuclide release from the repository is again calculated using the near-field model STRENG [Grindrod et al., 1990] and is read by PICNIC from “HARTLEY”-file format source files. The nuclide release from the repository near-field into the geosphere depends on the water flow rate at the interface of near-field and geosphere, thus the three different sources had to be calculated. The total inventory of the repository is allocated to the three sources according to their relative cross-sectional area.

The transport in this network can be evaluated by performing a separate PICNIC calculation for each leg. The result is called “assembled PICNIC”, analogous to the “assembled RANCHMD” calculations in section 4.4.3. The PICNIC results (solid lines in Figure 5.4) and the “assembled PICNIC” results (dots in Figure 5.4) are in nearly perfect agreement. Table 5.4 presents the maximum release rate of each nuclide and the corresponding time of maximum, (a) at the inflow to the mixing tank, and (b) at the release to the *hcf* for both the PICNIC and the “assembled PICNIC” calculations.

The differences in the maximum release rate and time to maximum release at the mixing tank are so small for all the nuclides that they need not be discussed. Table 5.5 presents a detailed comparison of the release curves for ^{238}U and ^{234}U , those nuclides with the highest maximum release rates. The two calculations are in near perfect agreement for the time-dependence of the release fluxes at the mixing tank for ^{238}U (left hand side of Table 5.5a) and ^{234}U (left hand side of Table 5.5b).

At the outflow into the *hcf*, the predicted times of maximum release rate for both calculation methods are in nearly perfect agreement, see Table 5.4b. The rising edge of the release curve for ^{238}U shows good agreement, within 1%, even at nine orders of magnitude below the maximum, while for ^{234}U the same level of agreement is seen from eight decades below the maximum. For the trailing edge the agreement is within 0.2% for the period up to $10^8[\text{a}]$, the end of the calculation time. This cut-off time is a factor of ten greater than the time to maximum release and sufficient for safety assessment purposes.

The tiny differences between the two calculations could be due to the fact that for the PICNIC calculation only a convolution of the response function of the network is performed with the source,

⁵⁶ The hydraulic transmissivity of the network is higher than that of the single vein presented in section 5.2.1; hence, the length of the flow path was increased to achieve a reasonable transport time.

while for the “assembled PICNIC” calculations the release curve at the mixing tank is evaluated first in a resolution of 36 output times per decade. This output is then used as the source of the departing legs 4, 5 and 6. For each of these legs the source is then convoluted in individual PICNIC calculations for each leg with the response functions of these legs.

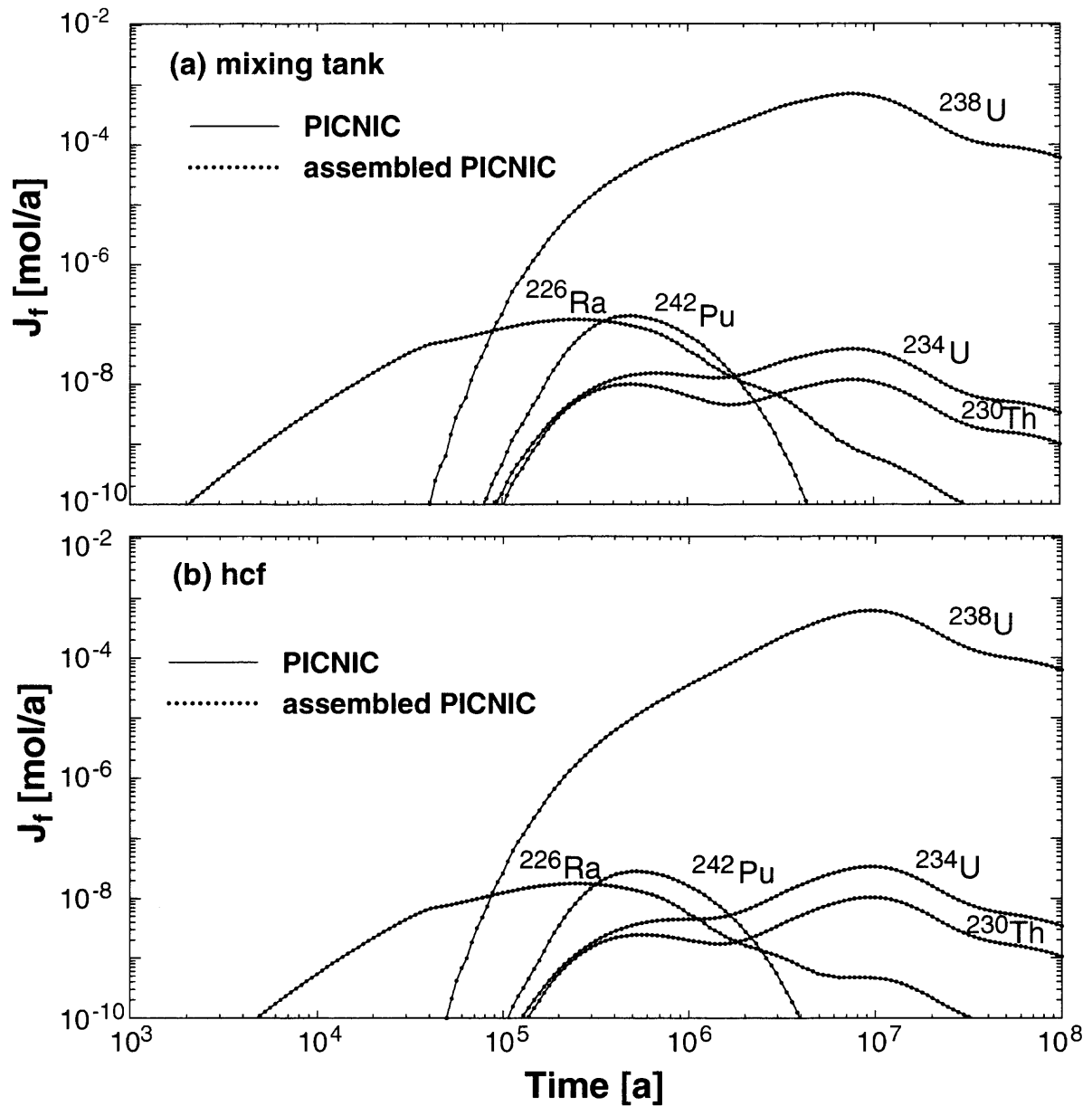


Figure 5.4. Release curves (a) at the mixing tank and (b) at the *hcf* presented on a double-logarithmic scale. Considered is the transport of the 4N+2 decay chain in the vein network, see Figure 4.32. PICNIC calculations (solid lines) and “assembled PICNIC” calculations (dots) are shown for comparison.

(a) mixing tank	maximum of J_f [mol / a]			time t_{\max} [a] of maximum		
nuclide	PICNIC	assembled PICNIC	diff. [%]	PICNIC	assembled PICNIC	diff. [%]
^{246}Cm	1.089E-16	1.089E-16		6.391E+04	6.391E+04	
^{242}Pu	1.398E-07	1.397E-07	< 0.1	4.948E+05	4.948E+05	
^{238}U	7.087E-04	7.088E-04	< 0.1	7.743E+06	7.743E+06	
^{234}U	3.877E-08	3.877E-08		7.743E+06	7.743E+06	
^{230}Th	1.187E-08	1.187E-08		7.743E+06	7.743E+06	
^{226}Ra	1.211E-07	1.211E-07		2.448E+05	2.448E+05	

(b) <i>hcf</i>	maximum of J_f [mol / a]			time t_{\max} [a] of maximum		
nuclide	PICNIC	assembled PICNIC	diff. [%]	PICNIC	assembled PICNIC	diff. [%]
^{246}Cm	1.201E-17	1.201E-17		6.391E+04	6.391E+04	
^{242}Pu	2.866E-08	2.863E-08	< 0.1	5.275E+05	5.275E+05	
^{238}U	6.214E-04	6.211E-04	< 0.1	9.380E+06	9.380E+06	
^{234}U	3.410E-08	3.408E-08	< 0.1	9.380E+06	9.380E+06	
^{230}Th	1.046E-08	1.046E-08		9.380E+06	9.380E+06	
^{226}Ra	1.781E-08	1.781E-08		2.448E+05	2.448E+05	

Table 5.4. Comparison of maxima and time of maxima of PICNIC and assembled PICNIC output for the six-leg vein network, (a) at the mixing tank, and (b) at the highly conducting feature (*hcf*). The 4N+2 nuclide chain is considered. The first column specifies the nuclides. The maximum release rate and the time of that maximum as calculated by PICNIC are given in columns 2 and 5 respectively. The corresponding assembled PICNIC results are given in columns 3 and 6 respectively. Columns 4 and 7 present the relative differences between the results of the two calculations.

(a) ^{238}U	mixing tank			hcf		
	time [a]	PICNIC	assembled PICNIC	diff. [%]	PICNIC	assembled PICNIC
2.0E+03	1.931E-29	1.929E-29	0.07	7.947E-26	7.969E-26	-0.27
3.0E+03	2.382E-26	2.381E-26	0.05	1.470E-27	1.489E-27	-1.26
5.0E+03	4.956E-23	4.954E-23	0.03	3.860E-24	3.997E-24	-3.45
1.0E+04	1.469E-18	1.468E-18	0.07	1.577E-19	1.584E-19	-0.44
2.0E+04	2.217E-14	2.216E-14	0.04	2.673E-15	2.844E-15	-5.99
3.0E+04	4.404E-12	4.403E-12	0.01	6.096E-13	6.126E-13	-0.48
5.0E+04	7.095E-10	7.096E-10	-0.01	1.103E-10	1.111E-10	-0.66
1.0E+05	1.463E-07	1.464E-07	-0.07	2.633E-08	2.638E-08	-0.19
2.0E+05	3.972E-06	3.973E-06	-0.02	8.072E-07	8.090E-07	-0.21
3.0E+05	1.356E-05	1.356E-05	-0.00	2.988E-06	2.990E-06	-0.08
5.0E+05	3.995E-05	3.995E-05	0.00	1.003E-05	1.003E-05	-0.05
1.0E+06	1.112E-04	1.112E-04	0.00	3.558E-05	3.560E-05	-0.06
2.0E+06	2.521E-04	2.521E-04	0.00	1.082E-04	1.082E-04	0.00
3.0E+06	4.037E-04	4.037E-04	-0.00	2.063E-04	2.063E-04	-0.00
5.0E+06	5.995E-04	5.995E-04	0.00	4.053E-04	4.053E-04	0.02
1.0E+07	6.482E-04	6.482E-04	0.00	6.189E-04	6.185E-04	0.06
2.0E+07	2.545E-04	2.546E-04	-0.04	2.978E-04	2.981E-04	-0.10
3.0E+07	1.322E-04	1.322E-04	-0.00	1.544E-04	1.547E-04	-0.18
5.0E+07	9.380E-05	9.380E-05	0.00	1.010E-04	1.010E-04	-0.00
1.0E+08	6.003E-05	6.003E-05	0.00	6.233E-05	6.234E-05	-0.02

(b) ^{234}U	mixing tank			hcf		
	time [a]	PICNIC	assembled PICNIC	diff. [%]	PICNIC	assembled PICNIC
3.0E+03	3.208E-29	3.205E-29	0.10	1.893E-30	1.900E-30	-0.36
5.0E+03	6.681E-26	6.682E-26	-0.01	5.202E-27	5.391E-27	-3.52
1.0E+04	1.952E-21	1.951E-21	0.05	2.094E-22	2.104E-22	-0.48
2.0E+04	2.858E-17	2.856E-17	0.05	3.448E-18	3.664E-18	-5.88
3.0E+04	5.496E-15	5.494E-15	0.04	7.602E-16	7.636E-16	-0.44
5.0E+04	8.376E-13	8.375E-13	0.02	1.301E-13	1.309E-13	-0.57
1.0E+05	1.502E-10	1.502E-10	0.00	2.697E-11	2.700E-11	-0.11
2.0E+05	3.083E-09	3.083E-09	0.00	6.260E-10	6.264E-10	-0.07
3.0E+05	7.939E-09	7.939E-09	-0.00	1.750E-09	1.751E-09	-0.06
5.0E+05	1.418E-08	1.418E-08	0.00	3.559E-09	3.560E-09	-0.04
1.0E+06	1.393E-08	1.393E-08	0.00	4.481E-09	4.482E-09	-0.02
2.0E+06	1.454E-08	1.454E-08	0.00	6.301E-09	6.301E-09	0.00
3.0E+06	2.184E-08	2.185E-08	-0.01	1.126E-08	1.126E-08	-0.01
5.0E+06	3.263E-08	3.263E-08	-0.00	2.218E-08	2.217E-08	0.05
1.0E+07	3.550E-08	3.550E-08	0.00	3.397E-08	3.395E-08	0.06
2.0E+07	1.395E-08	1.394E-08	0.07	1.635E-08	1.637E-08	-0.12
3.0E+07	7.251E-09	7.251E-09	-0.00	8.483E-09	8.494E-09	-0.13
5.0E+07	5.153E-09	5.153E-09	0.00	5.550E-09	5.550E-09	-0.00
1.0E+08	3.299E-09	3.299E-09	0.00	3.425E-09	3.426E-09	-0.03

Table 5.5. Comparison between PICNIC and assembled PICNIC calculations for (a) ^{238}U and (b) ^{234}U for the six-leg vein network. In the first column, time is given and in the second and fifth columns the PICNIC results at the mixing tank and the highly conducting feature, respectively. In the third and sixth columns, the assembled PICNIC results are presented. For comparison of the data at the selected times, a cubic spline interpolation on a double-logarithmic scale was used. The fourth and seventh columns give the relative differences of PICNIC and assembled PICNIC results. Maximum release and time to maximum release are given in Table 5.4.

5.3. Summary

As step II in the verification scheme in this section we verified the capability of PICNIC to deal with a cylindrical rock matrix; see the detailed verification matrix in Table 5.6. Transport of a single nuclide in a single vein was evaluated and compared to RANCHMD calculations for a limited and an effectively unlimited rock matrix. This was done using parameters of the Grimsel dipole experiment with the tracer uranine. Then test cases related to the Kristallin-I safety assessment were considered. A parameter variation of the transport of the $4N+2$ decay chain in a single leg was used as an example. The PICNIC calculations were compared in a code inter-comparison to results from RANCHMD calculations. Thereby the capacity of the code for dealing with the decay of nuclide chains in combination with rock matrix diffusion in a vein geometry was verified. PICNIC and RANCHMD calculations showed a very good agreement for the vein case with matrix diffusion considered here. For the test of the network facility in PICNIC, transport from a repository through a network of veins of differing hydraulic properties was analysed. Results from a simulation of this case using PICNIC were compared to so-called “assembled PICNIC” calculations. The excellent agreement in this self-consistency test between PICNIC and “assembled PICNIC” results verified the network capability of PICNIC for veins in combination with the decay of nuclide chains. Together with verification step I in section 4 and the considerations in section 3 this verified the capability of PICNIC to deal also with the cylindrical vein geometry for rock matrix.

single vein		(a) single nuclide			(b) nuclide decay chain		
cylindrical rock matrix geometry		ZG	ZC	AI	ZG	ZC	AI
source in Laplace domain	δ -pulse						
	simple-leaching						
source in time domain	short pulse	C ⁵⁷					
	long top-hat						
	band-release						
	general		C		C ⁵⁸	C	

pathway of veins		(c) single nuclide			(d) nuclide decay chain		
cylindrical rock matrix geometry		ZG	ZC	AI	ZG	ZC	AI
source in Laplace domain	δ -pulse						
	simple-leaching						
source in time domain	short pulse						
	long top-hat						
	band-release						
	general						

vein network		(e) single nuclide			(f) nuclide decay chain		
cylindrical rock matrix geometry		ZG	ZC	AI	ZG	ZC	AI
source in Laplace domain	δ -pulse						
	simple-leaching						
source in time domain	short pulse						
	long top-hat						
	band-release						
	general				C ⁵⁹	C	

Table 5.6. Performed test calculations for cylindrical vein geometry. Note: All test cases represented by empty fields in the scheme were implicitly verified by any of the specified examples. Such a procedure is strongly based on the internal structure of PICNIC as outlined in more detail in section 3. Legend: C: comparison with other computer code.

⁵⁷ Comparison with RANCHMD.

⁵⁸ Comparison with RANCHMD. The same for ZC.

⁵⁹ Comparison with assembled PICNIC. The same for ZC.

6. Using the Embedded Finite-Element Method to Approximate Matrix Diffusion into a Homogeneous One-Dimensional Planar Rock Matrix

In the calculations of the previous sections, the rock matrix response was calculated in PICNIC by implemented analytical formulae. In this section we introduce the **embedded finite-element method** (FEM) for calculation of the rock matrix response, see section 2.4.3. We consider (almost) one-dimensional rock matrix diffusion into a homogeneous planar rock matrix using the embedded FEM.

In cases where a one-dimensional finite element mesh is used in PICNIC, we use the abbreviation “1D-FEM”, while “2D-FEM” is used in cases where PICNIC uses a two-dimensional finite-element mesh for the calculation of the rock matrix response. This is step III of the verification of PICNIC; cf. the verification strategy in section 3.4.3. The case of a homogeneous planar rock matrix is the only rock matrix geometry that can be treated in PICNIC using both the embedded FEM and the method with implemented one-dimensional analytical solution of the rock matrix response (1D-AS). Because the **1D-AS** option uses an exact **analytical solution for the rock matrix response**, this method yields a more accurate result than the FEM option, where the rock matrix response in the Laplace domain is approximated by a **finite-element calculation**. Thus the comparison of the FEM results with the 1D-AS results performed in this section gives first estimate of the validity and accuracy of the FEM results and acts as a solid base for the further verification steps in the next sections for more complex rock matrix geometries. For the parameter definition and the balance equations for the rock matrix geometries of this section see sections 2.4 and 2.5.1.

We start in section 6.1 with a **single nuclide** and a **nuclide decay chain in a single leg** as hypothetical variations of the Grimsel dipole parameters for uranine.

In section 6.2 it is investigated whether **“weakly two-dimensional matrix diffusion”** has an effect on the accuracy of the results.

For different **single nuclides in a single leg** with Kristallin-I performance assessment parameters for a constant source, the effect of a **refined finite-element mesh** is investigated in section 6.3. The **steady-state release** is compared to the **analytical result**.

In section 6.4 the effect of **multiple rock layers** with the same properties (i.e. subdividing the rock matrix) on the numerical result is investigated.

In section 6.5 it is shown that **rock matrix areas of extremely different size** lead to a slightly reduced accuracy of the PICNIC results.

In section 6.6 the transport of a **single nuclide** and a **nuclide decay chain** in a 26-leg **network** is considered.

Section 6.7 gives a summary.

6.1. One-Dimensional Matrix Diffusion

In this subsection, for two **different refinements** of the finite-element mesh, we compare the FEM results in PICNIC with the respective 1D-AS results which use an analytically calculated rock matrix response. The transport of a **single nuclide** and a **nuclide decay chain** in a **single leg** with Grimsel uranine parameters are considered.

First we compute nuclide flow rates in a single leg together with one-dimensional matrix diffusion in a homogeneous rock matrix (Figure 6.1) using both the 1D-FEM and - for comparison purposes - the 1D-AS.

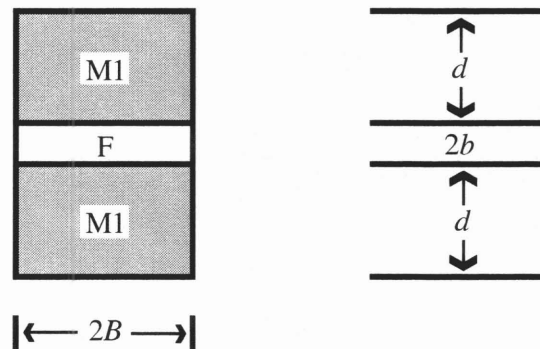


Figure 6.1. Sketch of the cross-section of a leg with an area of flowing water (F) and a matrix layer (M1) below and above the area of flowing water. The sketch is not to scale. The aperture of the area of flowing water is $2b$ and the (here irrelevant) width is $2B$. The thickness of the rock layer is d .

As an example we consider the transport of uranine in the 5 m dipole experiment with a δ -function source and the zero-gradient outlet boundary condition, compare sections 4.1 and 4.2. The result calculated by PICNIC using the 1D-AS method is given as a solid line on a linear timescale in Figure 6.2a and on a logarithmic scale in Figure 6.2b. Time is given on a logarithmic scale. The PICNIC result using the 1D-FEM option in standard resolution is given as dash-dotted lines. Figure 6.2c gives the relative difference function of the 1D-FEM result with respect to the 1D-AS result. The overall form of the release curves is in excellent agreement, while there are slight differences in some details. The 1D-FEM result slightly oscillates around the 1D-AS result. The rising edge and the trailing edge of the 1D-AS result are somewhat earlier, while the peak region is at the most 2% below the 1D-FEM result. The maximum of the relative difference function is at the beginning of the hump in the breakthrough curve at about 0.02 [a] and is below 10%.

PICNIC can be forced to use a refined mesh for the finite-element calculation of the rock matrix response. This can be entered to PICNIC by the command "REFINE 4", while the standard resolution calculation is performed using the command "REFINE 2", compare section 2.4.3 and especially Table 2.1. The calculation with the refined mesh (dashed lines) is even closer to the 1D-AS result, while the overall oscillatory behaviour of the relative difference function is similar. The difference in the peak region is now below 1% and the maximum relative difference at the hump at about 0.02 [a] is within 3%. Note that the calculation using the finer mesh sometimes needs about 10 times more execution time. The small differences in the breakthrough curves and the converging behaviour for the finer mesh gives, on the one hand, initial confidence that the 1D-FEM option

works correctly and, on the other hand, indicates what accuracy we should expect at best from the FEM option in PICNIC.

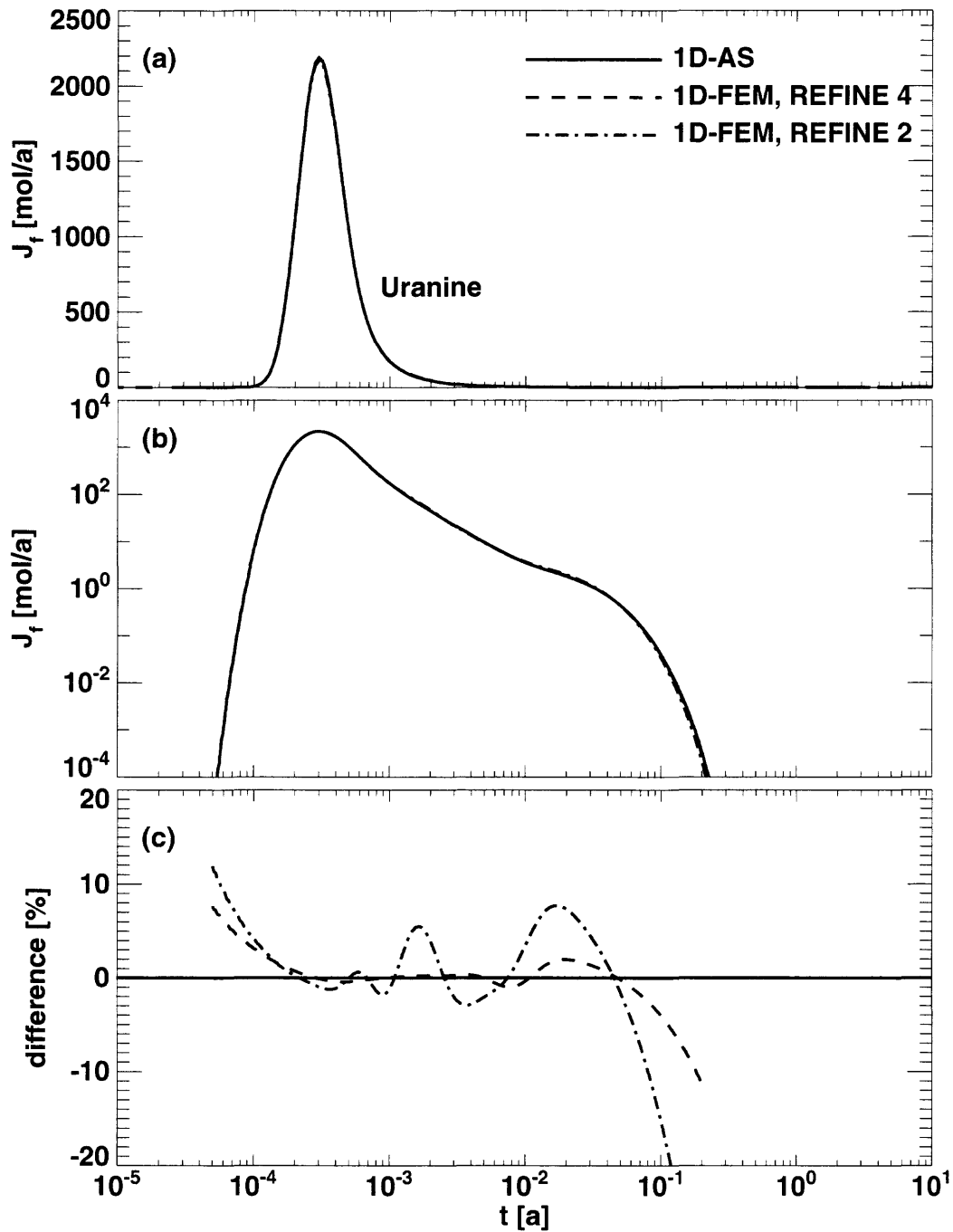


Figure 6.2. The result of a PICNIC calculation for the release of uranium using the (finite-element) 1D-FEM option with standard resolution "REFINE 2" (dash-dotted lines) and increased refinement "REFINE 4" (short-dashed lines) is compared to the respective PICNIC result for the ("analytical") 1D-AS option (solid lines), compare also Figure 4.9. A δ -function source is considered. The release curves are given in (a) on a linear scale and in (b) on a logarithmic scale. The relative difference functions with respect to the 1D-AS result are given in (c).

To test also the accuracy for a **nuclide decay chain** we consider a hypothetical variation of the uranine case. As in section 4.2, Figures 4.10 to 4.12, we consider a nuclide decay chain $\text{ANUC} \rightarrow \text{BNUC} \rightarrow \text{CNUC}$, where the half-life of ANUC is $10^{-3}[\text{a}]$, the half-life of BNUC is $10^{-4}[\text{a}]$ and CNUC is assumed to be stable. ANUC, BNUC and CNUC are assumed to have the same properties as uranine except for the retardation factor in the rock matrix. ANUC has the same retardation factor as uranine, $R_p = 1.0$, while BNUC has $R_p = 2.0$ and CNUC has $R_p = 10.0$. A δ -function source of the parent ANUC is considered.

We first consider the release curve of ANUC in Figure 6.3. Using a standard mesh (REFINE 2), again a similar kind of oscillatory behaviour of the FEM result around the 1D-AS result is observed as for the non-decaying case in Figure 6.2. Now, however, the curve (dash-dotted lines) is earlier, both for the rising and the trailing edge. The maximum of the relative deviation is now slightly increased and is in the order of 15%. The overall behaviour is still in very good agreement with the 1D-AS result. The oscillations, however, could lead to misinterpretations, e.g. when the calculations are used for the analysis of experiments. Again, the increased refinement results (REFINE 4) agree in the entire relevant region within about 3% with the 1D-AS result, which should also be sufficient for the interpretation of experiments. The accuracy of the fast decaying nuclide BNUC (Figure 6.4) shows similar behaviour to its parent. The end of the decay chain, CNUC, shows a very long tailing in the release curve (Figure 6.5). The deviation of the standard mesh (REFINE 2) result from the 1D-AS result again shows a number of oscillations with a maximum deviation in the order of 12%. The maximum of the release curve is underestimated by 3 to 4% for "REFINE 2" and the decrease of the release curve is somewhat earlier. The agreement using a refined mesh (REFINE 4) is again much better so that the plots in Figure 6.5a,b nearly coincide. The maximum is underestimated by only about 1% to 2% and the agreement within the relevant region is within 4%.

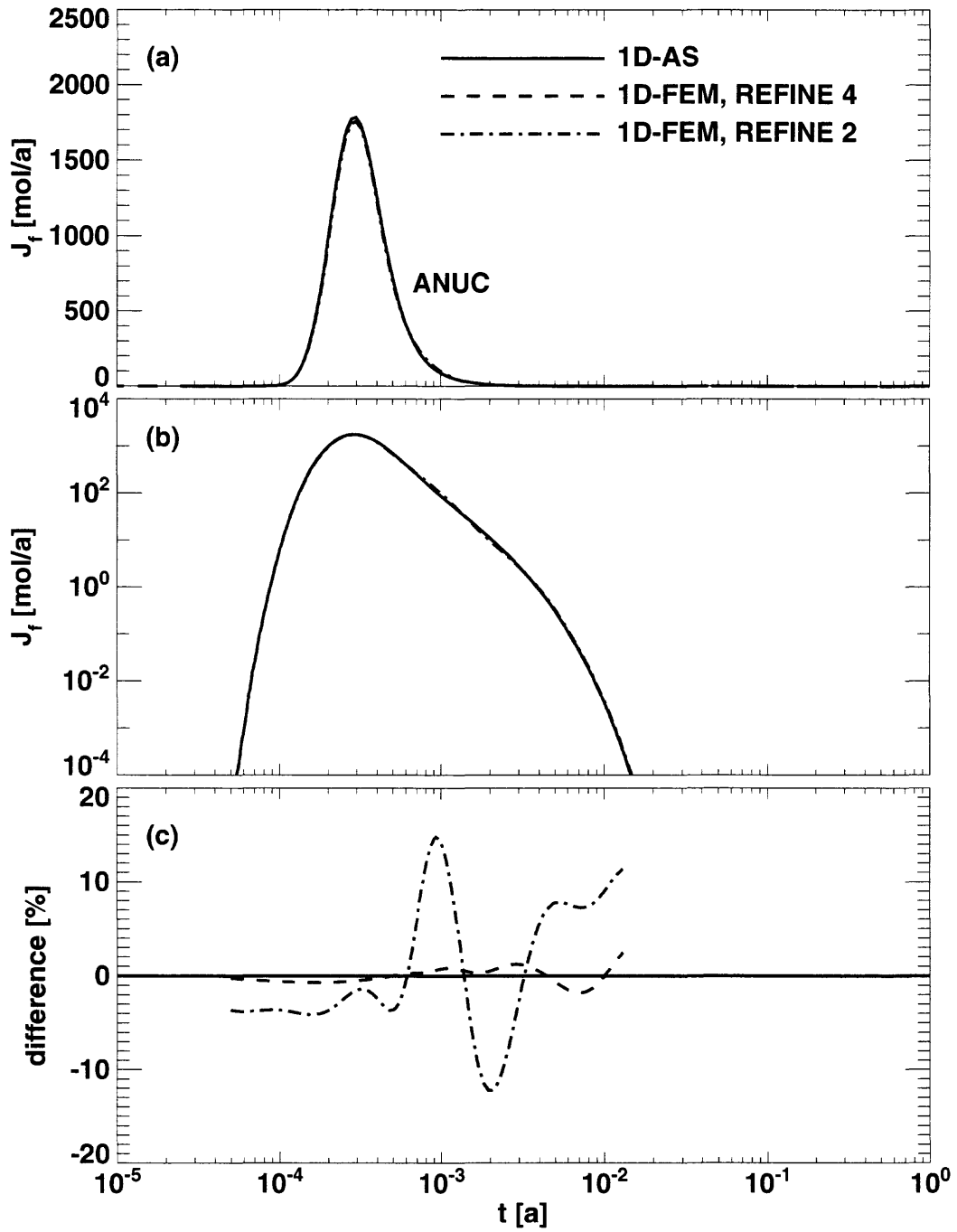


Figure 6.3. Hypothetical variation of the Grimsel uranium dipole experiment for a nuclide decay chain. Presented is the nuclide ANUC of the decay chain $\text{ANUC} \rightarrow \text{BNUC} \rightarrow \text{CNUC}$. A δ -function source of the parent ANUC is considered. The nomenclature is as in Figure 6.2.

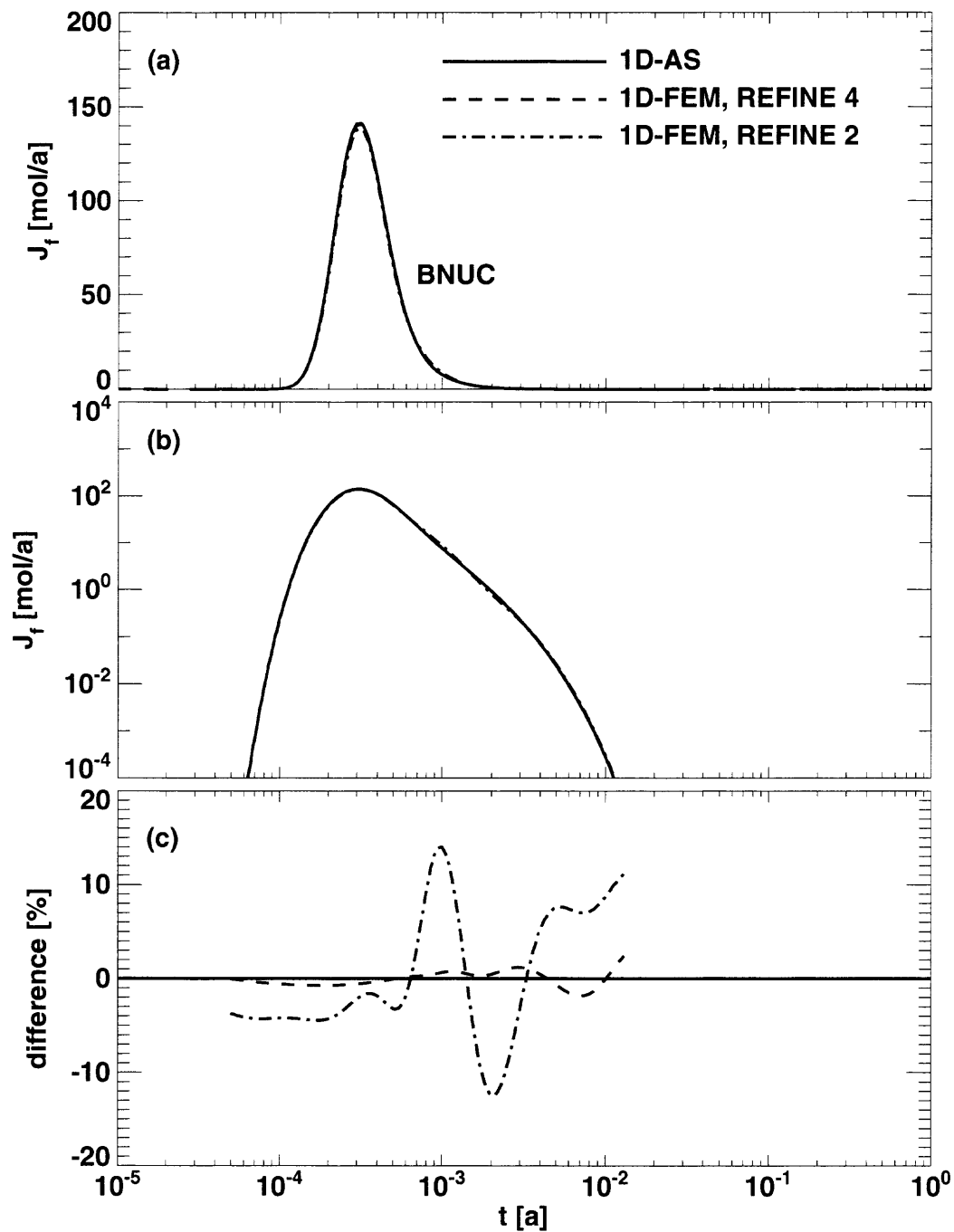


Figure 6.4. Hypothetical variation of the Grimsel uranium dipole experiment for a nuclide decay chain. Presented is the nuclide BNUC of the decay chain $\text{ANUC} \rightarrow \text{BNUC} \rightarrow \text{CNUC}$. A δ -function source of the parent ANUC is considered. The nomenclature is as in Figure 6.2.

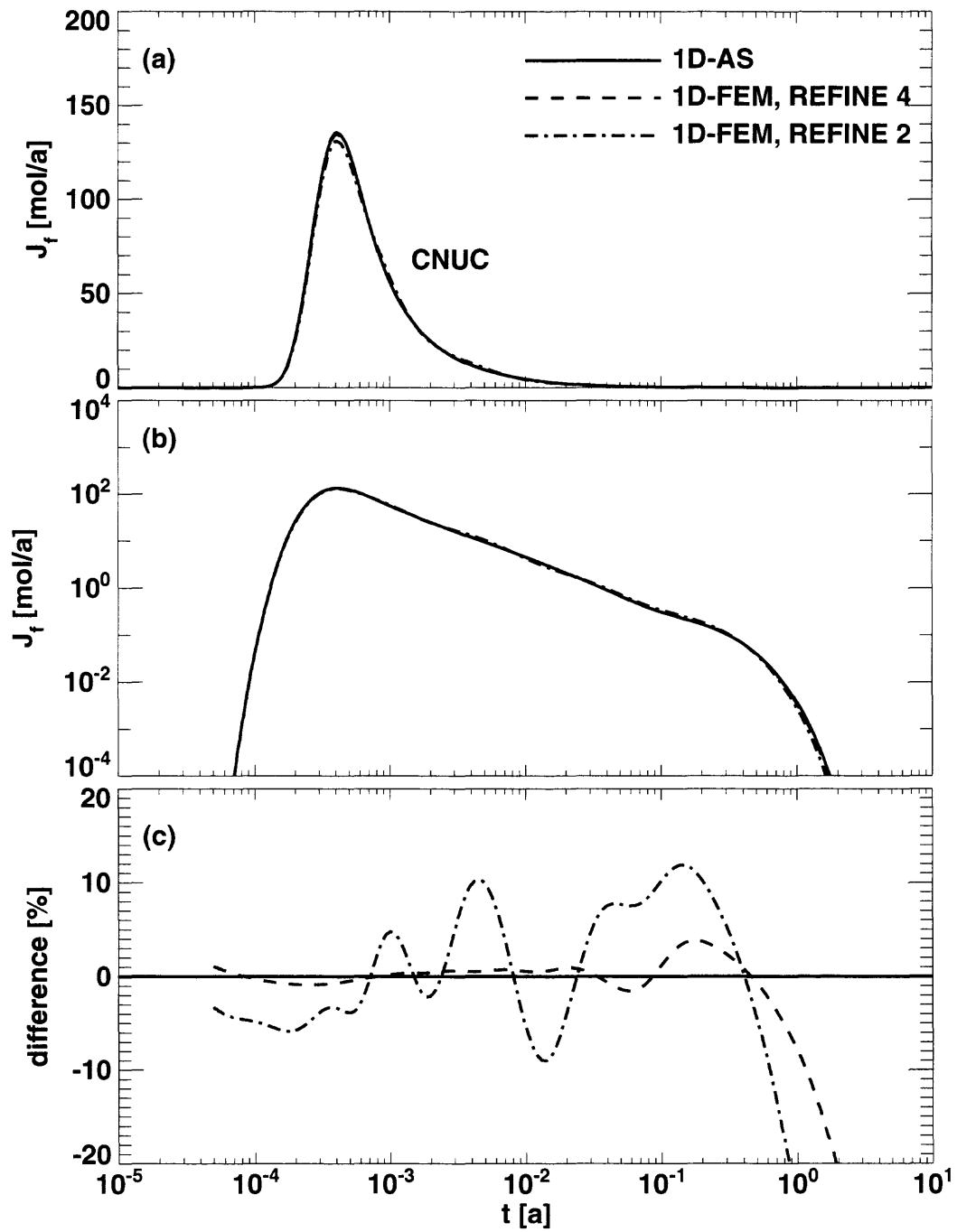


Figure 6.5. Hypothetical variation of the Grimsel uranium dipole experiment for a nuclide decay chain. Presented is the nuclide CNUC of the decay chain $ANUC \rightarrow BNUC \rightarrow CNUC$. A δ -function source of the parent ANUC is considered. The nomenclature is as in Figure 6.2.

6.2. Weakly Two-Dimensional Matrix Diffusion

In the previous subsection, for the geometry of Figure 6.1, PICNIC used a one-dimensional finite-element mesh to calculate the rock matrix response. In this subsection, for the geometry of Figure 6.6, a fracture is considered that is filled mainly with an area of flowing water (F) of width $2B = 10^{-4}$ [m] and, to a small degree, $2d_y = 9 \cdot 10^{-9}$ [m], with (nearly) impermeable rock (M0). Because there is presently no option in PICNIC to generate a perfectly impermeable rock, M0 is defined here as a rock matrix type with retardation constant $R_p = 1.0$ for all nuclides and the extremely small porosity $\varepsilon_p = 10^{-15}$. The aperture of the fracture is $2b = 93 \cdot 10^{-6}$ [m]. Below and above this fracture, there is a homogeneous layer of accessible rock matrix (M1) of thickness $d = 6.2 \cdot 10^{-3}$ [m]. This geometry of the leg cross-section forces PICNIC to use a **two-dimensional finite-element mesh**; we call the method applied 2D-FEM. However, because of the choice of the very small value of d_y relative to d and B , the physical behaviour is nearly the same as in the case of one-dimensional matrix diffusion. Thus, **matrix diffusion is “weakly two-dimensional”**. This means that nearly the same breakthrough curve is produced for uranine (Figure 6.7) as for the geometry of Figure 6.1. The relative deviations of the “REFINE 4” and “REFINE 2” calculations (Figure 6.7c) are also nearly the same as in Figure 6.2c.

For a first test of the two-dimensional finite-element mesh calculation in PICNIC for **nuclide decay chains**, the decay chain $\text{ANUC} \rightarrow \text{BNUC} \rightarrow \text{CNUC}$ described above is considered for the rock matrix geometry of Figure 6.6. The breakthrough curves for ANUC (Figure 6.8), BNUC (Figure 6.9) and CNUC (Figure 6.10) are also nearly the same as for the respective curves in Figures 6.3-5. These first tests indicate that the weakly two-dimensional finite-element calculation of the rock matrix response does not substantially increase the error already generated by the one-dimensional finite-element calculation considered in the previous subsection.

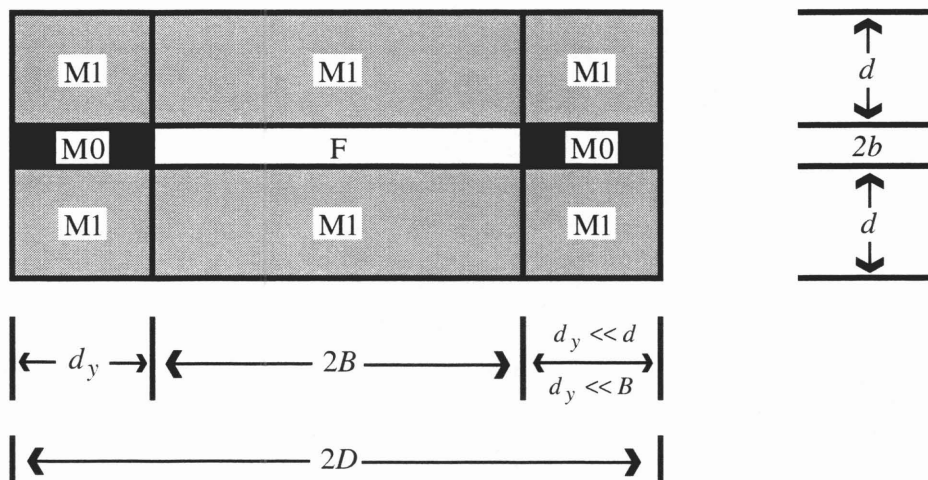


Figure 6.6. Sketch of the cross-section of a leg with a fracture that is mainly filled with an area of flowing water (F) of width $2B$ and to the left and right of F, with small stripes of (nearly) impermeable rock matrix (M0) of width d_y each. The sketch is not to scale. The width of the fracture is $2D$ and the aperture is $2b$. Below and above the fracture, a rock matrix layer (M1) is situated. The thickness of the rock layer is d .

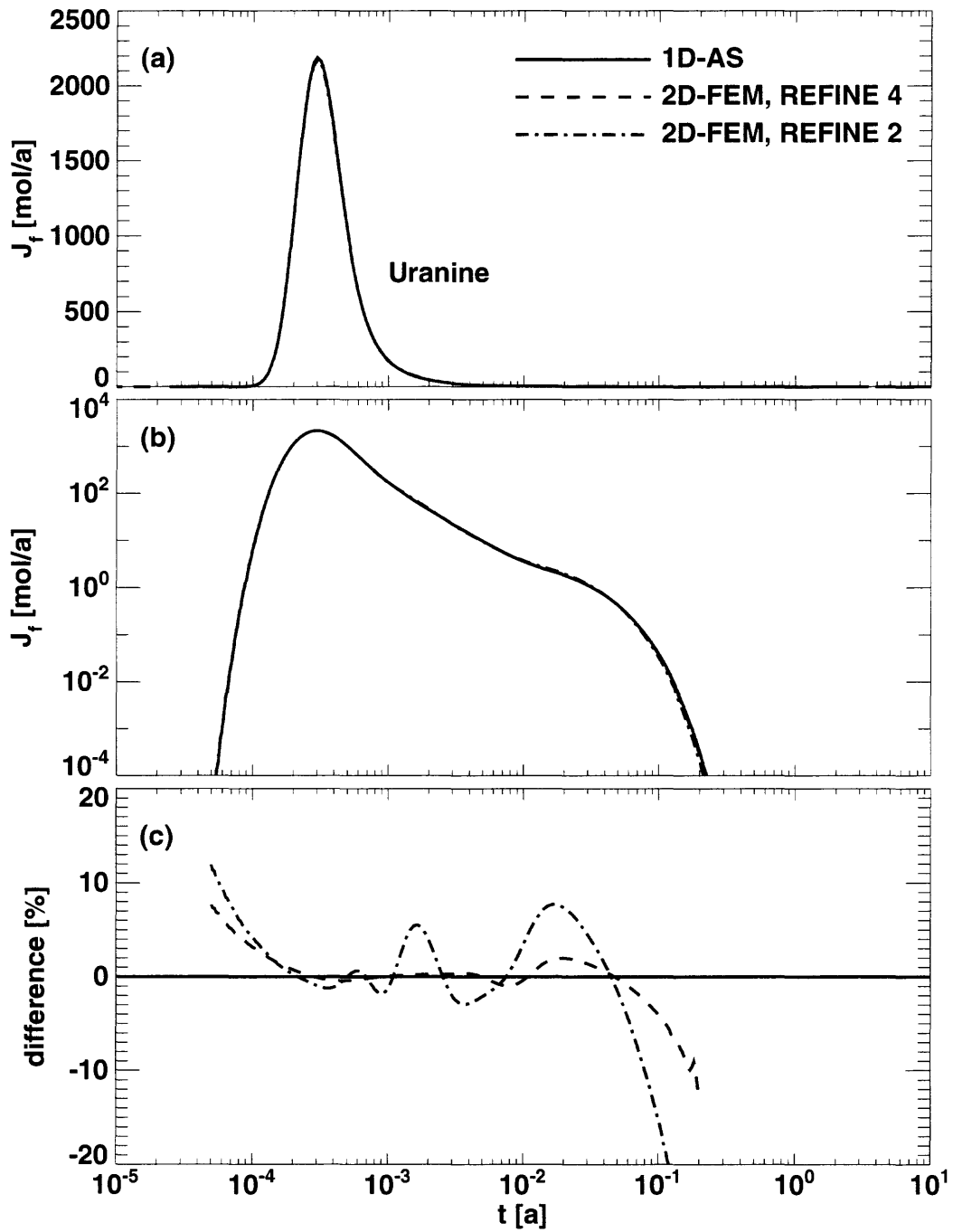


Figure 6.7. Hypothetical variation of the Grimsel uranine dipole experiment for the weakly two-dimensional rock matrix geometry of Figure 6.6. A δ -function source is considered. The nomenclature is as in Figure 6.2.

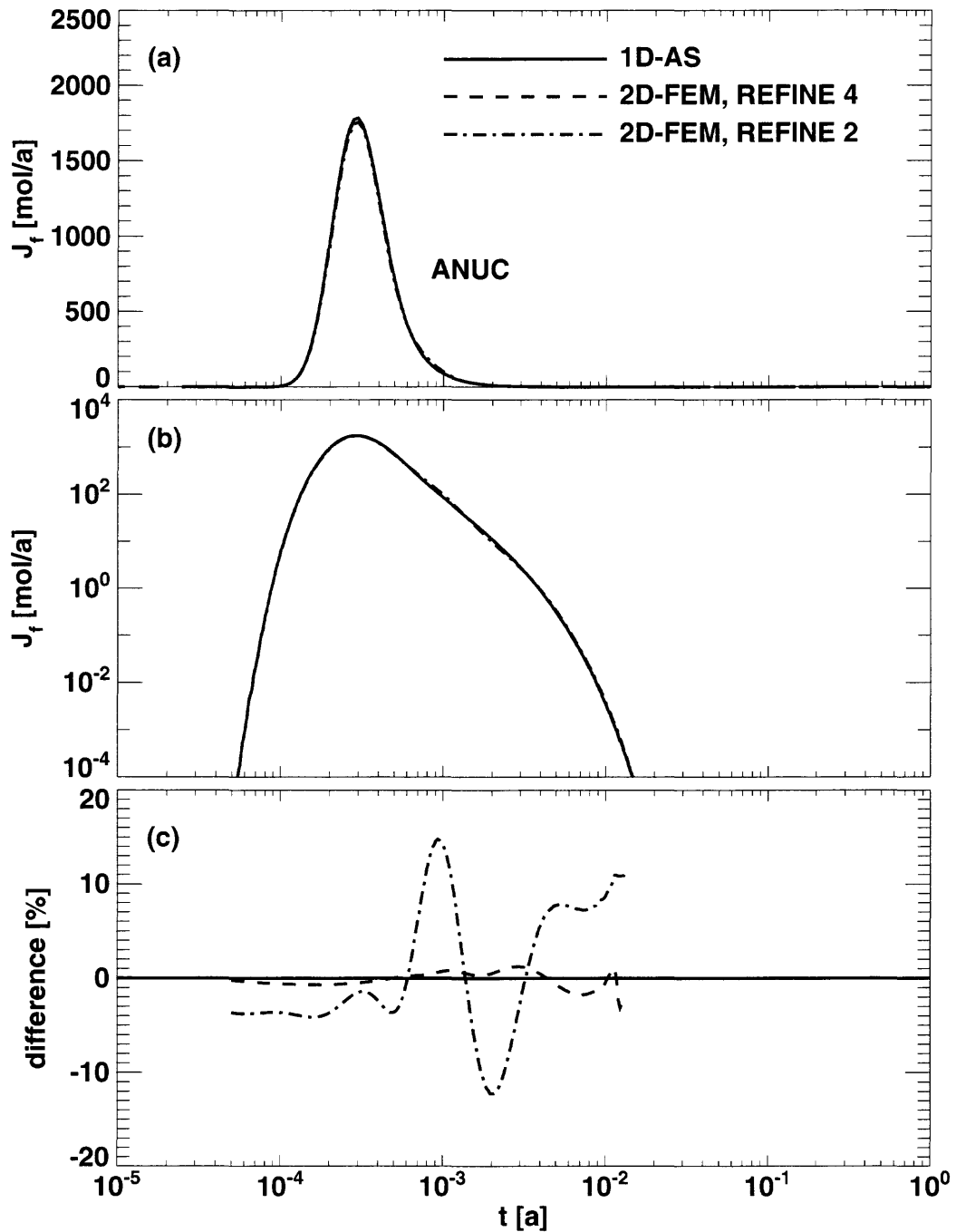


Figure 6.8. Hypothetical variation of the Grimsel uranium dipole experiment for a nuclide decay chain and the weakly two-dimensional rock matrix geometry of Figure 6.6. Presented is the nuclide ANUC of the decay chain $\text{ANUC} \rightarrow \text{BNUC} \rightarrow \text{CNUC}$. A δ -function source of the parent ANUC is considered. The nomenclature is as in Figure 6.2.

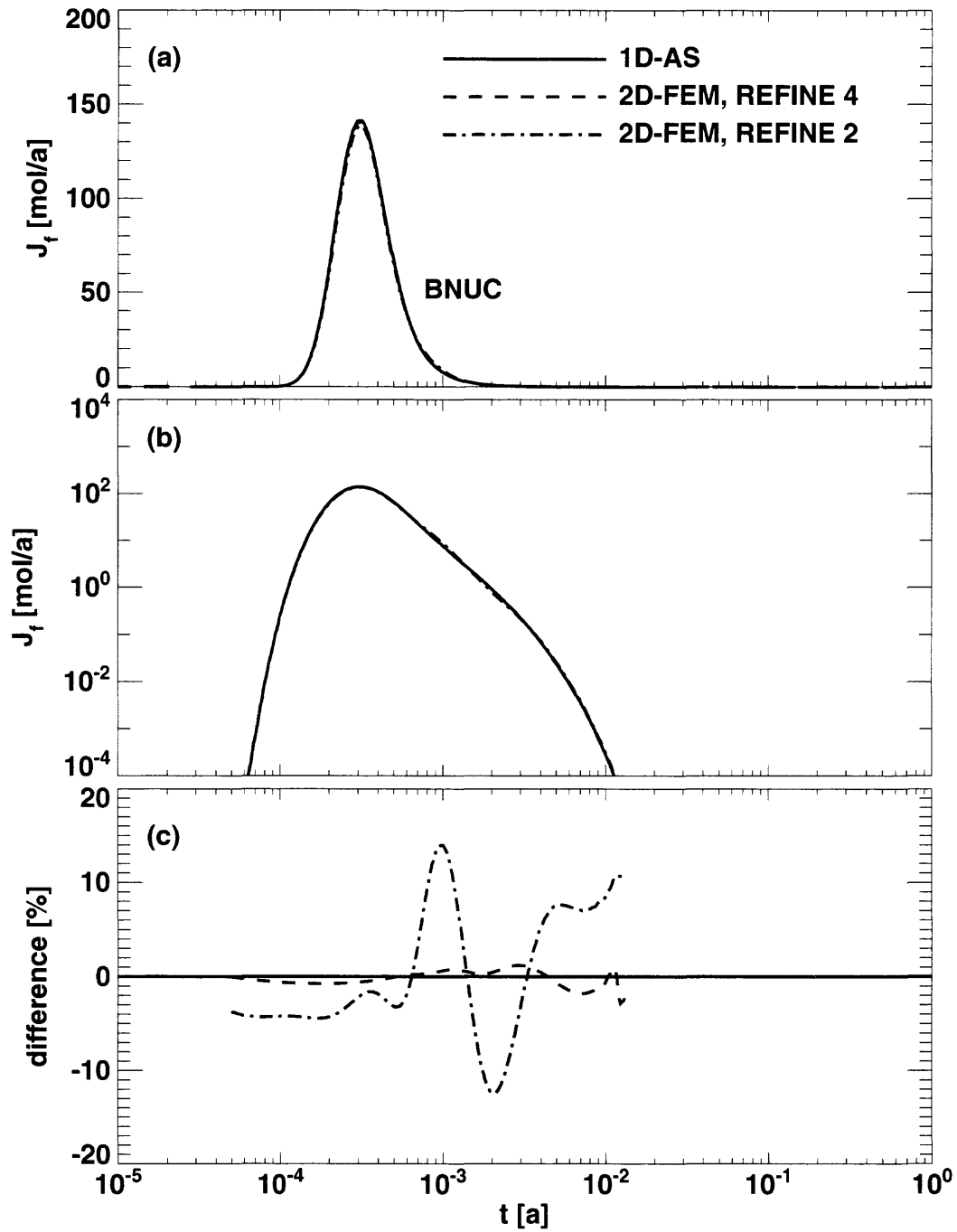


Figure 6.9. Hypothetical variation of the Grimsel uranium dipole experiment for a nuclide decay chain and the weakly two-dimensional rock matrix geometry of Figure 6.6. Presented is the nuclide BNUC of the decay chain $ANUC \rightarrow BNUC \rightarrow CNUC$. A δ -function source of the parent ANUC is considered. The nomenclature is as in Figure 6.2.

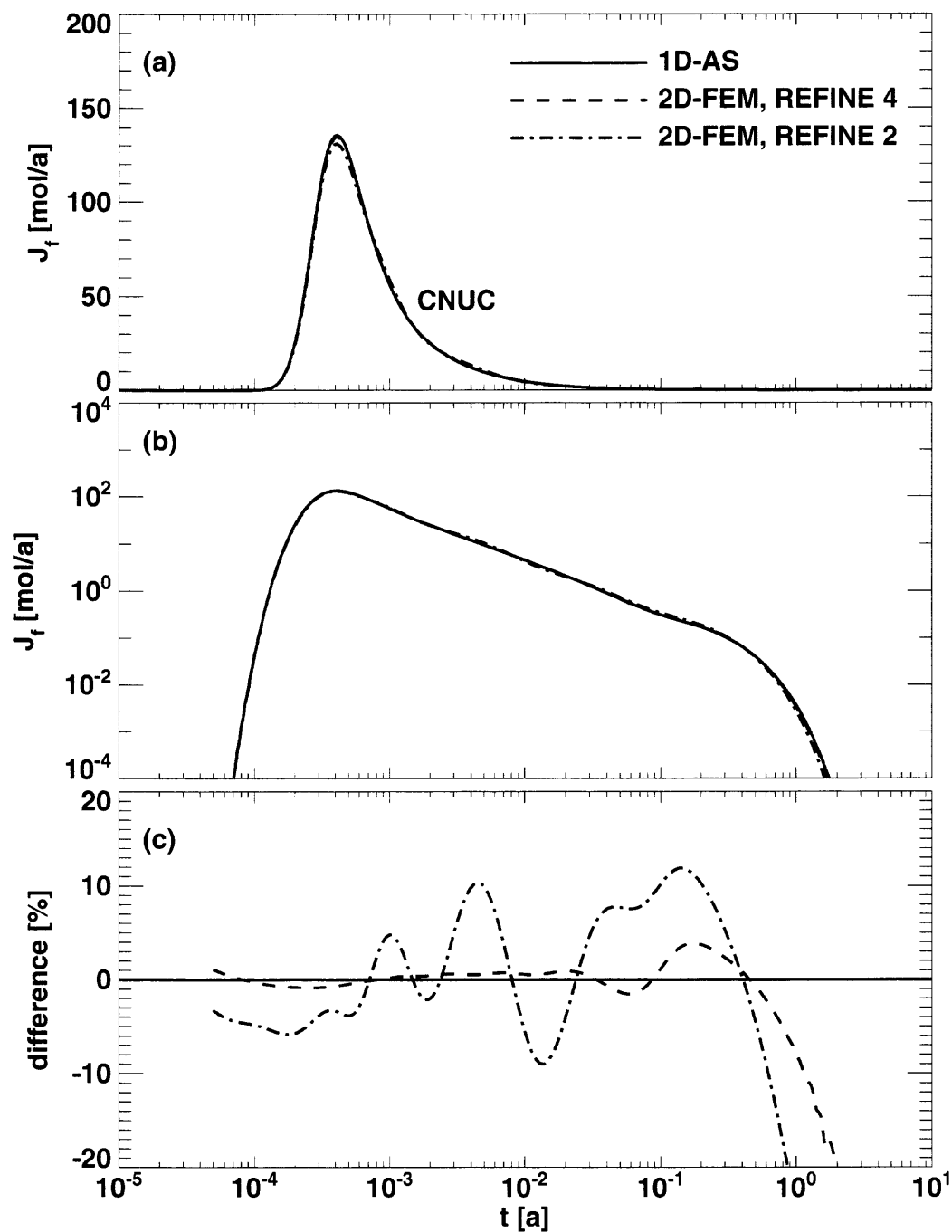


Figure 6.10. Hypothetical variation of the Grimsel uranium dipole experiment for a nuclide decay chain and the weakly two-dimensional rock matrix geometry of Figure 6.6. Presented is the nuclide CNUC of the decay chain $\text{ANUC} \rightarrow \text{BNUC} \rightarrow \text{CNUC}$. A δ -function source of the parent ANUC is considered. The nomenclature is as in Figure 6.2.

6.3. Test of Finite-Element Mesh Refinement

In this subsection we investigate in more detail the effect of **refinement of the finite-element mesh** in PICNIC (compare section 2.4.3) for **single nuclides** in a **single leg**. Different nuclides are considered for the Kristallin-I reference case, compare section 4.4.1. A constant nuclide source and the zero-concentration leg outlet boundary condition are considered. The constant source is entered to PICNIC as a top-hat release of $1[\text{mol/a}]$ over $10^8[\text{a}]$, which is larger than the timescales of interest. Considering a constant source is in particularly desirable, because, in the long time limit, it gives the steady-state release, which is considered extensively in the verification for more complex rock matrix geometries.

In Figure 6.11 the release curve for the nuclide ^{79}Se is calculated using the 2D-FEM with the standard finite-element mesh “REFINE 2” (dash-dotted lines) and an increased refinement “REFINE 3” (dashed lines) for the geometry of Figure 6.1. For comparison, this situation is also calculated using the 1D-AS option (solid lines). Figure 6.11c gives the absolute value of the relative difference function of the 2D-FEM results with respect to the 1D-AS result.

The effect of a further refined mesh is analysed in Figure 6.12 for the options REFINE 4 and REFINE 5 and in Figure 6.13 for the options REFINE 6 and REFINE 7. All these 2D-FEM calculations show similar behaviour. For early times, the increase of the release curves is slightly later than for the 1D-AS result. Between about 50000 and 100000 [a] the 2D-FEM results slightly overshoot the 1D-AS result. In the steady-state limit, the 2D-FEM results are again slightly below the 1D-AS result.

The agreement with the 1D-AS result improves with increased refinement from the REFINE 2 result up to the REFINE 5 result. It then stagnates or even deteriorates for REFINE 6 and REFINE 7. Considering the steady-state behaviour⁶⁰, the REFINE 2 result differs by only about 0.03% from the 1D-AS result; this reduces to only about 0.01% for REFINE 4 and 0.008% for REFINE 5. However, only 1/3 of the ^{79}Se nuclide decays in the leg. Thus the effect of radioactive decay is only moderate for this nuclide.

⁶⁰ Note that, in the steady-state, the “analytical” 1D-AS option produces the exact result within six to seven digits accuracy, cf. section 4.

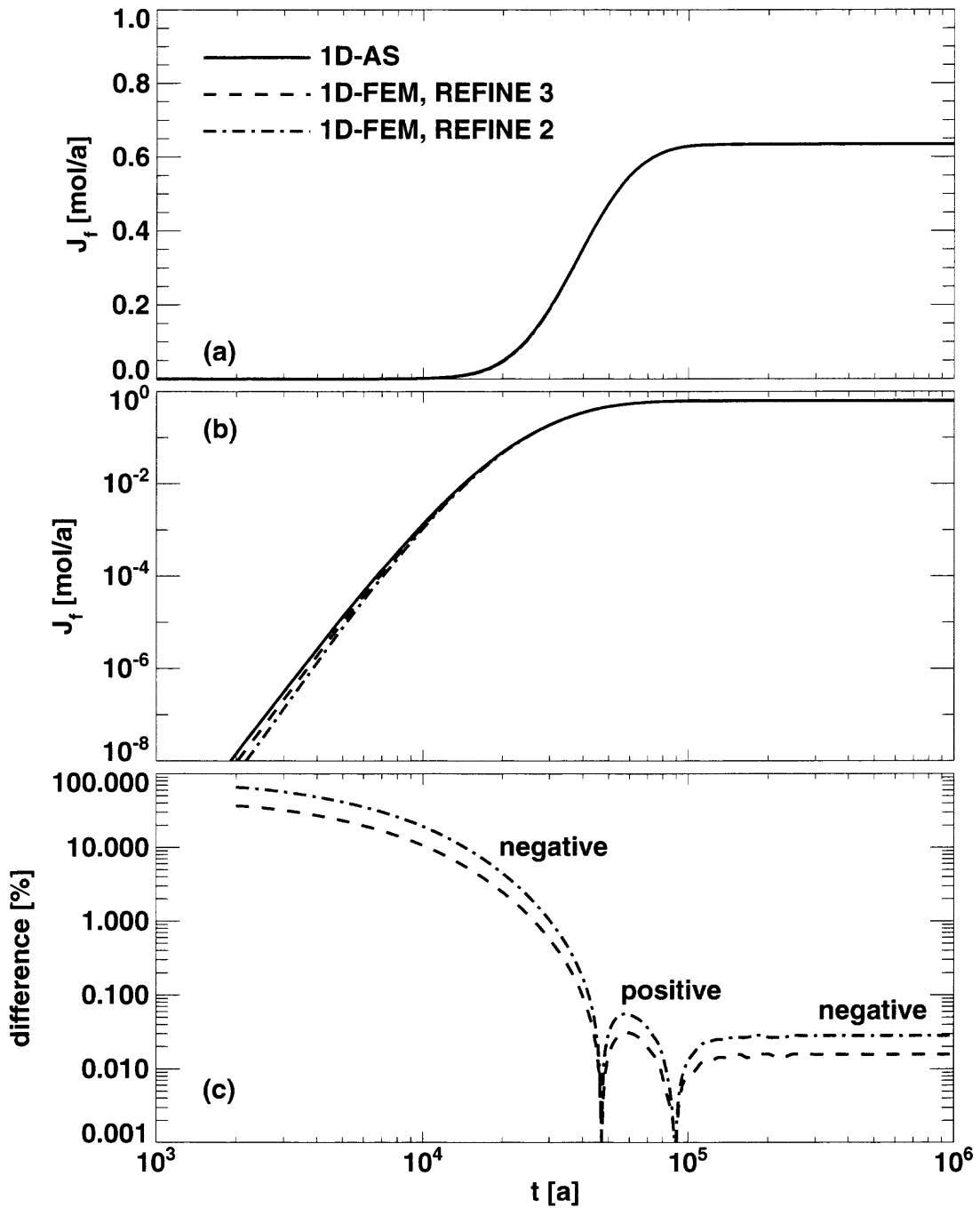


Figure 6.11. The result of a PICNIC calculation for the release of ^{79}Se using the (finite-element) 2D-FEM option with standard resolution "REFINE 2" (dash-dotted lines) and increased refinement "REFINE 3" (short-dashed lines) is compared to the respective PICNIC result for the ("analytical") 1D-AS option (solid lines). A constant source is considered. The release curves are given in (a) on a linear scale and in (b) on a logarithmic scale. The relative difference functions with respect to the 1D-AS result are given in (c).

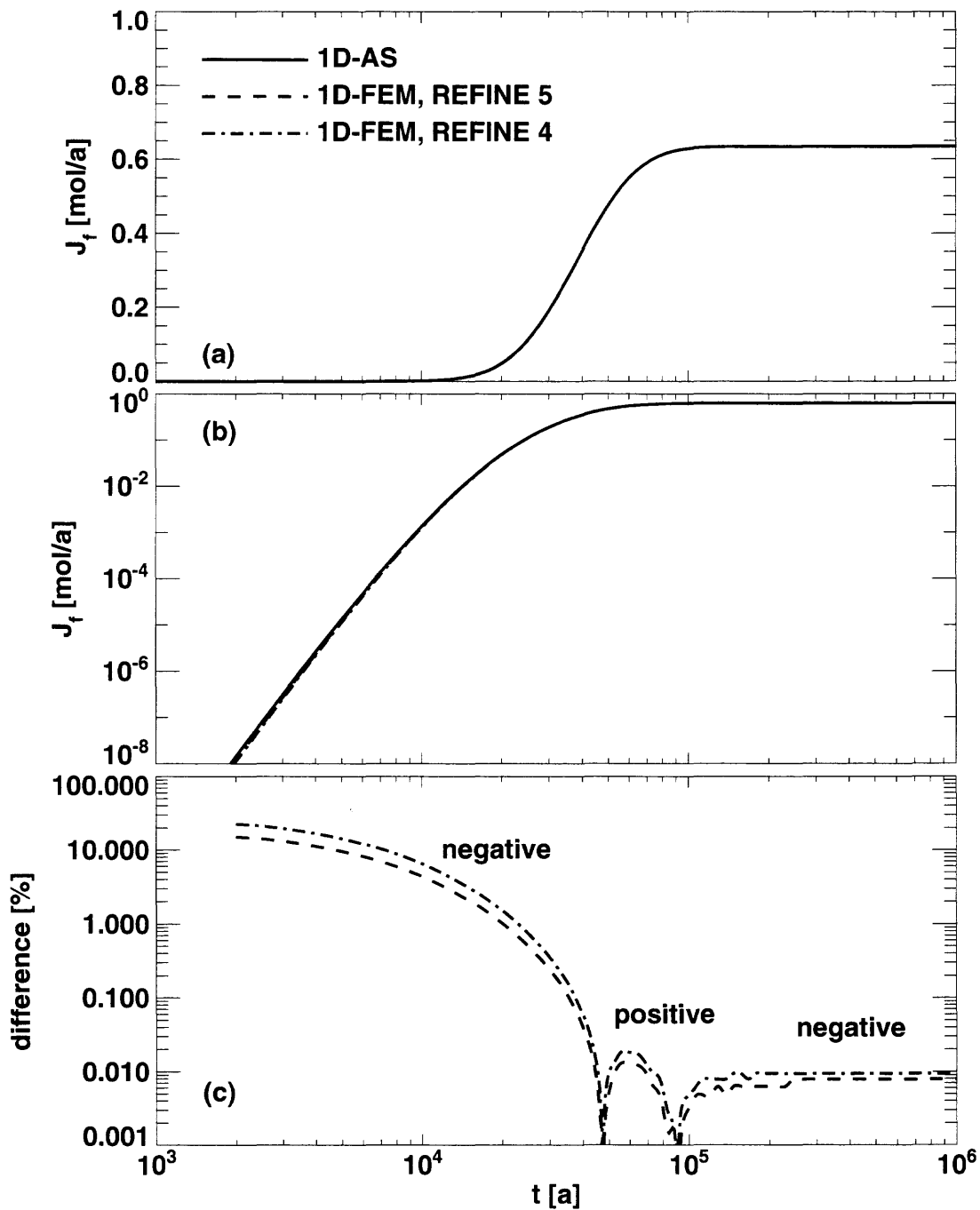


Figure 6.12. The result of a PICNIC calculation for the release of ^{79}Se using the (finite-element) 2D-FEM option with refinements "REFINE 4" (dash-dotted lines) and "REFINE 5" (short-dashed lines) are compared to the respective PICNIC result for the ("analytical") 1D-AS option (solid lines). A constant source is considered. The release curves are given in (a) on a linear scale and in (b) on a logarithmic scale. The relative difference functions with respect to the 1D-AS result are given in (c).

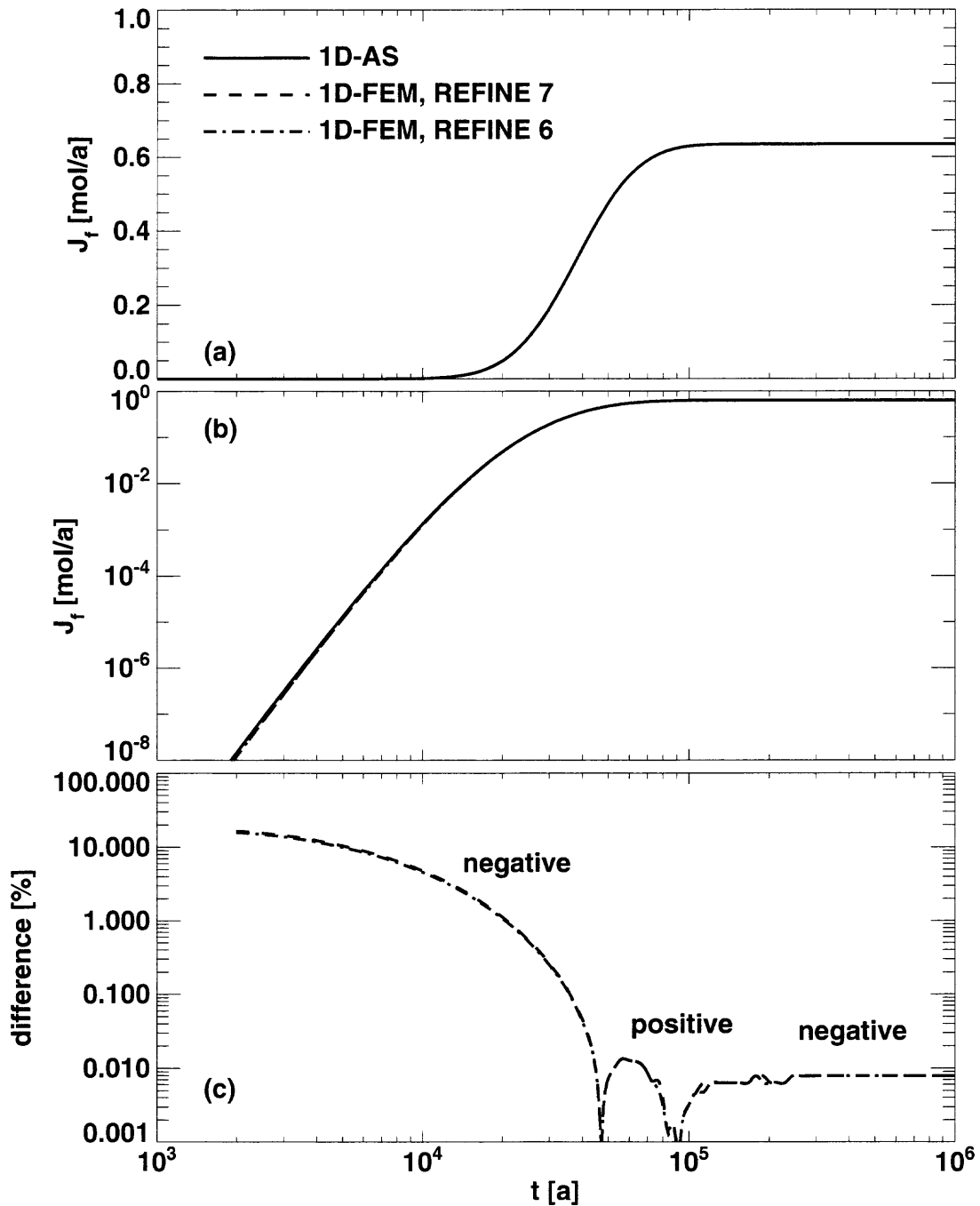


Figure 6.13. The result of a PICNIC calculation for the release of ^{79}Se using the (finite-element) 2D-FEM option with refinements "REFINE 6" (dash-dotted lines) and "REFINE 7" (short-dashed lines) are compared to the respective PICNIC result for the ("analytical") 1D-AS option (solid lines). A constant source is considered. The release curves are given in (a) on a linear scale and in (b) on a logarithmic scale. The relative difference functions with respect to the 1D-AS result are given in (c).

For a stronger effect of radioactive decay, we now consider (for the same situation) the nuclide ^{99}Tc , where only 0.9% of the nuclide survives the leg and 99% decays. Thus ^{99}Tc can be denoted as a “strongly decaying” nuclide. For this situation, the **inaccuracies in the rock matrix response are strongly amplified** as a consequence⁶¹ of the exponential functions in the leg response functions (see sections 2.1.7 and 2.3).⁶² For ^{99}Tc we consider in Figure 6.14 the 2D-FEM results for REFINE 2 and REFINE 3, in Figure 6.15 the results for REFINE 4 and REFINE 5, and in Figure 6.16 the results for REFINE 6 and REFINE 7. The overall forms of the release curves are still in very good agreement, while the amplitudes of the relative difference functions are considerably increased with respect to the “weakly decaying” ^{79}Se . The results for all 2D-FEM calculations are now below the 1D-AS result for all times. For all values of the REFINE parameter, the relative difference functions decrease with time until steady-state release is reached. As for ^{79}Se , the agreement with the 1D-AS result improves from REFINE 2 to REFINE 5, while it stagnates or even deteriorates for REFINE 6 and REFINE 7. For the steady-state release, the REFINE 2 result is about 4% below the 1D-AS result, while the difference is about 1.8% for the REFINE 4 result and about 1.2% for the REFINE 5, REFINE 6 and REFINE 7 results.

Overall, this shows that, for such performance assessment calculations, the standard option REFINE 2 is a good choice, while for improved accuracy the option REFINE 4 is the optimum choice. The comparison of the release of ^{79}Se with the ^{99}Tc case and also with the Grimsel cases shows that we should expect a different accuracy of the PICNIC FEM calculations for different nuclides and different situations.

⁶¹ Consider also the increased concentration gradients in the rock matrix.

⁶² Because of the small values evidently the absolute errors decrease, but the relative errors increase.

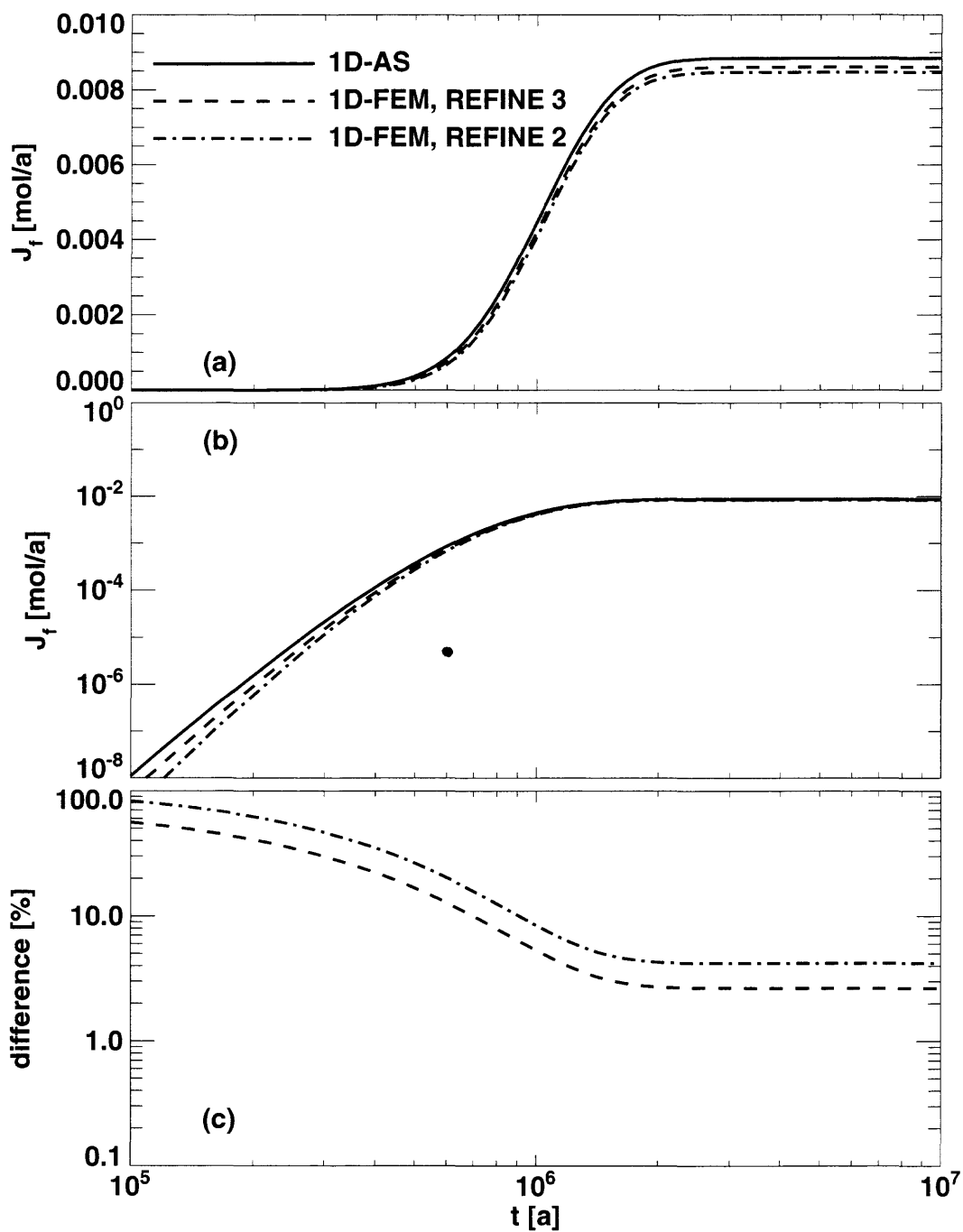


Figure 6.14. The result of a PICNIC calculation for the release of ^{99}Tc using the (finite-element) 2D-FEM option with standard refinement “REFINE 2” (dash-dotted lines) and increased refinement “REFINE 3” (short-dashed lines) is compared to the respective PICNIC result for the (“analytical”) 1D-AS option (solid lines). A constant source is considered. The release curves are given in (a) on a linear scale and in (b) on a logarithmic scale. The relative difference functions with respect to the 1D-AS result are given in (c).

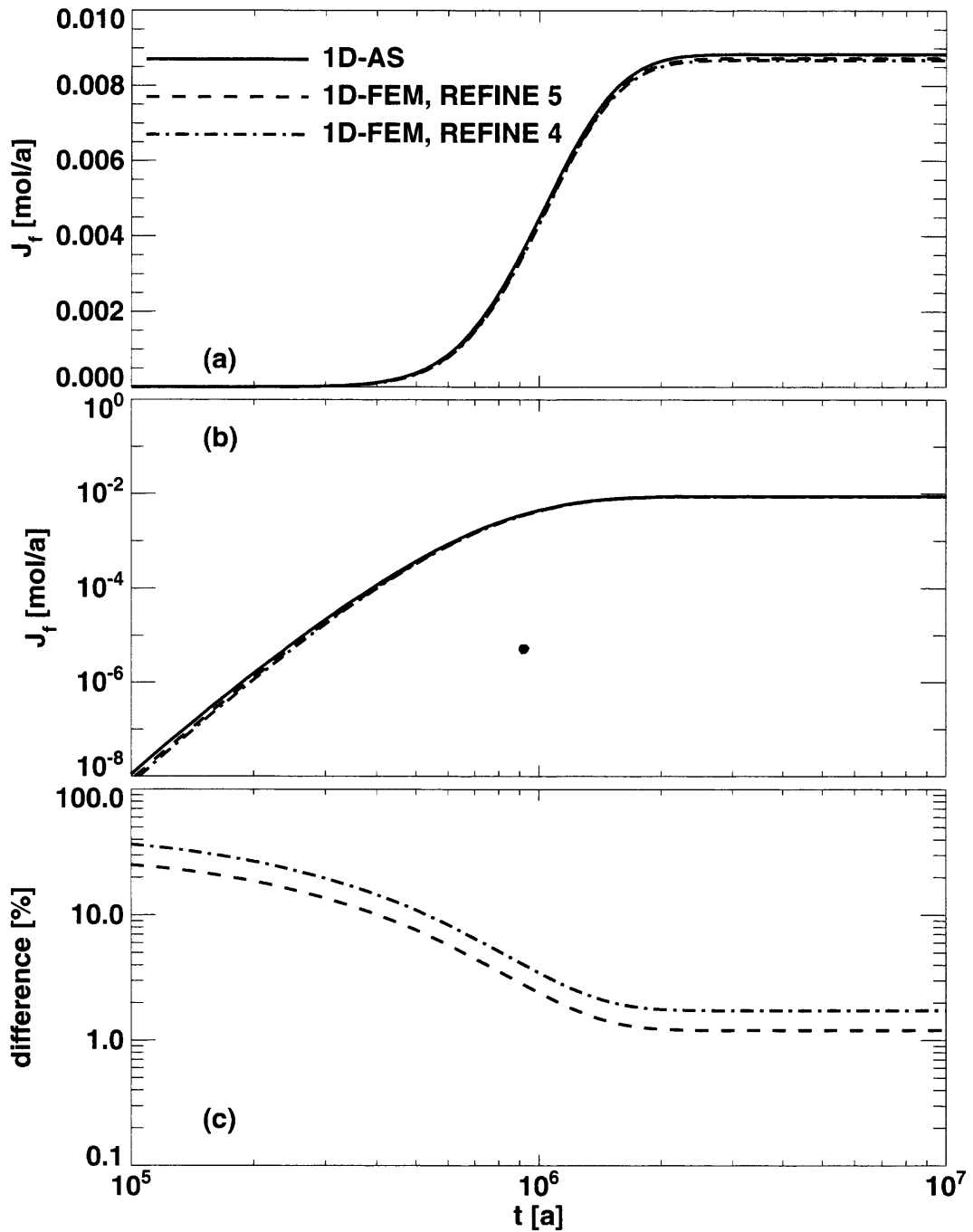


Figure 6.15. The result of a PICNIC calculation for the release of ^{99}Tc using the (finite-element) 2D-FEM option with the refinements “REFINE 4” (dash-dotted lines) and “REFINE 5” (short-dashed lines) are compared to the respective PICNIC result for the (“analytical”) 1D-AS option (solid lines). A constant source is considered. The release curves are given in (a) on a linear scale and in (b) on a logarithmic scale. The relative difference functions with respect to the 1D-AS result are given in (c).

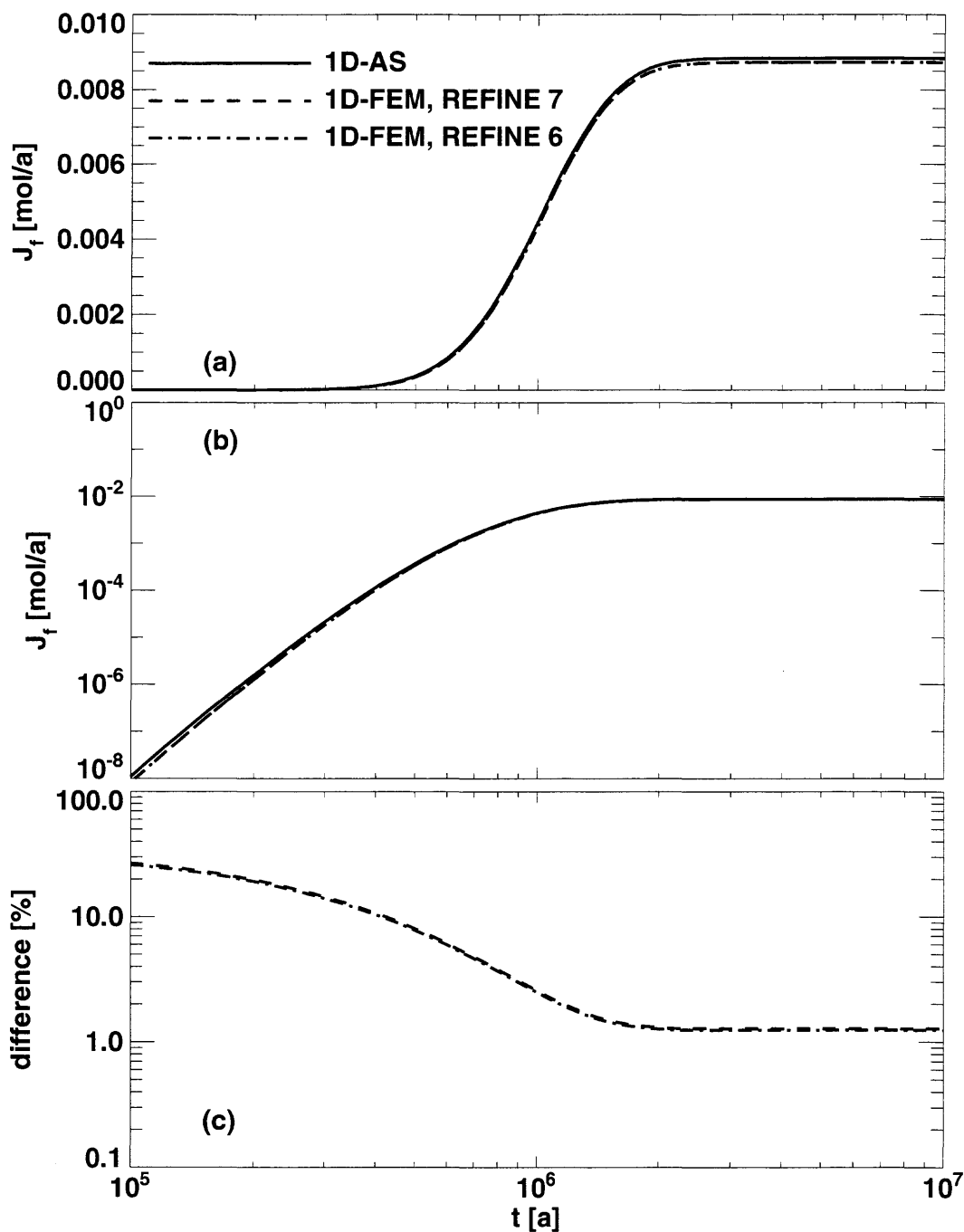


Figure 6.16. The result of a PICNIC calculation for the release of ^{99}Tc using the (finite-element) 2D-FEM option with the refinements “REFINE 6” (dash-dotted lines) and “REFINE 7” (short-dashed lines) are compared to the respective PICNIC result for the (“analytical”) 1D-AS option (solid lines). A constant source is considered. The release curves are given in (a) on a linear scale and in (b) on a logarithmic scale. The relative difference functions with respect to the 1D-AS result are given in (c).

6.4. Test of Multiple Rock Matrix Layers

In this subsection we investigate how PICNIC deals with the **subdivision of rock matrix layers**. This also tests how PICNIC deals with multiple, (here **two**) **rock matrix layers**, with the same properties. As a test case we again consider the variation of the Kristallin-I reference case with a constant source.

The rock matrix geometry of Figure 6.1 is again approximated by the weakly two-dimensional rock matrix geometry of Figure 6.17 to force PICNIC to generate a two-dimensional finite-element mesh for the calculation of the rock matrix response. For this geometry a fracture is considered that consists of an area of flowing water (F) of width $2B = 0.1$ [m] and a small part of width $2d_y = 2 \cdot 10^{-5}$ [m] with (nearly) impermeable rock (M0). Because PICNIC at present does not allow perfectly impermeable rock, M0 is defined here as a rock matrix where both porosity ϵ_p and rock density ρ_p are a factor of 10^{15} smaller than in the rock matrix type M1, which implies⁶³ that the retardation factor R_p is about the same as for M1. The aperture of the fracture is $2b = 10^{-3}$ [m] and, below and above the fracture, two layers of accessible rock matrix (both type M1) of thickness $h_1 = 0.02$ [m] and $h_2 = 0.0295$ [m] are situated. The choice of the value of d_y relative to d and B leads to physically nearly the same behaviour as considered with the 1D-AS.

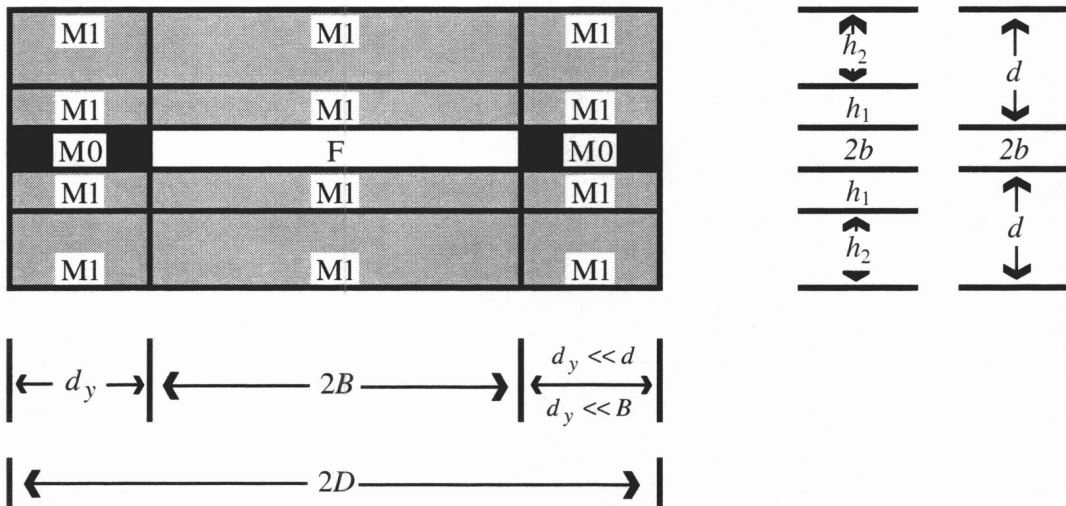


Figure 6.17. Sketch of the cross-section of a leg with a fracture that is mainly filled with an area of flowing water (F) of width $2B$ and, to the left and right of F, with small stripes of (nearly) impermeable rock matrix (M0) of width d_y . The sketch is not to scale. The width of the fracture is $2D$ and the aperture is $2b$. Below and above the area of flowing water, two matrix layers are situated, which have the same properties (M1). The thicknesses of the rock layers are h_1 and h_2 , respectively.

⁶³ This makes it clear that the factor $1/\epsilon_p$ in the retardation factor R_p (equation 2.176) cannot correctly describe the physical behaviour for an extremely small available rock matrix porosity ϵ_p .

Figure 6.18 gives the release curves for the 2D-FEM results for the two-layer rock matrix of Figure 6.17 for ^{79}Se (dash-dotted lines) and compares these to the 1D-AS result (solid lines). For comparison, the release curve for physically the same situation is given (dashed lines), but considering the rock matrix below and above the fracture as one rock layer of thickness $d = h_1 + h_2$ depicted in Figure 6.6. The relative difference function (dashed line in Figure 6.18c) of the single-layer result with respect to the 1D-AS result has the same magnitude and nearly the same form as already observed in Figure 6.11 for the rock type of Figure 6.1. Thus, considering the side-columns of width d_y has no adverse influence on the accuracy of the PICNIC result.

Also using the two-layer rock matrix (dash-dotted lines in Figure 6.18) has no adverse influence on the PICNIC results. On the contrary, this representation of the rock matrix clearly improves the PICNIC results. The 2D-FEM result is now consistently below the 1D-AS result. The relative difference function is, for all times considered, within 10% and decreases monotonically with time (apart from some small wiggles). For early times up to $t = 10^{-4}$ [a], the relative difference function is more than 10 times smaller than for the calculation with the single rock layer (dashed lines). Also the agreement with the 1D-AS result for the steady-state release increases by a factor of 3, such that the difference is only 0.01%.

Analysing the same situation in Figure 6.19 for the REFINE 4 option shows similar behaviour with an improved accuracy. The relative difference function (dashed line in Figure 6.19c) for the single-layer rock matrix with respect to the 1D-AS result decreases by a factor of 1.5 to 3 and is now within 20% for all times. The overshooting at $t \approx 6 \cdot 10^{-4}$ [a] is now below 0.001% and the agreement for the steady-state release is now within 0.02%. Again, the calculation for the two-layer representation of the rock matrix (dash-dotted lines) is much more accurate than the single-layer result. The agreement with the 1D-AS result is now within 3% for all times considered. However, the agreement for the steady-state release does not improve with respect to the REFINE 2 option and is still 0.01%.⁶⁴

We also consider the strongly decaying nuclide ^{99}Tc for the same rock types and using the options REFINE 2 (Figure 6.20) and REFINE 4 (Figure 6.21). As for ^{79}Se , the calculations for the single-layer rock type (dashed lines) agree almost perfectly with the results for the rock type without the side columns of widths d_y ; compare dashed lines in Figures 6.20 and 6.21 with dash-dotted lines in Figures 6.14 and 6.15. As for ^{79}Se the accuracy of the two-layer rock type (dash-dotted lines in Figures 6.20 and 6.21) is much better than the single-layer rock type. This means that the relative difference to the 1D-AS result is, for the option REFINE 2, within 10% for all times. Thus, it is reduced by a factor of 10 and more when compared to the single-layer case. For the steady-state release, the agreement with the 1D-AS result is now within 0.3%.

For the option REFINE 4 the two-layer rock type result also agrees about by a factor of 10 better with the 1D-AS result than the single-layer rock type result and is within 5% for all times considered. For the steady-state, the agreement with the 1D-AS result is now within 0.15%.

⁶⁴ Thus one might speculate that at least part of this very small difference is physically based on the additional rock matrix columns of widths $d_y = 10^{-5}$ [m], see Figure 6.17.

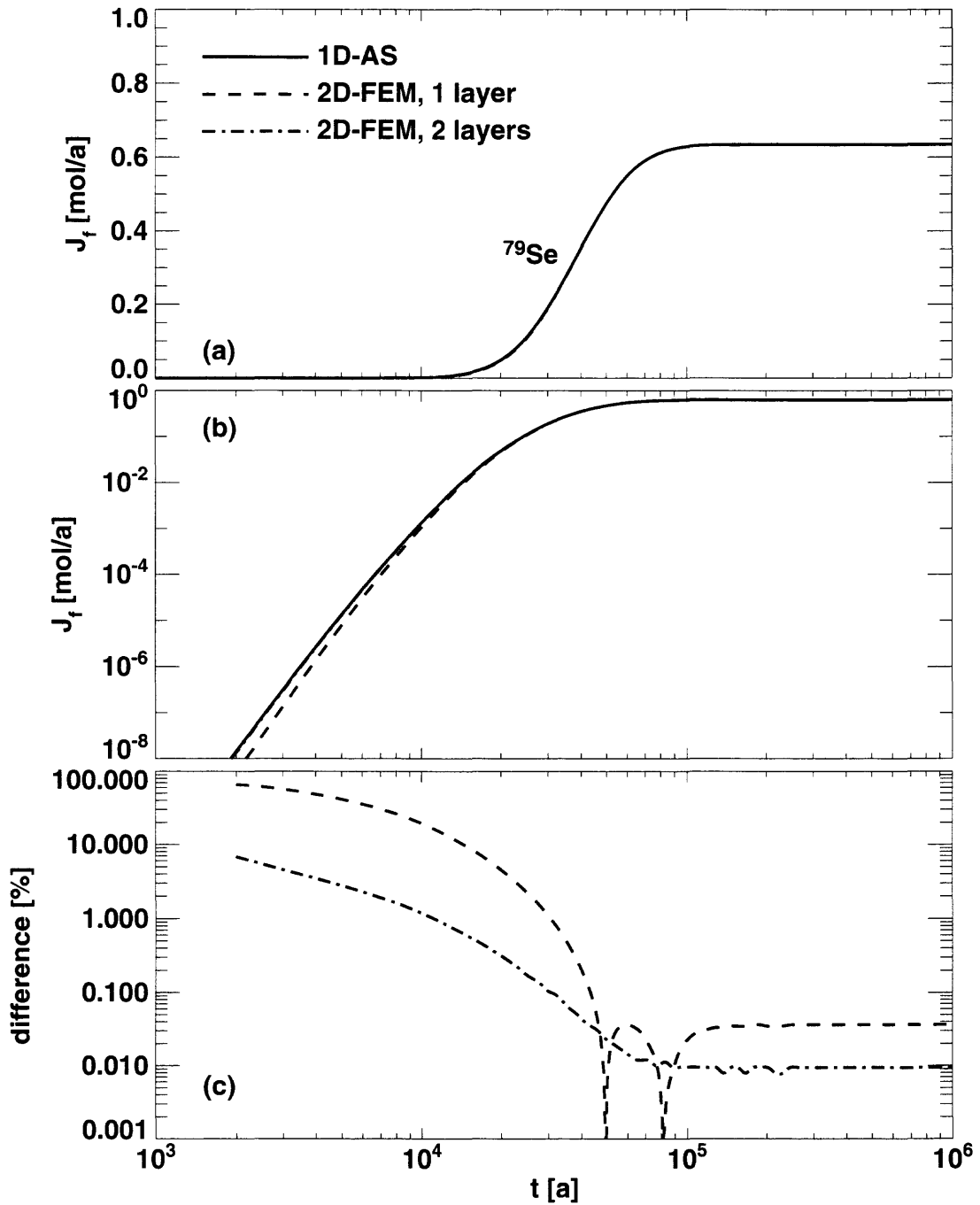


Figure 6.18. Kristallin-I reference case for ^{79}Se and a constant source. The release curves for the two-layer matrix geometry of Figure 6.17 (dash-dotted lines) and the single-layer matrix geometry of Figure 6.6 (dashed lines), both using the standard resolution “REFINE 2” and $d_y = 10^{-5}$ [m], are compared to the 1D-AS result (solid lines). The release curves are given in (a) on a linear scale and in (b) on a logarithmic scale. The relative difference functions with respect to the 1D-AS result are given in (c).

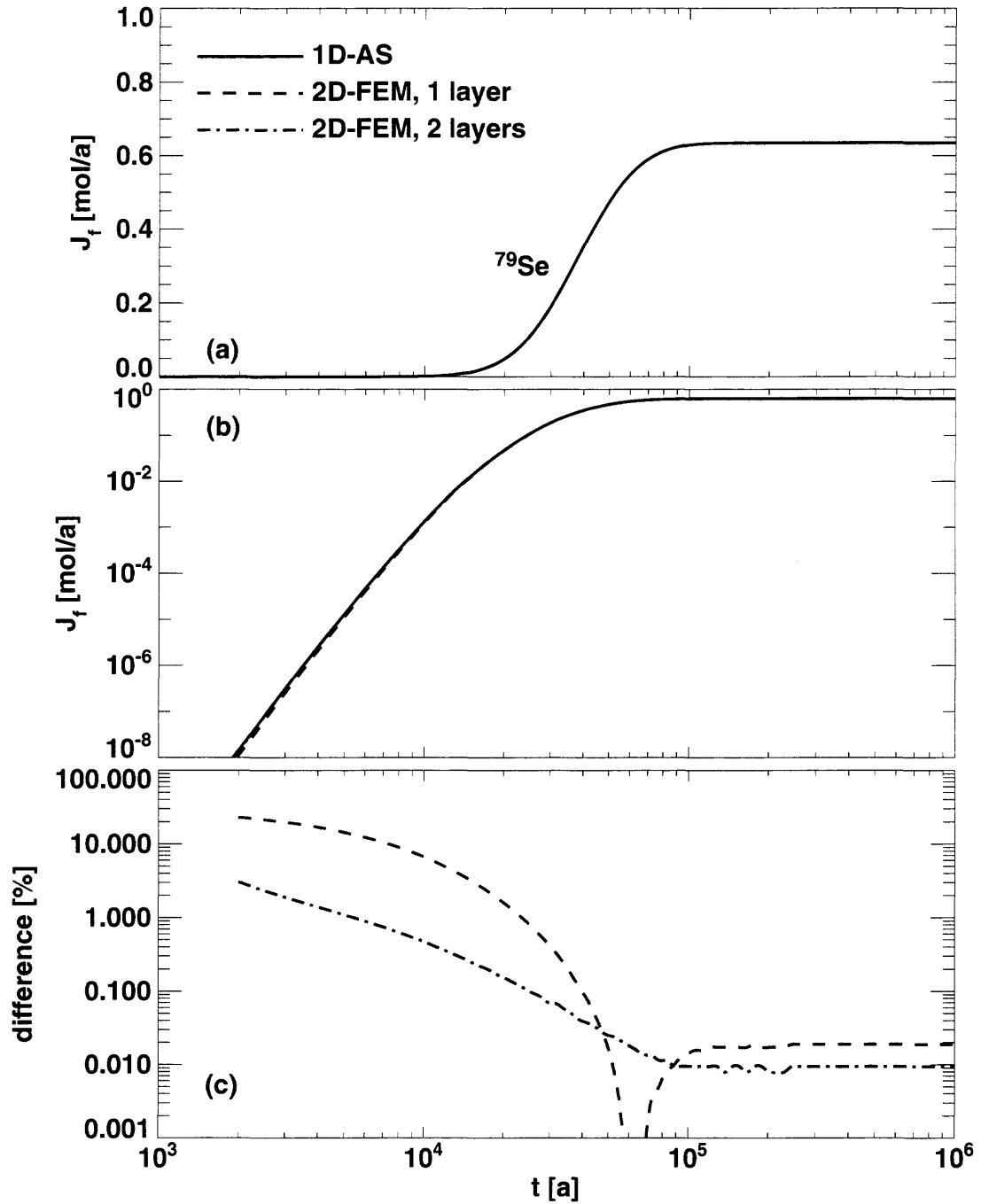


Figure 6.19. Kristallin-I reference case for ^{79}Se and a constant source. The release curves for the two-layer matrix geometry of Figure 6.17 (dash-dotted lines) and the single-layer matrix geometry of Figure 6.6 (dashed lines), both using the increased refinement “REFINE 4” and $d_y = 10^{-5}$ [m], are compared to the 1D-AS result (solid lines). The release curves are given in (a) on a linear scale and in (b) on a logarithmic scale. The relative difference functions with respect to the 1D-AS result are given in (c).

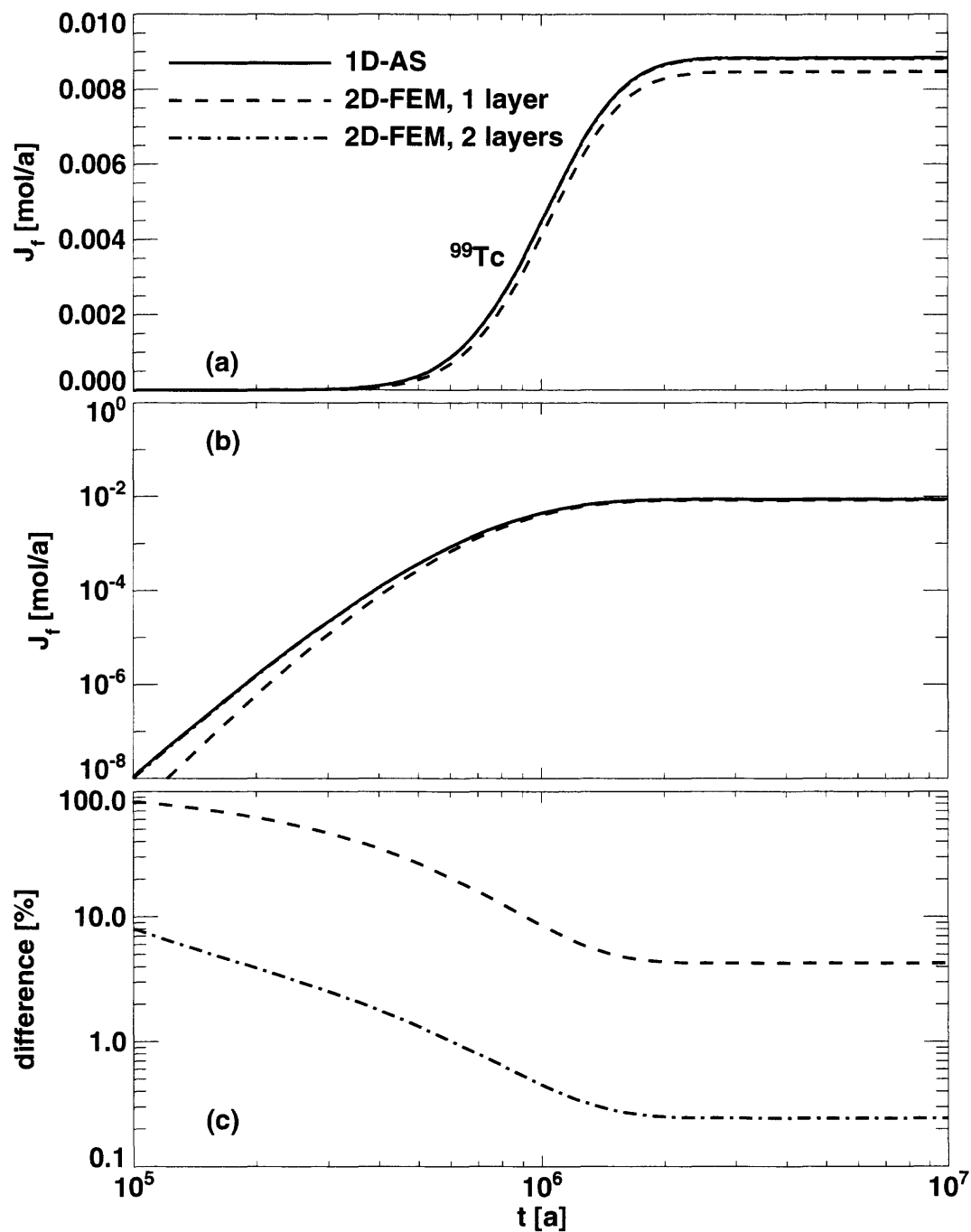


Figure 6.20. Kristallin-I reference case for ^{99}Tc and a constant source. The release curves for the two-layer matrix geometry of Figure 6.17 (dash-dotted lines) and the single-layer matrix geometry of Figure 6.6 (dashed lines), both using the standard resolution “REFINE 2” and $d_y = 10^{-5}$ [m], are compared to the 1D-AS result (solid lines). The release curves are given in (a) on a linear scale and in (b) on a logarithmic scale. The relative difference functions with respect to the 1D-AS result are given in (c).

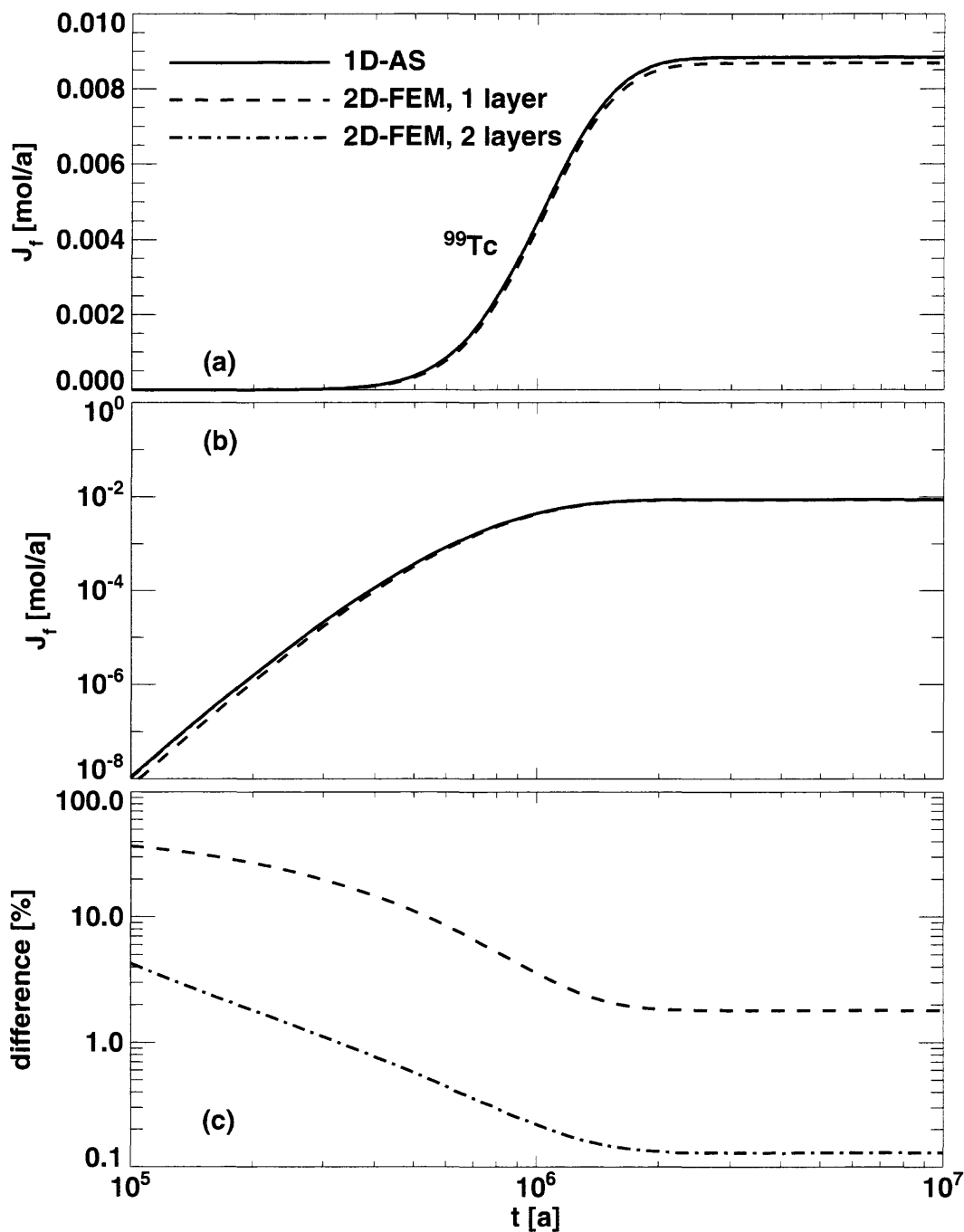


Figure 6.21. Kristallin-I reference case for ^{99}Tc and a constant source. The release curves for the two-layer matrix geometry of Figure 6.17 (dash-dotted lines) and the single-layer matrix geometry of Figure 6.6 (dashed lines), both using the increased refinement “REFINE 4” and $d_y = 10^{-5}$ [m], are compared to the 1D-AS result (solid lines). The release curves are given in (a) on a linear scale and in (b) on a logarithmic scale. The relative difference functions with respect to the 1D-AS result are given in (c).

To conclude, the subdivision of the rock matrix into layers appears to be highly beneficial to the accuracy of PICNIC. The reason behind this is an efficient refinement at the interface of different rock layers of the mesh for the calculation of the rock matrix response, compare section 2.4.3. The subdivision, together with the mesh refinement, is much more efficient than the internal REFINE option, at least for the test cases considered. This leads to the questions (i) if and how the internal REFINE option could be improved, and (ii) if the construction of the finite-element mesh at the outer boundaries of the rock matrix is appropriate or could be improved with a reasonable effort.

6.5. Extremely Small Areas of Rock Matrix

To test if PICNIC can deal with **rock matrix areas of extremely different size**, the rock types of the Figures 6.6 and 6.17 are examined, but reducing the **column width** to the **extremely small** value $d_y = 10^{-15}$ [m]. Using the option REFINE 4, the release of ^{79}Se (Figure 6.22) and ^{99}Tc (Figure 6.23) is considered. PICNIC can also deal with this situation, but the accuracy is reduced. Moreover, the amount of nuclides which are transported through the leg reduces when the amount of rock matrix reduces - this qualitative behaviour of the numerical results is physically not correct. Interestingly, for ^{79}Se the two-layer rock matrix result shows overshooting (dash-dotted lines), and for ^{99}Tc the two-layer rock matrix result is worse⁶⁵ (7% difference from the 1D-AS result) than the single-layer calculation (dashed lines).

⁶⁵ Note that this effect is observed for extremely small values of d_y only, which are below $d_y = 10^{-12}$ [m] for the geometry considered.

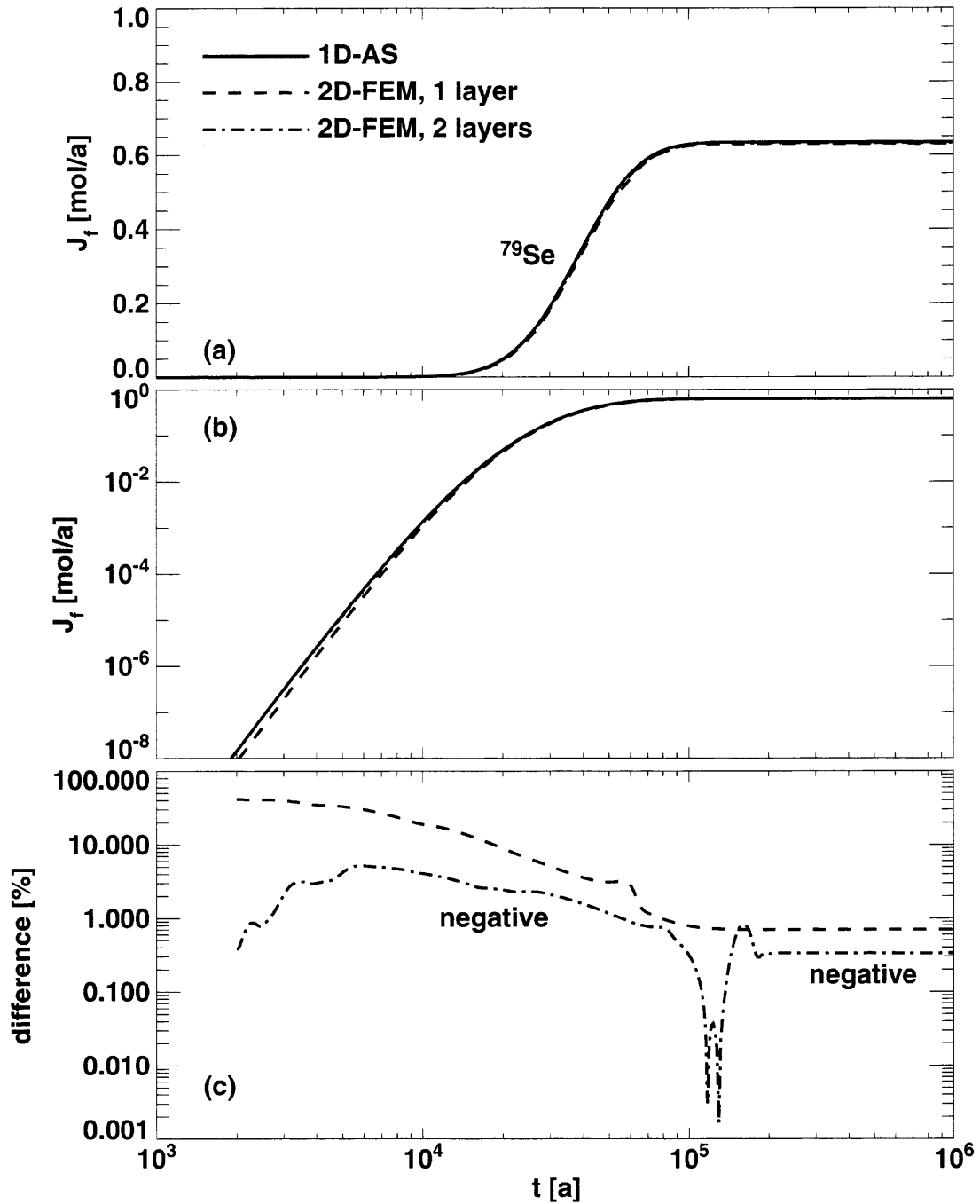


Figure 6.22. Kristallin-I reference case for ^{79}Se and a constant source. The release curves for the two-layer matrix geometry of Figure 6.17 (dash-dotted lines) and the single-layer matrix geometry of Figure 6.6 (dashed lines), both using the increased refinement “REFINE 4” and the extremely small $d_y = 10^{-15}$ [m], are compared to the 1D-AS result (solid lines). The release curves are given in (a) on a linear scale and in (b) on a logarithmic scale. The relative difference functions with respect to the 1D-AS result are given in (c).

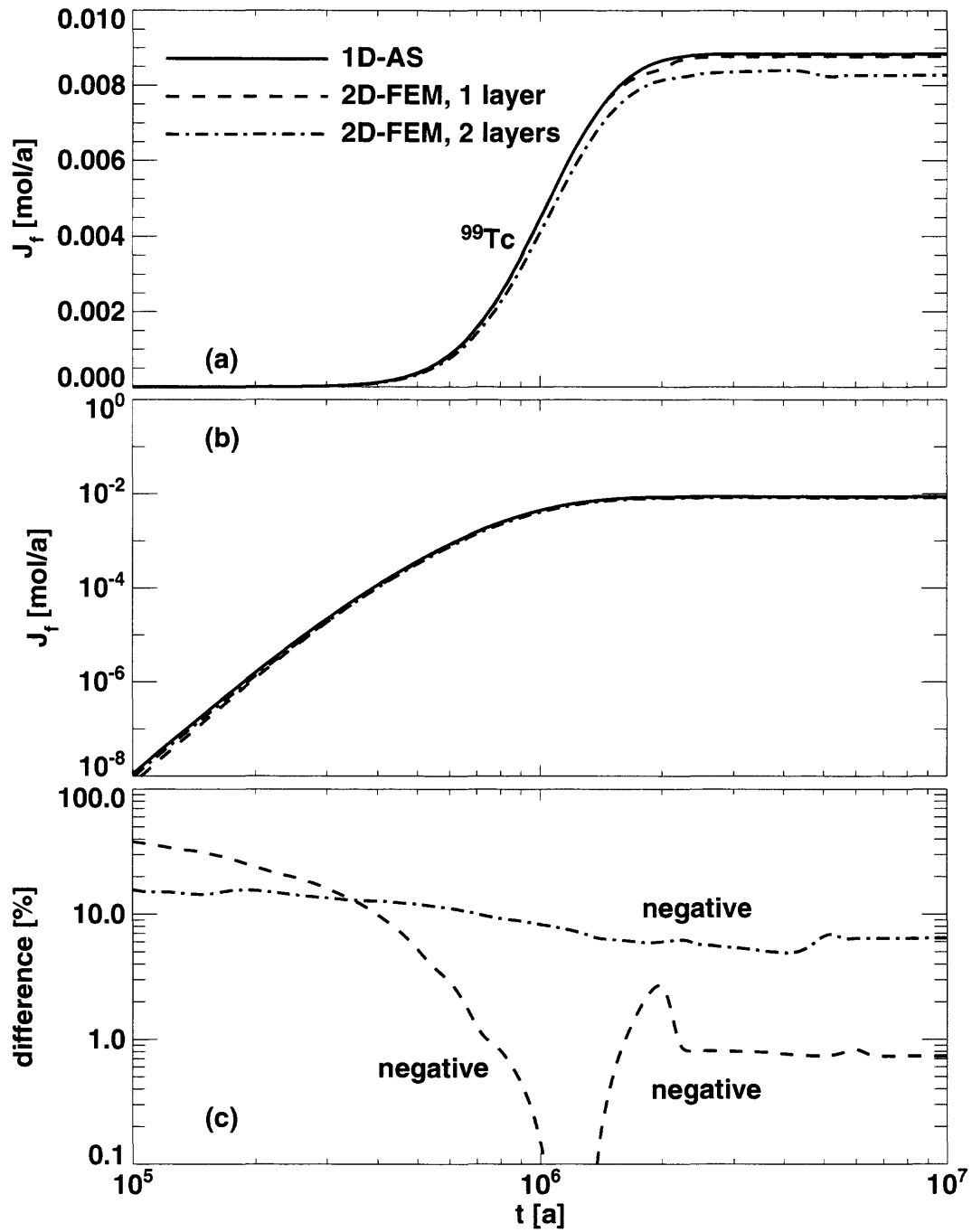


Figure 6.23. Kristallin-I reference case for ^{99}Tc and a constant source. The release curves for the two-layer matrix geometry of Figure 6.17 (dash-dotted lines) and the single-layer matrix geometry of Figure 6.6 (dashed lines), both using the increased refinement “REFINE 4” and the extremely small $d_y = 10^{-15}$ [m], are compared to the 1D-AS result (solid lines). The release curves are given in (a) on a linear scale and in (b) on a logarithmic scale. The relative difference functions with respect to the 1D-AS result are given in (c).

To check if the reason for the decreasing accuracy is mainly based on the extremely different properties of the rock matrix types M0 and M1, we consider a leg cross-section where the area of flowing water is in contact with rock matrix type M1 only. We compare, for a single-layer rock matrix, the geometry of Figure 6.24.⁶⁶ To test also a two-layer rock matrix, we subdivide the rock layer of thickness d into two rock layers of thickness h_1 and h_2 , see Figure 6.25.

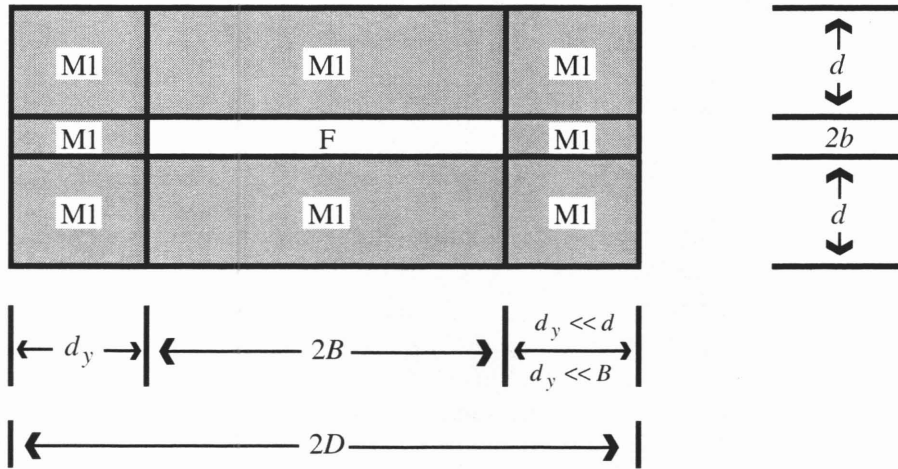


Figure 6.24. Sketch of the cross-section of a leg with a fracture that is mainly filled with an area of flowing water (F) of width $2B$ and, to the left and right of F, with small stripes of rock matrix type M1. The sketch is not to scale. The width of the fracture is $2D$ and the aperture is $2b$. Below and above the fracture, a rock matrix layer also of type M1 is situated. The thickness of the rock layer is d . Thus the area of flowing water is in contact with rock matrix of the type M1 only.

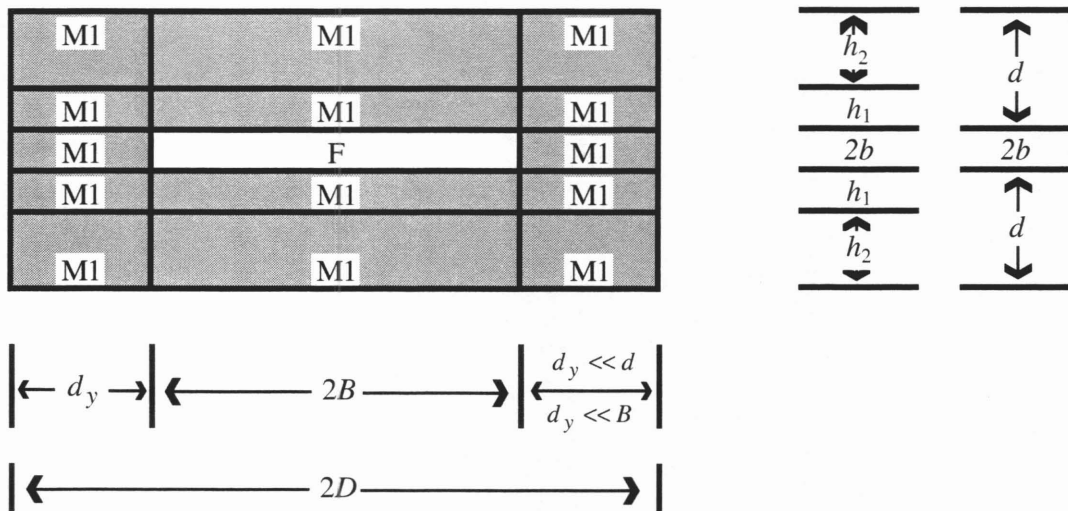


Figure 6.25. Sketch of the cross-section of a leg with a fracture that is mainly filled with an area of flowing water (F) of width $2B$ and, to the left and right of F, with small stripes of rock matrix type M1. The sketch is not to scale. The width of the fracture is $2D$ and the aperture is $2b$. Below and above the fracture, two matrix layers are situated, which have the same properties M1. The thicknesses of the rock layers are h_1 and h_2 , respectively.

⁶⁶ Compared to Figure 6.6, the matrix type M0 in the fracture is replaced by rock matrix type M1.

For the geometries of Figures 6.24 and 6.25 we consider again the nuclides ^{79}Se (Figure 6.26) and ^{99}Tc (Figure 6.27) for the extremely small rock matrix column $d_y = 10^{-15}$ [m].⁶⁷ The standard option REFINE 2 is used. PICNIC can also deal with this situation, but again with reduced accuracy. For both, ^{79}Se and ^{99}Tc , the accuracy for the two-layer geometry (dash-dotted lines) is quantitatively better than for the single-layer geometry (dashed lines). The result for the single-layer geometry underestimates the nuclide release for all times, while the result for the two-layer geometry slightly underestimates the release for early times and overestimates it for the main part of the release curve. The effect that, for ^{99}Tc in the two-layer geometry (dash-dotted line in Figure 6.27c), the nuclide release does reach the steady-state, but increases again for late times $t \approx 10^7$ [a], could lead to misinterpretations in other applications.

Overall we can conclude that, from a quantitative and performance assessment point of view, extremely small columns of rock matrix do not lead to really serious problems for the geometries considered. However, there are some inconsistencies⁶⁸ and in later applications of PICNIC, especially for more complex rock matrix geometries and other parameter regions, extended test series will not always be performed. It might be possible that extremely small columns of rock matrix could overstrain the code. Thus they should be avoided in PICNIC calculations or, at least should be considered with increased care.

⁶⁷ For $d_y = 10^{-5}$ [m], PICNIC calculations for the geometries of Figures 6.24 and 6.25 give nearly the same results as for the geometries of Figures 6.6 and 6.17 presented in Figures 6.18 and 6.20.

⁶⁸ For the rock matrix geometries considered, extremely small means side column widths smaller than $d_y = 10^{-12}$ [m], which are fortunately far from the intended application range of PICNIC.

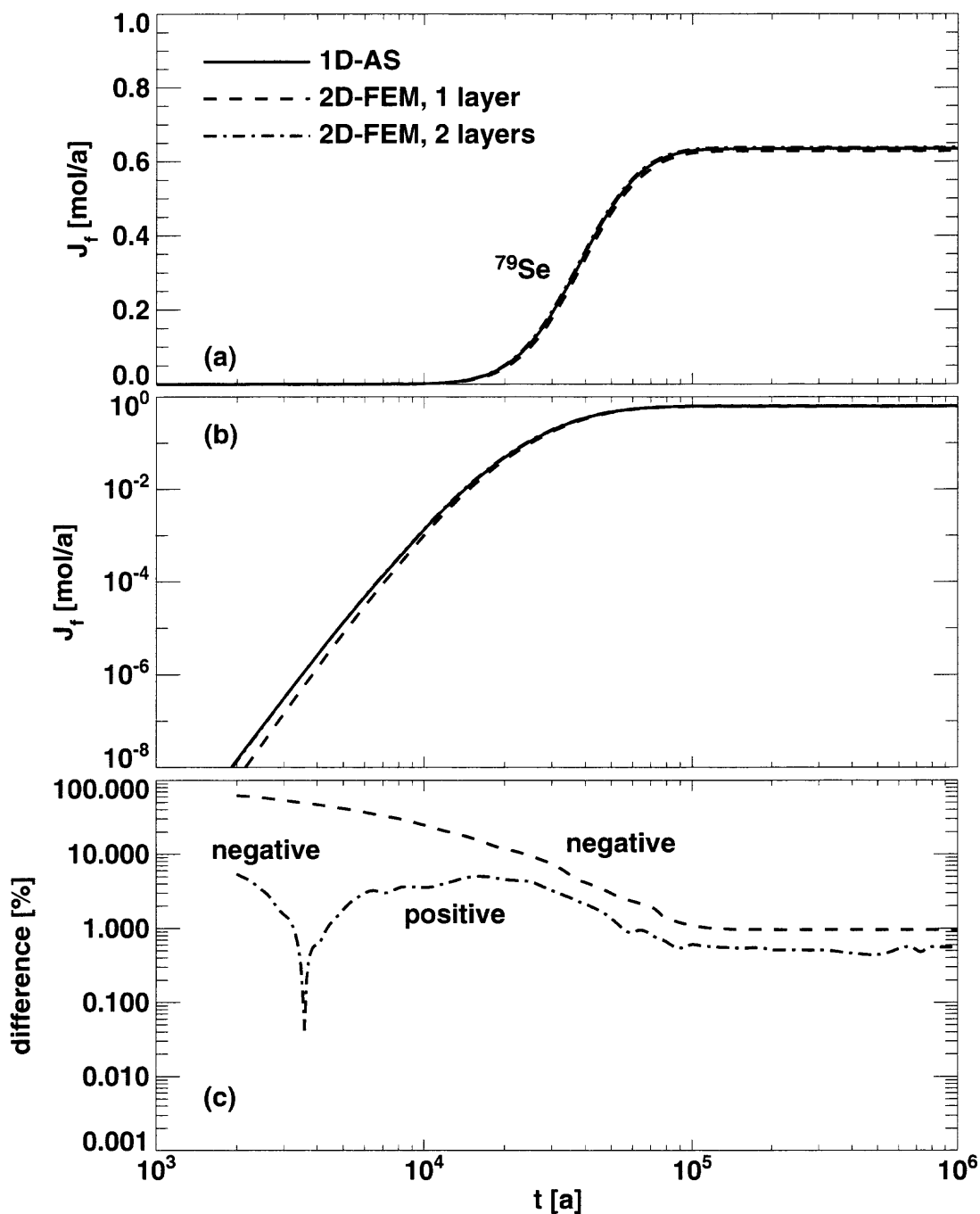


Figure 6.26. Kristallin-I reference case for ^{79}Se and a constant source. The release curves now for the two-layer matrix geometry of Figure 6.25 (dash-dotted lines) and the single-layer matrix geometry of Figure 6.24 (dashed lines), both using the standard refinement “REFINE 2” and the extremely small $d_y = 10^{-15}$ [m], are compared to the 1D-AS result (solid lines). The release curves are given in (a) on a linear scale and in (b) on a logarithmic scale. The relative difference functions with respect to the 1D-AS result are given in (c).

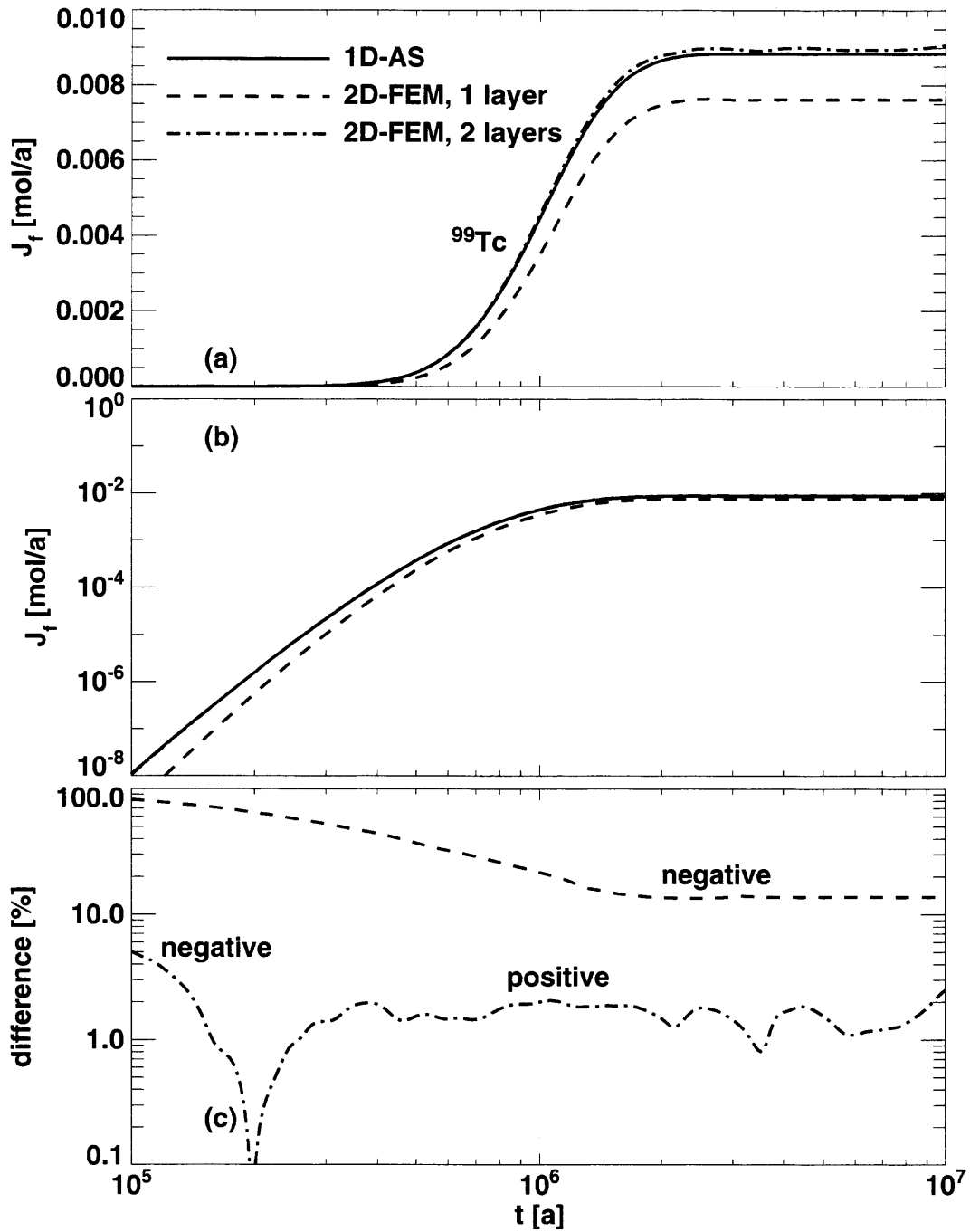


Figure 6.27. Kristallin-I reference case for ^{99}Tc and a constant source. The release curves for the two-layer matrix geometry of Figure 6.25 (dash-dotted lines) and the single-layer matrix geometry of Figure 6.24 (dashed lines), both using the standard refinement “REFINE 2” and the extremely small $d_y = 10^{-15}$ [m], are compared to the 1D-AS result (solid lines). The release curves are given in (a) on a linear scale and in (b) on a logarithmic scale. The relative difference functions with respect to the 1D-AS result are given in (c).

6.6. Transport in a Network

To test if the FEM together with transport in a **network** can be handled by PICNIC we use the 26-leg network with different rock matrices in different legs as the test case, see section 4.3.3. First we consider transport of a single non-decaying nuclide, compare Figure 4.25. The same parameters and source term are considered as specified in section 4.3.3.⁶⁹ However, we now use the 1D-FEM option for the calculation of the rock matrix response functions of the legs 10,11,12 (see Figure 6.28), which have a rock matrix geometry as sketched in Figure 6.1. The release for the standard mesh resolution “REFINE 2” is given in Figure 6.29 as dashed lines and is compared to the 1D-AS result (solid lines). The overall agreement for the nuclide release is good. Only the relative difference function (Figure 6.29c) is in the order of 10% in the maximum region, which is bigger than observed for the single leg case of Figure 6.2. As for the single leg test case, the 1D-FEM result is slightly retarded for early times with respect to the 1D-AS result. The typical oscillations of the relative difference function (dashed line in Figure 6.29c) already observed for the single leg case are within 15%.

For a refined finite-element mesh using the option REFINE 4 (dash-dotted lines), as expected we obtain a very good agreement within 3 to 5% with respect to the 1D-AS result for the relevant time domain. This is again slightly larger than for the single leg test case of Figure 6.2. Overall, the agreement with the 1D-AS result is however similar to the single leg cases.

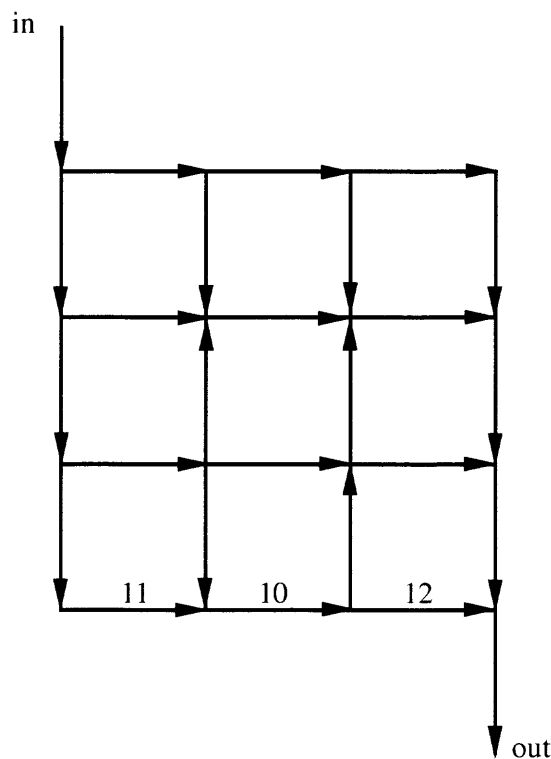


Figure 6.28. The legs 10, 11, 12 are indicated in the 26-leg network which is reproduced from Figure 4.24.

⁶⁹ Zero-gradient is again used as the boundary condition in each leg, and we use 129 Talbot points in the Laplace domain.

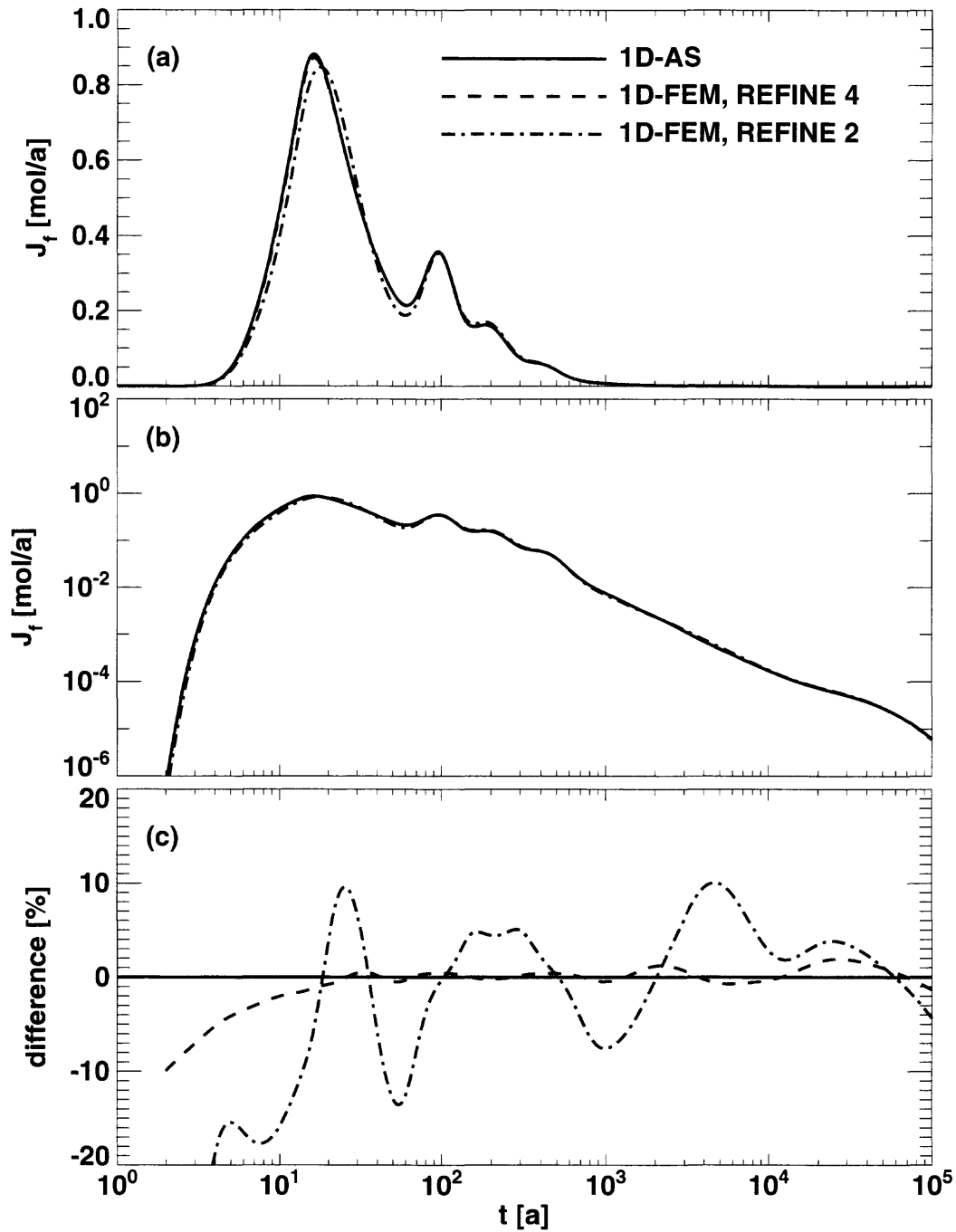


Figure 6.29. Transport of a non-decaying nuclide in a 26-leg network. The result of PICNIC calculations using the (finite-element) 1D-FEM option with standard resolution “REFINE 2” (dash-dotted lines) and increased refinement “REFINE 4” (short-dashed lines) for legs 10,11,12 are compared to the respective PICNIC result for the (“analytical”) 1D-AS option (solid lines), compare also Figure 4.25. The release curves are given in (a) on a linear scale and in (b) on a logarithmic scale. The relative difference functions with respect to the 1D-AS result are given in (c).

In the next step the transport of the **nuclide decay chain** $\text{ANUC} \rightarrow \text{BNUC} \rightarrow \text{CNUC} \rightarrow$ (see section 4.3.3 and Figures 4.26-4.28) in the 26-leg network is considered for the rock matrix geometries mentioned above. The accuracy of the parent ANUC (Figure 6.30) shows a similar form and oscillations as in the non-decaying case (Figure 6.29). As for the single leg test case (Figure 6.3), the relative difference functions with respect to the 1D-AS result are slightly increased, for both options REFINE 2 and REFINE 4.

The accuracy of the daughter BNUC (Figure 6.31) is in the same order as ANUC. This holds also for CNUC (Figure 6.32), consider particularly the relative difference functions in the time domain between 1 [a] and 1000 [a] in parts (c) of the Figures 6.30 to 6.32. The relative difference functions in this time range are reproduced for illustration in Figure 6.33 to show their similarity.

To conclude, the FEM option in PICNIC for the homogeneous one-dimensional planar rock matrix geometry of Figure 6.1 appears to work correctly also for transport in a network, both for a single nuclide and a nuclide decay chain. The standard REFINE 2 result should be sufficiently accurate for most performance assessment applications. When greater accuracy is needed, e.g. for modelling of transport experiments, an improved calculation of the rock matrix response is recommended, for example using the option REFINE 4.

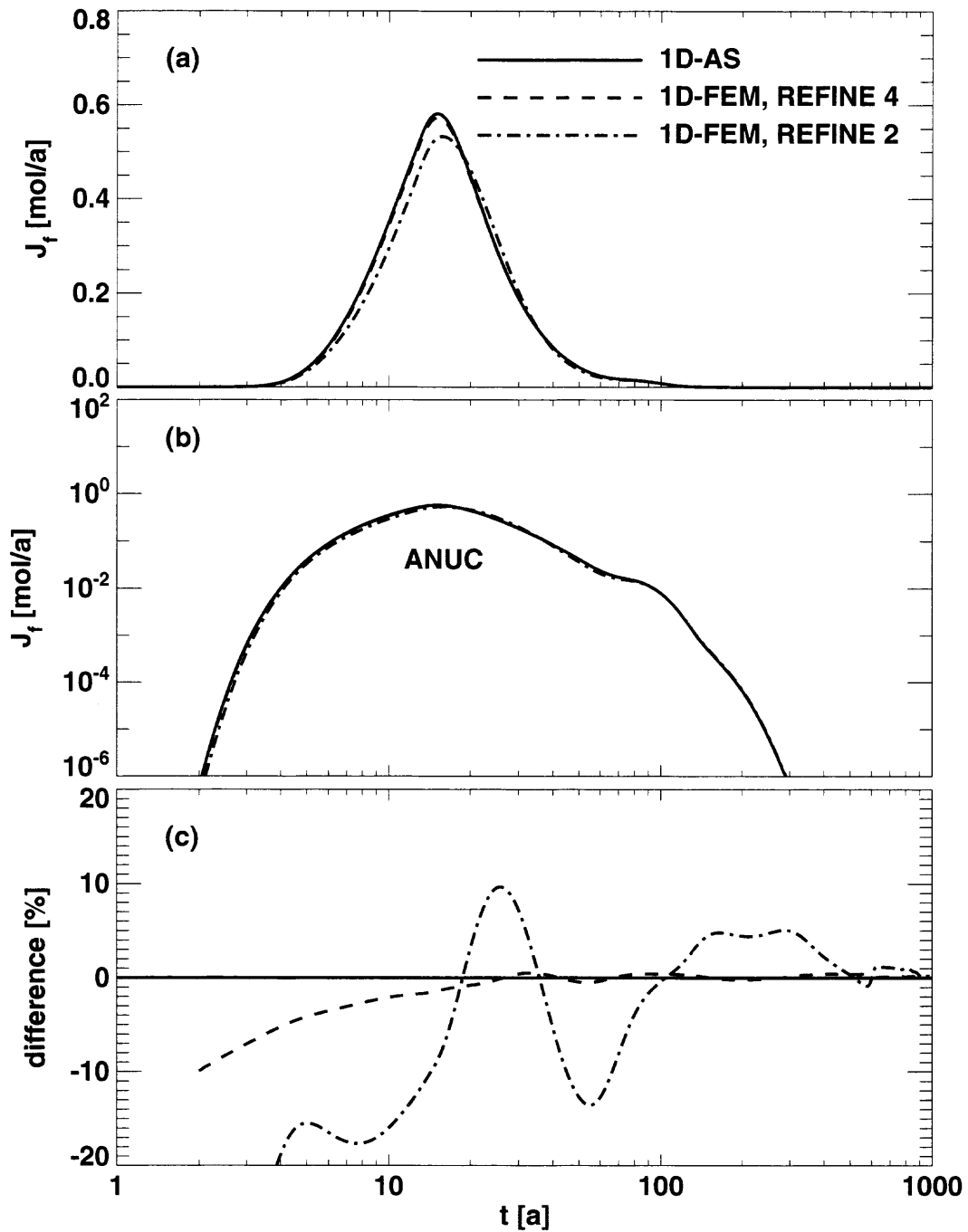


Figure 6.30. Same as Figure 6.29. The only difference is that the nuclide ANUC of the decay chain $\text{ANUC} \rightarrow \text{BNUC} \rightarrow \text{CNUC} \rightarrow$ is considered in the 26-leg network, compare also Figure 4.26. The result of PICNIC calculations using the (finite-element) 1D-FEM option with standard resolution "REFINE 2" (dash-dotted lines) and increased refinement "REFINE 4" (short-dashed lines) for legs 10,11,12 are compared to the respective PICNIC result for the ("analytical") 1D-AS option (solid lines). The release curves are given in (a) on a linear scale and in (b) on a logarithmic scale. The relative difference functions with respect to the 1D-AS result are given in (c).

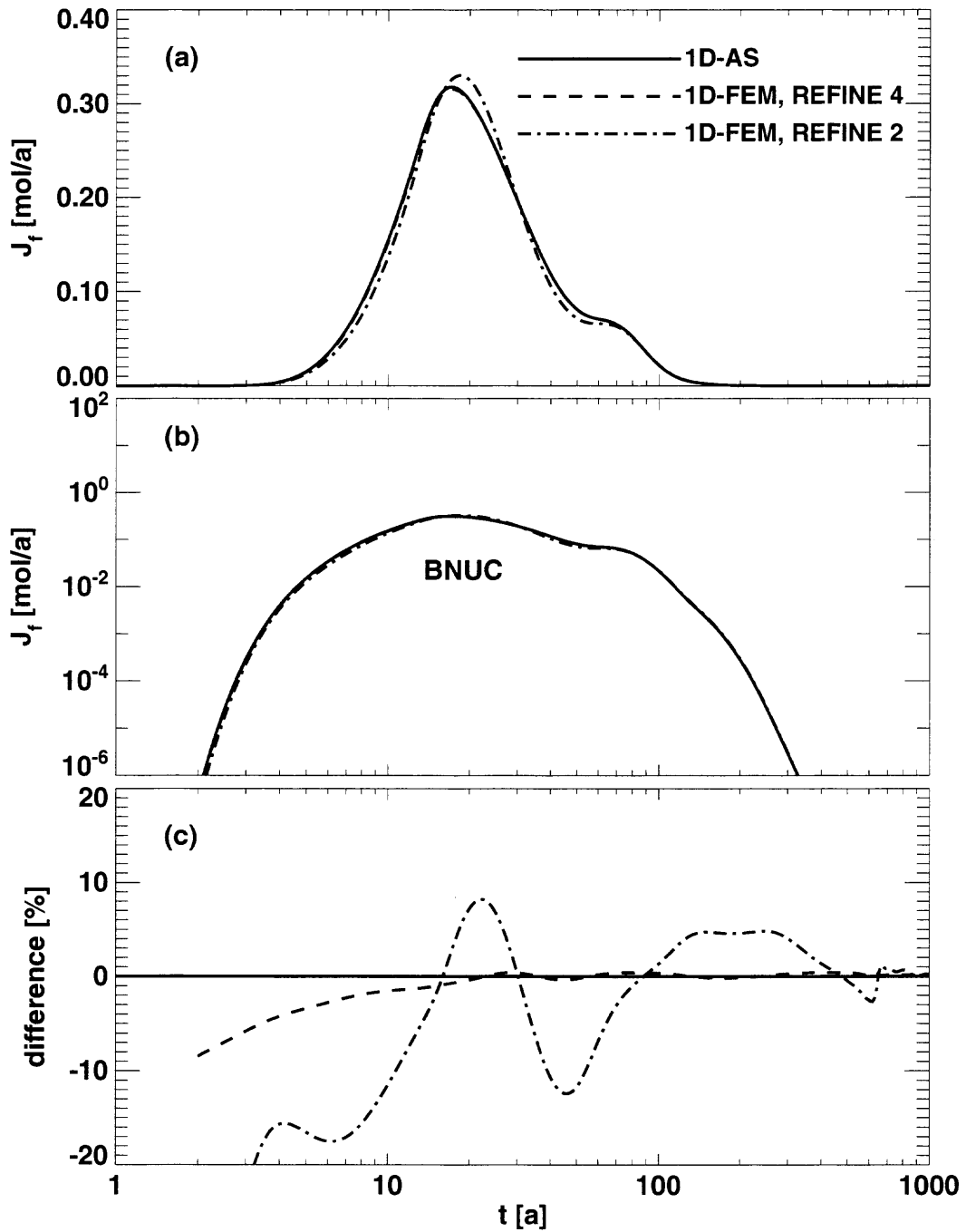


Figure 6.31. Same as Figure 6.29. The only difference is that the nuclide BNUC of the decay chain $ANUC \rightarrow BNUC \rightarrow CNUC \rightarrow$ is considered in the 26-leg network, compare also Figure 4.27. The result of PICNIC calculations using the (finite-element) 1D-FEM option with standard resolution "REFINE 2" (dash-dotted lines) and increased refinement "REFINE 4" (short-dashed lines) for legs 10,11,12 are compared to the respective PICNIC result for the ("analytical") 1D-AS option (solid lines). The release curves are given in (a) on a linear scale and in (b) on a logarithmic scale. The relative difference functions with respect to the 1D-AS result are given in (c).

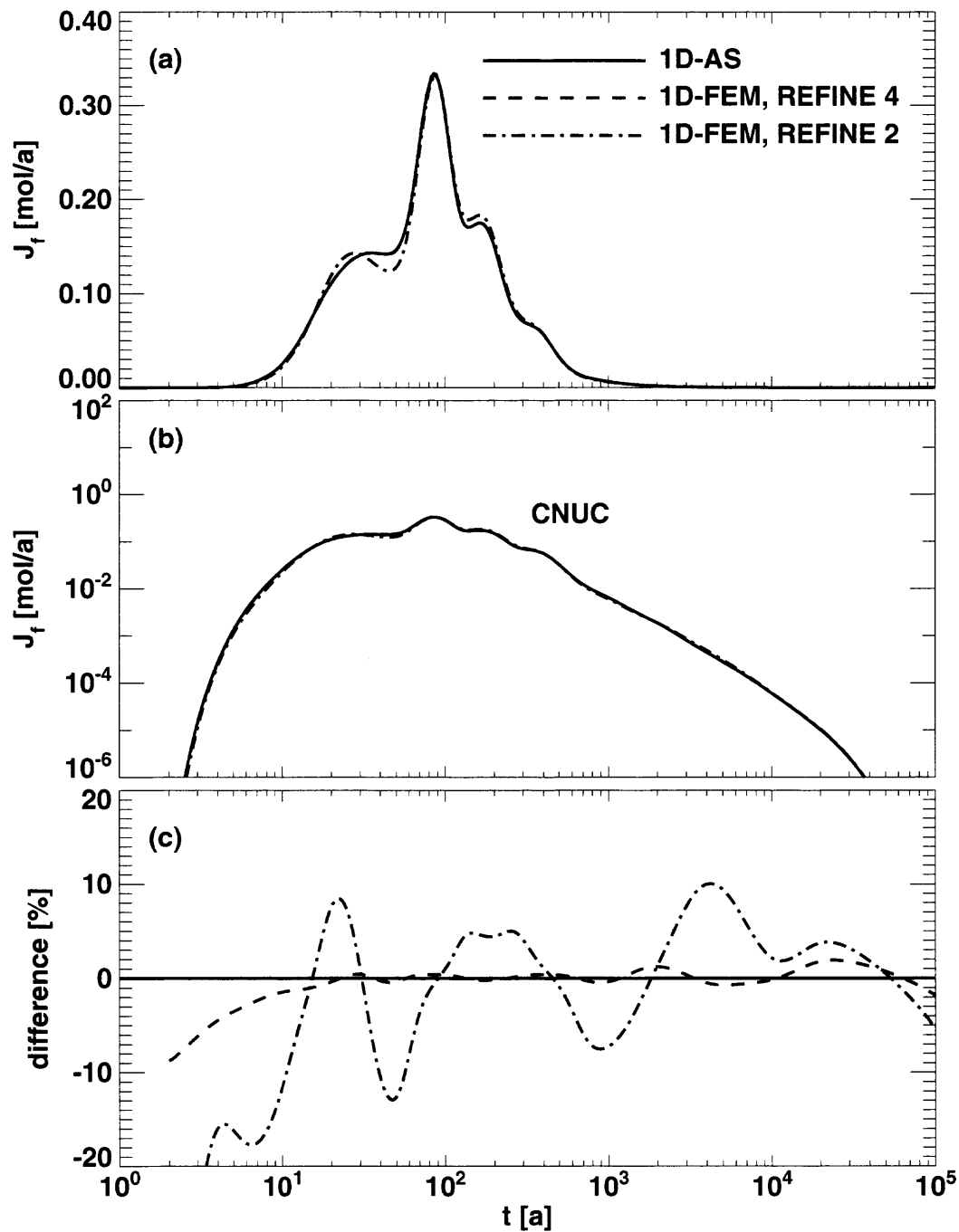


Figure 6.32. Same as Figure 6.29. The only difference is that the nuclide CNUC of the decay chain ANUC \rightarrow BNUC \rightarrow CNUC \rightarrow is considered in the 26-leg network, compare also Figure 4.28. The result of PICNIC calculations using the (finite-element) 1D-FEM option with standard resolution "REFINE 2" (dash-dotted lines) and increased refinement "REFINE 4" (short-dashed lines) for legs 10,11,12 are compared to the respective PICNIC result for the ("analytical") 1D-AS option (solid lines). The release curves are given in (a) on a linear scale and in (b) on a logarithmic scale. The relative difference functions with respect to the 1D-AS result are given in (c).

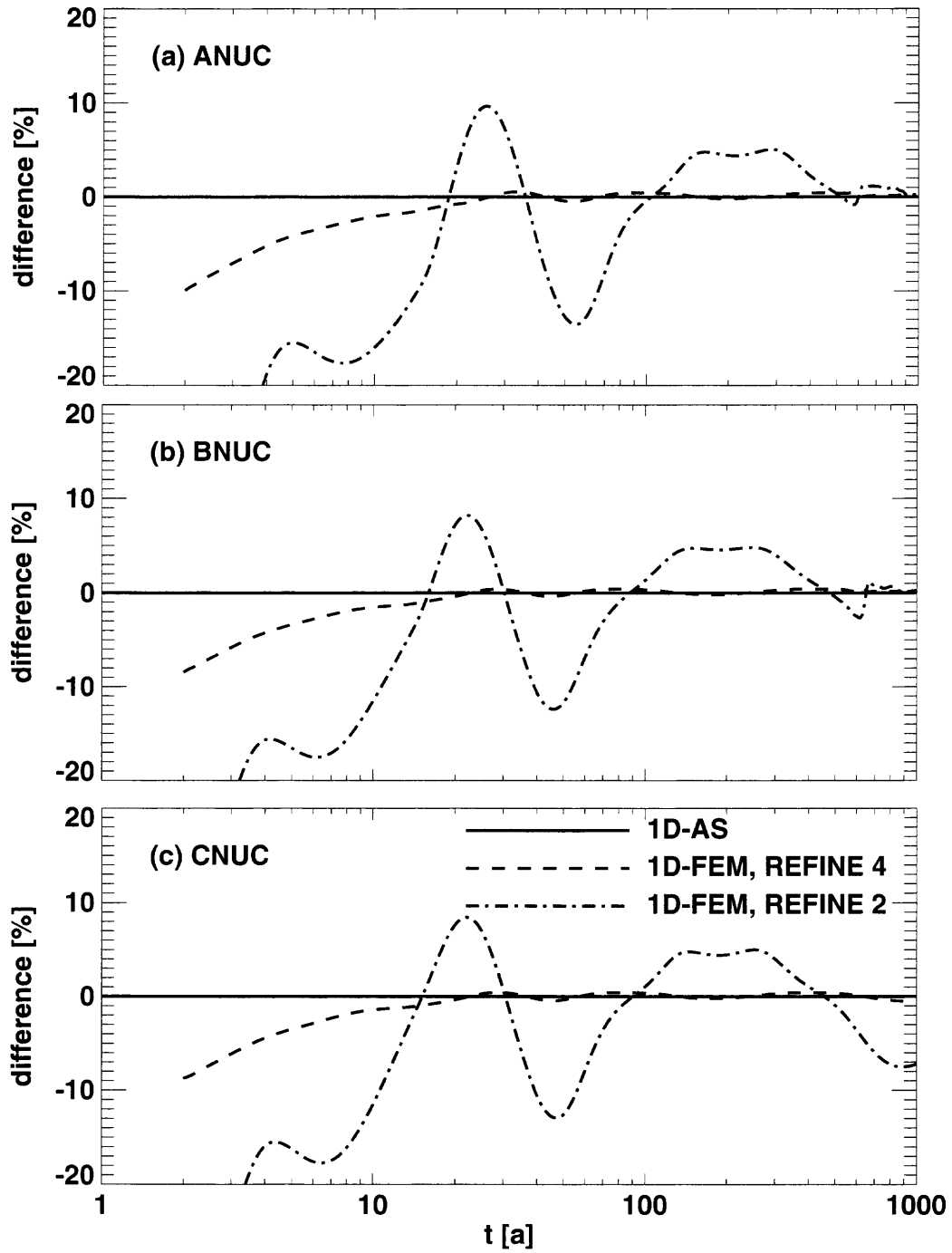


Figure 6.33. The relative difference functions of the nuclides of the decay chain $\text{ANUC} \rightarrow \text{BNUC} \rightarrow \text{CNUC} \rightarrow$ for transport in the 26-leg network are reproduced from Figures 6.30c, 6.31c and 6.32c for the same range of time.

6.7. Summary

As step III in the verification scheme in this section we have considered the capability of PICNIC to deal with a homogeneous planar rock matrix geometry using the finite-element method for calculation of the rock matrix response, see the detailed verification matrix in Table. 6.1. These tests were done by comparing the results of the embedded finite-element method (1D-FEM and 2D-FEM) with the respective PICNIC results for the analytically implemented rock matrix response (1D-AS). Thus, following the verification strategy in section 3, this verification step is based on the verification step I in section 4 where we used the “analytical” variant.

The capabilities for a single nuclide and a nuclide decay chain in a single leg were considered for Grimsel uranium parameters for two different refinements of the finite-element mesh. It was also shown that weakly two-dimensional matrix diffusion does not lead to a considerably increased numerical error.

For a weakly decaying and a strongly decaying single nuclide in a single leg with Kristallin-I performance assessment parameters, the effect of mesh refinement was analysed more in detail. The time-dependent release and the long-time limit for a constant source were considered. It was shown that subdivision of the rock matrix, forcing an increased number of meshes and especially a local mesh refinement in the finite-element method in PICNIC, can considerably increase the accuracy of the results. On the other hand, considering rock matrix regions of extremely different size should be avoided, because they can lead to reduced accuracy.

The capabilities for a single nuclide and a nuclide decay chain in a network were verified for two different refinements of the finite-element mesh. In the 26-leg network considered the rock matrix response of 3 legs was calculated using the embedded finite-element method.

Overall this comparison of the two different methods within PICNIC shows that the finite-element method for numerical calculation of the rock matrix response functions correctly for this homogeneous one-dimensional rock matrix geometry.

We have considered the magnitude and form of the (mainly small) relative difference functions between different PICNIC results using the finite-element method for different mesh refinements and for subdivided rock layers. We have observed that the relative difference functions of the standard refinement FEM results with respect to the 1D-AS results are in the same order of magnitude as the relative difference functions of the standard refinement FEM results with respect to the increased refinement FEM results.⁷⁰ This implies that considering relative difference functions between different refinement FEM results is a useful “tool”. This tool can give some hints as to the accuracy of the FEM and on the order of magnitude of the errors encountered.⁷¹ In the next sections for more complex (heterogeneous) rock matrix geometries, we will use this tool⁷² among others.

⁷⁰ This is because the relative difference functions of the increased refinement FEM results with respect to the 1D-AS results are small when compared to the relative difference functions of the standard refinement FEM results with respect to the 1D-AS results.

⁷¹ It is clearly not enough to consider these discretisation tests alone.

⁷² Note that there are no “analytical” PICNIC results available/implemented for more complex rock matrix geometries.

single leg		(a) single nuclide			(b) nuclide decay chain		
nearly planar geometry		ZG	ZC	AI	ZG	ZC	AI
source in Laplace domain	δ -pulse	R,P-I			R,P-I		
	simple-leaching						
source in time domain	short pulse						
	long top-hat		R,P-I,S ⁷³				
	band-release						
	general						

pathway		(c) single nuclide			(d) nuclide decay chain		
nearly planar geometry		ZG	ZC	AI	ZG	ZC	AI
source in Laplace domain	δ -pulse						
	simple-leaching						
source in time domain	short pulse						
	long top-hat						
	band-release						
	general						

network		(e) single nuclide			(f) nuclide decay chain		
nearly planar geometry		ZG	ZC	AI	ZG	ZC	AI
source in Laplace domain	δ -pulse						
	simple-leaching						
source in time domain	short pulse						
	long top-hat						
	band-release						
	general	R,P-I			R,P-I		

Table 6.1. Performed comparisons of FEM results with 1D-AS results for a (nearly) planar fracture geometry. Note: All test cases represented by empty fields in the scheme were implicitly verified by any of the specified examples. Such a procedure is strongly based on the internal structure of PICNIC as outlined in more detail in section 3. Legend: P-I: comparison of the “embedded finite-element” results in PICNIC with “analytically” implemented results in PICNIC; R: “discretisation test” considering different mesh refinements in the “finite-element” results in PICNIC; S: stationary behaviour tested.

⁷³ Comparison with analytical result.

7. Two-Layer One-Dimensional Planar Rock Matrix

In this section we consider the effect of **one-dimensional rock matrix diffusion into a two-layer planar rock matrix** shown in Figure 7.1. In this geometry, the area of flowing water (F) of aperture $2b$ is in contact with a rock matrix of type M1 and thickness d_1 . This is as for the homogeneous one-dimensional planar fracture geometry considered in sections 4 and 6. Behind this rock layer, now a second, different rock layer of type M2 and thickness d_2 follows. For the parameter definition and the balance equations for the rock matrix geometries of this section see sections 2.2, 2.4 and 2.5.4. This is step IV in the verification scheme of PICNIC, compare section 3.4.4. The geometry considered is the first example of a rock matrix geometry where the calculation of the rock matrix response is not implemented analytically in PICNIC. In verification step V in the next section, the verification of the capability of PICNIC to deal with different rock matrix geometries for one-dimensional matrix diffusion will be completed.

We start in section 7.1 with different **single nuclides in a single leg**, with parameters related to the Kristallin-I performance assessment. Thereby [Barten, Robinson and Schneider, 1998] is reviewed and extended. The **steady-state behaviour is compared to the analytical solution**. For the time-dependent behaviour, **discretisation tests** are performed considering different refinements in the embedded finite-element method (FEM) in PICNIC and subdivided rock matrix layers.

In section 7.2 a **single nuclide** and a **nuclide decay chain in a single leg** are considered using hypothetical variations of the Grimsel dipole parameters for uranine. An inter-comparison with the code RIP [Miller and Kossik, 1998] is performed for the full time-dependent behaviour of the nuclide release. Again different mesh refinements and the effect of subdividing the rock matrix are considered.

Section 7.3 gives a summary.

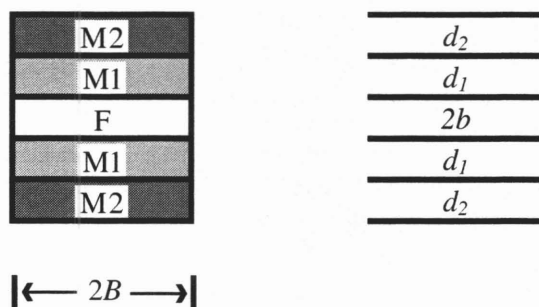


Figure 7.1. Sketch of the cross-section of a leg with an area of flowing water (F) and two-layer rock matrix below and above the area of flowing water. M1 and M2 indicate the two types of rock matrix. The sketch is not to scale. The aperture of the area of flowing water is $2b$ and the (here irrelevant) width is $2B$. The thicknesses of the rock layers are d_1 and d_2 respectively.

For this geometry the diffusion in the rock matrix is still one-dimensional and analytical solutions in the Laplace domain are still available. For single nuclides, which we mainly consider here, the second rock layer leads to a “correction” in the exponent

$$L\Lambda(s) = -[s + \lambda]\alpha - \gamma_1 \sqrt{s + \lambda} \tanh(\beta_1 \sqrt{s + \lambda}) f_2(s) \quad (7.1)$$

with the “correction function”

$$f_2(s) = \frac{1 + \frac{\gamma_2 \tanh(\beta_2 \sqrt{s + \lambda})}{\gamma_1 \tanh(\beta_1 \sqrt{s + \lambda})}}{1 + \frac{\gamma_2}{\gamma_1} \tanh(\beta_2 \sqrt{s + \lambda}) \tanh(\beta_1 \sqrt{s + \lambda})}, \quad (7.2)$$

compare Barten [1996a]; Robinson, Sharp and Kreisel [1998]; Barten, Robinson and Schneider [1998] and section 2.5.4 of this report. The values β_2 and γ_2 are defined according to the values β_1 and γ_1 for the first rock layer, compare equations (2.128) and (2.129). As mentioned above, this solution is however not implemented as an analytical solution in PICNIC, and we have to use the embedded finite-element option to deal with geometries such as that of Figure 7.1 in PICNIC.

7.1. Cases Related to Performance Assessment

In this subsection we consider the transport of different **single nuclides in a single leg** with variations of the Kristallin-I reference case as parameters. We start with a description of the geometry of a cataclastic zone to highlight the relevance of these cases for performance assessment. Then, for three different nuclides and different extents of the second rock matrix layer, the nuclide release for a constant source and a δ -function source are analysed. For different refinements of the finite-element mesh, the accuracy of the steady-state release is estimated with respect to the analytical solution. For a δ -function source, several discretisation tests are performed using different refinements of the finite-element mesh and considering subdivision of the rock matrix. The network feature of PICNIC is spot-checked with a self-consistency test. Finally, the accuracy of the steady-state release is considered for different porosities of the second rock layer.

7.1.1. Geometry of a Cataclastic Zone

The Kristallin-I reference case is based on cataclastic zones in the crystalline basement of Northern Switzerland, as observed in a drill cores and simplified for the purposes of transport modelling (Figure 7.2). The cataclastic zones were analysed by Thury et al. [1994] and their relevance for repository safety assessment was also pointed out by Smith et al. [1997]. On a small scale (say one metre), a typical cataclastic zone consists of an interconnected network of individual fractures (top left). This pattern is represented in the model as a set of parallel fractures (top right). These fractures are partially filled by porous infill material, with open channels in between. In these open channels, shown in the close-up (bottom figures), predominantly advective transport occurs.

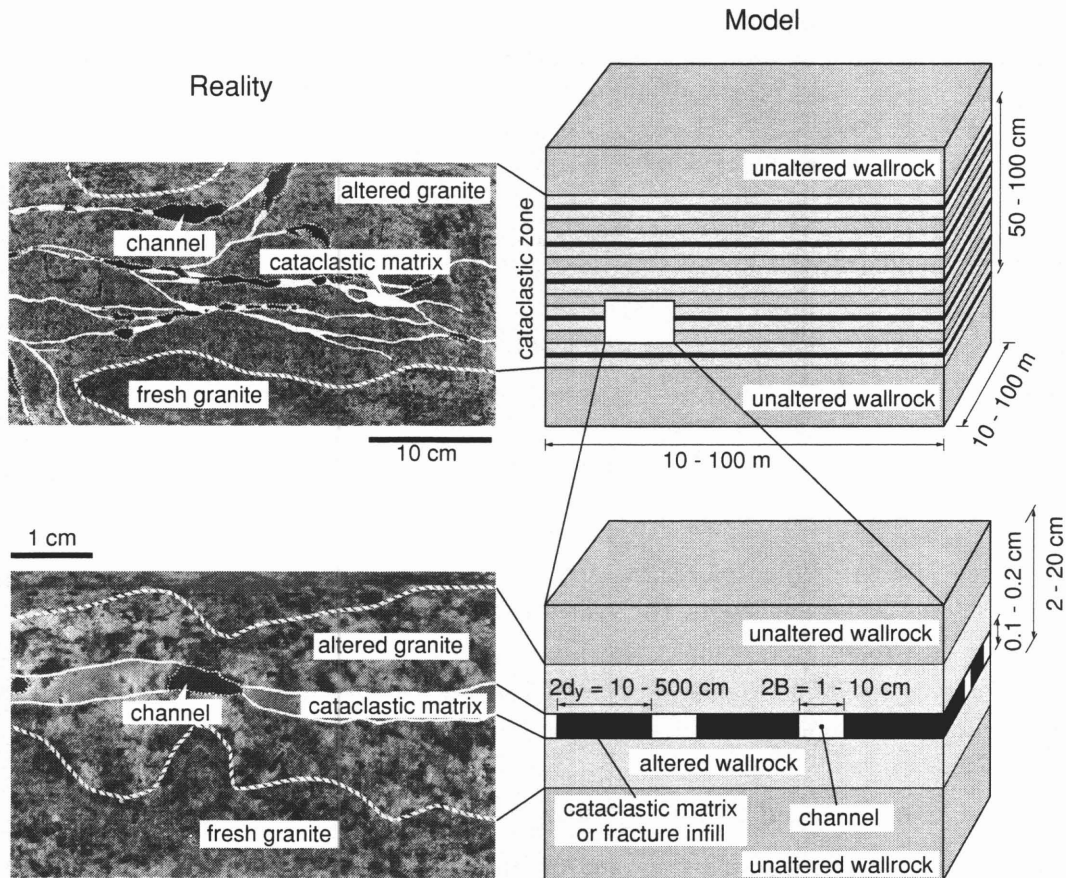


Figure 7.2. Cataclastic zones in the crystalline basement of Northern Switzerland, as observed in drill cores and as simplified for the purposes of transport modelling. Adapted from Thury et al. [1994].

In the Kristallin-I reference case [Nagra, 1994], the following parameter values were selected, consistent with the ranges given in Figure 7.2. The open channels have a width of $2B = 10$ cm and a spacing of 500 cm. In the direction perpendicular to the plates, the channels have an aperture of $2b = 1$ mm (Figure 7.1). The altered wallrock adjacent to the open channels is assumed to be accessible for matrix diffusion, with a porosity $\varepsilon_{p,1}$ of 5% and a matrix depth of d_1 with $d_1 + b = 5$ cm (Figures 7.1 and 7.2). Matrix diffusion into the unaltered wallrock (second matrix layer in Figure 7.1) is not considered in the reference case.

To assess the effect of a more realistic description of radionuclide transport on geosphere barrier efficiency, we assume that in addition to the altered wallrock, the unaltered wallrock is also accessible for matrix diffusion, with a porosity $\varepsilon_{p,2}$ of 0.25% [Nagra, 1994] and a depth d_2 varying between 10^{-5} m and 15 m. With these one-dimensional matrix diffusion calculations we still consider only the wallrock adjacent to the open channels of width $2B$ and we do not make use of the wallrock adjacent to the fracture infill.

Note that $d_2 = 10^{-5}$ m effectively corresponds to the reference case, while $d_2 = 15$ m is a hypothetical large value chosen to illustrate model behaviour. Field observations indicate that a value of $d_2 = 0.15$ m could be taken as representative [Nagra, 1994], considering that a typical water-conducting feature of the type "cataclastic zone" is usually composed of several closely-spaced fracture planes (Figure 7.2) and that matrix diffusion is consequently limited by geometry.

7.1.2. Release Curves and Geosphere Barrier Efficiency

In the Kristallin-I reference case, ^{135}Cs is the most important nuclide contributing to the annual individual dose. In Figure 7.3b release curves to the biosphere are considered for a δ -pulse of 1 mol of ^{135}Cs injected into the geosphere at $t = 0$. For the reference case the time to maximum release is about $0.14 \cdot 10^6$ [a], which is small compared to the ^{135}Cs half-life of $2.3 \cdot 10^6$ [a]. The time to maximum release is only slightly changed when a layer of unaltered wallrock is also taken into account. However the maximum reduces by a factor of five for $d_2 = 0.15$ m. Also the form of the release curve changes. For the reference case ($d_2 = 0$ m), diffusion into the rock matrix is a fast process ($\beta_1^2 = 0.005 \cdot 10^6$ [a]) acting as simple retardation like surface sorption. However, already for $d_2 = 0.15$ m, the tailing of the release curve appears which is typical for limited matrix diffusion. This has several consequences. The recovered mass (the time integral of the release curve) which is proportional to the release curve for a constant source (presented in Figure 3a) reaches steady-state much later. This means that most nuclides need several hundred thousand years longer to cross the geosphere. While in the reference case 5% of the ^{135}Cs nuclides decay in the geosphere, about 19% of the nuclides decay for $d_2 = 0.15$ m (Figures 7.3a and 7.4c). For a larger extent of the unaltered wallrock, $d_2 = 0.3$ m or $d_2 = 15$ m, also the typical $t^{-3/2}$ fingerprint [Hadermann and Heer, 1996] of unlimited matrix diffusion can be seen, especially when the release curves are re-scaled so that radioactive decay is neglected (Figure 7.3c). For $d_2 = 0.6$ m with $\tanh(\beta_2 \sqrt{\lambda}) \approx 1$ (Figure 7.4a) the rock matrix depth is effectively unlimited and a larger rock matrix extent does not lead to a higher geosphere barrier efficiency. The geosphere barrier efficiency is calculated by PICNIC using the standard option (REFINE 2) within an accuracy of 1% with respect to the analytical result of section 2.1.7 (squares in Figure 7.4b). With increased refinement of the finite-element mesh in the rock matrix (REFINE 4), the accuracy is within 0.2% (crosses in Figure 7.4b).

The nuclide ^{79}Se shows similar behaviour. However, because the timescale for the tailing for neglected radioactive decay (see Figure 7.5c) is in the same order of magnitude as the half-life of $0.065 \cdot 10^6$ [a], the tailing is masked when decay is considered (Figure 7.5b) and the barrier efficiency of the geosphere is higher (Figures 7.5a and 7.6c). The relative difference of the geosphere barrier efficiency from the analytical result revealed by PICNIC calculations is somewhat bigger (Figure 7.6a) than for ^{135}Cs . However it is in the same order of magnitude, and is especially nearly the same for the same $\tanh(\beta_2 \sqrt{\lambda})$ (Figure 7.6a) which measures how far the second rock layer can be regarded as unlimited.

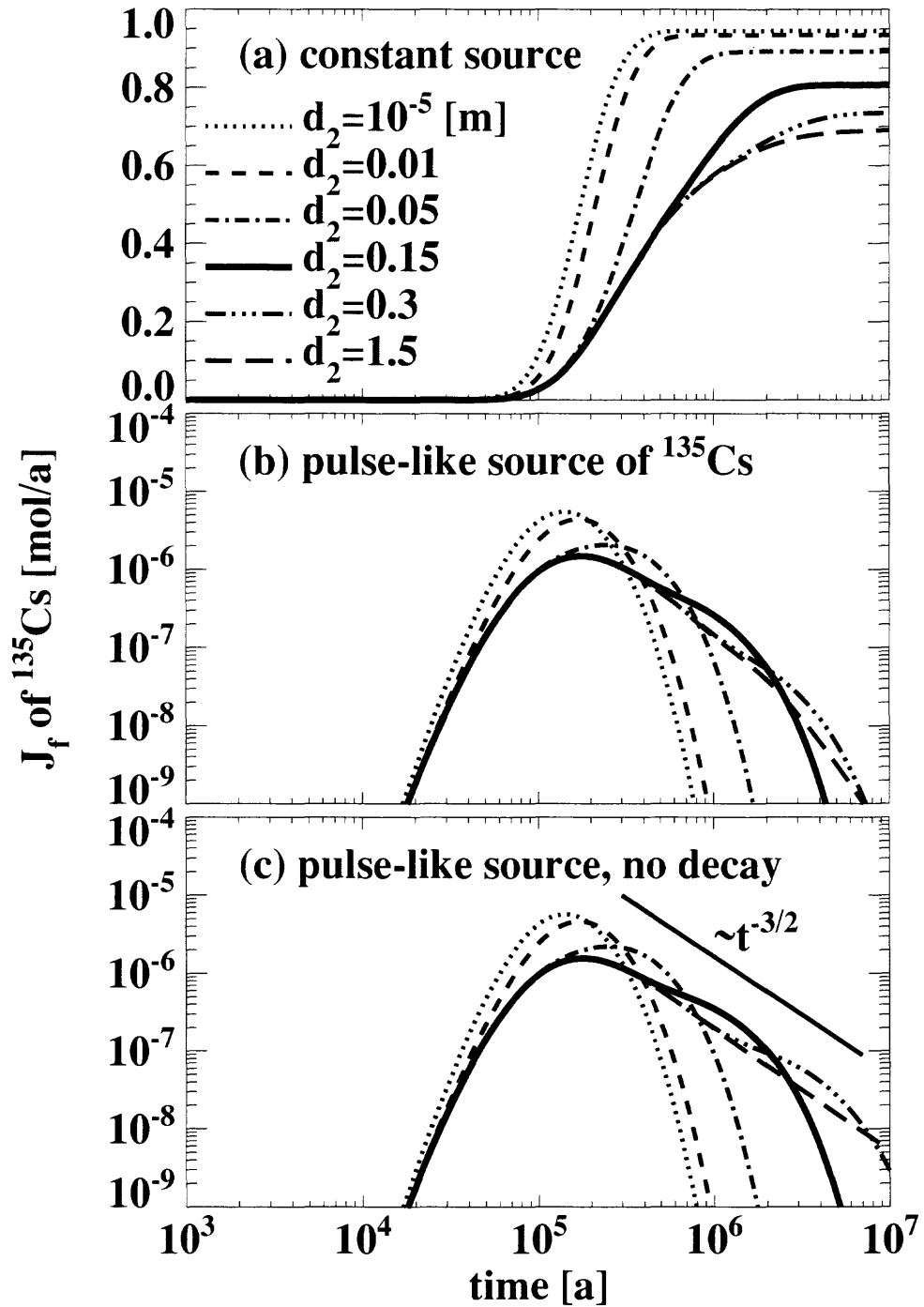


Figure 7.3. In (a) the nuclide outflow of ^{135}Cs for a constant source of 1 [mol/a] starting at $t = 0$ is presented for different extents d_2 of the unaltered wallrock. In (b) the nuclide release for a pulse-like injection of 1 [mol] of ^{135}Cs at $t = 0$ into the geosphere is given. In (c) the release curves for a pulse-like source are presented when radioactive decay is neglected. The $t^{-3/2}$ dependency in parts of the release curves for $d_2 = 0.15$ m to $d_2 = 1.5$ m, respectively, is indicative of unlimited matrix diffusion. For $d_2 = 0.3$ m and 1.5 m in the PICNIC calculation, a refined finite-element mesh in the rock matrix is used.

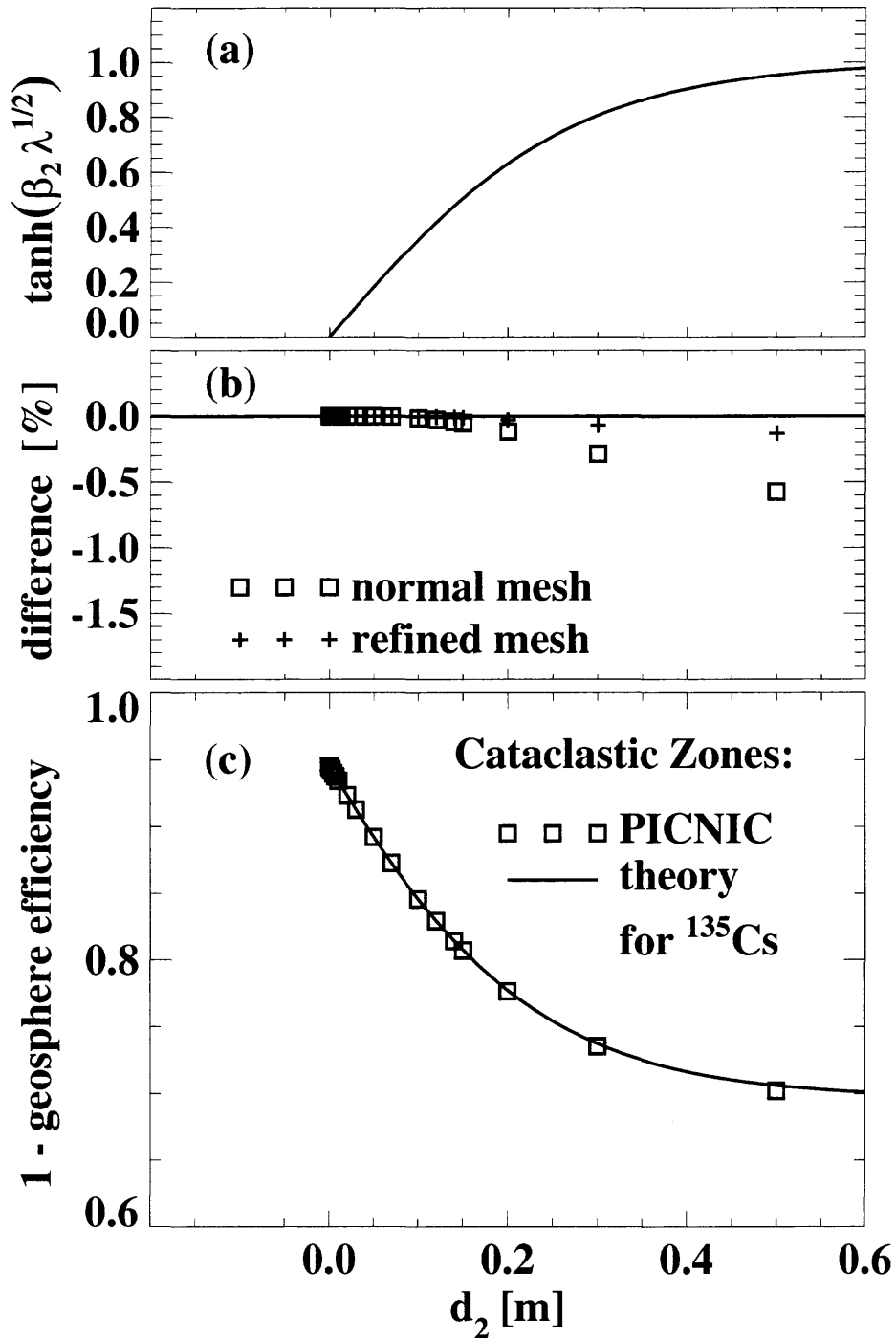


Figure 7.4. (a) gives the variation of $\tanh(\beta_2 \sqrt{\lambda})$ as a function of the extent d_2 of the unaltered wallrock for ^{135}Cs .

This quantity measures to what extent the second rock layer can be considered as unlimited. It enters into $\bar{\mathfrak{R}}(z=L, s=0) = (1 - \text{the geosphere efficiency})$ presented in (c). The PICNIC calculation (squares) is in very good agreement with the theoretical result (solid line). (b) shows the relative difference of the PICNIC calculation for $\bar{\mathfrak{R}}(z=L, s=0)$ with respect to the theoretical result. The agreement is even better for a refined finite-element mesh in the PICNIC calculation (crosses).

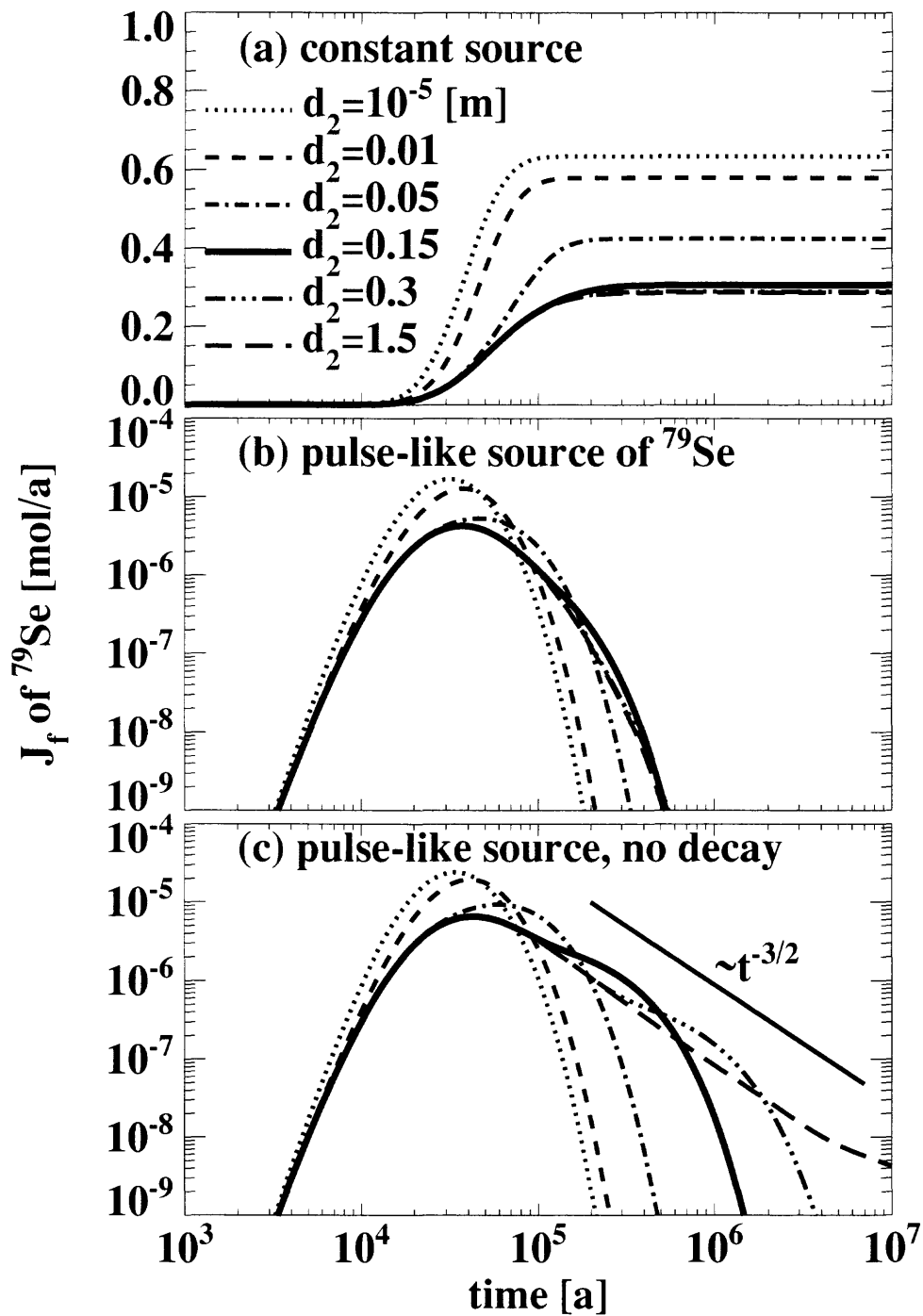


Figure 7.5. As Figure 7.3, but for ^{79}Se .

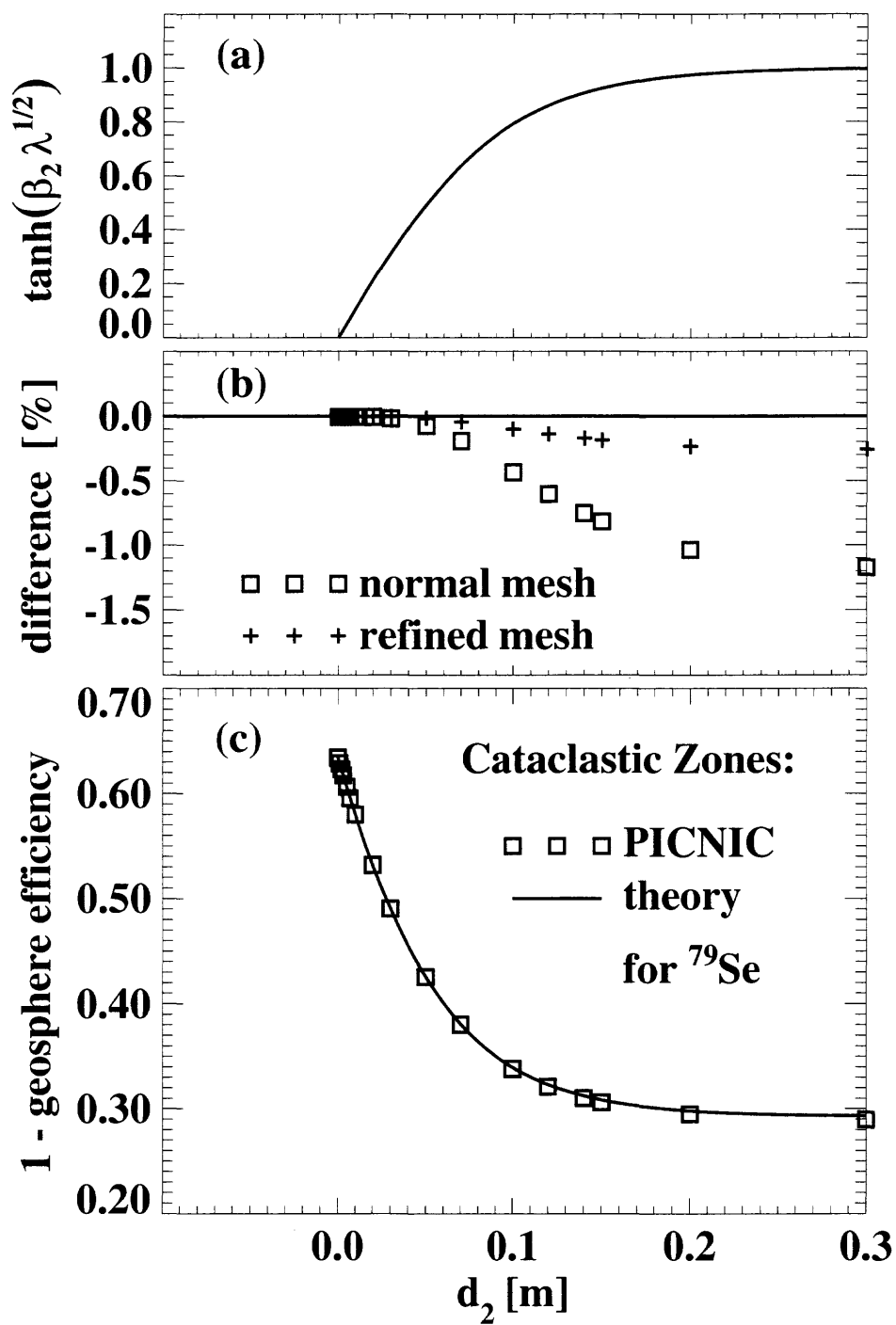


Figure 7.6. As Figure 7.4, but for ^{79}Se .

The $t^{-3/2}$ tailing exists also for ^{99}Tc when radioactive decay is neglected (Figure 7.7c). However the ^{99}Tc half-life of $0.213 \cdot 10^6[\text{a}]$ is much smaller than the time to maximum release which is at about $0.9 \cdot 10^6[\text{a}]$ (Figure 7.5b). Consequently the release curves for times larger than the half-life are dominated by radioactive decay. Thus, already in the reference case only 0.9% of the ^{99}Tc crosses the geosphere while more than 99% decays (Figures 7.7a and 7.8c). Taking into account the unaltered wallrock, only 0.2% of the nuclide pass the geosphere. Already for $d_2 = 5 \text{ cm}$ with $\tanh(\beta_2 \sqrt{\lambda}) \approx 1$ (Figure 7.6a) the rock matrix behaves as nearly unlimited. To ensure an accuracy of $\bar{\mathfrak{R}}(z = L; s = 0)$ within 1% it is also necessary to use a refined finite-element mesh in the rock matrix (crosses in Figure 7.8b).

To conclude for these three nuclides, the geosphere barrier efficiency is calculated very accurately. Generally the relative difference to the analytical result increases with increasing extent d_2 of the second layer. Only for ^{99}Tc is the agreement best for about $d_2 = 1 \text{ cm}$ and the relative difference to the analytical result increases for very small d_2 . In all cases the REFINE 4 option shows an agreement with the analytical result which is about a factor of three better than for the standard REFINE 2 option. This is similar to the single-layer case (section 6). These tests give a first indication that the two-layer case for one-dimensional matrix diffusion can also be dealt with accurately by PICNIC.

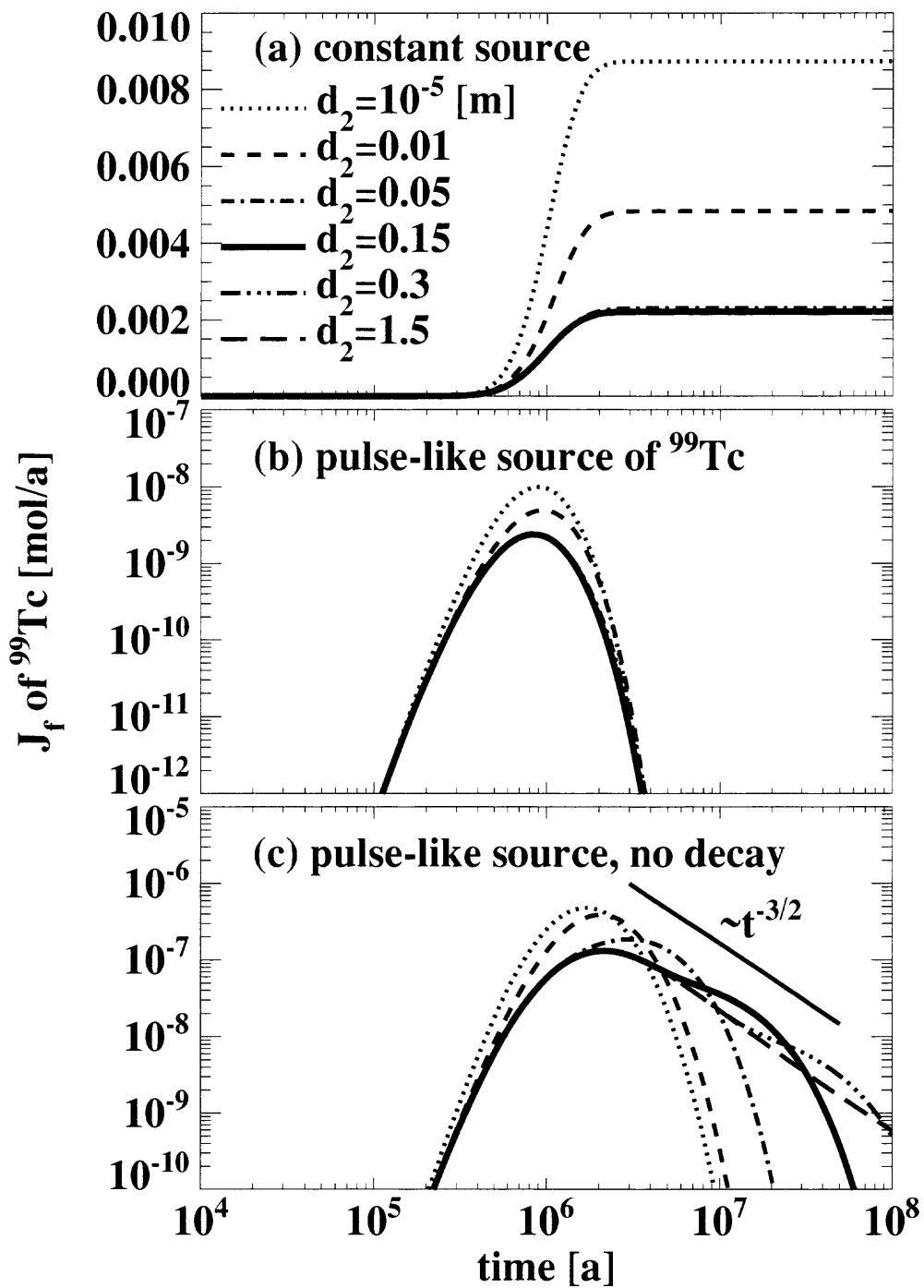


Figure 7.7. As in Figure 7.3, but for ^{99}Tc .

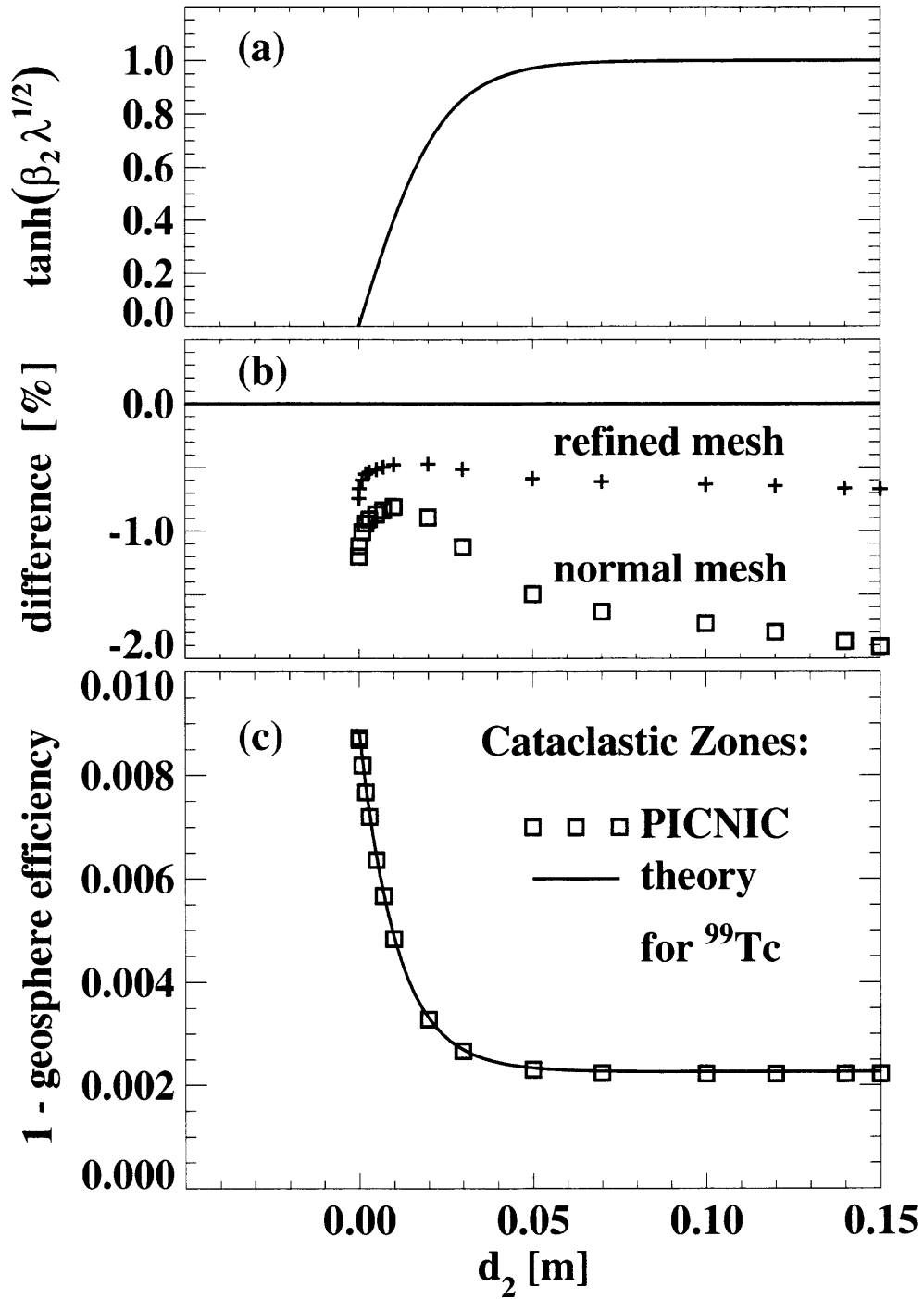


Figure 7.8. As Figure 7.4, but for ^{99}Tc .

7.1.3. Discretisation Tests with Subdivided Rock Matrix Layers

For discretisation tests of the time-dependent behaviour, we now enter the rock matrix geometry of Figure 7.9 to PICNIC. It considers, as in Figure 7.1, a two-layer rock matrix, but both rock **layers** are now **subdivided** into two parts with equal properties. As for the case of a single homogeneous rock layer (cf. section 6.4), the first rock layer (M1) of thickness $d_1 = 0.0495$ [m] is subdivided into two sub-layers of thickness $h_1 = 0.02$ [m] and $h_2 = 0.0295$ [m]. In addition, the second rock layer (M2) of thickness d_2 is subdivided into two sub-layers, here of the same thickness $h_3 = h_4 = \frac{1}{2}d_2$ for simplicity.

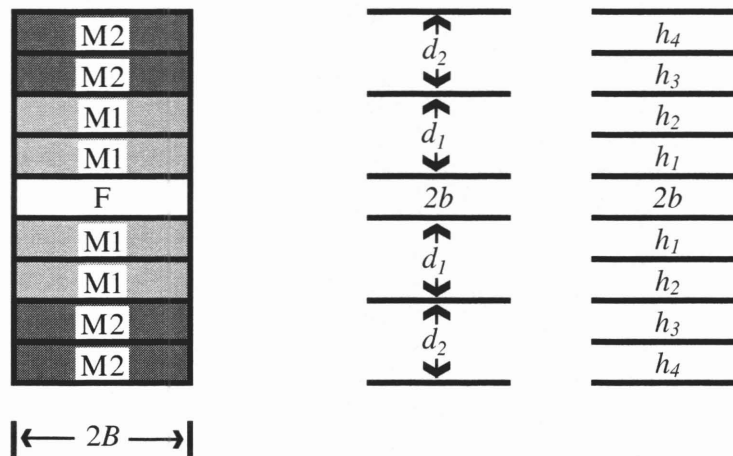


Figure 7.9. Sketch of the cross-section of a leg with an area of flowing water (F) and two-layer rock matrix types M1 and M2 below and above the area of flowing water, as in Figure 7.1. Differing to Figure 7.1 the rock layer M1 is subdivided into two parts of thickness h_1 and h_2 with $d_1 = h_1 + h_2$, and the rock layer M2 is subdivided into two parts of thickness h_3 and h_4 with $d_2 = h_3 + h_4$.

From the homogeneous rock matrix case considered in section 6 we have learned that the subdivision of the rock matrix area considerably increases the accuracy of the PICNIC calculation. Therefore, we first return to the nearly homogeneous case. We consider in Figure 7.10 the transport of ^{135}Cs in a single leg, but neglecting radioactive decay, for a δ -function source where the second rock layer has the thickness $d_2 = 10^{-5}$ [m],⁷⁴ compare dotted line in Figure 7.3c. The release curves for the standard calculation with REFINE 2 (long dashes) and the increased refinement REFINE 4 (dash-dotted lines) are given in Figure 7.10a,b. The results for the 2+2 sub-layers are presented for the options REFINE 2 (short dashes) and REFINE 4 (which should give the best result, solid line). The relative difference functions with respect to the latter calculation (presented in Figure 7.10c) are known from section 6 to be in the order of the relative difference to the result for the analytically implemented rock matrix response. All release curves agree very well with each other. The relative difference functions indicate that the lower refinement calculations show a slightly retarded increase of the release curve for early times, then overshooting within 0.5[%] in the maximum region, and finally an earlier decrease of the release curve for late times. As expected, the REFINE 2 result for the 2+2 layers agrees best with the REFINE 4 result for the 2+2 layers, followed by the REFINE 4

⁷⁴ Thus this very small second rock matrix layer should have virtually no effect on the nuclide release.

result without subdivision of the matrix layers, and finally the standard resolution result with REFINE 2.

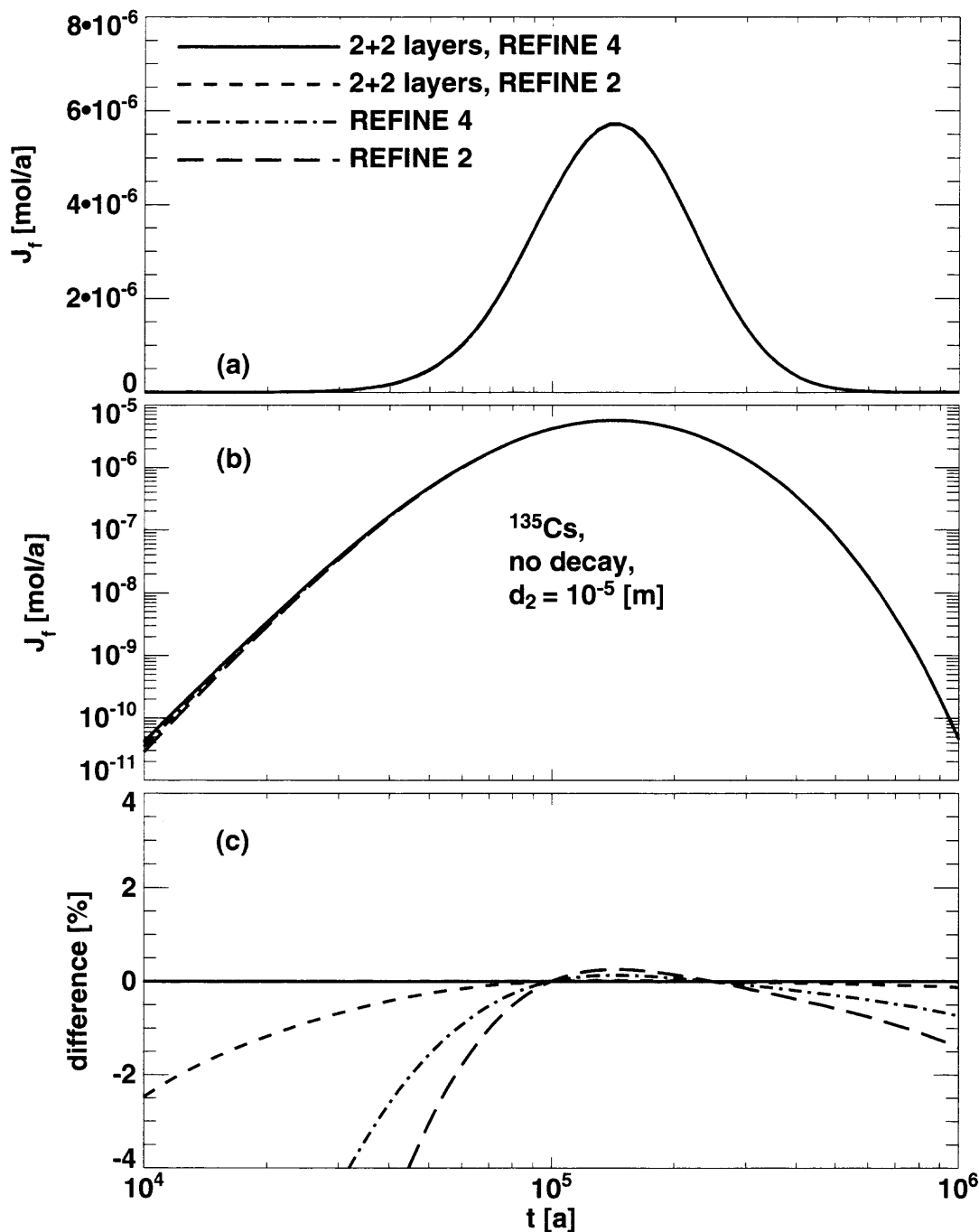


Figure 7.10. Transport of ^{135}Cs in a single leg, when radioactive decay is neglected, for a δ -function source. A two-layer rock matrix with width of the second rock layer $d_2 = 10^{-5}$ [m] is considered, compare the dotted line in Figure 7.3c (which represents the same release curve).

The same situation considered in Figure 7.11 for the finite rock layer thickness $d_2 = 0.15$ [m] (compare solid line in Figure 7.3c) shows similar behaviour. The overall agreement of the different calculations is again very good. For early times, the lower resolution results show a slightly retarded increase of the release curve for early times, and an earlier decrease of the release curve for late times. However the overshooting is now stronger and similar oscillations are observed as discussed in section 6.

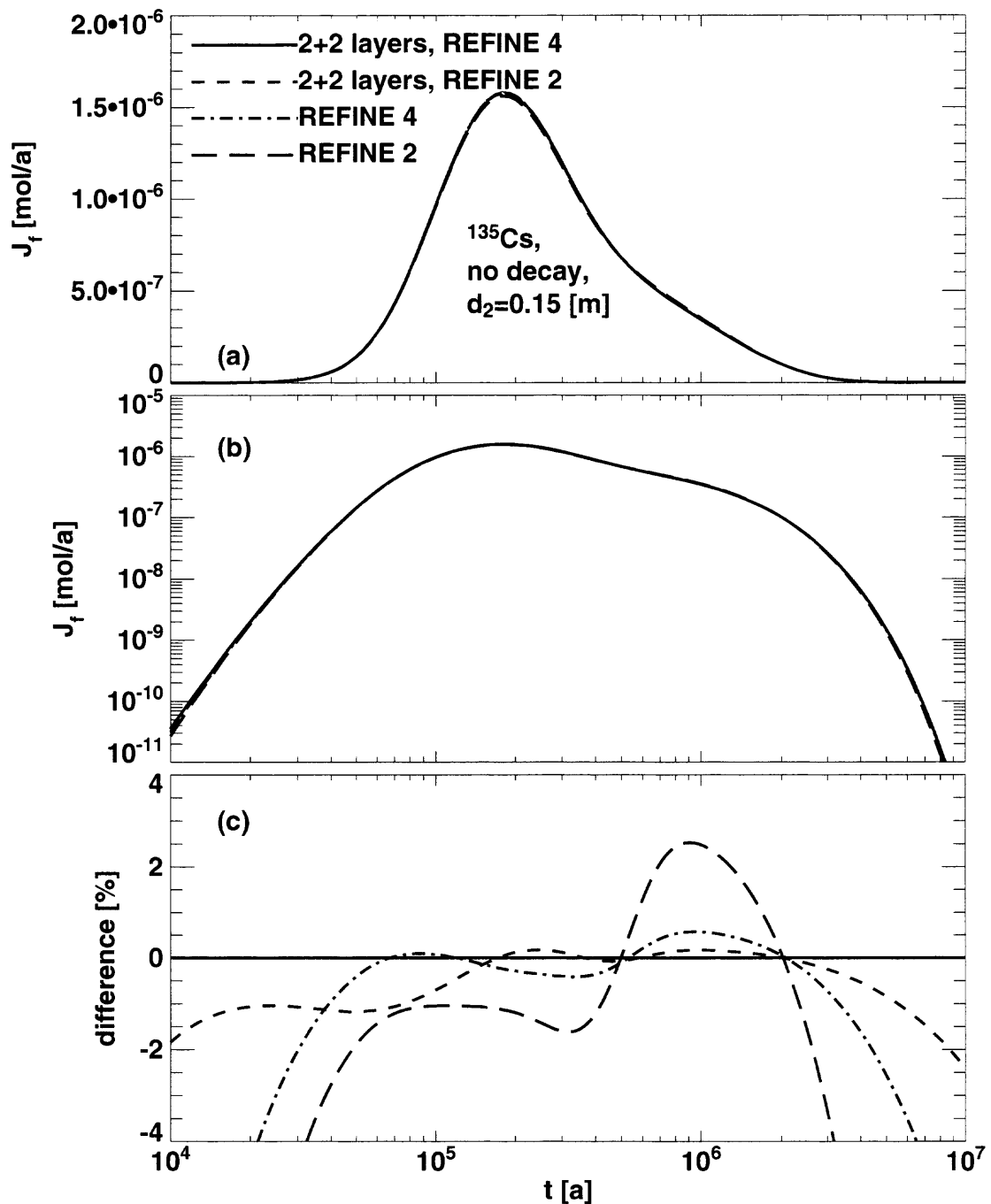


Figure 7.11. Transport of ^{135}Cs in a single leg when radioactive decay is neglected, for a δ -function source. A two-layer rock matrix with width of the second rock layer $d_2 = 0.15$ [m] is considered, compare the solid line in Figure 7.3c.

For a yet increased thickness of the second rock layer $d_2 = 15$ [m] (Figure 7.12) we observe the typical $t^{-3/2}$ fingerprint of nearly unlimited matrix diffusion; compare long-dashed line in Figure 7.3c. The overall agreement of the different calculations is again very good, at least for performance assessments standards. For early times the lower resolution calculations show a slightly retarded increase of the release curve and would show also an earlier decrease for late times not considered after 10^8 [a]. For early times ($< 2 \cdot 10^4$ [a]) and late times ($> 10^7$ [a]), as already for smaller d_2 , the REFINE 2 result for the 2+2 layers agrees best with the REFINE 4 result for the 2+2 layers, followed by the REFINE 4 result without subdivision of the matrix layers and finally the standard resolution REFINE 2. However, now more, stronger oscillations are observed in the long tail of the release curve due to nearly unlimited matrix diffusion, compare Figure 6.2 for a single-layer case. These oscillations are mainly observed for both calculations with REFINE 2 and are nearly suppressed for the calculations with REFINE 4. Interestingly, the oscillations are biggest for the 2+2 layers result for REFINE 2. Also in this case they are within 15[%]. Because the oscillations could mask algebraic tailing of release curves (like $t^{-3/2}$ here, see Figure 7.12c), they could invalidate calculations for the analysis of experiments and one should use the REFINE 4 option. However one should keep in mind that a further subdivision of the matrix layers (M2) could increase the accuracy considerably, considering the relatively large thickness $h_3 = h_4 = 0.75$ [m] compared to h_1 and h_2 .

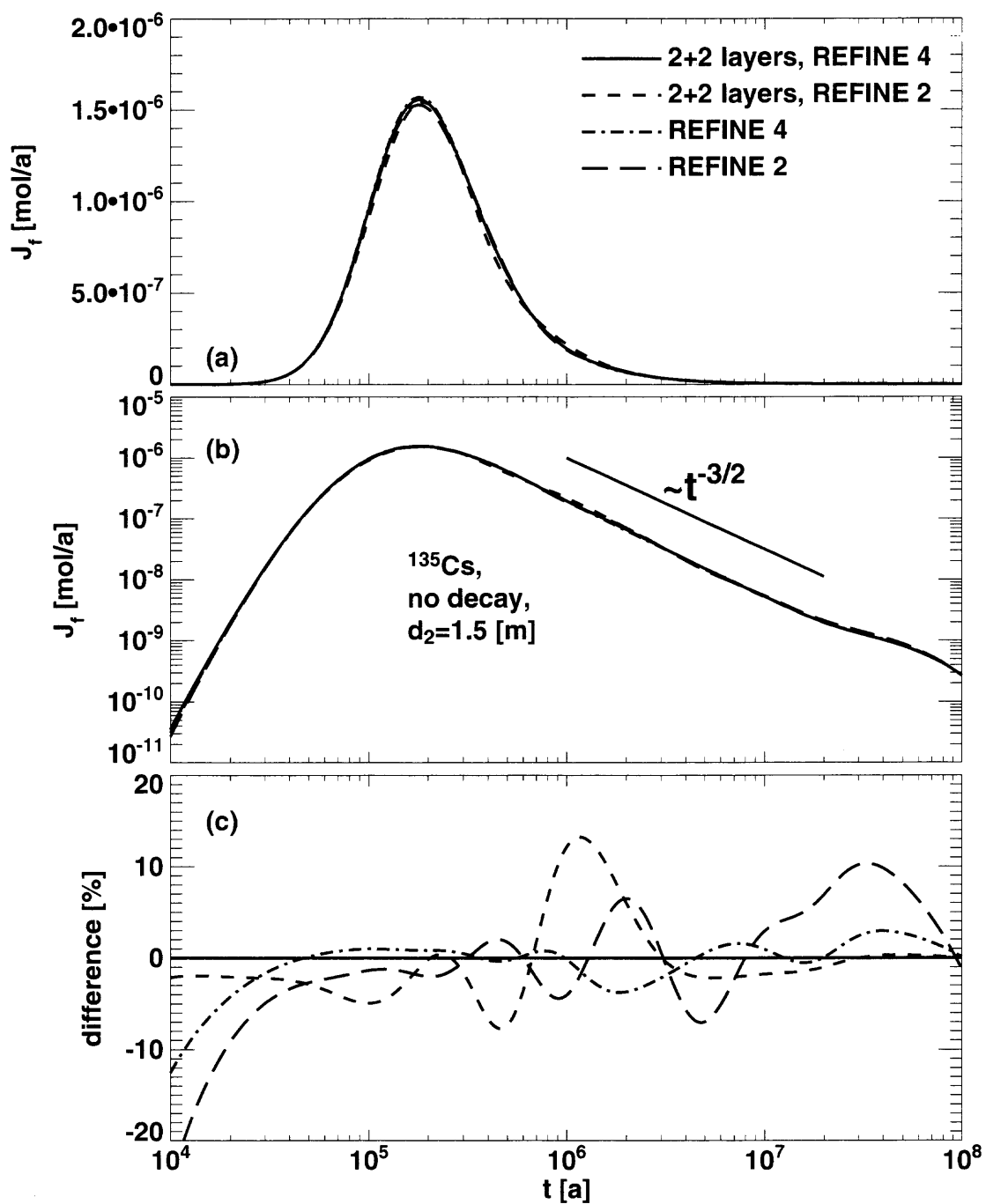


Figure 7.12. Transport of ^{135}Cs in a single leg, when radioactive decay is neglected, for a δ -function source. A two-layer rock matrix with width of the second rock layer $d_2 = 1.5$ [m] is considered, compare the long-dashed line in Figure 7.3c.

In the next test we also take radioactive decay into account and consider transport of the nuclide ^{79}Se and the thickness of the second rock layer is $d_2 = 0.15$ [m], compare solid line in Figure 7.5b. For this geometry, we compare in Figure 7.13 again PICNIC calculations for 2+2 layers and without subdivision, both for the increased refinement REFINE 4 and the standard resolution REFINE 2. As a further consistency check, the calculations for the 2+2 layers are performed neglecting radioactive decay; and then radioactive decay is incorporated by the analytical relation for single nuclides

$$\mathfrak{R}(t) = e^{-\lambda t} \mathfrak{R}_{\lambda \rightarrow 0}(t), \quad (7.3)$$

compare equation (2.140). In Figure 7.14 for ^{79}Se also $d_2 = 1.5$ [m] is considered, compare long-dashed line in Figure 7.5b. The agreement between the different calculations for these two geometries is again very good. Moreover, the relative differences are in the same order of magnitude as for ^{135}Cs and show a similar form, considering that there is no long tailing of the release curves because of radioactive decay.

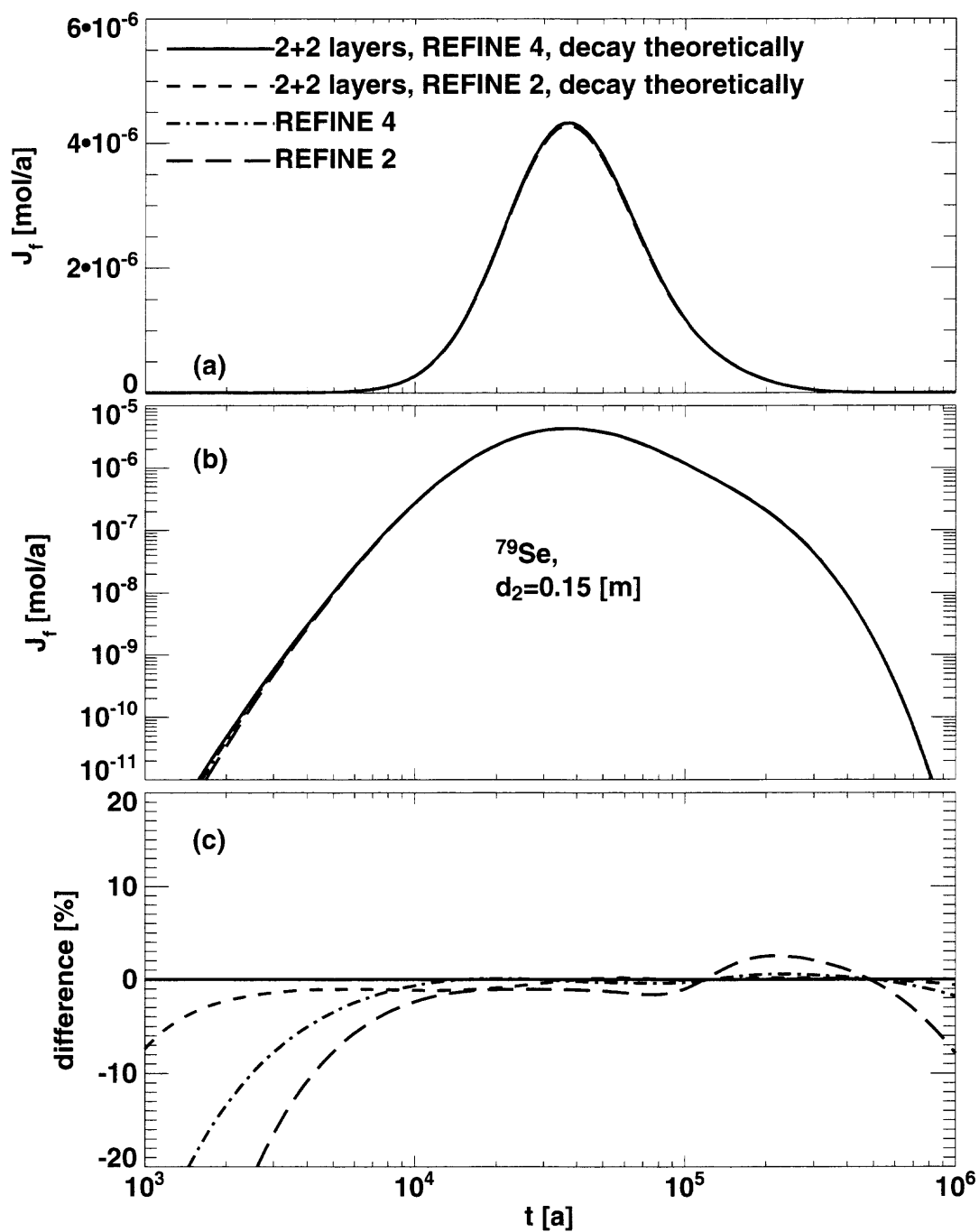


Figure 7.13. Transport of ^{79}Se in a single leg for a δ -function source. A two-layer rock matrix with width of the second rock layer $d_2 = 0.15$ [m] is considered, compare the solid line in Figure 7.5b. For the 2+2 layer calculations, radioactive decay is incorporated analytically, see text.

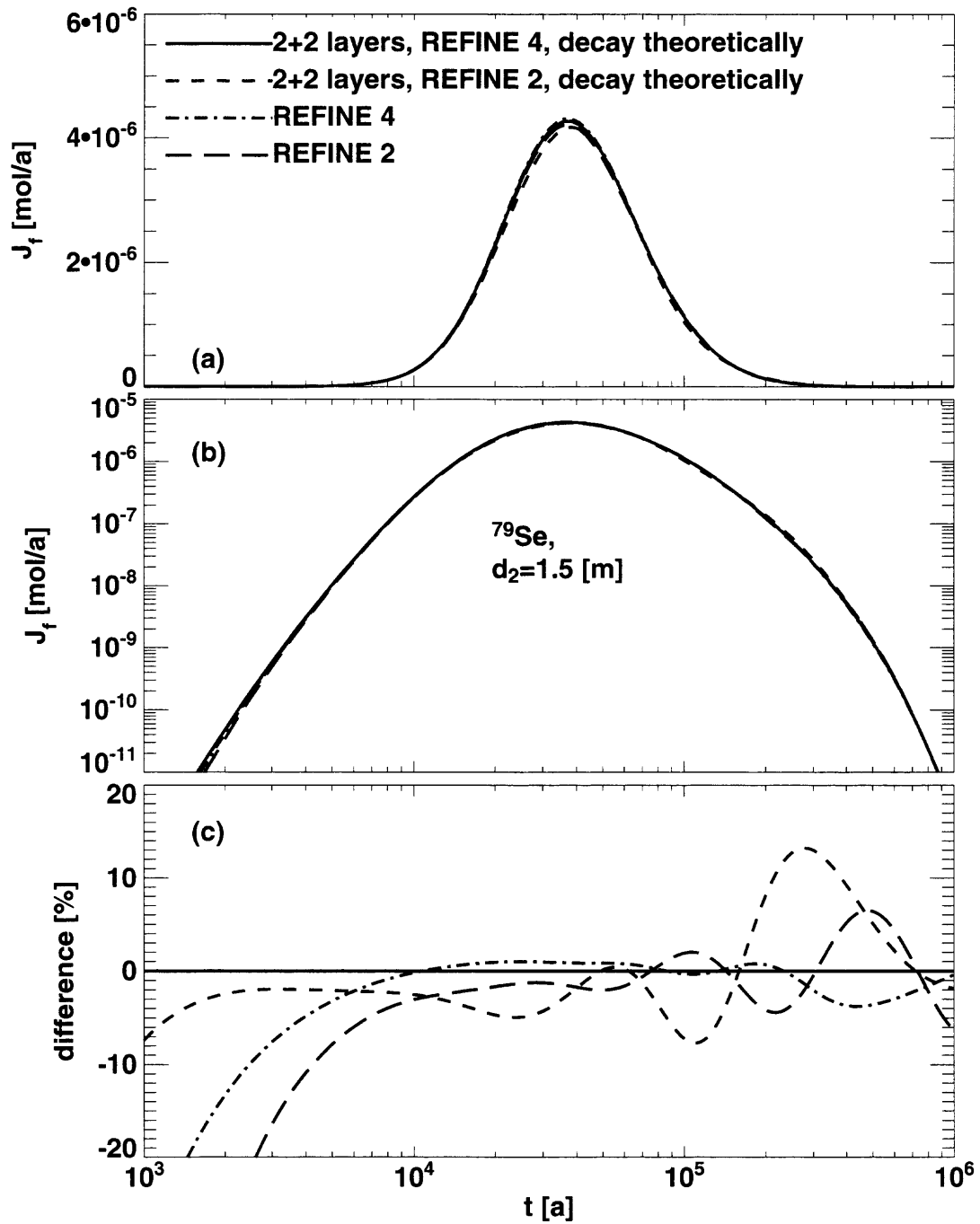


Figure 7.14. Transport of ^{79}Se in a single leg for a δ -function source. A two-layer rock matrix with width of the second rock layer $d_2 = 15$ [m] is considered, compare the long-dashed line in Figure 7.5b. For the 2+2 layer calculations, radioactive decay is incorporated analytically, see text.

For the strongly decaying nuclide ^{99}Tc we consider the extents $d_2 = 0.15$ [m] (Figure 7.15, compare also the solid line in Figure 7.7b) and $d_2 = 15$ [m] (Figure 7.16, long-dashed line in Figure 7.7b). The forms of the relative difference functions (Figures 7.15c and 7.16c) are similar to ^{135}Cs and ^{79}Se for early times and the maximum region. The trailing edge of the release curve is mainly dominated by radioactive decay for ^{99}Tc . Thus, the agreement between the different calculations indicates that PICNIC can also handle this situation. The user of PICNIC has to be aware that inaccuracies in the order of 5% are possible, also in the maximum region, for a strongly decaying nuclide.

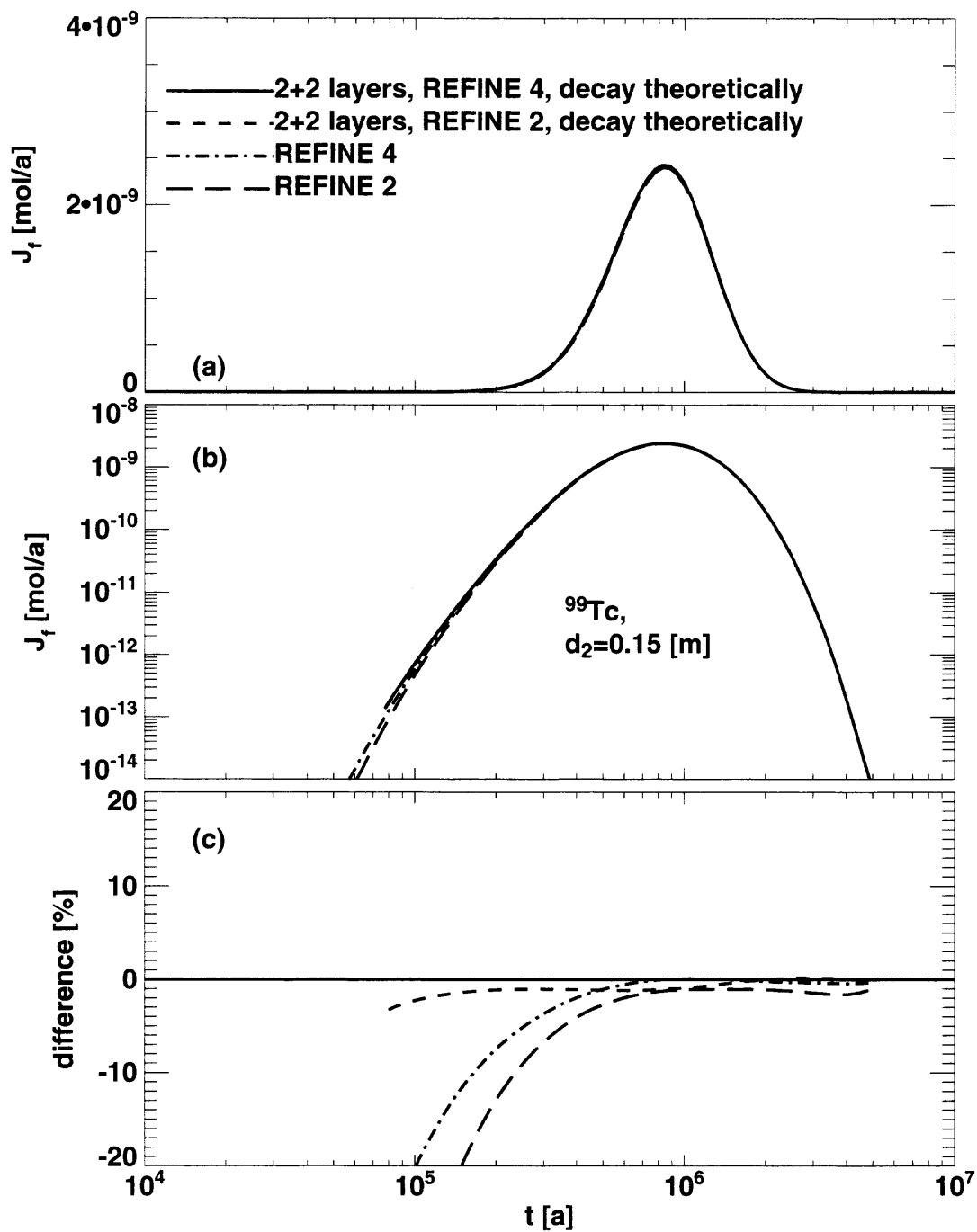


Figure 7.15. Transport of ^{99}Tc in a single leg for a δ -function source. A two-layer rock matrix with width of the second rock layer $d_2 = 0.15$ [m] is considered, compare the solid line in Figure 7.7b. For the 2+2 layer calculations, radioactive decay is incorporated analytically, see text.

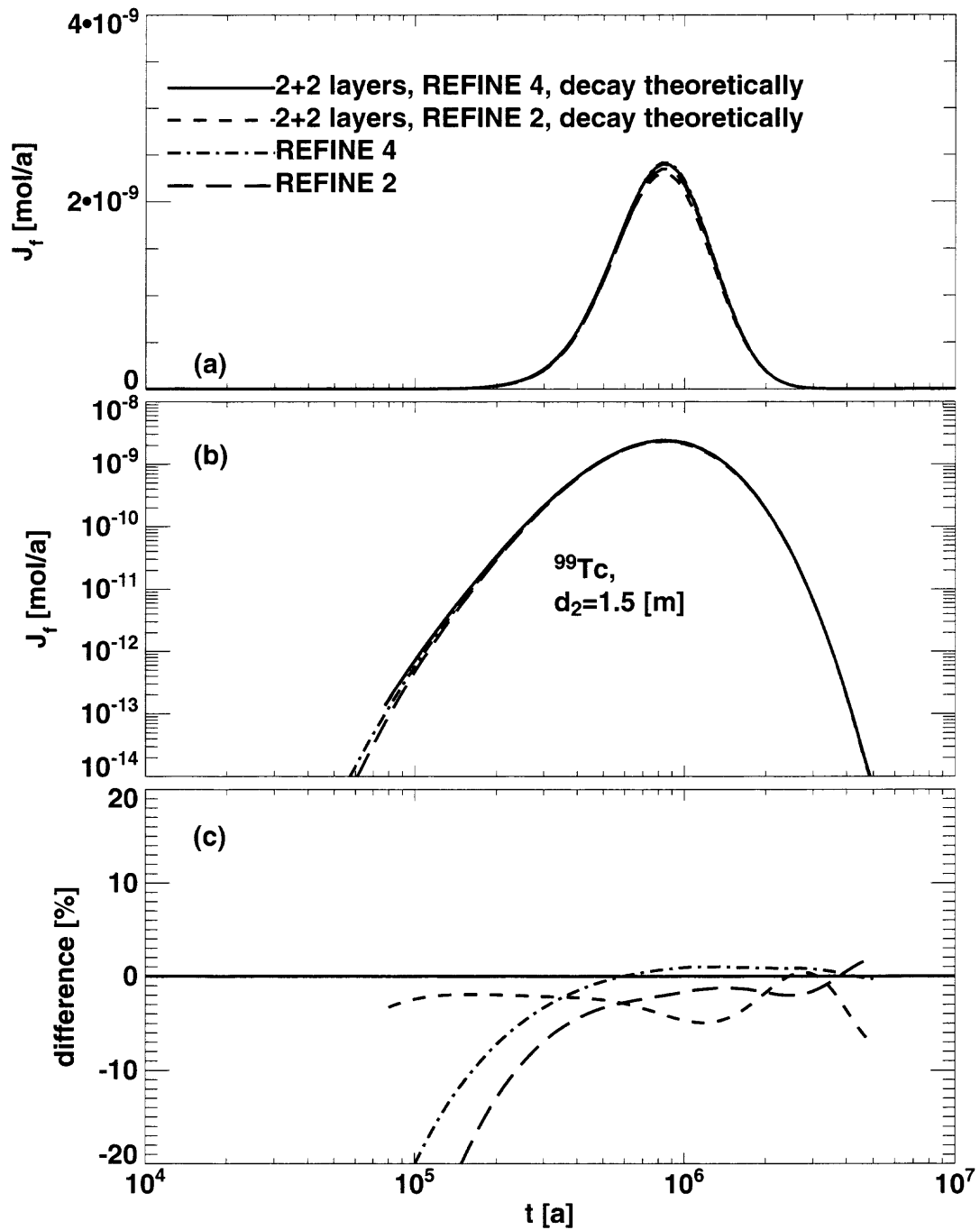


Figure 7.16. Transport of ^{99}Tc in a single leg for a δ -function source. A two-layer rock matrix with width of the second rock layer $d_2 = 1.5$ [m] is considered, compare the long-dashed line in Figure 7.7b. For the 2+2 layer calculations, radioactive decay is incorporated analytically, see text.

7.1.4. Self-Consistency Test of Network Feature

For the **network** feature of PICNIC, a self-consistency test is performed. As a test case, the transport of ^{79}Se in a single leg is considered and the extent of the second rock layer is $d_2 = 0.15$ [m]. This is the same as depicted in Figure 7.13, but the “at-infinity” option is chosen as the outlet boundary condition. The release curve is calculated with standard resolution REFINE 2 (short-dashed lines in Figure 7.17) and with increased refinement REFINE 4 (solid lines). The relative difference of these two calculations (short-dashed line in Figure 7.17c) is nearly the same as for the zero-concentration boundary condition in Figure 7.13. A network similar to Figure 4.8 is constructed with the same rock type around each leg to show the same transport behaviour as a single leg. This is possible using the at-infinity outlet boundary condition for each leg in the network, compare section 4.1.6. The respective release curves for the network for standard resolution REFINE 2 (long-dashed lines) and REFINE 4 (dash-dotted lines) are as expected virtually identical to the respective calculations for the single leg. This can be seen most clearly in the relative difference function of the network calculation for REFINE 4 with respect to the single leg calculation (dash-dotted line in Figure 7.17c), which shows some scatter only in the fifth digit of the calculations. The same holds for the option REFINE 2, where the relative difference (short-dashed and long-dashed line in Figure 7.17c) to the REFINE 4 result coincides in this graphical representation.

The same relations also hold for the strongly decaying nuclide ^{99}Tc presented in Figure 7.18. Thus, these self-consistency tests indicate, as expected, that the network feature of PICNIC is as reliable for calculations with the FEM option as with the “analytical” option.

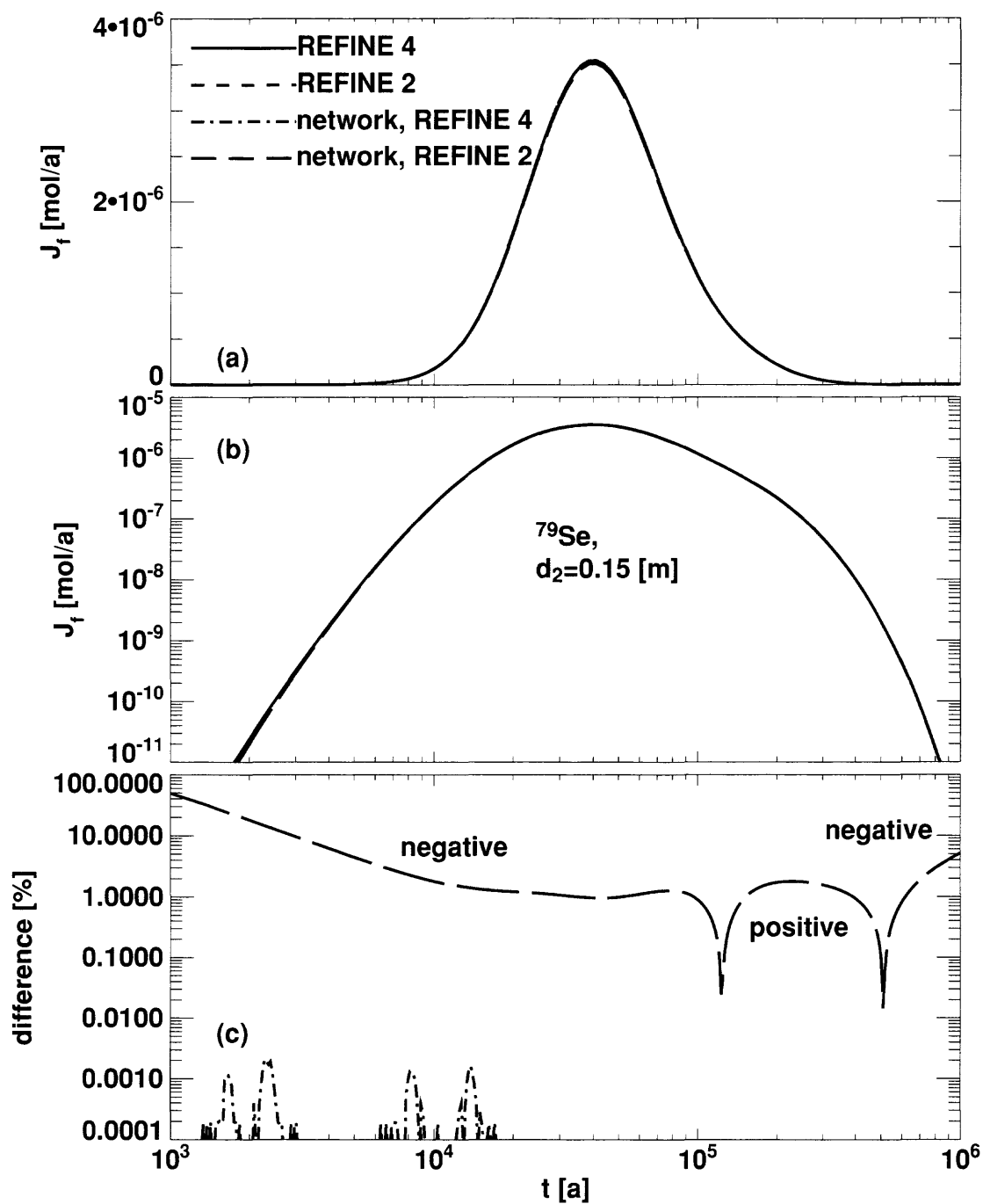


Figure 7.17. Transport of ^{79}Se in a single leg for a δ -function source. The at-infinity boundary condition is used. It is shown in (c) that the network behaves like the single leg within 0.01[%] relative difference.

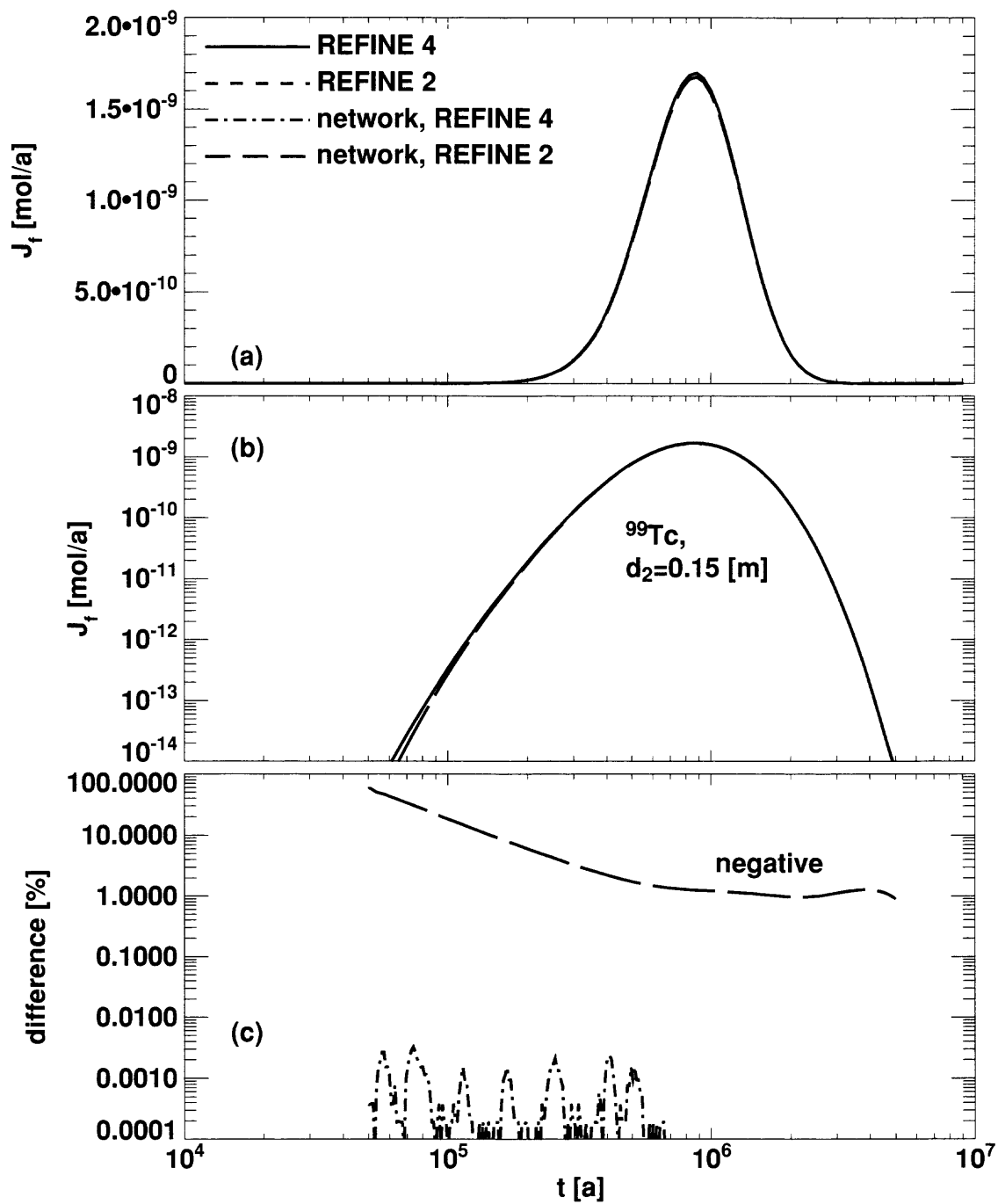


Figure 7.18. Same as in Figure 7.17, but for ^{99}Tc .

7.1.5. Varying the Porosity of the Second Rock Layer

Till now, for different nuclides with different decay rates and different retardation constants, we have varied the thickness d_2 of the second rock layer. For this test, we consider again a variation of the Kristallin-I reference case for the nuclide ^{79}Se . Transport in a single leg is considered. As depicted in Figure 7.1 in addition to the first layer of thickness $d_1 = 0.0495$ [m] and porosity $\varepsilon_{p,1} = 0.05$, a second rock layer of the same thickness $d_2 = d_1$ is assumed to follow the first rock layer. Now we consider the dependence on the porosity⁷⁵ $\varepsilon_{p,2}$ of the second rock layer to study model behaviour and behaviour of the code. The geosphere barrier efficiency (Figure 7.19) for very high porosities, $\varepsilon_{p,2} \rightarrow 1$, increases to values slightly above the value for a non-existent second layer, because the retardation constant, $R_{p,2} \rightarrow 1$ for $\varepsilon_{p,2} \rightarrow 1$, and the storage capacity of the second rock layer is small. On the other hand, for very small porosities, $\varepsilon_{p,2} \rightarrow 0$, the second rock layer becomes impermeable and the geosphere barrier efficiency reaches the limit of a non-existent second rock layer. However this limit is approached only slowly, because, using equation (2.175), the retardation constant⁷⁶, $R_{p,2} \sim \frac{1}{\varepsilon_{p,2}} \rightarrow \infty$, and the matrix diffusion time of the second layer, $\beta_2^2 \sim R_{p,2} \rightarrow \infty$, diverge for very small porosities. The rock matrix capacity of the second layer reaches a constant, $\beta_2 \gamma_2 \sim \varepsilon_{p,2} R_{p,2} \rightarrow \text{const.}$ The rock matrix delay time decreases only linearly with the porosity, $\gamma_2^2 \sim \varepsilon_{p,2}^2 R_{p,2} \sim \varepsilon_{p,2} \rightarrow 0$. The geosphere barrier efficiency is best for $0.001 < \varepsilon_{p,2} < 0.1$.

The PICNIC result (dots in Figure 7.19) agrees very well with the analytical result (solid line). The agreement is much better for a strongly limited second rock layer ($\varepsilon_{p,2} \rightarrow 1$) than for nearly unlimited matrix diffusion ($\varepsilon_{p,2} \rightarrow 0$), where the barrier efficiency is again slightly overestimated. To conclude, PICNIC can also deal with this situation and the magnitude of the inaccuracies is as expected.

⁷⁵ Note that the porosity of the second layer of the rock matrix enters into the balance equations in the rock matrix, the continuity equation at the interface of both rock layers and also into the retardation factor in the rock matrix.

⁷⁶ As already mentioned, for very small porosities this divergence is not expected to represent the behaviour in real rock.

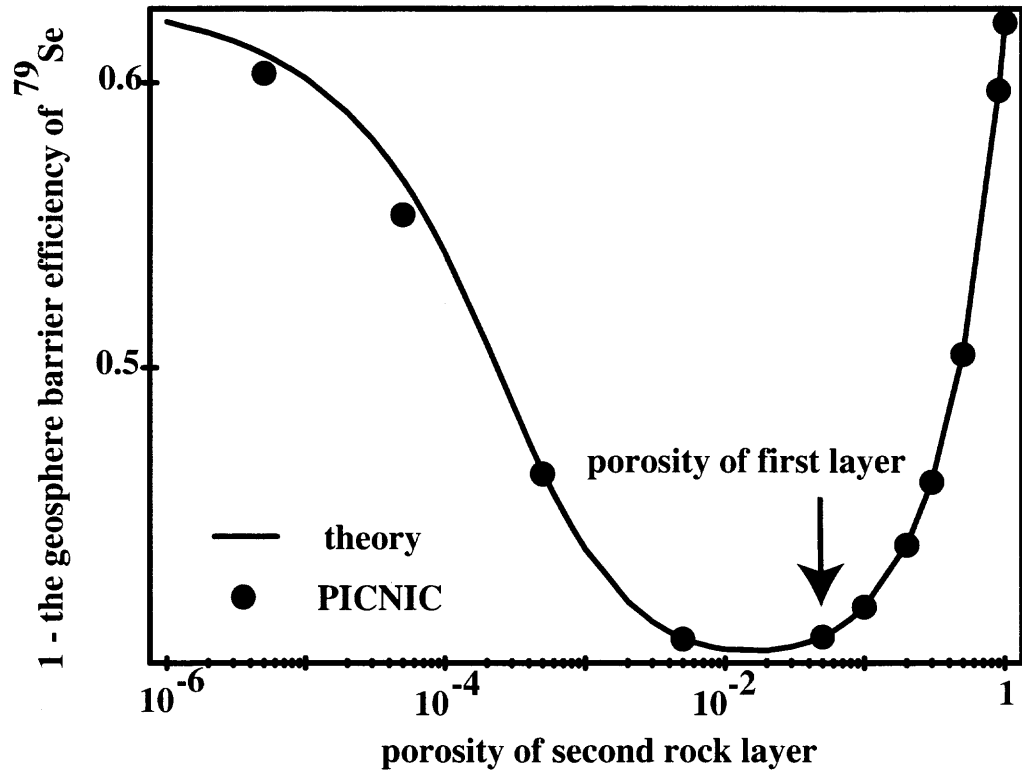


Figure 7.19. (1 - the geosphere barrier efficiency) for the nuclide ^{79}Se versus the porosity of the second rock layer $\epsilon_{p,2}$. The PICNIC results (dots) are compared to the analytical result (solid line).

7.2. Variations of the Grimsel Dipole Experiment

For the test cases related to the Kristallin-I performance assessment, the base case (without second rock layer) behaves like an advection-dispersion dominated system. This means that matrix diffusion into the first rock layer is a fast process and matrix diffusion acts like surface sorption. In this subsection we consider a case related to the transport of uranine in the Grimsel dipole experiment, which shows the typical behaviour related to matrix diffusion already for a single-layer rock matrix, compare sections 4.1 and 4.2. First a **single nuclide**, then a **nuclide decay chain**, are considered in a **single leg**. These test cases have been performed as a cross-comparison between RIP⁷⁷ and PICNIC. For this cross-comparison the at-infinity boundary condition is used for each leg throughout this subsection. The effect of different mesh refinements in the finite-element part of PICNIC is considered together with the effect of subdividing the rock matrix.

7.2.1. Single Nuclide

We consider transport in a single leg of length $L = 5$ [m], a δ -function source, and flow block and the first rock layer with the same properties as in the single-layer case. However, as discussed below, here the at-infinity outlet boundary condition is used. In addition the thickness of the first rock layer is reduced by a factor of 6.2 to $d_1 = 0.001$ [m]. Thus the matrix diffusion time of the first rock layer is reduced to $\beta_1^2 = 1.2675 \cdot 10^{-3}$ [a], which is a factor of 5 higher than the time to maximum release. This reduction of the matrix diffusion time gives the second rock layer the possibility to become important for times which are in the order of β_1^2 and larger. The second rock layer (Figure 7.1) is assumed to be half as thick as the first rock layer $d_2 = 0.0005$ [m], but the retardation is assumed to be ten times greater, $R_{p,2} = 10$. Thus the matrix diffusion time of the second rock layer, $\beta_2^2 = 3.1688 \cdot 10^{-3}$ [a] is only a factor of 2.5 larger than β_1^2 , which leads to an interplay of the diffusion processes in both layers.

For discretisation tests, this situation is modelled as in the preceding section in four different ways. The release curves for the standard calculation with REFINE 2 (long dashes) and the increased refinement REFINE 4 (dash-dotted lines) are given in Figure 7.20. As depicted in Figure 7.9, the rock matrix is also subdivided into 2+2 sub-layers of thickness $h_1 = h_2 = \frac{1}{2}d_1$ and $h_3 = h_4 = \frac{1}{2}d_2$. The results for the 2+2 sub-layers are presented for the options REFINE 2 (short dashes) and REFINE 4 (which should give the best result, solid line) in Figure 7.20. Again the relative difference functions with respect to the latter calculation are presented in Figure 7.20c. All release curves have the same structure and agree very well with each other. The relative difference functions given in Figure 7.20c are within 3% in the relevant region. The oscillations in the relative difference functions are typical for systems where matrix diffusion does not simply act as linear retardation. As usual, the lower resolution results decrease slightly earlier for late times. Interestingly, in the main part of the release curve, the agreement of the REFINE 4 result without subdivided layers with respect to the REFINE 4 result for 2+2 layers (which is within 1%) is better than for the REFINE 2 result with 2+2 layers. This resembles the behaviour of ¹³⁵Cs and ⁷⁹Se for $d_2 = 0.15$ [m] and $d_2 = 1.5$ [m] considered in Figures 7.11-7.14. However, differently from these cases, the increase of the release curves is now slightly earlier for the REFINE 2 option.

⁷⁷ A selection of the RIP simulations presented in this, and the next, section have been used in the verification of RIP.

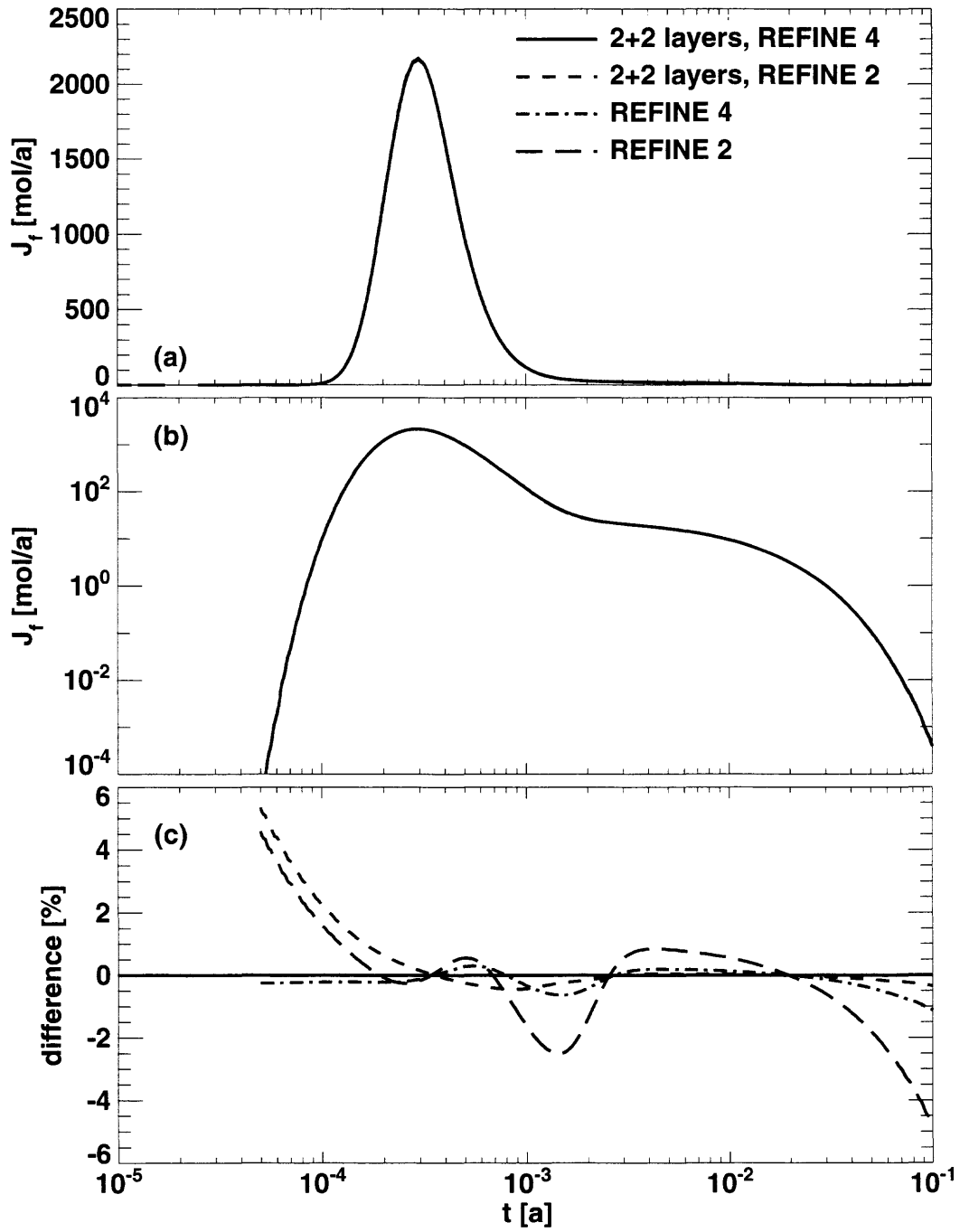


Figure 7.20. Hypothetical variation of the Grimsel dipole experiment for a two-layer rock matrix. (c) gives the relative difference functions with respect to the highest resolution PICNIC result (2+2 layers, REFINE 4). See text for more details.

Very recently the performance assessment code RIP [Miller and Kossik, 1998] has been further developed.⁷⁸ This gives the opportunity to compare the PICNIC results for 2+2 layers with option REFINE 4 (solid lines in Figure 7.21) with the RIP result (short-dashed line). The agreement is very good for times which are similar to the time to maximum release and later. In this time domain the relative difference function of the RIP result with respect to the PICNIC result is within 3% (dashed line in Figure 7.21c). Only for early times is the RIP result retarded by about $5 \cdot 10^{-6}$ [a] with respect to the PICNIC result. This retardation also causes the difference in the maximum region; see Figure 7.22 where the RIP result is shifted by $5 \cdot 10^{-6}$ [a] for comparison and a linear timescale is used.

To check how far this difference for very early times has its reason in the numerical error of the finite-element calculation of the rock matrix response in PICNIC, we compare also with the single-layer case of the Grimsel dipole experiment with $d_1 = 0.0062$ [m] (which is 6.2 times larger than in the two-layer case) and $d_2 = 0$. The same leg outlet boundary condition, at-infinity, is used. For times smaller than $\beta_1^2 = 1.2675 \cdot 10^{-3}$ [a] the release curve for this single-layer case should be the same as for the two-layer case, while for times which are in the order of magnitude of the matrix diffusion time of the first layer, β_1^2 , and for longer times there are differences.⁷⁹

For this single-layer geometry, the release curve of the 1D-FEM result (dash-dotted lines in Figures 7.21 and 7.22) agrees up to $t \approx 4 \cdot 10^{-4}$ [a] within 0.3% with the 1D-FEM result of PICNIC for the two-layer geometry. This agreement in the rising edge and the maximum region of the release curves for times up to $t \approx \frac{1}{3} \beta_1^2$ indicates that the additional second rock layer does not lead to a relevant increase of the numerical error of the FEM option in PICNIC.⁸⁰ Both PICNIC 1D-FEM results also show the well known (Figure 6.2), slightly too early increase of the release curve when compared to the 1D-AS result of PICNIC (long-dashed lines in Figure 7.21 and 7.22). However all PICNIC results agree, for these very early times, much better with each other than with the RIP result. To stay on the safe side, it can at least be inferred that the 1D-FEM option for the two-layer rock matrix does not lead to unexpected or large errors.

⁷⁸ RIP (Version 5.19) was used as a tool for total system performance assessment (TSPA) of the proposed Yucca Mountain repository [DOE, 1998]. Since version 5.21, RIP makes use of the linear response pathway method in the Laplace domain [Barten, 1996a] to calculate the transport of radionuclides in channel networks (denoted in RIP as pathway networks). For the numerical inverse Laplace transformation the variant of deHoog, Knight and Stokes [1982] of the method of Crump [1976] is used. As for PICNIC, this code is restricted to linear transport processes and time-independent parameters. As in PICNIC, the transport of single radionuclides and nuclide decay chains with the flow of water and micro-dispersion in one-dimensional channels are considered in combination with matrix diffusion into the surrounding rock matrix. RIP is presently restricted to the at-infinity boundary condition which is applied in each leg. One-dimensional matrix diffusion can be considered as in the 1D-AS option in PICNIC, and planar rock matrix geometries are considered. However also two independent two-layer areas for matrix diffusion can be considered where the first layer is the same.

⁷⁹ This is because, for these larger times, the release curve is influenced by nuclides which have reached the second rock layer in the rock matrix.

⁸⁰ Compare also magnitude and form of the relative differences functions of the single-layer case (Figure 7.20c) with the two-layer case (Figure 6.2c).

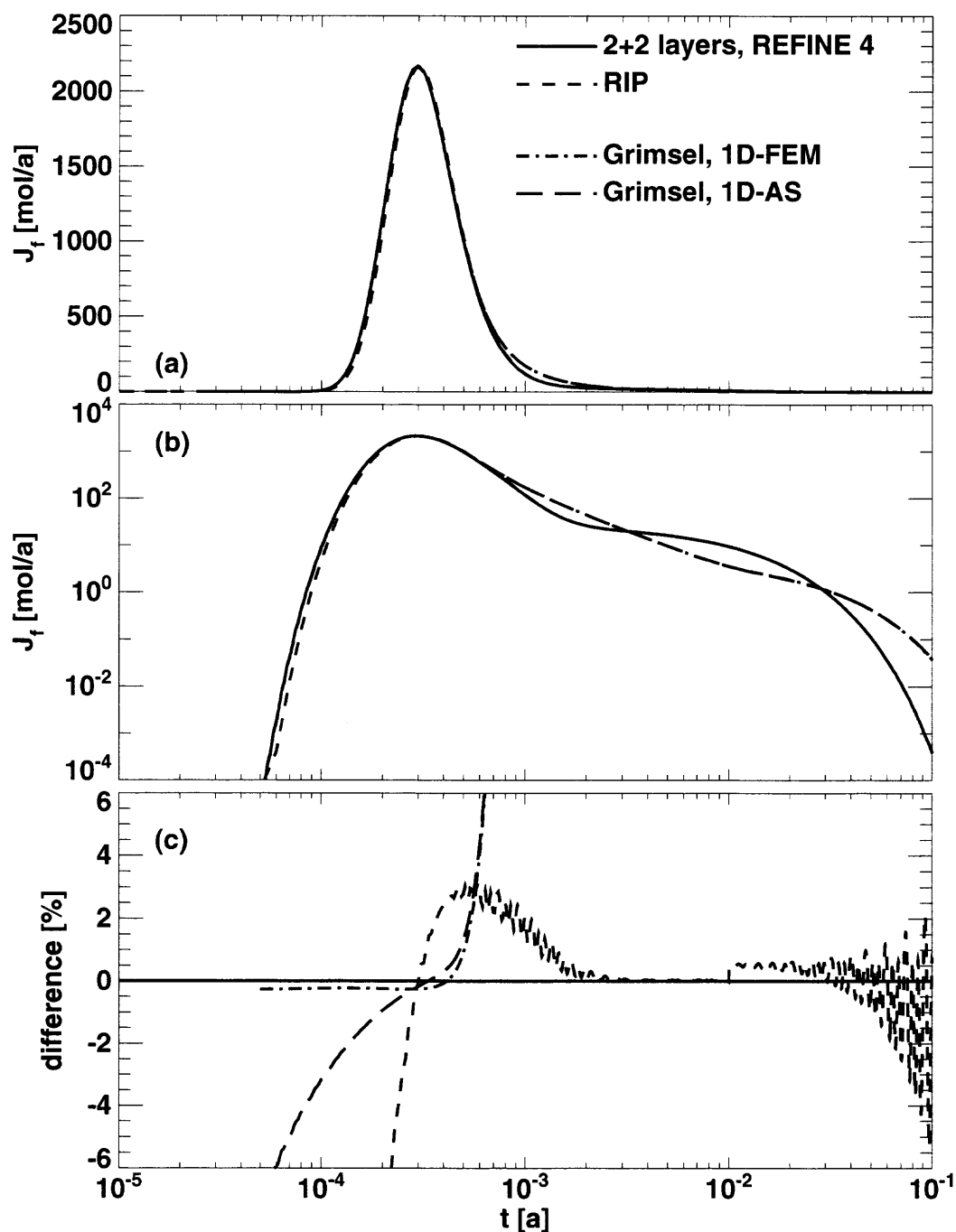


Figure 7.21. The hypothetical variation of the Grimsel dipole experiment for a two-layer rock matrix is compared to the homogeneous (single-layer) case. The solid lines (“2+2 layers, REFINE 4”) give the PICNIC 1D-FEM result for horizontally subdivided rock layers and a refined mesh. The short-dashed lines give the respective result of the RIP code. The dash-dotted lines (Grimsel, 1D-FEM) give the PICNIC FEM result for matrix diffusion into a homogeneous rock layer, which however is horizontally subdivided and using a refined mesh. The long-dashed lines (Grimsel, 1D-AS) give the respective result using the 1D-AS option in PICNIC for the single-layer case. The scatter in the relative difference function of the RIP result (short-dashed line in c) with respect to the PICNIC result is based on the numerical interpolation of the RIP printout. The relative difference functions of the homogeneous rock matrix case (dash-dotted line and long-dashed line in c) with respect to the two-layer case (2+2 layers, REFINE 4) is given in (c) for times relevant for verification purposes, up to $\beta^2 \approx 10^{-3}$ [a]. See text for further details.

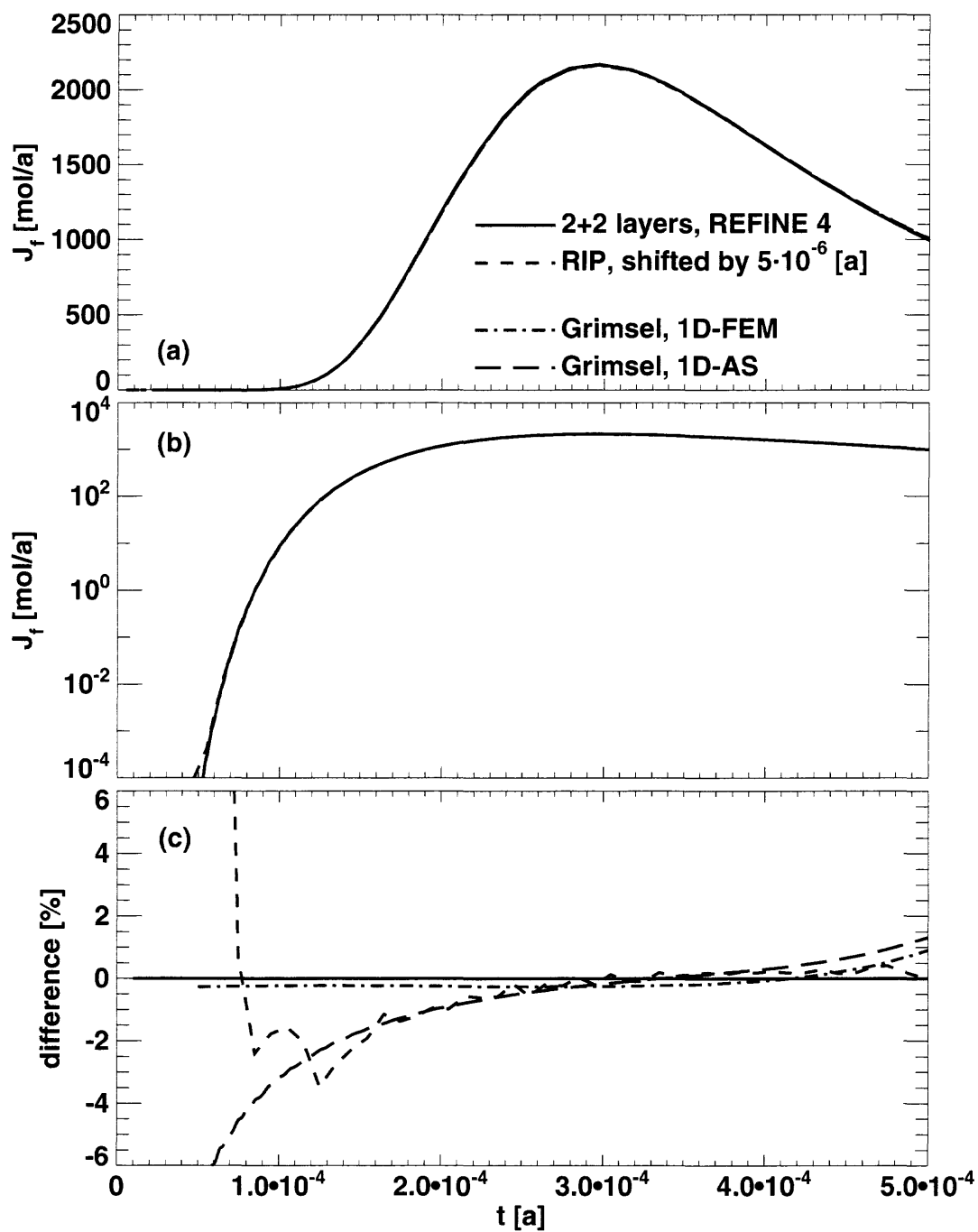


Figure 7.22. Hypothetical variation of the Grimsel dipole experiment for a two-layer rock matrix. The same curves as in Figure 7.21 are given now on a linear timescale for a better resolution of the maximum region. The RIP result, however, is shifted by $5 \cdot 10^{-6}$ [a] to earlier times to indicate the much better agreement in this situation.

7.2.2. Nuclide Decay Chain

To test also the accuracy for a **nuclide decay chain** for the two-layer rock matrix discussed above, we consider again the decay chain $\text{ANUC} \rightarrow \text{BNUC} \rightarrow \text{CNUC}$, where the half-life of ANUC is 10^{-3} [a], the half-life of BNUC is 10^{-4} [a] and CNUC is assumed to be stable, compare section 4.2. In the first rock layer, ANUC, BNUC and CNUC are assumed to have the same properties as uranine, apart from the retardation factor in the rock matrix. ANUC has the same retardation factor as uranine, $R_p = 1.0$, while BNUC has $R_p = 2.0$ and CNUC has $R_p = 10.0$. In the second rock layer the retardation factors for all nuclides are assumed to be ten times higher. Again a δ -function source of the parent ANUC is considered.

The same discretisation tests of PICNIC are performed as for the single nuclide case in Figure 7.20. See Figure 7.23 for ANUC, Figure 7.24 for BNUC, and Figure 7.25 for CNUC. All nuclides of the decay chain have in common that the relative difference from the highest refinement case is within 5% for all relevant times. Thus the agreement between the different PICNIC calculations is very good. The amplitudes of the relative difference functions are smaller than for the single-layer case (compare section 6.1). Similar to the single-layer case, the relative difference functions oscillate. As expected, the relative difference function for the standard resolution REFINE 2 option without subdivided rock layers is highest. The agreement of the RIP results with the highest resolution PICNIC results is very good. Overall, we can conclude that the 1D-FEM option for a two-layer rock matrix geometry does not appear to lead to an increased numerical error when compared to the 1D-FEM option for a homogeneous rock matrix (compare section 6.1), both for single nuclides and for nuclide decay chains.

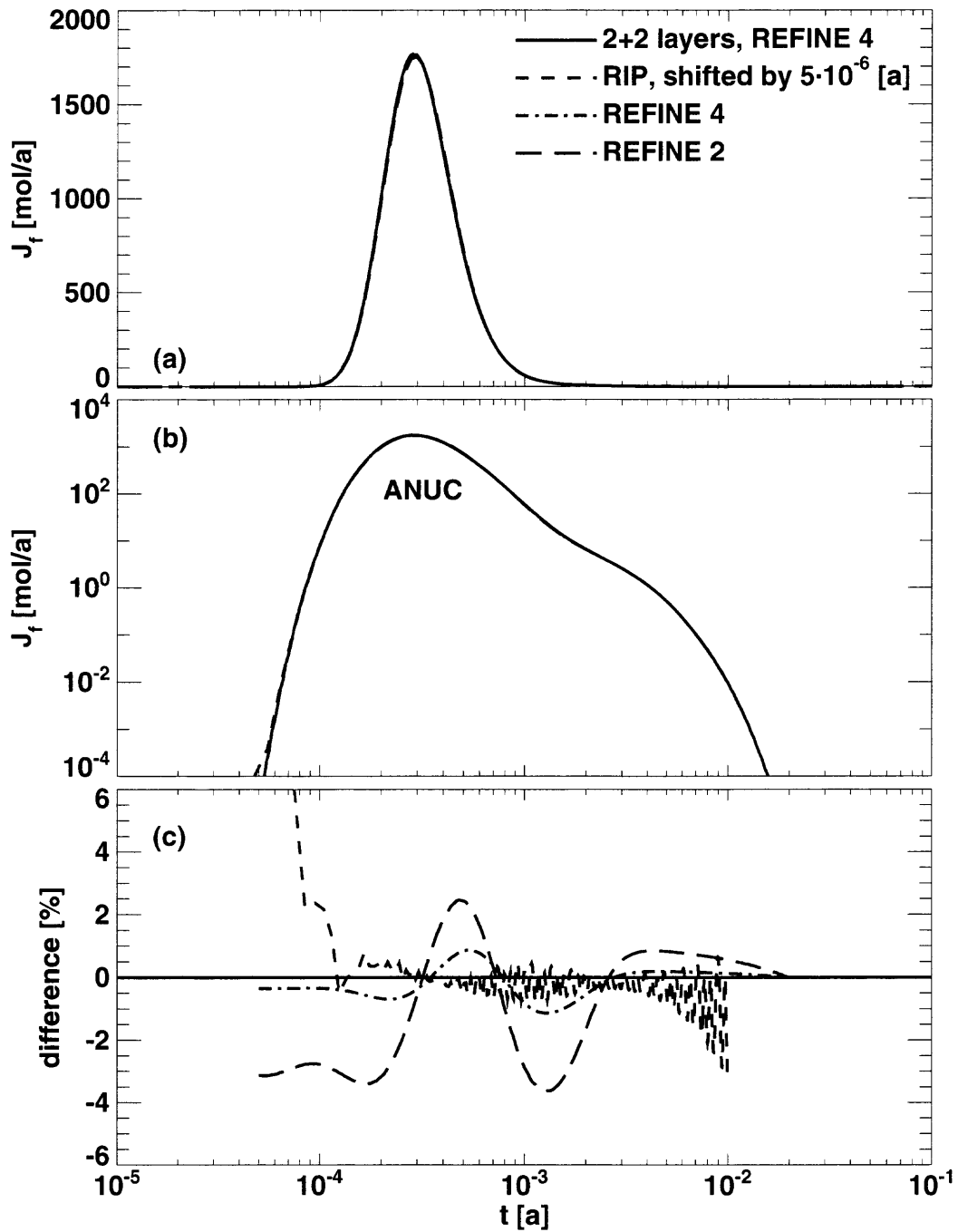


Figure 7.23. Hypothetical variation of the Grimsel dipole experiment for a two-layer rock matrix. Presented is the nuclide ANUC of the decay chain $\text{ANUC} \rightarrow \text{BNUC} \rightarrow \text{CNUC}$. The RIP result has been calculated up to $t \approx 10^{-2}$ [a] only. The nomenclature is as in Figure 7.20.

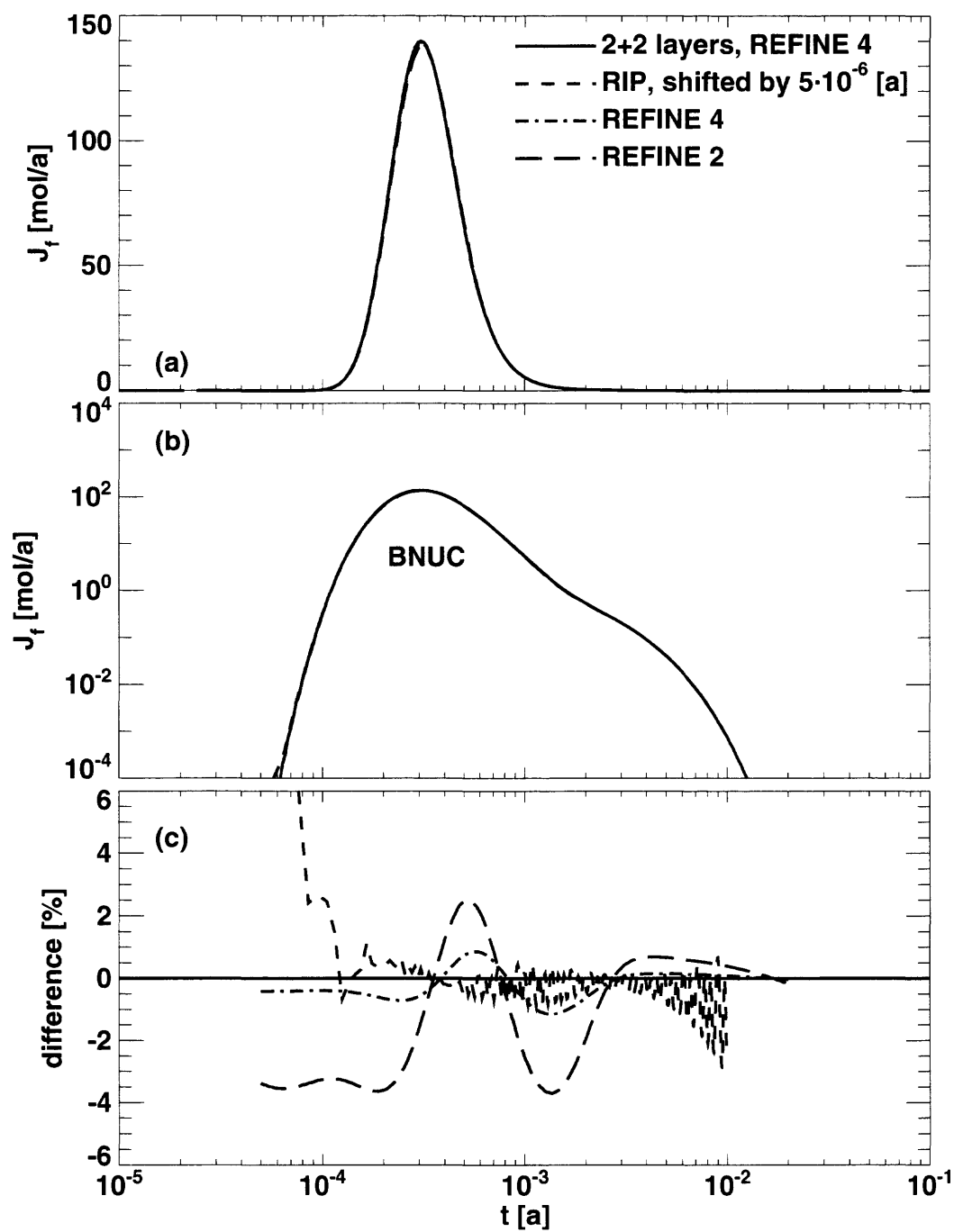


Figure 7.24. Hypothetical variation of the Grimsel dipole experiment for a two-layer rock matrix. Presented is the nuclide BNUC of the decay chain $ANUC \rightarrow BNUC \rightarrow CNUC$. The nomenclature is as in Figure 7.20. The RIP result has been calculated up to $t \approx 10^{-2}$ [a] only.

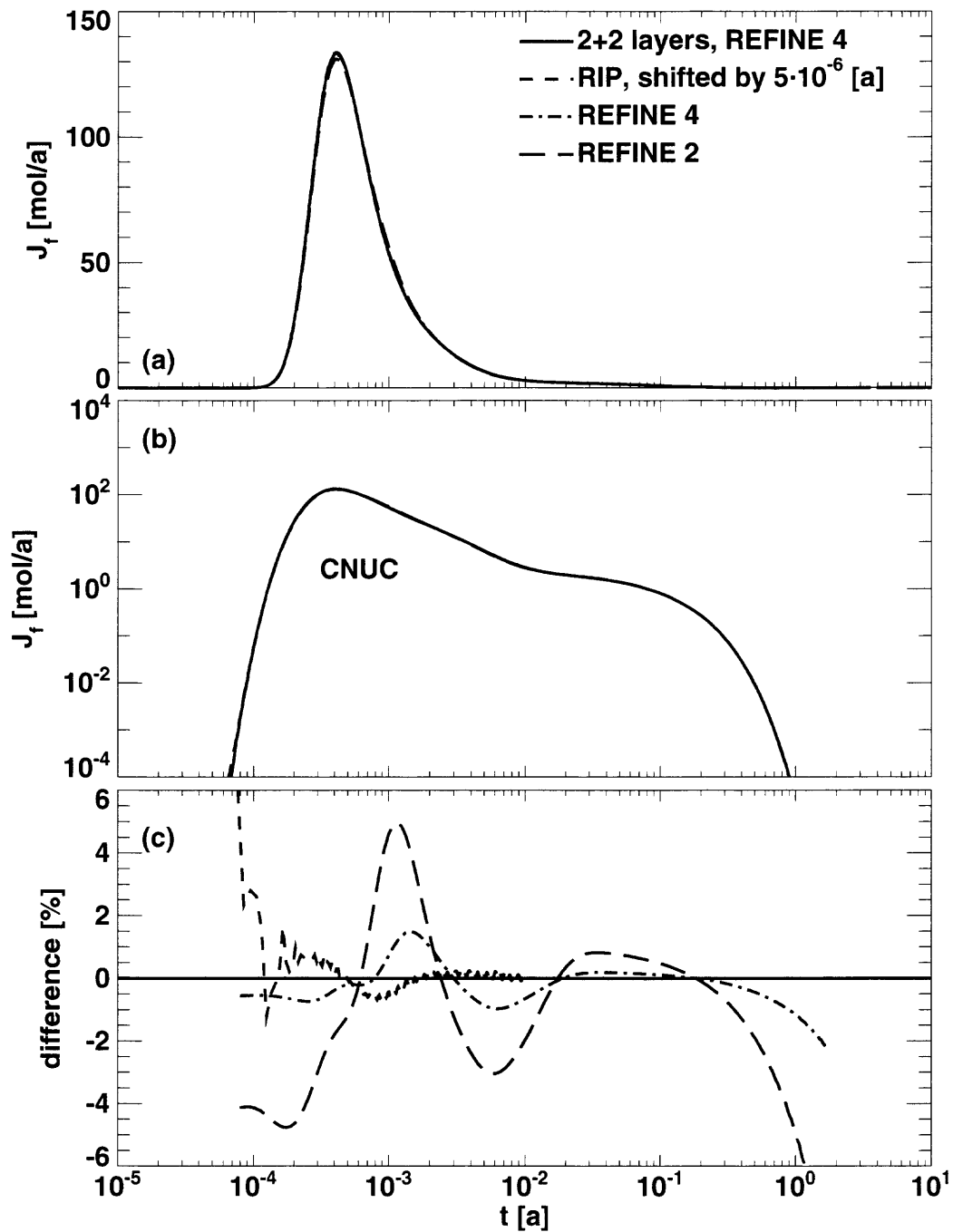


Figure 7.25. Hypothetical variation of the Grimsel dipole experiment for a two-layer rock matrix. Presented is the nuclide CNUC of the decay chain $\text{ANUC} \rightarrow \text{BNUC} \rightarrow \text{CNUC}$. The nomenclature is as in Figure 7.20. The RIP result has been calculated up to $t \approx 10^{-2}$ [a] only.

7.3. Summary

As step IV in the verification scheme, in this section, we have verified the capability of PICNIC to deal with a two-layer planar rock matrix for one-dimensional matrix diffusion using the finite-element method for calculation of the rock matrix response, see Table. 7.1. Following the verification strategy in section 3, we have concentrated on single nuclides and nuclide decay chains in single legs.

For two weakly decaying and one strongly decaying single nuclide and Kristallin-I performance assessment parameters, the effect of mesh refinement and subdivision of rock layers was analysed for different extents of the second rock layer. Physically, the second rock layer represents unaltered wallrock in a cataclastic zone, while the first rock layer is altered wallrock. It was shown that the long time limit of the nuclide release for a constant source differs only slightly from the analytical result derived for this verification. Moreover, it was shown that a refined finite-element mesh in PICNIC, as expected, further considerably reduced the difference to the analytical result. The effect of the porosity variation in the second rock layer was also investigated for the long time limit of the nuclide release. The network feature of PICNIC was successfully spot-checked with self-consistency tests.

For a single nuclide and a nuclide decay chain in a single leg with Grimsel uranium parameters, the full time-dependent behaviour was analysed. Discretisation tests were performed. A cross-comparison with the RIP code showed a very good agreement. This cross-comparison will be extended in section 8 to more complicated rock matrices.

Following the considerations in section 3, together with verification step I in section 4 and step III in section 6, this verifies the capability of PICNIC to deal also with one-dimensional matrix diffusion into a two-layer rock matrix.

single leg		(a) single nuclide			(b) nuclide decay chain		
		ZG	ZC	AI	ZG	ZC	AI
source in Laplace domain	δ -pulse		R	R,C ⁸¹	R		R,C ⁸²
	simple-leaching						
source in time domain	short pulse						
	long top-hat		R,S ⁸³				
	band-release						
	general						

pathway		(c) single nuclide			(d) nuclide decay chain		
		ZG	ZC	AI	ZG	ZC	AI
source in Laplace domain	δ -pulse						
	simple-leaching						
source in time domain	short pulse						
	long top-hat						
	band-release						
	general						

network		(e) single nuclide			(f) nuclide decay chain		
		ZG	ZC	AI	ZG	ZC	AI
source in Laplace domain	δ -pulse			K			
	simple-leaching						
source in time domain	short pulse						
	long top-hat						
	band-release						
	general						

Table 7.1. Performed calculations for the two-layer planar fracture geometry given in Figure 7.1 and for various boundary conditions. Note: All test cases represented by empty fields in the scheme were implicitly verified by any of the specified examples. Such a procedure is strongly based on the internal structure of PICNIC as outlined in more detail in section 3. Legend: C: comparison with other computer code; K: consistency tests; R: “discretisation test” considering different mesh refinements in the “finite-element” results in PICNIC; S: stationary behaviour tested.

⁸¹ Comparison with RIP.

⁸² Comparison with RIP.

⁸³ Comparison with analytical result.

8. One-Dimensional Matrix Diffusion into Heterogeneous Geometries

In this section we consider **heterogeneous geometries for one-dimensional rock matrix diffusion** which were not considered in sections 6 and 7. This is step V in the PICNIC verification scheme, which completes the verification for one-dimensional matrix diffusion, (see the verification strategy in section 3.4.5). The tests of this section have been performed as cross-comparisons of PICNIC with the codes PAWorks/LTG or RIP. Note that throughout this section we use two-dimensional finite-element meshes (2D-FEM) for calculation of the rock matrix response, while in section 7 we used one-dimensional finite element meshes (1D-FEM). The effects on the PICNIC results of mesh refinement and rock layer subdivision are considered in all cases.

We start in section 8.1 with the transport of a **single nuclide** and of a **nuclide decay chain** in a **single leg with matrix diffusion into two independent homogeneous areas of rock matrix**. A cross-comparison with PAWorks/LTG is performed.

In section 8.2 the transport of a **single nuclide** and of a **nuclide decay chain** in a **single leg with matrix diffusion into two independent two-layer areas of rock matrix** is considered. A cross-comparison with RIP is performed.

In section 8.3 the transport of **single nuclides** and of **nuclide decay chains** in different **pathways** is considered, where some legs have rock matrix geometries described in sections 8.1 and 8.2. Cross-comparisons with PAWorks/LTG and RIP are performed. All test cases of sections 8.1 to 8.3 use variations of Grimsel uranine parameters (compare sections 4.2 and 6.1).

In section 8.4, finally, the transport of a **single nuclide** and of a **nuclide decay chain** in a **26-leg network** is considered, compare sections 4.3 and 6.6. Three of the legs are assumed to have **two independent two-layer areas available for rock matrix diffusion**.

Section 8.5 gives a summary.

8.1. Two Independent Homogeneous Regions for Matrix Diffusion

As a first example we consider again in this subsection a hypothetical variation of the transport of uranine in the Grimsel dipole experiment for a δ -function source. Now, however, only **40% of the fracture surface is in contact with rock matrix type M1** and thickness $d_1 = 0.0062$ [m], see Figure 8.1a. This is done such that the surface of this rock matrix area, $2B_1$, which is in contact with the area of the flowing water, is reduced by a factor of 0.4 compared to the original uranine case. The aperture $2b$ of the fracture is the same as in the original case. The remaining **60% is assumed to be in contact with rock matrix of another type M2**, $\frac{B_2}{B_1 + B_2} = 0.6$. The thickness of this rock matrix block is $d_2 = 0.0005$ [m]. The rock matrix of type M2 (the same type of rock matrix discussed in section 4.2) is as M1, but the retardation factor, $R_{p,2} = 10$, is ten times higher.

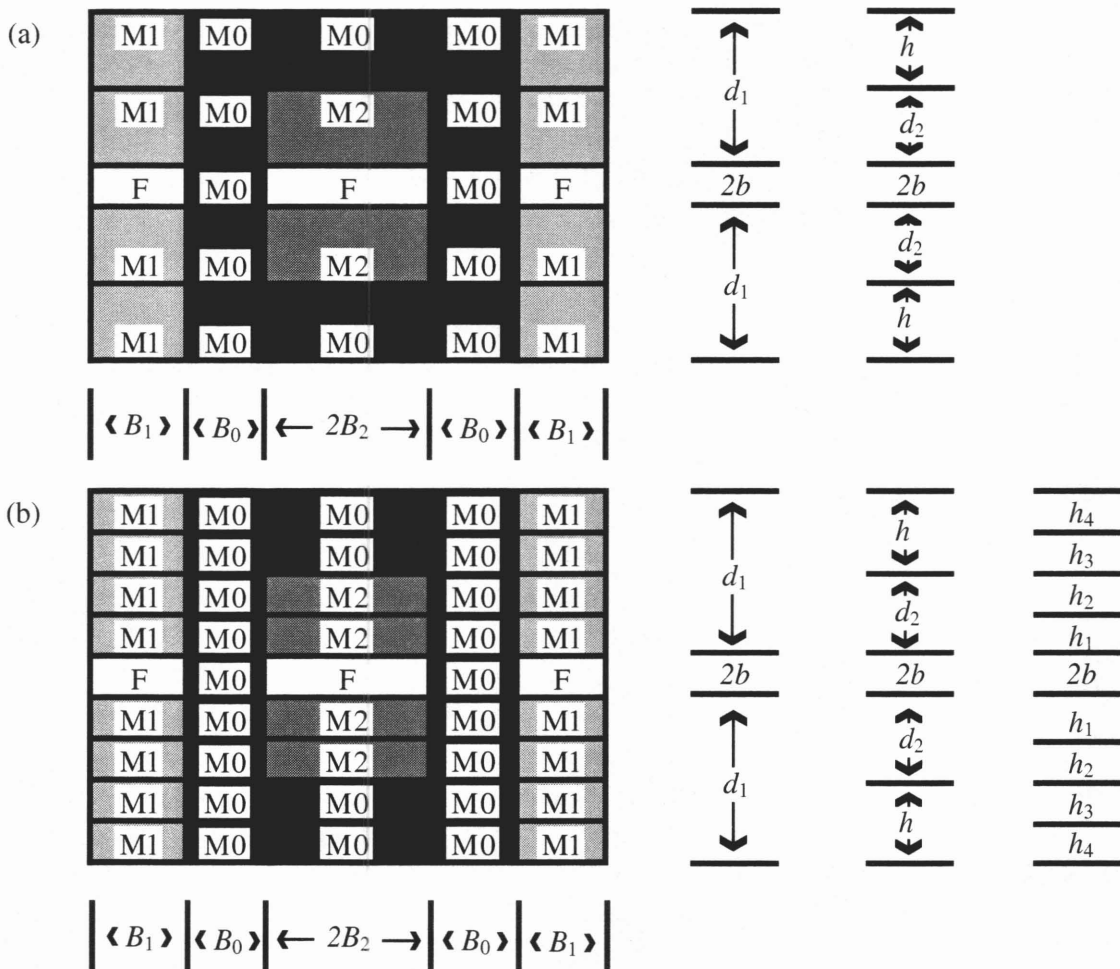


Figure 8.1. Sketch of the cross-section of a leg with a fracture where the area of flowing water (F) is in contact with two independent areas of rock matrix (M1 and M2) for one-dimensional matrix diffusion. The width of the interface to the rock matrix type M1 is $2B_1$, while it is $2B_2$ to the rock matrix type M2. The two blocks of rock matrix are separated by two stripes of impermeable rock (M0) of widths B_0 . This is such that matrix diffusion into the different rock blocks is independent and moreover one-dimensional. The aperture of the fracture is $2b$. The thickness of the rock layers types M1 and M2 are d_1 and d_2 , respectively. In (a) this is entered to PICNIC by two layers of rock matrix below and above the fracture of thickness d_2 and $h = d_1 - d_2$. In (b) the first rock layer of thickness d_1 is subdivided into two sub-layers of thickness h_1 and h_2 , such that $d_1 = h_1 + h_2$, and the second rock layer of thickness h is subdivided into two sub-layers of thickness h_3 and h_4 , such that $h = h_3 + h_4$.

To ensure that **diffusion** into the rock matrix regions of types M1 and M2 is **one-dimensional** and independent, the different matrix areas are separated from each other by strips of impermeable rock matrix (M0) of width B_0 .⁸⁴ Because d_1 is unequal to, and especially larger than, d_2 , the rock matrix below and above the fracture is separated into two layers to be consistent with the PICNIC input standards, one close to the fracture and of thickness d_2 , the other of thickness $h = d_1 - d_2$ following the first layer. This means that the rock matrix of type M1 and thickness d_1 is subdivided into two layers, and that, after the rock layer of type M2 and thickness d_2 , follows impermeable rock (M0) of thickness h .

The release curves for this geometry are depicted in Figure 8.2 for standard resolution REFINE 2 (long-dashed lines) and increased refinement REFINE 4 (dash-dotted lines). The timescales of the different rock matrix types can nicely be read from the release curve in the log-log representation. The time to maximum release is slightly before $\alpha + \frac{1}{6}\gamma_1^2 + \frac{1}{6}\gamma_2^2 = 3.7464 \cdot 10^{-4}$ [a], where the matrix delay time of the matrix type M1, $\gamma_1^2 = 1.98026 \cdot 10^{-5}$ [a], is a factor of 0.16 smaller, while the matrix delay time of the matrix type M2, $\gamma_2^2 = 4.45558 \cdot 10^{-4}$ [a], is increased by a factor of 3.6 with respect to the original uranine case. Also the timescales for matrix diffusion in the regions of type M1, $\beta_1^2 = 4.87236 \cdot 10^{-2}$ [a], and of type M2, $\beta_2^2 = 3.16881 \cdot 10^{-3}$ [a], can be seen in the two humps in the release curve (Figure 8.2b).

To achieve yet greater accuracy with PICNIC for another calculation, in addition to the option REFINE 4, each rock layer is subdivided into two layers of the same thickness, see Figure 8.1b. This means that the rock matrix region of type M2 is represented by two rock regions of thickness h_1 and h_2 with $h_1 = h_2 = \frac{1}{2}d_2$. The rock matrix region of type M1 is represented by four rock blocks of thickness h_1 , h_2 , h_3 , and h_4 with $h_3 = h_4 = \frac{1}{2}h$. The release curve for this rock type is given as solid lines in Figure 8.2. All PICNIC results agree again very well with each other. See especially in Figure 8.2c the differences to the PICNIC highest refinement result. As already observed for the layer rock matrix discussed in section 7, the relative difference functions show some oscillatory behaviour. The difference is biggest for the PICNIC calculation without subdivision and with standard resolution REFINE 2. However, also for this case, it is within 6% in the relevant region. This difference is again mainly based on the somewhat later increase of the release curve for early times and the somewhat earlier decrease of the release curve for late times.

The analytical solution for this situation with two independent regions for one-dimensional matrix diffusion can be calculated analytically in the Laplace domain. The response of the entire rock matrix is simply the sum of the response of the two independent rock areas,

$$\eta = \eta_1 + \eta_2. \quad (8.1)$$

⁸⁴ It should be noted that, although the system defined here is mathematically well specified, the presence of two separate flow blocks violates the basic physical assumption that the concentrations in the flow blocks are equal. That is to say, there is no physical mechanism that would ensure that the concentrations in these separate flow blocks are equal, which however is explicitly assumed in the PICNIC code. Thus it is arguable that PICNIC should not allow such a geometry to be specified. Connecting the areas of flowing water in the leg cross-sectional area would be a possible option to provide explicitly a physical mechanism that ensures equal concentrations in the flow blocks. The same argument holds for the rock matrix geometries depicted in Figures 8.6 and 8.26 below.

Compare section 5.5 in Barten [1996a] where, inter alia, one-dimensional matrix diffusion into two independent, but there orthogonal, rock matrix regions was considered, see also section 2.4 of this report. This solution, however, is not implemented in PICNIC as a 1D-AS.

As an alternative, we can compare with results of the code PAWorks/LTG [Dershowitz et al., 1998].⁸⁵ It should be recalled that PAWorks/LTG and PICNIC are in excellent agreement for transport in a single leg with a homogeneous rock matrix, see sections 6.8 and 6.9 in Shuttle and Eiben [1998] and section 4.2 in this report.

The PAWorks/LTG result (crosses in Figure 8.2) agrees very well with the PICNIC results. Moreover the difference of the PAWorks/LTG result to the highest refinement PICNIC result is in the order of the difference of the different PICNIC results. In the relevant region, the relative difference with respect to the highest refinement PICNIC result is within 1%. Only for very early times is the increase of the LTG result somewhat later; for very late times the decrease is somewhat later. From these small differences we can conclude that PICNIC also works also in this situation.

⁸⁵ The PAWorks/LTG code uses a new variant of the finite-element method in the Laplace domain [Sudicky, 1989, 1990]. For the numerical inverse Laplace transformation, as in the RIP code, the variant of deHoog, Knight and Stokes [1982] of Crump's [1976] method is applied. As for PICNIC and RIP, LTG is restricted to linear transport processes and time-independent parameters. The transport of radionuclide decay chains in one-dimensional channels is considered in combination with matrix diffusion into the neighbouring rock matrix. LTG is presently restricted to the zero-gradient boundary condition. In the present version of LTG, one-dimensional matrix diffusion into a planar matrix geometry can be considered, but no layer rock matrix and no two-dimensional matrix diffusion. Two or more independent matrix blocks for one-dimensional matrix diffusion, can however be considered.

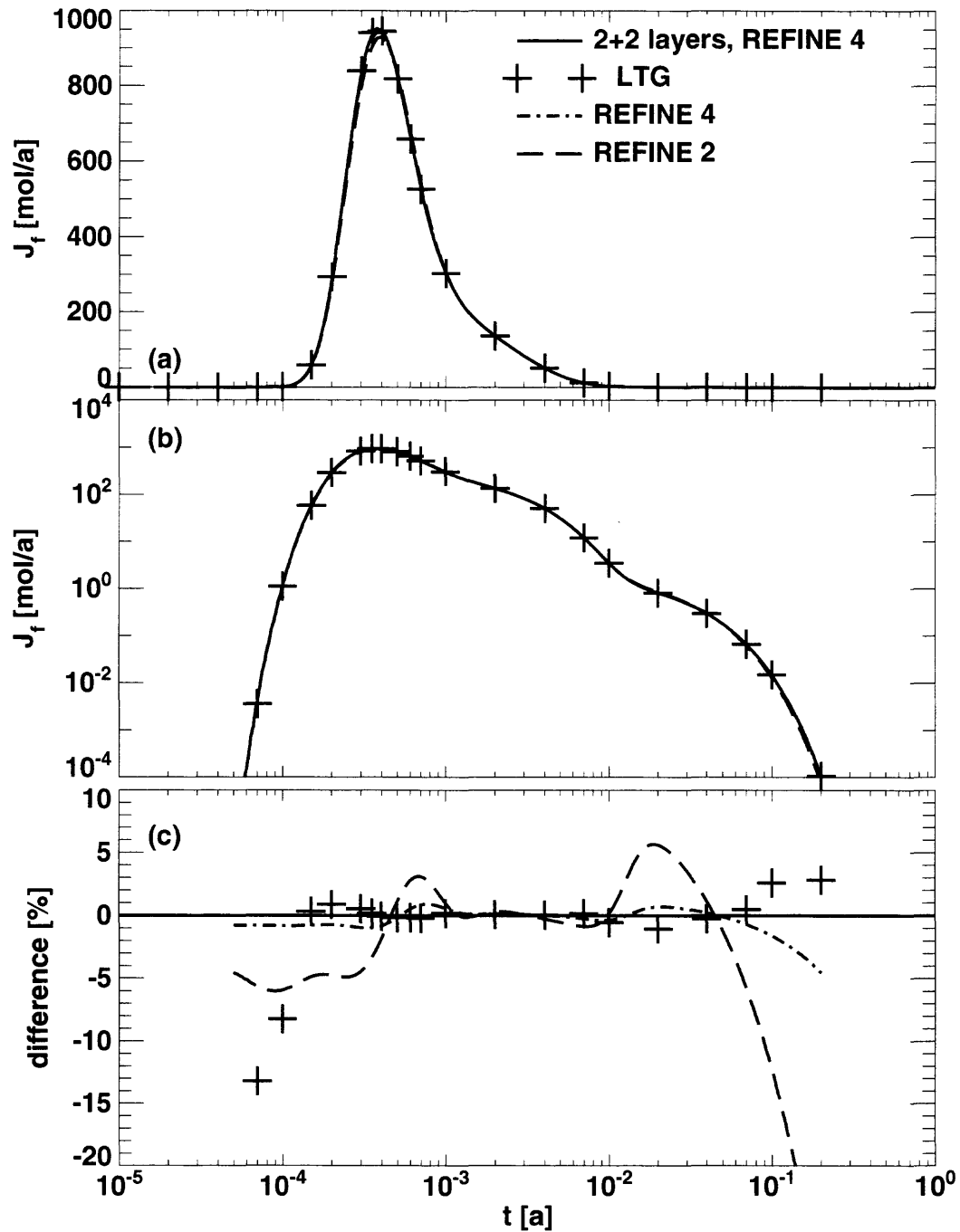


Figure 8.2. Hypothetical variation of the Grimsel dipole experiment for two independent areas for rock matrix diffusion. For more details see text. The PICNIC result for 2+2 layers (Figure 8.1b) with the option REFINE 4 (solid lines) is compared to the PICNIC result for 2 layers (Figure 8.1a) and the standard option REFINE 2 (long-dashed lines) and REFINE 4 (dash-dotted lines). A comparison with a PAWorks/LTG result (crosses indicate the data points available) is also performed. The release curves are given in (a) on a linear scale and in (b) on a logarithmic scale for the flux. The relative difference to the 2+2 layers PICNIC result with REFINE 4 is given in (c).

To test also the accuracy for a **nuclide decay chain** for the **two independent rock matrix areas** discussed above, we consider again the nuclide decay chain $\text{ANUC} \rightarrow \text{BNUC} \rightarrow \text{CNUC}$, where the half-life of ANUC is 10^{-3} [a], the half-life of BNUC is 10^{-4} [a] and CNUC is assumed to be stable, compare section 4.2. ANUC, BNUC, and CNUC are assumed to have the same properties as non-decaying uranine, except for the retardation factor in the rock matrix. ANUC has the same retardation factor as uranine, $R_p = 1.0$ in rock type M1 and $R_p = 10.0$ in rock type M2, while again the retardation factor of BNUC is two times higher and the retardation factor of CNUC is ten times higher. A δ -function source of the parent ANUC is considered.

Similar discretisation tests within PICNIC are performed as for the single nuclide case of Figure 8.2. See Figure 8.3 for ANUC, Figure 8.4 for BNUC, and Figure 8.5 for CNUC. All nuclides of the decay chain have in common that PICNIC calculations with option REFINE 4 and the PAWorks/LTG calculation agree excellently with each other. For all the nuclides of the chain the agreement is within a few percent. Again the PAWorks/LTG result increases somewhat later for early times. For late times the PAWorks/LTG results decrease somewhat earlier for ANUC and BNUC and somewhat later for CNUC. Only for the standard resolution result of PICNIC, are the differences slightly bigger, i.e. ranging from -15% to +5% in the maximum region. This should be acceptable for most performance assessment calculations, but for the analysis of experiments with decay chains the option REFINE 4 might be preferable.

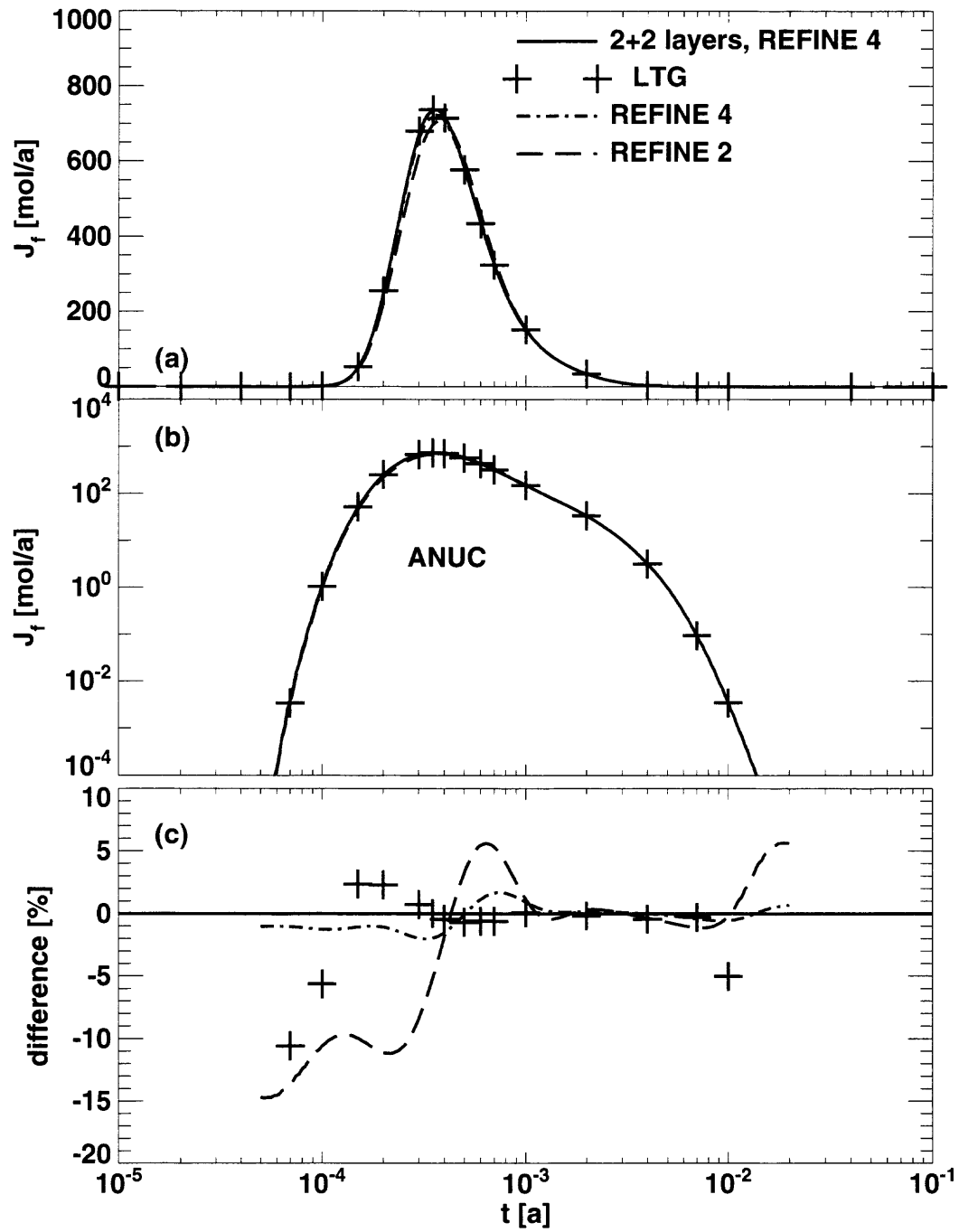


Figure 8.3. Hypothetical variation of the Grimsel dipole experiment for two independent areas for rock matrix diffusion. Presented is the nuclide ANUC of the decay chain $ANUC \rightarrow BNUC \rightarrow CNUC$. The nomenclature is as in Figure 8.2.

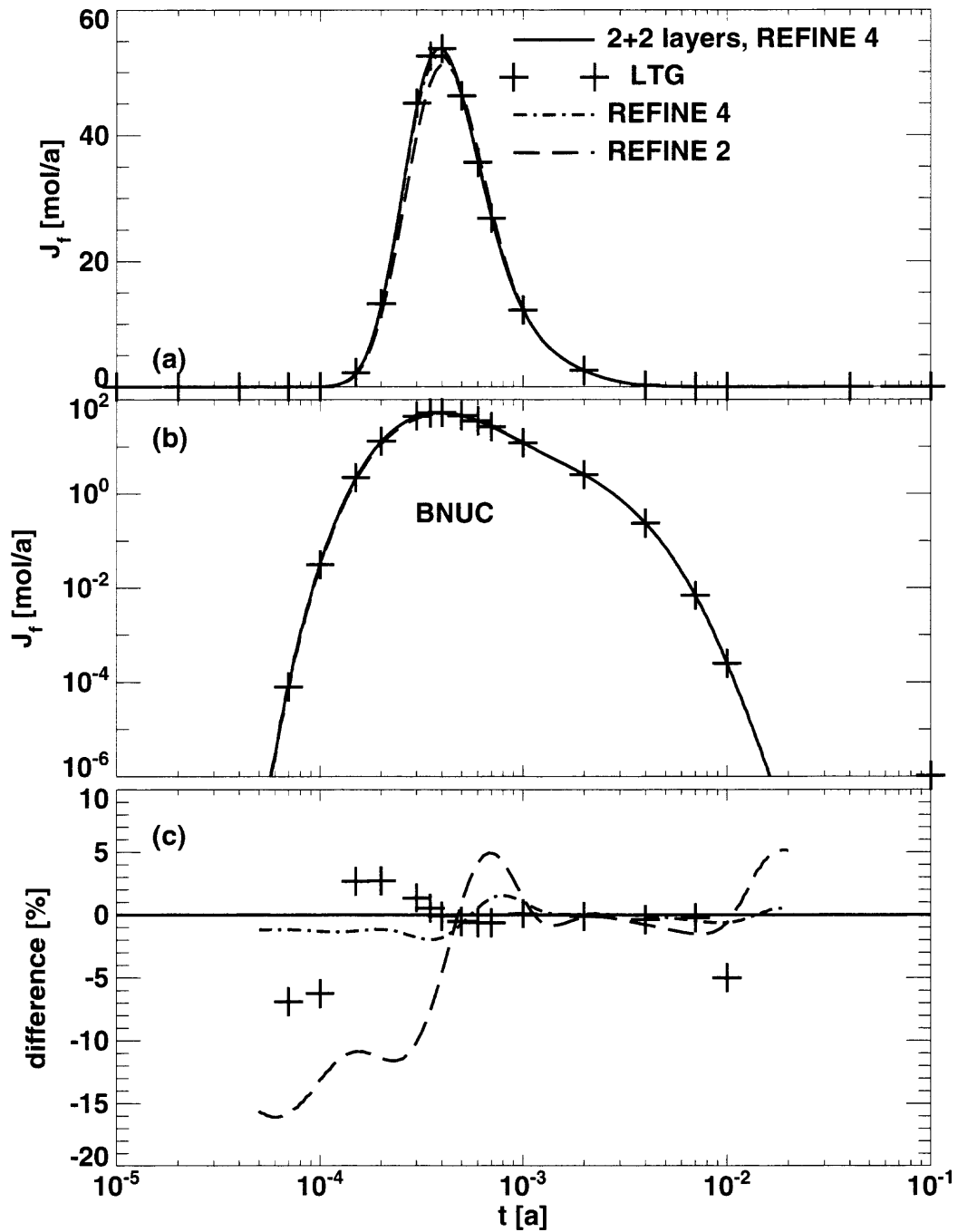


Figure 8.4. Hypothetical variation of the Grimsel dipole experiment for two independent areas for rock matrix diffusion. Presented is the nuclide BNUC of the decay chain $ANUC \rightarrow BNUC \rightarrow CNUC$. The nomenclature is as in Figure 8.2.

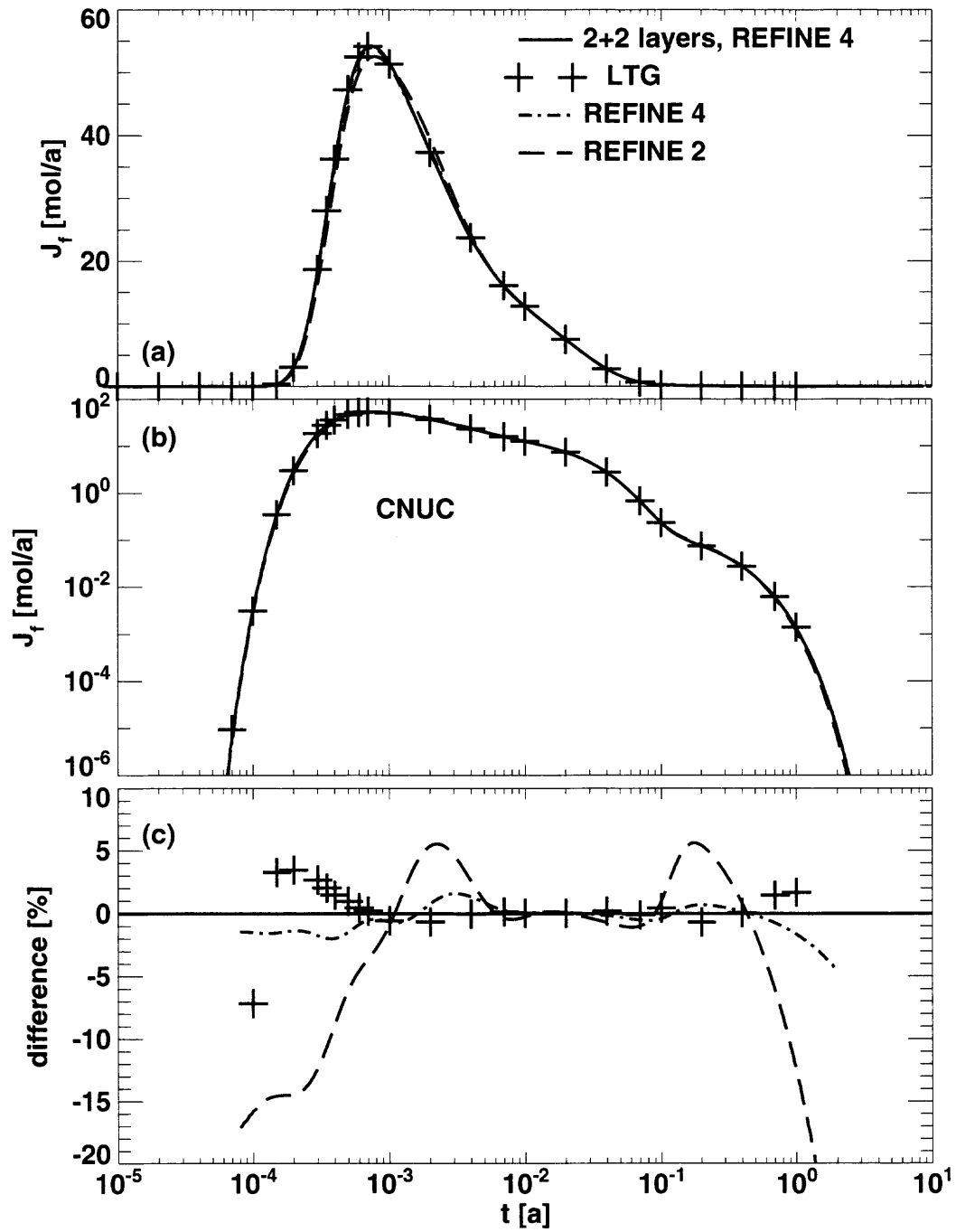


Figure 8.5. Hypothetical variation of the Grimsel dipole experiment for two independent areas for rock matrix diffusion. Presented is the nuclide CNUC of the decay chain ANUC \rightarrow BNUC \rightarrow CNUC. The RIP result has been calculated up to $t \approx 1$ [a]. The nomenclature is as in Figure 8.2.

8.2. Two Independent Two-Layer Regions for Matrix Diffusion

As the next test case one-dimensional diffusion into **two independent rock matrix regions** is considered again, as in the preceding section, Now, however, the **matrix regions are two-layer**. As in the preceding section, a hypothetical variation of the uranium case is considered, where 40% of the fracture surface is in contact with one matrix region and 60% is in contact with the other matrix region. The difference is that the area of flowing water is now in contact with rock matrix of type M3 and thickness $d_3 = 0.001$ [m] and, after this layer, a rock matrix region of type M1 follows in one matrix region, while rock matrix of type M2 follows in the other matrix region, see Figure 8.6a. The matrix types M1 and M2 and their respective extents are as in the preceding section. The matrix type M3 is as M1, but with a 6 times higher retardation constant, $R_p = 6.0$. Here the at-infinity boundary condition (equation 2.51c) is used.

The release curves for this geometry are depicted in Figure 8.7 for standard resolution REFINE 2 (long-dashed lines) and increased refinement REFINE 4 (dash-dotted lines). To achieve a yet higher accuracy with PICNIC in addition to the option REFINE 4, for another calculation each rock layer is subdivided into two sub-layers of the same thickness, see Figure 8.6b. This means that the rock matrix region of type M3 is represented by two rock blocks of thickness h_5 and h_6 with $h_5 = h_6 = \frac{1}{2}d_3$. The rock matrix regions of type M1 and M2 are represented as already described for the geometry of Figure 8.1. The release curve for this rock type is given as solid lines in Figure 8.7. The PICNIC results with REFINE 4 again agree very well with each other. See especially in Figure 8.7c the differences to the PICNIC highest refinement result. The agreement for the PICNIC standard resolution can also be regarded as good. However, the relative differences from -10% to +5% in the maximum region might be judged as too high for special applications, but are still acceptable for standard performance assessment purposes.

As for the single region for diffusion into a two-layer rock matrix, we compare also here with results from a RIP calculation (short-dashed lines in Figure 8.7). This agrees well with the PICNIC calculations. In the maximum region the relative difference to the REFINE 4 PICNIC results is within several percent. Only at the rising edge of the release curve does the RIP result⁸⁶ increase somewhat later than the PICNIC result. Also for long times $t > 10^{-2}$ [a], the RIP result starts to oscillate around the PICNIC result.

⁸⁶ For this case, more time steps are used in the RIP calculations than in the earlier RIP calculations, so that the time shift by $5 \cdot 10^{-6}$ [a] (see discussion in section 7.2.1) is not appropriate here.

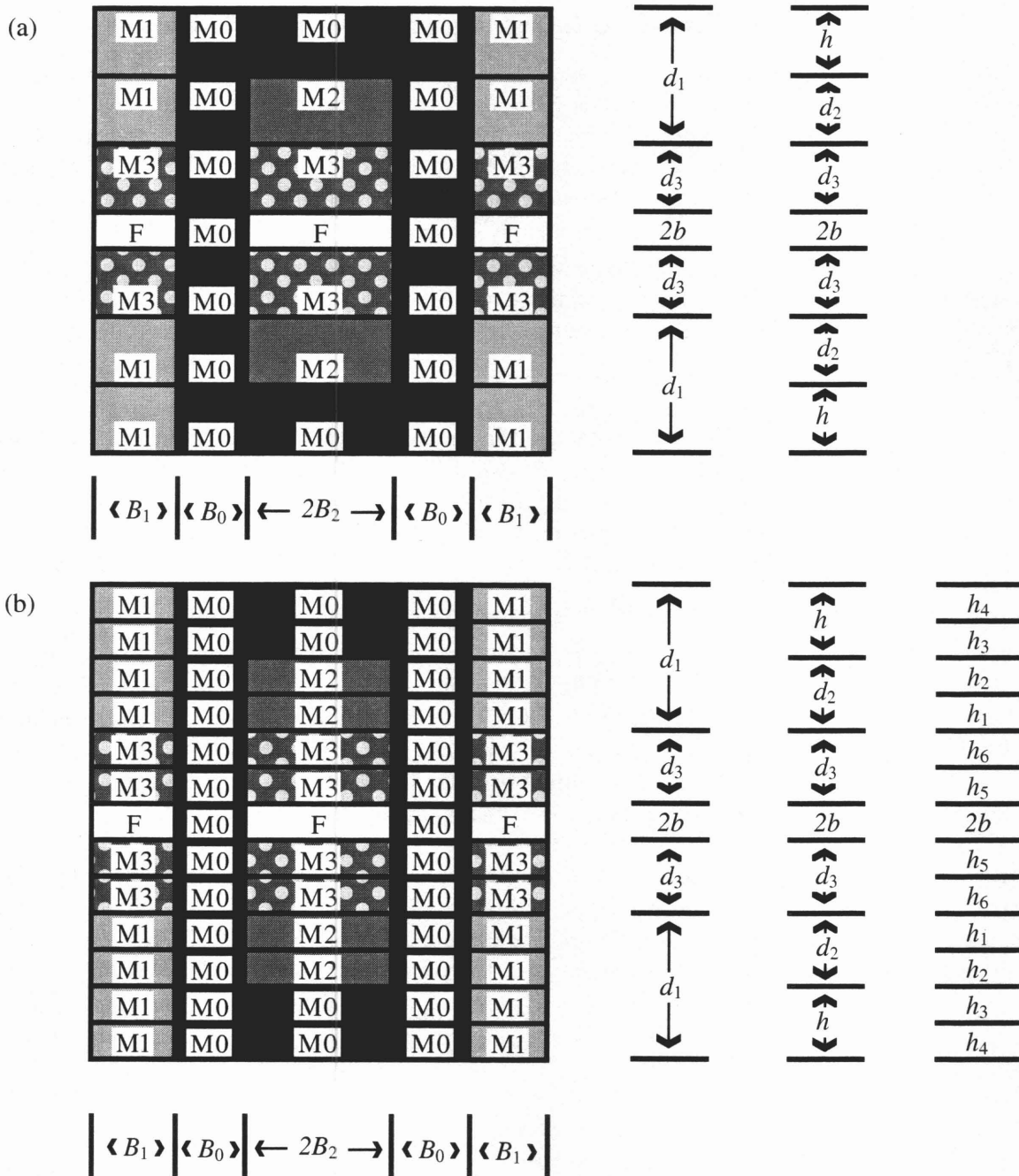


Figure 8.6. Sketch of the cross-section of a leg with two independent regions for one-dimensional matrix diffusion into a layer rock matrix. The difference to Figure 8.2 is that a rock layer of type M3 and thickness d_3 is in contact with the area of flowing water and, after this type of rock matrix, two independent rock regions of type M1 and M2 follow. In (a) this is entered to PICNIC by three layers of rock matrix below and above the fracture of thickness d_3 , d_2 and $h = d_1 - d_2$. In (b) the first rock layer of thickness d_3 is subdivided into two sub-layers of thickness h_5 and h_6 such that $d_3 = h_5 + h_6$, the second rock layer of thickness d_1 is subdivided into two sub-layers of thickness h_1 and h_2 such that $d_1 = h_1 + h_2$, and the third rock layer of thickness h is subdivided into two sub-layers of thickness h_3 and h_4 such that $h = h_3 + h_4$.

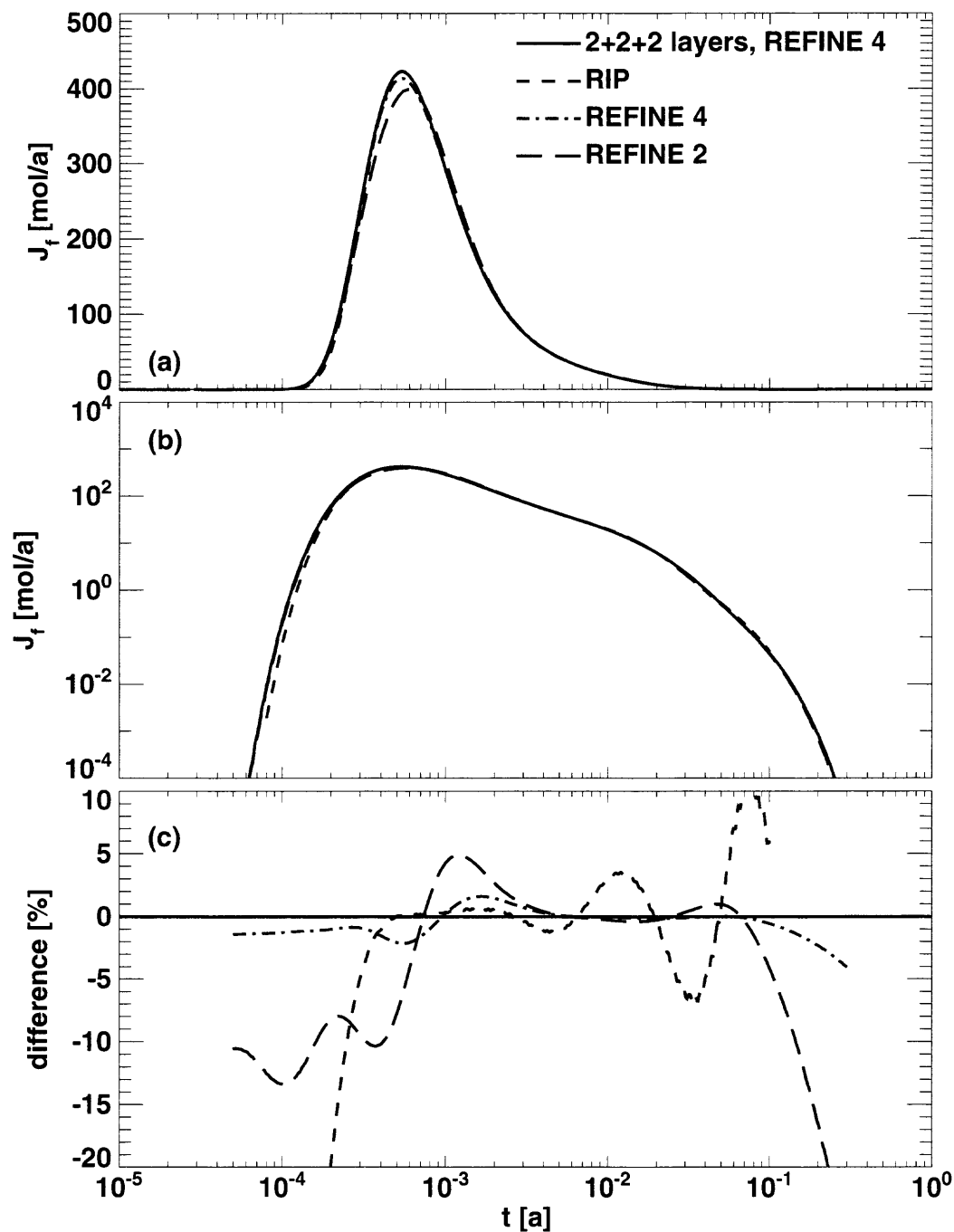


Figure 8.7. Hypothetical variation of the Grimsel dipole experiment for two independent areas for two-layer rock matrix diffusion. For more details see text. The PICNIC result for 2+2+2 layers (Figure 8.6b) with the option REFINE 4 (solid lines) is compared to the PICNIC result for 3 layers (Figure 8.6a) and the standard option REFINE 2 (long-dashed lines) and REFINE 4 (dash-dotted lines). The result of a RIP calculation is given as short-dashed lines. The release curves are given in (a) on a linear scale and in (b) on a logarithmic scale. The relative difference functions with respect to the 2+2+2 layers PICNIC result with REFINE 4 are given in (c).

To test also the accuracy for a **nuclide decay chain** for the **two independent two-layer rock matrix areas** discussed above, we consider again the decay chain $\text{ANUC} \rightarrow \text{BNUC} \rightarrow \text{CNUC}$, where the half-life of ANUC is 10^{-3} [a], the half-life of BNUC is 10^{-4} [a] and CNUC is assumed to be stable, compare sections 4.2 and 8.1. ANUC, BNUC and CNUC are assumed to have the same properties as the non-decaying nuclide, except for the retardation factor in the rock matrix. ANUC has the same retardation factor as uranine, while again in each rock matrix type the retardation factor of BNUC is two times higher and the retardation factor of CNUC is ten times higher.

The same discretisation tests are performed as for the single nuclide case in Figure 8.7. See Figure 8.8 for ANUC, Figure 8.9 for BNUC, and Figure 8.10 for CNUC. The relative difference functions for the different PICNIC results are now about twice as high as for the single nuclide. This means that the two different results for REFINE 4 agree for all times within 5%. For REFINE 2 the differences in the maximum region, best visible on a linear scale, range from -25% to +10%. In some applications this might be judged as too high.

As for the single nuclide, we compare with results from a RIP calculation (short-dashed lines). This agrees very well with the PICNIC calculations. In the maximum region the relative difference to the REFINE 4 PICNIC results is again within several percent. At the rising edge of the release curve the RIP result increases again somewhat later than the PICNIC result. Again for long times the RIP result starts to oscillate around the PICNIC result.

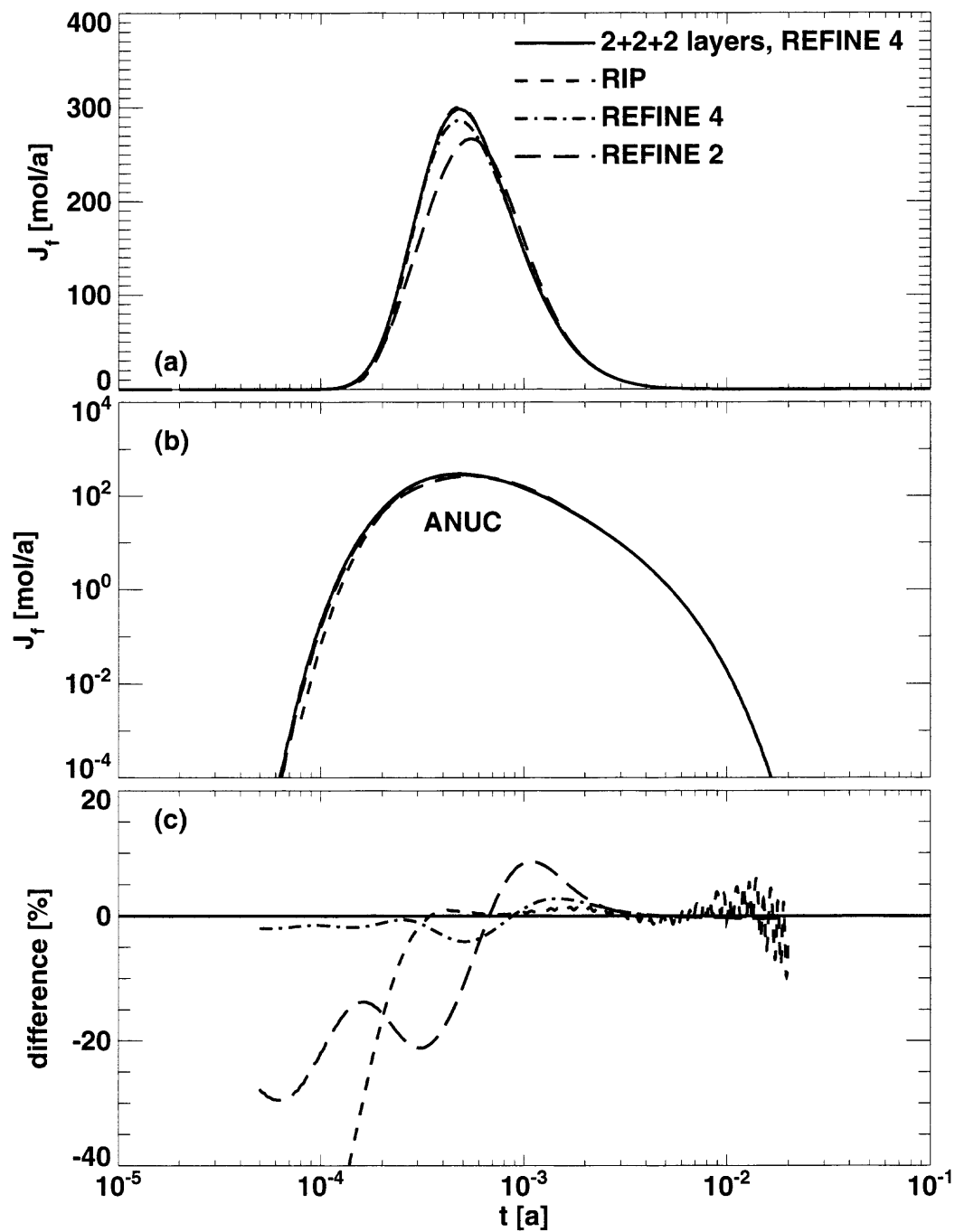


Figure 8.8. Hypothetical variation of the Grimsel dipole experiment for two independent areas for two-layer rock matrix diffusion. Presented is the nuclide ANUC of the decay chain $\text{ANUC} \rightarrow \text{BNUC} \rightarrow \text{CNUC}$. The nomenclature is as in Figure 8.7.

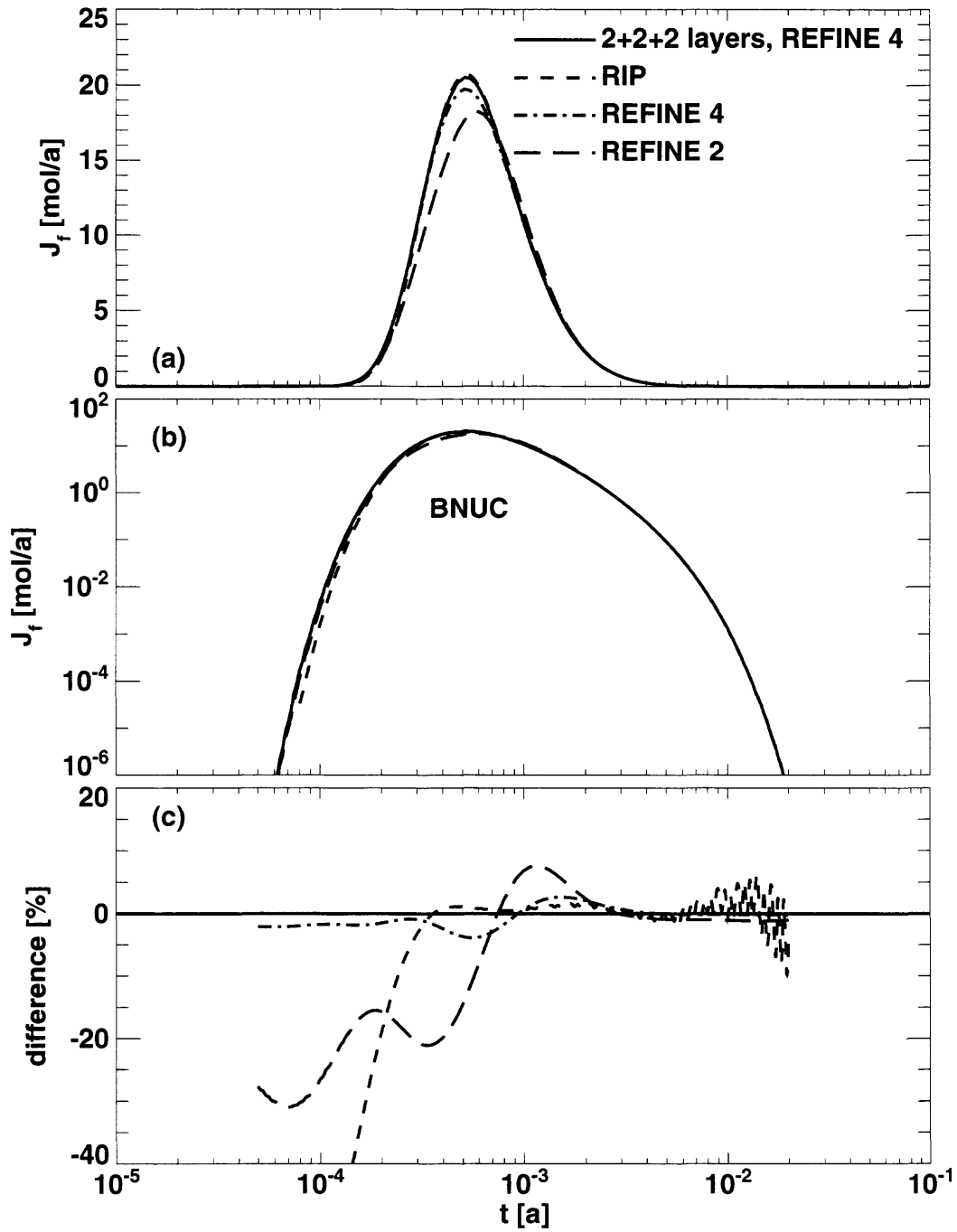


Figure 8.9. Hypothetical variation of the Grimsel dipole experiment for two independent areas for two-layer rock matrix diffusion. Presented is the nuclide BNUC of the decay chain $ANUC \rightarrow BNUC \rightarrow CNUC$. The nomenclature is as in Figure 8.2.

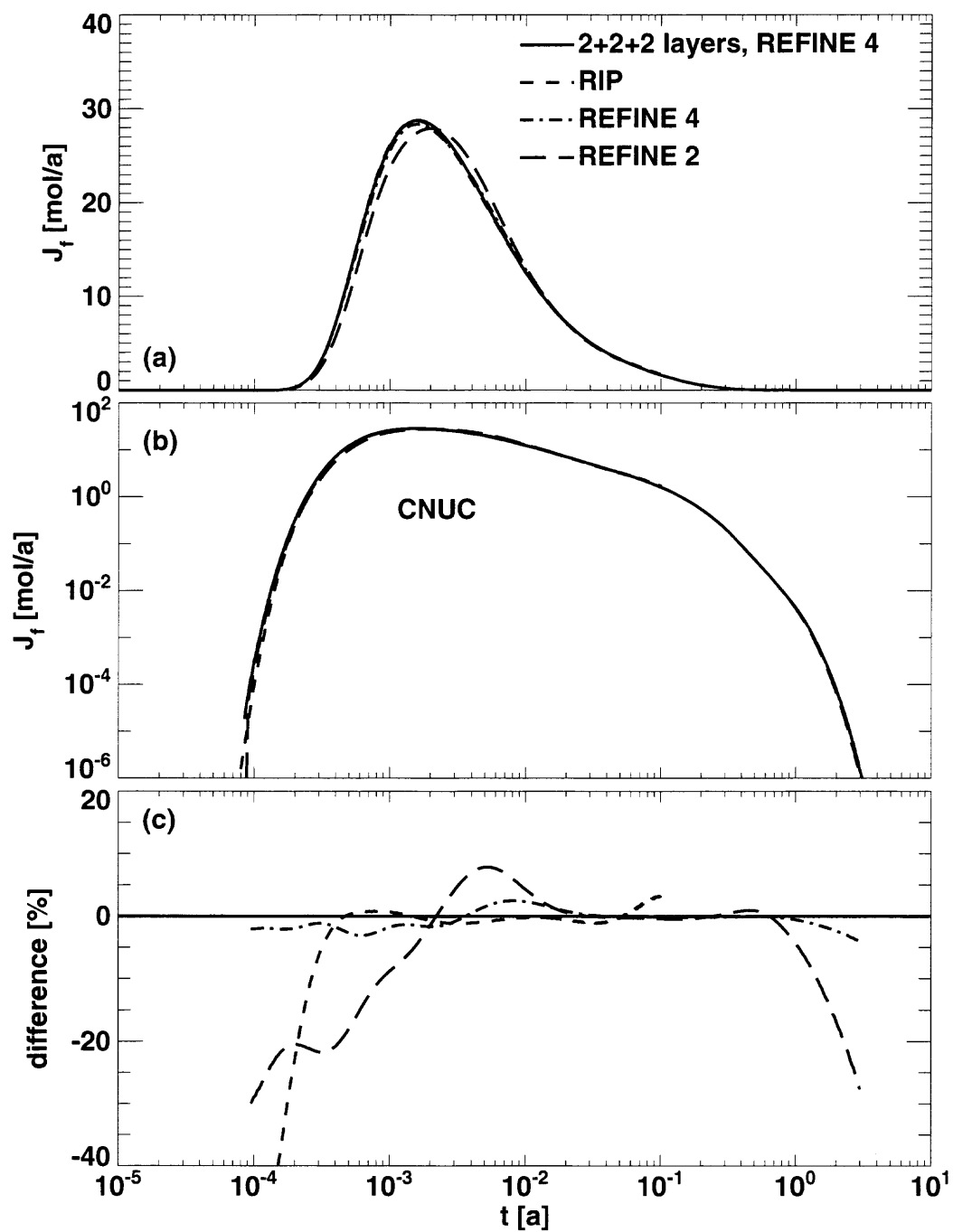


Figure 8.10. Hypothetical variation of the Grimsel dipole experiment for two independent areas for two-layer rock matrix diffusion. Presented is the nuclide CNUC of the decay chain $ANUC \rightarrow BNUC \rightarrow CNUC$. The RIP calculation has been performed up to $t = 0.1$ [a]. The nomenclature is as in Figure 8.6.

8.3. Transport in a Pathway

The rock matrix geometries considered for single legs in the previous subsections will now also be considered in **pathways**.

8.3.1. Two Independent Homogeneous Matrix Areas and 3 Legs

For a test of the network feature in PICNIC we also consider transport in a pathway consisting of three legs, see Figure 8.11. Again a hypothetical variation of the transport of uranine in the Grimsel dipole experiment is considered. The third leg is defined such that it behaves as the leg considered in section 8.1. The leg has length $L = 5$ [m] and **40% of the interface of the area of flowing water is in contact with rock matrix type M1** and thickness d_1 , while **60% of the interface of the area of flowing water is in contact with rock matrix type M2** and thickness d_2 . The first leg is assumed to be of length $L = 2$ [m] and the area of the flowing water is in contact with rock matrix of type M1 and thickness d_1 . The second leg is assumed to be of length $L = 3$ [m] and the area of the flowing water is in contact with rock matrix of type M2 and thickness d_2 . Thus these two legs are be modelled using the 1D-AS option. The cross-sectional area of the first and the second leg are assumed to be three times smaller, and the Darcy velocity is assumed three times higher, than in the third leg. A δ -function source is assumed at the inlet of the first leg.

	leg 1	leg 2	leg 3
length:	2 [m]	3 [m]	5 [m]
rock matrix:	M1	M2	40% M1 and 60% M2 (according to Figure 8.1)
CSA:	1 [m ²]	1 [m ²]	3 [m ²]

Figure 8.11. Pathway consisting of three legs. In leg 3, at the end of the pathway, one-dimensional matrix diffusion into two different and independent porous zones M1 and M2 is assumed. For further details see text.

This is again considered for the **single non-decaying nuclide** case (Figure 8.12), and the nuclides of the **decay chain** ANUC (Figure 8.13), BNUC (Figure 8.14) and CNUC (Figure 8.15). For the decay chain case again a δ -function source of the parent ANUC is assumed. The same discretisation tests within PICNIC and the comparison with the code PAWorks/LTG are performed as for the single leg case in section 8.1. To compare with the code PAWorks/LTG, the outlet boundary conditions of all legs are assumed to be zero-gradient (equation 2.51a). The agreement between the different PICNIC calculations is very similar to the single leg case. This also holds for the comparison to the PAWorks/LTG result. Only for early times is the increase of the release curves now slightly earlier for the LTG result. Thus, considering the pathway does not lead to increased differences.

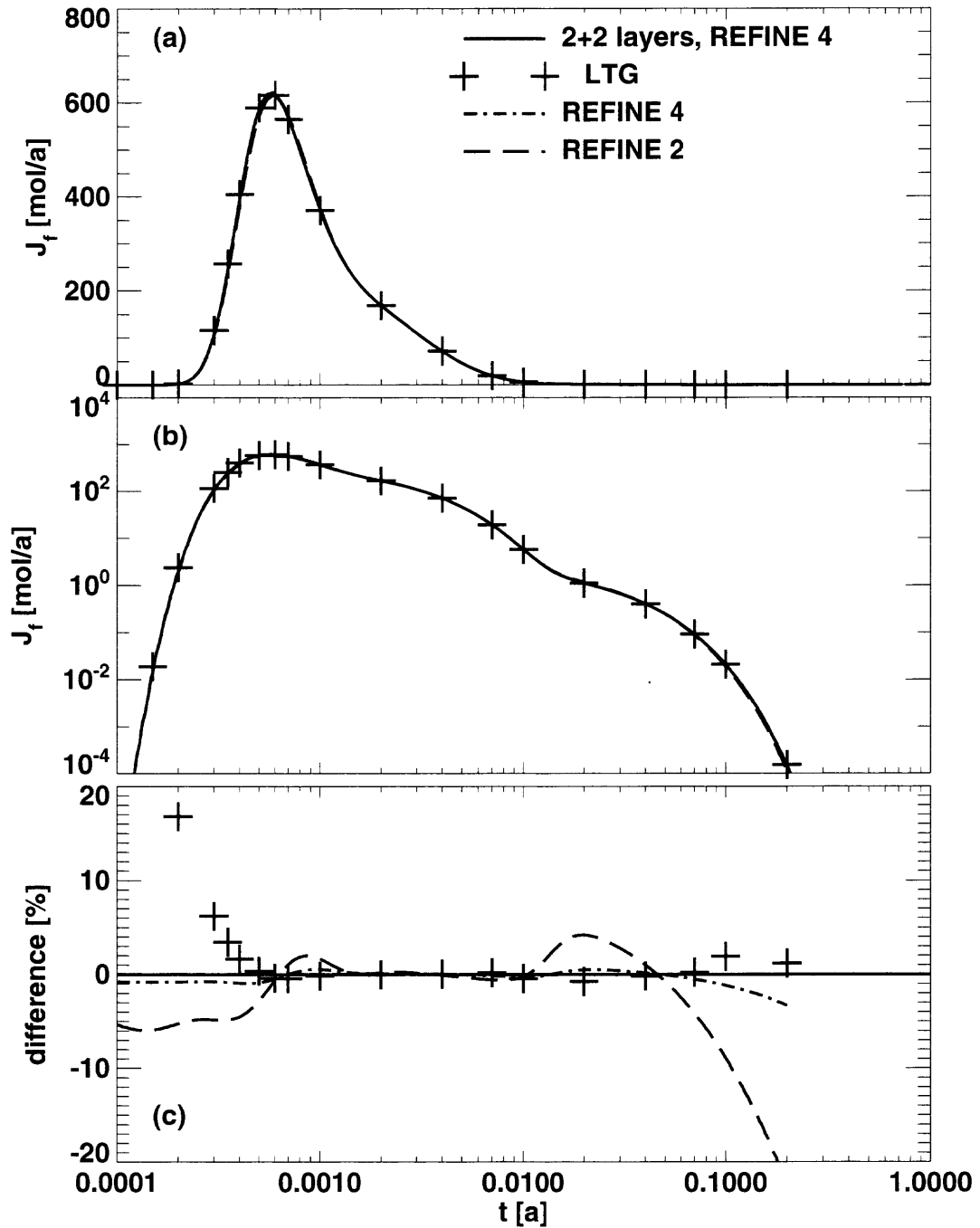


Figure 8.12. Hypothetical variation of the Grimsel dipole experiment for the 3-leg pathway of Figure 8.11. In one of the legs two independent areas for rock matrix diffusion are assumed. For more details see text. The PICNIC result for 2+2 layers of rock matrix in this leg (Figure 8.1b) with the option REFINE 4 (solid lines) is compared to the PICNIC result for 2 layers (Figure 8.1a) and the standard option REFINE 2 (long-dashed lines) and REFINE 4 (dash-dotted lines). The result of a PAWorks/LTG calculation is given as (crosses connected by short-dashed lines). The release curves are given in (a) on a linear scale and in (b) on a logarithmic scale for the flux. The relative difference functions with respect to the 2+2 layers PICNIC result with REFINE 4 is given in (c).

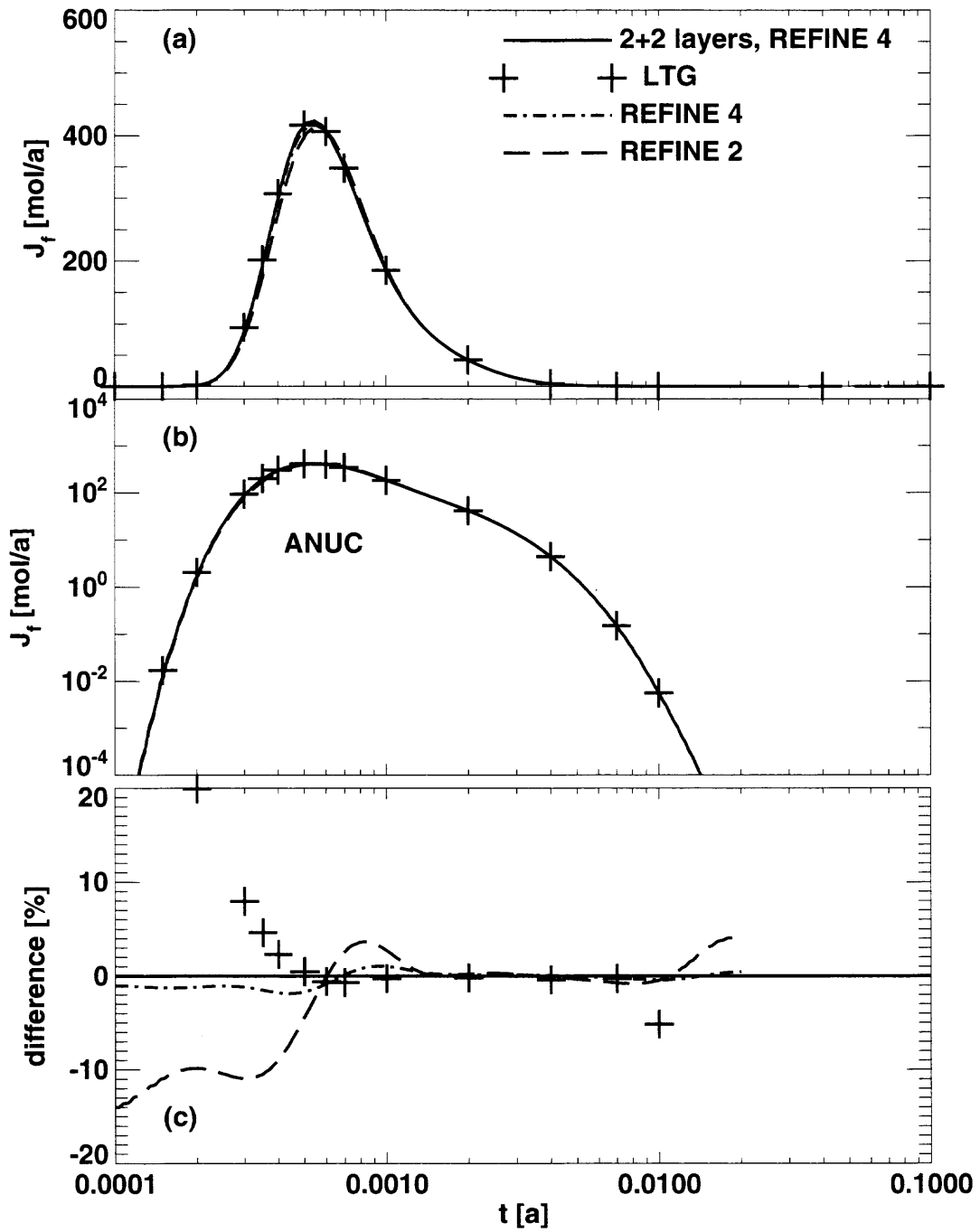


Figure 8.13. Hypothetical variation of the Grimsel dipole experiment for the 3-leg pathway of Figure 8.11. Presented is the nuclide ANUC of the decay chain $ANUC \rightarrow BNUC \rightarrow CNUC$. The nomenclature is as in Figure 8.12.

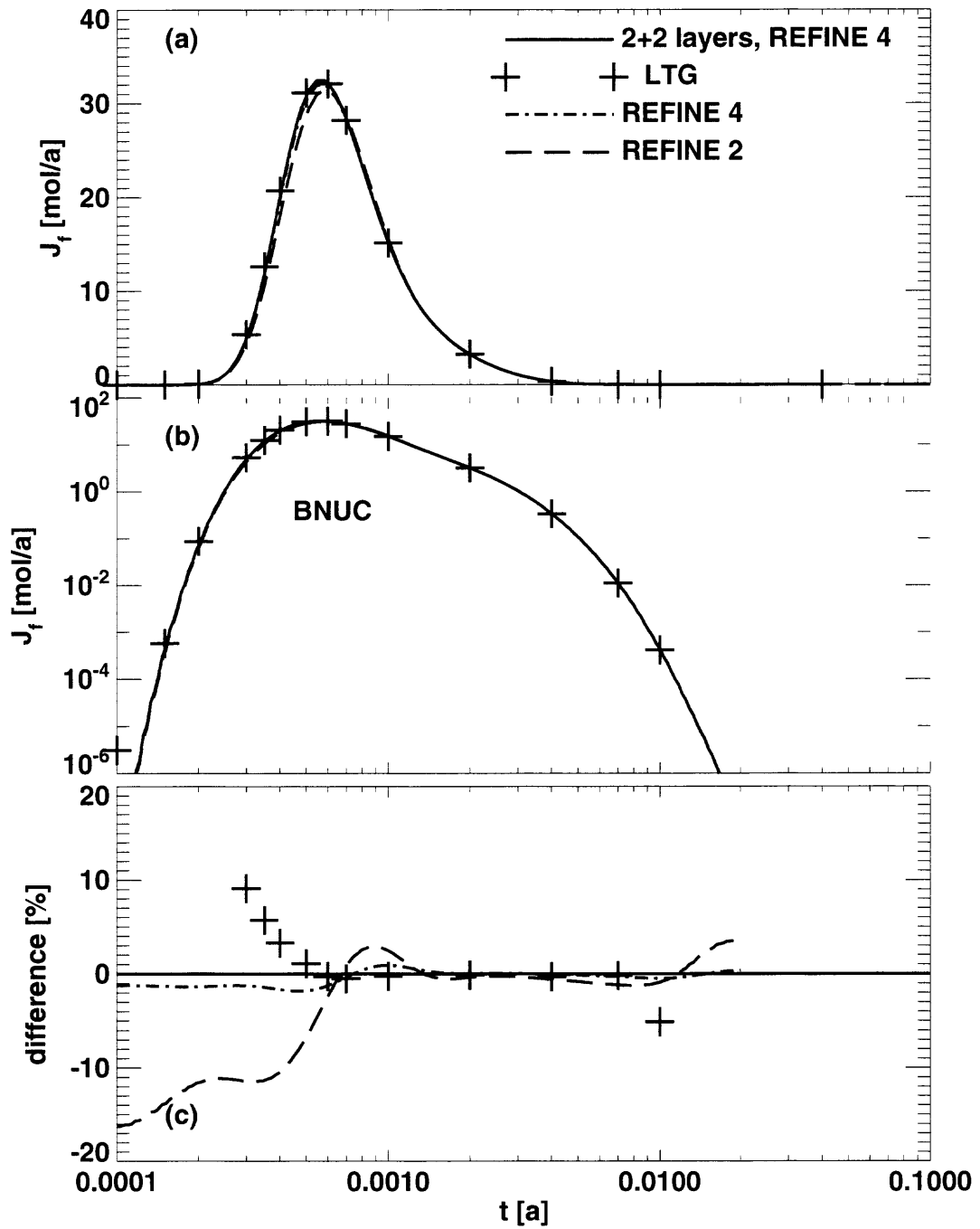


Figure 8.14. Hypothetical variation of the Grimsel dipole experiment for the 3-leg pathway of Figure 8.11. Presented is the nuclide BNUC of the decay chain $\text{ANUC} \rightarrow \text{BNUC} \rightarrow \text{CNUC}$. The nomenclature is as in Figure 8.12.

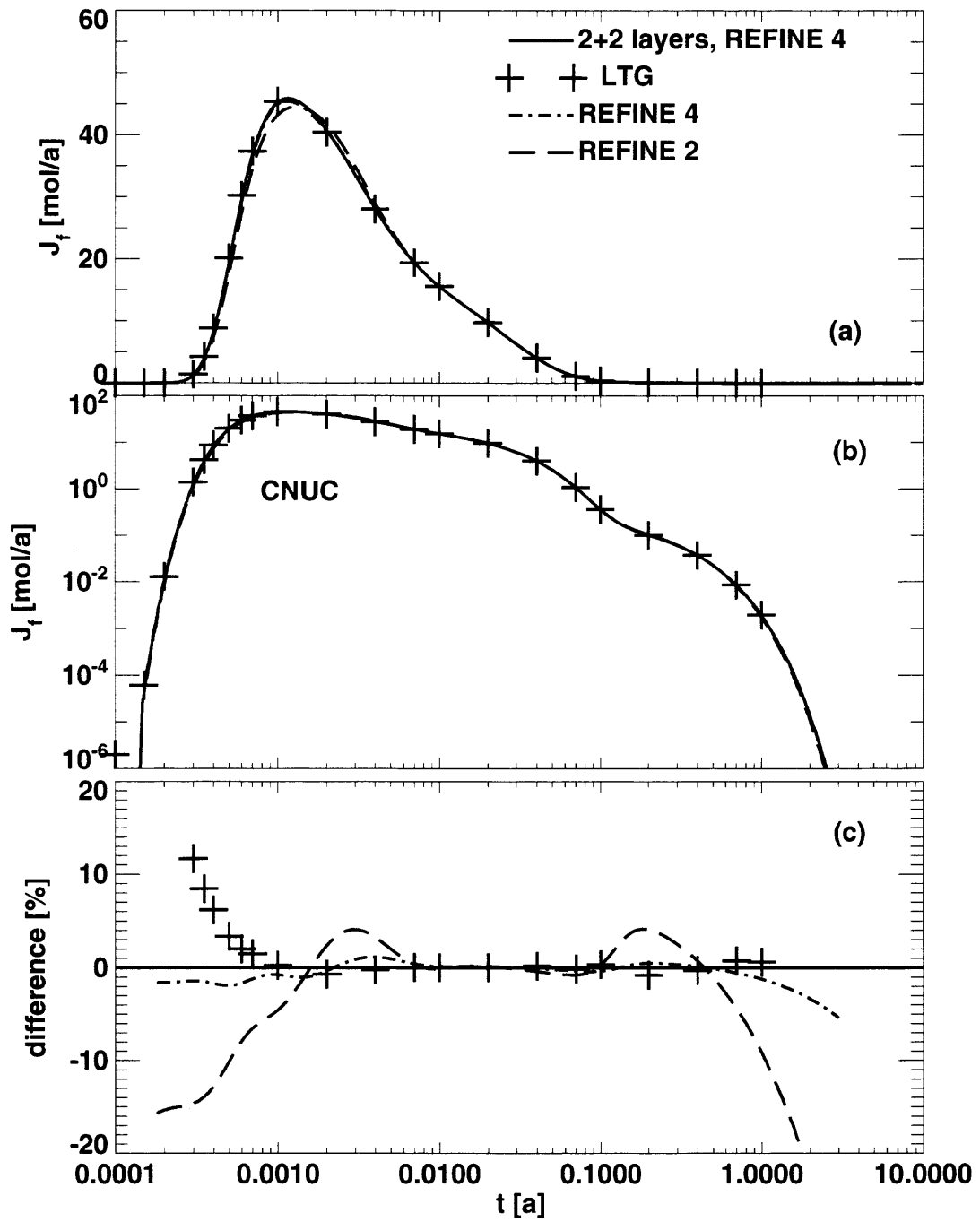


Figure 8.15. Hypothetical variation of the Grimsel dipole experiment for the 3-leg pathway of Figure 8.11. Presented is the nuclide CNUC of the decay chain $ANUC \rightarrow BNUC \rightarrow CNUC$. The PAWorks/LTG calculations have been performed up to $t = 0.1[a]$. The nomenclature is as in Figure 8.12.

8.3.2. Two Independent Homogeneous Matrix Areas and 5 Legs

In the previous subsection we considered a 3-leg pathway. Now we consider a **pathway consisting of five legs**, see Figure 8.16. The first three legs and the source are as in Figure 8.11. The fourth and the fifth leg have the same properties as the first and the second leg, but the cross-sectional areas of the first and the second leg are assumed to be twenty times smaller, and the Darcy velocity is assumed to be twenty times higher, than in the third leg.

	leg 1	leg 2	leg 3	leg 4	leg5
length:	2 [m]	3 [m]	5 [m]	2 [m]	3 [m]
rock matrix:	M1	M2	40% M1 and 60% M2 (according to Figure 8.1)	M1	M2
CSA:	1 [m ²]	1 [m ²]	3 [m ²]	20 [m ²]	20 [m ²]

Figure 8.16. Pathway consisting of five legs. In leg 3, in the middle of the pathway, one-dimensional matrix diffusion into two different and independent porous zones M1 and M2 is assumed. For further details see text.

This is again considered for the **single non-decaying nuclide** case (Figure 8.17) and the nuclides of the **decay chain** ANUC (Figure 8.18), BNUC (Figure 8.19) and CNUC (Figure 8.20). The same discretisation tests within PICNIC and the comparison with the code PAWorks/LTG are performed as for the single leg case in section 8.1. To compare with the code PAWorks/LTG, the outlet boundary conditions of all legs are assumed to be zero-gradient. The agreement between the different PICNIC calculations and with the PAWorks/LTG result is similar to the 3-leg case. To some extent, the differences between the different calculations are even smaller.

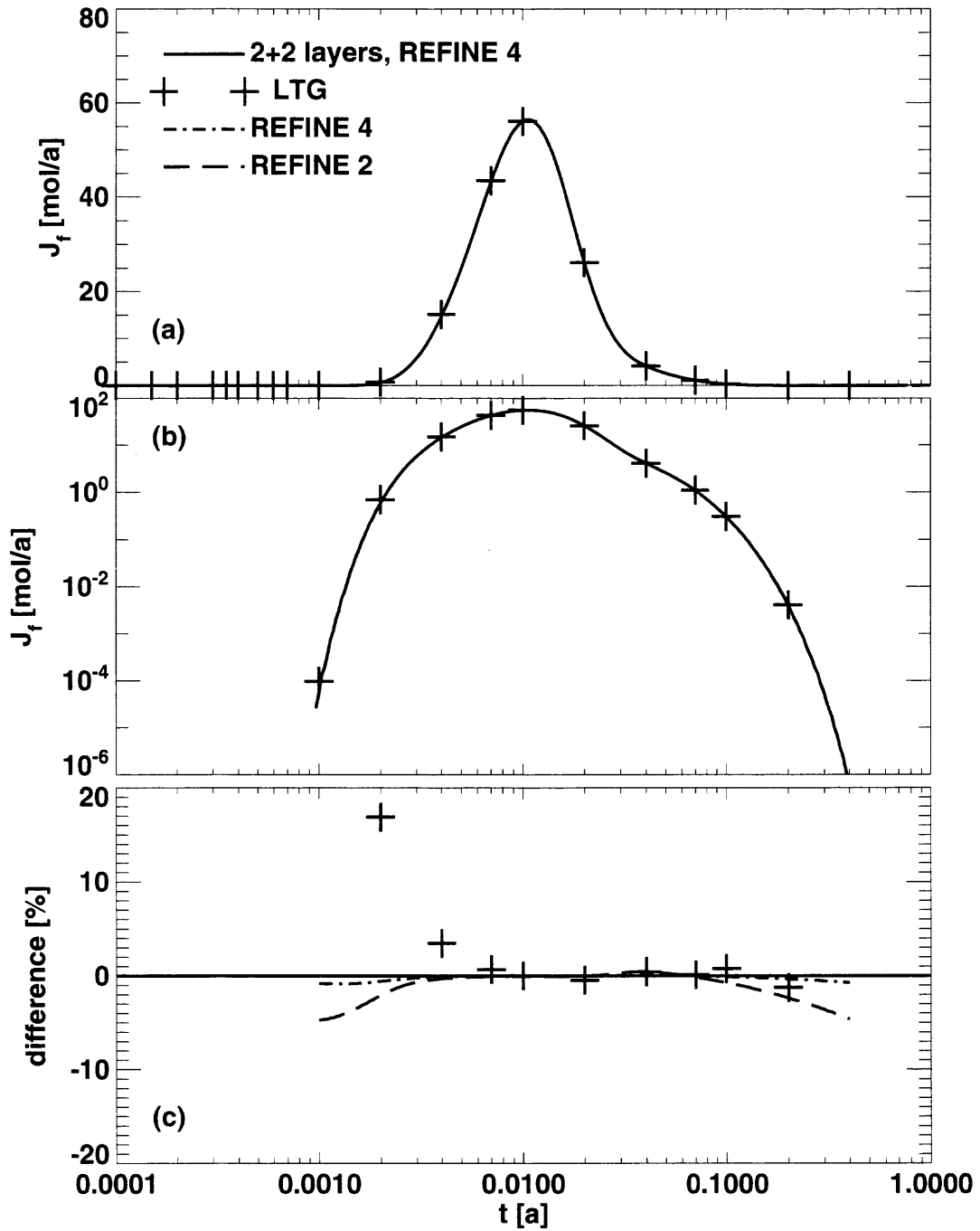


Figure 8.17. Hypothetical variation of the Grimsel dipole experiment for the 5-leg pathway of Figure 8.16. In one of the legs two independent areas for rock matrix diffusion are assumed. For more details see text. The nomenclature is as in Figure 8.12.

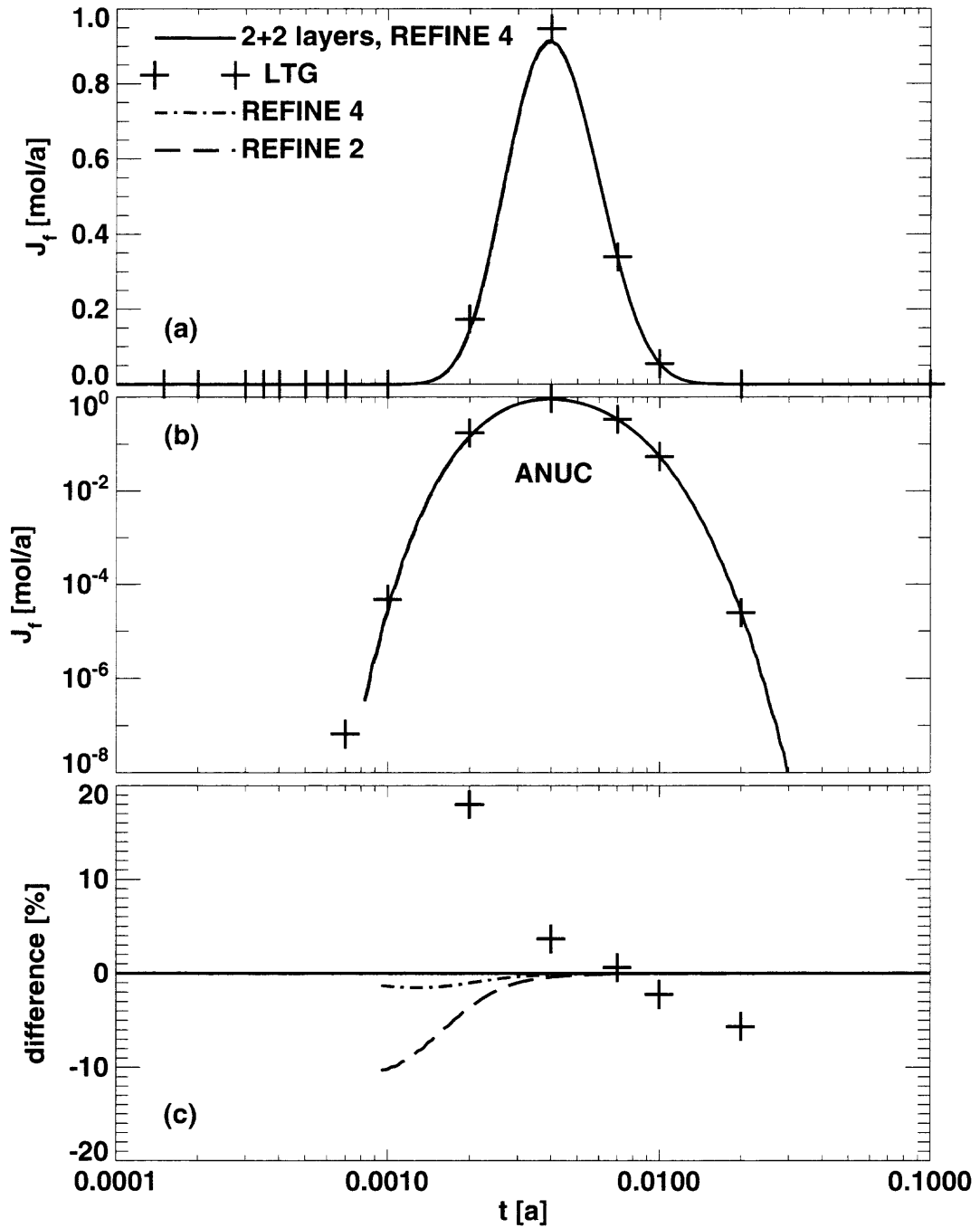


Figure 8.18. Hypothetical variation of the Grimsel dipole experiment for the 5-leg pathway of Figure 8.16. Presented is the nuclide ANUC of the decay chain $\text{ANUC} \rightarrow \text{BNUC} \rightarrow \text{CNUC}$. The nomenclature is as in Figure 8.12.

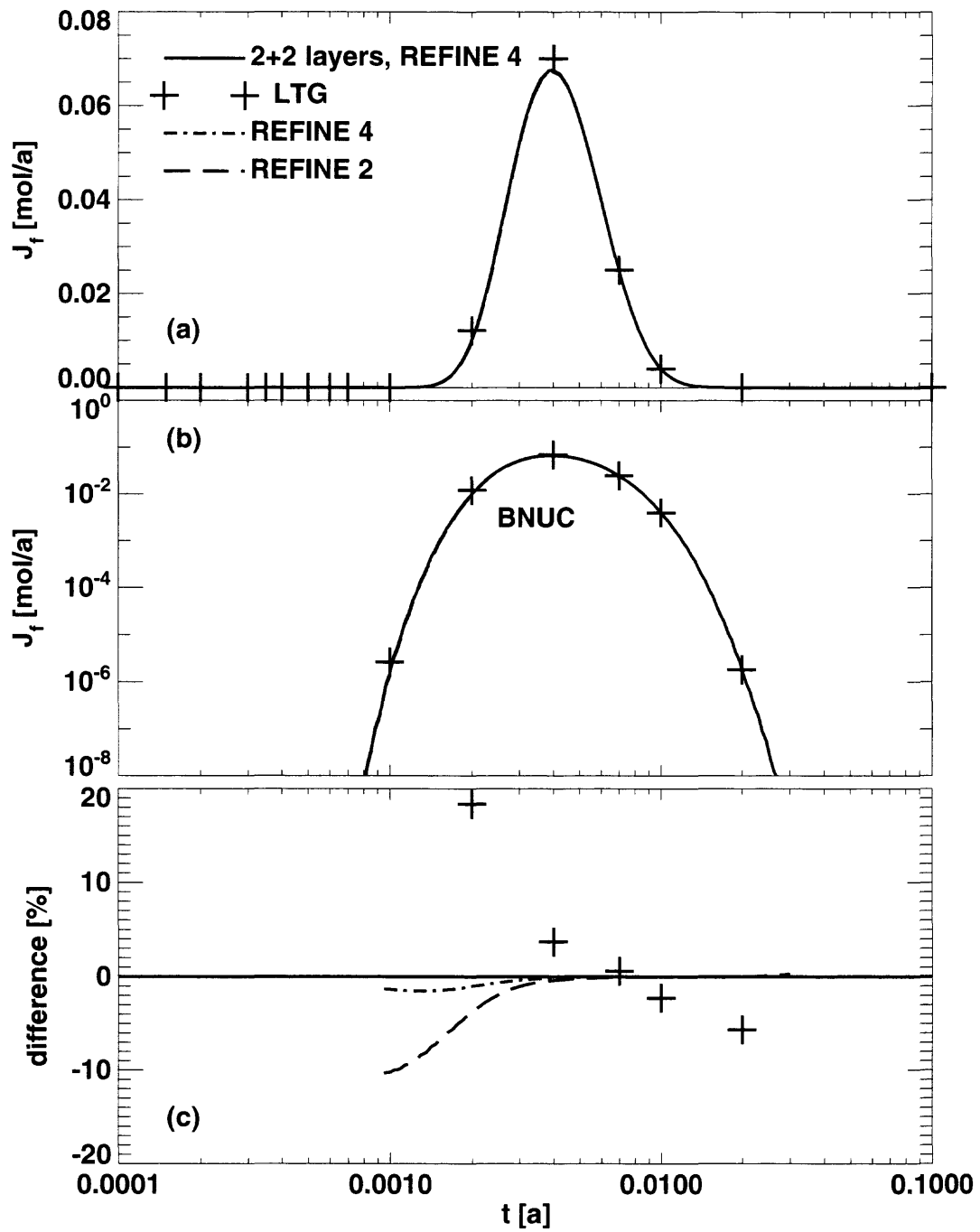


Figure 8.19. Hypothetical variation of the Grimsel dipole experiment for the 5-leg pathway of Figure 8.16. Presented is the nuclide BNUC of the decay chain $ANUC \rightarrow BNUC \rightarrow CNUC$. The nomenclature is as in Figure 8.12.

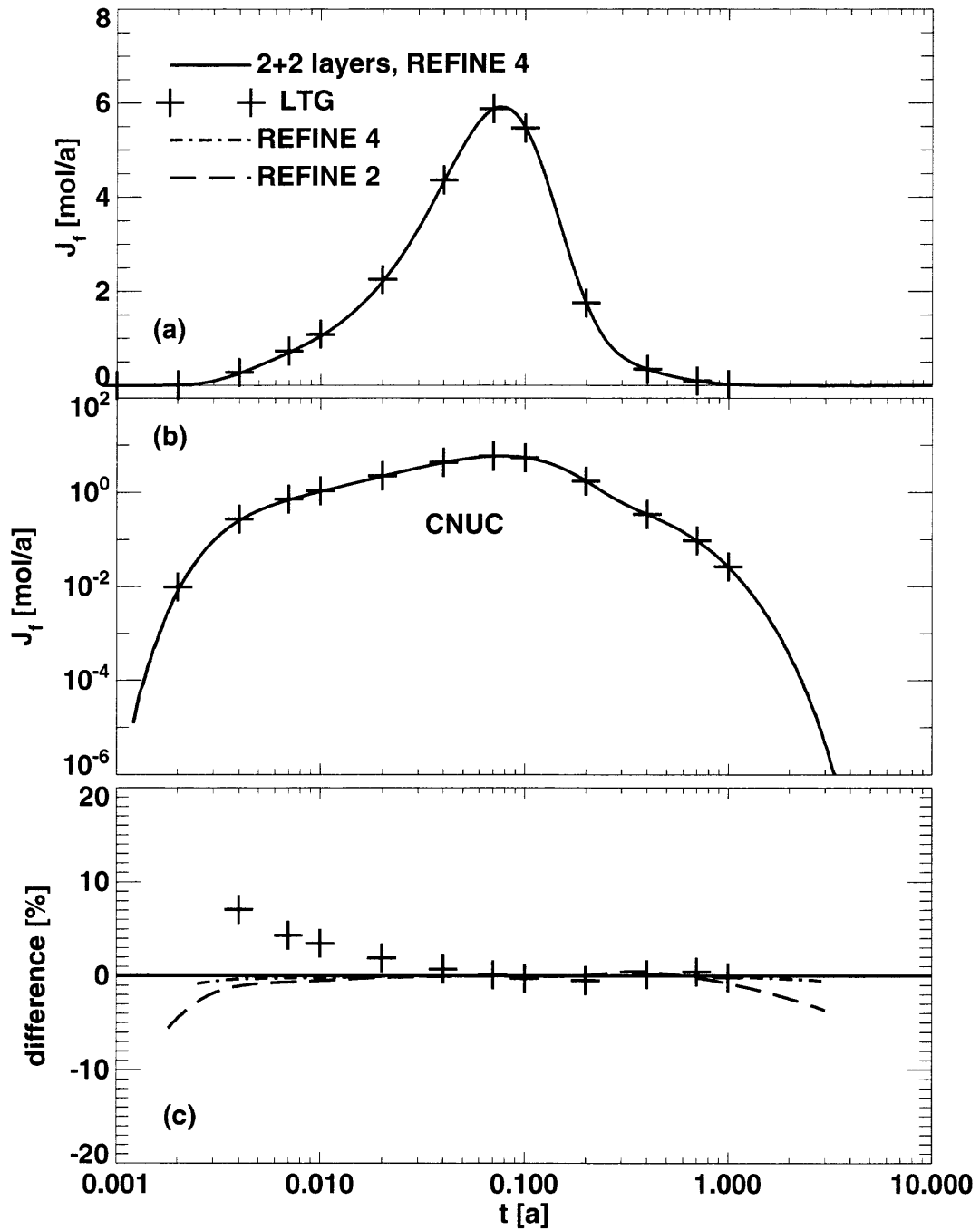


Figure 8.20. Hypothetical variation of the Grimsel dipole experiment for the 5-leg pathway of Figure 8.16. Presented is the nuclide CNUC of the decay chain $\text{ANUC} \rightarrow \text{BNUC} \rightarrow \text{CNUC}$. The PAWorks/LTG calculations have been performed up to $t = 1$ [a]. The nomenclature is as in Figure 8.12.

8.3.3. Two Independent Two-Layer Matrix Areas and 5 Legs

As the next test we consider again a **pathway consisting of five legs**, see Figure 8.21. The first three legs and the source are as in Figure 8.11 and 8.16. The fourth and the fifth leg have the same properties in the flowing water as in the five-leg pathway of Figure 8.16, but the rock matrix is now much more complex and consists of **two independent two-layer areas** as in Figure 8.6.

	leg 1	leg 2	leg 3	leg 4	leg5
length:	2 [m]	3 [m]	5 [m]	2 [m]	3 [m]
rock matrix:	M1	M2	40% M1 and 60% M2 (according to Figure 8.1)	40% M3 followed by M1 and 60% M3 followed by M2 (according to Figure 8.6)	
CSA:	1 [m ²]	1 [m ²]	3 [m ²]	20 [m ²]	20 [m ²]

Figure 8.21. Pathway consisting of five legs. In leg 3, one-dimensional matrix diffusion into two different and independent porous zones M1 and M2 is assumed. In leg 4 and leg 5 there is one-dimensional matrix diffusion into two two-layer zones (M3 followed by M1 and M3 followed by M2). For further details see text.

This is again considered for the **single non-decaying nuclide** case (Figure 8.22) and the nuclides of the **decay chain** ANUC (Figure 8.23), BNUC (Figure 8.24) and CNUC (Figure 8.25). The outlet boundary conditions of all legs are assumed to be at-infinity. For the single nuclide the agreement between different PICNIC calculations is very good. The increase for the lower resolution cases is just somewhat later for early times and somewhat earlier for late times. The agreement in the maximum region is within 1%. Considering the nuclide decay chain, the variations of the different PICNIC calculations are larger than for the single nuclide and especially larger than for the previous 3-leg and 5-leg cases. The increased magnitude of the relative difference functions appears to be dominated by the rock matrix of the legs 4 and 5; compare the relative difference functions for the single leg case in section 8.2. In the maximum region there is a variation within 10% for ANUC and BNUC. This increased numerical error of the PICNIC results identified here will be considered in more detail for two-dimensional matrix diffusion in sections 9 and 10.

As for the single leg in section 8.2, we compare also here with results from a RIP calculation (short-dashed lines). The RIP result agrees very well with the highest refinement PICNIC result. The agreement with the PICNIC calculations for the maximum region is again - within few percent - very good. In the region of the peak maximum, the relative difference to the REFINE 4 PICNIC results is within a few percent. At the rising edge of the release curves, the RIP results increase somewhat later than the PICNIC results for the single non-decaying nuclide and somewhat earlier for the members of the decay chain. In the tailing region, the RIP results decrease slightly earlier than the PICNIC results.

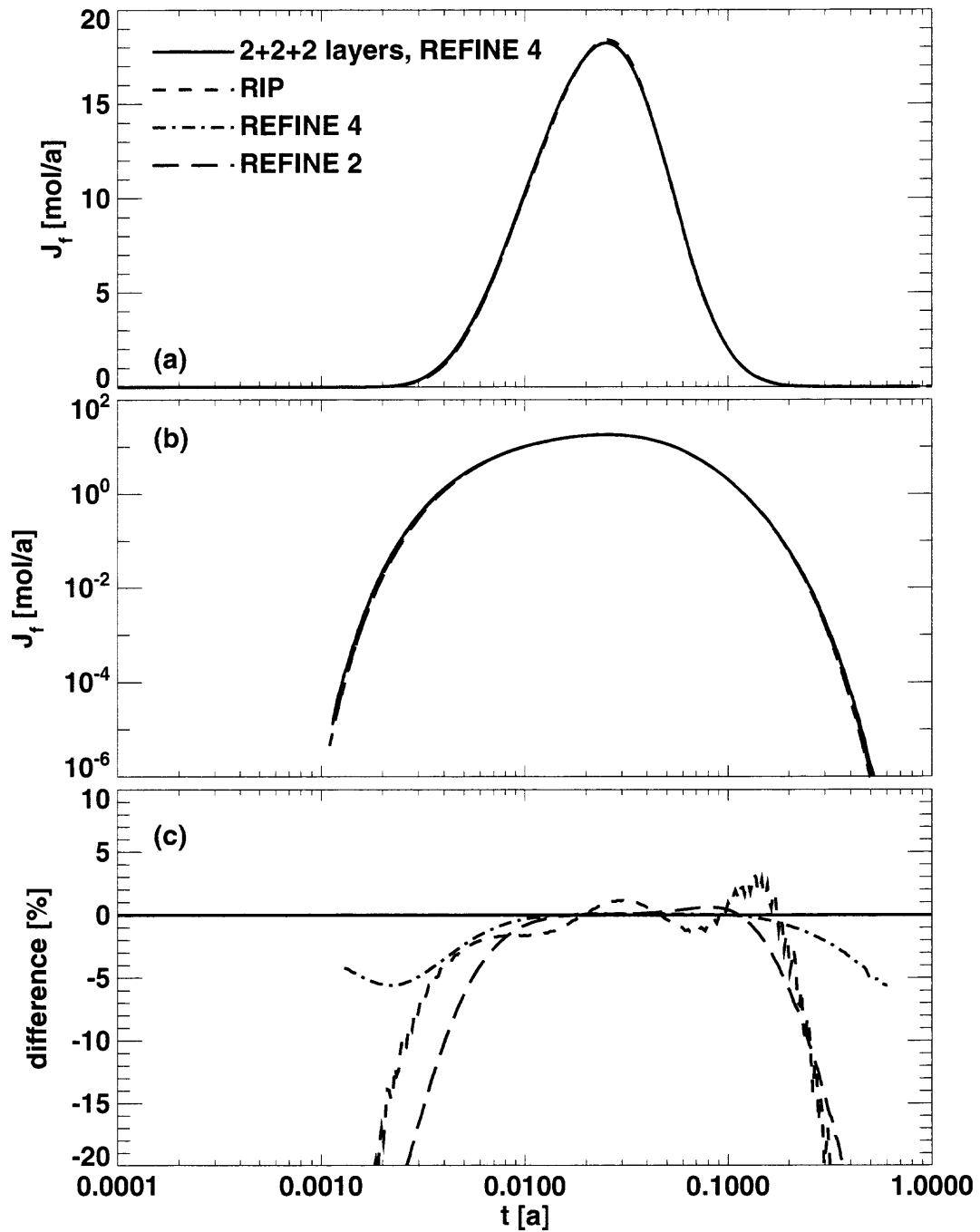


Figure 8.22. Hypothetical variation of the Grimsel dipole experiment for the 5-leg pathway of Figure 8.21. In two of the legs two independent two-layer areas for matrix diffusion are assumed. For more details see text. Presented is the single nuclide. The nomenclature is as in Figure 8.7.

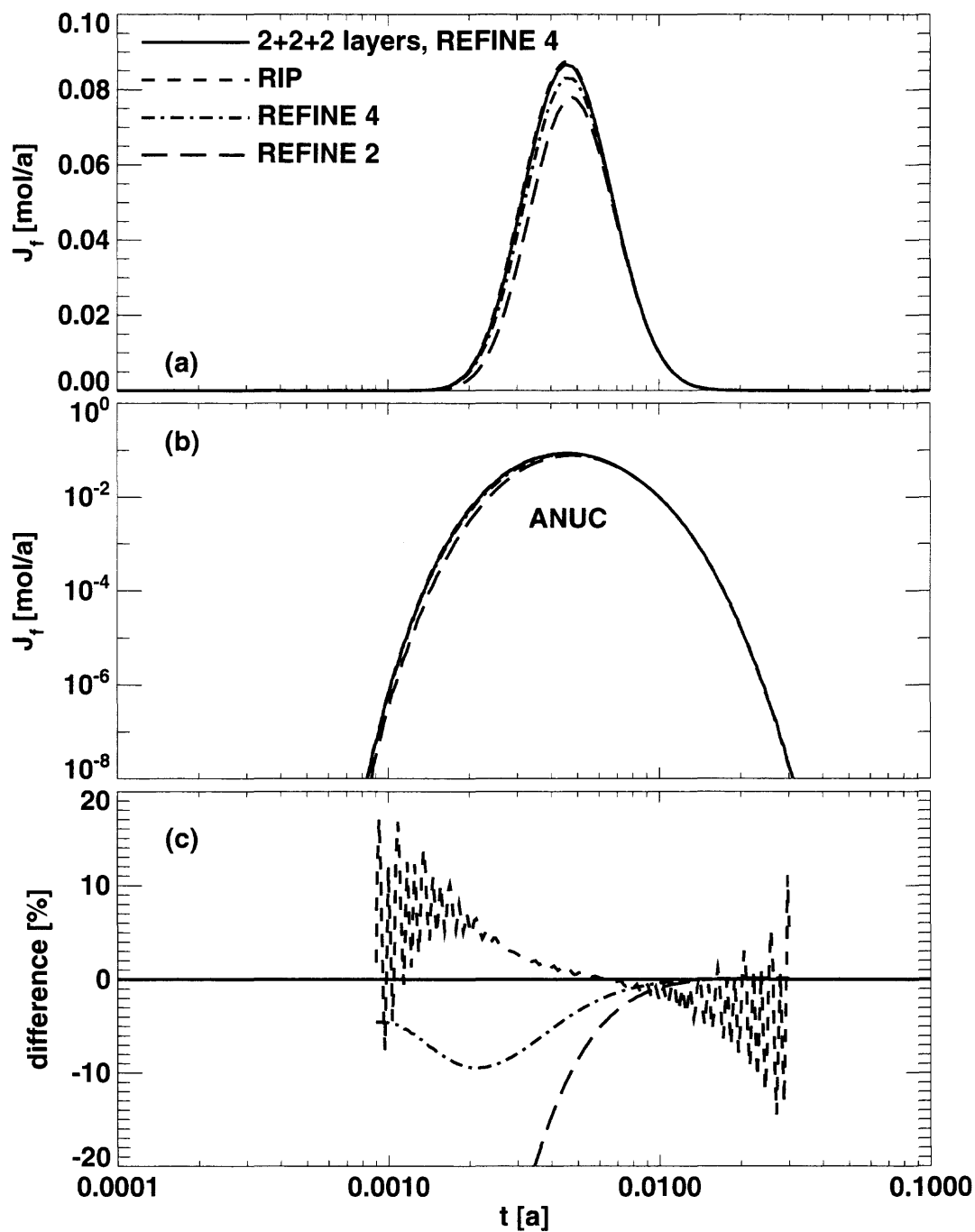


Figure 8.23. Hypothetical variation of the Grimsel dipole experiment for the 5-leg pathway of Figure 8.21. Presented is the nuclide ANUC of the decay chain ANUC \rightarrow BNUC \rightarrow CNUC. The oscillations in the short-dashed lines in (c) are due to the procedure which interpolates the output points. The nomenclature is as in Figure 8.7.

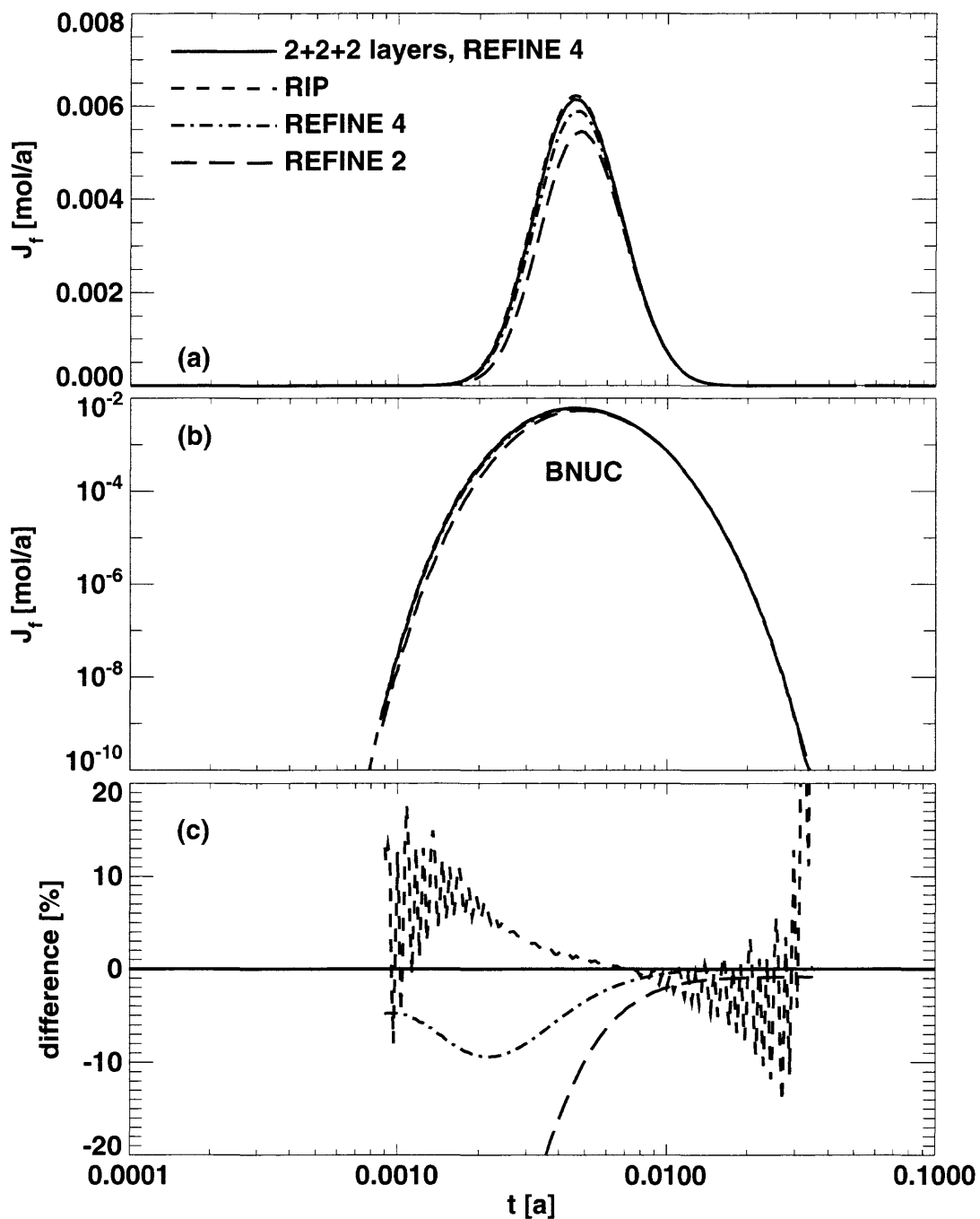


Figure 8.24. Hypothetical variation of the Grimsel dipole experiment for the 5-leg pathway of Figure 8.21. Presented is the nuclide BNUC of the decay chain $\text{ANUC} \rightarrow \text{BNUC} \rightarrow \text{CNUC}$. The oscillations in the short-dashed lines in (c) are due to the procedure which interpolates the output points. The nomenclature is as in Figure 8.7.

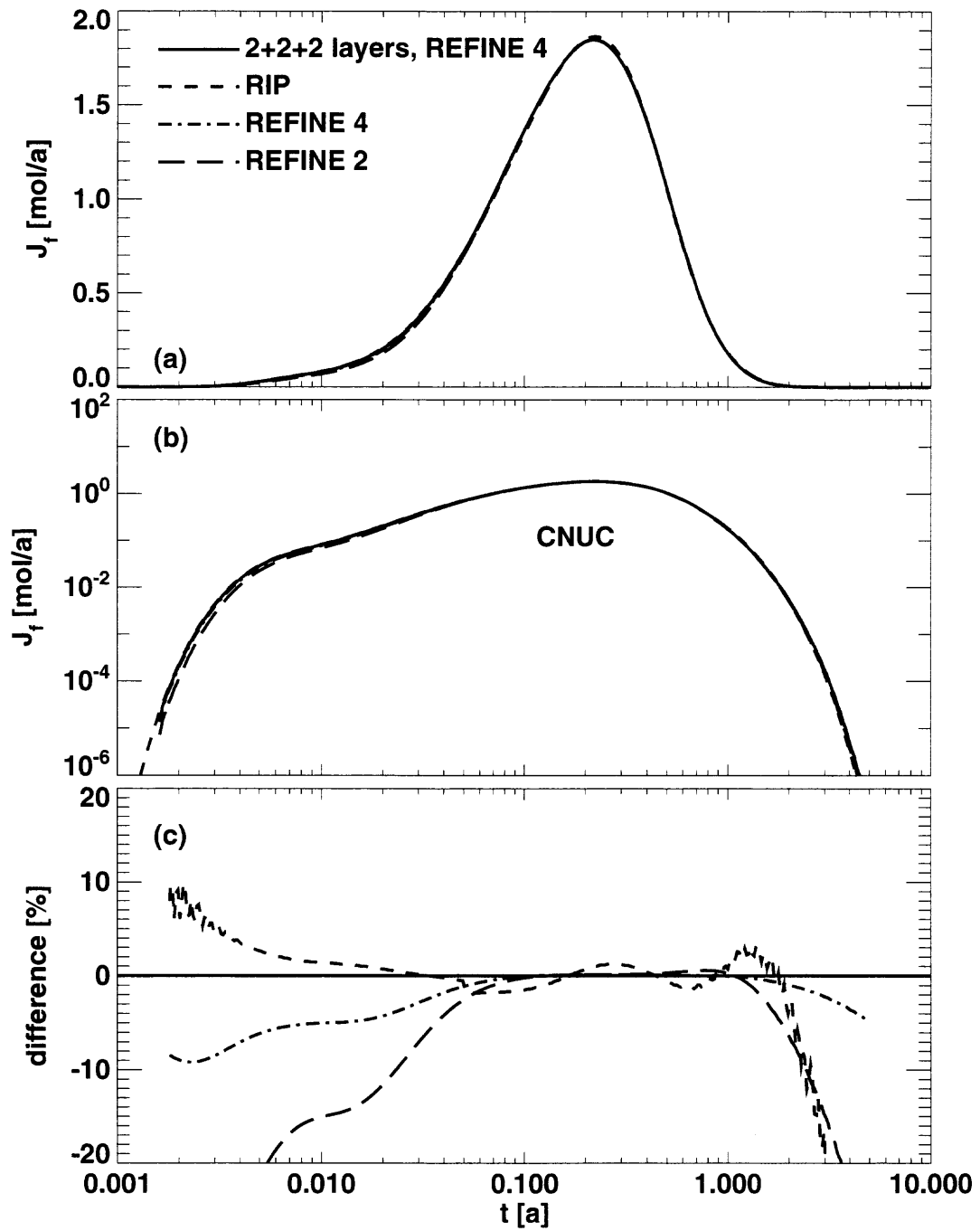


Figure 8.25. Hypothetical variation of the Grimsel dipole experiment for the 5-leg pathway of Figure 8.21. Presented is the nuclide CNUC of the decay chain ANUC → BNUC → CNUC. The nomenclature is as in Figure 8.7.

8.4. Transport in a Network

As the next step we consider transport of a **single nuclide** and a **nuclide decay chain** in a 26-leg **network**. This is a variation of the network with different rock matrices in different legs considered in sections 4.3.3 and 6.6. The same parameters and the top-hat source over $10[a]$ are considered. However the legs 10,11,12 (see Figure 4.22 or 6.28) are now defined such that they have a rock type with two independent regions for one-dimensional diffusion into a two-layer rock matrix as sketched in Figure 8.26.⁸⁷ As for the network with the homogeneous rock matrices, the area of flowing water of the legs 10,11,12 is in contact with rock matrix of type M4, but with thickness $d_4 = 0.01 [m]$ only. After this layer, a rock matrix of type M1 follows with thickness $d_1 = 1.0 [m]$ for 40% of the fracture surface and $d_2 = 0.1 [m]$ for 60% of the fracture surface. All other legs are as for the network in sections 4.3.3 and 6.6. M1 denotes the type of rock matrix that is in contact with the legs 1,2,3. The at-infinity outlet boundary condition is used in each leg for comparison purposes with the RIP code.

The release curves for this geometry are depicted in Figure 8.27 for standard resolution REFINE 2 (long-dashed lines) and increased refinement REFINE 4 (dash-dotted lines). To achieve yet greater accuracy with PICNIC, for another calculation, in addition to the option REFINE 4, each rock layer is subdivided into two layers, see Figure 8.26b. The two sub-layers representing the rock matrix region of type M4 are represented by two rock blocks of thicknesses h_5 and h_6 , with $h_5 = h_6 = \frac{1}{2}d_4$. The layer of thickness d_2 is also represented by two sub-layers of thickness $h_1 = h_2 = \frac{1}{2}d_2$. For a better resolution close to the rock matrix interfaces, the two sub-layers $h_3 = 0.1 [m]$ and $h_4 = 0.8 [m]$ are chosen to be of different thickness.

This is again considered for the **single non-decaying nuclide** case (Figure 8.27) and the nuclides of the **decay chain** ANUC (Figure 8.28) → BNUC (Figure 8.29) → CNUC (Figure 8.30) →. Similar discretisation tests within PICNIC are performed as for the 5-leg case in section 8.3.3.⁸⁸ The PICNIC result agree very well with each other. In the maximum region, and also in the tailing region, the different PICNIC calculations agree within 1%. Only for early times are the lower resolution results somewhat delayed.

As for the single leg and the pathway in sections 8.2 and 8.3, we compare here also with results from RIP calculations (short-dashed lines). The RIP result agrees well with the PICNIC results. For all nuclides, the increase of the release curves at the rising edge is somewhat later for the RIP result with respect to the PICNIC result. Interestingly there is agreement within few percent of the RIP and the PICNIC result for $10[a] < t < 30[a]$. For about $30[a] < t < 300[a]$, the RIP result is consistently in the order of 10% smaller than the PICNIC result. For longer times, the RIP results oscillate around the PICNIC results in a range between -20% and +30%.⁸⁹

⁸⁷ As in section 4.3 we use 129 points in the Laplace domain.

⁸⁸ These nuclides are different to the nuclides considered in sections 8.2 and 8.3.

⁸⁹ Considering the much better agreement of PICNIC and RIP for the single leg and the pathway cases one might speculate that the reason for these increased relative differences is due to a small parameter inconsistency in this very late test case. Note that the agreement for the transport in a network of PICNIC and RIP is much better than the agreement between PAWorks/LTG and PICNIC, see section 4.3. Consider also section 6.6 where we have shown, for a similar network, that the relative difference functions between PICNIC results of differently refined finite-element meshes are of similar oscillatory behaviour and magnitude to the relative difference functions between the

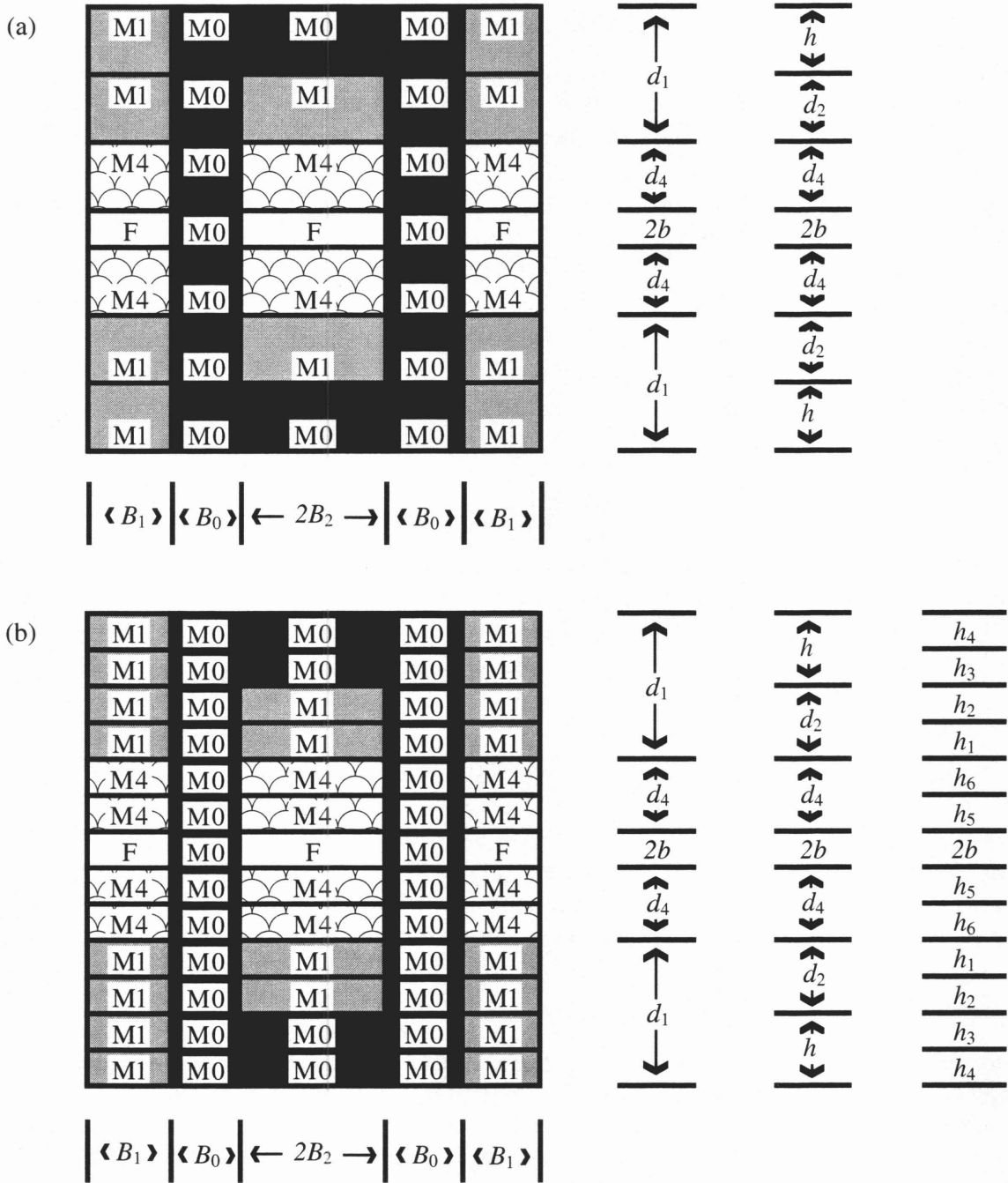


Figure 8.26. Sketch of a leg cross-section with two independent regions for one-dimensional matrix diffusion into a layer rock matrix. The difference to Figure 8.6 is that a rock layer of type M4 and thickness d_4 is in contact with the area of flowing water and, after this type of rock matrix, two independent rock regions of the same type (M1) follow, but with different thicknesses d_1 and d_2 . In (a) this is entered to PICNIC by three layers of rock matrix below and above the fracture of thicknesses d_4 , d_2 and $h = d_1 - d_2$. In (b) the first rock layer of thickness d_4 is subdivided into two sub-layers of thickness h_5 and h_6 such that $d_4 = h_5 + h_6$, the second rock layer of thickness d_1 is subdivided into two sub-layers of thickness h_1 and h_2 such that $d_1 = h_1 + h_2$, and the third rock layer of thickness h is subdivided into two sub-layers of thickness h_3 and h_4 such that $h = h_3 + h_4$.

RIP and the PICNIC results here.

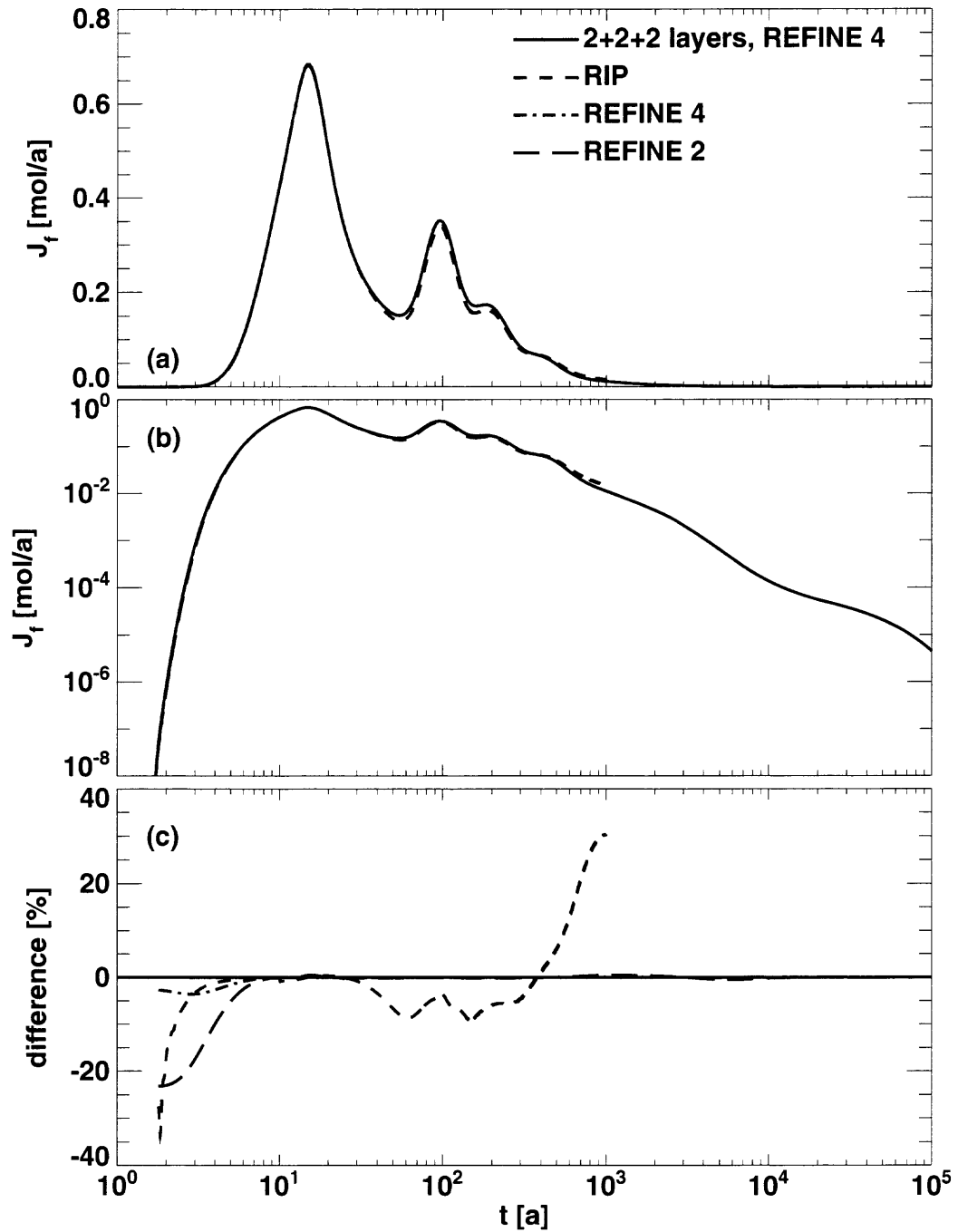


Figure 8.27. Transport of a single nuclide in a 26-leg network where, in three of the legs, one-dimensional matrix diffusion into two independent two-layer porous regions is considered. For more details see text. The RIP calculation has been performed up to $t = 10^3$ [a]. The nomenclature is as in Figure 8.7.

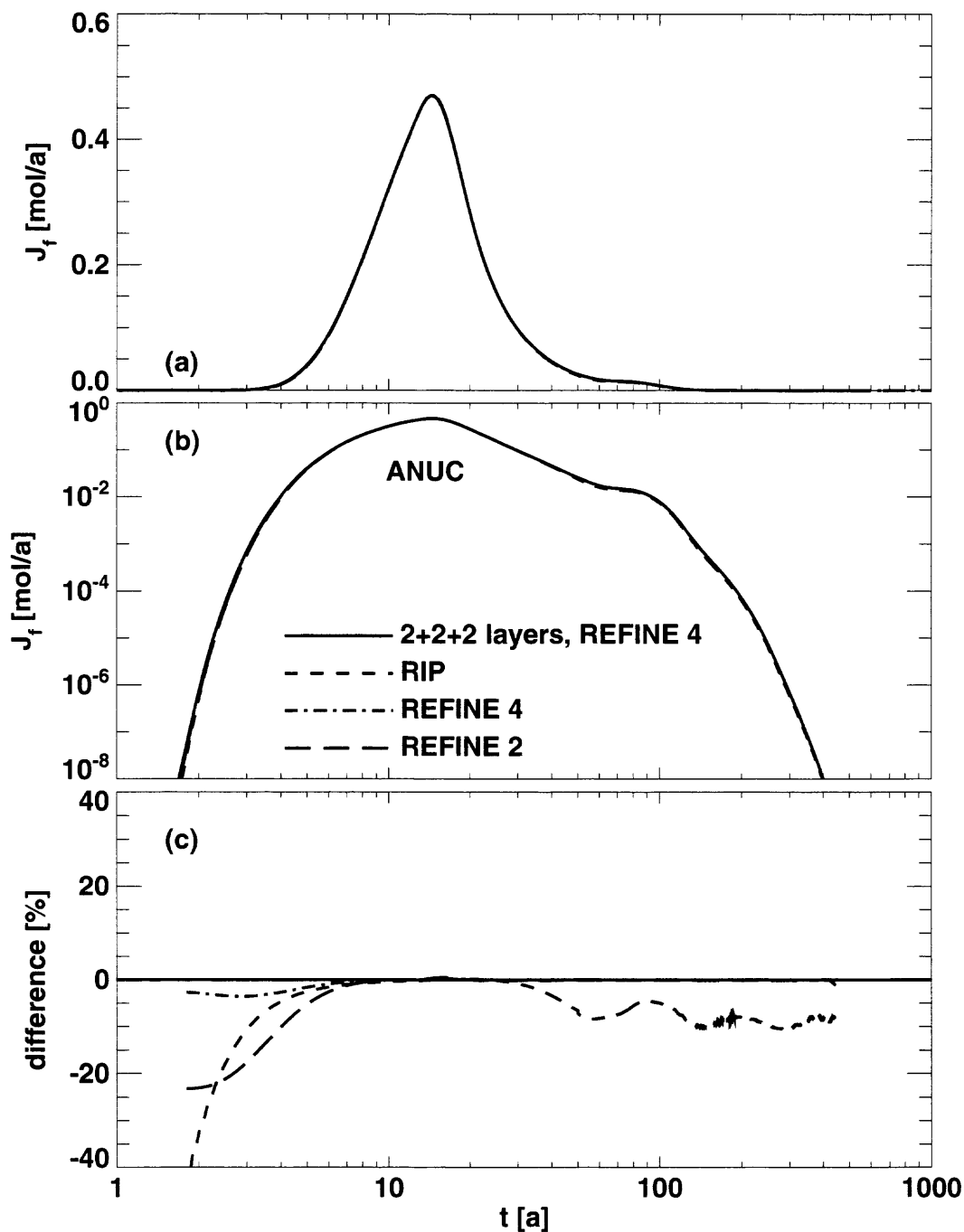


Figure 8.28. Transport in a 26-leg network where, in three of the legs, one-dimensional matrix diffusion into two independent two-layer porous regions is considered. For more details see text. Presented is the nuclide ANUC of the decay chain $ANUC \rightarrow BNUC \rightarrow CNUC$. For more details see text. The nomenclature is as in Figure 8.7.

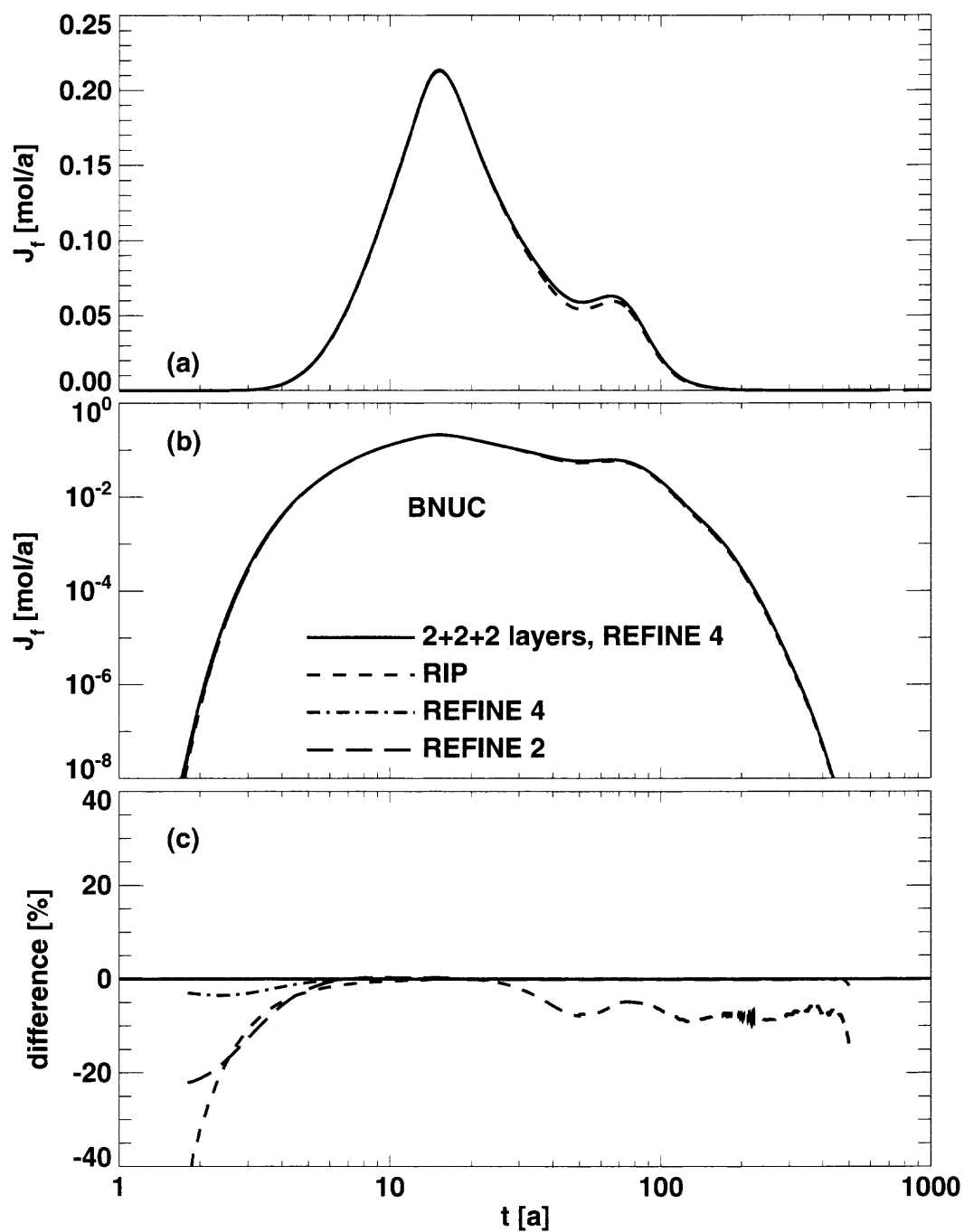


Figure 8.29. Transport in a 26-leg network where, in three of the legs, one-dimensional matrix diffusion into two independent two-layer porous regions is considered. For more details see text. Presented is the nuclide BNUC of the decay chain $\text{ANUC} \rightarrow \text{BNUC} \rightarrow \text{CNUC}$. The nomenclature is as in Figure 8.7.

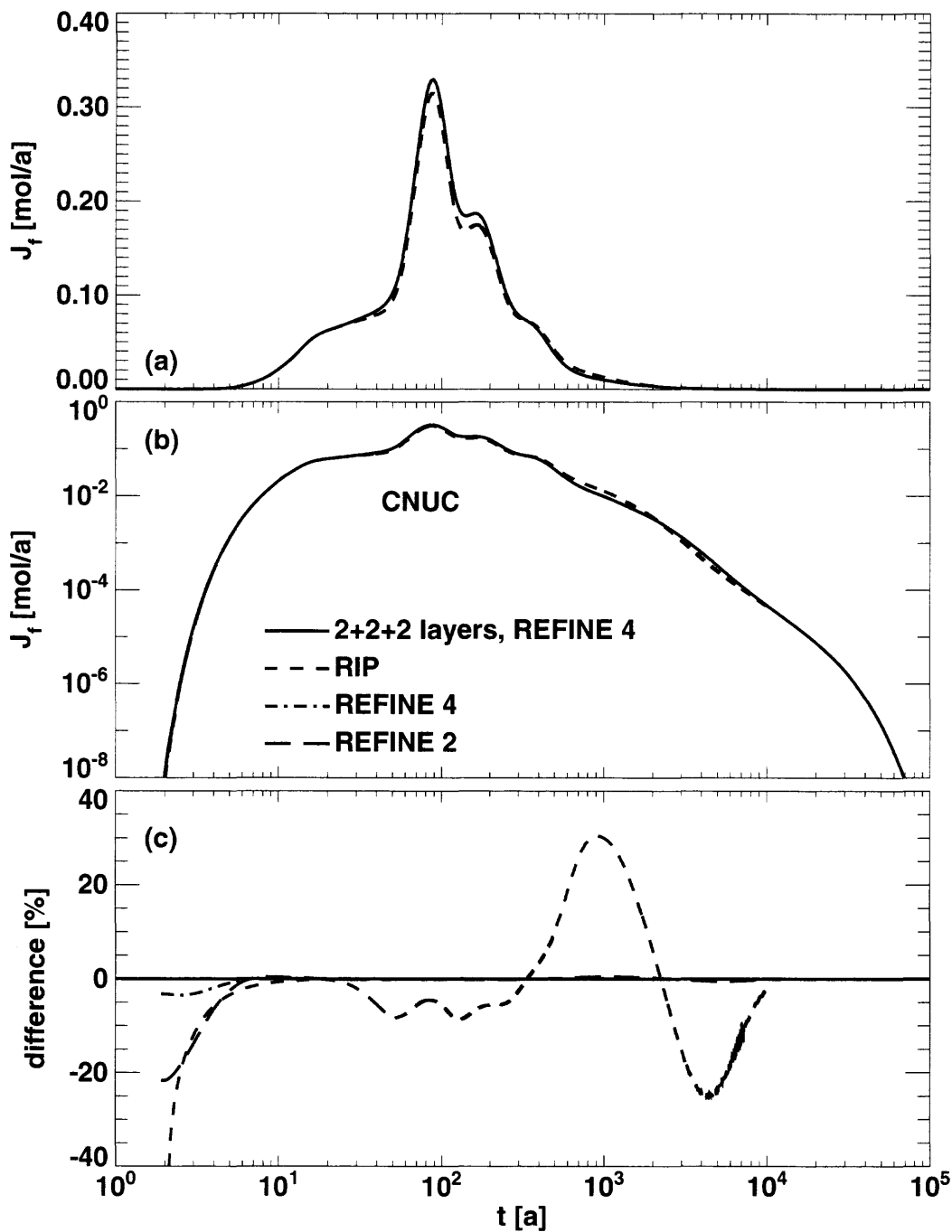


Figure 8.30. Transport in a 26-leg network where, in three of the legs, one-dimensional matrix diffusion into two independent two-layer porous regions is considered. For more details see text. Presented is the nuclide CNUC of the decay chain ANUC \rightarrow BNUC \rightarrow CNUC. The RIP calculation has been performed up to $t = 10^4$ [a]. The nomenclature is as in Figure 8.7.

8.5. Summary

In this section as step V in the verification scheme of Table 3.4, we have completed the verification of the ability of PICNIC to deal with one-dimensional matrix diffusion into different (heterogeneous) rock matrix geometries; see the detailed verification matrix in Table. 8.1. In the test cases, the effects of mesh refinement and of subdividing the rock matrix are analysed.

The capability of the finite-element method to deal with one-dimensional matrix diffusion into two independent homogeneous areas of rock matrix was verified for a single nuclide and a nuclide decay chain in a single leg and a 3-leg and a 5-leg pathway. This was done as a cross-comparison with the code PAWorks/LTG.

The capability of the finite-element method to deal with one-dimensional matrix diffusion into two independent two-layer areas of rock matrix was verified for a single nuclide and a nuclide decay chain in a single leg and a 5-leg pathway. For other parameters also a single nuclide and a nuclide decay chain in a network were considered. This verification was done as a cross-comparison with the code RIP. The agreement of RIP and PICNIC was very good. For this rock matrix geometry, which looks for PICNIC very much like two-dimensional matrix diffusion because a two-dimensional finite element mesh is used, the variation of the PICNIC results with different mesh refinements was somewhat increased with respect to the previous test cases in section 7, where one-dimensional finite-element meshes were used. This is especially true for nuclide decay chains. This somewhat decreased accuracy of the lower resolution PICNIC results will also be considered in the verification for two-dimensional matrix diffusion in the next sections.

Overall in this section we have verified the checkerboard-like technique for entering a rock matrix geometry for one-dimensional matrix diffusion into various rock matrix geometries to the finite-element method for numerical calculation of the rock matrix response. Following the considerations in section 3, together with verification step I in section 4, step III in section 6 and step IV in section 7, this verifies the capability of PICNIC to deal with various rock matrix geometries for one-dimensional matrix diffusion. Using discretisation tests and by code cross-comparisons, we have estimated the accuracy of the PICNIC results. The verification for one-dimensional matrix diffusion will be used as a basis for the further verification steps in the next sections for two-dimensional matrix diffusion.

Single leg		(a) single nuclide			(b) nuclide decay chain		
one-dimensional matrix diffusion into heterogeneous rock matrices		ZG	ZC	AI	ZG	ZC	AI
source in Laplace domain	δ -pulse	R,C ⁹⁰		R,C ⁹¹	R,C ⁹²		R,C ⁹³
	simple-leaching						
source in time domain	short pulse						
	long top-hat						
	band-release						
	general						

pathway		(c) single nuclide			(d) nuclide decay chain		
one-dimensional matrix diffusion into heterogeneous rock matrices		ZG	ZC	AI	ZG	ZC	AI
source in Laplace domain	δ -pulse	R,C ⁹⁴		R,C ⁹⁵	R,C ⁹⁶		R,C ⁹⁷
	simple-leaching						
source in time domain	short pulse						
	long top-hat						
	band-release						
	general						

network		(e) single nuclide			(f) nuclide decay chain		
one-dimensional matrix diffusion into heterogeneous rock matrices		ZG	ZC	AI	ZG	ZC	AI
source in Laplace domain	δ -pulse						
	simple-leaching						
source in time domain	short pulse						
	long top-hat						
	band-release						
	general			R,C ⁹⁸			R,C ⁹⁹

Table 8.1. Performed calculations for the “one-dimensional” rock matrix geometries depicted in Figures 8.1, 8.6, and 8.26. Note: All test cases represented by empty fields in the scheme were implicitly verified by any of the specified examples. Such a procedure is strongly based on the internal structure of PICNIC as outlined in more detail in section 3. Legend: C: comparison with other computer code; R: “discretisation test” considering different mesh refinements in the “finite-element” results in PICNIC.

⁹⁰ Comparison with PAWorks/LTG.

⁹¹ Comparison with RIP.

⁹² Comparison with PAWorks/LTG.

⁹³ Comparison with RIP.

⁹⁴ Comparison with PAWorks/LTG.

⁹⁵ Comparison with RIP.

⁹⁶ Comparison with PAWorks/LTG.

⁹⁷ Comparison with RIP.

⁹⁸ Comparison with RIP.

⁹⁹ Comparison with RIP.

9. Homogeneous Two-Dimensional Planar Rock Matrix

In this section we consider the effect of **two-dimensional rock matrix diffusion into a homogeneous rock matrix block**, see Figure 9.1. In this geometry, the area of flowing water (F) of aperture $2b$ is as for the homogeneous one-dimensional planar fracture geometry in contact with a rock matrix of type M1 and thickness d . Now, however, it is assumed that the flow of water is only within channels of widths $2B$ within the fracture. The channel centres have distance $2D$ and the rest of the fracture is filled with areas of impermeable rock (M0) of widths $d_y = D - B$.¹⁰⁰ Thus, as depicted in Figure 9.1a, to every channel of width $2B$ belongs a rock matrix layer of width $2D$. For the parameter definition and the balance equations for the rock matrix geometries of this section, see sections 2.2 and 2.4. This is step VI of the verification of PICNIC, which is the main part of the testing for two-dimensional matrix diffusion, cf. section 3.4.6. In step VII in the next section, the verification the ability of PICNIC to deal with two-dimensional matrix diffusion will be completed.

The flexibility of PICNIC to deal with this, and even more complicated, rock matrix geometry was the reason to implement the finite-element method (FEM) for calculation of the rock matrix response in the Laplace domain. For this two-dimensional rock matrix geometry, no analytical solution of the rock matrix response $\bar{\eta}(s)$ is available. No computer code for comparison purposes was found that can deal generally with two-dimensional matrix diffusion and particularly this geometry considered, see also section 4.1.2. Because this considerably reduces the possibilities for code verification, the verification rests primarily on discretisation tests considering different refinements in the finite-element method in PICNIC and considering subdivided rock matrix layers. These forms of the relative difference functions between different PICNIC calculations will be discussed and compared to the respective ones in the previous sections. It was also possible to compare PICNIC results for steady-state release of a single nuclide to a result derived from an ADINA-T calculation. Thereby the test cases presented in [Barten, Robinson and Tirbonod, 2000] are reviewed and extended.

We start in section 9.1 with different **single nuclides in single legs** with different influence of radioactive decay on the release curve. The applied parameters are related to the Kristallin-I performance assessment. The steady-state behaviour of the nuclide release is compared to a solution derived from results of the code ADINA-T [ADINA, 1992]. For the time-dependent behaviour, discretisation tests considering different refinements in the finite-element method in PICNIC and considering subdivided rock matrix areas are performed.

In section 9.2 a **single nuclide** and a **nuclide decay chain in a single leg** are considered as a hypothetical variation of the Grimsel dipole parameters for uranine. Again different mesh refinements and the effect of subdividing the rock matrix are considered in discretisation tests.

In section 9.3 the transport of a **single nuclide** and of a **nuclide decay chain** in a 26-leg **network** are considered with **two-dimensional matrix diffusion** in part of the legs, compare sections 4.3, 6.6 and 8.4.

Section 9.4 gives a summary.

¹⁰⁰ The direction for one-dimensional matrix diffusion ($d_y = 0$) is denoted as the x -direction for historical reasons, and the direction of the flowing water is the z -direction.

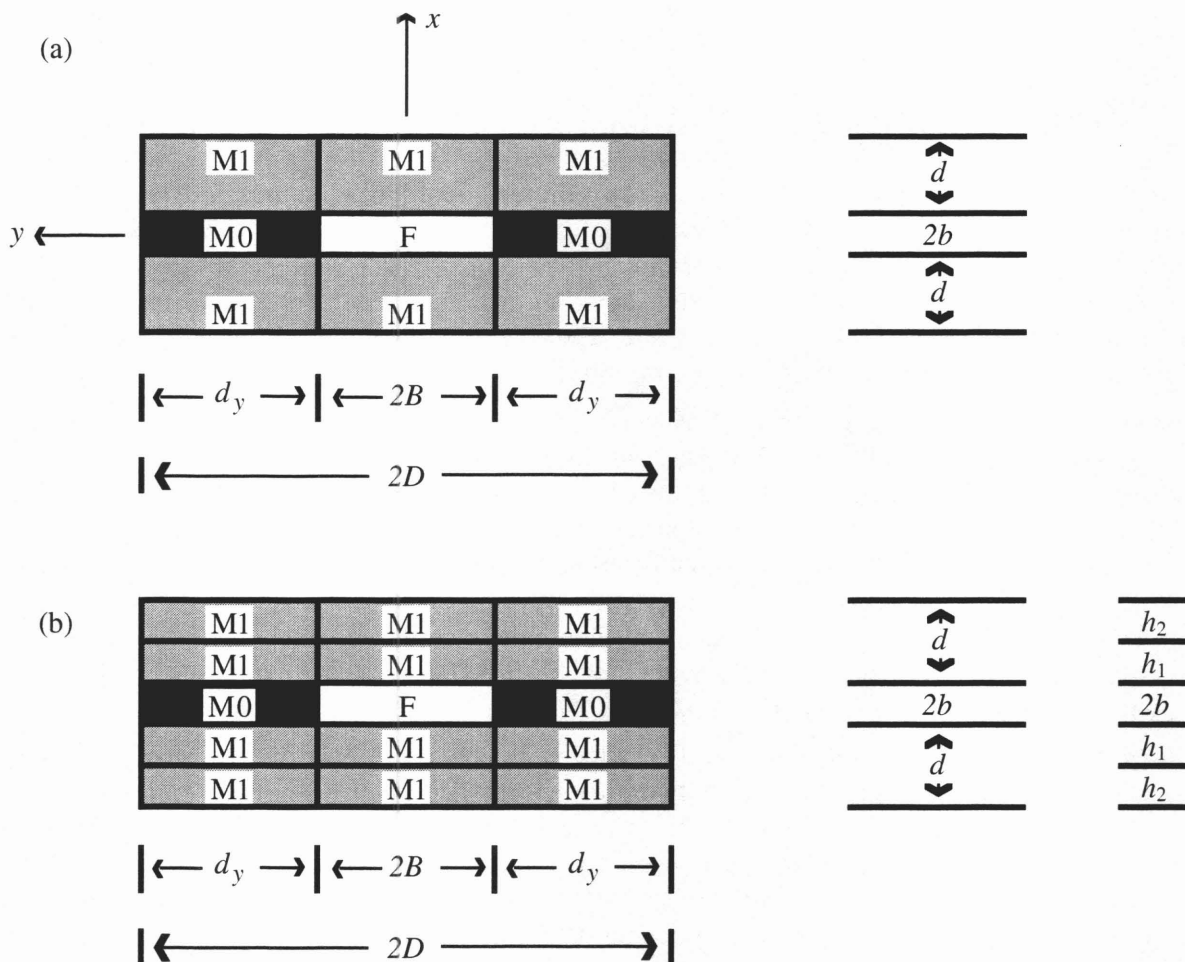


Figure 9.1. (a) Sketch of the cross-section of a leg with a fracture that is filled with an area of flowing water (F) of width $2B$ and the rest of the fracture (to the left and right of the channel with flowing water) is filled with impermeable rock matrix (M0) of width d_y . The sketch is not to scale. The width of the fracture is $2D$ and the aperture is $2b$. Below and above the fracture a rock matrix layer (M1) is situated. The thickness of the rock layer is d . In (a) this is entered to PICNIC by one layer of rock matrix below and above the fracture of thickness d . In (b) this rock layer is subdivided into two sub-layers of (in general unequal) thickness h_1 and h_2 such that $d = h_1 + h_2$.

For this geometry, diffusion in the rock matrix is now two-dimensional. For single nuclides the extended rock matrix layer leads to a “correction” in the exponent

$$L\Lambda(s) = -[s + \lambda]\alpha - \gamma\sqrt{s + \lambda} \tanh(\beta\sqrt{s + \lambda})f_2(s), \tag{9.1}$$

compare also equation 7.1. To the best of our knowledge, an analytical expression for the correction function $f_2(s)$ in terms of simple functions is not available, unlike the case for one-dimensional rock matrix diffusion.

9.1. Cases Related to Performance Assessment

In this subsection we consider the transport of different **single nuclides in a single leg**. The parameters are variations of the Kristallin-I reference case. As discussed in section 7.1.1, the Kristallin-I reference case is based on cataclastic zones in the crystalline basement of Northern Switzerland. The open channels in the cataclastic zone are considered to have a width of $2B=10$ cm and an aperture $2b=1$ mm (compare the leg cross-section in Figure 9.1a with the geometry of a cataclastic zone depicted in Figure 7.2). The rock matrix type M1 represents altered wallrock accessible for matrix diffusion, with a porosity ε_p of 5% and a matrix depth of size d , with $d+b=5$ cm. In the Kristallin-I reference case, only matrix diffusion into the rock adjacent to the channels was considered. (This means $d_y=0$ [m] and $D=B$ in Figure 9.1.) To assess the effect of two-dimensional matrix diffusion on the radionuclide transport, we consider rock matrix layer widths varying between $D=B=0.05$ [m] (corresponding to the Kristallin-I reference case) and $D=21B=1.05$ [m]. The geometry of Figure 9.1 does not make use of matrix diffusion into the unaltered wallrock which was considered in section 7.1, see especially Figure 7.2.

Because this is the first performance assessment-related application of the effect of two-dimensional matrix diffusion, the transport behaviour is considered in more detail. For three different nuclides and different widths, $2D$, of the rock matrix layer, the nuclide release for a constant source and a δ -function like source are analysed.

For different refinements of the finite-element mesh the accuracy of the steady-state release is estimated by comparing the results of the different refinements. For one of these nuclides, fortunately, it is possible to compare to results from the code ADINA.

For the δ -function source, the time-dependent behaviour is analysed with discretisation tests for different refinements of the finite-element mesh and considering subdivision of the rock matrix.

9.1.1. Release Curves and Geosphere Barrier Efficiency

We start again with ^{135}Cs , which is the most important nuclide in the Kristallin-I reference case. In Figure 9.2b, release curves to the biosphere are considered for a δ -pulse of 1 [mol] of ^{135}Cs injected into the geosphere at $t=0$. The release curves in Figure 9.2 are calculated in PICNIC using the option REFINE 4 and entering the geometry of Figure 9.1b with two sub-layers of thickness $h_1=0.02$ [m] and $h_2=0.0295$ [m] to PICNIC. For the reference case, the time to maximum release is at about $0.14 \cdot 10^6$ [a], which is small compared to the ^{135}Cs half-life of $2.3 \cdot 10^6$ [a]. For the reference case ($d=0.0495$ [m] and $d_y=0$ [m]), diffusion into the rock matrix is moreover a one-

dimensional, fast process ($\beta^2 = \frac{d^2 R_p}{D_p} = 0.005 \cdot 10^6$ [a]) acting as simple retardation like surface sorption.

Note that for one-dimensional matrix diffusion, $D=B$, the matrix thickness d , or the respective matrix diffusion time $\beta_d^2 = \frac{d^2 R_p}{D_p}$ defined in equation (2.128), is the only parameter necessary to

describe the geometry of the rock matrix, see section 2.5.2. For two-dimensional matrix diffusion ($D>B$) the length scales D and B are also required to describe the geometry of the rock matrix. Equivalently to these length scales, we can define the respective timescales for diffusion across the

channel width,

$$\beta_B^2 = \frac{B^2 R_p}{D_p} \quad (9.2)$$

and across the rock matrix layer,

$$\beta_D^2 = \frac{D^2 R_p}{D_p}. \quad (9.3)$$

For the case considered, diffusion in the y -direction across the channel width is always a fast process $\beta_B^2 \approx \beta_d^2$, i.e. it is especially small with respect to the nuclide half-life and the time to maximum release for one-dimensional matrix diffusion. This means that, for times larger than β_B^2 and for nuclides entering the porous rock matrix at arbitrary positions at the channel/matrix interface¹⁰¹, the system is **not** translational-invariant in the y -direction.¹⁰² Thus for times in the order of magnitude of, and larger than, β_B^2 it is **relevant** that matrix diffusion is two-dimensional (if D is not too close to B).

The timescale for diffusion in the y -direction across the rock matrix layer β_D^2 is up to $D = 3B$ below $0.05 \cdot 10^6$ [a]. Thus diffusion in the y -direction is a fast process compared to the time to maximum release. Because diffusion in the x -direction is also a fast process, the diffusion in the whole rock matrix is a fast process and acts like surface sorption in the area of flowing water.

For $D = 10B$, however, $\beta_D^2 \approx 0.5 \cdot 10^6$ [a] is in the order of magnitude of the time to maximum release, and the type of release curve changes. In particular, the release curve becomes broader. This is even more expressed for $D = 21B$ with $\beta_D^2 \approx 2 \cdot 10^6$ [a], where the hump like tailing in the release curve can be seen, which is typical for reflection at the outer boundaries of the rock matrix. When radioactive decay is neglected (Figure 9.2c), the release curve is double-humped. The typical $t^{-3/2}$ finger print of unlimited one-dimensional matrix diffusion into a planar rock matrix geometry, however, is not encountered for the parameters considered here.

The increase of the rock matrix width has several consequences. The recovered mass which is proportional to the release curve for a constant source (presented in Figure 9.2a) reaches steady-state much later. This means that most nuclides need several hundred thousand years longer to cross the geosphere. While in the reference case 5% of the ¹³⁵Cs decays in the geosphere, about 40% decays for $D = 10B$, and nearly 60% for $D = 21B$ (Figure 9.2a and 9.3c). For $D = 21B$ with

¹⁰¹ This means that also the nuclides entering the rock matrix at $y = 0$ by diffusion can reach the position $y = B$ during this time.

¹⁰² A quantitative theory for two-dimensional matrix diffusion is lacking. Besides the qualitative arguments and the "order of magnitude" discussions of the timescales presented here, the development of such a theory is left to future work.

$\tanh(\beta_D \sqrt{\lambda}) \approx 0.7$ (Figure 9.3a) the rock matrix still cannot be considered unlimited. The geosphere barrier efficiency (section 2.1.7) is calculated by PICNIC in different ways: representing the rock matrix by two layers of the same type and using the option REFINE 4 (solid line in Figure 9.3c), using the option REFINE 4 (crosses) and using the standard option REFINE 2 (squares). All PICNIC results agree within about 0.5%, see the relative difference from the highest refinement PICNIC result in Figure 9.3b of $(1 - \text{the geosphere barrier efficiency})$. The PICNIC results for the option REFINE 4 agree within 0.1% (crosses in Figure 9.3b).

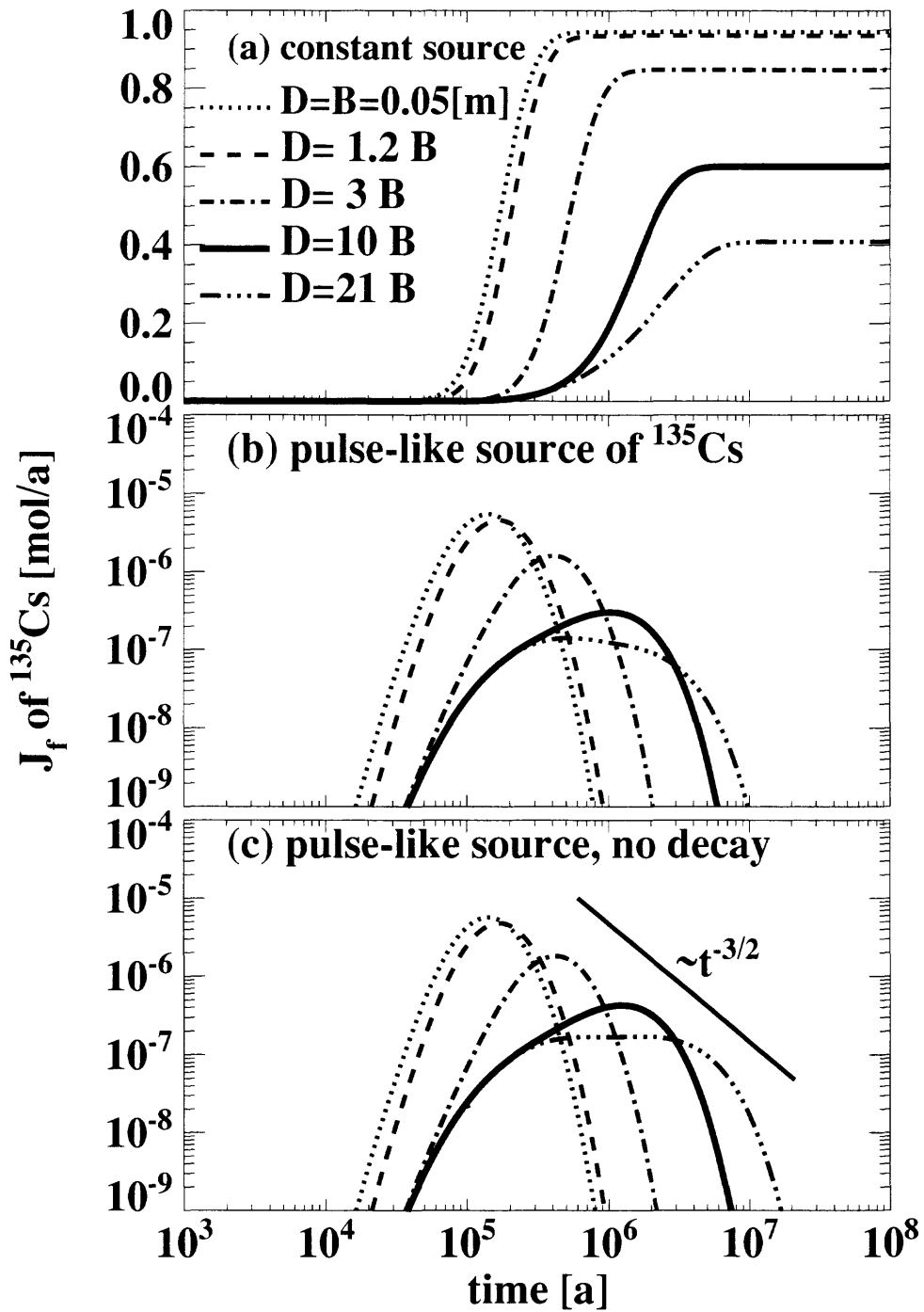


Figure 9.2. In (a) the nuclide outflow rate of ^{135}Cs for a constant source of 1 [mol/a] starting at $t = 0$ is presented for different widths D of the unaltered wallrock. In (b) the nuclide release for a pulse-like injection of 1 [mol] of ^{135}Cs at $t = 0$ into the geosphere is given. In (c) the release curves for a pulse-like source are presented when radioactive decay ($T_{1/2} = 2.3 \cdot 10^6$ [a]) is neglected.

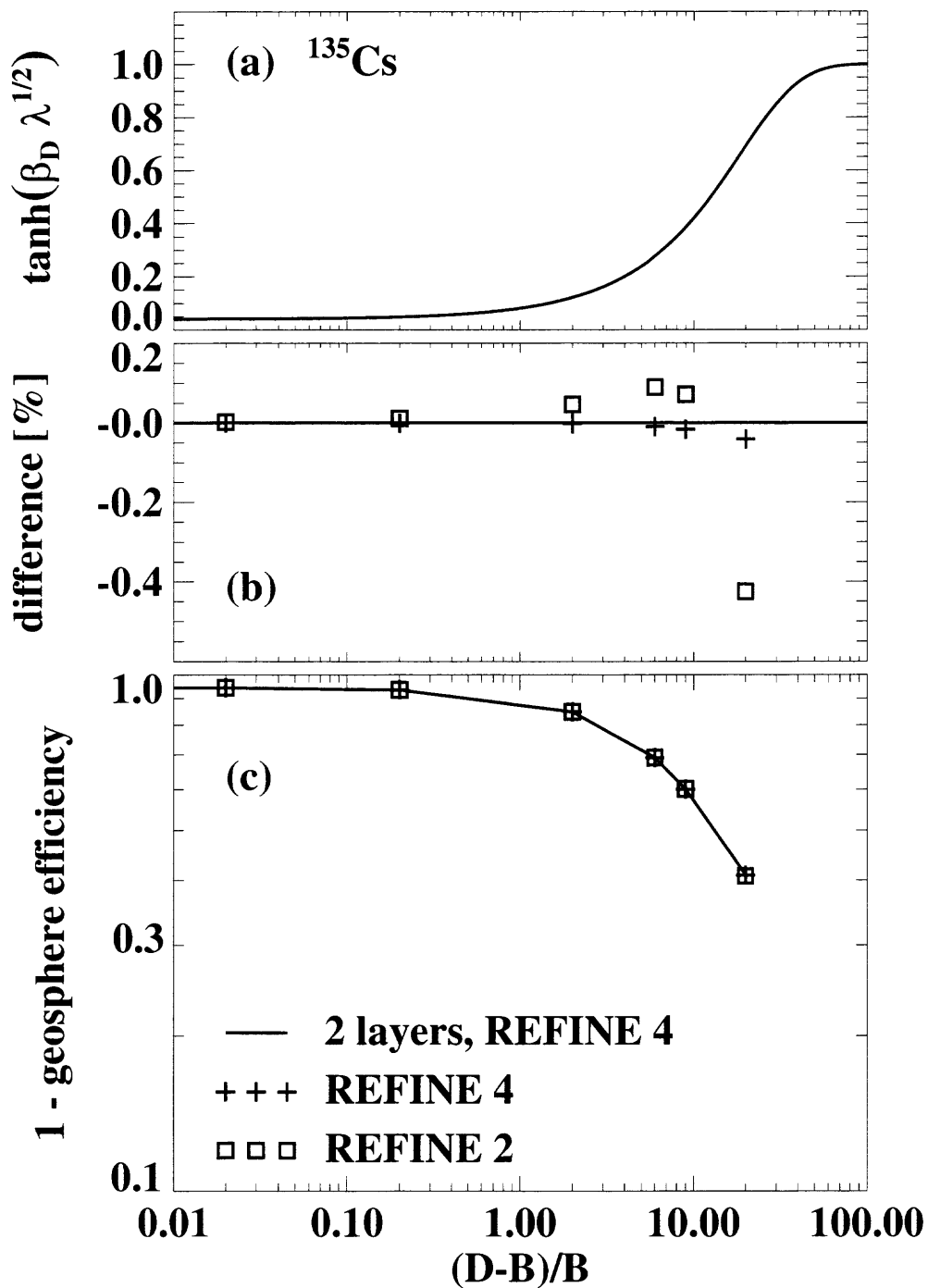


Figure 9.3. (a) gives the variation of $\tanh(\beta_D \sqrt{\lambda})$ of equation (9.1) as a function of the width D of the wallrock for ^{135}Cs . This quantity measures to what extent the wallrock can be considered unlimited in the y -direction. (c) gives $\bar{\chi}(z=L, s=0) = (1 - \text{the geosphere barrier efficiency})$. This is calculated by PICNIC in different ways: representing the rock matrix by two layers and using the option REFINE 4 (the solid line is a linear interpolation of the calculated values), using a single layer and the option REFINE 4 (crosses) and using the standard option REFINE 2 (squares). (b) shows the relative difference of the PICNIC calculation for $\bar{\chi}(z=L, s=0)$ with respect to the highest refinement PICNIC result presented.

When radioactive decay is neglected, the release curves of ^{99}Tc behave similarly to ^{135}Cs (Figure 9.4c). The ^{99}Tc half-life of $0.213 \cdot 10^6$ [a], however, is much smaller than the time to maximum release, which is in the order of 10^6 [a] when radioactive decay is taken into account (Figure 9.4b). Consequently the release curves for times longer than the half-life are dominated by radioactive decay. Thus, already in the reference case only 0.9% of the ^{99}Tc crosses the geosphere, while more than 99% decays (Figures 9.4a). For small D values, $D \approx B$, the different PICNIC results agree within 5% and within 2% for PICNIC calculations with REFINE 4 (Figure 9.5b). For $D \geq 7B$ with $\tanh(\beta_D \sqrt{\lambda}) \approx 1.0$ (Figure 9.5a), the rock matrix can be considered unlimited in the y -direction and only about 0.005% of the nuclide crosses the geosphere (Figures 9.4a and 9.5c). Thus the steady-state release (1 - the geosphere barrier efficiency) has decreased by a factor of more than hundred. A larger rock matrix extent D does not lead to a higher geosphere barrier efficiency. For these large D values, the different PICNIC results agree within 25%, and within 6% for PICNIC calculations with REFINE 4 (Figure 9.5b).

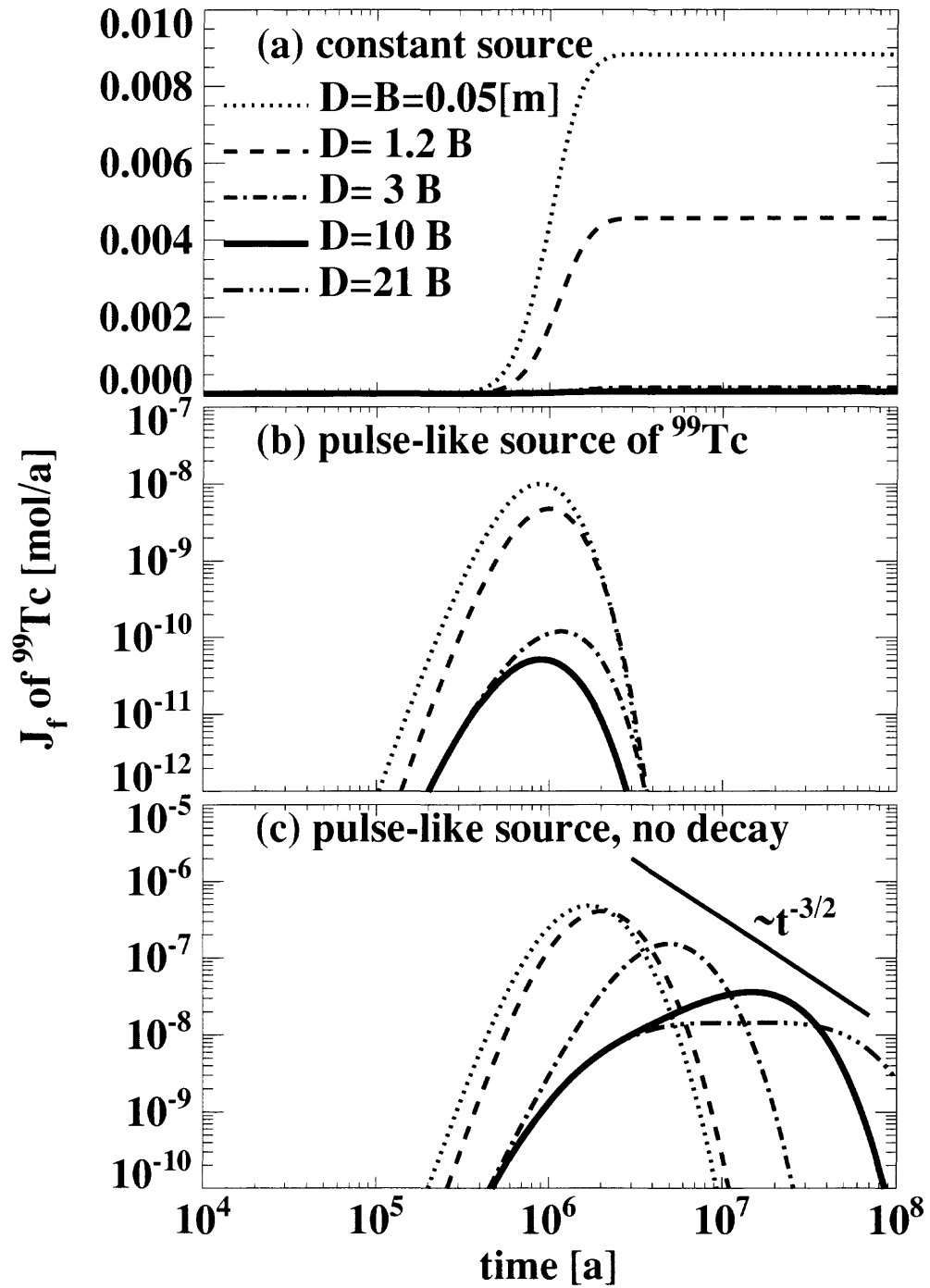


Figure 9.4. As in Figure 9.2, but for ^{99}Tc ($T_{1/2} = 0.213 \cdot 10^6$ [a]).

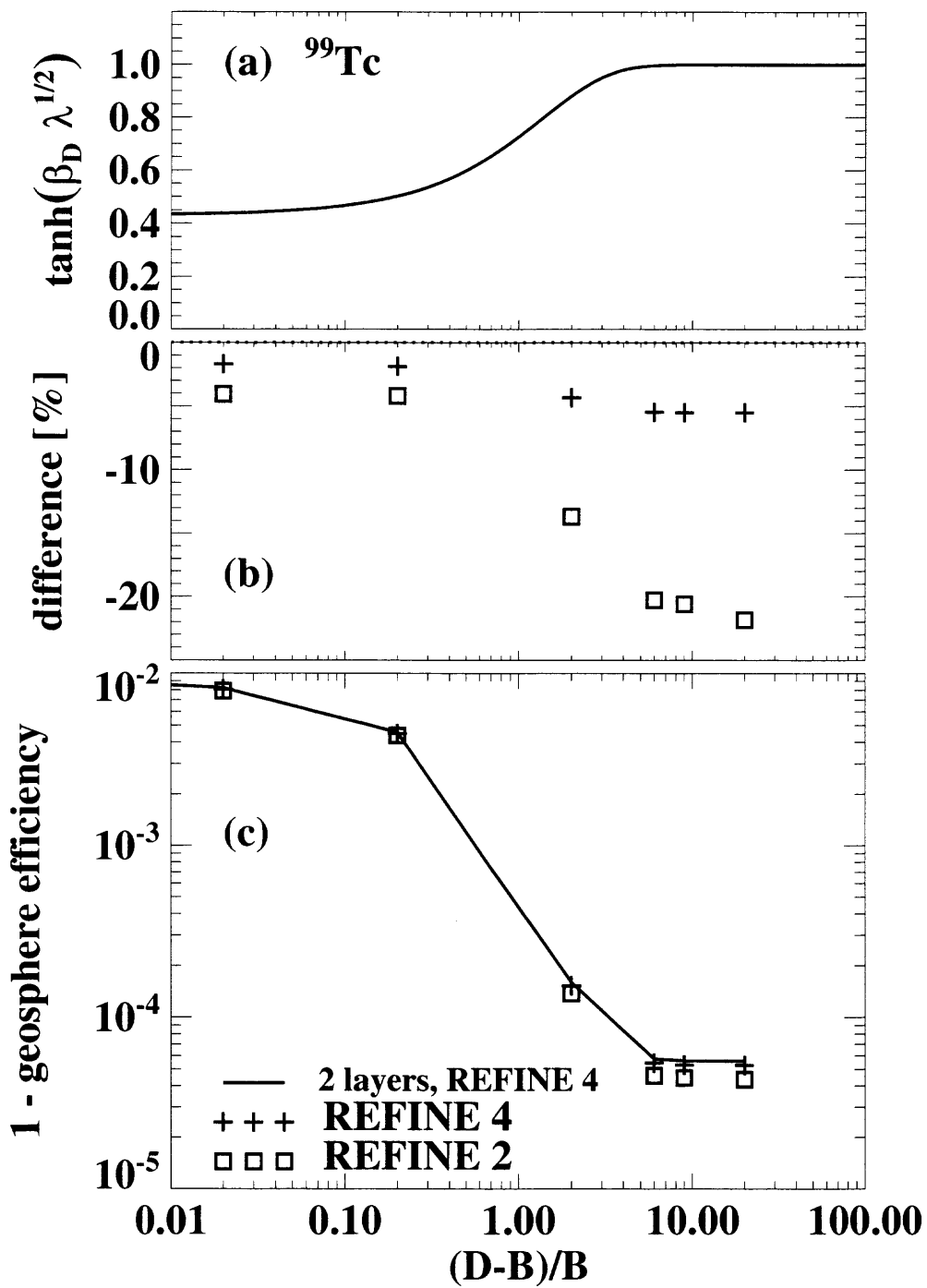


Figure 9.5. As in Figure 9.3, but for ^{99}Tc .

The nuclide ^{79}Se (Figures 9.6 and 9.7) shows similar behaviour to ^{135}Cs . Because the timescale for the tailing behaviour, when radioactive decay is neglected (see Figure 9.6c), is in the same order of magnitude as the half-life of $0.065 \cdot 10^6$ [a], the tailing is masked by radioactive decay (Figure 9.6b). The barrier efficiency of the geosphere is higher (Figures 9.6a and 9.7c). For $D = 21B$ with $\tanh(\beta_D \sqrt{\lambda}) \approx 0.99$ (Figure 9.7a), the rock matrix can be considered as nearly unlimited in the y -direction. The relative differences of the geosphere barrier efficiency revealed from the different PICNIC calculations are somewhat bigger (Figure 9.7b) than for ^{135}Cs , but stay within 5% (and within 0.5% for the results with REFINE 4).

For comparison with the PICNIC result, the geosphere barrier efficiency has also been calculated using the finite-element code ADINA-T [ADINA, 1992]. The ADINA results for the barrier efficiency (triangles in Figure 9.7b,c) agree well with the PICNIC results. For $D = 10B$ also a calculation with an increased refinement finite-element mesh has been performed using ADINA (diamonds in Figure 9.7b,c). The reduction of the steady-state release ($1 -$ the geosphere barrier efficiency) of the ADINA result with the refined mesh indicates that ADINA slightly overestimates the steady-state release (Figure 9.7b). The PICNIC results for the steady-state release are consistent with this observation, because they are below the ADINA results (except for the small D -values where the PICNIC results and the ADINA results nearly perfectly agree). Moreover, the PICNIC results and the ADINA results converge with increased mesh refinement. This indicates that PICNIC slightly underestimates the steady-state release, while ADINA slightly overestimates it. This is also consistent with the tests of PICNIC for one-dimensional matrix diffusion into a single-layer rock matrix (section 6.3) and a two-layer rock matrix (section 7.1).

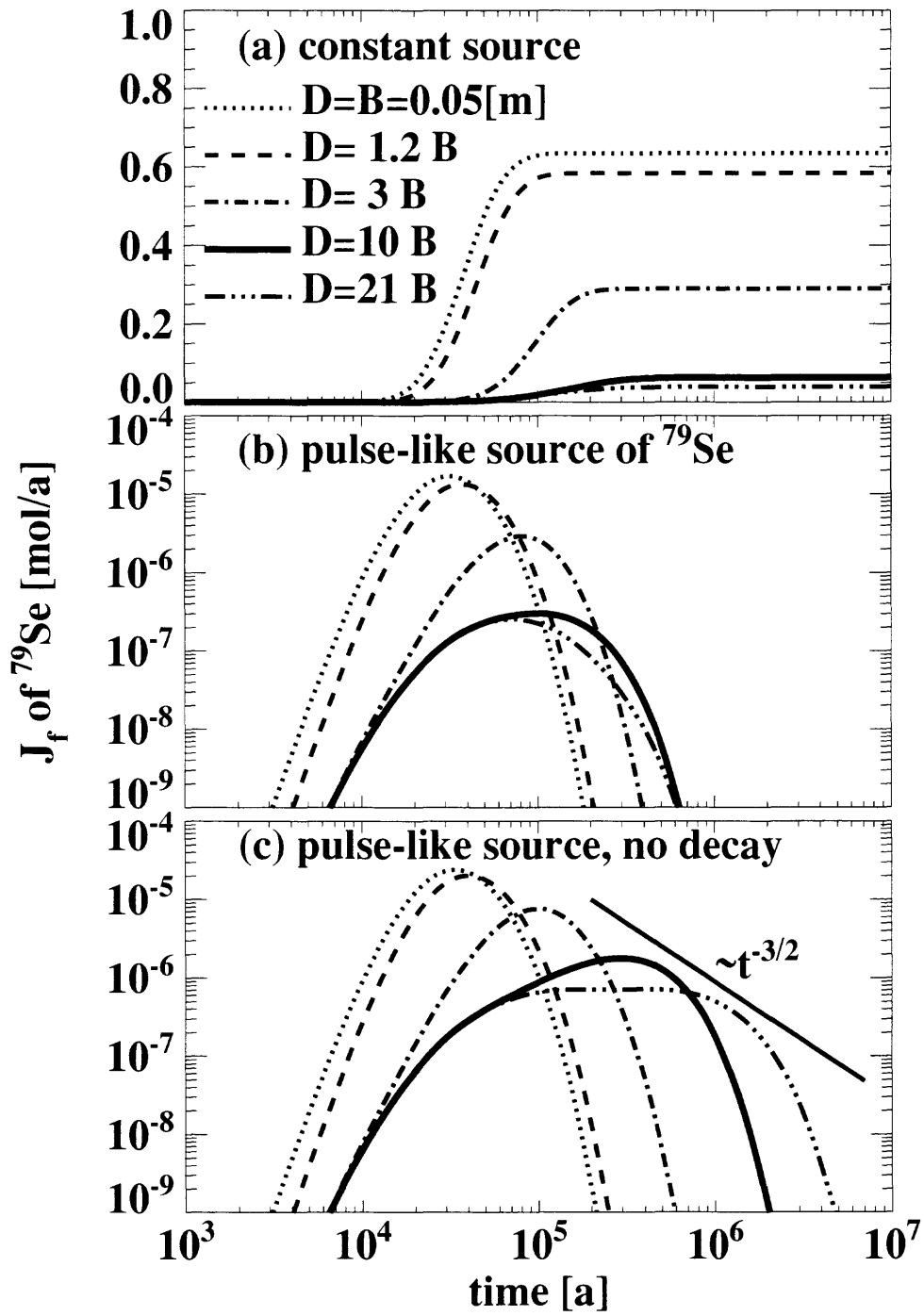


Figure 9.6. As in Figure 9.2, but for ^{79}Se ($T_{1/2} = 0.065 \cdot 10^6 [a]$).

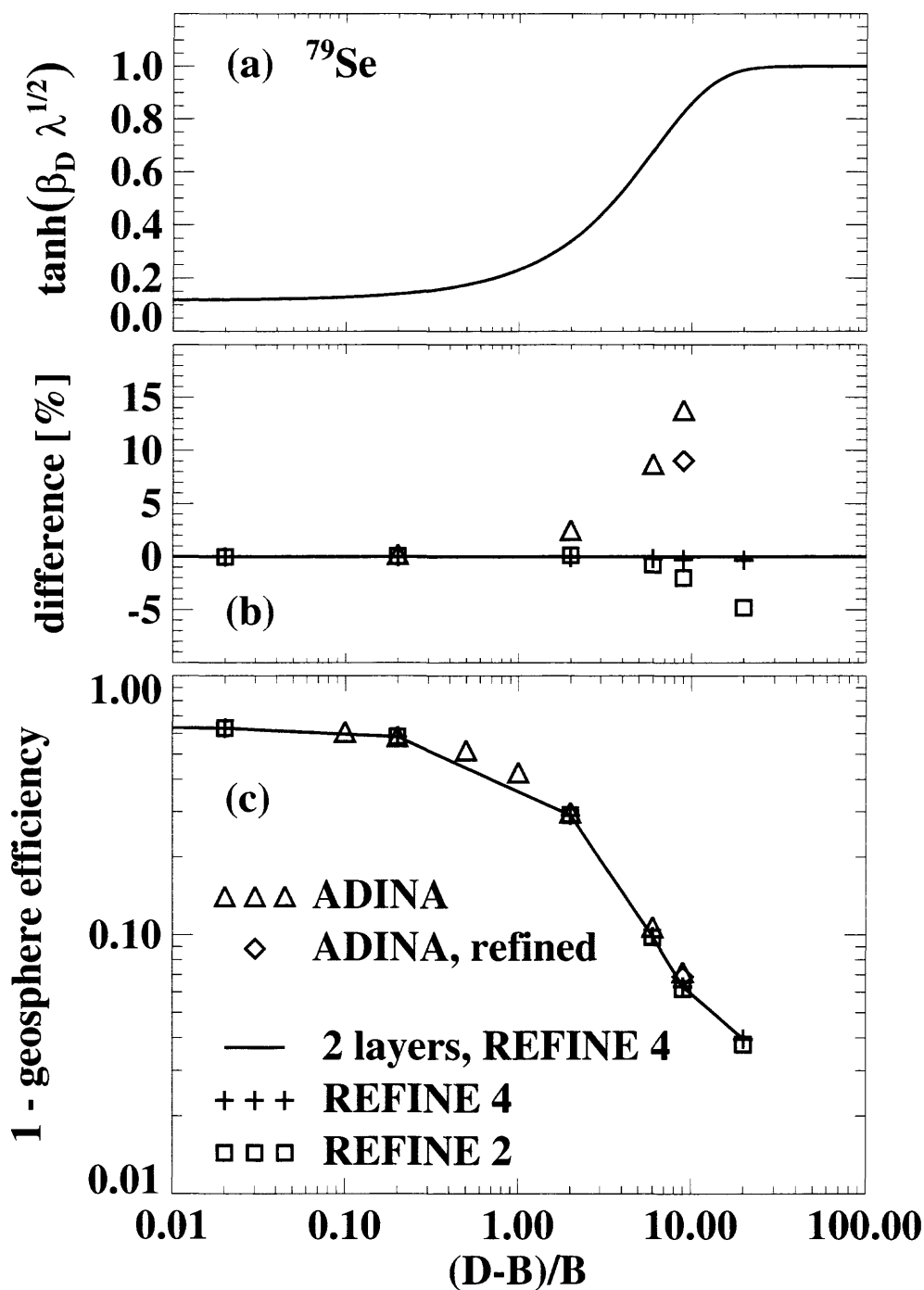


Figure 9.7. As in Figure 9.3, but for ^{79}Se . Results calculated using the finite-element code ADINA are given as triangles. For $D = 10B$ also a refined finite-element mesh has been used in ADINA (diamond). (b) shows the relative difference of the different ADINA and PICNIC calculations for $\Re(z = L, s = 0)$ with respect to the highest refinement PICNIC result presented.

The ADINA results for the geosphere barrier efficiency of ^{79}Se have been derived as follows: For the geosphere barrier efficiency (section 2.1.7) the leg response function $\overline{\mathfrak{R}}_{ZC}(z=L; s=0)$ has to be calculated for the value $s=0$. Using analytical relations (section 2.3), the leg response function is determined by the rock matrix response $\overline{\eta}(s=0)$. As described in sections 2.4.2 and 2.4.3, the rock matrix response can be calculated by solving the two-dimensional stationary diffusion problem in the Laplace domain, equations (2.87-88), for the geometry of Figure 9.1a using the relation

$$-A_m \left\langle \overline{\mathbf{j}}_p \cdot \mathbf{e}_n \right\rangle_{A_m} (s) = \overline{\eta}(s) \left[\text{a mol/m}^3 \right] \quad (9.4)$$

when the nuclide concentration in the area of flowing water is fixed as $\overline{C}_f = 1 \left[\text{a mol/m}^3 \right]$. This has been done using ADINA for different D values. Because of symmetry reasons, only a quarter of the leg cross-section needs to be analysed, compare the discussion in section 2.4.1. Moreover, because of the impermeable rock matrix type (M0), only diffusion in the rectangular rock block ($b \leq x \leq [b+d], 0 \leq y \leq D$) presented in Figure 9.8.a needs to be considered, together with the boundary conditions

$$\overline{C}_p(x=b, y; s=0) = 1 \left[\text{a mol/m}^3 \right] \quad \text{for} \quad 0 \leq y \leq B, \quad (9.5a)$$

$$\partial_x \overline{C}_p(x=B, y; s=0) = 0 \quad \text{for} \quad B \leq y \leq D, \quad (9.5b)$$

$$\partial_x \overline{C}_p(x=[b+d], y; s=0) = 0 \quad \text{for} \quad 0 \leq y \leq D, \quad (9.5c)$$

$$\partial_y \overline{C}_p(x, y=0; s=0) = 0 \quad \text{for} \quad b \leq x \leq [b+d], \quad (9.5d)$$

$$\partial_y \overline{C}_p(x, y=D; s=0) = 0 \quad \text{for} \quad b \leq x \leq [b+d]. \quad (9.5e)$$

Because there is no nuclide flux between the area of flowing water and the impermeable rock matrix of type M0, nuclide flux into the area of flowing water is at the interface at $|x|=b$ only. Thus the rock matrix response is calculated as

$$\begin{aligned} \overline{\eta}(s) \left[\text{a mol/m}^3 \right] &= -4B \Delta z \left\langle \overline{\mathbf{j}}_x \right\rangle (x=b; s) = -4B \Delta z \left\langle -\varepsilon_p D_p \partial_x \overline{C}_p \right\rangle (x=b; s) \\ &= 4B \Delta z \varepsilon_p D_p \frac{1}{B} \int_0^B dy \left[\partial_x \overline{C}_p \right] (x=b, y; s) \end{aligned} \quad (9.6)$$

and is determined by the average of the concentration gradient in the rock matrix (Figure 9.8b) at the channel/matrix interface. The non-zero nuclide flux for $y > B$ is a numerical artefact of the

ADINA code which is due to the non-continuous boundary condition at the channel/matrix interface at $|y|=B$ (compare equation 9.5a with 9.5b). Moreover, the very strong increase of the nuclide flux when y approaches $|y|=B$ for large D values must be resolved with sufficient accuracy by the numerical code. Because a similar finite-element method is used in PICNIC, the local increase of the flux and the non-continuous boundary condition could be the reasons for the reduced accuracy of the PICNIC calculations for two-dimensional matrix diffusion compared with one-dimensional matrix diffusion.

To conclude for these three nuclides, the geosphere barrier efficiency shows very good accuracy, at least for the REFINE 4 option. Generally the relative differences between different PICNIC results and also to the ADINA result increase with increasing width D of the rock layer. In all cases the REFINE 4 option shows an agreement with the highest refinement PICNIC result presented, which is about a factor of three or more better than for the standard REFINE 2 option. This is similar to the single-layer (section 6) and two-layer (section 7) geometries for one-dimensional matrix diffusion. This gives the first indications that two-dimensional matrix diffusion can also be accurately handled with PICNIC. The accuracy, however, is reduced compared to the one-dimensional case.

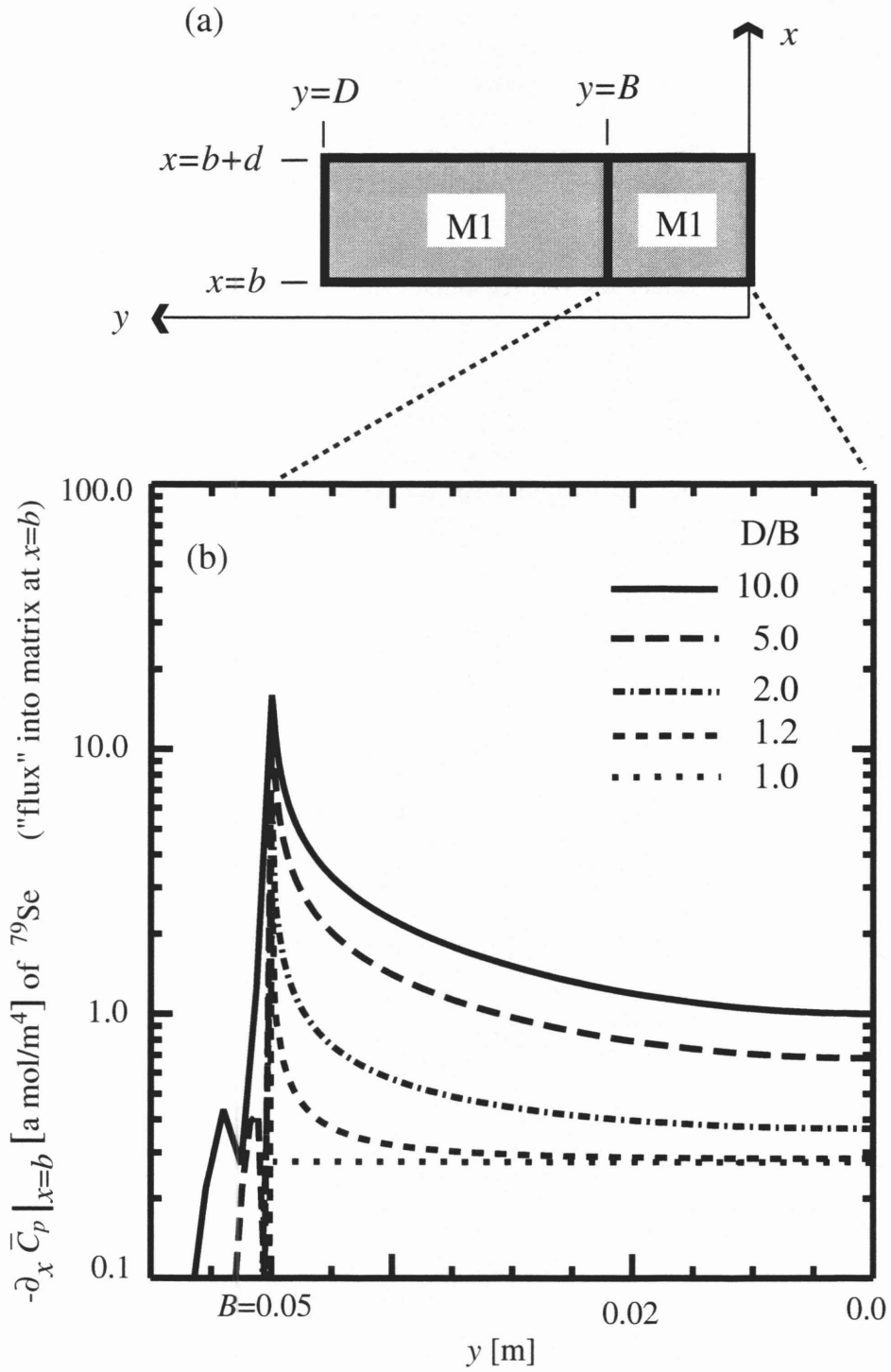


Figure 9.8. (a) Sketch of a quarter of the rock matrix for two-dimensional matrix diffusion into a single-layer rock matrix considered for ADINA calculations (see also Figure 9.1a). In (b) the local spatial x -derivative of the steady-state concentration field at the channel/matrix interface calculated by the code ADINA is given for the nuclide ^{79}Se for different widths $2D$ of the rock layer. The width of the fracture channel is fixed ($2B = 10[\text{cm}]$). Note for $D > B$ the extreme increase of the concentration gradient (given on a logarithmic scale) for y -values close to the boundary of the channel at $y = B$.

9.1.2. Effect of Mesh Refinement for a Pulse-Like Source

In this subsection we test the effect of **mesh refinement** for the full time-dependent behaviour in the case of a δ -function source. Different nuclides and different widths of the rock matrix are considered. As a first test case we consider in the transport of the nuclide ^{135}Cs in the matrix geometry with $D = 10B$, compare solid line in Figure 9.2b. The nuclide release curves for the standard calculation with REFINE 2 (long dashes) and the increased refinement REFINE 4 (dash-dotted lines) are given in Figure 9.9a on a linear scale and in Figure 9.9b on a logarithmic scale. The results for the 2 sub-layers are presented for the options REFINE 2 (short dashes) and REFINE 4 (which should give the best results, solid lines). The relative difference functions with respect to the latter are presented in Figure 9.9c. All release curves have the same structure and are in good agreement. The relative difference functions indicate that the lower resolution calculations show a delayed increase of the release curves for early times, then overshooting in the maximum region, and an earlier decrease of the release curves for late times. The results with the REFINE 4 option agree best with each other. The agreement of the standard resolution REFINE 2 result is worst: the increase for early times is about $10^3[\text{a}]$ later with respect to the increased refinement result and the overshooting in the maximum region is within 2%.

Similar discretisation tests for transport of the nuclide ^{79}Se are given for $D = 1.2B$ (Figure 9.10) and $D = 10B$ (Figure 9.11), compare dashed line and solid line in Figure 9.6b. The relative difference functions are in the same order of magnitude and have a similar form as for the ^{135}Cs case discussed above. Only for the ^{79}Se $D = 10B$ case is the overshooting slightly behind the maximum region. This means that the lower resolution results using the option REFINE 2 still underestimate the nuclide release in the maximum region by about 2-4%. Together with the underestimation of the nuclide release for early times, this leads to the underestimation of the steady-state release depicted in Figure 9.7.

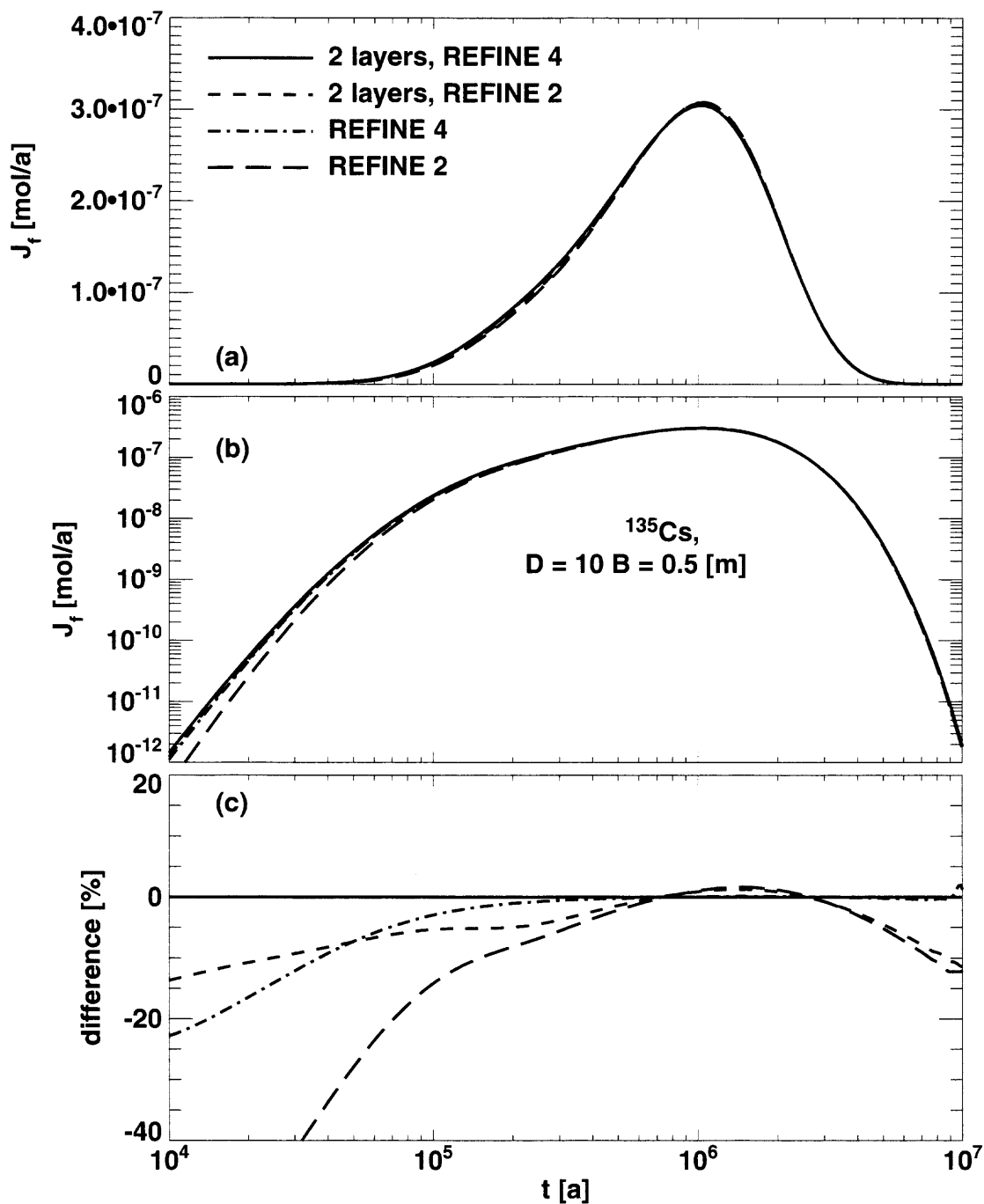


Figure 9.9. Transport of ^{135}Cs in a single leg for a δ -function source. The width of the channel is $2B = 0.1$ [m], while the width of the rock layer is $2D$ with $D = 10B = 0.5$ [m], compare the solid line in Figure 9.2b. For more details see text.

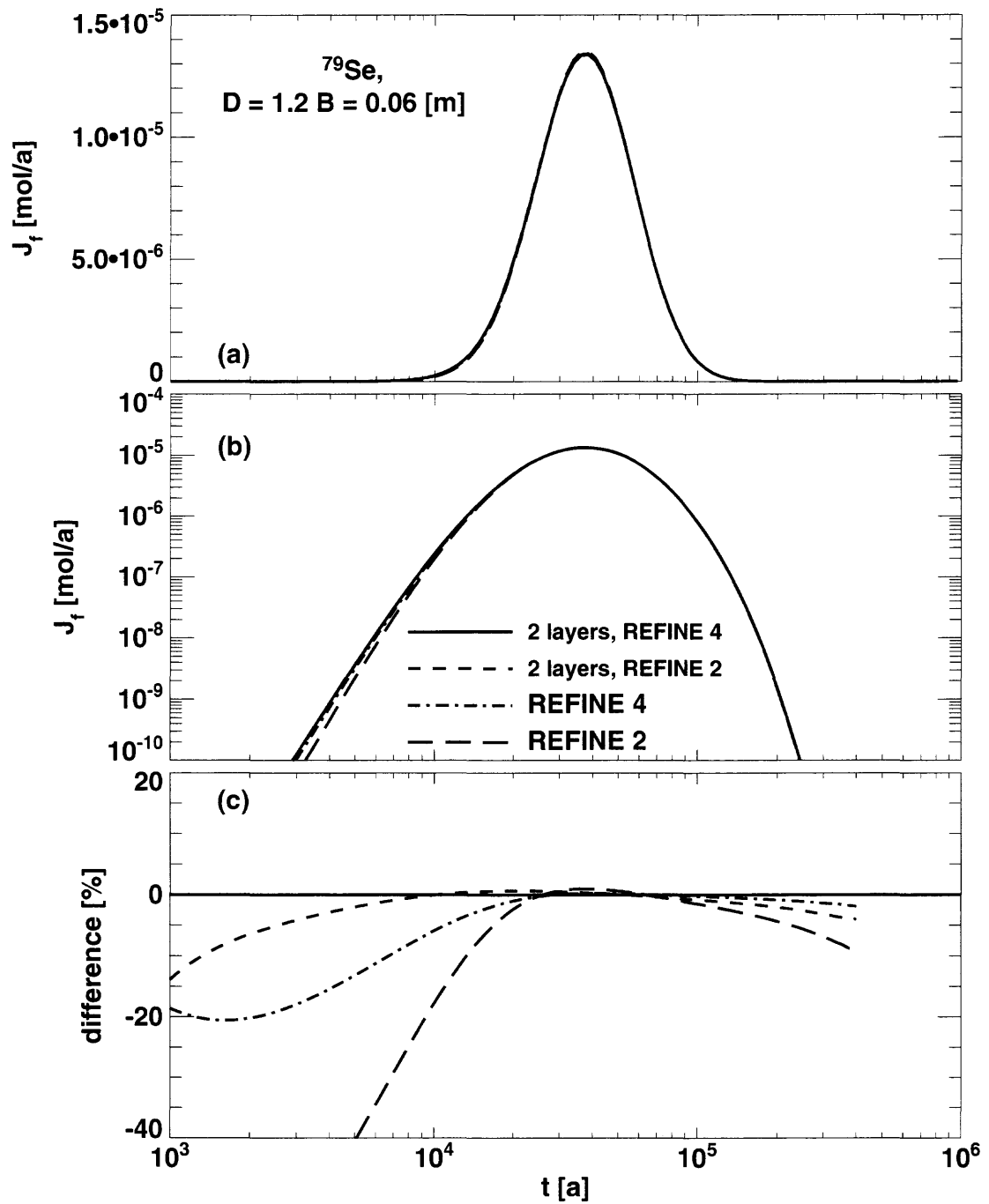


Figure 9.10. Transport of ^{79}Se in a single leg for a δ -function source. The width of the channel is $2B = 0.1 \text{ [m]}$, while the width of the rock layer is $2D$ with $D = 1.2B = 0.06 \text{ [m]}$, compare the dashed line in Figure 9.6b. For more details see text.

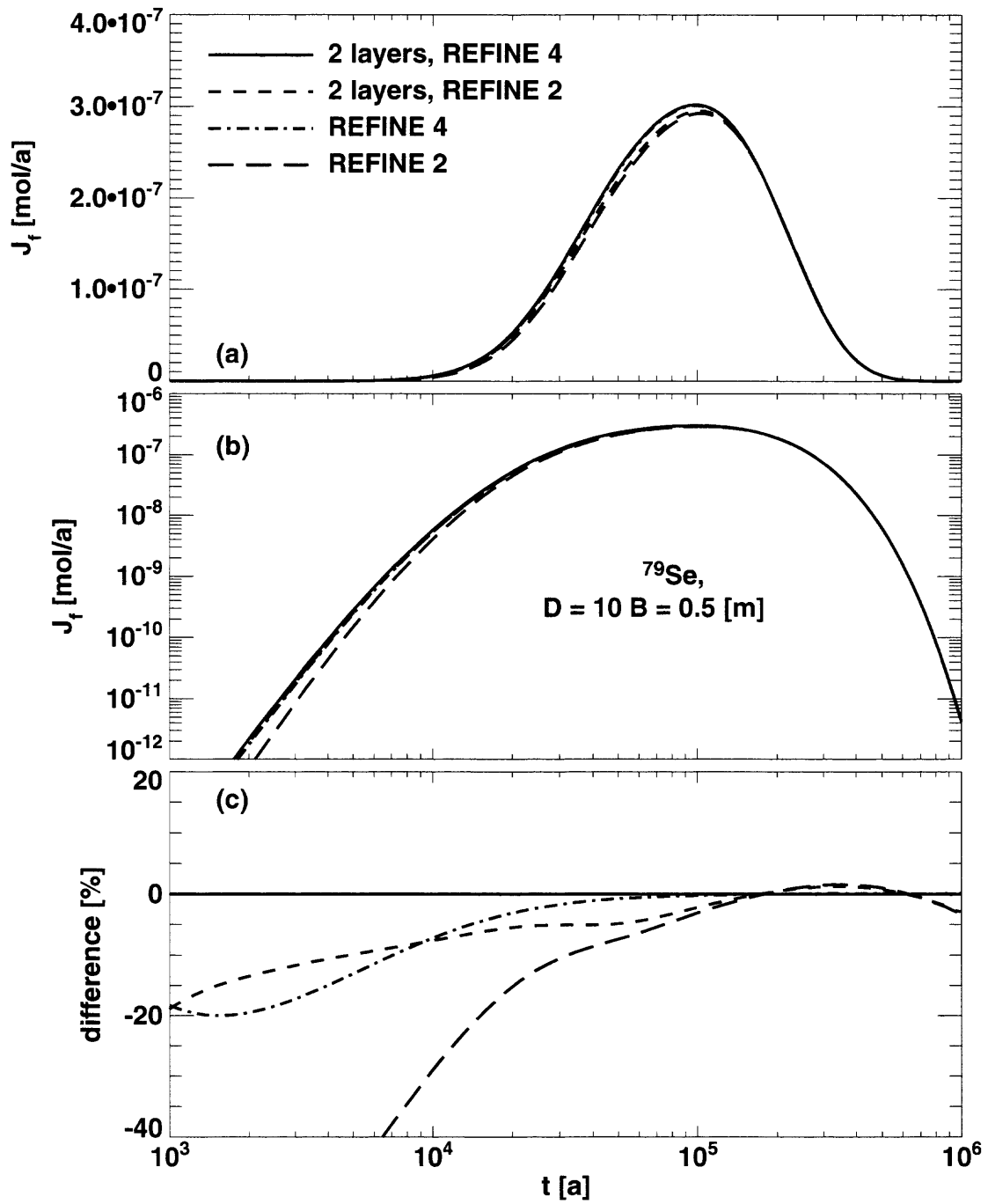


Figure 9.11. Transport of ^{79}Se in a single leg for a δ -function source. The width of the channel is $2B = 0.1$ [m], while the width of the rock layer is $2D$ with $D = 10B = 0.5$ [m], compare the solid line in Figure 9.6b. For more details see text.

For the nuclide ^{99}Tc the relative differences between the PICNIC calculations are larger than for the other two nuclides considered. Therefore we start with tests for the nearly one-dimensional case $D = 1.0002B$ (Figure 9.12); compare the dotted line in Figure 9.4b which is the one-dimensional case. Here we know from section 6.4 that the PICNIC calculation with 2 layers is very close to the 1D-AS result for an analytical solution of the rock matrix response. As expected from the calculation for a constant source (Figures 6.20 and 6.21), the lower resolution results are slightly delayed for early times, show a slight overshooting in the maximum region (or shortly behind the maximum), and decrease slightly earlier for late times. This is also observed in the relative difference functions for the ^{135}Cs and ^{79}Se cases.

For $D = 1.2B$ (Figure 9.13) and $D = 10B$ (Figure 9.14), the relative differences between the different PICNIC calculations increase, while the forms of the relative difference functions are similar, compare dashed line and solid line in Figure 9.4b. This can be understood as a shift of the region of overshooting of the lower resolution calculations to later times, which we have already observed for ^{79}Se . Especially for $D = 10B$ (Figure 9.14c), the overshooting region appears to be shifted to longer times, after the release curve has decreased again. The lower resolution calculations underestimate the release for all times presented, which in turn leads to the overestimation of the geosphere barrier efficiency (Figure 9.5). Especially the nuclide release calculated with the PICNIC standard resolution (long dashes in Figure 9.14) is in the order of 20% below the increased refinement results, even in the maximum region.

Thus, the agreement between the different calculations indicates that PICNIC can also handle this situation, but with different accuracy. The user of PICNIC has to be aware that inaccuracies in the order of 20% are possible for strongly decaying nuclides, also in the maximum region. For some applications, the standard mesh refinement in PICNIC may be not sufficient.

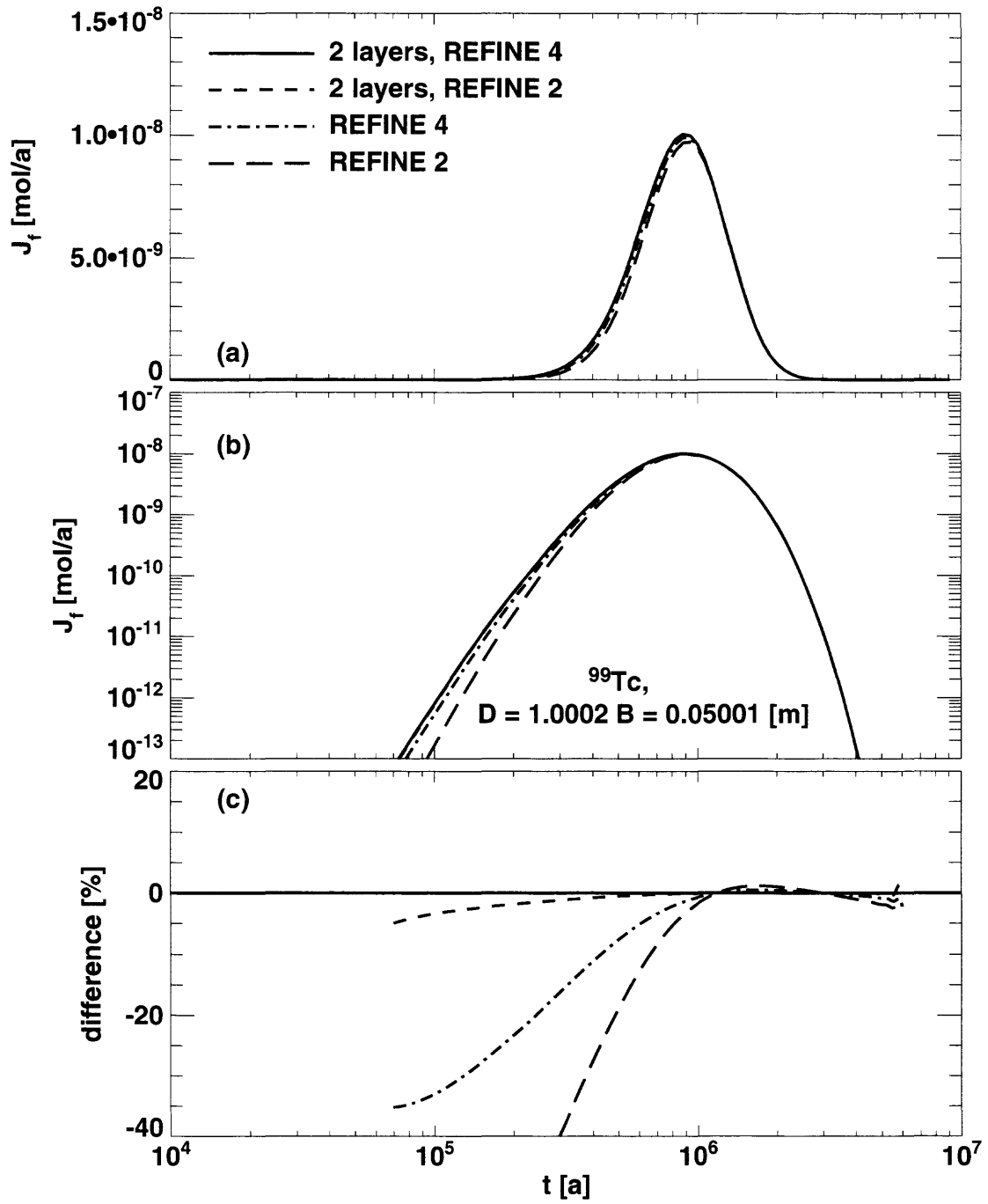


Figure 9.12. Transport of ^{99}Tc in a single leg for a δ -function source. The width of the channel is $2B = 0.1$ [m], while the width of the rock layer is $2D$ with $D = 1.0002 B = 0.05001$ [m], compare the nearly identical dotted line in Figure 9.4b. For more details see text.

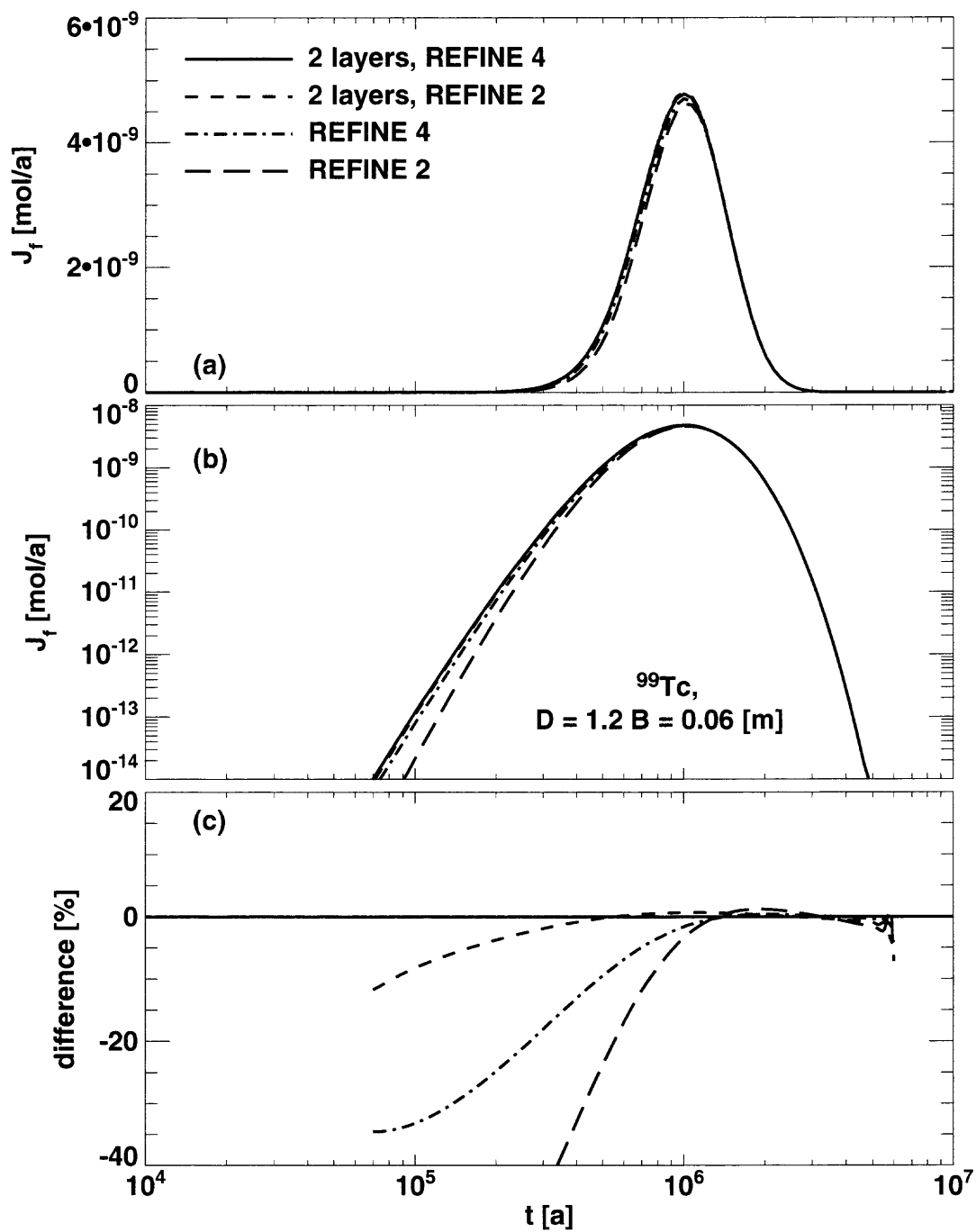


Figure 9.13. Transport of ^{99}Tc in a single leg for a δ -function source. The width of the channel is $2B = 0.1$ [m], while the width of the rock layer is $2D$ with $D = 10B = 0.06$ [m], compare the dashed line in Figure 9.4b. For more details see text.

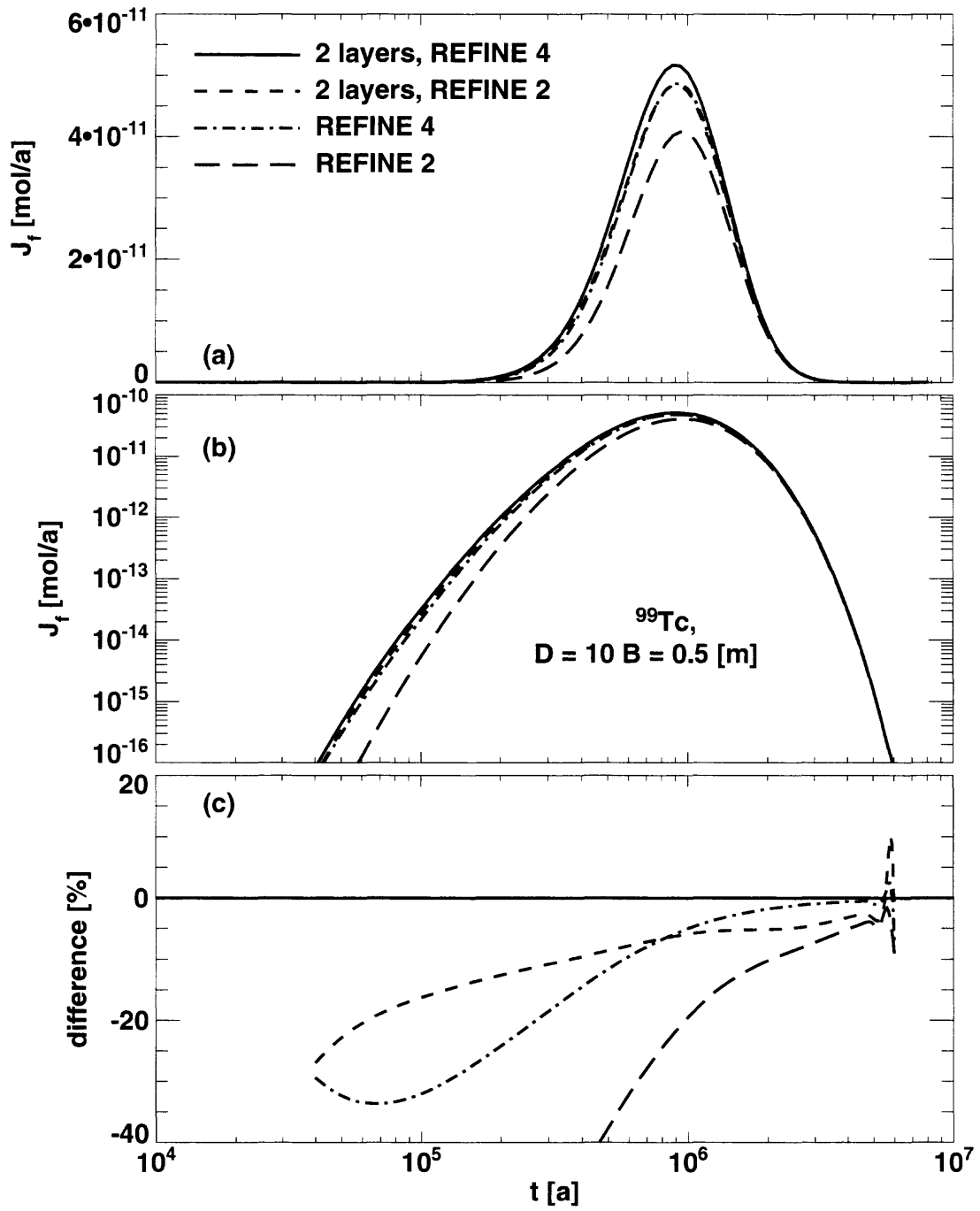


Figure 9.14. Transport of ^{99}Tc in a single leg for a δ -function source. The width of the channel is $2B = 0.1$ [m], while the width of the rock layer is $2D$ with $D = 10B = 0.5$ [m], compare the solid line in Figure 9.6b. For more details see text.

9.1.3. Spot-Check for an Even More Refined Mesh

We briefly discuss now the influence of **different mesh refinements** in the rock matrix. We concentrate on the example of the geosphere barrier efficiency for the transport of ^{99}Tc which shows the largest effects. As a reference we still use the PICNIC calculations for 2 sub-layers and the option REFINE 4. In Figure 9.5 we have considered the PICNIC results where the rock layer was not subdivided and the options REFINE 2 and REFINE 4. Comparing now, in Figure 9.15, the options REFINE 3 (squares) and REFINE 5 (crosses), we find that the agreement with the reference result improves with increasing level of refinement, such that the agreement is best for the option REFINE 5 and is within 4% for all D -values considered.

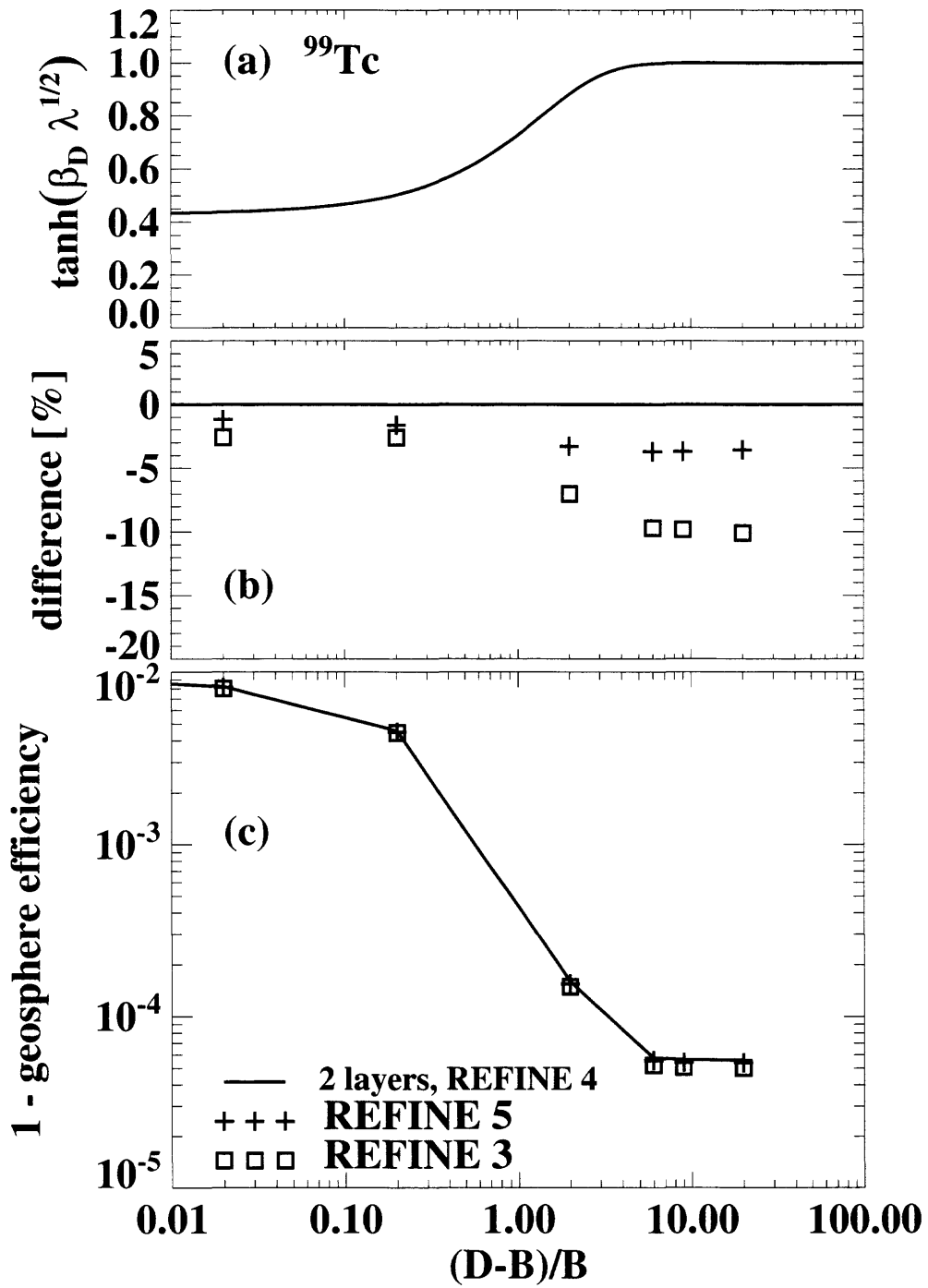


Figure 9.15. Geosphere barrier efficiency for ^{99}Tc as in Figure 9.5. Now, however, the PICNIC results for the options REFINE 3 (squares) and REFINE 5 (crosses) are given.

9.1.4. Vertically Subdivided Rock Matrix

Till now we have analysed the effect of **subdividing the rock matrix layer horizontally**. Now we consider also the effect of **vertically subdividing** the side-columns of the rock matrix in addition to the horizontal subdivision. This means that the side columns of width d_y are vertically subdivided into two columns of widths H_1 and H_2 such that $d_y = H_1 + H_2$, see geometry in Figure 9.16b. Here

$H_1 = \frac{1}{2}d_y$ is chosen for $d_y < 0.02[\text{m}]$ and $H_1 = 0.01[\text{m}]$ is chosen for $d_y \geq 0.02[\text{m}]$. In Figure 9.17 this geometry for the options REFINE 2 (squares) and REFINE 4 (crosses) is considered. As a reference, again the PICNIC calculation for 2 horizontal sub-layers without vertical subdivision (solid line in Figure 9.17c) is used. The effect of the vertical subdivision is only small. Both calculations with the option REFINE 4 agree within 1%. This difference is about 10 times smaller than the difference of the two calculations with the same horizontal and vertical subdivision, but different REFINE level.

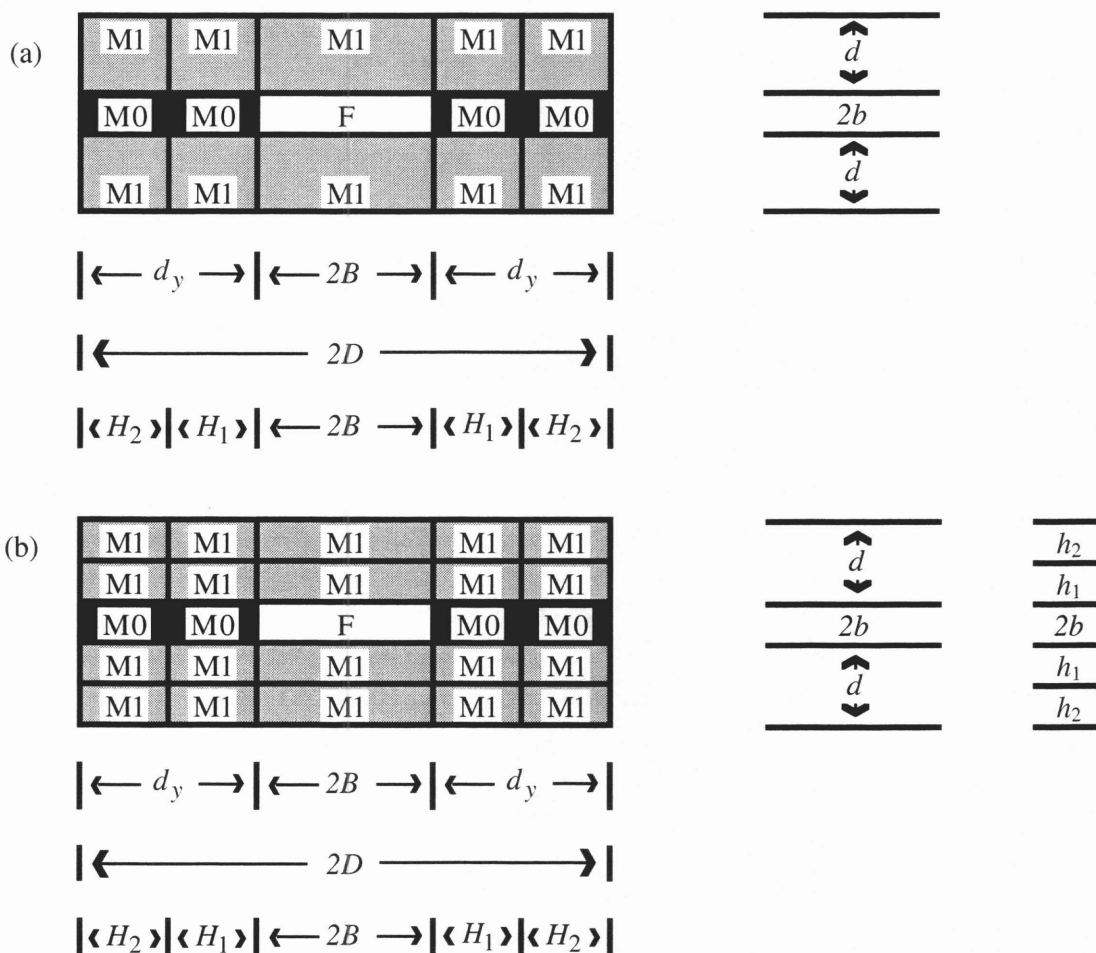


Figure 9.16. Sketch of the cross-section of a leg with the same geometry as in Figure 9.1. Different to Figure 9.1, the side columns of the rock layer of widths d_y each are subdivided into two columns of widths H_1 and H_2 such that $d_y = H_1 + H_2$. In (b), as in Figure 9.1b, the rock matrix layer is also horizontally subdivided into two sub-layers of thicknesses h_1 and h_2 .

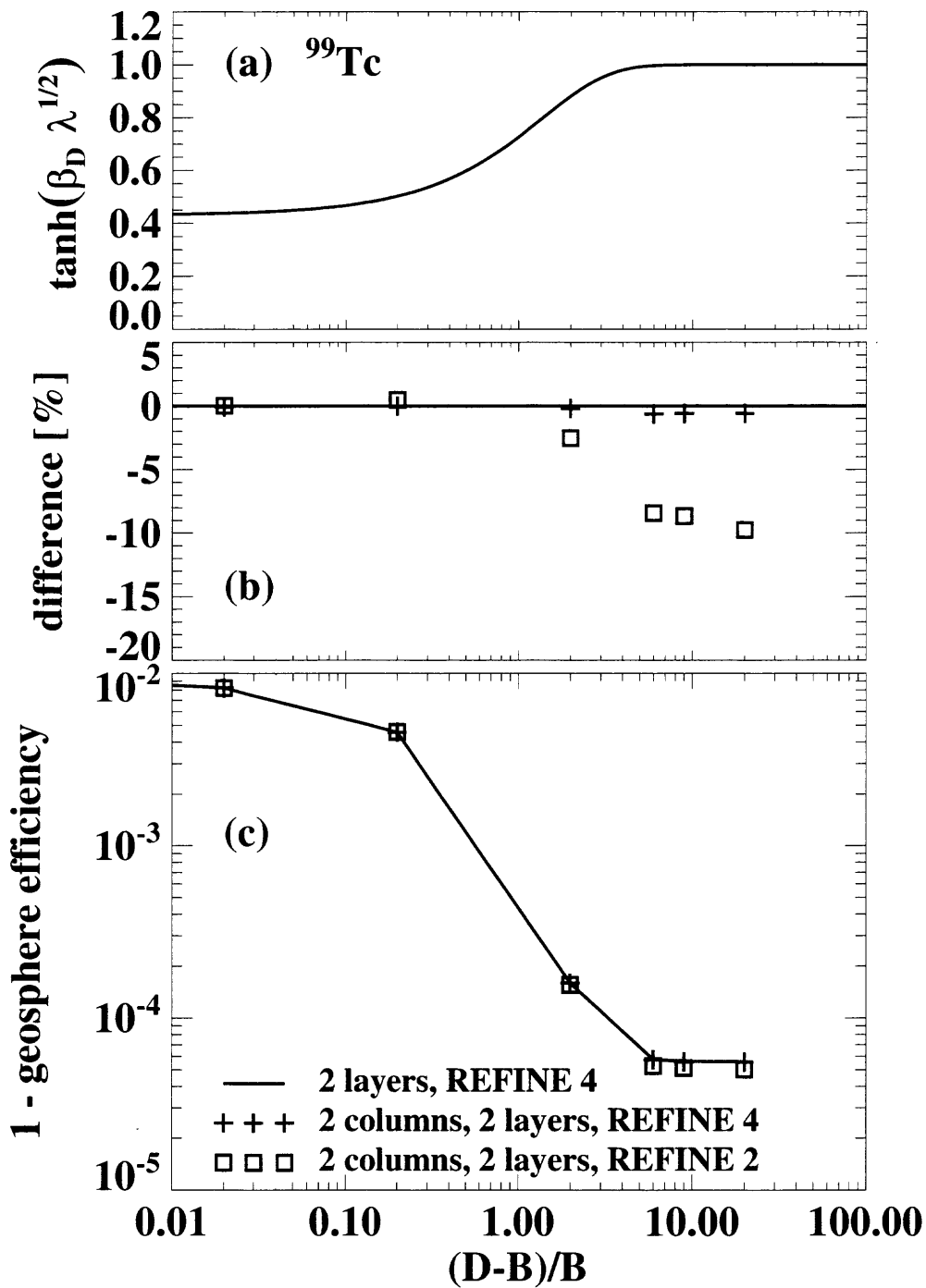


Figure 9.17. Geosphere barrier efficiency for ^{99}Tc as in Figure 9.5. Now, however, the PICNIC results for subdivided rock layers and subdivided side columns of the rock layer are given together with the options REFINE 2 (squares) and REFINE 4 (crosses).

In Figure 9.18, for the option REFINE 5 the cases of a horizontally (crosses) and a vertically and horizontally subdivided rock matrix (squares) are considered. As a reference, again the PICNIC calculation for 2 horizontal sub-layers without vertical subdivision (solid line in Figure 9.18c) is used. The three different calculations considered agree within 1%. Thus, again the effect of the vertical subdivision is only small and is within 0.5%. Also the effect of using the option REFINE 5 is within 1% only, with respect to the option REFINE 4.

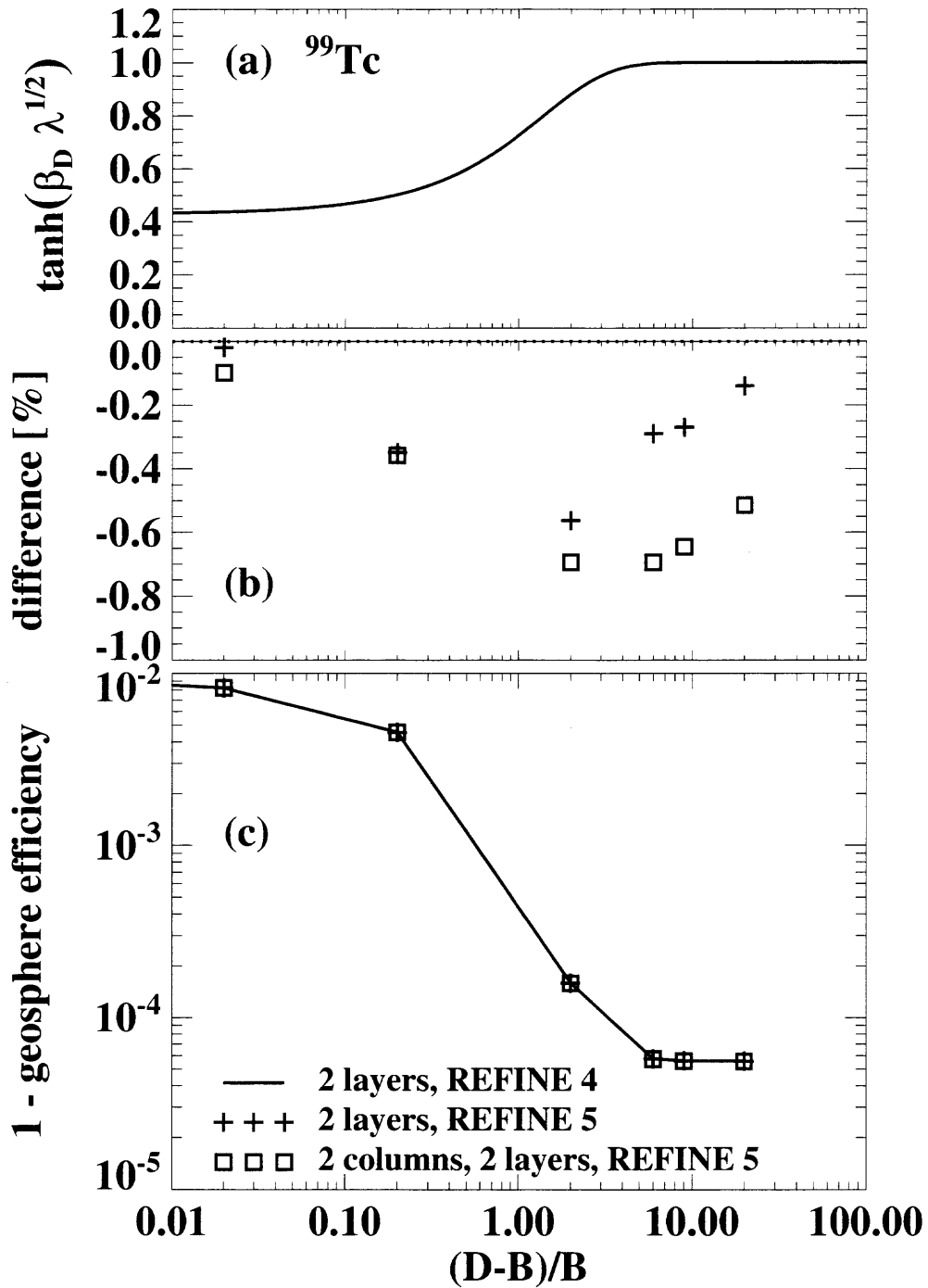


Figure 9.18. Geosphere barrier efficiency for ^{99}Tc as in Figure 9.5. Now, however the PICNIC results for subdivided rock layers and using the option REFINE 5 without (squares) and with subdivided side-columns of the rock layer are given.

9.2. Variations of the Grimsel Dipole Experiment

For the cases related to the Kristallin-I performance assessment, as already mentioned, the base case, $D = B$, behaves like an advection-dispersion system. Now we consider again a case related to the transport of uranine in the Grimsel dipole experiment, which shows the typical behaviour related to matrix diffusion already for one-dimensional geometries, compare sections 4.1 and 4.2. First a **single nuclide**, then a **nuclide decay chain** are considered in a **single leg**.

9.2.1. Single Nuclide

We consider transport in a **single leg** of length $L = 5$ [m] and a δ -function source. Flow block and rock matrix layer have the same properties as in the one-dimensional case. The zero-gradient outlet boundary condition is used. The thickness of the rock layer is $d = 6.2 \cdot 10^{-3}$ [m] and thus the matrix diffusion time is $\beta^2 = 48.7236 \cdot 10^{-3}$ [a]. Different to the Grimsel case, here we assume water flow in channels of width $2B$ in the fracture and the width of the rock matrix available for matrix diffusion is $2D$, see Figure 9.1a. We concentrate on the case that $D = 10B$. To see a strong effect of two-dimensional matrix diffusion, the channel width is assumed to be small compared to the rock matrix layer thickness, $2B = 0.1 \cdot 10^{-3}$ [m]. Thus, diffusion in the rock matrix¹⁰³ across the width of the channel is a fast process, $\beta_B^2 = 3.1688 \cdot 10^{-6}$ [a], while the timescale for diffusion in the y -direction in the rock layer, $\beta_D^2 = 0.31688 \cdot 10^{-3}$ [a], is in the same order of magnitude as the time to maximum release.

For a discretisation test this situation is modelled in four different ways. The release curves for the standard calculation with REFINE 2 (long dashes) and the increased refinement REFINE 4 (dash-dotted lines) are given in Figure 9.19. In further calculations, as depicted in Figure 9.16a, the side columns of widths d_y of the rock matrix are also vertically subdivided into 2 sub-columns of widths H_1 and H_2 such that $d_y = H_1 + H_2$, see geometry in Figure 9.1ab. Here $H_1 = B = 0.05 \cdot 10^{-3}$ [m] and $H_2 = 0.4 \cdot 10^{-3}$ [m] are chosen. The results for the 2 sub-columns case are presented for the options REFINE 2 (short dashes) and REFINE 4 in Figure 9.19. The relative difference functions with respect to the latter are presented in Figure 9.19c.

All release curves have the same form and agree very well with each other. The release curves show no indication of $t^{-3/2}$ behaviour — the release is much more flat. The relative difference functions are largest for early times and in the maximum region. There the results using the option REFINE 2 are about 10% larger than for the increased refinement using the option REFINE 4. This overestimation of the release for early times and in the maximum region is large when compared to the cases considered for one-dimensional matrix diffusion. The vertical subdivision of the side columns has a very small effect within 2% only. The slight oscillations in the relative difference function again are typical for systems where matrix diffusion does not simply act as linear retardation. As usual, the lower resolution results decrease slightly earlier for late times.

¹⁰³ From structural geological investigations, $2B$ is expected to be roughly in the order of 0.1[m] [M. Mazurek, private communication]. For a channel width $2B = 0.1$ [m] with the very large $\beta_B^2 = 3.1688$ [a], however, we found that two-dimensional matrix diffusion, $D > B$, has nearly no effect on the release curves. This might explain the fact that it was sufficient to consider one-dimensional matrix diffusion in the Grimsel experiment.

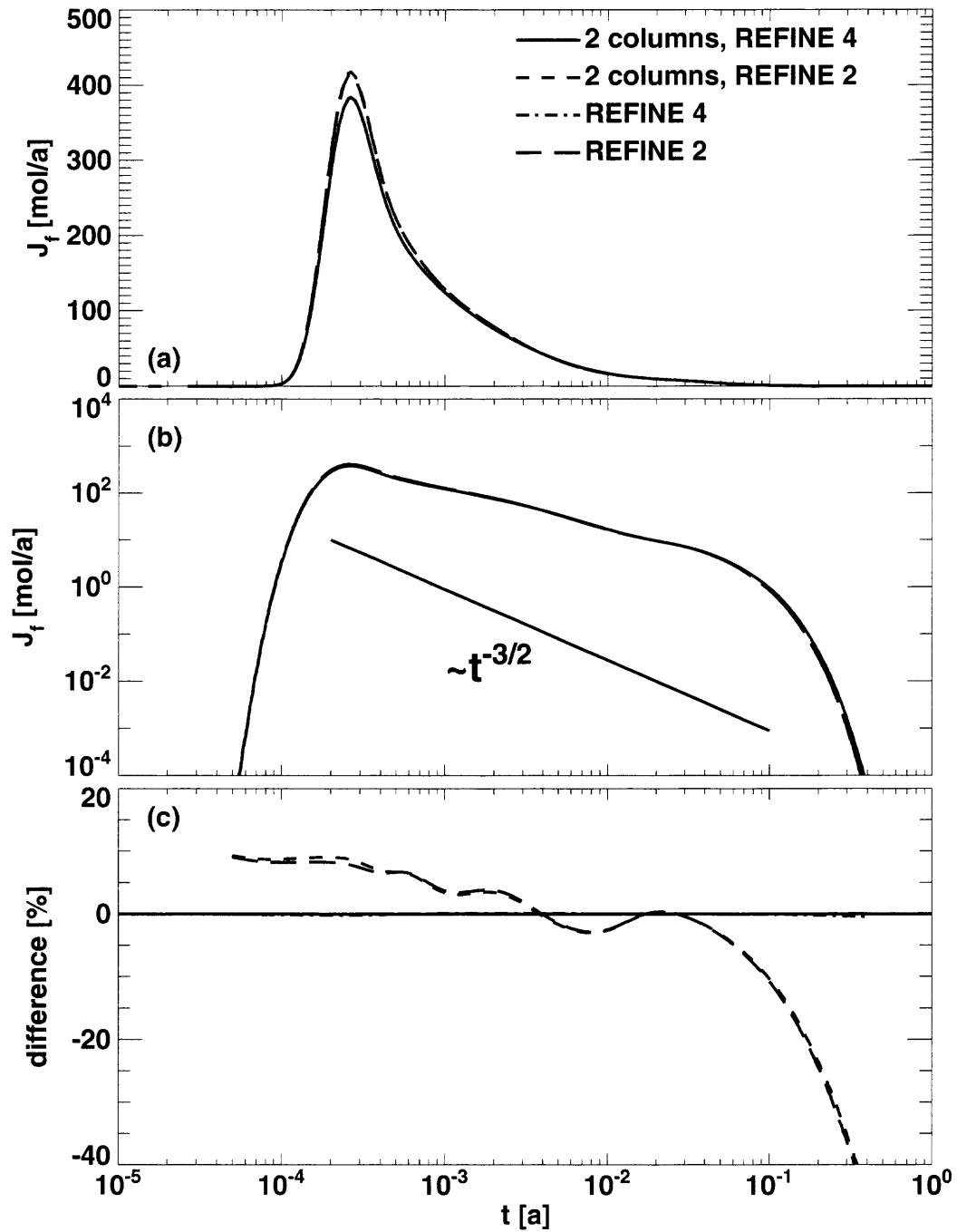


Figure 9.19. Hypothetical variation of the Grimsel dipole experiment using uranium parameters for a homogeneous rock layer available for two-dimensional matrix diffusion. For more details see text.

9.2.2. Nuclide Decay Chain

To test also the accuracy for a **nuclide decay chain** for two-dimensional matrix diffusion into a homogeneous layer, we consider again the nuclide decay chain $\text{ANUC} \rightarrow \text{BNUC} \rightarrow \text{CNUC}$, where the half-life of ANUC is 10^{-3} [a], the half-life of BNUC is 10^{-4} [a] and CNUC is assumed to be stable, compare section 4.2. ANUC, BNUC, and CNUC are assumed to have the same properties as uranine in the rock layer, apart from the retardation factor in the rock matrix. ANUC has the same retardation factor as uranine, $R_p = 1.0$, while BNUC has $R_p = 2.0$ and CNUC has $R_p = 10.0$. Again a δ -function source of the parent ANUC is considered.

The same discretisation tests of PICNIC are performed as for the single nuclide case in Figure 9.19. See Figure 9.20 for ANUC, Figure 9.21 for BNUC and Figure 9.22 for CNUC. All nuclides of the decay chain have in common that the relative difference of the REFINE 2 cases from the REFINE 4 cases is within 10% for all relevant times. Different to the single nuclide case the lower resolution result underestimates the release for early times and at the maximum in the order of 5 to 10%. Again the typical oscillations in the relative difference functions are seen. As for the single nuclide case, the decrease of the CNUC release is slightly later for the lower resolution cases, while the release is earlier for ANUC and BNUC. The vertical subdivision of the side columns again has a very small effect within 2% only.

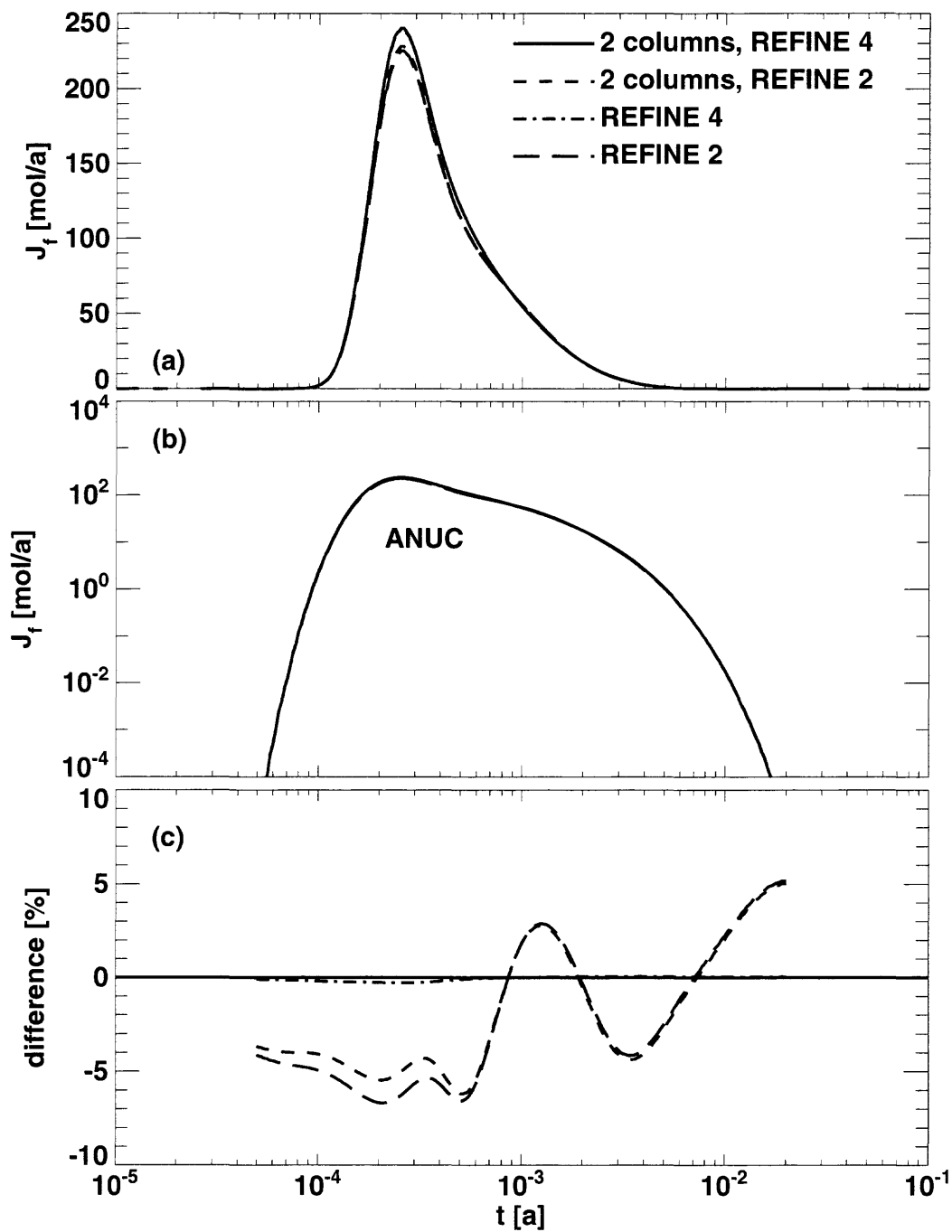


Figure 9.20. Hypothetical variation of the Grimsel dipole experiment for a homogeneous rock layer available for two-dimensional matrix diffusion. Presented is the nuclide ANUC of the decay chain $\text{ANUC} \rightarrow \text{BNUC} \rightarrow \text{CNUC}$. The nomenclature is as in Figure 9.19.

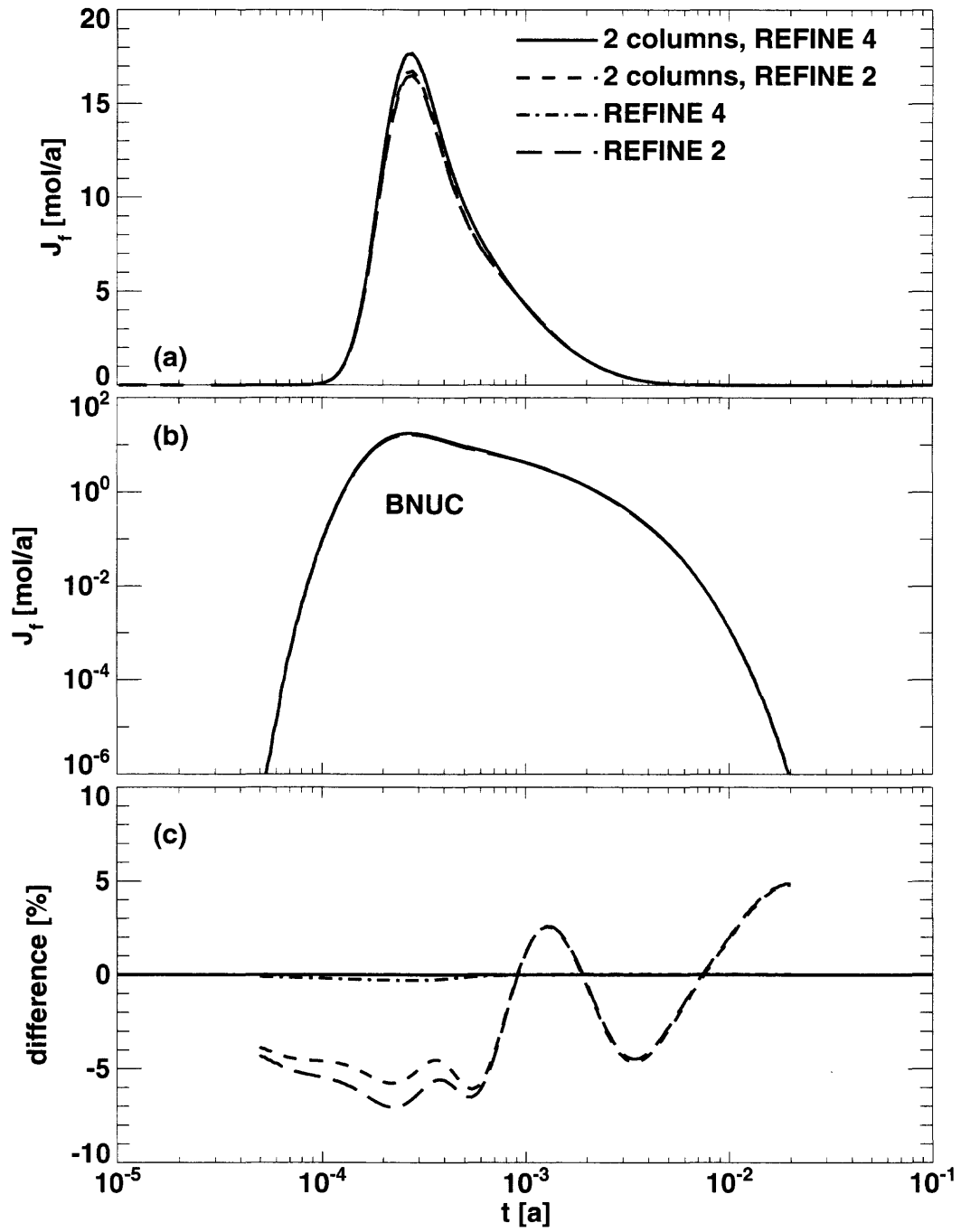


Figure 9.21. Hypothetical variation of the Grimsel dipole experiment for a homogeneous rock layer available for two-dimensional matrix diffusion. Presented is the nuclide BNUC of the decay chain $ANUC \rightarrow BNUC \rightarrow CNUC$. The nomenclature is as in Figure 9.19.

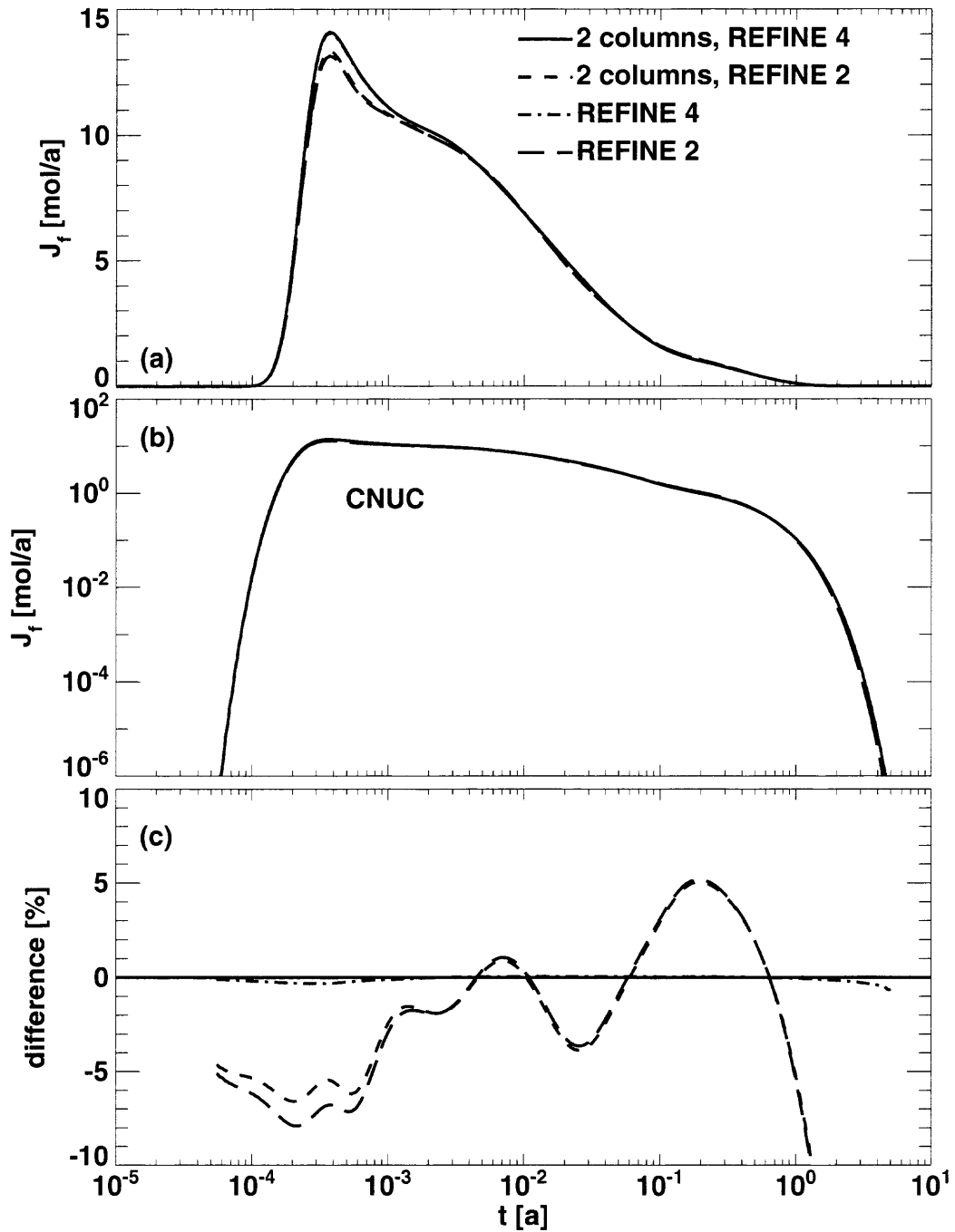


Figure 9.22. Hypothetical variation of the Grimsel dipole experiment for a homogeneous rock layer available for two-dimensional matrix diffusion. Presented is the nuclide CNUC of the decay chain $\text{ANUC} \rightarrow \text{BNUC} \rightarrow \text{CNUC}$. The nomenclature is as in Figure 9.19.

9.2.3. The “Numerical Effect” of Rotating the Rock Matrix

In the next step we consider the numerical effect of **exchanging the x - and y -axes** in the cross-section of a leg. This is analysed for the rock matrix geometry of Figure 9.23a, which is repeated from Figure 9.1a. The three member nuclide decay chain ANUC (Figure 9.24) \rightarrow BNUC (Figure 9.25) \rightarrow CNUC (Figure 9.26) is considered. The release functions for the original geometry of Figure 9.23a using the option REFINE 4 are given as solid lines. The standard resolution result with REFINE 2 is given as short-dashed lines. This is compared to the results for the rotated geometry (Figure 9.23b) with the option REFINE 4 (dash-dotted lines) and REFINE 2 (long-dashed lines). The rotated geometry describes the same physical system considered in another coordinate system and thus should give the same release curves. There are, however, differences generated by the numerical calculations. The differences in the release curves of the rotated variant with respect to the original geometry are within 3% for the REFINE 2 cases and within 3% for the REFINE 4 cases. The relative difference functions are largest for early times and in the maximum region. These differences are due to an x - y asymmetry in the generation of the finite-element mesh for calculation of the Laplace transformed rock matrix response in the applied PICNIC version, leading to different degrees of discretisation in the x - and y -direction.

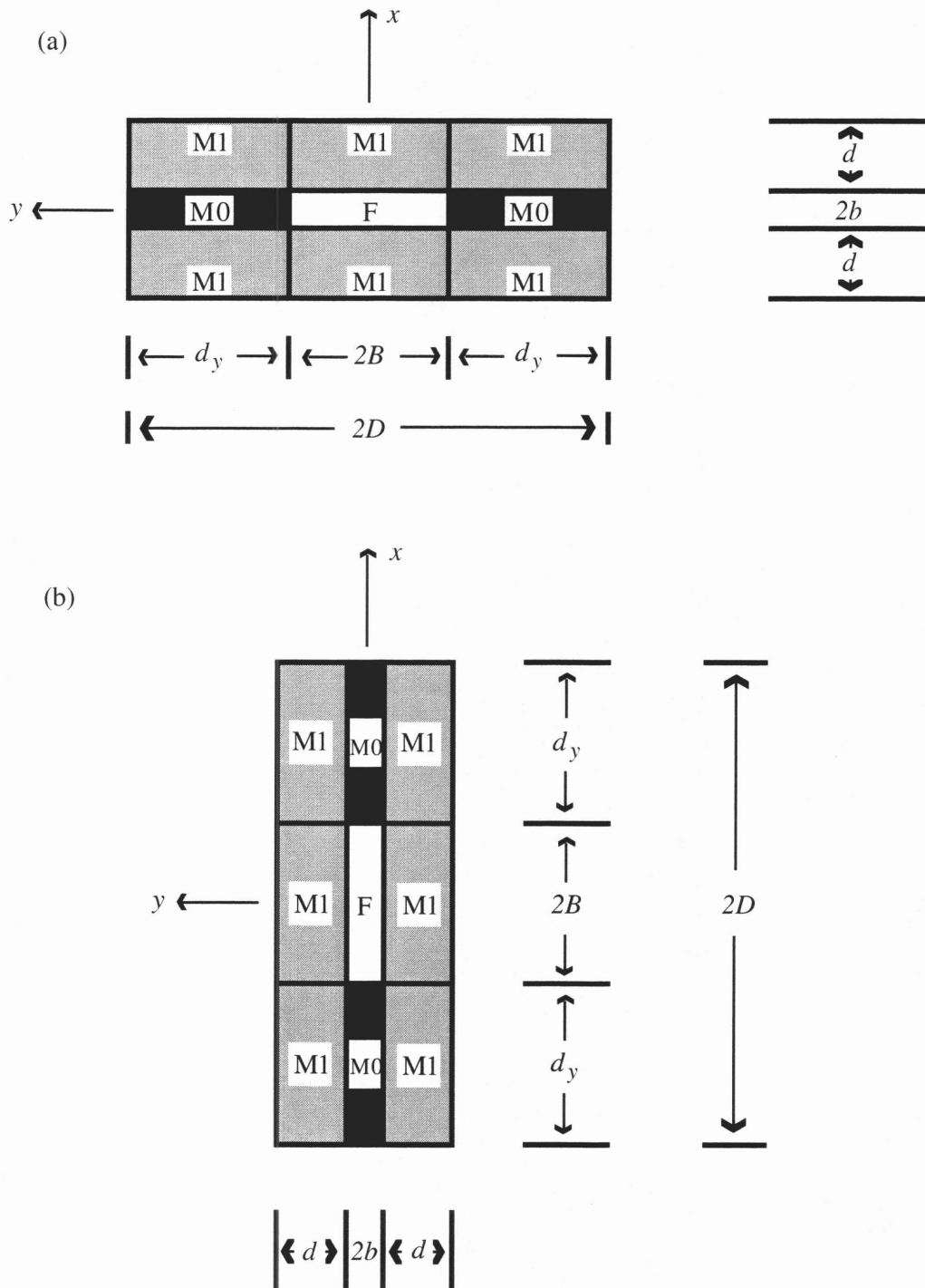


Figure 9.23. (a) Cross-section of the rock matrix geometry as specified in Figure 9.1a. (b) is the rotated version.

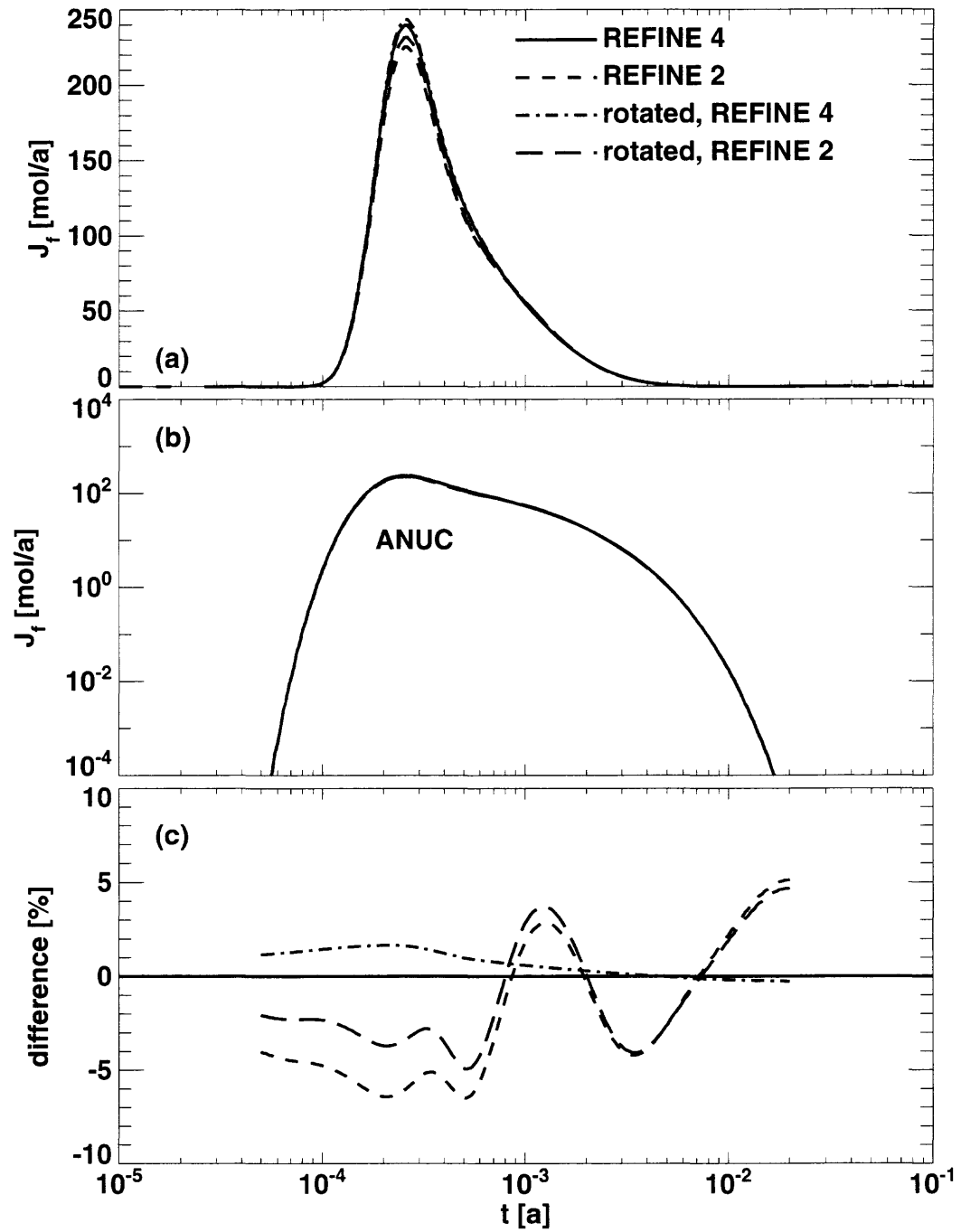


Figure 9.24. Hypothetical variation of the Grimsel dipole experiment using uranium parameters for a homogeneous rock matrix rock layer available for two-dimensional matrix diffusion. Presented is the nuclide ANUC of the decay chain $ANUC \rightarrow BNUC \rightarrow CNUC$. For more details see text.

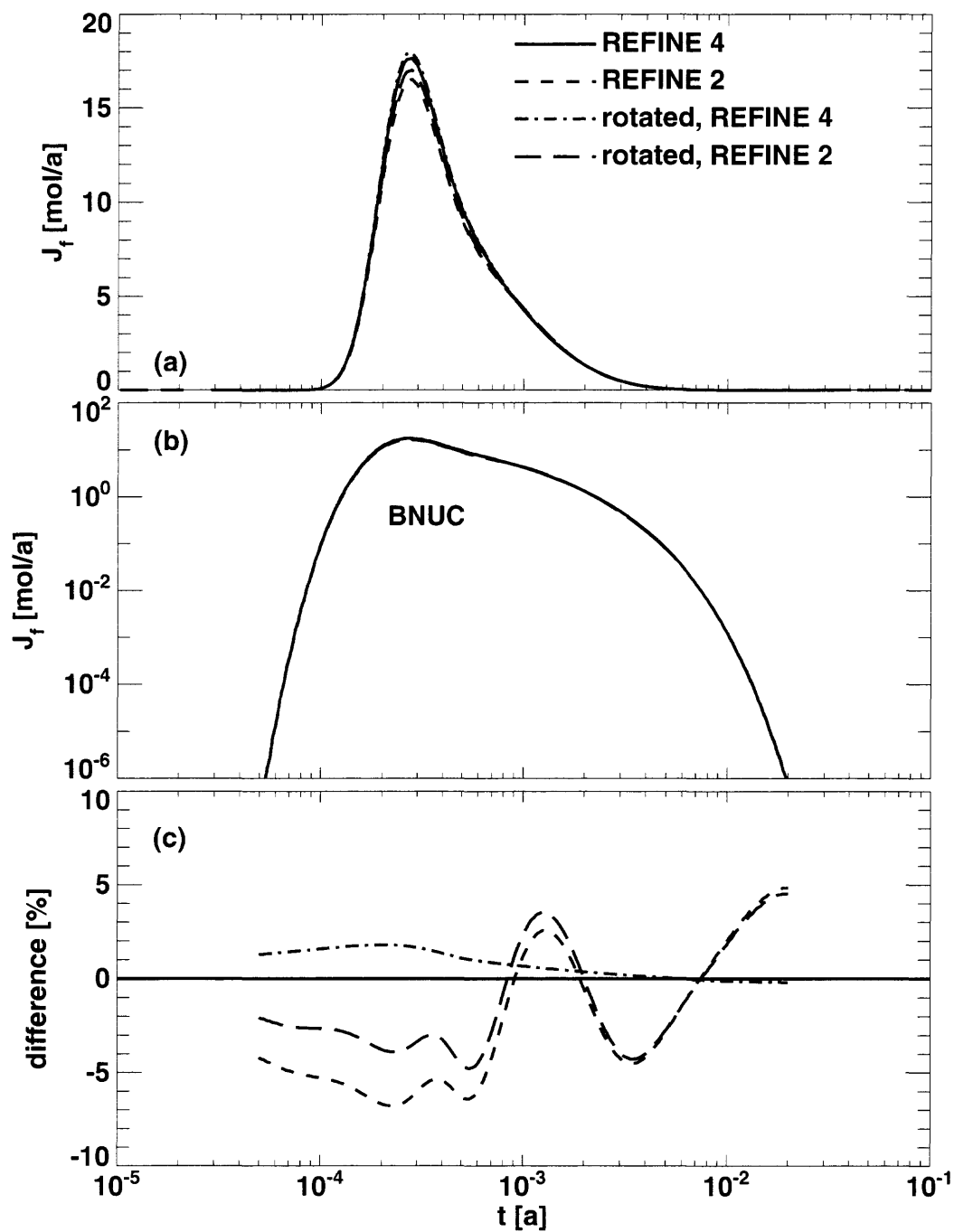


Figure 9.25. Hypothetical variation of the Grimsel dipole experiment using uranium parameters for a homogeneous rock layer available for two-dimensional matrix diffusion. Presented is the nuclide BNUC of the decay chain $ANUC \rightarrow BNUC \rightarrow CNUC$. The nomenclature is as in Figure 9.24.

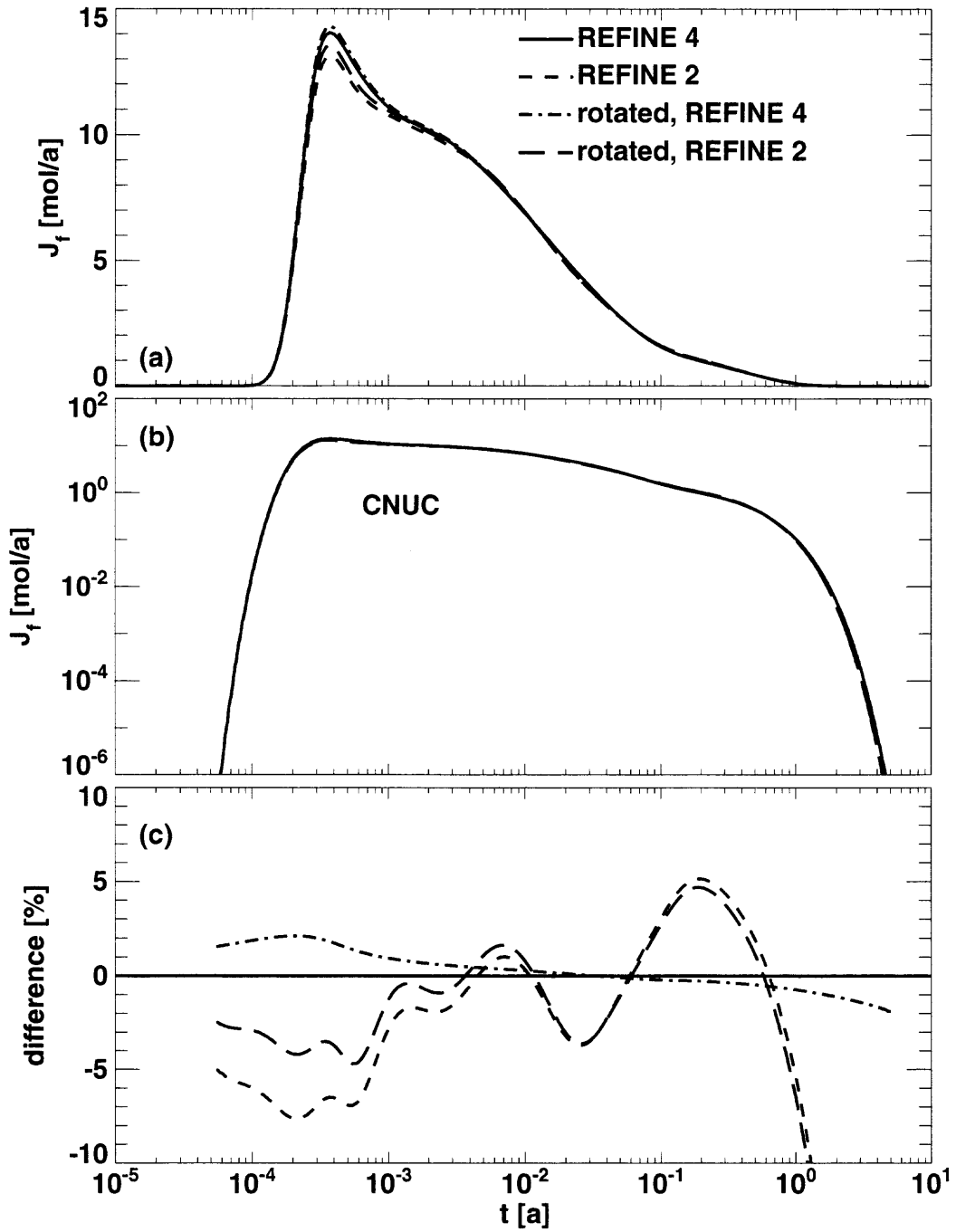


Figure 9.26. Hypothetical variation of the Grimsel dipole experiment using uranine parameters for a homogeneous rock layer available for two-dimensional matrix diffusion. Presented is the nuclide CNUC of the decay chain ANUC \rightarrow BNUC \rightarrow CNUC. The nomenclature is as in Figure 9.24.

9.2.4. The “Numerical Effect” of a Daughter on its Parent

In the next step we compare transport of the non-decaying uranine with the decaying ANUC, which is defined to have the same properties as uranine. Thus, for a δ -function source the release curves of ANUC and uranine are analytically related. The solid lines in Figure 9.27, give as a reference, the release of ANUC calculated from the PICNIC-generated release of uranine using the relation $\mathfrak{R}(t) = e^{-\lambda t} \mathfrak{R}_{\lambda \rightarrow 0}(t)$. The option REFINE 4 is used in all calculations. This is compared to the release of ANUC from the decay chain calculation by PICNIC also using the option REFINE 4, see the dash-dotted lines in Figure 9.27. Theoretically these releases should be exactly the same. However, in the main parts of the release curves the decay chain result is up to 25% below the uranine result (dash-dotted line in Figure 9.27c). The maximum of the relative difference function is close to the time to maximum release. The reason for this relatively large difference is based on the fact that PICNIC uses, for all nuclides in a decay chain, the same finite-element mesh for calculation of the rock matrix response. PICNIC searches for a common optimum of the finite-element mesh for all nuclides of the decay chain.¹⁰⁴ By this numerical effect, the release curve of ANUC does indeed depend on the properties of BNUC and CNUC, which is physically not correct.

This can be seen even more clearly in another calculation when the retardation constants in the rock matrix of BNUC and CNUC are further increased to $R_p^{(\text{BNUC})} = 10$ and $R_p^{(\text{CNUC})} = 100$. The maximum of the relative difference function of the respective release curve for ANUC (long dashes) with respect to the uranine result is now over 30%. Inconveniently, the maximum of the relative difference function is close to the time to maximum release.

Using the same properties (half-lives are still different) for all nuclides of the decay chain, i.e. $R_p^{(\text{BNUC})} = 1$ and $R_p^{(\text{CNUC})} = 1$, the uranine result and the ANUC result (short dashes) almost coincide.

Overall, we note that the accuracy of the PICNIC results for two-dimensional matrix diffusion into a homogeneous rock layer is considerably reduced when compared to cases with one-dimensional matrix diffusion. Thus the respective PICNIC results for two-dimensional rock matrix geometries should be interpreted with care, especially when moving to another parameter region.

¹⁰⁴ Since the retardation constants in the rock matrix are different for the different nuclides, the optimum mesh for ANUC is not the same as for BNUC.

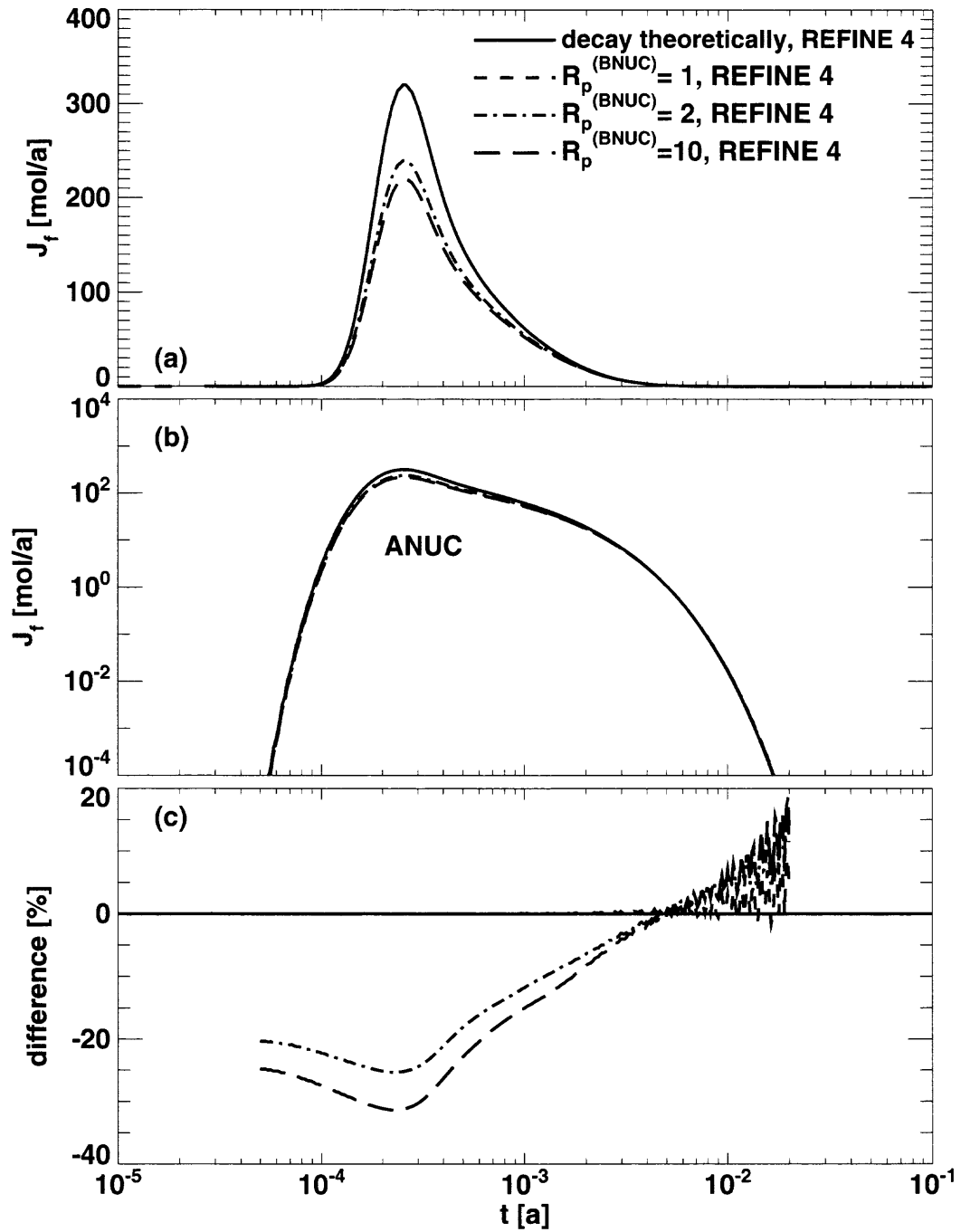


Figure 9.27. Hypothetical variation of the Grimsel dipole experiment using uranium parameters for a homogeneous rock layer available for two-dimensional matrix diffusion. Presented are different PICNIC results for transport of the nuclide ANUC of the decay chain $ANUC \rightarrow BNUC \rightarrow CNUC$. For more details see text.

9.3. Transport in a Network

As the next step we consider transport of a **single nuclide** and a **nuclide decay chain** in a 26-leg **network**. This is a variation of the network with different rock matrices in different legs considered in sections 4.3.3 and 6.6. The same parameters and the top-hat source over $10[a]$ are considered.¹⁰⁵ However the legs 10,11,12 (see Figure 4.22 or 6.28) are now defined in such a way that matrix diffusion is two-dimensional into a homogeneous rock layer as sketched in Figure 9.1a. In these legs $D = 10B = 0.5 [m]$, instead of the one-dimensional geometry ($D = B$) considered in sections 4.3.3 and 6.6.

The release curves for this geometry are depicted in Figure 9.28a,b for standard resolution REFINE 2 (short-dashed lines) and increased refinement REFINE 4 (solid lines). For comparison, the results for the 26-leg network with one-dimensional matrix diffusion are presented also for standard resolution REFINE 2 (long-dashed lines in Figure 9.28a,b) and increased refinement REFINE 4 (dash-dotted lines). The release curves for $D = 10B$ have a similar structure as for $D = B$. See also section 6.6 where different discretisation tests for the 26-leg network with $D = B$ were performed. The main differences are in the peak region, where the two-dimensional matrix diffusion result is in the order of 10% lower than the one-dimensional ($D = B$) result, and the later decrease in the tailing of the two-dimensional ($D = 10B$) result for very long times. The relative difference functions of the REFINE 2 results with respect to the REFINE 4 results given in Figure 9.28c for $D = 10B$ (short-dashed line) and $D = B$ (long-dashed line) also have a similar order of magnitude within 20% and also a similar form. Especially in the maximum region, where the results of the two 26-leg networks differ by about 10%, the magnitudes of the relative differences are very similar and agree within about 2%.

This network is also considered for the nuclides of the **decay chain** ANUC (Figure 9.29) → BNUC (Figure 9.30) → CNUC (Figure 9.31) →, described in section 4.3.3.¹⁰⁶ The same discretisation tests within PICNIC are performed. The main result is that the relative difference functions for the two-dimensional rock matrix ($D = 10B$) in the legs 10, 11,12 stay in the same order of magnitude as for the network with one-dimensional matrix diffusion ($D = B$) in all legs.

¹⁰⁵ We use again 129 points in the Laplace domain.

¹⁰⁶ These nuclides are different to the nuclides considered in section 9.2.

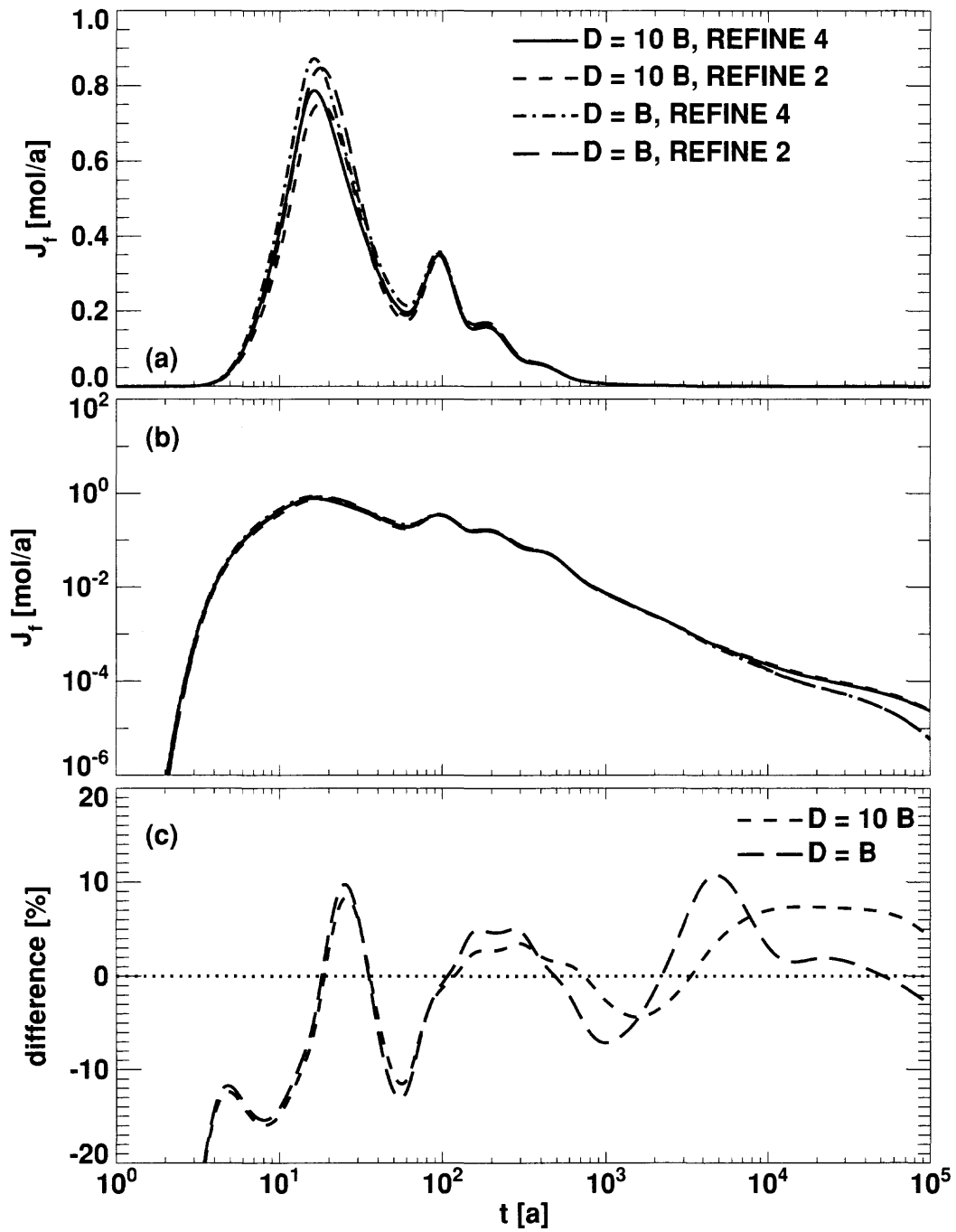


Figure 9.28. Transport of a single nuclide in a 26-leg network where, in three of the legs, two-dimensional matrix diffusion into a homogeneous rock block is considered. For more details see text. In (c) the relative difference functions of the REFINE 2 results with regard to the respective REFINE 4 results are given.

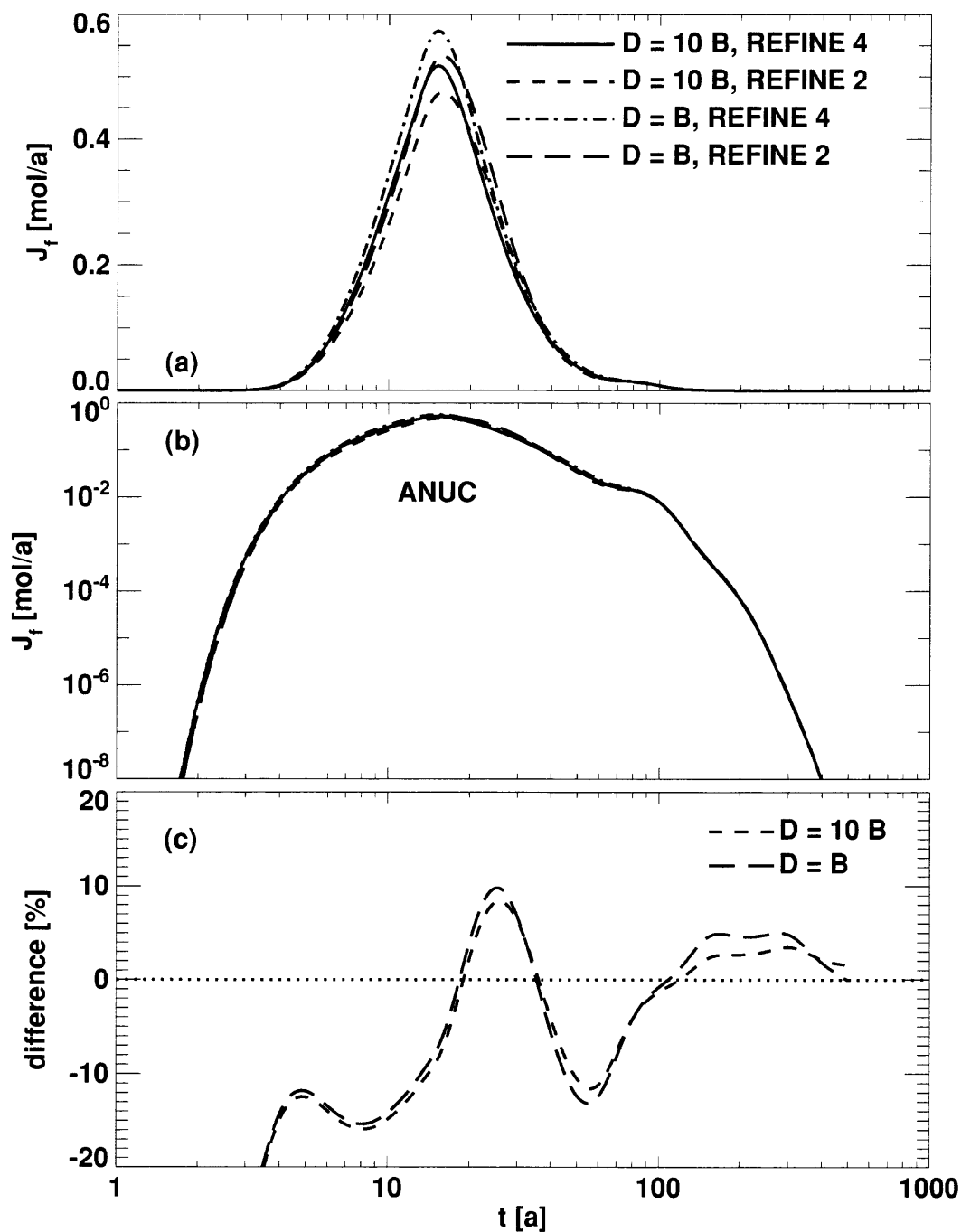


Figure 9.29. Transport in a 26-leg network, where in three of the legs, two-dimensional matrix diffusion into a homogeneous rock block is considered. Presented is the nuclide ANUC of the decay chain $\text{ANUC} \rightarrow \text{BNUC} \rightarrow \text{CNUC} \rightarrow \dots$. In (c) the relative difference functions of the REFINE 2 results with regard to the respective REFINE 4 results are given. The nomenclature is as in Figure 9.28.

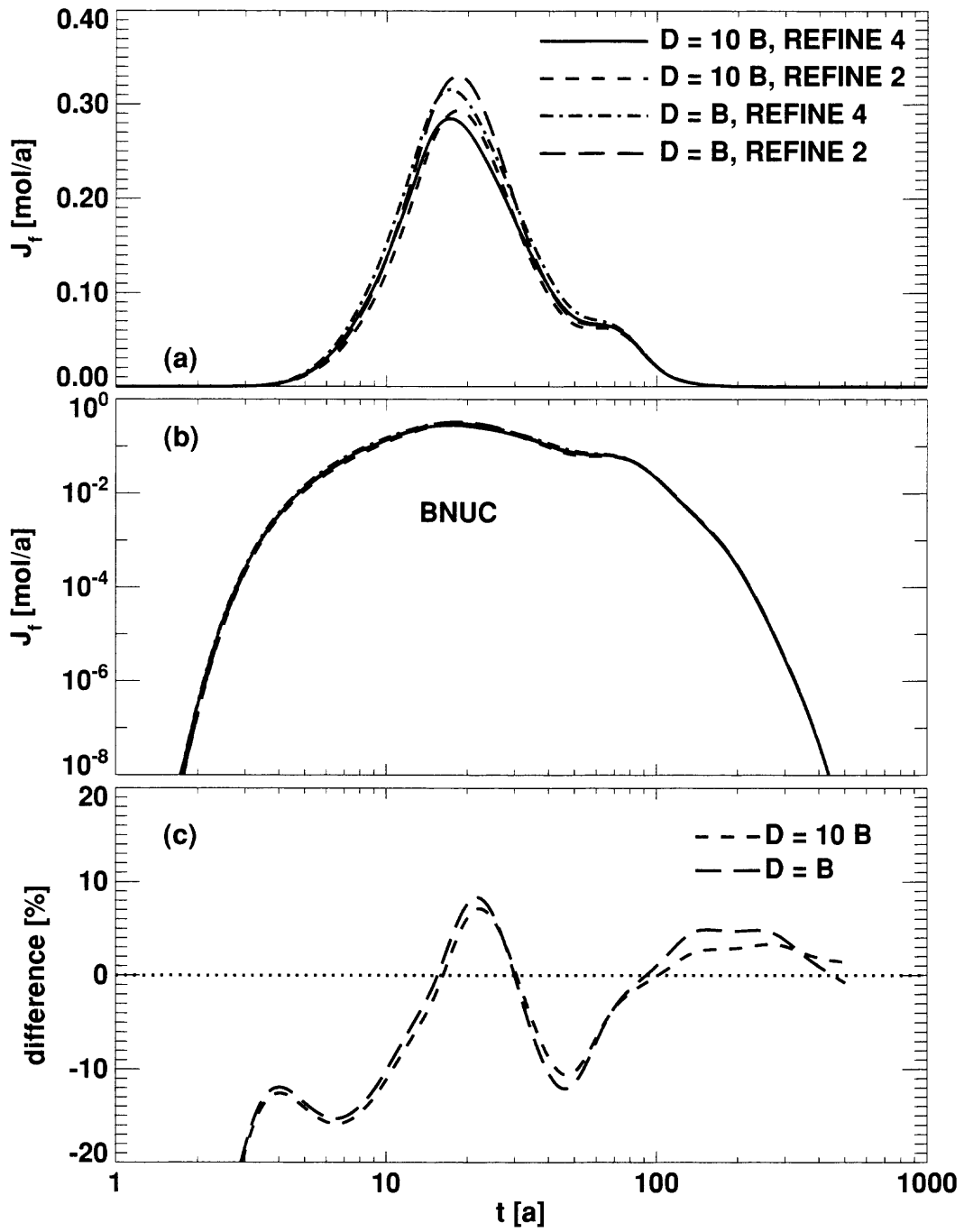


Figure 9.30. Transport in a 26-leg network where, in three of the legs, two-dimensional matrix diffusion into a homogeneous rock block is considered. Presented is the nuclide BNUC of the decay chain $ANUC \rightarrow BNUC \rightarrow CNUC \rightarrow \dots$. In (c) the relative difference functions of the REFINE 2 results with regard to the respective REFINE 4 results are given. The nomenclature is as in Figure 9.28.

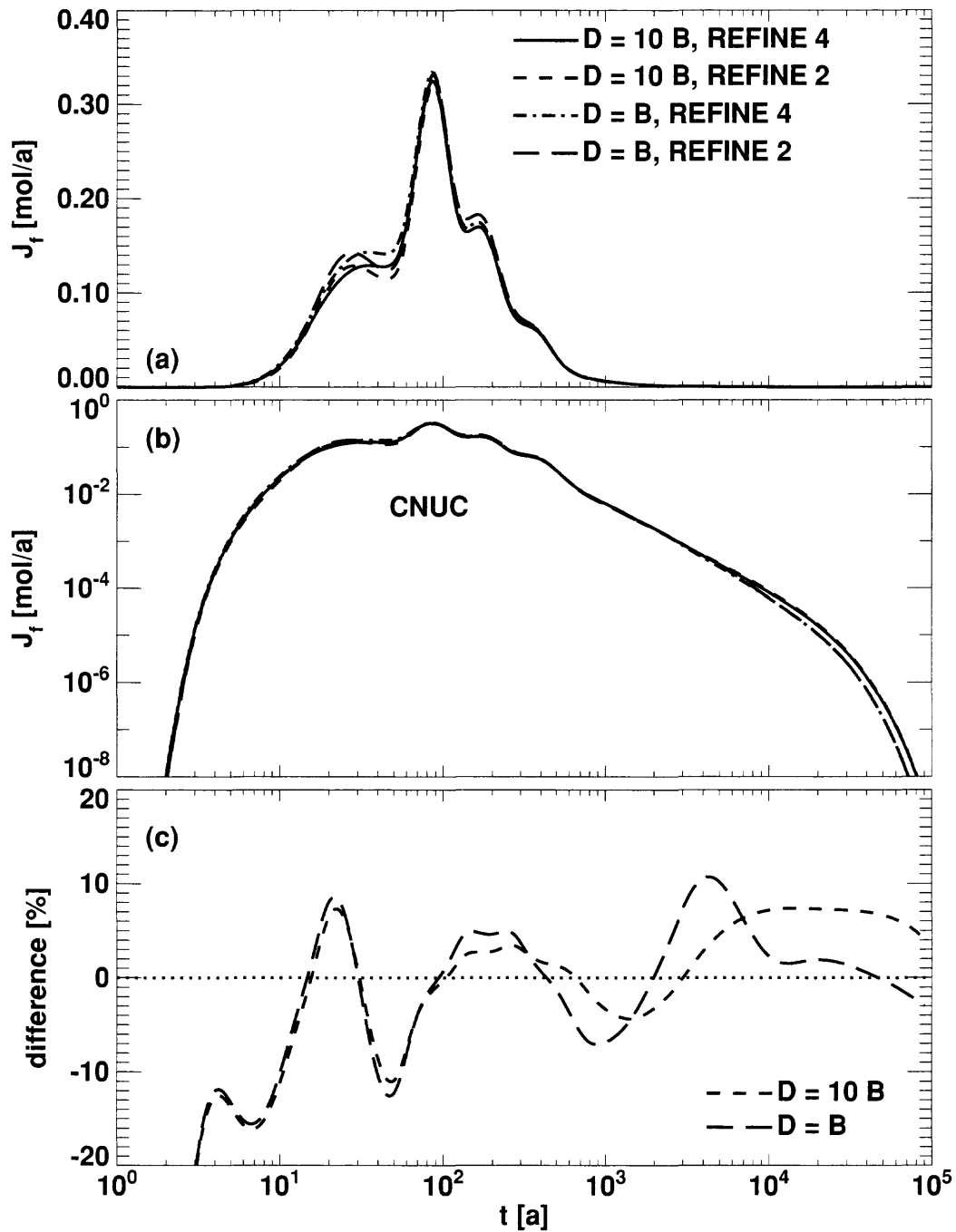


Figure 9.31. Transport in a 26-leg network where, in three of the legs, two-dimensional matrix diffusion into a homogeneous rock block is considered. Presented is the nuclide CNUC of the decay chain $ANUC \rightarrow BNUC \rightarrow CNUC \rightarrow \dots$. In (c) the relative difference functions of the REFINE 2 results with regard to the REFINE 4 results are given. The nomenclature is as in Figure 9.28.

9.4. Summary

In this section, as step VI in the verification scheme, we have verified the capability of PICNIC to deal with two-dimensional matrix diffusion into a homogeneous rock matrix layer; see the detailed verification matrix in Table 7.1. Following the verification strategy in section 3, we have concentrated on single nuclides and nuclide decay chains in single legs.

For two weakly decaying and a strongly decaying single nuclide with Kristallin-I performance assessment parameters, the effect of mesh refinement and subdivision of rock layers was analysed for different widths of the rock layer. To test the full time-dependent behaviour of the nuclide release, no code for inter-comparison was found. However, for the steady-state release for a constant source of one of these nuclides, a comparison with the finite-element code ADINA was possible. A very good agreement was achieved and the differences between the results of both codes further decreased considerably when a refined finite-element mesh was used in the codes. The differences in the steady-state release calculated from PICNIC with different mesh refinements were however somewhat increased when compared to the respective relative difference functions encountered in the previous sections for one-dimensional matrix diffusion. Moreover, the relative differences of the different calculations increased almost monotonically with the width of the rock matrix layer, D , from the nearly one-dimensional case, $D \approx B$ (see also section 6), to the strongly two-dimensional case, $D \gg B$.¹⁰⁷ The lower resolution results slightly underestimate the steady-state nuclide flow rate. This is qualitatively similar to the behaviour for one-dimensional matrix diffusion. The increase of the relative difference functions between different PICNIC calculations was also found consistently for the full time-dependent behaviour of the nuclide release for a δ -function source. Overall, the accuracy for the standard mesh used in PICNIC was estimated to be of acceptable magnitude.

Moving to another parameter region and considering transport of a single nuclide and a nuclide decay chain in a single leg as a hypothetical variation of the Grimsel dipole parameters for uranine, the effects of mesh refinements and of subdividing the rock matrix were considered. Similar to the performance assessment parameters, the agreement of different PICNIC results was very good. Also consistent with the tests with performance assessment parameters, the relative difference functions in discretisation tests increased when compared to the tests for one-dimensional matrix diffusion considered in the previous sections. It must however be stated that PICNIC standard mesh results were found to underestimate the maximum nuclide release in the order of 10%. This accuracy might be too low in some situations with high demands, but should be sufficient in most performance assessment applications. In high-demand situations, a refined finite-element mesh in PICNIC should be used, which can, however considerably increase the calculation times.

In further tests it was found that PICNIC shows a small asymmetry of a few percent in the results, when the two axes in the cross-section of the legs are exchanged.¹⁰⁸ It was also found, in self-consistency tests for nuclide decay chains, that the behaviour of a parent nuclide numerically depends to some degree on the parameters of the daughter, which is physically not correct. The reason behind this is that the same finite-element mesh is used for all nuclides of a decay chain. The

¹⁰⁷ A user of PICNIC must keep this in mind and must balance the accuracy requirements for a specific application with the fact that the calculation time can greatly increase with increased mesh refinement.

¹⁰⁸ In the 1999 version of PICNIC this bug is fixed. In some spot-checks with the new version of the code, the differences to the version used in this report showed up in the same order or smaller than the effect of the asymmetry in this report. In the next section this asymmetry is briefly reconsidered.

PICNIC user must be aware, that in such a situation, the time to the maximum release region appears unfortunately to be the most inaccurate part of the release curve of the parent. The maximum release of the parent was observed to be underestimated in extreme situations in the order of 30%, also for a refined finite-element mesh in PICNIC. This numerical error will be reconsidered by a spot-check in the next section.

The network feature of PICNIC is successfully spot-checked with confirmation runs for a single nuclide and a nuclide decay chain. The agreement between different PICNIC calculations was consistent with the findings discussed above.

Besides the two small inconsistencies mentioned above, we can conclude that the capability of PICNIC is verified as far as is presently possible for this rock matrix geometry. All in all it was verified that the finite-element method for numerical calculation of the rock matrix response also works correctly for two-dimensional matrix diffusion into a homogeneous rock matrix layer. Checks for the mesh refinement and rock matrix subdivision in the finite-element method provided estimates of the accuracy of the embedded finite-element option in PICNIC.

single leg		(a) single nuclide			(b) nuclide decay chain		
two-dimensional matrix diffusion into a homogeneous rock layer		ZG	ZC	AI	ZG	ZC	AI
source in Laplace domain	δ -pulse	R	K, R		K, R		
	simple-leaching						
source in time domain	short pulse						
	long top-hat		R, S ¹⁰⁹				
	band-release						
	general						

pathway		(c) single nuclide			(d) nuclide decay chain		
two-dimensional matrix diffusion into a homogeneous rock layer		ZG	ZC	AI	ZG	ZC	AI
source in Laplace domain	δ -pulse						
	simple-leaching						
source in time domain	short pulse						
	long top-hat						
	band-release						
	general						

network		(e) single nuclide			(f) nuclide decay chain		
two-dimensional matrix diffusion into a homogeneous rock layer		ZG	ZC	AI	ZG	ZC	AI
source in Laplace domain	δ -pulse						
	simple-leaching						
source in time domain	short pulse						
	long top-hat						
	band-release						
	general	R			R		

Table 9.1. Performed calculations for two-dimensional matrix diffusion into the homogeneous rock matrix geometry in Figure 9.1. Note: All test cases represented by empty fields in the scheme were implicitly verified by any of the specified examples. Such a procedure is strongly based on the internal structure of PICNIC as outlined in more detail in section 3. Legend: K: consistency tests; R: “discretisation test” considering different mesh refinements in the “finite-element” results in PICNIC; S: stationary behaviour tested.

¹⁰⁹ Comparison of steady-state release with ADINA result.

10. Two-Dimensional Matrix Diffusion into Heterogeneous Geometries

In this section we consider the effects of two further geometries for **two-dimensional rock matrix diffusion**. This is the last step, VII, of the verification of PICNIC, which completes the verification for two-dimensional matrix diffusion, compare section 3.4.7. Because there is no code available for cross-comparison and there is presently no result available for the steady-state behaviour, the options for verification and the use of the tests are considerably reduced, and we restrict these to self-consistency tests and discretisation tests using Grimsel uranine parameters.

In section 10.1 we consider the transport of a **single nuclide** and a **nuclide decay chain in a single leg** with **two-dimensional matrix diffusion into a two-layer rock matrix**. Again the effects of mesh refinement and rock layer subdivision on the PICNIC results are analysed to obtain indications of the accuracy of the results. This geometry should indicate if there are problems in PICNIC with two-dimensional matrix diffusion at the interface of two different rock matrix areas.

In section 10.2 finally the **two inconsistencies/inaccuracies of the embedded finite-element method** in PICNIC observed in section 9 considering the (x, y) -asymmetry and considering the “numerical effect” of a daughter on its parent are reconsidered for a simple heterogeneous rock matrix geometry for two-dimensional matrix diffusion.

Section 10.3 gives a summary.

10.1. Two-Layer Rock Matrix

In this subsection we consider **two-dimensional diffusion into a two-layer rock matrix geometry** as depicted in Figure 10.1a. There the area of flowing water (F) has aperture $2b$ and is in contact with a layer of rock matrix (M1) of thickness d_1 . After this first rock matrix layer, a second rock matrix layer (M2) of thickness d_2 follows as for the one-dimensional geometry of Figure 7.1 and discussed in section 7.2. It is assumed that flow of water is only within channels of width $2B$ within the fracture, and the channel centres are separated from each other by the distance $2D$. The rest of the fracture is filled with areas of impermeable rock (M0) of width $d_y = D - B$. This is as for the single-layer case depicted in Figure 9.1 and discussed in section 9.2.

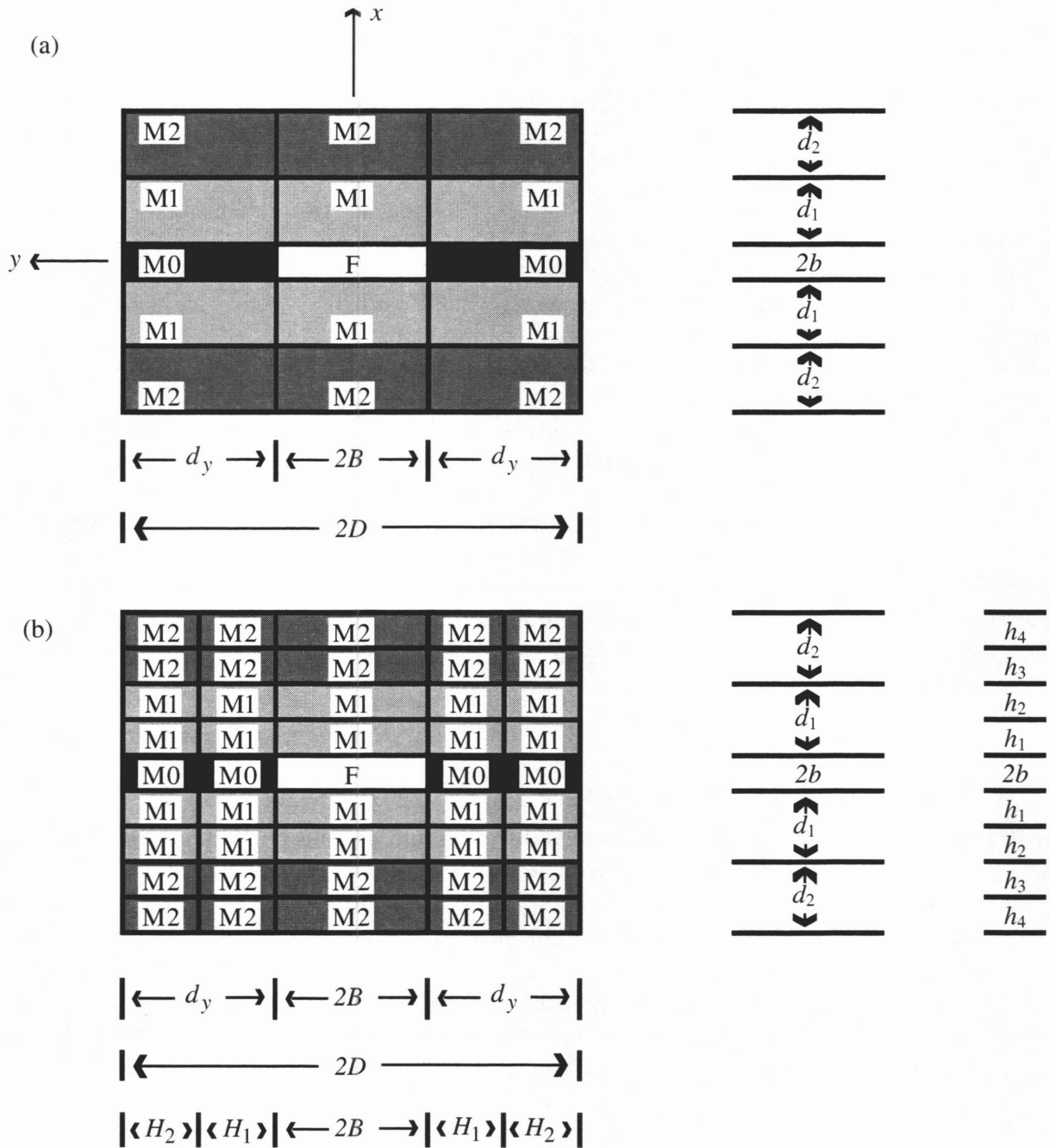


Figure 10.1. (a) Sketch of the cross-section of a leg with a fracture that is filled with an area of flowing water (F) of width $2B$ and the rest of the fracture (to the left and right of the channel with flowing water) is filled with impermeable rock matrix (M0) of width d_y . The sketch is not to scale. The width of the fracture is $2D$ and the aperture is $2b$. Below and above the fracture, a rock matrix layer (M1) is situated. The thickness of the rock layer is d_1 . After the first rock layer, a second rock layer (M2) of thickness d_2 follows. In (a) a two-layer system is considered with rock matrix below and above the fracture and with three columns of widths $d_y, 2B, d_y$. In case (b) the two rock layers below and above the fracture are horizontally subdivided into two sub-layers each, such that $d_1 = h_1 + h_2$ and $d_2 = h_3 + h_4$. Also the two side columns are vertically subdivided into two sub-columns of widths H_1 and H_2 each, such that $d_y = H_1 + H_2$.

10.1.1. Single Nuclide

For this hypothetical variation of the Grimsel uranine case, again a **single nuclide** in a **single leg** of length $L = 5$ [m] and a δ -function source are considered. Flow block and the first rock layer (M1) have the same properties as in the single-layer case. The zero-gradient outlet boundary condition is used. As discussed in section 7.2, the thickness of the first rock layer is reduced by a factor of 6.2 to a value $d_1 = 0.001$ [m], which gives the second rock layer the chance to become important for times which are in the order of $\beta_1^2 = 1.2675 \cdot 10^{-3}$ [a] and greater. The second rock layer is assumed to be half as thick as the first rock layer $d_2 = 0.0005$ [m], but the retardation is assumed to be ten times greater, $R_{p,2} = 10$. Thus $\beta_2^2 = 3.1688 \cdot 10^{-3}$ [a] is now only a factor of 2.5 larger than β_1^2 , which leads to an interplay of the diffusion processes in both layers.

To see a strong effect of two-dimensional matrix diffusion, the channel width, $2B = 0.1 \cdot 10^{-3}$ [m], is assumed to be small with respect to the rock matrix layer thicknesses d_1 and d_2 . We concentrate on the case that $D = 10B$, as in section 9.2. Thus, diffusion in the first rock matrix layer (M1) across the width of the channel is a fast process, $\beta_{1,B}^2 = 3.1688 \cdot 10^{-6}$ [a], while the timescale for diffusion in the y -direction in this rock layer, $\beta_{1,D}^2 = 0.31688 \cdot 10^{-3}$ [a], is about four times smaller than diffusion over the rock layer thickness. The timescales for diffusion in y -direction in the second rock layer are ten times larger; thus $\beta_{2,B}^2 = 31.688 \cdot 10^{-6}$ [a] is still small, but $\beta_{2,D}^2 = 3.1688 \cdot 10^{-3}$ [a] is in the same order of magnitude as the timescales for diffusion in the x -direction.

The breakthrough curves are given in Figure 10.2. For this two-dimensional geometry, the time to maximum release is slightly earlier with respect to the one-dimensional case in Figure 7.20, but the maximum value is reduced by a factor of about five.¹¹⁰ The hump in the release curve for longer times is much bigger than observed earlier for one-dimensional matrix diffusion, i.e. consider that the hump is also clearly visible in the linear scale for the nuclide flow rate in Figure 10.2a. For discretisation tests, this situation is calculated in four different ways. The release curves for the standard mesh with REFINE 2 (long dashes in Figure 10.2) and the refined mesh using REFINE 4 (dash-dotted lines) are calculated. In other calculations, the rock matrix layers are each horizontally subdivided into two sub-layers of thickness $h_1 = h_2 = \frac{1}{2}d_1$ and $h_3 = h_4 = \frac{1}{2}d_2$, see Figure 10.1b. The side columns of the rock matrix of width d_y are also vertically subdivided into 2 sub-columns of widths H_1 and H_2 , such that $d_y = H_1 + H_2$. Here $H_1 = B = 0.05 \cdot 10^{-3}$ [m] and $H_2 = 0.4 \cdot 10^{-3}$ [m] are chosen as for the homogeneous rock layer considered in section 9.2. The results for the 2+2 sub-layers and the 2 side columns are presented for the options REFINE 2 (short dashes in Figure 10.2) and REFINE 4 (which is expected to give the best result, solid line). Again the relative difference functions with respect to the latter are presented in Figure 10.2c.

¹¹⁰ There might be algebraic behaviour of the breakthrough curve in the range of time $0.4 \cdot 10^{-3}$ [a] $< t < 3 \cdot 10^{-3}$ [a], but from this brief inspection it is not clear if it is a $t^{-3/2}$ behaviour, indicative of unlimited one-dimensional matrix diffusion into a planar rock matrix geometry.

All release curves have the same structure and agree very well with each other. The effect of the subdivision of the rock matrix is only moderate. The standard REFINE 2 result is somewhat earlier for early times and late times. Also the maximum is about 10% higher than for the REFINE 4 results. Note that relative difference functions of similar form and also of this order of magnitude were also encountered for the case of two-dimensional matrix diffusion into a homogeneous rock matrix layer.

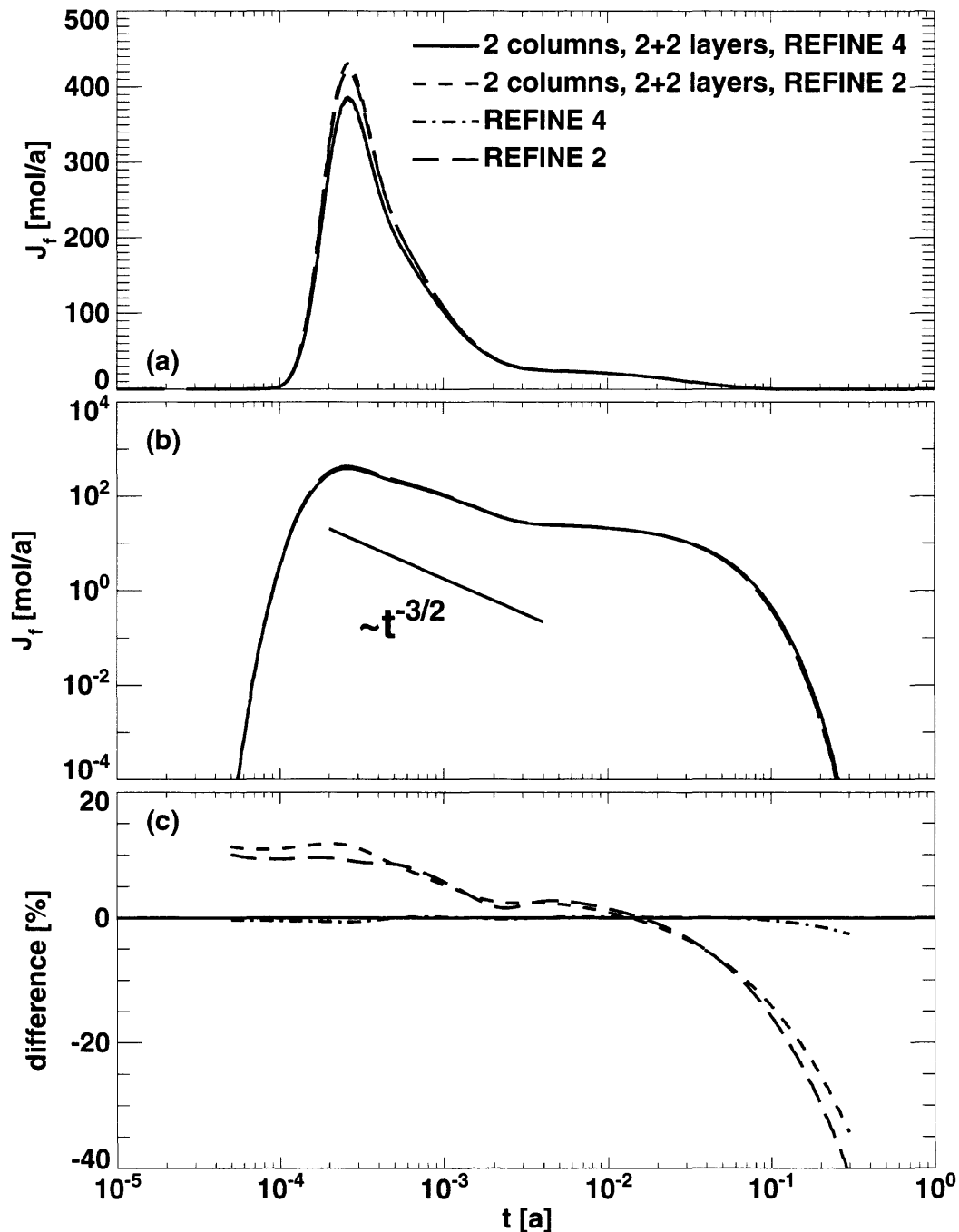


Figure 10.2. Hypothetical variation of the Grimsel dipole experiment for a two-layer rock matrix available for two-dimensional matrix diffusion. In (a) and (b) the breakthrough curves are plotted for two different subdivisions and two different discretisations as indicated in the legend. In (c) the relative difference functions of the results with respect to the calculations with two columns, 2+2 sub-layers and REFINE 4 are shown.

10.1.2. Nuclide Decay Chain

To test also the accuracy for a **nuclide decay chain** for **two-dimensional matrix diffusion into a two-layer rock matrix**, we consider again the nuclide decay chain $\text{ANUC} \rightarrow \text{BNUC} \rightarrow \text{CNUC}$, where the half-life of ANUC is 10^{-3} [a], the half-life of BNUC is 10^{-4} [a] and CNUC is assumed to be stable, compare sections 4.2, 7.22 and 9.2.2. ANUC, BNUC, and CNUC are assumed to have the same transport properties as uranine in the rock layer, apart from the retardation factor in the rock matrix layer of type M1. ANUC has the same retardation factor as uranine, $R_p = 1.0$, while BNUC has $R_p = 2.0$ and CNUC has $R_p = 10.0$. The retardation constants in the rock matrix of type M2 are again ten times higher for each nuclide. Again a δ -function source of the parent ANUC is considered and the zero-gradient boundary condition.

The same discretisation tests of PICNIC are performed as for the single nuclide case in Figure 10.2. See Figure 10.3 for the nuclide release of ANUC, Figure 10.4 for BNUC and Figure 10.5 for CNUC. All nuclides of the decay chain have in common that the relative difference functions of the REFINE 2 cases with respect to the REFINE 4 cases lie within 10% for all relevant times. Different to the single nuclide case, the lower resolution results (REFINE 2) underestimate the release for early times and at the maximum nuclide release in the order of 5 to 10%. Again the typical oscillations in the relative difference functions are seen. As for the single nuclide case, the decrease in the CNUC release is slightly later for the lower resolution cases, while for ANUC and BNUC the release is earlier. The vertical subdivision of the side columns again has a rather small effect within 2 to 3% only. This description of the relative difference functions is almost a duplicate of the case of two-dimensional matrix diffusion into a homogeneous rock layer. Thus we can infer that the second rock layer does not lead to increased inconsistencies between the different PICNIC calculations.

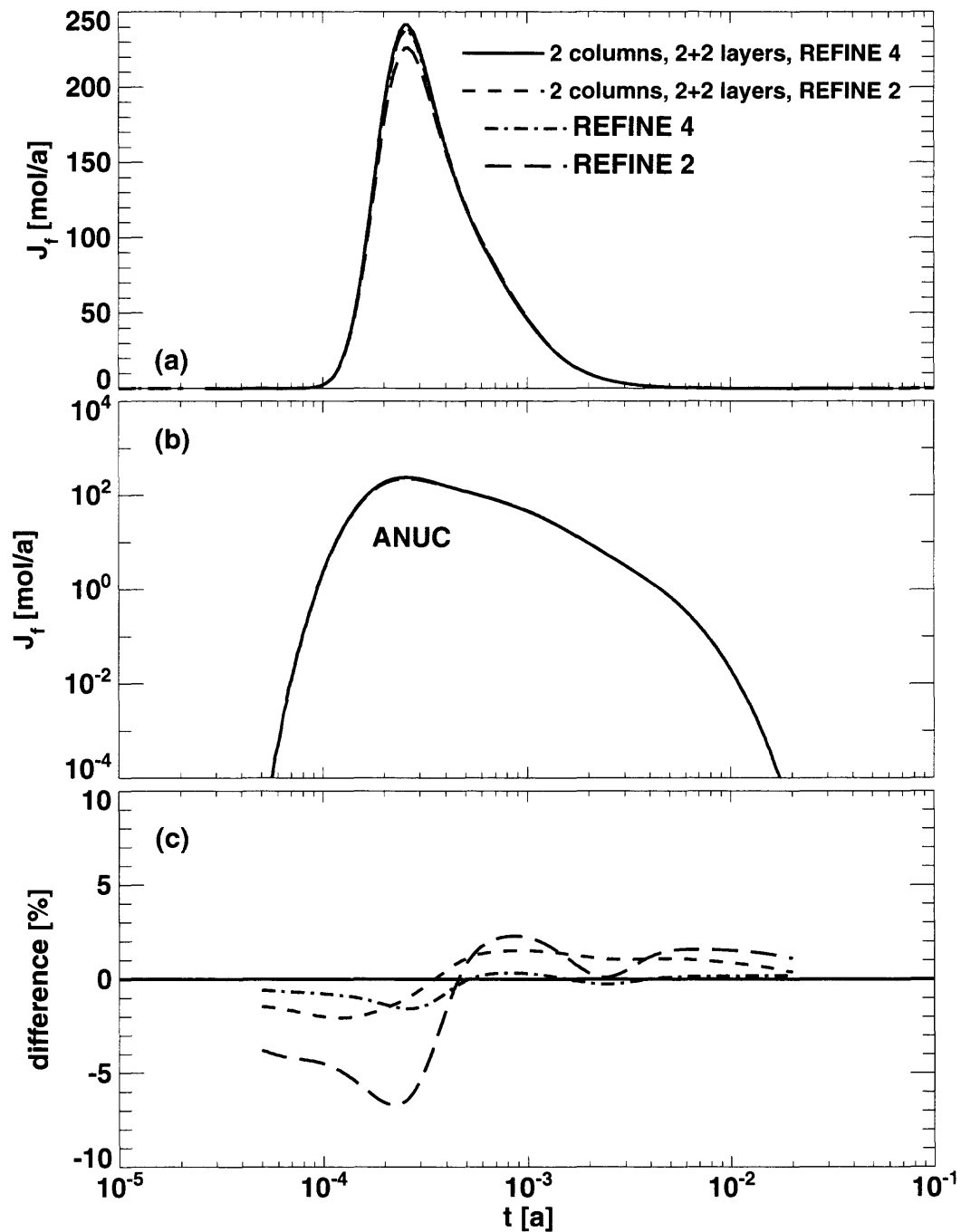


Figure 10.3. Hypothetical variation of the Grimsel dipole experiment for a two-layer rock matrix available for two-dimensional matrix diffusion. Presented is the nuclide ANUC of the decay chain $ANUC \rightarrow BNUC \rightarrow CNUC$. The nomenclature is as in Figure 10.2. For more details see text.

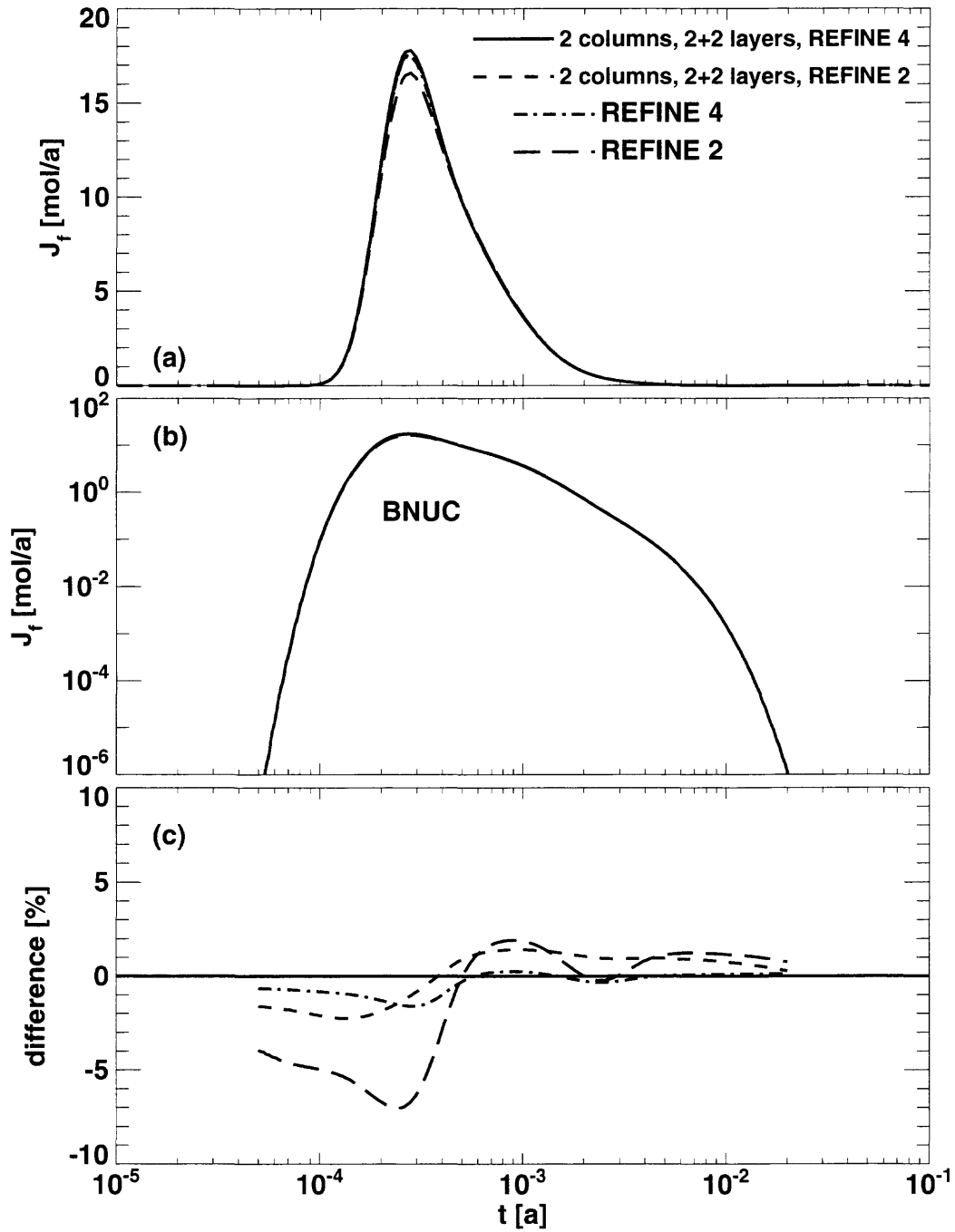


Figure 10.4. Hypothetical variation of the Grimsel dipole experiment for a two-layer rock matrix available for two-dimensional matrix diffusion. Presented is the nuclide BNUC of the decay chain $\text{ANUC} \rightarrow \text{BNUC} \rightarrow \text{CNUC}$. For more details see text.

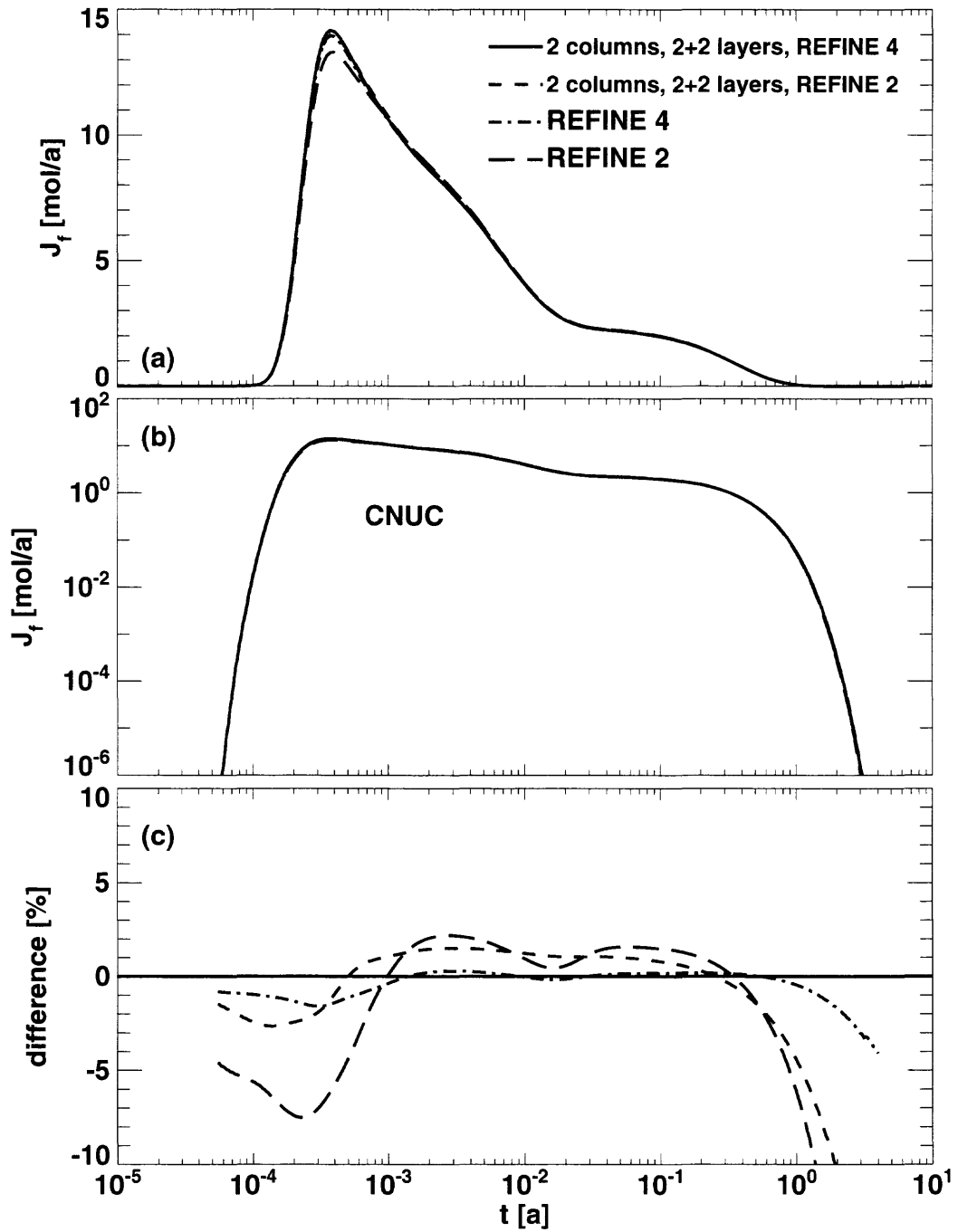


Figure 10.5. Hypothetical variation of the Grimsel dipole experiment for a two-layer rock matrix available for two-dimensional matrix diffusion. Presented is the nuclide CNUC of the decay chain ANUC \rightarrow BNUC \rightarrow CNUC. The nomenclature is as in Figure 10.2. For more details see text.

10.2. Rock Matrix within the Fracture

We end our investigations with a case of a rock matrix geometry which is very similar to the geometry considered in Figure 9.1a. The area of flowing water (F) with aperture $2b$ is in contact with a rock matrix of type M1 and thickness d , see Figure 10.6a. Also the flow of water is only within channels of width $2B$ within the fracture, and the channel centres are separated from each other by the distance $2D$. The rest of the fracture is filled with areas of impermeable rock (M0) of width $d_y = D - B$. Here we concentrate again on the case that $D = 10B$. Now, however it is assumed that the rest of the fracture of widths $d_y = D - B$ is filled with a rock matrix of type (M2) and is accessible for matrix diffusion. Matrix diffusion in the two rock types is not independent, because the two rock types are in contact with each other.

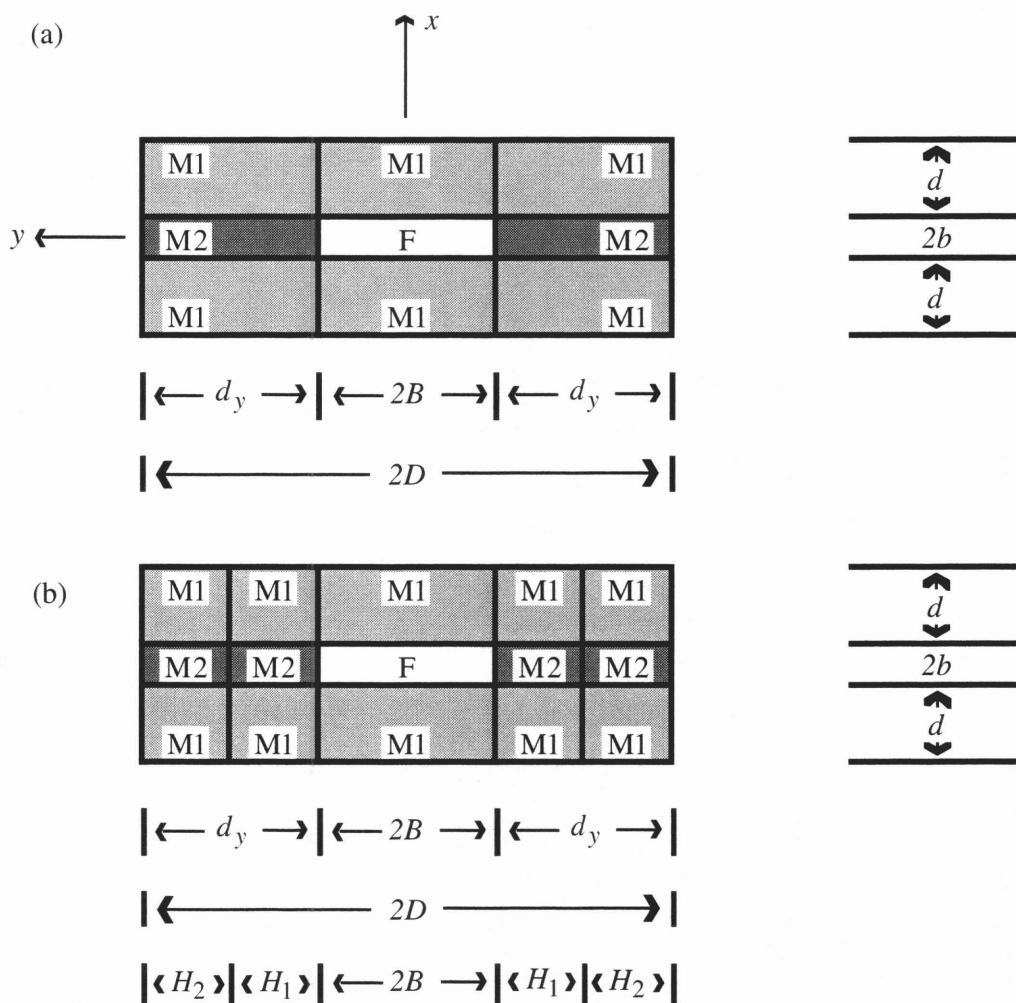


Figure 10.6. (a) Sketch of the cross-section of a leg with a fracture that is filled with an area of flowing water (F) of width $2B$ and the rest of the fracture is filled on both sides with rock matrix of type (M2) with width d_y . The sketch is not to scale. The width of the fracture is $2D$ and the aperture is $2b$. Below and above the fracture, a rock matrix layer (M1) is situated. The thickness of the rock layer is d . In (b) the two side-columns are vertically subdivided into two sub-columns of widths H_1 and H_2 each, such that $d_y = H_1 + H_2$, and $H_1 \neq H_2$.

A reason for choosing this geometry was to exclude, in a spot-check, that the extreme parameter values of the impermeable rock type M0 used in many test cases are the reason for increased errors in some self-consistency tests. In this subsection the observed x - y asymmetry in PICNIC calculations and the non-physical influence of the properties of daughter nuclides on their parent are tested. Note that the forms of the release curves are considerably different to section 9.

10.2.1. The “Numerical Effect” of Rotating the Rock Matrix

For this hypothetical variation of the Grimsel uranine case, again a single leg of length $L = 5$ [m] and a δ -function source are considered. Flow block and the rock layer (M1) have the same properties as in the original case. The thickness of the rock layer (M1) is reduced by a factor of 6.2 to $d_1 = 10^{-3}$ [m], to reduce its importance relative to the importance of the rock matrix type M2. To obtain a strong effect of two-dimensional matrix diffusion in the breakthrough curve, the channel width is assumed to be small compared to the rock matrix layer thickness, $2B = 0.1 \cdot 10^{-3}$ [m]. Apart from the geometry, the properties of the rock matrix type M2 are as described in section 10.1. The zero-gradient outlet boundary condition is used. As can be seen in Figure 10.7, we obtain a double-humped structure in the release curves, where the second hump is much more marked than the first hump.

For self-consistency tests, this example is computed in four different ways using the standard option REFINE 2. The release curves for the standard calculation are given as short-dashed lines in Figure 10.7. In another calculation, the side columns of width d_y of the rock matrix are also vertically subdivided into 2 sub-layers of widths H_1 and H_2 , such that $d_y = H_1 + H_2$; see geometry in Figure 10.6b. Here $H_1 = B = 0.05 \cdot 10^{-3}$ [m] and $H_2 = 0.4 \cdot 10^{-3}$ [m] are chosen. The results for the 2 sub-columns case are presented as solid lines. The relative difference function with respect to the latter case is presented in Figure 10.7c.

In two further calculations the numerical effects of exchanging the x - and y -direction in the geometries of Figure 10.6ab are considered, compare section 9.2.3. The results with subdivided side columns are given as dash-dotted lines in Figure 10.7, and the results without subdivision are given as long-dashed lines.

All release curves agree within $\pm 10\%$. The vertical subdivision of the side columns has a small effect within 5%. The difference of the rotated variant to the geometries of Figure 10.6 is within 3% in the relevant region. Only for the strong decrease of the release curve in the tailing do the differences slightly increase. Thus the differences due to the $(x - y)$ -asymmetry in PICNIC in the generation of the finite-element mesh for calculation of the Laplace transformed rock matrix response are not serious, at least for the case considered.

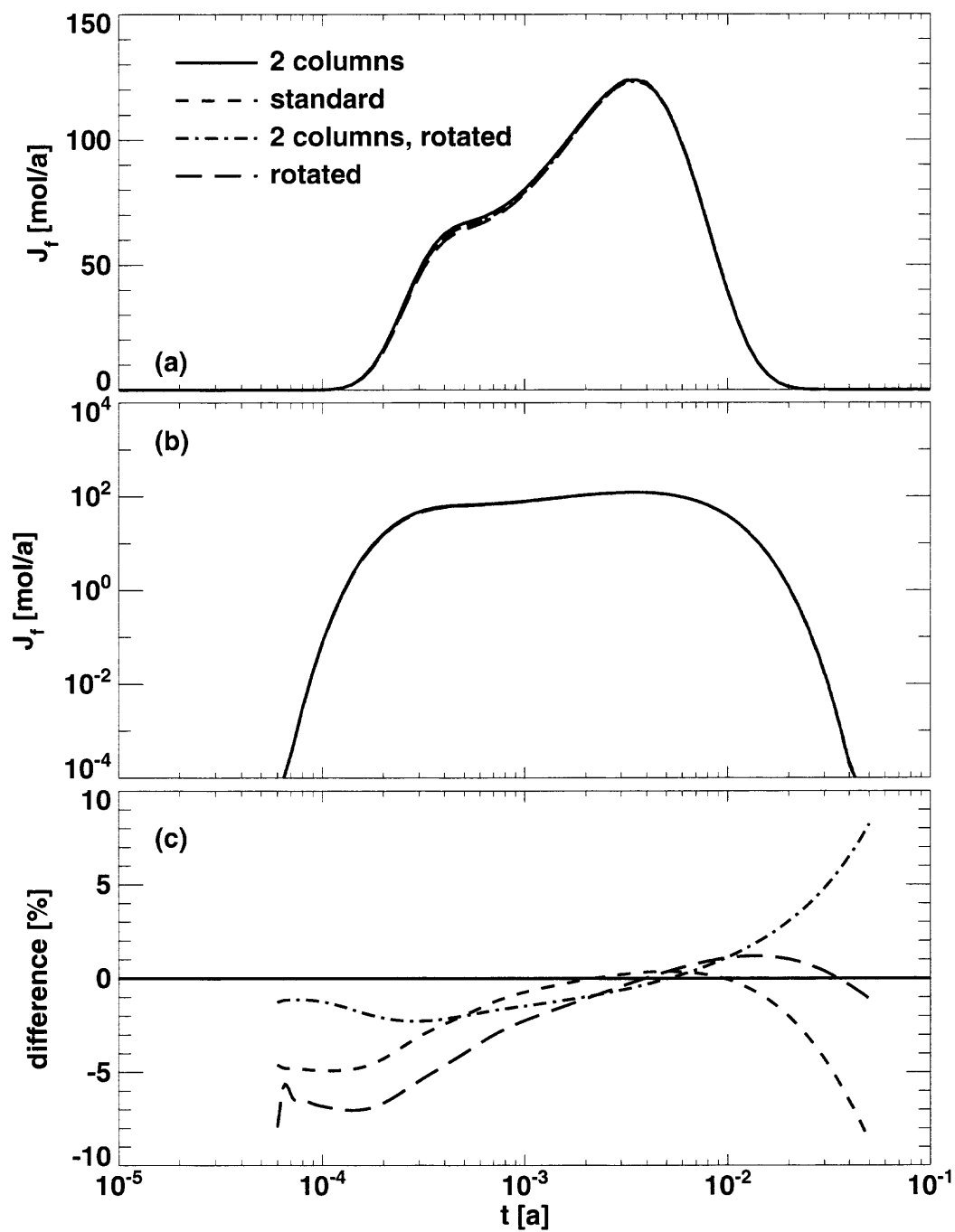


Figure 10.7. Hypothetical variation of the Grimsel dipole experiment using uranine for two-dimensional matrix diffusion into the rock matrix geometry depicted in Figure 10.6. For more details see text.

10.2.2. The “Numerical Effect” of a Daughter on its Parent

Finally we test, for the rock matrix geometry of Figure 10.6, the (non-physical) influence of the parameters of a **nuclide decay chain** $\text{ANUC} \rightarrow \text{BNUC} \rightarrow \text{CNUC}$ on the parent ANUC, compare section 9.2.4. The half-life of ANUC is 10^{-3} [a], the half-life of BNUC is 10^{-4} [a] and CNUC is assumed to be stable. ANUC is assumed to have the same transport properties as the non-decaying nuclide considered in section 10.2.1. BNUC, and CNUC are assumed to have the same transport properties as ANUC, apart from the retardation factors in the rock matrix. Again a δ -function source of the parent ANUC is considered. Figure 10.8 gives the release curves of the parent ANUC. The second hump of the release curve is strongly reduced by radioactive decay to a shoulder; compare to the non-decaying nuclide in Figure 10.7.

The release of the parent ANUC is calculated in four different ways, which all use the increased refinement option REFINE 4. The short-dashed lines give the release of ANUC when the rock matrix retardation constants of BNUC and CNUC are the same as for ANUC. Hence, a three member decay chain is considered where all the nuclides have the same transport parameter values, except of course, for the different half-life. The dash-dotted lines give the release of ANUC when the rock matrix retardation constants of BNUC are 2 times higher and of CNUC are 10 times higher with respect to ANUC. The long-dashed lines consider that the rock matrix retardation constants of BNUC are 10 times higher and of CNUC are 100 times higher than for ANUC. For the solid lines, a non-decaying nuclide was considered and radioactive decay was analytically taken into consideration using the relation $\mathfrak{R}(t) = e^{-\lambda t} \mathfrak{R}_{\lambda \rightarrow 0}(t)$. Let us call this the “uranine” nuclide release. The relative differences to the latter are given in Figure 10.8c. Using the same properties for all nuclides of the decay chain, the uranine result and the ANUC result (short dashes) almost coincide. However, when the properties of BNUC and CNUC differ from the properties of ANUC, in the main parts of the release curves and especially in the maximum region, the decay chain result is about 20% below the uranine result. This is similar to the case of two-dimensional matrix diffusion into a homogeneous rock layer, see Figure 9.27.

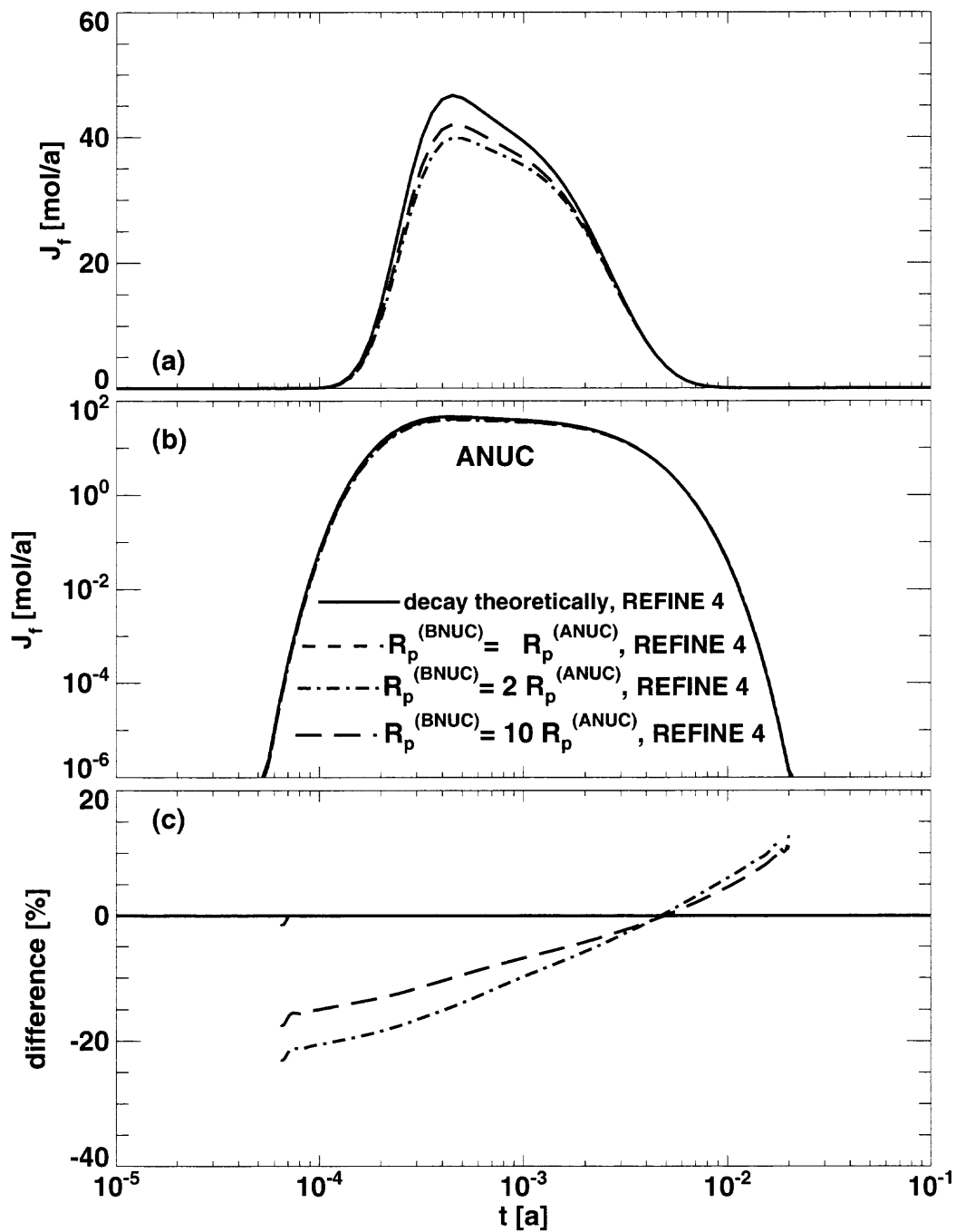


Figure 10.8. Hypothetical variation of the Grimsel dipole experiment using uranium parameters for two-dimensional matrix diffusion into the rock matrix geometry depicted in Figure 10.6. Presented are different PICNIC results for transport of a parent nuclide ANUC. For more details see text.

10.3. Summary

In this section, as step VII of the verification scheme presented in section 3, we come to the end of the verification of PICNIC's ability to deal with two-dimensional matrix diffusion into different (heterogeneous) rock matrix geometries; see the detailed verification matrix of this section in Table. 10.1. In this step, in all cases considered, Grimsel uranine parameters are used and transport in a **single leg** is considered.

The capability of the embedded finite-element method to deal with two-dimensional matrix diffusion into a two-layer rock matrix does not show any indication of an increased numerical error compared to the homogeneous case for two-dimensional matrix diffusion considered in section 9.2.

For a rock matrix geometry where - adjacent to the open channels - a further zone of porous rock matrix is accessible for diffusion, we have shown that the two inconsistencies of the finite-element method in PICNIC are not enhanced when compared to the homogeneous case for two-dimensional matrix diffusion.

These test cases round off the verification of the finite-element method in PICNIC to deal with one- and two-dimensional matrix diffusion performed in sections 6-10. From self-consistency tests and discretisation tests with different refinements of the finite-element mesh, estimates of the accuracy of the code are available. Given these estimates, PICNIC can be applied with confidence. As long as no results from other codes are available, a more extended verification plan would be of restricted use only.

single leg		(a) single nuclide			(b) nuclide decay chain		
two-dimensional matrix diffusion into heterogeneous rock geometries		ZG	ZC	AI	ZG	ZC	AI
source in Laplace domain	δ -pulse	R, K			R, K		
	simple-leaching						
source in time domain	short pulse						
	long top-hat						
	band-release						
	general						

pathway		(c) single nuclide			(d) nuclide decay chain		
two-dimensional matrix diffusion into heterogeneous rock geometries		ZG	ZC	AI	ZG	ZC	AI
source in Laplace domain	δ -pulse						
	simple-leaching						
source in time domain	short pulse						
	long top-hat						
	band-release						
	general						

network		(e) single nuclide			(f) nuclide decay chain		
two-dimensional matrix diffusion into heterogeneous rock geometries		ZG	ZC	AI	ZG	ZC	AI
source in Laplace domain	δ -pulse						
	simple-leaching						
source in time domain	short pulse						
	long top-hat						
	band-release						
	general						

Table 10.1. Performed calculations for the two-dimensional rock matrix geometries depicted in Figures 10.1 and 10.6. Note: All test cases represented by empty fields in the scheme were implicitly verified by any of the specified examples. Such a procedure is strongly based on the internal structure of PICNIC as outlined in more detail in section 3. Legend: K: consistency tests; R: “discretisation test” considering different mesh refinements in the “finite-element” results in PICNIC.

11. Conclusions and Outlook

In this report we have presented the state-of-the-art discrete fracture network model PICNIC developed for the description of migration of radionuclides/contaminants in the geosphere. The heterogeneity of the geosphere on different spatial scales is accounted for in a conceptually simple geometrical approach, which is easy to handle but highly powerful. PICNIC has grown from the conceptualisation at the very beginning, through the derivation and elaboration of the mathematical fundamentals, to implementation in a numerical code and the careful verification with iterative improvement of the code. As applications and examples for the verification, we mainly considered cases related to the Kristallin-I repository performance assessment and cases related to experiments on the field scale.

11.1. Fundamentals and Capabilities of the Code

The movement of radionuclides in saturated fractured rock from the near-field of a radioactive waste repository to the biosphere is modelled as part of a model chain ("geosphere transport model") in repository performance assessment. The PICNIC project has been established as a cooperation between PSI/Nagra and QuantiSci to provide a new geosphere transport model for Swiss performance assessments of radioactive waste repositories. PICNIC can deal with all processes considered in the geosphere model RANCHMD generally used, e.g. in the Kristallin-I safety assessment, and in addition explicitly accounts for the heterogeneity of the geosphere on different scales. In order to use the potential of the geosphere as a barrier to radionuclide migration, PICNIC takes account of both small-scale and large-scale flowpath heterogeneities. In addition to the transport on large spatial scales and on large timescales typical for performance assessment, PICNIC can also deal with the small timescales and transport distances considered typically in transport experiments in the field and the laboratory.

To ensure the reliability of such a code and to estimate its accuracy, verification is of primary importance. Therefore, a verification strategy suited to the program was developed in section 3, which is specifically based on the mathematical fundamentals of PICNIC. The verification presented forms the main part of this report.

PICNIC is based on the very efficient combination of a hierarchical linear response concept with Laplace transformation methods. The inverse Laplace transformation is performed numerically using Talbot's method. The heterogeneity on the large scale is taken into account in PICNIC by modelling transport in a network of legs using methods from graph theory. The legs are only in contact with each other at their end points, the junctions. The properties of an individual leg are constant, while the parameters can differ from leg to leg. In each leg, advective and dispersive transport of single nuclides or of nuclide decay chains are considered. PICNIC also contains the capability for branching and recombining nuclide decay chains. The small-scale heterogeneity of the rock adjacent to the area of flowing water is taken into account by additionally considering diffusion of the nuclides into the stagnant porewater of the surrounding rock matrix (possibly heterogeneous). Therefore one-dimensional matrix diffusion into a *homogeneous* planar or cylindrical rock matrix was implemented in the code by means of analytical relations in the Laplace domain. To account also for one-dimensional or two-dimensional matrix diffusion into *heterogeneous* rock matrices, an alternative embedded finite-element method in the Laplace domain was implemented for the

calculation of the rock matrix response. These options, and particularly their verification, are now discussed.

11.2. Analytically Implemented One-Dimensional Matrix Diffusion

In a first phase, as one PICNIC option, matrix diffusion was considered as one-dimensional into a homogeneous planar or cylindrical rock matrix. These two different rock matrix geometries together with the transport in a single leg, were the typical modelling approaches considered in recent performance assessments where RANCHMD was used for the transport in the geosphere. Consequently, for the verification of this phase, cross-comparisons with RANCHMD were of great use considering transport in a single leg. The excellent agreement found in this cross-comparison in particular indicated that PICNIC can be used with confidence in performance assessments and modelling of transport experiments. This confidence was increased by self-consistency tests of PICNIC checking analytical relations. For verification of the network capability in PICNIC using a new network technique, a sequence of RANCHMD calculations for each individual leg in the network were combined to finally obtain the nuclide release of a network. This so-called “assembled RANCHMD” result was cross-compared to a PICNIC result. In another case, similarly defined so-called “assembled PICNIC” calculations were compared to PICNIC results in a kind of self-consistency check. Cross-comparisons with the codes GIMRT and PAWorks/LTG further strengthened the verification. The conceptual differences of PICNIC to the PAWorks/LTG code regarding the boundary conditions at inner junctions in a network were considered. The capability of PICNIC to calculate the flow of water from hydraulic conductivities of the legs and hydraulic heads at some junctions was also verified. According to the verification strategy, the capabilities of PICNIC to deal with transport in a pathway and a network of pathways, with leg outlet boundary conditions and with single or multiple sources of different form were verified. The further verification for other geometries of the rock matrix for matrix diffusion concentrated mainly on the transport of single nuclides and nuclide decay chains in a single leg with appropriate sources. The capabilities for transport in pathways and networks were spot-checked for different rock matrix geometries.

11.3. Embedded Finite-Element Method for One-Dimensional Matrix Diffusion Into a Heterogeneous Rock Matrix

In a second development phase, the capability of PICNIC was extended to deal more realistically with small-scale heterogeneity. Now the cross-section of legs could be entered easily, in a geometrical and flexible way, to the code. The leg cross-section was represented in rectangular cells in a checkerboard manner. The properties of the leg cross-section may vary from cell to cell, but are constant within individual cells. Each cell describes either an area of flowing water or a rock matrix area. This increased flexibility of the code was at the cost of a more complex code and increased computation times. While in the option of the first phase, the rock matrix response was implemented as analytical formulae in the code, in this phase a finite-element method was embedded which solves a kind of stationary diffusion equation (with radioactive decay and ingrowth) to calculate the response of the rock matrix in the Laplace domain. Because of the inaccuracies inevitable in the finite-element method, considerations with respect to mesh refinements were of great importance for the verification of the numerical results.

For this hybrid type of model which uses graph theory, analytical and numerical Laplace transformation methods together with a finite-element method combined in a hierarchical linear response concept, we distinguish between cases for one-dimensional matrix diffusion and two-

dimensional matrix diffusion.

For one-dimensional matrix diffusion, the rock matrix response is still possible analytically in the Laplace domain, but is approximated in PICNIC by the finite-element method. For a homogeneous one-dimensional planar layer of rock matrix, a cross-comparison to the PICNIC option with the analytical rock matrix response in PICNIC was performed in detail. The excellent agreement with the latter indicated the accuracy of the finite-element method for this type of geometry, and the very small relative difference functions were used to measure the agreement. The forms of the relative difference functions acted as “calibration curves” to be used as references for more complicated rock matrix geometries. For the code verification, the steady-state nuclide flow (i.e. “1 - the geosphere barrier efficiency”) for a constant source of a single nuclide was compared to the analytical result derived for the verification. The small differences encountered, as expected, depended on the rock layer properties, the refinement of the finite-element mesh and the relevant timescales for transport, especially the nuclide half-life. Very recently, a cross-comparison to the code RIP was possible. Very good agreement for the full time-dependent behaviour was found, both for a single nuclide and a nuclide decay chain. The small differences again depended on the mesh refinement.

For one-dimensional matrix diffusion into two independent homogeneous areas of rock matrix, very recently a cross-comparison to the PAWorks/LTG code was possible. Very good agreement for the full time-dependent behaviour was found, both for a single nuclide and a nuclide decay chain.

For one-dimensional matrix diffusion into two independent two-layer areas of rock matrix, a cross-comparison with the RIP code was possible for a single nuclide and a nuclide decay chain. A good agreement with the RIP code was found, but the differences increased with respect to the previous cases. Also the differences between different PICNIC calculations increased somewhat. Note that these inaccuracies could become relevant in some applications. In such cases, an increased refinement of the finite-element mesh in PICNIC should be used.

To conclude, the very good agreement between different PICNIC calculations, in the code cross-comparison with PAWorks/LTG and RIP, and the agreement with the analytical result for steady-state nuclide release show that PICNIC can be used with confidence for different types of one-dimensional matrix diffusion.

11.4. Embedded Finite-Element Method for Two-Dimensional Matrix Diffusion

For two-dimensional matrix diffusion, no analytical solution for the rock matrix response is available, either for a single nuclide or for a nuclide decay chain. Thus the embedded finite-element method could show its full strength. Moreover, the capability of PICNIC to account for two-dimensional matrix diffusion into heterogeneous rock matrices is to our knowledge unique in fracture network modelling. However this also means that there was no code available for cross-comparison of the time-dependent behaviour, and the options for verification of the code were considerably reduced. Thus the verification for these geometries rested mainly on the verification of the embedded finite-element method for one-dimensional matrix diffusion and on discretisation tests comparing different refinements of the finite-element mesh. It was also checked that the relevant timescales for transport can be observed in the release curves.

For two-dimensional matrix diffusion into a homogeneous layer of rock matrix, the PICNIC results

for the steady-state release (“geosphere barrier efficiency”) of a single nuclide were also verified quantitatively. The PICNIC result was compared to results derived from an ADINA calculation of the rock matrix response in the Laplace domain. The PICNIC result for this agreed very well with the ADINA result. The small differences encountered, as expected, depended again on the rock layer properties, the refinement of the finite-element mesh and the relevant timescales for transport, especially the nuclide half-life. With refined meshes used in both codes, as expected, the results converged. The relative differences between different PICNIC calculations however were increased, e.g. compared to one-dimensional matrix diffusion into a two-layer rock matrix, because of the increased complexity of the transport behaviour and the finite-element meshes used internally in PICNIC. Tests for other parameters and also nuclide decay chains showed similar increase of relative difference functions between different PICNIC calculations with different finite-element meshes.

Similar consistency checks for two-dimensional matrix diffusion into a two-layer rock matrix showed similar forms and magnitudes of relative difference functions between different PICNIC results. Overall, PICNIC showed itself to be a reliable code also for these two-dimensional matrix diffusion cases. It must however be stated that PICNIC standard mesh results were found to underestimate the maximum nuclide release in the order of 10%. This might be too low in some situations with high demands, but should be sufficient in most applications, in particular in performance assessments. In situations with a higher demand of accuracy, a refined finite-element mesh in PICNIC should be used¹¹¹, which can however considerably increase the calculation times.

In several tests we experienced that the subdivision of the rock matrix into layers and the associated local refinement of the finite-element mesh was mostly highly beneficial to the accuracy of PICNIC. Thus, for practical applications, it should be borne in mind that the rock layer subdivision is often much more efficient than the internal mesh refinement option. This might also give indications for a possible further development of PICNIC aimed at an increased accuracy and code efficiency.

11.5. Remaining Open Questions and Restrictions

Few open questions with the code remain. For large Peclet numbers (mainly above $Pe = 100$ and higher), the code can encounter a numerical instability. Because such high Peclet numbers are mostly outside the range observed in natural systems and used in performance assessments, this is not really serious. It was also found that the tendency towards this instability is reduced with increasing strength of matrix diffusion compared to the influence of advection. Note also that the main application range of PICNIC is for an important effect of matrix diffusion. The instability for high Peclet numbers appears to be inherent to Talbot’s method, which is actually implemented in PICNIC for inverse Laplace transformation.¹¹²

The accuracy of the embedded finite-element method is inevitably reduced compared to the method of embedded analytical rock matrix response. For two-dimensional matrix diffusion, the numerical error in the maximum region was observed to be in the order of 10%.¹¹³ A reason for these

¹¹¹ The verification tests suggest that a careful user of the code will perform discretisation tests when moving to a new parameter region.

¹¹² In the 1999 version of PICNIC, a small bug is eliminated, thereby reducing some inaccuracies for high Peclet numbers. The main problem, however, is not solved.

¹¹³ For two-dimensional matrix diffusion, when the x and y -axis are exchanged, there was additionally a small asymmetry observed in the order of 3% in the PICNIC results. In the interim, in the 1999 version of PICNIC this

inaccuracies might be strong spatial variations of the nuclide flux in the rock matrix and particularly discontinuities of the nuclide flux at the flowing water/rock matrix interface.

In PICNIC calculations for the release of nuclide decay chains, the finite-element mesh is the same for all nuclides in the decay chain. This ensures, in a simple way, conservation of mass in the code results. Because the selected finite-element mesh depends on the properties of all nuclides in the decay chain, the results for the parent depend numerically on the retardation properties of the daughter (which contradicts the laws of physics). One has to be aware that the maximum release of the parent was sometimes underestimated in the order of 30% for some cases with two-dimensional matrix diffusion, also using a refined finite-element mesh, but for extremely different retardation properties of the parent and the daughter in the rock matrix. It would require some effort to overcome this problem, which is presently not regarded as pressing. It might be possible to use different meshes for different nuclides in the decay chain. If necessary, the implementation should be done very carefully, to maintain the conservation of mass in the code and to avoid artificial numerical diffusion in the rock matrix.

Because of the tree technique for the network calculation in PICNIC, for large and complex networks memory problems are encountered in PICNIC. Thus, on present computers, realistically several dozens of legs could be considered, depending on the complexity of the network. In the case that large networks need to be considered, going back to the original pathway method could solve these memory problems — as long as the calculation times do not increase too much. The implementation of another, recently suggested much more efficient network technique would need a somewhat increased coding effort. For stability reasons, it might then also be necessary to use another method for the numerical inverse Laplace transformation.

The capabilities for more complex matrix geometries in PICNIC are quite restricted; e.g. it might be useful to consider matrix diffusion into heterogeneous cylindrical vein geometry, or into the spherical geometry of homogeneous or heterogeneous nuggets. However, in the present PICNIC version such geometries cannot be considered.

PICNIC assumes that the nuclide exchange between different legs is dominated by advective transport at the junctions of the network. Thus, in cases where the nuclide exchange between different legs is strongly influenced by other mechanisms, such as dispersive or diffusive transport, PICNIC results should be interpreted with care. Presently, PICNIC is also restricted to the assumption of perfect mixing of the nuclide flow from different legs at the junctions of the network.

In PICNIC, matrix diffusion is assumed to be orthogonal to the direction of the water flow. Thus PICNIC is not applicable in cases where matrix diffusion parallel to the direction of the water flow is of great importance.

Due to its underlying mathematical structure, PICNIC cannot take into account time-dependent parameters and non-linear effects, such as non-linear sorption and most chemical reactions. Note that over the times that have to be considered in performance assessments, it is likely that the flow field, at least, will change, as a result, for example of changing climate. Calculations to address the effects of such changes could not be directly undertaken using PICNIC. However, various calculations with constant flow fields and rock properties could be undertaken using PICNIC to

small bug is eliminated. It was spot-checked with some tests that the influence of this bug is indeed in the order of the observed asymmetry only.

scope the effects of changes to the flow fields or rock properties.

11.6. Performance Assessment Modelling Aspects

Many of the cases considered in this report are related to performance assessment, here mainly the Kristallin-I study, because the parameters used in this study are well founded and readily available. Because of restrictions in the available codes at the time, the Kristallin-I study mainly considered one-dimensional matrix diffusion into a homogeneous rock layer. These results are well reproduced by PICNIC. A great deal of structural geological investigations is available, which could only be used in a restricted way in the geosphere transport modelling in the performance assessment. It has been shown in two ways that much more credit can be taken for these investigations in the case of the small-scale heterogeneity of a cataclastic zone. When one-dimensional matrix diffusion into a two-layer rock matrix is considered, it was shown that the second rock layer representing unaltered wallrock could have a strong positive influence on the transport behaviour in the geosphere. For the case of two-dimensional matrix diffusion into the first layer, representing the altered wallrock, an even larger positive influence on the performance of the geosphere has been shown. The combination of both effects, two-dimensional matrix diffusion into a two-layer rock matrix, is also considered in this report. The effect of such a combination would be even larger. The results of these investigations have shown for the first time that this geological information, simplified for performance assessment, can be modelled easily with PICNIC. More important, taking into account this kind of information has the potential to considerably increase the calculated performance of the geosphere.

11.7. Experiment Modelling Aspects

The other type of cases considered in this report is related to modelling of transport experiments. As an example, the Grimsel dipole experiment was considered and PICNIC reproduced the earlier modelling results for these experiments very well. This showed even more complex transport behaviour than the performance assessment cases, especially when more complex rock matrix geometries were considered as variations of the original case. However, to obtain this more complex behaviour, we had to select the geometry of the rock matrix appropriately to see the small-scale heterogeneity of the geosphere also in the release curves.¹¹⁴

11.8. Outlook

We now briefly consider the development options. Following the development and verification of PICNIC, it can now be used with confidence in performance assessment of the disposal of radioactive waste and modelling of transport experiments in the water-saturated underground environment.

With regard to applications of PICNIC to field tracer tests, we mention the still ongoing modelling work for the Äspö migration experiments. There, one-dimensional matrix diffusion into a homogeneous planar rock matrix and a 2-leg “network” is considered [Jakob and Heer, 1998; 1999].

¹¹⁴ For instance, for the Grimsel dipole experiment we have speculated that two-dimensional matrix diffusion could not be seen and appears indeed to be irrelevant for the parameters considered, because of the geometry of the rock matrix. On the other hand this means that it is likely that relevant transport processes on a large timescale such as two-dimensional matrix diffusion, are overlooked or misinterpreted in transport experiments on a small timescale. This is a typical and also well-known general problem of up-scaling from small-scale experiments to behaviour on large spatial and timescales.

However, more complex applications will follow.

Related to this, it would be very useful, if clear indications could be found of two-dimensional matrix diffusion in geological media, in addition to the structural geological investigations, which were related e.g. to the Kristallin-I investigations of granite [Thury et al., 1994] and e.g. to the marl at Wellenberg [Nagra, 1997]. Therefore a thorough understanding of two-dimensional matrix diffusion should be aimed for. The timescale parameters (λ , α , $\alpha + \beta\gamma$, β_1^2 , β_D^2 , γ_1^2 , Pe, ...) considered for one-dimensional and two-dimensional matrix diffusion into single-layer and two-layer rock matrices [Hadermann and Heer, 1996; Barten, 1996a; Heer and Smith, 1998; Barten, Robinson and Schneider, 1998; this report and references cited therein] could be a good starting-point. Transport experiments clearly indicating two-dimensional matrix diffusion, as distinct from one-dimensional matrix diffusion, would be very helpful.

A main application range of PICNIC aims [Klos and Barten, 1995] at the performance assessment of radioactive waste repositories. The first applications of Schneider et al. [1996]; Smith et al. [1997]; Schneider et al. [1998] and the test cases with performance assessment parameters in this report show that it should be possible to take yet more credit for the available structural geological knowledge of the geosphere surrounding a repository.

It is hoped that it will be possible sometime to make more use of information on hydrology at a repository site for performance assessment.¹¹⁵ Related to this, it will probably be necessary in the future to consider larger networks for radionuclide transport. To do this with PICNIC, going back from the tree method to the pathway method might be considered as a first attempt, followed by the use of the recently suggested, much more efficient network technique [Barten, 1997].¹¹⁶

¹¹⁵ An appropriate interface of PICNIC with an available state-of-the-art hydrology tool such as, e.g., NAPSAC, is currently under development (cf. Schneider et al. [1998] for a first step); compare Barten [1994] and Smith and Robinson [1995] for the initial concept of PICNIC.

¹¹⁶ As an aside we would like to mention that a variant of the new "junction sequence method" can also be used for some nonlinear effects, like nonlinear sorption, in connection with transport in a network, see Barten, Niemeyer and Jakob [2000] for a first application. These nonlinear effects, however, are outside the scope of the PICNIC code which works in the Laplace domain.

12. Acknowledgements

The “PICNIC project” has strongly benefited from the contributions of a series of people, during the concept and the code development and especially during the verification phase. We would like to thank warmly

Urs R. Berner for his support and many practical hints

Neill S. Cooper (Cooper and Caulcott/UK, formerly at QuantiSci) for help in the coding of PICNIC

Jörg Hadermann for a series of stimulating discussions and suggestions and for his promotion of the PICNIC project

Walter Heer for help in designing and for performing cross-comparisons with the RANCHMD code and for patiently sharing his experience with matrix diffusion

Andreas Jakob for his engaged and helpful comments on the verification of PICNIC and particularly on this report, with many stimulating discussions

Matthias J. Niemeyer (Colenco) for help in designing and for performing cross-comparisons with the RANCHMD code and his explanations on performance assessment

Jürg W. Schneider (Nagra) for useful discussions on transport in a cataclastic zone and on performance assessment and his continuing interest in the PICNIC project

Dawn A. Shuttle (Golder/US) for jointly designing and performing cross-comparisons of PICNIC with the PAWorks/LTG and the RIP codes. The PAWorks/LTG calculations (performed at Golder) have been funded by JNC/Japan as part of the PAWorks/LTG verification procedure. A selection of the RIP simulations (performed at Golder) have been used in the verification of RIP

Paul A. Smith (SAM/UK, formerly at QuantiSci) for contributions in the design of the PICNIC project in an early phase and a hint on a bug in PICNIC for the vein geometry case

Josep M. Soler for contributing GIMRT calculations for a code cross-comparison

Bernard Tirbonod for the collaboration on two-dimensional matrix diffusion and for providing ADINA calculations for code cross-comparisons.

Special thanks to Linda McKinley for editing the English language in the manuscript and Enzo Curti and Christophe Grenier (CEA/France) for the translations of the abstract.

This report was externally reviewed by David Lever (AEA technology plc/UK). His thorough and careful review has provided a number of thoughtful hints for the improvement of this report.

Partial financial support by Nagra is gratefully acknowledged. Without that support, this work would not have been possible.

13. Notation

quantity	units	description
1D-AS		denotes the “analytical” option for calculation of the rock matrix response for one-dimensional matrix diffusion
1D-FEM		denotes the finite-element option for calculation of the rock matrix response using a one-dimensional finite-element mesh in the rock matrix
2D-FEM		denotes the finite-element option for calculation of the rock matrix response using a two-dimensional finite-element mesh in the rock matrix
A_f	$[m^2]$	cross-sectional area of a leg
A_i	$[m^2]$	part of the cross-sectional area of a leg which is wetted with flowing water
a_L	$[m]$	longitudinal dispersion length of a leg
A_m	$[m^2]$	area perpendicular to the flowing water of side-walls of specified volume in the area of flowing water
an		denotes an ancestor of a junction
An		denotes the set of ancestors of a junction
ar		denotes an arriving leg of a junction
Ar		denotes the set of arriving legs of a junction
AI		at-infinity boundary condition
b	$[m]$	half-width of aperture of fracture
B	$[m]$	half-width of channel within fracture, in y -direction
C_f	$[mol/m^3]$	nuclide concentration in flowing water
C_p	$[mol/m^3]$	nuclide concentration in the porewater of the rock matrix
d	$[m]$	thickness of rock matrix layer
d_y	$[m]$	width in y -direction
D	$[m]$	half-width of rock matrix layer
D_f	$[m^2/a]$	dispersion coefficient
da		denotes a daughter of a junction
Da		denotes the set of daughters of a junction
dp		denotes a departing leg of a junction
Dp		denotes the set of departing legs of a junction
e_n	$[-]$	normal vector
f		index for area of flowing water
\bar{f}	$[f] \cdot [a]$	Laplace transform of a function f
F		denotes an area of flowing water in the leg cross-section

$f_2(s)$	$[-]$	“correction” function in rock matrix response
h	$[m]$	width in x -direction
H	$[m]$	width in y -direction
hd		denotes a head of a leg of a junction
(i)		index for a nuclide in a decay chain
I		number of nuclides in a decay chain
\mathbf{I}	$[-]$	identity function or identity function tensor
(j)		index for a nuclide in a decay chain
in		denotes a junction with a nuclide source
In		denotes the set of junctions with a nuclide source
In	$[mol/a]$	nuclide flow rate entering a leg
j_f	$[mol/(m^2 \cdot a)]$	nuclide flux in flowing water
J_f	$[mol/a]$	nuclide flow rate in the flowing water (nuclide release), index “f” is sometimes omitted
j_p	$[mol/(m^2 \cdot a)]$	nuclide flux in the rock matrix
\mathbf{j}_p	$[mol/(m^2 \cdot a)]$	nuclide flux vector in the rock matrix
J_p	$[mol/a]$	nuclide flow rate in the rock matrix
ju		denotes a junction
K	$[1/m]$	eigenvector
$K_{a,f}$	$[m]$	surface-based linear sorption equilibrium distribution coefficient, in flowing water
$K_{d,f}$	$[m^3/kg]$	volume-based linear sorption equilibrium distribution coefficient, in flowing water
$K_{d,p}$	$[m^3/kg]$	volume-based linear sorption equilibrium distribution coefficient, in the rock matrix area
L	$[m]$	length of leg
\mathbf{L}^{-1}		inverse Laplace transformation
lg		denotes a leg
$M1$		denotes a type of rock matrix, same for M0, M2, etc.
N		operator, describing transport in a leg
N_f	$[mol]$	amount of nuclides in a specified volume in the area of flowing water
N_p	$[mol]$	amount of nuclides in a specified volume in the rock matrix
Out	$[mol/a]$	nuclide flow rate out of a leg
p		index for area of porous rock matrix
Pe	$[-]$	Peclet number
q_f	$[m/a]$	Darcy velocity (specific discharge), index “f” is sometimes omitted
Q_f	$[m^3/a]$	water flow rate (discharge), index “f” is sometimes omitted

Q_s	$[m^3/a]$	source of water at a junction
Q_t	$[m^3/a]$	amount of water entering (or leaving) a junction
r	$[m]$	radial coordinate perpendicular to direction of the water flow
R	$[m]$	vein radius
\Re	$[-]$	response function or tensor of response functions of a leg
R_f	$[-]$	retardation constant in flowing water
R_p	$[-]$	retardation constant in the rock matrix
$R_{0,f}$	$[-]$	base retardation in flowing water
$R_{0,p}$	$[-]$	base matrix retention in the rock matrix
REFINE		option for refinement of the finite-element mesh
s	$[1/a]$	Laplace variable
S	$[mol/a]$	nuclide source at a junction
t	$[a]$	time
T	$[-]$	response function for nuclide flow rate at a junction for a source at another junction
$T_{1/2}$	$[a]$	nuclide half-life
tl		denotes a tail of a leg
v	$[m/a]$	velocity of flowing water, $= q_f / \varepsilon_f$
V_f	$[m^3]$	volume in the area of flowing water
V_i	$[m^3]$	volume in the area of flowing water
V_p	$[m^3]$	volume in the rock matrix
w		probability of nuclides entering a leg at a junction or index for a pathway
x	$[m]$	direction perpendicular to water flow
X	$[m]$	x -position in the rock matrix
y	$[m]$	direction perpendicular to direction of water flow
Y	$[m]$	y -position in the rock matrix
z	$[m]$	direction parallel to direction of water flow
ZC		the zero-concentration boundary condition
ZG		the zero-gradient boundary condition
α	$[a]$	advection time
β	$[a^{1/2}]$	square root of the matrix diffusion time
γ	$[a^{1/2}]$	square root of the matrix delay time
δ	$[-]$	Dirac delta function or Kronecker-delta
ε_f	$[-]$	flow porosity
ε_i	$[-]$	infill porosity

ε_p	$[-]$	porosity of porous rock matrix
λ	$[1/a]$	nuclide decay constant
Λ	$[1/m]$	eigenvector, in the case of infinite Peclet number
Γ	$[1/m]$	eigenvector, in rock matrix calculations
η	$[m^3/a]$	rock matrix response function or function tensor
ρ_f	$[kg/m^3]$	solid density of fracture infill material
ρ_p	$[kg/m^3]$	solid density of rock matrix
θ	$[-]$	Heaviside step function
χ	$[-]$	(part of an) eigenvalue
∂_t	$[1/a]$	partial derivative in time
∂_x	$[1/m]$	partial derivative in x -direction, similar for ∂_r , ∂_y , ∂_z
∂_x^2	$[1/m^2]$	second partial derivative in x -direction
∇	$[1/m]$	Nabla operator
∇_{\perp}	$[1/m]$	portion of Nabla operator perpendicular to water flow
∇_{\perp}^2	$[1/m^2]$	portion of Laplace operator perpendicular to water flow

These quantities can have additional indices. All these quantities are in SI units¹¹⁷, with the only exception that the time-scale is given in units of a year, $1[a]$.

¹¹⁷ It is possible to use an arbitrary, consistent system of units, as long as the form of the partial differential equations is conserved. Thus one might try to make use of this, e.g. by substituting **all** length scales by $1[\text{inch}]$ and **all** timescales by $1[\text{hour}]$. However substituting all timescales would also mean, e.g. giving the nuclide half-life in units of $1[\text{hour}]$. As another example, it is also possible to use activity units, $1[\text{becquerel}/a]$, or mass units, $1[\text{kg}/a]$, for the flow of single nuclides. However for nuclide decay chains this is not possible in a straightforward way, because the partial differential equations for the nuclide flow in activity units or mass units are different to the partial differential equations implemented in PICNIC, which are for the nuclide flow given in particle units, e.g. $1[\text{mol}/a]$. In a later phase, it might be considered to implement a pre-processor in PICNIC for the conversion of units.

14. References

- Abell, M. L., and Braselton, J. P.** 1994a. Section 10: Graph theory: The Networks Package, in The Maple V Handbook, AP Professional, Boston, p. 489-552.
- Abell, M. L., and Braselton, J. P.** 1994b. Differential Equations with Maple V, AP Professional, Boston.
- ADINA R & D, Inc.** 1992. ADINA Theory and Modeling Guide, Report, ARD 92-8, Watertown MA, USA.
- Barker, J. A.** 1982. Laplace Transform Solutions for Solute Transport in Fissured Aquifers, Adv. Water Resources, 5, 98-104.
- Barker, J. A.** 1985. Block-Geometry Functions Characterizing Transport in Densely Fissured Media, J. Hydrol., 77, 263-279.
- Barten, W.** 1994. Konzept eines linearen Respons-Modells für Transport in einem Klufnetzwerk, PSI Technical Note, AN-44-94-11, Würenlingen and Villigen.
- Barten, W.** 1995. Input File and Fundamentals for the First Phase of PICNIC, PSI Technical Report, TM-44-95-01, Würenlingen and Villigen.
- Barten, W.** 1996a. Linear Response Concept Combining Advection and Limited Rock Matrix Diffusion in a Fracture Network Transport Model, Water Resour. Res., 32, 3285-3296.
- Barten, W.** 1996b. Network Model Using a Linear Response Concept for Contaminant Transport in Heterogeneous Fractured Rock, in Calibration and Reliability in Groundwater Modelling (Proceedings of the ModelCARE 96 conference held at Golden, Colorado, USA, 24.-26. September 1996), edited by K. Kovar and P. van der Heijde, IAHS Publication no. 237, IAHS press, Wallingford, Oxfordshire, UK, p. 333-342.
- Barten, W.** 1996c. PICNIC-I Test Cases: Fracture Case, PSI Technical Report, TM-44-96-12, Würenlingen and Villigen.
- Barten, W.** 1997. Proposal for an Efficient Network Modelling in PICNIC and Marrying Nonlinearity with Network Effects, PSI Technical Report, TM-44-97-07, Würenlingen and Villigen.
- Barten, W., Niemeyer, M. J., and Heer, W.** 1997. PICNIC-I Test Cases: Vein Case, PSI Technical Report, TM-44-97-06, Würenlingen and Villigen.
- Barten, W., Niemeyer, M. J., and Jakob, A.** 2000. Efficient Junction Sequence Method for Transport in a Directed Network, Water Resour. Res., 36, 1333-1337.
- Barten, W., and Robinson, P. C.** 1996. PICNIC: A Code to model Migration of Radionuclides in Fracture Network Systems with Surrounding Rock Matrix, in HYDROINFORMATICS 96, volume 2 (Proceedings of the second international conference on Hydroinformatics, Zürich, Switzerland, 9.-13. September 1996), edited by A. Müller, A. A. Balkema, Rotterdam, The Netherlands, p. 541-548.
- Barten, W., Robinson, P. C., and Schneider, J. W.** 1998. PICNIC-II: A code to simulate contaminant transport in fracture networks with heterogeneous rock matrices, in

Advances in Hydro-Science and -Engineering, Volume III, Proceedings of the 3rd International Conference on Hydro-Science and Engineering, Cottbus/Berlin, Germany, 1998, edited by K. P. Holz, W. Bechteler, S. S. Y. Wang, and M. Kawahara, The University of Mississippi, Center for Computational Hydroscience and Engineering, MS 38667, USA, abstract on p. 152 and full paper on CD-ROM.

- Barten, W., Robinson, P. C., and Tirbonod, B.** 2000. Verification of a Fracture Network Transport Model Including Two-Dimensional Rock Matrix Diffusion, for International Conference on Calibration and Reliability in Groundwater Modelling, Coping with Uncertainty (ModelCARE' 99 conference held at ETH Zürich, Switzerland, 20.-23. September 1999), edited by F. Stauffer, W. Kinzelbach, K. Kovar, and E. Hoehn, IAHS Publication no. 265, IAHS press, Wallingford, Oxfordshire, UK, p. 3-9.
- Bateman, H.** 1908-1910. The Solution of a System of Differential Equations Occurring in the Theory of Radio-Active Transformations, Proc. Camb. Phils. Soc., 15, 423-427.
- Bear, J., Tsang, C. F., and deMarsily, G.** (eds.), 1993. Flow and Contaminant Transport in Fractured Rock, Academic Press, San Diego.
- Berkowitz, B.** 1994. Modelling flow and contaminant transport in fractured media, in Advances in Porous Media, Volume 2, edited by M. Y. Corapcioglu, Elsevier, Amsterdam, p. 397-451.
- Bradbury, M. H., and Baeyens, B.** 1997a. Far-Field Sorption Data Bases for Performance Assessment of a L/ILW Repository in a Undisturbed Palfris Marl Host Rock, PSI Report, 97-15, Würenlingen and Villigen; and Nagra Technical Report, NTB 95-05, Nagra, Wettingen.
- Bradbury, M. H., and Baeyens, B.** 1997b. Far-Field Sorption Data Bases for Performance Assessment of a L/ILW Repository in a Disturbed/Altered Palfris Marl Host Rock, PSI Report, 97-16, Würenlingen and Villigen; and Nagra Technical Report, NTB 95-06, Nagra, Wettingen.
- Cacas, M. C., Ledoux, E., deMarsily, G., Barbreau, A., Calmels, P., Gaillard, B., and Margritta, R.** 1990. Modelling fracture flow with a stochastic discrete fracture network: Calibration and validation, 2, The transport model, Water Resour. Res., 26, 491-500.
- Clemo, T., and Smith, L.** 1997. A hierarchical model for solute transport in fractured media, Water Resour. Res., 33, 1763-1783.
- Crump, K. S.** 1976. Numerical Inversion of Laplace Transforms Using Fourier Series Approximation, J. Assoc. Comp. Mach., 23, 89-96.
- Davis, B., and Martin, B. L.** 1979. Numerical Inversion of Laplace Transforms: a Critical Evaluation of Methods, J. Comp. Phys., 33, 1.
- de Hoog, F. R., Knight, J. H., and Stokes, A. N.** 1982. An Improved Method for Numerical Inversion of Laplace Transforms, SIAM J. Stat. Comput., 3, 357-366.
- Dershowitz, W., Foxford, T., Sudicky, E., Shuttle, D. A., and Eiben, Th.** 1998. PAWorks: Pathway Analysis for Discrete Fracture Networks with LTG Solute Transport, User Documentation, Version 1.5; Internal Report, Golder Associates, Redmont WA, USA.
- DOE,** 1998. Viability Assessment of a Repository at Yucca Mountain, Volume 3: Total System Performance Assessment, DOE/RW-0508/V3, U.S. Department of Energy, Office of

Civilian Radioactive Waste Management, North Las Vegas, Nevada, USA.

- Dverstorp, B., Andersson, J., and Nordquist, W.** 1992. Discrete fracture network interpretation of field tracer migration in sparsely fractured rock, *Water Resour. Res.*, 28, 2327-2343.
- Foster, S. S. D.** 1975. The Chalk Groundwater Tritium Anomaly — A Possible Explanation, *J. Hydrol.*, 25, 159-165.
- Grindrod, P., Williams, M., Grogan, H. A., and Impey, M.** 1990. STRENG: A Source Term Model for Vitrified High Level Waste, Nagra Technical Report, NTB 90-48, Wettingen.
- Grindrod, P., Herbert, W., Roberts, D., and Robinson, P. C.** 1991. NAPSAC Technical Document, Stripa Project Technical Report, 91-31, Swedish Nucl. Fuel and Waste Manage. Co., Stockholm.
- Grisak, G. E., and Pickens, J. F.** 1980. Solute Transport Through Fractured Media: 1. The Effect of Matrix Diffusion, *Water Resour. Res.*, 16, 719-730.
- Hadermann, J.** 1980a. Radionuclide Transport Through Heterogeneous Media, *Nucl. Technol.*, 47, 312-323.
- Hadermann, J.** 1980b. BATEM, ein Rechenprogramm zur numerischen Berechnung der Bateman-Lösungen für radioaktive Zerfallsketten, EIR Technical Report, TM-45-80-11, Paul Scherrer Institute, Würenlingen and Villigen.
- Hadermann, J.** 1981. Radionuklidtransport durch Rissysteme und Matrixdiffusion, EIR Technical Report, TM-45-81-42, Paul Scherrer Institute, Würenlingen and Villigen.
- Hadermann, J., and Heer, W.** 1996. The Grimsel Migration Experiment: Integrating Field Experiments, Laboratory Investigations and Modelling, *J. Contam. Hydrol.*, 21, 87-100.
- Hadermann, J., and Rösel, F.** 1983. INTRACOIN Level 1 Benchmark Calculations with EIR Codes CONZRA, RANCH and RANCHN, EIR Report, 491, Paul Scherrer Institute, Würenlingen and Villigen; and Nagra Technical Report, NTB 83-10, Wettingen.
- Hadermann, J., and Rösel, F.** 1985. Radionuclide Chain Transport in Inhomogeneous Crystalline Rocks — Limited Matrix Diffusion and Effective Surface Sorption, EIR Report, 551, Paul Scherrer Institute, Würenlingen and Villigen; and Nagra Technical Report, NTB 85-40, Wettingen.
- Heer, W., and Hadermann, J.** 1994. Grimsel Test Site, Modelling Radionuclide Migration Field Experiments, PSI Report, 94-13, Würenlingen and Villigen; and Nagra Technical Report NTB 94-18, Wettingen.
- Heer, W., and Hadermann, J.** 1997. Breakthrough and Diffusion in Fracture and Vein Geometry, in preparation.
- Heer, W., and Smith, P. A.** 1998. Modelling the Radionuclide Migration Experiments at Grimsel. What have we learned?, in *Scientific Basis for Nuclear Waste Management XXI (MRS'97)*, MRS Symposium in Davos, Switzerland, 28. September - 3. October 1997, edited by I.G. McKinley and C. McCombie, Symposium Proceedings Volume 506, Materials Research Society, Warrendale, Pennsylvania, p. 663-670.
- Herbert, A. W., and Lanyon, G.** 1992. Modelling tracer transport in fractured rock at Stripa, Stripa Project Technical Report, 92-01, Swedish Nucl. Fuel and Waste Manage. Co., Stockholm.
- Hodgkinson, D. P., and Maul, P. R.** 1988. 1D-Modelling of Radionuclide Migration Through

- Permeable and Fractured Rock for Arbitrary Length Decay Chains Using Numerical Inversion of Laplace Transforms, *Ann. Nucl. Energy*, 15, 175-189.
- Jakob, A.** 1997. Modelling Solute Transport Using the Double Porous Medium Approach, in *Modelling in Aquatic Chemistry*, edited by I. Grenthe and I. Puigdomenech, OECD Nuclear Energy Agency, Paris, p. 525-576.
- Jakob, A., and Hadermann, J.** 1994. INTRAVAL Finnsjön Test - Modelling Results for some Tracer Experiments, PSI Report, 94-12, Würenlingen and Villigen.
- Jakob, A., and Heer, W.** 1998. Blind-Predictions of the Task 4E Tracer Migration Experiments at the TRUE-1 Site, PSI Technical Report, TM-44-98-03, Würenlingen and Villigen.
- Jakob, A., and Heer, W.** 1999. Blind-Predictions of the Äspö STT2 Tracer Test, PSI Technical Report, TM-44-99-03, Würenlingen and Villigen.
- Klos, R. A., and Barten, W.** 1995. *Description of an Output Option of PICNIC for TAME*, PSI Technical Note, AN-44-95-09, Würenlingen and Villigen.
- Kubo, R.** 1966. The Fluctuation-Dissipation Theorem, *Reports on Progress in Physics*, 29, 255-284.
- Küpper, J. A., Schwartz, F. W., and Steffler, P. M.** 1995. A comparison of fracture mixing models, 1. A transfer function approach to mass transport modeling, *J. Contam. Hydrol.*, 18, 1-32.
- Lever, D. A., and Bradbury, M. H.** 1985. Rock-Matrix Diffusion and its Implications for Radionuclide Migration, *Mineralogical Magazine*, April 1985, 245-254.
- Miller, I., and Kossik, R.** 1998. RIP, Integrated Probabilistic Simulator for Environmental Systems, Theory Manual & User's Guide (version 5.21), Golder Associates, Redmond WA, USA.
- Nagra** (National Cooperative for the Disposal of Radioactive Waste), 1994. Kristallin-I, Safety Assessment Report, Nagra Technical Report, NTB 93-22, Wettingen.
- Nagra**, 1997. Geosynthese Wellenberg 1996, Ergebnisse der Untersuchungsphasen I und II, Textband, Nagra Technical Report, NTB 96-01, Wettingen.
- National Research Council**, 1996. *Rock Fractures and Fluid Flow: Contemporary Understanding and Applications*, Natl. Acad. Press, Washington D.C.
- Neretnieks, I.** 1980. Diffusion in the Rock Matrix: An Important Factor in Radionuclide Retardation?, *J. Geophys. Res.*, 85, 4379-4397.
- Niemeyer, M. J., and Barten, W.** 1997. PICNIC-I Test Cases: Fracture Geometry Cases in Kristallin-I, PSI Technical Report, TM-44-97-05, Würenlingen and Villigen.
- Nordquist, A. W., Tsang, Y. W., Tsang, C. F., Dverstorp, B., and Andersson, J.** 1992. A variable aperture fracture network model for flow and transport in fractured rock, *Water Resour. Res.*, 28, 1703-1713.
- Nordquist, A. W., Tsang, Y. W., Tsang, C. F., Dverstorp, B., and Andersson, J.** 1996. Effects of high variance of fracture transmissivity on transport and sorption at different scales in a discrete model for fractured rocks, *J. Contam. Hydrol.*, 22, 39-66.
- Novakowski, K. S., and Bogan, J. D.** 1999. A semi-analytical model for the simulation of solute transport in a network of fractures having random orientations, *International Journal for Numerical and Analytical Methods in Geomechanics*, 23, 317-333.

- OECD Nuclear Energy Agency (NEA)**, 1992. Disposal of Radioactive Waste, Radionuclide Sorption from the Safety Evaluation Perspective, Proceedings of an NEA Workshop, October, 16-18, 1991, in Interlaken, Switzerland; (Paris, France).
- Prudnikov, A. P., Brychkov, Y. A., and Marichev, O. I.** 1992. Integrals and Series, vol. 5, Inverse Laplace Transforms, Gordon and Breach, Newark, New Jersey.
- Rasilainen, K.** 1997. Matrix Diffusion Model, In Situ Tests Using Natural Analogues, Ph. D. Thesis, Helsinki University of Technology, Finland; VTT Technical Research Centre of Finland, Espoo.
- Robinson, P. C.** 1984. Connectivity, flow and transport in network models of fractured media, Ph. D. Thesis, TP 1072, St. Catherine's College, Oxford University, Oxford, UK.
- Robinson, P. C.** 1993. Approaches to Modelling Matrix Diffusion in More Complex Geometries, QuantiSci Internal Report, IM3803-1, Henley-on-Thames, UK.
- Robinson, P. C.** 1997a. PICNIC Version 2.0, Technical Details, Nagra Unpublished Report, Wettingen.
- Robinson, P. C.** 1997b. PICNIC GUI Version 2.0, User's Guide, Nagra Unpublished Report, Wettingen.
- Robinson, P. C., and Cooper, N. S.** 1997. PICNIC Solver Version 2.0, User Guide, Nagra Unpublished Report, Wettingen.
- Robinson, P. C., and Maul, P. R.** 1991. Some Experience with the Numerical Inversion of Laplace Transforms, Math. Eng. Ind., 3, 111-131.
- Robinson, N. I., Sharp, J. M., and Kreisel, I.** 1998. Contaminant Transport in Sets of Parallel Finite Fractures with Fracture Skins, J. Contam. Hydrol., 31, 83-109.
- Schneider, J., Zuidema, P., Smith, P., Gribi, P., and Niemeyer, M.** 1996. Recent Developments in the Safety Assessment of a Repository for High-Level Radioactive Waste Sited in the Crystalline Basement of Northern Switzerland, in Proc. Int. Conf. on Deep Geological Disposal of Radioactive Waste, in Winnipeg, Manitoba, Canada, 16-19 September 1996, Canadian Nuclear Society, Toronto, Ontario, Canada, p. 8-109 - 8-118.
- Schneider, J., Zuidema, P., Smith, P. A., Gribi, P., Hugli, M., and Niemeyer, M. J.** 1998. Novel and practicable approach to modelling radionuclide transport through heterogeneous geological media, in Scientific Basis for Nuclear Waste Management XXI (MRS'97), MRS Symposium in Davos, Switzerland, 28. September - 3. October 1997, edited by I. G. McKinley and C. McCombie, Symposium Proceedings Volume 506, Materials Research Society, Warrendale, Pennsylvania, p. 821-828.
- Shuttle, D. A., and Ahlstrom, E.** 1999. PAWorks/PICNIC Cross Verification, Report (prepared for JNC, Tokai Japan), Golder Associates, Redmont WA, USA.
- Shuttle, D. A., and Eiben, Th.** 1998. Verification Plan: PAWorks 1.5 including PAWorks/LTG Version 1.08, Internal Report, Golder Associates, Redmont WA, USA.
- Smith, P. A.** 1991. The Role of the Geosphere as a Barrier to Radionuclide Migration, PSI Technical Report, TM-41-91-36, Würenlingen and Villigen.
- Smith, P. A., Gautschi, A., Vomvoris, S., Zuidema, P., and Mazurek, M.** 1997. The Development of Safety Assessment Model of the Geosphere for a Repository Sited in the Crystalline Basement of Northern Switzerland, J. Contam. Hydrol., 26, 309-324.

- Smith, P. A., and Robinson, P. C.** 1995. Transport Code for NAGRA Safety Assessments: A Proposal to Develop a Code to Handle Geosphere Heterogeneity over a Range of Scales, QuantiSci Internal Report, IM4286, Henley-on-Thames, UK.
- Steeffel, C. I., and Yabusaki, S. B.** 1996. OS3D/GIMRT, Software for Multicomponent - Multidimensional Reactive Transport: User's Manual and Programmer's Guide. PNL-11166, Pacific Northwest National Laboratory, Richland, WA.
- Stenhouse, M. J.** 1995. Sorption Databases for Crystalline, Marl and Bentonite for Performance Assessment, Nagra Technical Report, NTB 93-06, Wettingen.
- Sudicky, E. A.** 1989. The Laplace Transform Galerkin Technique: A Time-Continuous Finite-Element Theory and Application to Mass Transport in Groundwater, *Water Resour. Res.*, 18, 1634-1642.
- Sudicky, E. A.** 1990. The Laplace Transform Galerkin Technique for Efficient Time-Continuous Solution of Solute Transport in Double-Porosity Media, *Geoderma*, 46, 209-232.
- Sudicky, E. A., and Frind, E. O.** 1984. Contaminant Transport in Fractured Porous Media: Analytical Solution for a Two-Member Decay Chain in a Single Fracture, *Water Resour. Res.*, 20, 1021-1029; and Comment Reply, *Water Resour. Res.*, 20, 1323-1324; on Comment from Davis, G. B., and Johnston, C. D., *Water Resour. Res.*, 20, 1321-1322.
- Sudicky, E. A., and McLaren, R. G.** 1992. The Laplace transform Galerkin technique for large-scale simulation of mass transport in discretely fractured porous formations, *Water Resour. Res.*, 28, 499-514.
- Talbot, A.** 1979. The accurate numerical inversion of Laplace transforms, *J. Inst. Maths Applics*, 23, 97-120.
- Tang, D. H., Frind, E. O., and Sudicky, E. A.** 1981. Contaminant Transport in Fractured Porous Media: Analytical Solution for a Single Fracture, *Water Resour. Res.*, 17, 555-564.
- Thury, M., Gautschi, A., Mazurek, M., Müller, W. H., Naef, H., Pearson, F. J., Vomvoris, S., and Wilson, W.** 1994. Geology and Hydrogeology of the Crystalline Basement of Northern Switzerland, Nagra Technical Report, NTB 93-01, Wettingen.